Contents

REVIEW OF DIAGNOSTICS FOR NEXT GENERATION LINEAR ACCELERATORS

M. Ross, Stanford Linear Accelerator Center, Stanford, CA 94309, USA

Abstract

New electron linac designs incorporate substantial advances in critical beam parameters such as beam loading and bunch length and will require new levels of performance in stability and phase space control. In the coming decade, e- (and e+) linacs will be built for a high power linear collider (TESLA, CLIC, JLC/NLC), for fourth generation X-ray sources (TESLA FEL, LCLS, Spring 8 FEL) and for basic accelerator research and development (Orion). Each project assumes significant instrumentation performance advances across a wide front.

This review will focus on basic diagnostics for beam position and phase space monitoring. Research and development efforts aimed at high precision multi-bunch beam position monitors, transverse and longitudinal profile monitors and timing systems will be described.

1 INTRODUCTION

Next generation linacs have smaller beam sizes, increased stability and improved acceleration efficiency. They will be used for single pass free electron lasers (FEL) [1], linear colliders (LC) [2] and advanced accelerator research and development [3]. Table 1 shows the evolution of beam parameters from the SLAC Linear Collider (SLC) toward the next generation projects. Performance improvements of a factor 10 are typical. If we consider older, more conventional linacs, the relative changes in performance parameters are more impressive, often as much as a factor of 1000. In addition, there are special locations within the linac system where the beam requirements are much more stringent: for example at the LC interaction point or within the FEL undulator.

Table 1: Next generation linac parameter comparison for SLC (1985), the SLAC Linac Coherent Light Source (LCLS) and the Next Linear Collider (NLC).

	SLC	LCLS	NLC
σ_x (μm)	90	30	7
σ_y (μm)	50	30	1
σ_z (μm)	1300	30	100
peak I (A)	700	3400	1000
power density (W/m^2)	2e13	1e12	1e18

It is evident that new technology and different physical principles, such as diffraction radiation and Compton scattering, are needed in order to extend the performance of diagnostics to meet the challenge [4]. In this paper we will review ideas and tests of diagnostics for measuring electron beam position, profile (transverse and longitudinal) and loss.

2 POSITION

2.1 Purposes

High peak current linacs require accurate, well referenced, beam position monitors (BPM's) to suppress the interaction between the RF structure and the beam. In addition, equally as important, the small beam must pass close to the center of each quadrupole magnet in order to avoid emittance dilution arising from the dispersion generated from a small dipole kick. Some LC designs include two separate BPM systems in each linac. Typical requirements are shown in table 2.

Table 2: NLC Linac quadrupole BPM performance requirements

Parameter	Value	Conditions
Resolution	300 nm rms	@ 10^{10} e^- single bunch
Position Stability	1 μm	over 24 hours
Position Accuracy	200 μm	wrt the quad magnetic center
x,y dynamic range	±2 mm	
Q dynamic range (per bunch)	5×10^8 to 1.5×10^{10} e^-	

The most challenging requirement is the long-term position stability, ~ 2×10^{-4} r_0 (r_0=BPM radius). The planned resolution is ~ 6×10^{-5} r_0; both are a factor of 50 improvement over BPMs used in the SLC.

The BPM's are in continual use by an automated steering loop that keeps the beam centered in the accelerating structure and the quadrupole magnets. The model for operation of the linac assumes that a second, presumably more intrusive, automatic quadrupole beam centering procedure is implemented once per day, as required by long term BPM drifts.

BPM system requirements for the FEL are tightest in the undulator itself. For full coherent emission saturation, the beam and the light it has generated must remain superimposed throughout the undulator. Surprisingly, longitudinal considerations rather than transverse set the steering tolerances. The difference between the x-ray photon path length and the electron beam must remain less than a full x-ray wavelength (0.1 nm for LCLS) integrated over the full undulator length. Beam-based alignment is used to correct the trajectory in the absolute sense, so that it is as straight as the optical path. For LCLS, the proposed beam based alignment scheme uses trajectory data taken at very different energies, down to 1/3 of the nominal energy. Transverse overlap, also important, requires beam-x ray profile monitors and x-ray flux monitors [5].

2.2 Designs

Table 1 shows the beam power density increase between SLC, the prototype linear collider, and NLC. Roughly half of the increase is from raising the number of bunches accelerated on each linac pulse from 1 to ~100. The BPM system must be able to resolve the position of single bunches (or groups of bunches) spaced at 2.8 ns. A proposed design for a multi-bunch BPM [6] uses a heterodyne receiver, tuned near the peak response frequency of the pickup buttons, followed by broadband digitizer electronics. Calibration is done using both a local oscillator tone generator and the single bunch impulse response. Design challenges include deconvolving the multi-bunch signal and reducing the cost of the broadband digitiser.

3 TRANSVERSE PROFILE

3.1 Operational considerations

For both an LC and an FEL, the beam size is a critical operational parameter. The luminosity L of an LC is:

$$L = \frac{P_B}{E_{CM}} \times \frac{N_e}{4\pi\sigma_x^*\sigma_y^*} \times H_D$$

where P_b is the beam power, E_{cm} is the center of mass energy, N_e is the number of particles in a single bunch, $\sigma_{x,y}^*$ is the beam size at the interaction point and H_D is the enhancement from the inter-bunch focusing effect. In practice, once the machine is built, the beam size is controlled more effectively than the other parameters. Since there is no transverse equilibrium condition in a linac, $\sigma_{x,y}^*$ is determined by the beam source and the sum (or product) of dilutions in the acceleration and delivery system. The primary function of the transverse profile monitor is as a predictor of luminosity. Second, if implemented in groups along the linac length, they can be used to determine sources of emittance dilution.

Profile monitors fall into two categories: 1) particle density samplers (e.g wire scanners) and 2) optical devices (imagers of phosphorescence, transition radiation or synchrotron radiation). In the next section we will examine examples of each of these.

A predictor of luminosity, the absolute measurement produced by the monitor is extremely important. However, given the sparse distribution of profile monitors it is difficult to verify their performance. In contrast, the ubiquitous BPM's can be used to check each other and can be compared with the expected beam motion from magnetic field changes. Techniques for verifying profile monitor performance include 1) redundancy, 2) using the centroid motion as a BPM, 3) combining monitors of different technologies and 4) use of flexible beam optics for producing a variety of beam conditions.

A good example of the implementation of these checks can be seen at the Accelerator Test Facility at KEK (ATF) [7, 8]. The primary purpose of the ATF is to test the generation of beams for an LC. As such, it produces 1.3 GeV, 20 bunch, damped electron beams with emittance $\varepsilon_{x,y}$ = 2 x 0.02 nm (1 nC), some of the smallest beams ever produced. The ATF beam is extracted from its damping ring and delivered to a transport that includes a diagnostic system. A sequence of five wire scanners is used for measuring $\varepsilon_{x,y}$.

In principle, only three independent measurements of beam size are required to determine the volume of beam phase space in a given direction (σ_x ,$\sigma_{x'}$) and its correlation($\sigma_{xx'}$). Each measurement must be done with a different rotation of beam phase space. Typically the rotation is naturally given by the spacing of a group of monitors or is directly implemented for a single monitor by changing upstream focus magnets. In practice, the quantity

$$\beta_{mag}\varepsilon = \frac{1}{2}\left[\beta\tilde{\gamma} - 2\alpha\tilde{\alpha} + \gamma\tilde{\beta}\right]\varepsilon,$$

where β_{mag} is an indicator of beam to lattice mismatch and the '~' indicates the measured optical functions, is both a more useful approximation of the eventual beam size following filamentation in the linac and a more accurately and simply measured quantity[9]. For a perfectly beta-matched beam, $\beta_{mag} = 1$.

The fully filamented emittance, $\beta_{mag}\varepsilon$, can be estimated from the measured beam size matrix [10] and the design optics,

$$\sigma = \begin{bmatrix} \sigma_{11} & \sigma_{12} \\ \sigma_{21} & \sigma_{22} \end{bmatrix} \text{ and } A = \frac{1}{\sqrt{\beta}}\begin{bmatrix} \beta & 0 \\ -\alpha & 1 \end{bmatrix}$$

(the phase space rotation between each of the scans must be well known) using

$$\hat{\sigma} = A^{-1}\sigma\left(A^{-1}\right)^T,$$

then $\beta_{mag}\varepsilon = \frac{1}{2}Tr(\hat{\sigma})$. In the presence of errors, the estimated emittance ($\varepsilon = \sqrt{\det(\sigma)}$) can be imaginary, but $\beta_{mag}\varepsilon$ is always positive.

Both an LC and an FEL include phase space manipulation systems for longitudinal compression. The compressor optics are usually quite complex and require high quality, tight tolerance magnets. Accurate phase space monitors are required before and after the bunch compressor.

3.2 *Designs - Laser based scanners*

Laser based scanners will be required for the LC due to the very high beam power density [11], well beyond the failure threshold of any wire material. Recently, a new type of laser based scanner, built at ATF / KEK, [12] has produced results and can be added to the two types tested at SLAC [13][14]. The device, shown in figure 1, perhaps best suited for rings or CW linacs, uses a transversely mounted resonant Fabry-Perot optical resonant cavity focused so that a very fine laser waist is produced at its center. In this case, the Q of the cavity amplifies the incoming CW laser power by a factor of 300. Compton scattered photons are detected following a bending magnet.

3.3 *Designs - Optical Transition Radiation Profile Monitors*

Transition radiation tests of both a high resolution optical monitor [15] and diffraction or edge radiation have been done in the ATF extraction line. Figure 3 shows the 2 μm resolution optical transition radiation monitor. Backward transition radiation, emerging at the angle of specular reflection, is easiest to image since the microscope objective can be located quite close to the target. The monitor shown in figure 3 has a optical working distance of 35 mm. Tests done at ATF with a $\sigma_{x,y}$=20 μm x 12 μm, 1 nC bunch showed target surface damage after a few hundred pulses at 1 Hz. Forward radiation is collinear with the beam and presumably less affected by surface defects. Unfortunately, since a mirror is required to deflect the transition radiation away from the beam path, achieving very small working distances will be difficult.

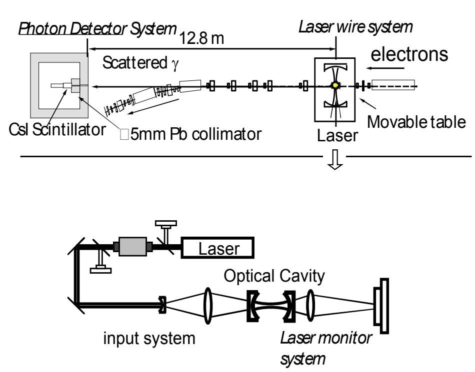

Figure 1: ATF CW laser-based profile monitor schematic.

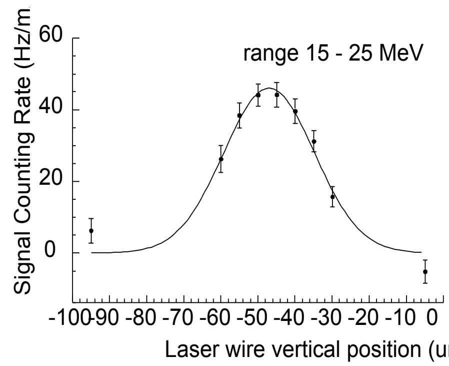

Figure 2: ATF resonant optical cavity beam size scan.

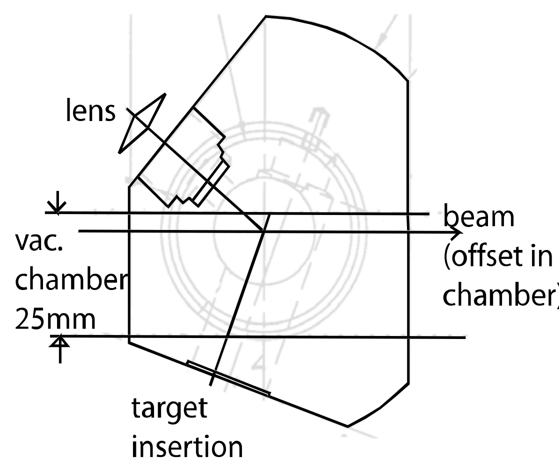

Figure 3: High-resolution optical transition radiation monitor tested at ATF/KEK. The monitor is displaced when the target is inserted in order to bring the beam close to the lens.

4 LONGITUDINAL PROFILE

4.1 *Challenge*

Most LC and FEL designs include one or more stages of bunch length compression, where the bunch is rotated in longitudinal phase space, exchanging energy spread for bunch length. In the LCLS FEL design, each stage is followed by a linac section, which reduces the fractional energy spread. An aggressive bunch compression scheme, shown in figure 4, involves generating a strong correlation between E and z with offset phase RF and using a sequence bend magnets or chicane to provide different path lengths for the head and tail particles. The scheme relies on careful cancellation between the longitudinal beam wakefield and the slope of the S-band RF. Because the beam is far from the RF crest in the section of linac where the correlation is generated, the pulse to pulse phase stability and beam loading stability tolerances are extreme: 0.1 degrees S-band for ~ 35 klystrons and 0.2% beam intensity at 1 nC.

The z distributions shown in figure 4 illustrate the challenge of measuring the bunch length. It is clear that the two traditional methods of bunch length monitoring, the streak camera and the inverse transform of the emitted radiation do not have the required resolution. The best streak cameras have resolution approaching 0.3 fs, ~100 μm, about 6 times the effective σ_z of LCLS.

Coherent radiation on the other hand is expected to be a significant source of emittance dilution at a short wavelength FEL. There will be ample opportunity to study this relatively new beam diagnostic tool. However, since coherent radiation monitors provide only radiated power spectrum information, without phase, they will not yield shape information for the highly asymmetric bunches with close to 10 μm detail.

4.2 Design - LCLS Bunch Length Monitor

The solution adopted for LCLS is an old idea [16] that relies on a transverse deflecting TM_{11} disk loaded waveguide structure [17]. The design parameters of the LCLS bunch length monitor are shown in Table 3 and the scheme is shown in Figure 5. The S-band TM_{11} deflecting field is used to tilt the beam, introducing a $y - z$ correlation. The phase of the deflection is offset slightly so that the centroid of the beam receives a small kick directing it onto a downstream screen. This allows operation of the monitor in 'parasitic' mode, so that only those machine pulses during which the deflection RF is on are intercepted by the screen and all other beam pulses proceed to the undulator downstream. By alternating the sign of the $y - z$ correlation, incoming correlations, such as those generated by wakefields, can be checked and corrected for.

Table 3: LCLS Bunch length monitor parameters for the SLAC S-band 8 foot TM_{11} deflecting structure.

RF deflector voltage	20 MV
Peak input power	25 MW
RF deflector phase (crest at 90°)	3.3 deg
Nominal beam size	80 μm
Beam size with deflector on (two-phase mean)	272 μm
Beam energy at deflector	5.4 GeV
RMS bunch length	24 μm

The bunch length is given by a function of the accelerator properties, the structure gradient and the screen measurements:

$$\sigma_z = \frac{\lambda_{rf}}{2\pi} \frac{\sqrt{E_d E_s}}{\left| eV_0 \sin\Delta\psi \cos\varphi \right|} \sqrt{\frac{\left(\sigma_y^2 - \sigma_{y0}^2\right)}{\beta_d \beta_s}}$$

where λ_{rf} is the RF wavelength, $E_{d,s}$ is the beam energy at the deflector and screen, $\Delta\psi$ is the betatron phase advance between the deflector and the screen, φ is the phase offset of the RF (≡0 at the zero crossing), σ_y is the measured beam size on the screen, σ_{y0} is the beam size without the y-z correlation and $\beta_{d,s}$ are the beta functions at the screen and deflector.

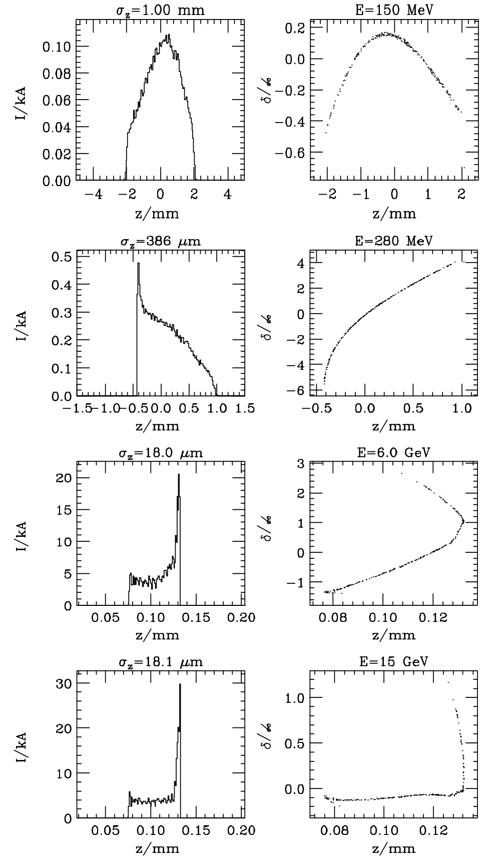

Figure 4: Evolution of longitudinal phase space in the LCLS. The plots show the z distribution and the E – z correlation following (from top to bottom): a) the gun capture section, b) the first compressor section, c) the second compressor and d) at the end of the linac.

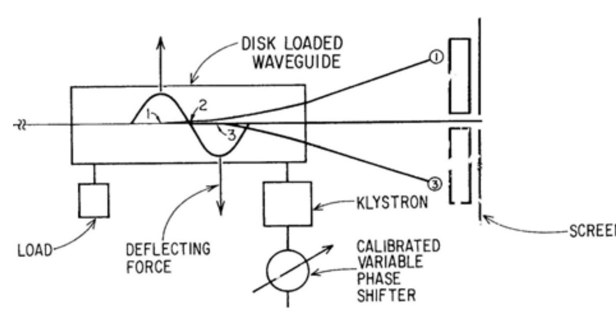

Figure 5: Schematic of bunch length monitor using RF transverse deflecting structure.

4.3 Beam phase monitoring

Both an LC and an FEL use linac structures far from the peak gradient in order to take advantage of the derivative of the gradient. Roughly 1/3 of the LCLS linac is operated 45 degrees from crest. The tolerance for phasing the bunches with respect to the RF is reduced by a factor of 10 from earlier linacs. In addition, next generation linac systems have non-isochronous systems between accelerating structures, as at KEK [18, 19] and TJNAF.

At an LC, the timing system is coupled with a beam phase monitoring so that the timing system requirements are defined only for the production of a pilot beam. The beam phase detection system then locks onto the difference between the beam and RF phase closes the loop. The two innovative components are the timing distribution system, with a tolerance of 1 degree X-band (0.2 ps) over time scales of 1 minute throughout the 15 km typical distribution length, [20] and the beam phase system.

REFERENCES

[1] J. Arthur et.al., LINAC Coherent Light Source Design Study Report, SLAC-R-0521, 1998.
[2] A. Wagner et.al., TESLA: the Superconducting Electron Positron Linear Collider with an Integrated X-Ray Laser Laboratory, Technical Design Report, DESY, 2001. http://tesla.desy.de/new_pages/TDR_CD/start.html
[3] Proceedings of the 9th Advanced Accelerator Concepts Workshop, Santa Fe, NM, 2000 (AIP Proceedings to be published). http://www-project.slac.stanford.edu/orion /Presentations/orion%20aac.pdf
[4] M. Ross, 'Linear Collider Diagnostics', Presented at the 9th Beam Instrumentation Workshop, Cambridge MA, 2000, AIP Conference Proceedings 546, 147:163. (SLAC –PUB-8437).
[5] E. Gluskin, et.al., 'Predicted Performance of the LCLS X-Ray Diagnostics', http://www-ssrl.slac.stanford.edu/lcls/technotes/LCLS-TN-00-13.pdf
[6] S. Anderson, et.al., 'Design of a Multi-bunch BPM for the Next Linear Collider', these proceedings.
[7] H. Hayano, ' Wire Scanners for Small Emittance Beam Measurement in ATF', presented at the 20th International Linac Conference, Monterey, CA, 2000.
[8] K. Kubo, 'Recent Progress in Accelerator Test Facility at KEK', presented at the 18th International Conference on High Energy Accelerators, Tsukuba, 2001.
[9] F. Decker et.al., 'Dispersion and Betatron Matching into the Linac', presented at the IEEE 1991 Particle Accelerator Conference, San Francisco, CA, 1991. (SLAC-PUB-5484)
[10] K. Brown, et.al., 'TRANSPORT/360', SLAC-R-091, 1970.
[11] C. Field, et.al., 'Wire Breakage in SLC Wire Profile Monitors' presented at the 8th Beam Instrumentation Workshop, Stanford, CA, 1998 (SLAC-PUB-7832).
[12] H. Sakai, et.al., 'Measurement of an Electron Beam Size with a Laser Wire Beam Profile Monitor', Phys.Rev.ST Accel.Beams 4:022801,2001.
[13] M. Ross, et.al., 'A High Performance Spot Size Monitor', presented at the 18th International Linac Conference, Geneva, 1996.
[14] T. Shintake, et.al., 'Experiments of Nanometer Spot Size Monitor at FFTB using Laser Interferometry', presented at 1995 IEEE Particle Accelerator Conference, Dallas, TX, 1995.
[15] M. Ross, et.al., 'A Very High Resolution Optical Transition Radiation Beam Profile Monitor', to be presented at 2001 IEEE Particle Accelerator Conference, Chicago, IL, 2001.
[16] G. A. Loew and O. H Altenmueller, 'Design and Applications of RF Separator Structures at SLAC', presented at the 5th International Conference on High-Energy Accelerators, Frascati, 1965. and O. Altenmueller, et.al., 'Investigations of Traveling Wave Separators for the Stanford 2-Mile Accelerator', Rev.Sci.Instrum. 35:438-442,1964.
[17] P. Krejcik, et. al., 'A Transverse RF Deflecting Structure for Bunch Length and Phase Space Diagnostics', to be presented at 2001 IEEE Particle Accelerator Conference, Chicago, IL, 2001. and P. Emma, et.al., 'A Transverse RF Deflecting Structure for Bunch Length and Phase Space Diagnostics', LCLS-TN-00-12, http://www-ssrl.slac.stanford.edu/lcls/technotes/LCLS-TN-00-12.pdf .
[18] A. Enomoto, et.al., 'Construction Status of the KEK B 8-GeV Injector Linac', presented at 1st Asian Particle Accelerator Conference, Tsukuba, 1998.
[19]Y. Ogawa, et.al., 'New Streak Camera System for the KEK B Linac', presented at 1st Asian Particle Accelerator Conference, Tsukuba, Japan, 1998.
[20] J. Frisch, et.al., 'The RF Phase Distribution and Timing System for the NLC', presented at 20th International Linac Conference, Monterey, CA, 2000 (SLAC-PUB-8578).

Instrumentation and Diagnostics Using Schottky Signals

F. Nolden, GSI, Darmstadt, Germany

Abstract

Schottky signal measurements are a widely used tool for the determination of longitudinal and transverse dynamical properties of hadron beams in circular accelerators and storage rings [1]. When applied to coasting beams, it is possible to deduce properties as the momentum distribution. the $Q_{x,y}$ values and the average betatron amplitudes. Scientific applications have been developed in the past few years, as well, namely nuclear Schottky mass spectrometry and lifetime measurements.

Schottky signals from a coasting beam are random signals which appear at every revolution harmonic and the respective betatron sidebands. Their interpretation is more or less straightforward unless the signal is perturbed by collective effects in the case of high phase space density.

Schottky signals from bunched beams reveal the synchrotron oscillation frequency, from which the effective rf voltage seen by the beam can be deduced.

The detection devices can be broad-band or narrow-band. The frequency range is usually in the range between a few hundred kHz up to about 150 MHz. In connection with stochastic cooling, Schottky signals are used at frequencies up to 8 GHz. Narrow-band devices are needed if signal-to-noise problems arise, e.g. in the case of antiproton beams. Heavy ion beams require less effort, it is relatively easy to detect single circulating highly charged ions.

1 SCHOTTKY SPECTRA

1.1 Coasting beam current

Imagine a detector at some given location in the storage ring. The beam current at this given place is the sum of the currents from each charged particle passing by. Let us assume that the beam is composed of N particles of a single species with charge qe. These particles are characterized in the longitudinal phase plane by their revolution period T_n (which we assume to be constant). Secondly, they are ordered randomly along the ring circumference. One way to parameterize this random placement is to stop the time t_n the particle passes by the detector during the revolution $k = 0$. The beam current is the sum over all particles n:

$$I(t) = qe \sum_{n=1}^{N} \sum_{k=-\infty}^{\infty} \delta(t - t_n - kT_n) \qquad (1)$$

The frequency spectrum, i.e. the Fourier transform of this current is an infinite train of delta functions, as well,

$$\tilde{I}(\Omega) = qe \sum_{n=1}^{N} \omega_n \sum_{k=-\infty}^{\infty} \delta(\Omega - k\omega_n) \exp(-i\Omega t_n) \qquad (2)$$

i.e. the current spectrum consists of peaks at each harmonic of the revolution frequency $\omega_n = 2\pi/T_n$ with a random phase. The mathematics of this Fourier correspondence can be found in most textbooks on signal theory. Because of the random phase, the expectation value of $\tilde{I}(\Omega)$ vanishes. However, the cancellation of the phases is never complete due to the finite number of particles in the beam. Therefore the power spectrum of the random process $I(t)$ can be detected, as we shall see. Before doing so, let us look at the distribution of the frequencies ω_n. The variation of the revolution frequencies around their mean value ω_0 is proportional the the deviation of the particle momenta p from their mean p_0:

$$\frac{\delta\omega}{\omega_0} = \eta \frac{\delta p}{p_0} \qquad (3)$$

with the frequency dispersion

$$\eta = \gamma^{-2} - \alpha_p \qquad (4)$$

Here, γ is the relativistic Lorentz factor, and α_p is the momentum compaction factor of the ring lattice. α_p is related to the transition γ_t by $\alpha_p = \gamma_t^{-2}$. Once η is known, it is possible to infer from the beam current frequency spectrum the momentum width of the beam. It is sufficient to measure the spectrum at one given harmonic. This is one of the main applications of Schottky diagnosis. If the momentum distribution is bounded by a momentum deviation $\pm\delta p_{\max}$, then there is a harmonic $k_{\max}$ above which the correspondence $\Omega(\delta p)$ ceases to be unique, i.e. where the Schottky harmonics begin to overlap:

$$k_{\max} > \frac{1}{2} \left| \eta \frac{\delta p_{\max}}{p_0} \right|^{-1} \qquad (5)$$

The width of the frequency distribution is proportional to the harmonic number.

Signal detectors are linear devices which respond to the beam with a voltage

$$u(t) = \frac{qeZ_L}{2} \sum_{n=1}^{N} \omega_n \sum_{k=-\infty}^{\infty} S(x_{kn}, y_{kn}, t) * \delta(t - t_n - kT_n) \qquad (6)$$

Here, Z_L the line impedance. S is called the sensitivity of the detector. One should note that the position (x, y) changes from revolution to revolution if the particle performs betatron oscillations around the closed orbit. The signal from a coasting depends on the variation of S over the range of betatron amplitudes. The position of the nth particle at the kth revolution is given by its coordinates x and y. $*$ denotes a convolution in the time domain, i.e. $f(t)*g(t) = \int d\tau\ f(\tau)\, g(t-\tau)$. The form of the pulse train $S(\ldots, t)$ determines the frequency response of the device. Let us first look at the signal from a longitudinal pick-up.

1.2 Longitudinal Signal of a Coasting Beam

We assume that the signal is independent of position, because the sensitivity is constant over the range of betatron amplitudes at the detector: $S(x, y, \ldots) \approx S_0$. Then the signal spectrum is directly proportional to the current spectrum. Let the momentum distribution $\Psi\,(\delta p/p_0)$ be normalized to N. In the case of non-overlapping Schottky bands at the frequency $\Omega(\delta p) = k\omega_0(1 + \eta\delta p/p_0)$ the power spectrum is

$$P(\Omega) = \frac{(qef_0)^2}{4Z_L} \left|\tilde{S}_0(\Omega)\right|^2 \frac{\Psi\,(\delta p/p_0)}{|\eta k|} \tag{7}$$

i.e. the spectrum has the following properties:

- The total power at each harmonic is proportional to N. Once the sensitivity at Ω has been gauged, e.g. by comparison with a beam current transformer, the total power is therefore a good measure for the beam current. This is particularly helpful at low intensity, if the current transformer response is well below the noise limit.
- It is proportional to the square of the charge state. Highly charged heavy ions are therefore easy to be seen in a Schottky spectrum.
- The width of the signal is proportional to the harmonic number k, the power density is inversersely proportional to the absolute value of both k and η.

Fig. 1 shows the longitudinal Schottky spectrum of a hypothetical Gaussian momentum distribution with an extremely large $\eta\sigma = 2\%$, bounded at $\delta\omega_{\max}/\omega_0 = \pm 5\%$. This is an unusually broad spectrum drawn only for illustrated purposes in order to show the properties discussed above in an overview.

1.3 Transverse Signal of a Coasting Beam

Detectors for transverse signals are usually take the difference signal from a pair of opposite electrodes. The sensitivity is then approximately linear around the center of the beam pipe. For example a horizontal pick-up can be characterized by a sensitivity

$$\tilde{S}(x, y, \Omega) \approx x\ \left.\frac{\partial \tilde{S}(x, y, \Omega)}{\partial x}\right|_{x=y=0} := xS'(\Omega) \tag{8}$$

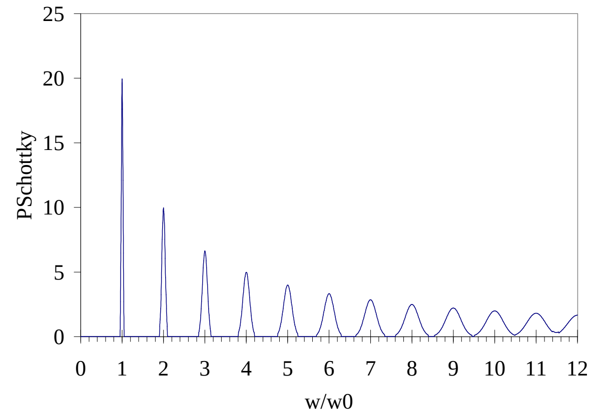

Figure 1: Hypothetical Schottky spectrum of bounded Gaussian distributed beam

Imagine a beam performing betatron oscillations around the electrical center $x = 0$ of the detector,

$$x_{kn} = A_n \sin 2\pi Q_x k + \mu_n \tag{9}$$

A_n is the betatron amplitude related to the one-particle emittance $\epsilon_{x,n}$ and the horizontal beta function β_x at the detector via $A_n = \sqrt{\epsilon_{x,n}\beta_x}$. μ_n is the random betatron phase. According to Eq. 6, the detector output changes sign in the rhythm of the betatron oscillations. The modulation produces sidebands around the revolution harmonics

$$\begin{aligned} \omega_{k,\pm} &= (k \pm Q_x)\,\omega \\ &= \omega_0\,(k \pm Q_{x0}) \left(1 + \eta\frac{\delta p}{p_0}\right) \pm Q_{x0}\xi_x \frac{\delta p}{p_0} \\ &+ O\left(\frac{\delta p}{p_0}\right)^2 \end{aligned} \tag{10}$$

If the effect of the chromaticity ξ_x can be neglected at sufficiently high harmonics $k \gg Q_{x0}\xi_x/\eta$, the power spectrum is (assuming that left and right sidebands do not overlap)

$$P(\omega_{k,\pm}) = \langle\epsilon_x\rangle\,\beta_x \frac{(qef_0)^2}{16Z_L}\,|S'(\Omega)|^2\,\frac{\Psi\,(\delta p/p_0)}{|\eta k|} \tag{11}$$

where $< \epsilon_x >$ is the mean emittance at the given momentum deviation. Therefore the measurement of transverse Schottky power spectra allows

- to infer the linear chromaticity at low harmonics,
- to infer the fractional part of the Q value,
- to deduce the mean emittance, even as a function of off-momentum, if the power spectral density is properly gauged.

1.4 Longitudinal Signal of a Bunched Beam

A bunched beam at constant energy (no acceleration or deceleration) gives rise to coherent lines which are not the subject of this paper. However, there is also a random (Schottky) contribution in the signal. A bunch exists because it is stabilized by synchrotron oscillations. These can be characterized by an amplitude and a random phase. The synchrotron oscillations have the frequency ω_s and give rise to a series of sidebands around the revolution harmonics at frequencies $k\omega + j\omega_s$. Although the synchrotron frequency becomes amplitude-dependent at large amplitudes, the small-amplitude synchrotron oscillation frequency can often be measured. It is given by

$$\omega_s = \frac{\omega_0}{\beta}\sqrt{\frac{\eta h q e V}{2\pi m \gamma c^2}} \tag{12}$$

The synchrotron satellites can therefore be used to determine the effective accelerating voltage V seen by the beam, including effects like transit time etc.

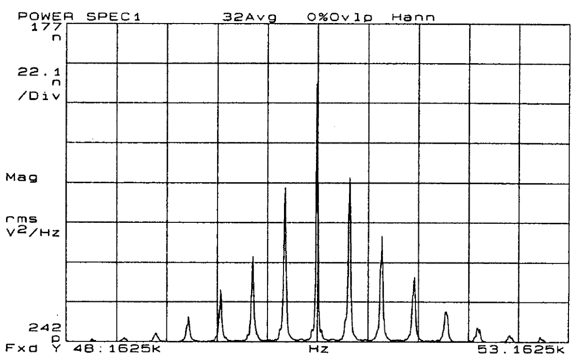

Figure 2: Bunched beam Schottky spectrum with synchrotron sidebands

2 SIGNAL SUPPRESSION

The interpretation of Schottky spectra is straightforward unless signal suppression enters into the game. Signal suppression is caused by collective effects inside the beam which effectively screen the signal from the detector. The effects are well-understood quantitatively [2] and can be analyzed by ways of a Vlasov equation formalism. In the case of the longitudinal spectrum, the screening is described by a dielectric function ϵ. it is sufficient to take Eq. 7 and perform the replacement

$$\Psi\left(\delta p/p_0\right) \mapsto \frac{\Psi\left(\delta p/p_0\right)}{\left|\epsilon(\Omega,k)\right|^2} \tag{13}$$

A detailed discussion of the screening effect can be found in [2]. It becomes significant if the beam approaches the Keil-Schnell circle, i.e if

$$\frac{qeI}{|\eta|\beta^2\gamma mc^2\left(\delta p/p_0\right)^2}\left|\frac{Z_{\|}(\Omega)}{k}\right| \approx 1 \tag{14}$$

The Keil-Schnell criterion is proportional to the beam current I, the beam impedance and inversely proportional to the square of the momentum width $\delta p/p_0$. Screening effects are often observed in machines with strong cooling and with non-relativistic beams that exhibit a large space charge impedance. A round beam of radius a in a round vacuum chamber of radius b has a purely imaginary space charge impedance

$$\mathrm{Im}\left.\frac{Z_{\|}}{k}\right|_{\text{(space charge)}} = -\frac{Z_0}{2\beta\gamma^2}\left(1+\ln\frac{b}{a}\right) \tag{15}$$

where $Z_0 = 377\Omega$ is the wave impedance of the vacuum. In screened Schottky spectra, the total power is no more proportional to N. The spectral density in the center of the distribution is reduced and peaks appear on the left and right hands of the center which can be attribution to propagating and counter-propagating acoustic plasma waves. Below transition, the left-hand wave is more pronounced, as it becomes unstable above the stability limit. It is important to be aware of these effects even if one does not see the screened 'ears' in the Schottky spectra at first sight, as the screening destroys the possibility of measuring beam intensities as well as momentum width.

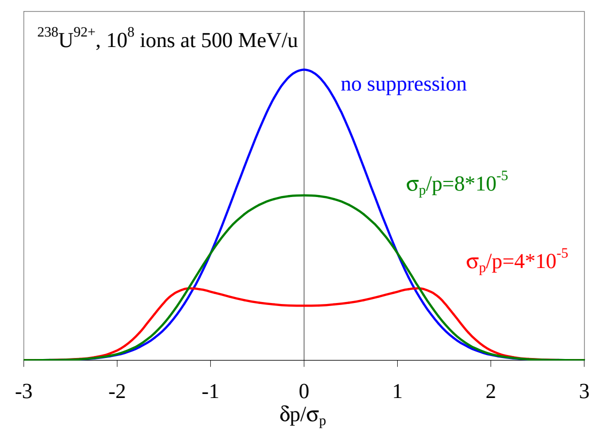

Figure 3: Calculated spectra of signal suppression due to space charge

3 DETECTORS

3.1 General considerations

Two main considerations dictate the choice and construction of a Schottky detector: bandwidth and sensitivity. Large bandwidth is desirable for all-purpose devices used not only for Schottky diagnosis but also for the detection of instabilities, the observation of coherent lines of bunched beam during acceleration or deceleration, and so on. On the other hand, high sensitivity is needed if one needs a high temporal resolution, wants to measure unstable beams, or if the product q^2N is so small that one has to cope with signal-to noise problems.

3.2 Broad-band devices

Useful broad-band devices are quarter-wave or capacitive Schottky detectors working at frequencies of up to 150 MHz. Typical harmonic numbers that occur in small rings with circumference between 100 m and 200 m are of the order of some ten. A completely different class of detector are the Schottky pick-ups used in stochastic cooling loops, which may work at frequencies up to 8 GHz. Here harmonic numbers of some 1000 come into play. The frequency curve of quarter-wave or capacitive devices is roughly sinusoidal,

$$S(\ldots, 2\pi f) \propto \sin\left(\frac{f}{f_c}\right) \tag{16}$$

The center frequency f_c for quarter-wave devices is given by

$$f_c = \frac{c}{2\,(1+\beta^{-1})\,L} \tag{17}$$

where L is the mechanical length of the pick-up plates.

3.3 Narrow-band devices

Narrow-band devices consist of high-Q cavities with critical coupling, i.e. the unloaded Q is twice as large as the Q with coupling.

3.4 Broad-band devices with lumped resonant circuits

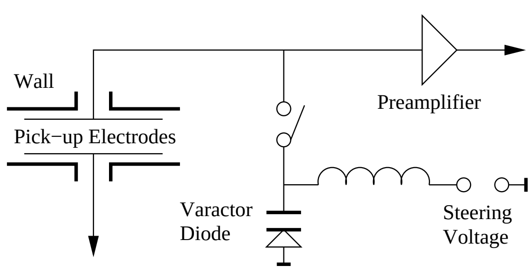

Figure 4: Broad-band pick-up with tunable exterior circuit

If the working frequency is not too high, a broad-band Schottky pick-up can be made resonant [3], if it is connected to a resonant circuit consisting of a cable and a tunable varactor diode. With such a simple circuit, the sensitivity can be enhanced by more than 6 dB. It is also possible to use the resonant cable at its second (or higher) harmonic.

3.5 Amplifiers

The signal to noise ratio is determined by the effective temperature of the pick-up and the noise number of the first preamplifier. A quantitative treatment of thermal noise problems is beyond the scope of this paper. Examples can be found, e.g in [3], [4],

4 SPECTRUM ANALYSIS

4.1 Analog Spectrum Analyzers

Analog spectrum analyzers are easy-to-use measurement devices which measure the spectral power inside a small band, the width of which is given by the resolution bandwidth (RBW). This process is repeated for N_p adjacent bands until one gets a spectrum of typically $N_p = 1000$ points. If the signal is random (as in Schottky signals), the power is not time-constant. It is effectively averaged by using a low-pass filter after the power detector with a bandwidth which is called the video bandwidth (VBW). With random signals, it makes sense to choose $VBW = R_{BW/10}$. It is useful to combine the effect of the video filtering with digital power averaging of many consecutive spectra. The measurement time T_S per spectrum is given by the Fourier limit of the RBW or the VBW, hence it is of the order $T_S \approx 2N_p/\min(RBW, VBW)$.

4.2 Digital Systems

The analog spectrum analyzers are getting replaced more and more by their digital relatives. In digital spectrum analyzers, the rf frequency band to be measured is converted into the low-frequency range using a stable reference frequency and a single sideband or image reject mixer. The signal is sampled at the sampling frequency f_s, and converted to digital. With a sampling rate of up to 10 MHz, 18 bit ADC's are nowadays available. This digital signal is Fourier analyzed. Even with the sampling rate mentioned above, real-time Fourier analysis is now available with fast digital signal processors (DSP's). Low pass-filtering (in order to avoid aliasing) and windowing in the time domain (in order to avoid spurious spectral sidelobes) are standard procedures discussed in many textbooks on digital signal analysis. If a spectral resolution Δf is required, the necessary record length is $2.56/\Delta f$. The factor 2.56 is larger than the Nyquist factor 2 because of the necessity of windowing. Note that the requirements on Δf are inversely proportional to the harmonic number because the width of Schottky spectra increases proportional to frequency. If spectral resolution is a critical issue, one should chose the highest possible revolution harmonic where signal to noise problems are still tolerable. The sampling rate f_s, on the other hand, determines the maximum usable bandwidth W that is observed simultaneously: $W = f_s/2.56$. The factor 2.56 expresses the necessity to keep the maximum band frequency away from aliasing frequencies. Spectral averaging over $N_{\rm avg}$ averages is needed because of the random nature of the Schottky signals. The estimated error of the power in a given line is simply $N_{\rm avg}^{-1/2}$. This has always to be taken into account in the quantitative analysis of digital Schottky spectra. The optimum signal to noise ratio depends on the signal to noise ratio of the rf signal behind the first preamplifier. It should never be deteriorated by unnecessary low rf levels in long cables, by low-quality IRM's, or unstable reference signals.

5 EXAMPLES

5.1 Cooling diagnosis

An important application of Schottky diagnosis is the observation of beam cooling (electron cooling, stochastic cooling, laser cooling). An instructive example is shown in figure 5. It shows vertical Schottky spectra taken during stochastic cooling of a uranium beam using a commercial Tektronix 3066 spectrum analyzer. The signal was taken directly from the stochastic cooling signal using a directional coupler.The lowest spectrum is displayed at the bottom, the time between successive curves is 80 ms. Each curve is an average of 250 non-overlapping single frames taken during 320 μs. The Fourier transform of each frame yields a spectrum of 641 frequency points in a bandwidth of 2 MHz. The sampling rate was 5 MHz with a resolution of 12 bits. As the beam was not well centered with respect to the pick-up,the longitudinal part of the spectrum is also seen. Because of the longitudinal cooling, the width decreases, but the area remains stable because there was no particle loss. The width of the vertical sidebands decreases simultaneously, of course, but the area of the vertical sidebands decreases, as well. This can be used for the diagnosis of vertical cooling. However, these curves have not been published, because the stochastic cooling loop was not opened for the measurement. The closed loop may lead to signal suppression. This could be the reason why there is a slight asymmetry in the upper spectra.

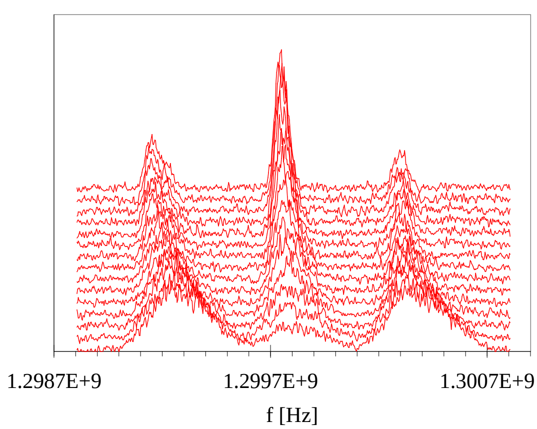

Figure 5: Waterfall diagram of vertical Schottky spectra at high harmonic taken during stochastic cooling of a uranium beam ($7 * 10^5$ fully stripped ions)

5.2 Nuclear Spectroscopy

An application to nuclear spectroscopy is displayed in figure 6. If there are different nuclear species stored in a ring like the ESR at GSI, the frequencies of the centroids are determined by their mass to charge ratio A/q:

$$\frac{\delta f}{f} = -\alpha_p \frac{\delta(A/q)}{A/q} \tag{18}$$

With electron cooled beams and good power supplies, extremely sharp Schottky spectra can be measured, which can even be used to infer nuclear masses. The figure shows a spectrum measured in a band of 300 Hz with a resonant probe as discussed in section 3.4. The spectra were taken at 3 kHz span, and 200 spectral averages were used in the off-line analysis. The time between subsequent spectra is 96 s. Shown are secondary ions produced by shooting a lead beam on a target at 800 MeV/u. The secondary ions shown in the figure were measured at 400 MeV/u. The most prominent line in the middle is due to fully stripped $^{206}\,\mathrm{Tl}^{81+}$. This ion has an isomeric state with a half life in the rest frame of 3.74 min, which is populated, as well. The half life seen in the laboratory is longer due to Lorentz time dilatation. The frequency difference seen between the two $^{206}\,\mathrm{Tl}^{81+}$ lines shows nicely how a difference in excitation energy is turned into a difference in rest mass. The third line on the right is due to the beta decay of $^{206}\,\mathrm{Tl}^{81+}$ into $^{206}\,\mathrm{Pb}^{81+}$. This is a so-called bound beta decay because the decay electron is captured in the electronic K-shell of the daughter nucleus. Time-resolved measurements as these allow to infer decay rates. The measurement also shows a small drift of the revolution frequency during the measurement. It is of the order of 10^{-6} and can be attribution to the dipole magnet power supplies or the electron cooler voltage. A small spurious line on the low-frequency part of the spectrum does not show this variation. The total number of particles in the spectrum is less than 1000. Single ions have been identified in Schottky spectra like these.

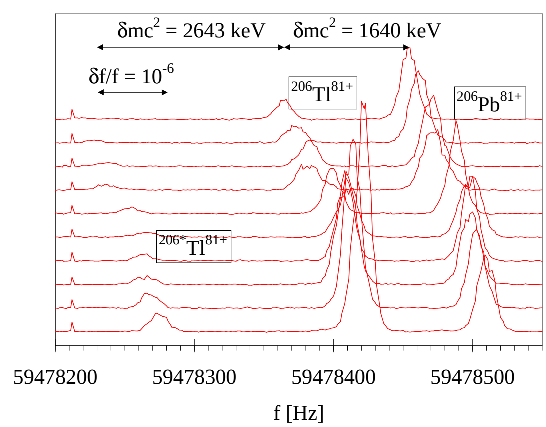

Figure 6: Spectra showing decay and decay products with three nuclear species

6 REFERENCES

[1] D. Boussard, CERN Report 95-06, 749-782

[2] S. Cocher, I. Hofmann, Part. Acc. 34, 189 (1990)

[3] U. Schaaf, PhD Thesis, GSI Report 91-22

[4] C. Gonzalez, F. Pedersen, Proc. PAC 1999, 474-476

DIAGNOSTICS AND INSTURMENTATION FOR FEL

M. E. Couprie, Service de Photons, Atomes et Molécules, Saclay, and Laboratoire d'Utilisation du Rayonnement Électromagnétique, Orsay, France

Abstract

Free Electron Laser are coherent sources of radiation based on the interaction of a relativistic electron beam in an undulator field. According to the energy of the accelerator, they presently cover a wide spectral range, from the infra-red to the VUV. FELs combine the diagnostics of typical laser systems (for the measurement of spectral and temporal characteristics, the transverse mode pattern, the polarisation) and the diagnostics of relativistic electron beams. The electron beam is characterised in order to evaluate and control the FEL performances, but also in order to measure the effect of the FEL on the electron beam. The FEL characteristics are monitored with various types of detectors, depending mainly on the spectral range. Diagnostics for Linac based Infra Red FELs and storage ring FELs in the UV-VUV will be described. Particular instrumentation, required for FEL operation, such as the optical resonator, possible diagnostics inside the undulator will also be analysed.

1 INTRODUCTION

The development of FELs followed the pioneering ideas [1] and experiment led by J. M. J. Madey in 1977 in the infra-red at Stanford on a linear accelerator [2]. The second FEL oscillation was then achieved in Orsay, on the storage ring ACO, in the visible range in 1983 [3]. Since then, a large number of simple and advanced undulators have been built and integrated into FELs. FEL facilities provide a fully coherent tuneable light in a wide spectral range for scientific applications in various domains.

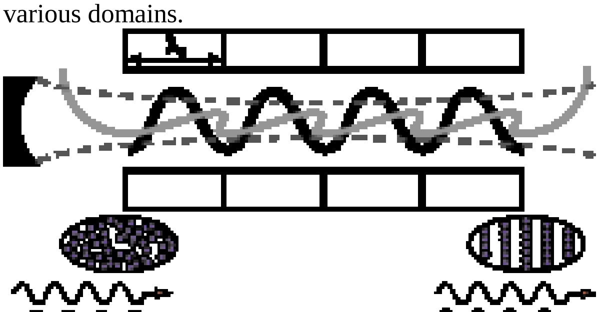

Fig.1 FEL principle

As illustrated in figure 1, Free Electron Laser (FEL) oscillation results from the interaction of an optical wave with a relativistic electron beam circulating in the periodic ppermanent magnetic field of an undulator (period λ_o and peak magnetic field B_o along the vertical direction y). The relativistic particles are transversely accelerated and emit synchrotron radiation, at the resonant wavelength λ_r and its harmonics :

$$\lambda_r = \frac{\lambda_0}{2\gamma^2}\left(1+K^2/2\right) \qquad (1)$$

with the deflection parameter K = 0.94 λ_o(cm) B_o(T) and γ the normalised energy of the electrons. The interaction between the optical wave and the electron bunch occurs along the undulator progression. Generally, an optical resonator, the length of which is adapted to the recurrence of the electron bunches, allows the radiation to be stored and the interaction to take place at each passage. The optical wave and the charged particles exchange energy, which can lead to a modulation of the electronic density at the wavelength of light (microbunching), phasing the emission and reinforcing the coherence of the produced radiation. An additional second order energy exchange between the optical wave and the electron beam leads to a non linear amplification of the stored towards saturation is reached (the gain of the system becomes equal to the cavity losses); meanwhile the spectral and temporal widths narrow. Through the system constituted by the relativistic electron beam in the undulator, coherent harmonics can be produced from an external laser source or from the FEL itself.

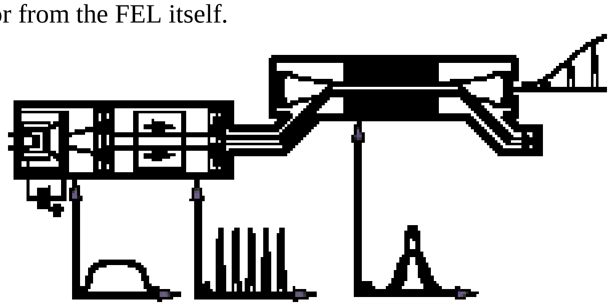

Fig. 2 : LINAC based FEL

By changing the deflection parameter K or the electron energy, one changes the resonant wavelength. As result, the FEL is intrinsically a tuneable source of radiation. The undulator period is typically a few cm long, therefore the higher the electron energy, the shorter the wavelength. FELs on low energy accelerators (MeV range) operate in the microwave and far infra red ranges, FELs on intermediate energy accelerators (50 MeV) cover the mid infra-red and ultra-violet ranges, and systems on higher energy accelerators (100 MeV-GeV) reach the UV, VUV and X-ray ranges. The gain is lower for higher energies, and optics are easily available in the infra-red. Therefore, the FEL was developed faster in the infrared (the first FEL oscillation was achieved in the UV in 1988 in ovosibirsk [4]) and the shortest wavelength was generated by coherent harmonics at 100 nm on Super-ACO in 1990 [5]. Very recently, amplification was observed in the SASE regime on the TESLA-TTF experiment at 80 nm [6].

The most popular type of accelerator used in the infra-red is the conventional RF linear accelerator (LINAC) (see fig.2). The electron beam, produced by a cathode, consists in a series of several µs pulses, emitted at a repetition rate ranging between 1 and 100 Hz. Following the passage of the beam through the RF accelerating structure, the macropulse is bunched into a few thousands of picosecond micropulses, with a spacing given by the RF field wavelength (typically 0.3-1 ns). A superconducting RF LINAC provides longer macropulses (typically 1 ms). Recent use of a photocathode produces very short micropulses (in the femtosecond range). The electron beam goes to a beam dump, and a “new” bunch interacts at each passage with the FEL. Several user facilities are currently operating in the infra-red, exploiting the high average power associated to the wide tunability for scientific applications. Average FEL power as high as a few hundred watts in the infra-red has been recently obtained at Jefferson Lab. (USA) [7] and JAERI (Japan) [8]. In order to insure a proper synchronisation between the optical pulse which reflects back and forth between the mirrors and the succesive bunches, the distance between the mirrors should be an integer of the electron bunch distance.

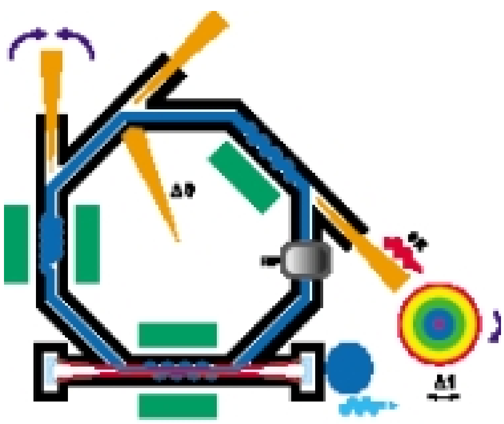

Fig. 3 : Storage ring based FEL

In the UV range, the majority of FELs are built on storage rings (see fig.3). In that case, the beam is recirculated from pass to pass and keeps memory from its interaction with the FEL. Besides, the FEL radiation can be coupled with synchrotron radiation, with which it is naturally synchronised, for pump-probe two-colour experiments [9]. In this case, the storage ring FEL (SRFEL) reproduces the pulsed MHz structure (although the filling should be limited to a few bunches in order to avoid inter-bunch longitudinal instabilities). Unlike LINACs, one may operate a large circulating current in the storage ring (few hundred mA) which implies a large circulating power (1 GW). The power of a storage ring FEL is nevertheless limited by the electron energy spread induced by the electron beam.

2 CONSTITUTING ELEMENTS OF THE FEL

2.1 Electron beam characterization

The usual electron beam characterisations both for LINACs and storage ring are used to determine the beam transverse and longitudinal dimensions, the energy spread. They are required for a careful gain evaluation. In addition, the stability of the electron bunch should be carefully checked. The usual accelerators measurements are not detailed here, but particular experimental set-up were proposed and tested with FEL accelerators. For instance, sub-picosecond electro-optic measurement of relativistic electron pulses were demonstrated on FELIX [10]. Using an ultrafast electro-optic sensor close to the electron beam, the longitudinal profile of the electric field was measured with subpicsecond time resolution and without time-reversal ambiguity. The electric field induces abirefringence in the electro-optical crystal (Zn-Se for example), which is probed by a synchronised Ti:Sapphire pulse.

2. 2.2 Undulator

The choice of the insertion device for the FEL operation provides some specific constraints. As the FEL and the electron beam should interact along the undulator, additional detectors can be installed. Besides, an optical klystron [11] is generally employed for a storage ring FEL, in order to artificially enhance the gain. The optical klystron consists of two undulators separaed by a dispersive section creating a wide wiggle of magnetic field. Its spectrum is then the result of the interference of the two undulators radiation spectra, as for the Young slits. From the depth of the modulation rate (the equivalent to the optical contrast), one can deduce the energy spread of the beam [12].

2.3 Optical cavity

Various characterisations can be performed on the mirrors of the optical resonator. The roughness, which defines the scatter losses can be measured by a picometer profilemeter developed at ESPCI (see fig. 4) and by a Zygo apparatus. Cavity losses can be measured using the Herbelin method [13], the absorption of the layers can be characterised using the photothermal deflection method [13]. Transmission can be checked with a spectrometer. Different optical techniques are used in order to measure the mirror radius of curvature, for the resonator stability.

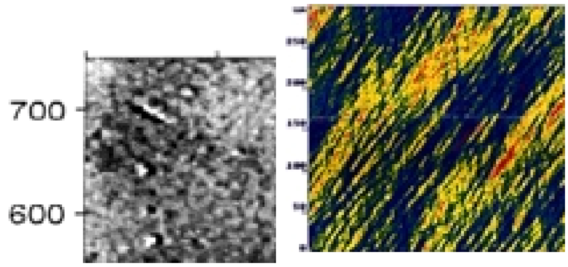

Fig. 4 : Mirror roughness measurement. On the left, 3.4 Å roughness measured with a picometer interferometer at Ecole de Physique et Chimie Industrielles (paris), on the right, 8.7 Å characterised with a ZYGO interferometer at SESO on a different sample.

3 FEL CHARACTERIZATION

3.1 Intensity measurements

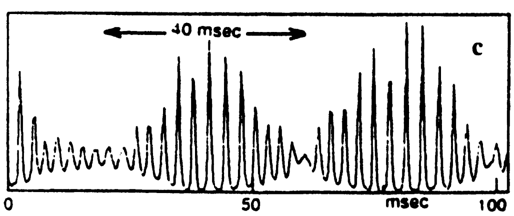

Fig. 5: Evolution of the macrotemporal structure of the Super-ACO FEL in presence of a low frequency modulation.

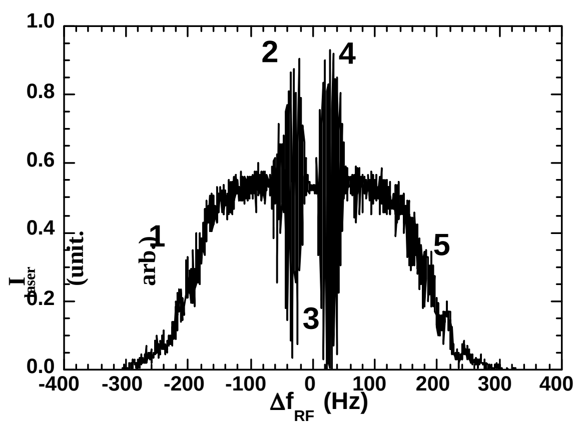

Fig.6: Super-ACO FEL intensity versus the difference between the revolution frequency of the electrons in the ring and the round trip time of the photons in the optical resonator. I = 90 mA.

The intensity measurements depend on the spectral range. In the Infra-red, Hg-Cd-Te detectors are used. In the visible down to the VUV, photomultipliers (PM) can be employed (see fig. 5). Such detectors allow to follow the behaviour of the FEL when one parameter is changed. In fig.6, a ramp is changing the tuning condition of the FEL (the synchronisation between the optical pulses bouncing in the resonator and the electron bunches stored in the ring). The signal of the PM versus the frequency changed is acquired on an ocilloscope. One can then distinguish five zones, zone three for a CW laser around perfect tuning, zones two and four where the laser is pulsed, and zone 1 and 5 where the laser is again CW.

3.2 Spectral characterisation

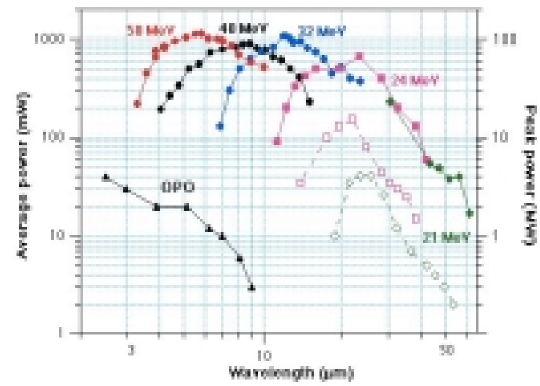

Fig. 7 : Intensity measurement of the CLIO infra-red FEL

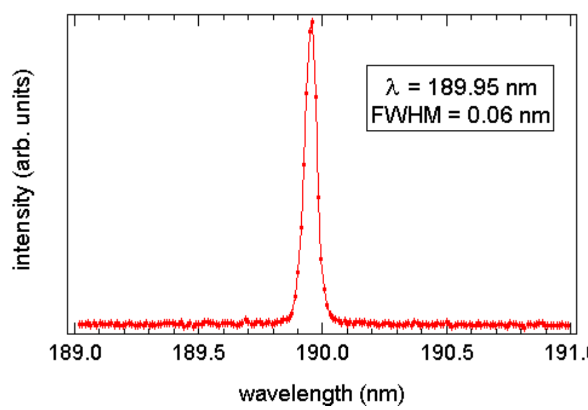

Fig. 8 : Spectral line of the ELETTRA FEL at 190 nm (the world record of the shortest wavelength in the FEL oscillator mode, 2001)

Grating monochromators are generally used for characterising the spectral features of the FELs. The light, after a slit selection, is sent to a system of gratings, which separates its spectral content. The exit light detector depends on the spectral range of the FEL source. The chosen photocathode is selected according to the spectral range. An example of CLIO tuneability in the infra-red is shown in fig. 7. From these measurements, it appears than the relative spectral range typically is in the 0.1-1% range for an Infra-red LINAC based FEL, and of 0.01 % for a storage ring FEL. A measurement of the spectral width of the ELETTRA FEL in the VUV at 190 nm is given in fig. 8. Further resolution can be achieved by using a scanning Fabry-Perot interferometer [14].

3.3 Temporal measurements

Different temporal detector are used according to the temporal width of the phenomenon to be studied. Nanosecond down to several dizains of picosecond can be measured with photomultipliers and fast photodiodes. The sensitive material of the photocathode is selected according to the spectral range. Picosecond range phenomena are characterised by stroboscopic techniques such as the dissector for phenomenon having a fixed period of reproducibility, or with a streak camera. In that case, the light pulse strikes a photocathode which yields an electronic pulse proportional to the incident intensity. In a streak camera, this pulse is then swept very quickly by two electrodes which are triggered at the frequency of the accelerator (synchroscan tube). It provides different fast sweep time scales in the ps up to the ns range. The typical resolution is of 2ps, but up to 500 fs can be reached in the single sweep mode. In addition, for double sweep streak cameras, a horizontal slow sweep shifts light pulses on the CCD (Charge Couple Device) screen versus different sweep ranges available between 100 ns and 1 s. The light intensity profile is provided by a vertical cut of the image (see fig. 9). The evolution of the longitudinal distribution in time is followed along by the horizontal time axis.

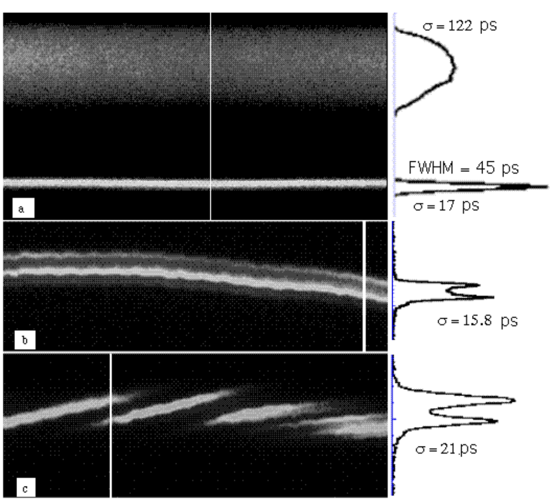

fig. 9 : Example of the Super-ACO FEL (Orsay). Cw FEL (area 3), 1a, Vertical scale = 1.7 ns, Horizontal scale = 1 ms; 1b, 300 ps, 10 ms; 1c, 300 ps, 10 ms; the current, I = 50 mA. The laser temporal distribution with their width RMS, associated to vertical slices for each image, are also plotted.

The different detuning zones of operation of the FEL can then be followed using the double sweep streak camera, as shown in Fig. 10.

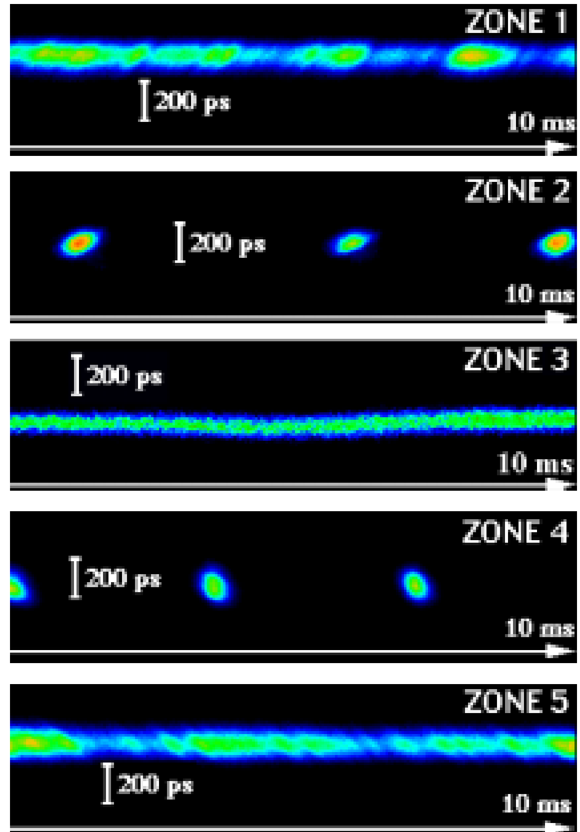

Fig. 10 : Super-ACO FEL pulse measured for different detuning with the double sweep streak camera (Hamamatsu). zone 1 : Δf_{RF} = -50 Hz, zone 2 : Δf_{RF} = -10 Hz, zone 3 : Δf_{RF} = 0 Hz, zone 4 : Δf_{RF} = +10 Hz, zone 5 : Δf_{RF} = +50 Hz

In a dissector [15], the electron beam from the photocathode is deflected onto the plane of a slit by a radio frequency voltage. For a period of deflection voltage equal or multiple of the repetition rate of the pulse, only a portion of the electron distribution goes through the slit, whose width determines principally the geometrical resolution of the device. Subsequently this part of electrons is amplified by a series of dynodes and transformed in an electric signal that is sent to a scope. A low frequency sweeping voltage superposed to the radiofrequency deflection one completes the measurement by scanning the whole electron density distribution. As a result, the characteristic time intervals observed on the scope are correlated to the real time intervals by a known fixed calibration factor. Besides, the frequency of the sweeping voltage gives the measurement time rate, which can be as high as 5 kHz. The dissector signal can then processed electronically, and the position of the FEL pulse can be measured with respect to a reference position as shown in fig. 11a, versus the detuning. Fig. 11b gives the imultaneously measured detuning curve, using the same trigger from the ramp generator.

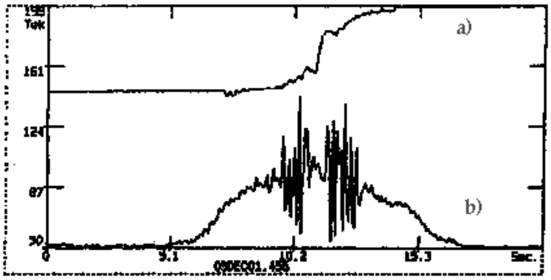

Fig.11: Super-ACO FEL position and intensity versus the difference between the revolution frequency of the electrons in the ring and the round trip time of the photons in the optical resonator. I = 90 mA.

A detuning curve can also be plotted with the double sweep streak camera by applying a proper trigger to the dual sweep tube, as shown in fig. 12.

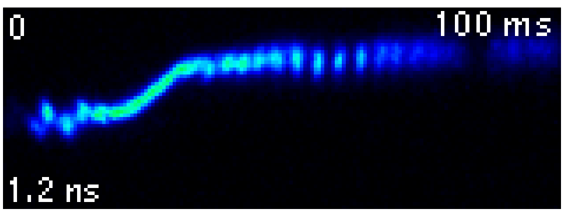

Fig. 12 : Detuning curve of the Super-ACO FEL measured with the double sweep streak camera.

Femtsosecond range measurements can be achieved with autocoreelators [16]. Rapid-scanning cross-correlation techniques probing the field birefringence in ZnTe with a 10 fs Ti:Sapphire laser have also been demonstrated [17]. Frequency resolved optical gating (FROG) measurements on the Superconducting Accelerator (SCA) mid-IR free-electron laser (FEL) have also been at Stanford [18]. FROG retrieves complete amplitude and phase content of an optical pulse.

3.4 Transverse modes measurements

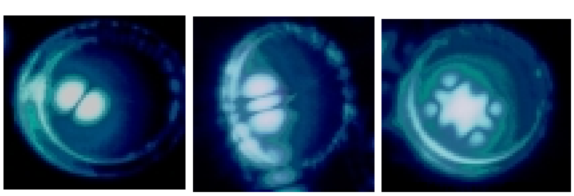

Fig. 13 : Transverse modes observed on the Super-ACO FEL, resulting from a cavity misalignement with respect to the magnetic axis of the undulator (TEM01, TEM02, TEM23).

The transverse mode pattern can be measured with a CCD camera. The profile can then be analysed. Example of different modes of the Super-ACO FEL are shown in fig. 13.

3.5 Polarisation measurements

The FEL polarization depending on the undulator type (planar, helical), it is measured with standard analysers and polarisers.

4 FEL INDUCED MODIFICATION OF THE ELECTRON BEAM

The FEL and the electron beam can be measured together. The beam stabilisation induced by the FEL in presence of saw-tooth instability is shown in fig. 14.

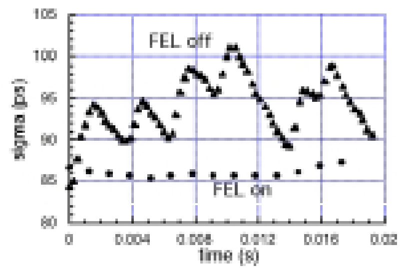

Fig. 14 : Super-ACO FEL stabilizing the electron measured with a double sweep streak camera.

5 CONCLUSION

FEL combine the diagnostics of accelerator and of conventional lasers. They could themselves even be considered as machine diagnostics since they are extremely sensitive to the stability of the accelerator.

REFERENCES

[1] J.M.J. Madey *Jou. Appl. Phys*., **42**, 1906 (1971).;
[2] J.M.J. Madey *Phys. Rev. Lett.*, **36**, 717 (1976). D.A.G. Deacon et al, *Phys. Rev. Lett.*, **38**, 892-894,1977
[3] M. Billardon et al, *Phys. Rev. Lett*. **51**, 1652 (1983)
[4] Kulipanov G.N et al *Nucl. Instr. Meth*., A**296**, 1-3 (1990)
[5] R. Prazeres et al *Europhys. Lett.*, **4** (7), 817-822 (1987);
[6] J. Rossbach Proced. EPAC, Austria, 26-30 June 2000
[7] S. Benson et al. Nucl. Inst. Meth. A 429 (1999) 27-32
[8] E.J. Minehara et al Nucl. Inst. Meth. A 429 (1999) 9-11
[9] M. Marsi et al, *Appl. Phys. Lett.* **70**(7) (1997) 895-897;
[10] X. Yan et al Phys. Rev. Lett.85(16), 2000, 3404-3407
[11] N.A.Vinokurov, A.N. Skrinsky Preprint INP77.59 Novossibirsk 1977; P. Elleaume: Optical Klystron, J. Phys. (Paris) 44, C1-353 (1983)
[12] R.J. Bakker et al *Proc. EPAC'96, S. Myers*, A. Pacheco, R.R. Pascual, Ch. Petit-Jean Genaz, J. Poole Ed. (Inst. of Phys. Publishing, Bristol and Philadelphia, (1996) 667-669
[13] D. Nutarelli et al. 20th Intern. FEL Conf 1998, G. R. Neil and S.V. Benson (Eds.) 1999 Elsevier Science B.V. II-63
[14 T. Hara et al *Nucl. Inst. Meth.* **A375** (1996) 39-45
[15] E.I. Zinine *Nucl. Instr. Meth.*, **A208**, 439-441, 1983.
[16] F. Glotin et al, Phys. Rev. Lett., **71**, 2587 (1993)
[17] G. M. H. Knippels et al Phys. Rev. Lett. 83 (8), Aug. 1999 1578-1581

REVIEW OF EMITTANCE AND STABILITY MONITORING USING SYNCHROTRON RADIATION MONITORS

K.Holldack, J.Feikes and W.B. Peatman, BESSY, Berlin, Germany

Abstract

Different techniques of emittance and stability monitoring using bend magnet and undulator radiation will be reviewed. Besides imaging methods for emittance monitoring , the problem of XBPM's used for the measurement of the centre of mass position of the undulator beams will be treated in detail. The key feature of these monitors is a careful electron optical design to take account of gap dependent changes of the shape and photon energy of the undulator beam as well as spurious signals from dipoles and high heat load. The reason for the fact that these monitors work well on low energy machines like BESSY II but often fail due in high energy machines will be demonstrated by experimental results obtained on different types of BESSY II insertion devices such as undulators, wavelength shifters, multipole wigglers and electromagnetic undulators. Experimental results of global and local orbit monitoring and a proof of principle of a XBPM-based local feedback will be shown.

1 INTRODUCTION

Experiments with Synchrotron Radiation (SR) which make use of the low emittance of the electron beam on third generation storage rings are closely related to stored beam parameters. Early predictions that orbit fluctuations of the order of 1/10 of the beam’s emittance dimensions [1] can be significant have been confirmed also at BESSY II where the opening angle of the monochromatic photon beam in insertion device beam lines is dominated by the electron beam divergence rather than by the photon beam itself. For a nominal vertical opening angle of the electron beam of 25 µrad and 20µm beam size at 1% coupling in the BESSY II high beta straight sections an orbit stability of 2.5 µm and 2 µrad is required. Hence, vertical emittance changes of 5 pmrad can already be a problem in particular for high resolution monochromators, where the source is stigmatically imaged to a slit of the order of 10 µm or less. The horizontal stability is usually a factor of 10 more relaxed due to the larger horizontal beam shape and/or divergence and due to the fact that the monochromators usually work with vertical dispersion.

In order to measure and eventually to stabilise the beam to these small values, several types of optical monitors in addition to the usual machine diagnostics have been designed and used at other facilities. Here, after a short review, experiences with optical emittance monitors and a review of high heat load photon beam position monitors (XBPM) and their present status together with results obtained on BESSY II will be presented.

2 OPTICAL SOURCE SIZE AND EMITTANCE MONITORS

2.1 Basic designs

The design parameters for the measurements of the beam cross section and divergence by means of SR can be estimated according to a theoretical work of Hoffmann and Meot [2]. Applying the formulas therein to third generation storage rings it becomes clear that a simple optical image of the beam in the visible is diffraction limited and yields only a blurred information for beam sizes less than about 100µm because of the angular aperture produced by the beam itself. In order to overcome the limit given by Fraunhofer diffraction one has to image the beam with shorter wavelengths to achieve a resolution of 10µm or less [3] or to use interference methods utilising the spatial coherence of SR to obtain the beam size indirectly [4]. For a fast direct X-ray imaging, however, the quality of the optics (slope errors), aberrations as well as the heat load stability of the optics has to be rather high to preserve the diffraction limited resolution which can be of the order of 1µm depending on the wavelength and the type of optics employed.

Several kinds of X-ray and VUV optics have been used for this purpose: Grazing incidence optics in a Kirkpatrick-Baez mirror scheme at the ALS diagnostic beamline [5], crystal based X-ray Bragg-Fresnel lenses at the ESRF [6-7]. X-ray transmission zone plates at the APS [8-9]. At BESSY, multilayer Bragg-Fresnel lenses have been tested at BESSY I and installed in the first diagnostic front end at BESSY II [10]. A monitor based on a transmission zone plate is being installed for the SLS storage ring [11]. Another type of X-ray optics, the pinhole camera , which was in operation at BESSY I from 1993 to 1999 [12] and since the first day of commissioning of BESSY II [13]. It has been successfully used at the ESRF [13] and at the APS [14] for a routine observation of the source point in a dipole and was used to determine the emittance from an undulator source [15]. At BESSY, the system was updated to a pinhole array such that a regular array of images of the dipole beam can be used to obtain the vertical divergence as well as the beam size simultaneously [10]. Presently, there are three such monitors at different source points in the BESSY II ring featuring a diffraction limited resolution of 11µm. This is close to the principle resolution limit of the pinhole camera but small enough to obtain quantitative information of the source size of usually 50µm rms on the dipole. At high energy machines the vertical photon beam divergence can be less than the angular acceptance of the pinhole and the images have to be corrected [13]. For BESSY dipoles with $1/\gamma$=0.3 mrad at 1.7 GeV this is not the case but it can be a problem trying to image a high energy undulator source with a pinhole because here the divergence is reduced by $N^{-1/2}$, where N is the number of periods.

2.2 Experiences at BESSY II

The Bragg-Fresnel Monitor as described in detail in [10] has a high nominal image resolution of 3µm and yields high quality images of the source as depicted in figure 1. Besides the image of the electron beam circular background structures arising from zero order reflection of the two lenses appear. This fact needs a sophisticated automatic image analysis to obtain correct size values. In addition, the diagnostic front end is exposed to light all the time leading to long term damage of the multilayer lenses by surface contamination due to pressure spikes (commissioning shifts) and a long term degradation of the multilayer, although it was actively cooled. After substituting the first lens, the system can be now used on request by opening a special shutter. Much better reliability despite of somewhat less resolution has been obtained using the pinhole array monitors. Vertical emittance changes of 3pmrad and position changes of 2µm can be detected using a fast image analysis of the source size. The data are logged via EPICS and together with the measured lattice parameters and the emittance as determined from the source points can be monitored every 0.3 seconds.

The general experience with these monitors is that sophisticated optical systems such as Bragg Fresnel Optics are feasible for a high resolution determination of the source size, but monitors based on the pinhole camera principle are the method of choice for a fast routine monitoring if the source size expected is not smaller than ~10µm. An example of source images using the pinhole monitor which operates at 16keV is shown in figure 2. Also shown are monochromatic maps of the radiation cone of the U49/1 monochromator at different coupling situations (2-5%) obtained using a scannable pinhole located 13 m from the middle of the undulator in the front end together with the beamline/monochromator as detector. It indicates that the global compensation of coupling leads to a small dipole source and to high brilliance of the insertion device beam in the next upstream straight section. Usually the emittance coupling is below 2% and an increase to 5% already means a loss of 30% intensity on the U49 SGM monochromator [16]. Therefore, a steady monitoring of the source point is very crucial for a stable beamline operation here but more relaxed on other systems without entrance slits and strong demagnification of the source.

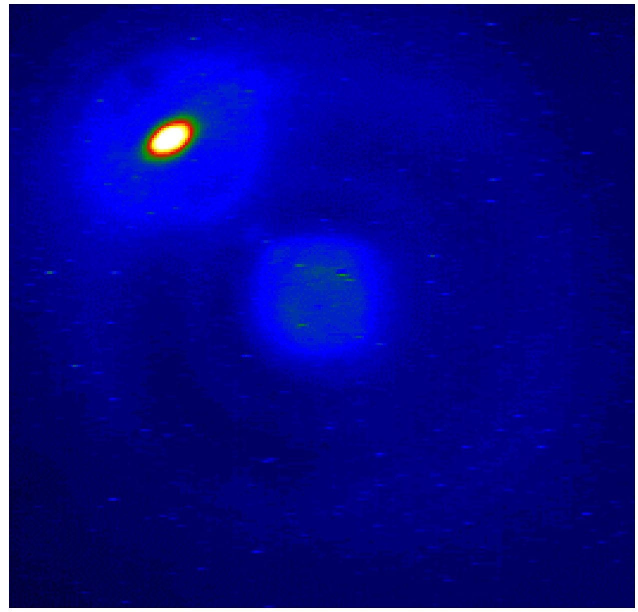

Figure 1: Source image taken with the Bragg-Fresnel-telescope before coupling was routinely compensated by skewed quadrupoles. (filed of view 1.5x1.5 mm).

For a direct emittance determination from the photon beam using undulator radiation one needs to determine the source image and electron beam divergence independently as performed in [15]. At BESSY good results were achieved using monochromatic mapping of undulator angular distributions using the scannable pinhole on the blue edge of the first harmonic. The total gaussian shapes of the monochromatic beam in this blue edge case (figure 2) can be written as follows [17]:

$$\sigma^2 = \varepsilon(\beta + \frac{a^2}{\beta}) + \frac{1}{2}\left(\sigma_r{}^2 + a^2\sigma_r{}'^2\right) \qquad (1)$$

where a is the distance to source and σ_r and σ_r' are the diffraction blurring values of size and divergence, respectively. We have to rely on the β-functions, but they are well known within a beta-beat of 10%. Moreover, it is easy to see that the most relevant term $(\beta+a^2/\beta)$ is very insensitive against absolute variations of β. The dispersion terms and additional blurring by the energy width of the beam (on higher harmonics) do not contribute here. The second term goes to zero for $\lambda\rightarrow0$. Hence, we measured the size of the spot for different wavelengths, λ, and the beam emittance can be determined from (1) in the limit $\lambda\rightarrow0$. The measurement was performed on the blue edges of the first harmonic while the undulator K-value (and thus, the wavelength) was varied. Here the spot has a clear 2D-gaussian shape and a 2D-gaussian fit routine was employed to obtain the σ-values. The influence of diffraction is very small for all photon energies but using the λ-variation one obtains:

$$\varepsilon_x=(5.3+-0.5)\mathit{nmrad}\ \mathit{and}\ \varepsilon_y=(90+-30)\mathit{pmrad}.$$

These values correspond to those determined from the electron beam images itself and to the design emittance of 6 nmrad of BESSY II. To check the sensitivity of the maps, coupling was introduced and the vertical blow up of the source images on the dipoles leads to a corresponding change of the maps as in figure 2. The maximum brightness of the undulator beam is achieved for the normal user run.

3 PHOTOEMISSION MONITORS (XBPM)

Synchrotron radiation monitors have been used for years to measure the intrinsic stability of the electron beam in addition to the rf-BPMs in the ring. [18,19]. They have even been used in fast feedback loops to stabilise the electron beam [20,21]. For third generation storage rings heat load stability and reliability are key parameters if these monitors are to achieve a feedback capability. The basic technical principle was solved using thin blades of tungsten [22] or diamond [23] mounted to actively cooled copper blocks by heat conducting insulating shims. At BESSY our staggered pair monitor (SPM) concept [12,24] is successfully used for vertical position detection of dipole, wiggler and wavelength shifter radiation. They are now being implemented into the global orbit feedback which is based on rf-BPMs.

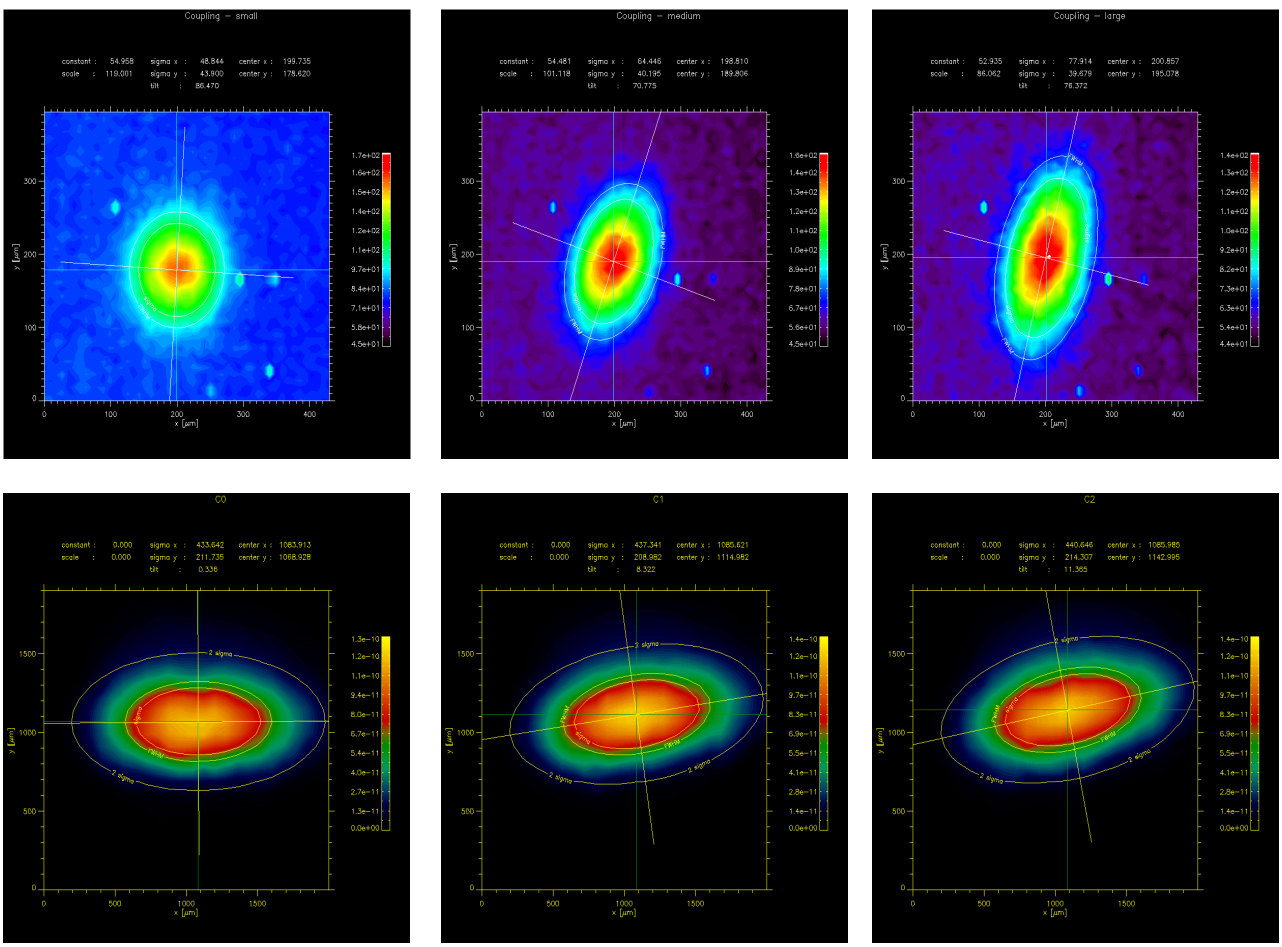

Figure 2: Comparison of the dipole source (X-ray pinhole camera) with a monochromatic map of the undulator radiation of U49/1 at the blue edge of the first harmonic at 400 eV with a bandwidth less than 10^{-4}. Emittance coupling was varied using a skewed quadrupole and is increasing from left to right. (units on the plots are in mm)

3.1 Soft X-ray undulator XBPMs

It is well known that for undulators with a variable gap the situation is quite complicated [25]. In order to optimise the resolution of the monitors, the angular and energy distribution of the undulator radiation f(ξ,ψ,E) has to be weighted by the spectral efficiency of the blade material according to:

$$I(\xi,\psi) = \int f(\xi,\psi,E)q(E)dE \qquad (2)$$

where q(E) is the total yield of photoemission [26]. The intensity distribution the blades “see” I(ξ,ψ) has then to be convoluted in space with the blade geometry (step functions) to calculate the monitor calibration curves.

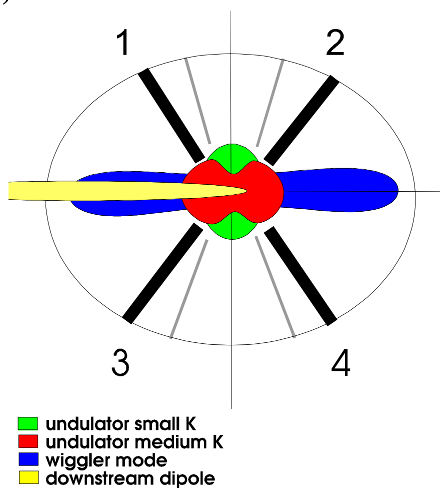

Figure 3: Polychromatic radiation pattern looking upstream into an undulator front-end. Because the dipole source is closer to the observer it is narrower than the undulator beam. (downstream blades: bold, upstream blades: light grey, vertical aperture 13 mm)

For the VUV range at BESSY this was done using the WAVE code [27]. Because q(E) has significant features in the photon energy range from 1 eV to 1keV the pattern can be significantly different from the gaussian power distribution as confirmed by polychromatic mapping of BESSY II undulators [16]. For high energy undulators with first harmonics above 1keV the photoemission cross sections decrease rapidly, and that the broad band dipole radiation covering also the low energy thresholds of the blade material dominates . This is more relaxed for the VUV range but the gap dependent shape variation (medium K) as depicted in figure 3 can lead to a smaller linear range and to xy-crosstalk if the beam is not on the axis. For large K the horizontal width of I(ξ,ψ) roughly increases with K/γ and the horizontal sensitivity to position changes decreases. At very small K-values the field of the undulator becomes weak and the signal of mainly the downstream dipole radiation is left though it is geometrically separated. Measuring the usual difference over sum asymmetry A , the sensitivity versus K is as shown in figure 4 for the case of the U180 electromagnetic insertion device [28] at 1.7 GeV.

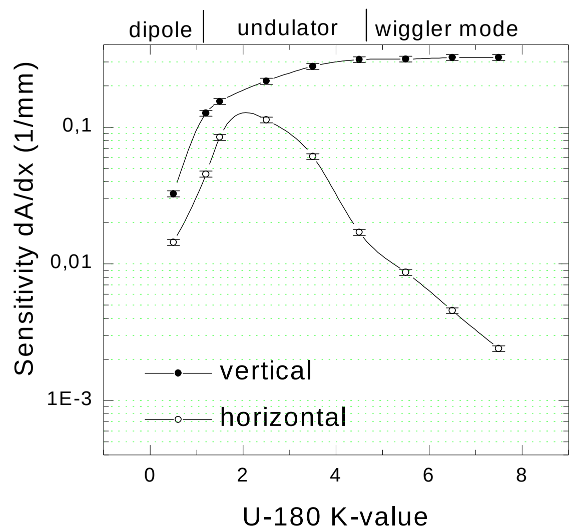

Figure 4: Sensitivity curves of a monitor XBPM 1 at 9.3 m distance from the source at U180 (PTB) of 180 mm period length (first harmonic from 5 to 100 eV).

Here, the device covers well the low energy maximum of the photoyield cross section and with increasing K the vertical sensitivity increases because it is better tuned to the central cone radiation. Below K=1 the low energy tail of the dipole radiation, which is far off the ring plane and off the central axis, causes a decrease both in vertical and in horizontal sensitivity. The dipole contamination ranges from 10% at low K to a few 0.1% at large K. Both, the low K and the high K tails can be influenced by discriminating low energy photoelectrons using a partial yield electron detection technique, but not the general fact that a horizontal sensitivity is available only over a limited K range. A very narrow band detection of direct photoelectrons lead to very sharp off axis features of I(ξ,ψ) and thus to strong xy-crosstalk of the position response.

At BESSY the 14 operating undulator XBPMs with spectrometer option allow either the detection of indirectly detected electrons after passing a bandpass filter or a direct photoemission from the blades, where a low energy threshold can be set by a positive voltage applied to the blades. The latter needs an additional electrode in the monitor on negative voltage to avoid crosstalk. The operational experience is that the second mode is much more reliable. On some insertion devices the low energy threshold is not necessary because a geometrical suppression of the dipole background is sufficient.

3.2 Operation example

With optimised performance the monitors feature a sub-micron position resolution with the constraints above. Because their bandwidth is 2kHz they have at least vertically a feedback capability also for very tiny beam position changes arising from seismic or internally

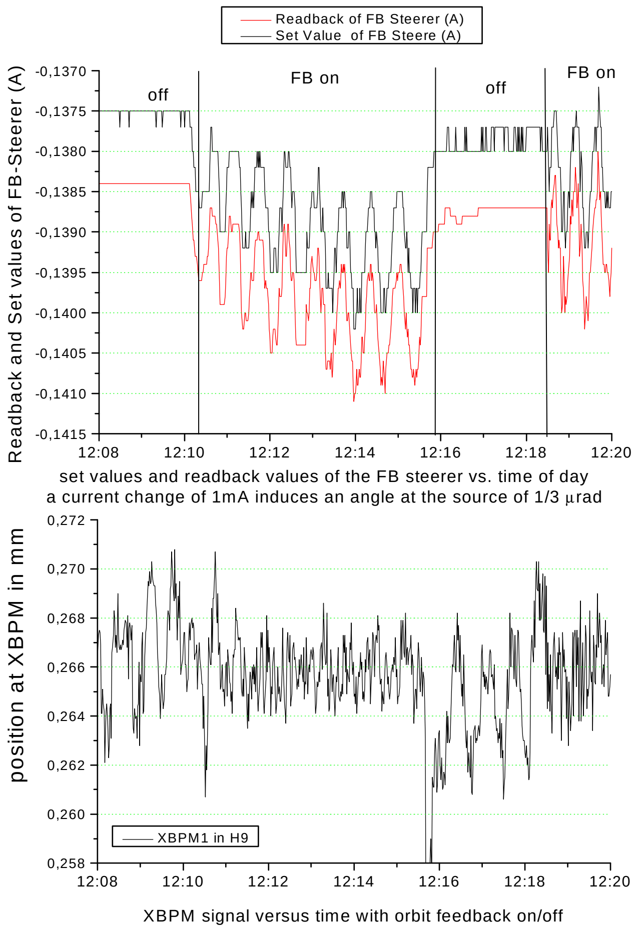

Figure 5: Local orbit feedback test at U49/1 using a closed loop realised with EPICS. The orbit was vertically corrected to the downstream XBPM 2 while the figure shows the upstream XBPM 1 signal control channel.

caused beam noise such as the 10 Hz or 50 Hz components in the beam. A proof of principle for this purpose is demonstrated below by removing the slow beam movement caused by cooling water cycles leading to peak amplitudes of 1,4 µm at the rf-BPMs and to 5 µm at XBPMs. This is residual noise not corrected by the rf-BPM based automatic global orbit feedback.

4 CONCLUSIONS

Optical beam size monitors based on X-ray pinhole camera arrays are the working horses for fast beam size and emittance determination. The BESSY solution allows them to be installed on any dipole to obtain a global online information on the source points. Imaging systems based on X-ray or VUV-optics yield somewhat better resolution and are helpful for machine studies on very low emittance operation.

While photoemission monitors are successfully in operation at dipoles and wigglers it needs more commissioning work at undulators to find tailored settings for each individual insertion device.

REFERENCES

[1] R.O.Hettel, Nucl. Instr. Meth. A 266 (1988) 155-163
[2] A.Hoffmann, F.Meot, Nucl. Instr. Meth. 203 (1982) 483-493
[3] K.Holldack, W.B.Peatman, A.Erko and T.Noll: Nucl. Instr. Meth. (A) 365 (1995) 40-45
[4] M.Katoh, T.Mitsuhasi, Proc. PAC'99, New York, 2307, 1999
[5] T.R.Renner, H.A.Padmore, R.Keller, Rev. Sci. Instrum. 67 (9), 1996, p. 1
[6] E. Tarazona et al., Rev. Sci. Instrum. 65 (6) 1994, p. 1959.
[7] Ya. Hartman et al. Rev. Sci Instrum. 66 (2), 1995, p 1978.
[8] Z. Cai, et al. AIP Conf. Proc., 417, AIP, (1997) p. 101
[9] W. Yun et al., Rev. Sci. Instrum., 70, (9), 1999, p..3537
[10] W.B.Peatman, K.Holldack, J.Synchr.Rad. 5 (1998) 639
[11] V.Schlott, Swiss Light Source, private commun.
[12] K.Holldack , W.B.Peatman, Proc. SRI'99, Stanford, CA.:AIP Conf. Proc. Vol. 521, p. 354
[13] P. Elleaume, C. Fortgang, C. Penel, E. Tarazona, J.Synchr. Rad. (1995). 2, 209-214.
[14] M. Borland et al., EPAC'98, Stockholm, Vol. 2 p. 1556 (1998)
[15] B. X. Yang, A. H. Lumpkin, PAC'99, New York City, March 1999, Vol., 3, p. 2161
[16] J. Bahrdt et al., J. Synchrotron Rad. (1998). 5, pp. 443-444
[17] H.Wiedemann in "Particle Accelerator Physics I"
[18] R.O.Hettel , IEEE Trans. Vol. NS-30, 2238 (1983)
[19] L.H.Yu,R.J.Nawrocky,J.Galayda, IEEE Trans. Nucl. Sci. NS-32, 3394 (1985)
[20] M. Bergher IEEE Trans.Nucl.Sci. Vol.NS-26,No.3,3857(1979)
[21] R.Mortazavi et al. Nucl.Instr.Meth A, 246 (1986) 389
[22] E.Johnson, T.Oversluizen, Rev.Sci.Instrm 60 (1989) 1947
[23] J.Barraza,D.Shu,T.M.Kuzay, Nucl.Instr.Meth. A347 (1994)591
[24] K.Holldack, W.B.Peatman, PROC. SRI 2000,Berlin Nucl.Instr.Meth. A, in press
[25] T. Warwick et al. Rev. Sci. Instr. 66 (2) 1995
[26] J.J.Yeh: "Atomic Calculation of Photoionization Parameters", Gordon&Breach 1993
[27] WAVE code developed by M.Scheer (BESSY)
[28] R. Klein, J. Bahrdt, D. Herzog and G. Ulm J . Synchrotron Rad. (1998). **5**, 451-452

RESULTS WITH LHC BEAM INSTRUMENTATION PROTOTYPES

C. Fischer, CERN, Geneva, Switzerland

Abstract

The beam instrumentation foreseen to provide the necessary diagnostics in the transfer lines and in the main rings of the LHC was conceived in the past years. The requirements expected from the different systems are now being closely analyzed and specified. In a few cases, tests of prototypes have already been performed, profiting from the facilities offered by existing machines.

The beam position measurement system had to be tackled first, as the pick-ups had to be integrated into the cryogenic part of the machine. Over the last two years other topics started to be experimentally investigated in order to define the best way to meet the requirements for the LHC era. Amongst these different studies are luminosity monitoring devices, various instruments for the measurement of the transverse beam distributions, the use of head-tail sampling to measure the beam chromaticity and quadrupole gradient modulation to derive the local amplitude of the lattice function.

The paper discusses the results of these tests.

1 BEAM POSITON MEASUREMENT

Along the two LHC rings about 1000 position monitors will be distributed, one per ring and per quadrupole, each with four electrodes to provide the beam excursion in both the horizontal and the vertical planes. The signal treatment is based on a Wide Band Time Normalizer as sketched in Figure 1. More details are provided in [1]. After normalization, the signal is transmitted via optical link outside the machine tunnel, where it is digitised. The Digital Acquisition Board, (DAB), treats then the data. Three prototypes of the normalizer card have been tested in the laboratory and some results on linearity and reproducibility are presented in Figures 2 and 3.

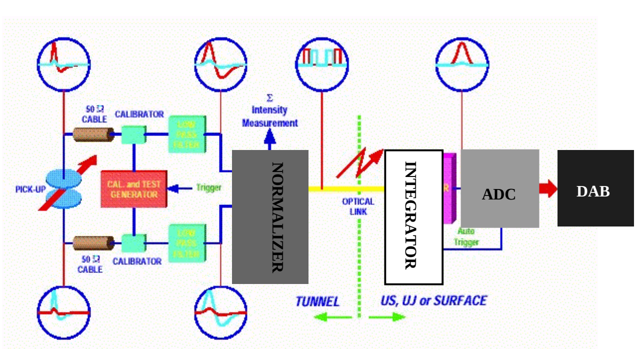

Figure 1: LHC BPM signal treatment block diagram.

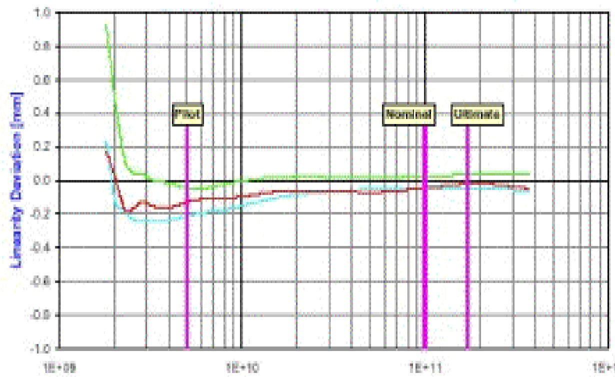

Figure 2: Normalizer card linearity vs bunch current at the LHC bunch frequency (40 MHz).

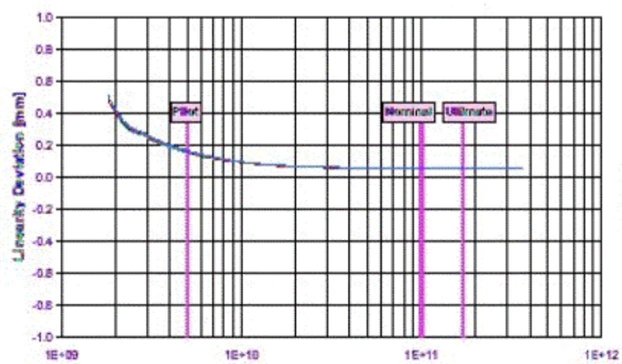

Figure 3: Signal rms deviation vs bunch current

Three bunch current levels are considered, first the pilot bunch intensity of 5. 10^9 protons which will be used during the machine setting-up, and then the nominal and an ultimate bunch current levels of respectively 1.1 10^{11} and 1.7 10^{11} protons. At the nominal bunch current and above, the linearity is good for the three samples, whereas for the pilot bunch current, deviations up to 200 µm are observed, (Figure 2). These results are quite satisfactory. The measurement rms noise is 50 µm at nominal current and remains below 200 µm for pilot bunches, (Figure 3).

A prototype position monitor equipped with the complete LHC control system was tested last year in the SPS. Comparison with the data from a standard SPS MOPOS) monitor is made in Figure 4. The agreement is quite good. The prototype monitor was also used during a test on “AC dipole “ excitation [2], and results are presented in Figure 5. It is possible to appreciate the difference between this type of maintained beam oscillations and the more classical excitation from a classical kick, which is very quickly damped.

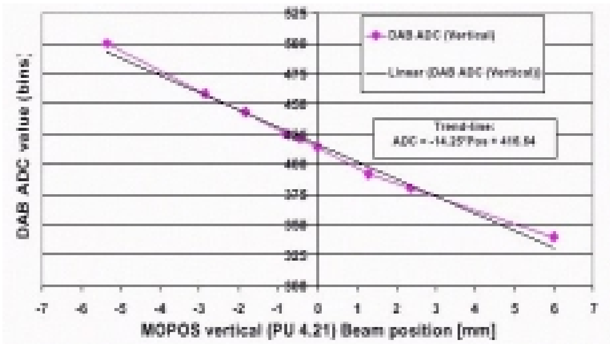

Figure 4: Comparison between LHC prototype BPM and standard MOPOS SPS monitor

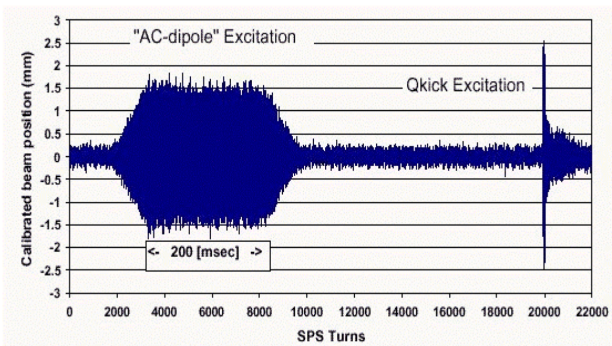

Figure 5: Detection of "AC Dipole" type excitation with the LHC prototype BPM in the SPS

2 Q' MEASUREMENT BY HEAD-TAIL SAMPLING

The method, presented in [3], uses the fact that in presence of chromaticity, the head and the tail of a bunch respond with different phase to the same excitation. Recording the periodic phasing and de-phasing between the two signals allows to determine the chromaticity within the bunch. This is illustrated in Figure 6 with respectively in a) and b) the response of the bunch head and tail, in c) the phase difference and in d) the corresponding value of the measured chromaticity, (Q'=1.7). Figure 7 compares data from this method with the one from tune measurement at different radial positions got by changing the RF frequency. The factor of 2.2 found between the two methods is being investigated.

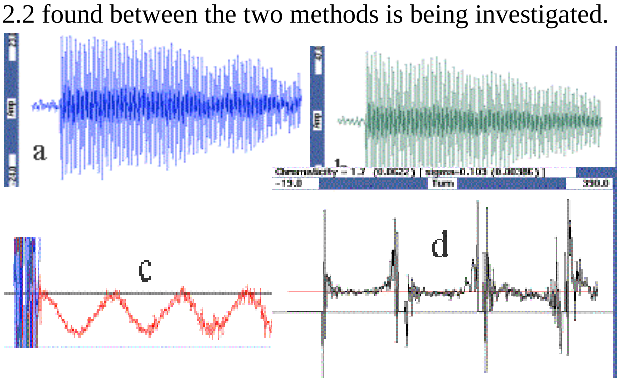

Figure 6: Q' measurement by head-tail sampling.

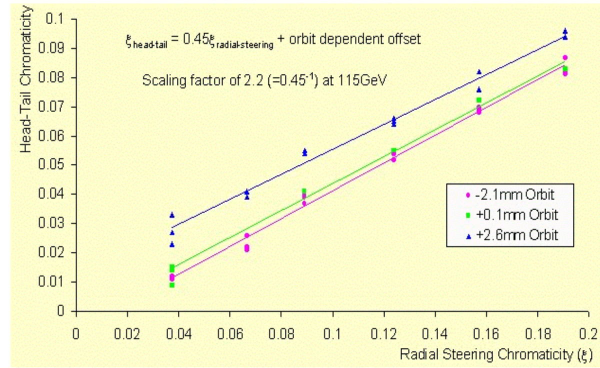

Figure7: Comparison of head-tail chromaticity measurements with radial displacement data.

The head-tail sampling method was also used to measure the chromaticity variation with radial beam position, Q". This is illustrated in Figure 8.

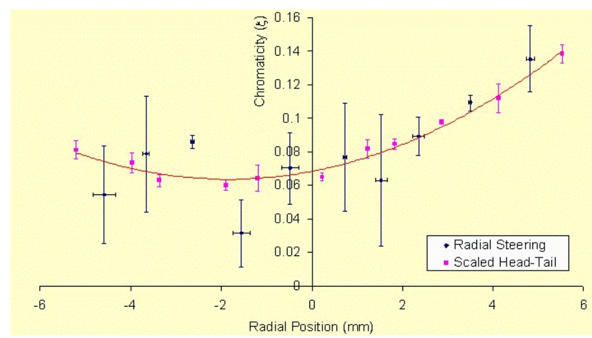

Figure 8: Chromaticity variation (Q") across the SPS aperture measured by head-tail sampling ().

3 INDIVIDUAL BUNCH MEASUREMENT SYSTEM

This system measures the population of each individual bunch, at the nominal LHC bunch frequency of 40 MHz, by looking at the maxima, (peaks), and minima, (valleys), of the analog signal from a fast current transformer [4], as shown in Figure 9. When the timing is adjusted to properly trigger measurements within the right time slots, individual bunch currents are provided from the difference between consecutive top and valley values (Figure 10)

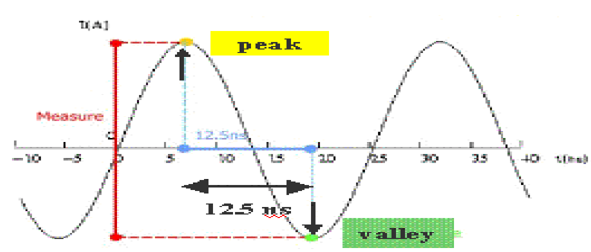

Figure 9: Principle of the Individual Bunch Measurement System sampling mode.

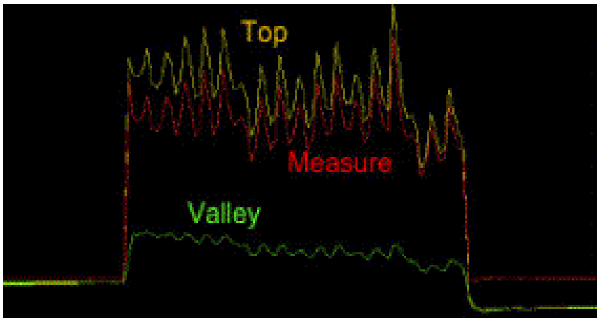

Figure 10: Current of a train of 72 bunches spaced by 25 ns, (LHC batch), on one turn, by difference between peak and valley signals.

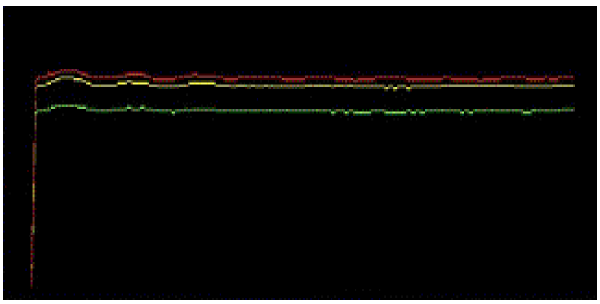

Figure 11: Turn by turn current evolution of 3 particular bunches over 20 ms, (850 turns).

Within a given bunch train, (batch), data relative to individual bunches are available for each passage and can be monitored, (Figure 11).

4 INTERACTION RATE DETECTORS

On each side of the LHC experimental insertions, the flux of secondary particles coming from the insertion point, directly related to the interaction rate, will be monitored with detectors installed within absorbers. Two types of detectors have been investigated for that purpose.

4.1 Ionization Chambers

Tests with ionization chambers were performed in the SPS experimental lines , using proton beams at 450 GeV, [5]. Some of the results are summarized in Figure 12.

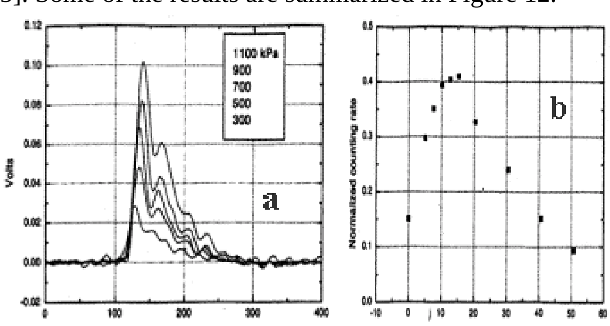

Figure 12: Ionization chamber data: a) signal response for different gas pressures; b) rate versus Fe absorber thickness.

Figure 12a exhibits the recorded pulse shape for various gas pressures. In all cases, the pulse length is of the order of 175 ns. This is significantly longer than the nominal bunch spacing of 25 ns, which, if confirmed, would not permit to sample at the bunch collision frequency of 40 MHz. The maximum shower rate is observed after an Fe absorber thickness of about 15 cm, (Figure 12b), which is in agreement with simulations.

4.2 CdTe Photoconductors

Polycrystalline CdTe photoconductors have also been tested [6]. First they were exposed to a picosecond laser source, with wavelength of 1060 nm, and their time response was studied. Figure 13.shows typical results.

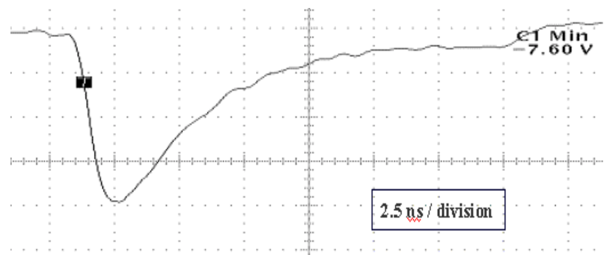

Figure 13: Time response of a CdTe photoconductor sample to a laser source at 1060 nm.

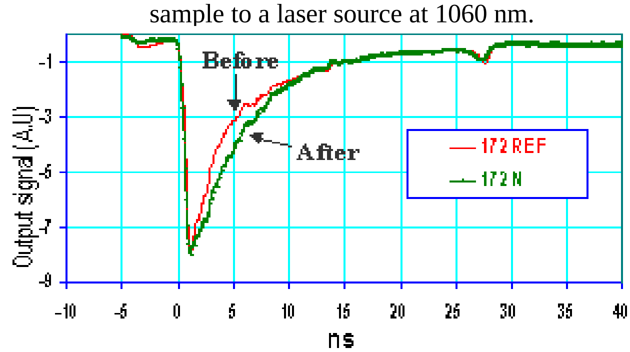

Figure 14: Time response before and after irradiation under 10^{15} n/cm^2.

The total pulse length of the photo-conductor response is about 10 ns, (Figure13), and fits very well the nominal 40 MHz LHC event rate. Samples have also be exposed in a reactor to a dose of 10^{15} neutrons /cm^2 without any significant change of sensitivity or speed, (Figure 14). The tests will be resumed up to about 10^{18} neutrons /cm^2, which is the dose the detectors will have to withstand during the LHC operation lifetime.

5 TRANSVERSE PROFILE MEASUREMENTS

5.1 Luminescence Profile Monitor

This monitor makes use of the light emitted by the gas molecules when they return to ground state after excitation by the beam. Promising data has been obtained in the SPS with Nitrogen, which has a good cross-section for this process and is easy to pump [7].

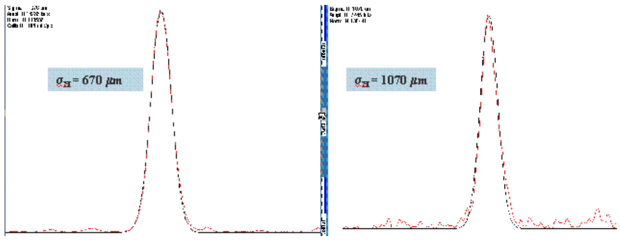

Figure 15: Profiles taken over 840 SPS turns under 6.10^{-7}hPa of N_2 pressure; left:2.10^{13} p; right:9.10^{8} Pb ions.

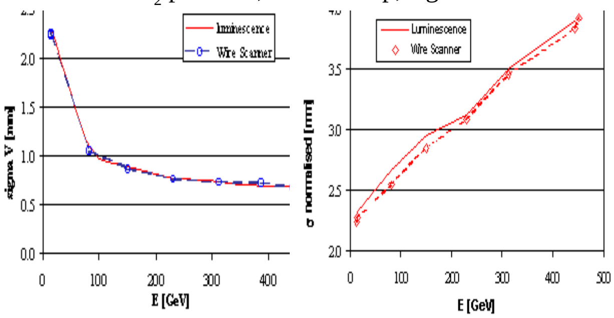

Figure 16: Vertical beam rms value variation recorded with the luminescence monitor and with the wire scanner.

In Figure 15, horizontal profiles acquired at 450 GeV on 840 SPS revolutions of, left, a proton beam and, right, a Pb ion beam, are represented. Data got with the luminescence monitor throughout an SPS acceleration cycle from 14 GeV to 450 GeV are compared in Figure 16 to corresponding ones made with the wire scanner, the usual reference. The agreement is good: both devices indicate an emittance blow-up when the rms beam dimension is normalised with the energy, (Figure 16, right).

5.2 Optical Transition Radiation Screens

Thin Titanium foils of a few micrometers can be left in beam, making it possible to record, with such monitors, beam profiles for several hundreds of consecutive turns. Hence injection matching studies can be performed, [8], as illustrated in Figure 17: oscillations of the beam size, resulting from imperfect tuning between the transfer line and the ring optics, occur in both H and V planes at injection. A constant blow-up is observed, (straight line slope), as the screen is left in the beam for the exercise.

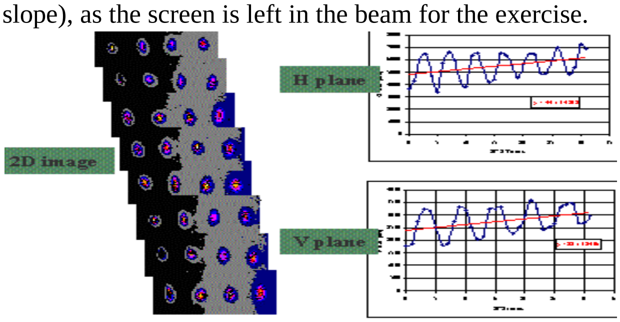

Figure 17: Oscillation of the horizontal and vertical rms beam size at injection into the SPS on the first 35 turns, and associated 2D image.

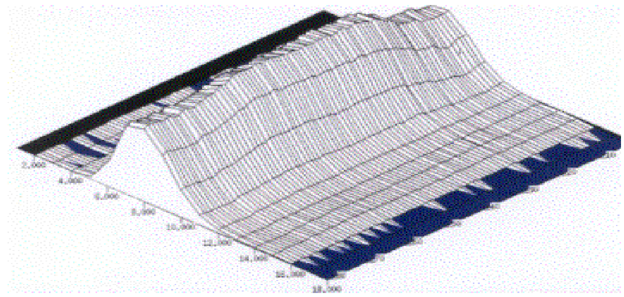

Figure 18: Train of 80 bunches, spaced by 25 ns, recorded on one passage in a SPS transfer line.

OTR screens are also used to sample at 40 MHz the individual bunch profiles belonging to a given LHC train, [9]. Such data is shown in Figure 18.

5.3 Rest Gas Ionisation Profile Monitor

A monitor analysing the signal from electrons produced due to the ionisation of the residual gas molecules by the beam is installed for tests in the SPS, [10]. Very good data has been recorded, as illustrated in Figure 19, following the evolution of a bunch of 6 10^{10} protons, (half the LHC nominal current), throughout an acceleration cycle. Horizontal profiles, integrated on 850 SPS revolutions, are well defined down to rms values of 700 µm. The residual pressure is around 10^{-8} hPa.

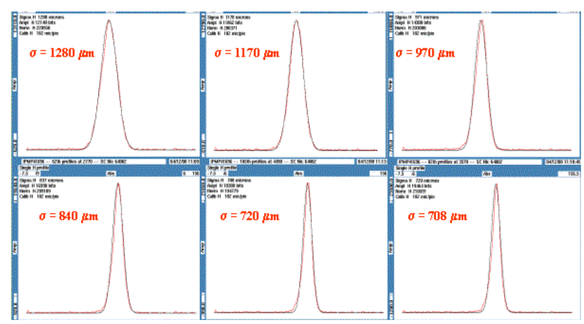

Figure 19: Horizontal dimension evolution of a bunch of 6 10^{10} protons during acceleration from 26 GeV to 120 GeV. The residual gas pressure is below 10^{-8} hPa

The residual gas monitor can also acquire turn by turn data, [10]. Such data are displayed in Figure 20 for a beam made of 40 bunches of 3.5 10^{10} protons each, monitored on 500 consecutive turns after injection into the SPS.

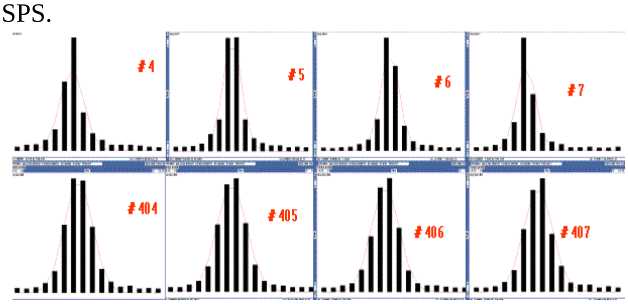

Figure 20: Turn by turn horizontal profiles of a beam of 1.4 10^{12} protons after injection into the SPS. The spatial resolution is 3mm /strip.

In this mode, the advantage, compared for example to an OTR screen, is that matching studies can be performed in a fully passive way for the beam, (no blow-up).

6 β FUNCTION MEASUREMENT BY K-MODULATION

The aim is to determine the average β function within a quadrupole by applying the smallest possible gradient variation, in order to not perturb the circulating beams, while getting a precision in the per cent range, [11]. This is achieved by modulating the magnet gradient, repeating numerous measurements to gain on statistics. The method was tested on a super-conducting quadrupole in LEP, using a square wave modulation, Figure 21.

Figure 21: Tune variation in LEP by square wave modulation of a SC quadrupole gradient at 0.25 Hz.

Results from this method are compared in Figure 22 to data got using the classical static method whereby gradient perturbations applied in several steps are left IN, and the associated tune variation recorded. <β> is given by the slope of the curve Δq(Δk). The static method leads to $\langle\beta_V\rangle$ = 165 m, Figure 22 left, whereas the k-modulation result averaged over several measurements gives $\langle\beta_V\rangle$ = 162.9 m, Figure 22 right.

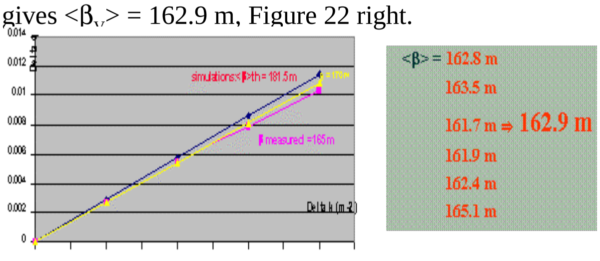

Figure 22: $\langle\beta_V\rangle$ measurement within a SC quadrupole: in LEP: left, static k – right, k-modulation results.

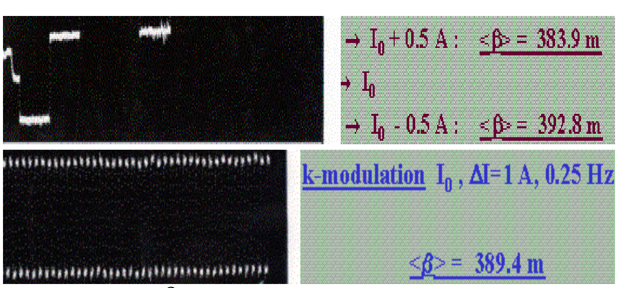

Figure 23: $\langle\beta_V\rangle$ measurement within a SC quadrupole in LEP: top, static k - bottom, k-modulation results.

Figure 23 gives another set of data acquired parasitically during a physics period, with two 103.4 GeV beams colliding in LEP. The value of $\langle\beta_V\rangle$ measured by k-modulation with a current I_0 in the SC quadrupole fits well between the values measured by the static method at currents of I_0+0.5 A and I_0-0.5 A. The method is very sensitive and does not perturb the beams.

7 CONCLUSION

Interesting results were recently obtained on prototype instruments developed for the LHC. However this is not an exhaustive review of all the beam instrumentation foreseen to operate the machine. Other fields are being investigated like synchrotron radiation monitors, beam loss detection, special pick-ups and shakers, and, in the CERN PS/BD group, DC beam current transformers.

ACKNOWLEDGMENTS

This paper reports on the work of many of my colleagues of the CERN-SL/BI group where most of the reported topics are handled, with the participation of external institutes. In particular, the collaboration with TRIUMF, LBNL, BNL, DESY, GSI, LYON1, the LETI is acknowledged as is the valuable help of colleagues from other groups at CERN to prepare and install the monitors, or to arrange their tests.

REFERENCES

[1] D. Cocq et Al., First beam tests for the prototype LHC orbit and trajectory system in the CERN SPS. These proceedings.
[2] J. P. Koutchouk et Al., Excitation of large transverse beam oscillations without emittance blow-up using the “AC dipole” principle. These proceedings.
[3] R. Jones, H. Schmickler, The measurement of Q’ and in the CERN SPS by head-tail phase shift analysis. These proceedings.
[4] A. Guerrero et Al., The SPS individual bunch measurement system. These proceedings.
[5] J.F. Beche et Al., An ionisation chamber shower detector for the LHC luminosity monitor, correspondence to wcturner@lbl.gov.
[6] E. Rossa et Al., New development of a radiation-hard polycrystalline CdTe detector for LHC luminosity monitoring. These proceedings.
[7] G. Burtin et Al., The luminescence profile monitor of the CERN SPS, CERN-SL-2000-031 BI, and EPAC2000, 26-30 June 2000, Vienna, Austria.
[8] C. Bovet et Al., The OTR screen betatron matching monitor of the CERN SPS, CERN-SL-99-050-BI, and DIPAC99, 16-18 May 1999, Chester, UK.
[9] G. Ferioli et Al., Beam profile measurements at 40 MHz in the PS to SPS transfer channel, CERN-SL-99-043-BI, and DIPAC99, 16-18 May 99, Chester, UK.
[10] G. Ferioli et Al., Sensitivity studies with the SPS rest gas profile monitor. These proceedings.
[11] O Berrig et Al., β function measurement with k-modulation. These proceedings.

MEASUREMENT OF SMALL TRANSVERSE BEAM SIZE USING INTERFEROMETRY

T. Mitsuhashi

High Energy Accelerator Research Organisation, Oho, Tsukuba, Ibaraki, 305-0801 Japan

Abstract

The principle of measurement of the profile or size of small objects through the spatial coherency of the light is known as the van Cittert-Zernike theorem. We developed the SR interferometer (interferometer for synchrotron radiation) to measure the spatial coherency of the visible region of the SR beam, and we demonstrated that this method is able to measure the beam profile and size. Since the small electron beam emits a SR beam which has a good spatial coherency, this method is suitable for measuring a small beam size. In this paper, the basic theory for the measurement of the profile or size of a small beam via the spatial coherency of the light, a design of the SR interferometer, and the results of beam profile measurement, examples of small beam size measurements and recent improvements are described.

1 INTRODUCTION

The measurements of beam profile and size are two of the most fundamental diagnostics in an electron storage ring. The most conventional method to observe the beam profile is known as a beam profile monitor via imaging of the visible SR beam[1]. The resolution of this monitor is generally limited by diffraction phenomena. In the usual configuration of the profile monitor the RMS size of diffraction (1σ of the point spread function) is no smaller than 50 μm. In the last 10 years, research and development in electron storage rings (especially in the area of emittance reduction) has been very remarkable. We can realise sub-diffraction-limited beam sizes in electron storage rings. So the above-mentioned profile monitor via imaging of the visible SR beam becomes useless in precise quantitative measurements of the beam profile and size. In the visible optics, opticians use an interferometer as the standard method to measure the profile or size of very small objects. The principle of measurement of the profile of an object by means of spatial coherency was first proposed by H.Fizeau [2] and is now known as the Van Cittert-Zernike theorem [3]. It is well known that A. A. Michelson measured the angular dimension (extent) of a star with this method [4]. Recently we developed the SR interferometer (an interferometer for SR beams) to measure the spatial coherency of the visible region of an SR beam, and as one of the results of investigations on the spatial coherence of SR beams, we demonstrated that this method is applicable to measure the beam profile and size at the KEK Photon Factory [5]. Since the SR beam from a small electron beam has good spatial coherency, this method is suitable for measuring a small beam size. The characteristics of this method are: 1) we can measure beam sizes as small as 3 and 4μm with 1μm resolution in a non-destructive manner; 2) the profile is easy to measure using visible light (typically 500 nm); 3) the measurement time is a few seconds for size measurement and few tens of seconds for profile measurement. In this paper we describe the van Cittert-Zernike theorem, the design of the SR interferometer and examples of the profile and the beam size measurements

e-mail: mitsuhas@mail.kek.jp

2 SPATIAL COHERENCE AND BEAM SIZE

According to van Citterut-Zernike's theorem, the profile of an object is given by the Fourier Transform of the complex degree of spatial coherence at longer wavelengths as in the visible light[3][6]. Let f denotes the beam profile as a function of position y, R denotes distance between source beam and the double slit, and γ denotes the complex degree of spatial coherence as a function of spatial frequency υ. Then γ is given by the Fourier transform of f as follows;

$$\gamma(\upsilon) = \int f(y)\exp(-2\pi i\upsilon \cdot y)dy, \quad \upsilon = \frac{2\pi \mathrm{D}}{\lambda R}.$$

We can measure the beam profile and the beam size via spatial coherence measurement with the interferometer.

3 SR INTERFEROMETER

To measure the spatial coherence of SR beams, a wavefront-division type of two-beam interferometer using polarized quasi-monochromatic rays was designed as shown in Fig.1[6].

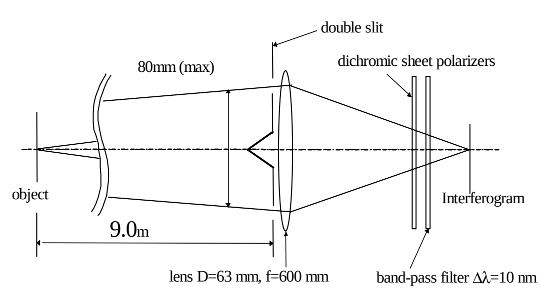

Fig.1 Outline of the SR interferometer.

In the vertical plane, the elliptical polarity of synchrotron radiation is opposite that in between the medium plane of the electron beam orbit. Therefore, there exists the π phase difference between the phases of the interferograms to correspond to the σ- and π-polarized components [5]. To eliminate the interferogram by π-polarized component, we mast apply a polarization filter. A typical interferogram observed with the SR interferometer is shown in Fig.2.

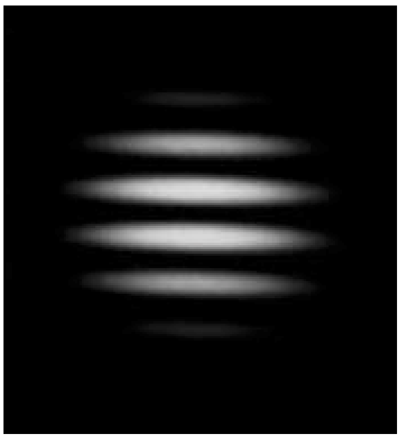

Fig. 2 A typical interferogram observed with the SR interferometer.

With this interferometer, the intensity of the interferogram is given by,

$$I(y,D) = (I_1 + I_2)\cdot\left\{\mathrm{sinc}\left(\frac{\pi\cdot a\cdot y\cdot\chi(D)}{\lambda\cdot f}\right)\right\}\cdot\left\{1+\gamma\cdot\cos\left(k\cdot D\cdot\left(\frac{y}{f}+\psi\right)\right)\right\}$$

$$\gamma = \left(\frac{2\sqrt{I_1\cdot I_2}}{I_1+I_2}\right)\left(\frac{I_{max}-I_{min}}{I_{max}+I_{min}}\right),\quad \psi = \tan^{-1}\frac{S(D)}{C(D)}$$

where y denotes position in the interferogram, a denotes the half-height of a slit, and f denotes the distance between secondary principal point of the lens and the interferogram[6]. $S(D)$ is the sine component and $C(D)$ the cosine component of the Fourier transformation of the distribution function of the SR source. $\chi(D)$ in this equation represents an instrumental function of the interferometer; this term has a cosine-like dependence, and comes mainly from two sources: 1) a cosine term in the Fresnel-Kirchhoff diffraction formula [6] which represents the angular dependence between the incident and diffracted light of a single slit; 2) reduction of effective slit height as double slit separation D increases. This term χ is normally neglected in diffraction theory under the paraxial approximation, but we cannot neglect this term in the practical use of the interferometer.

4 BEAM PROFILE MEASUREMENT

We can measure the beam profile by Fourier transform of the spatial coherence. Figure 3 shows the absolute value the complex degree of the spatial coherence (|γ|, visibility) was measured by changing the double slit separation from 5 mm to 15 mm at the Photon Factory[5].

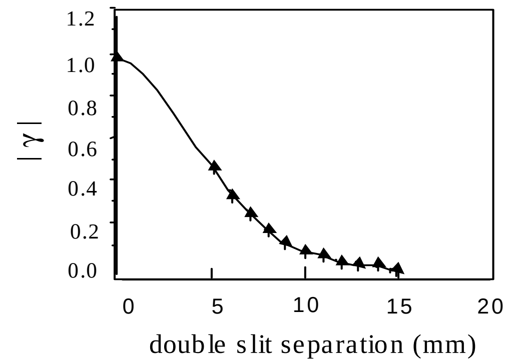

Fig 3. Result of |γ| at the Photon Factory

The result of beam profile by Fourier transform of the spatial coherence is shown Fig. 4.

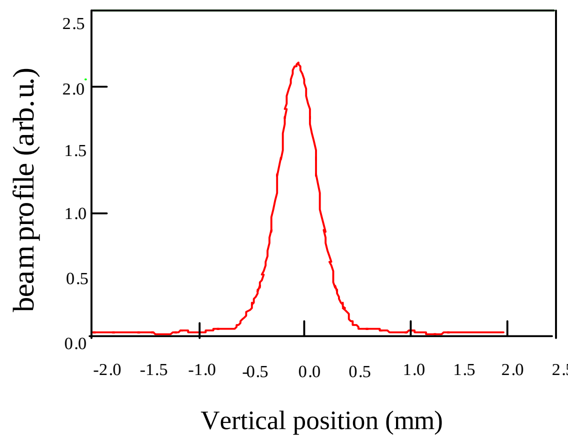

Fig. 4 Beam profile by the Fourier transform of the spatial coherence at the Photon Factory

5 SMALL BEAM SIZE MEASUREMENT BY MEANS OF GAUSSIAN APPROXIMATION OF BEAM PROFILE

We often approximate the beam profile with a Gaussian shape. With this approximation, we can skip any phase measurement. The Fourier transform of even function (Gaussian) is simplified to a Fourier cosine transform. A spatial coherence is also given by a Gauss function. We can evaluate a RMS width of spatial coherence by using q least-squares analysis. The RMS beam size σ_{beam} is given by the RMS width of the spatial coherence curve σ_γ as follows:

$$\sigma_{beam} = \frac{\lambda\cdot R}{2\cdot\pi\cdot\sigma_\gamma}$$

where R denotes the distance between the beam and the double slit. Experimentally, we must measure the |γ| (contrast of interferogram) as a function of slit separation D[6].

We can also measure the RMS. beam size from one data of visibility, which is measured at a fixed separation of double slit. The RMS beam size σ_{beam} is given by ,

$$\sigma_{beam} = \frac{\lambda \cdot F}{\pi \cdot D} \cdot \sqrt{\frac{1}{2} \cdot \ln\left(\frac{1}{\gamma}\right)}$$

where γ denotes the visibility, which is measured at a double slit separation of D[6].

With this technique, how small beam we can measure? In Fig. 5, it is shown a result of simulation. In this simulation, measuring condition of ATF is assumed ; the double slit separation is 50mm and distance between the source point and the interferometer is 7.4m. From this simulation, the beam size 4μm will gives the contrast 0.94 with 500nm and 0.91 with 400nm. The beam size 3μm will gives the contrast 0.97 with 500nm and 0.95 with 400nm. Since we can easily measure the intensity of light by 1% precision with CCD and image processor, we can measure a difference between the beam size 3 μm and 4 μm with a resolution better than 1μm.

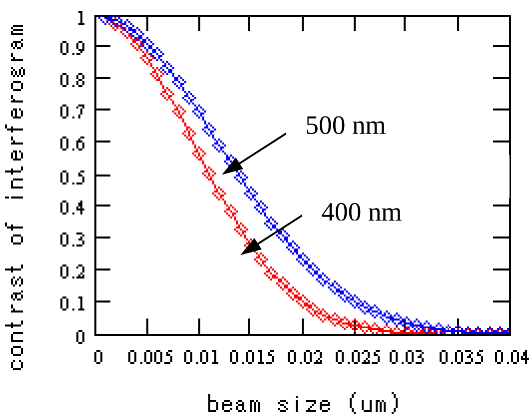

Fig. 5 Result of simulation about contrast of interferogram as a function of beam size .

6 SMALL BEAM SIZE MEASUREMENT

As mentioned in section 5, to assume the Gaussian profile, we can evaluate the beam size in the small-beam based on the degree of spatial coherence. We introduce two examples of small beam size measurements in this section.

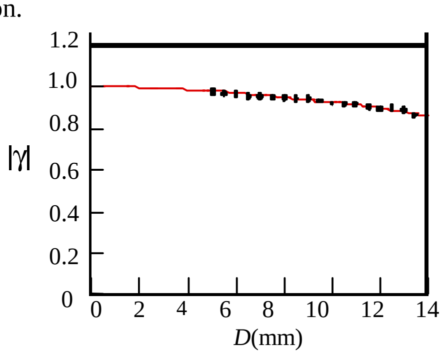

Fig. 6 Absolute value of the complex degree of spatial coherence in the vertical direction. Dotted line denotes measured |γ|, and solid line denotes the best-fit beam size of 16.5 ± 0.6μm.

One is the result of vertical beam size measurement at the AURORA[6] and other is the vertical and the horizontal beam size measurement the ATF damping ring at KEK[6].

Figure 6 shows the result of |γ| as a function of slit separation with a least-squares fitting by a Gaussian profile at the AURORA. The obtained beam size from this fitting is 16.5 μm.

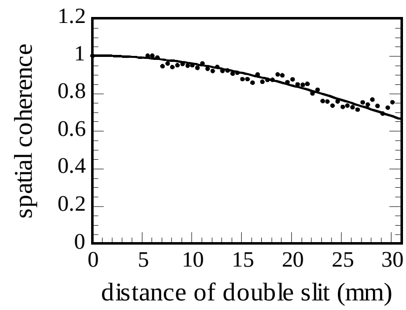

Fig. 7. Absolute value of the complex degree of spatial coherence in the vertical direction at ATF damping ring. Dotted line denotes measured |γ|, and solid line denotes the best-fit beam size of 14.7 ± 0.6μm.

The result of |γ| as a function of slit separation for vertical direction with a least-squares fitting by a Gaussian profile at the ATF damping ring is shown in Fig. 7. The result of |γ| as a function of slit separation for horizontal is shown in Fig. 8. A least-squares fitting of the |γ| in Figure 9 includes a field depth effect for the horizontal direction [6]. The obtained beam size from these fitting is 14.7 μm in the vertical and 39μm in the horizontal.

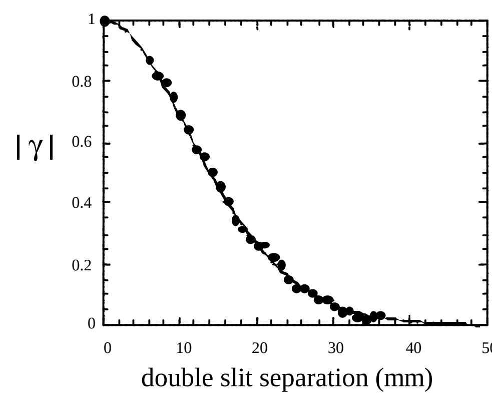

Fig. 8. Absolute value of the complex degree of spatial coherence in the horizontal plane at the ATF damping ring. The dotted line denotes measured |γ| and the solid line denotes the best-fit value of 39±1μm.

7 AUTOMATIC BEAM-SIZE MEASUREMENT IN KEK-B FACTORY

As described in section 5, with a Gaussan beam profile approximation again, we can estimate the RMS beam size from one data of visibility of one interferogram, which is measured at a fixed separation of double slit. Using this method, we can easily measure a beam size automatically from an analysis of interferogram taken at fixed separation of double slit D [7]. To find the visibility γ from the interferogram, we use the standard Levenberg-Marquart method for non-linear fitting. After the image processing of the interferogram, the results are relayed to a computer in the control room to display and further analysis. Figure 9 shows an example of the display panel for LER. A same panel is also displayed for HER. The interferogram, best fit curve and beam size trend graphs for vertical and horizontal directions are shown in the panel. By this automatic beam-size measurement system, we can measure the vertical and horizontal beam size in every second and which are extremely useful for beam tuning.

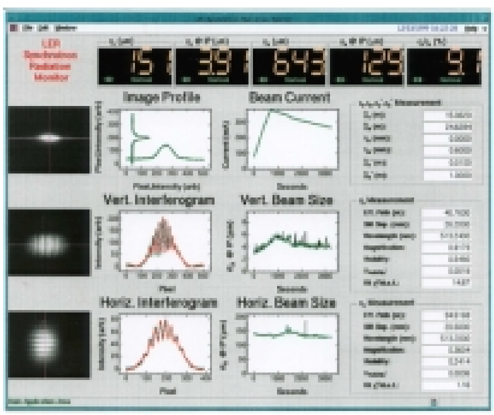

Fig. 9 SR Monitor panel in control room, showing LER vertical and horizontal beam sizes.

8 Recent improvements

In this section, It is described that some topics from recent improvements.

8-1 Linearity of CCD camera

Since we measure a contrast of interferogram in the beam size measurement, the linearity of the CCD camera is very important. In here, it is shown that some results of linearity measurements of CCD camera. The linearity of the CCD camera is measured by using accurately calibrated neutral-density filters. The optical density of these filters are calibrated by spectro-densitometer within 0.1% error in spectrum range from 400nm to 650nm. Since stability of the intensity of SR beam is less than 0.1% in a few minutes measurement at the Photon Factory, we used SR beam as the incident light. The measurement is performed in the intensity range from zero to saturation level.

A result of linearity measurement for commonly-used CCD camera is shown in Fig. 10. To see this figure, CCD camera is not always linear in the region which is far from its saturation.

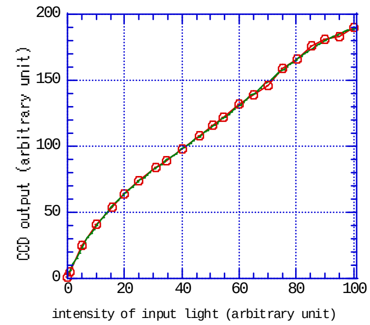

Fig. 10 A result of linearity measurement of commonly-used CCD camera.

Another result of linearity measurement for CCD camera is shown in Fig. 11. This camera is sold as a camera for quantitative measurement of intensity.

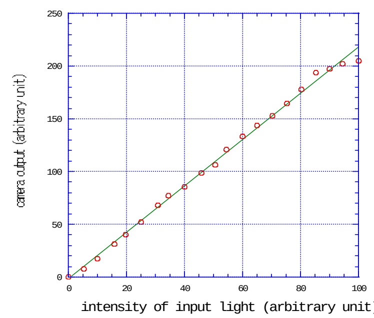

Fig. 11 A result of linearity measurement of CCD camera for quantitative measurement.

To see Fig. 11, the CCD camera which is sold for quantitative measurement has a good linearity. Right now, we check the linearity of the CCD camera before installation in the interferometer.

8-2 Effect of floor vibration

The vibration of floor of the accelerator building is not negligible smaller for interferometer measurements. To see an effect of floor vibration to interferometer, we measured the beam size as a function of exposure time of the CCD camera. A result of measurement at the Photon Factory is shown in Fig. 12.

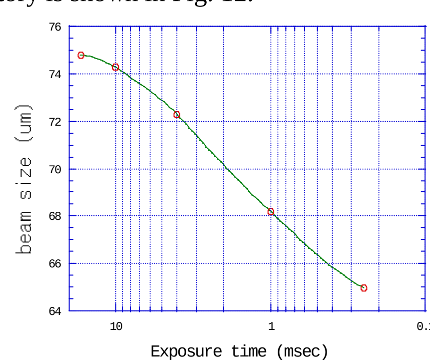

Fig.12 Beam size as a function of CCD exposure time.

From this result, decrease of the beam size is observed at shorter exposure time of CCD camera. From the view point of the accelerator physics, the beam size without an effect of floor vibration is more correct one, but an instantaneous beam size is often inconvenient for accelerator users, so we apply a exposure time 15msec.

8-3 Deformation of SR extraction mirror

The extraction mirror for SR beam deformed by strong irradiation of SR. The actual rays due to this deformation propagate different optical paths compare with ideal rays. So, Two optical paths of actual rays those come to double slit give a different separation from ideal ray's one. We must know true separation of two rays at the location of double slit. To measure wavefront error and true separation of two rays, we applied the Haltmann screen test[8]. In the Hartmann screen test, the wavefront is sampled by a number of rays normal to it, ray deviation at observation plane can be obtained. We used a 100-holes square-array screen as shown in Fig.13. The interval of hole is 5mm. The square-array screen is fixed on a X-Y moving stage.

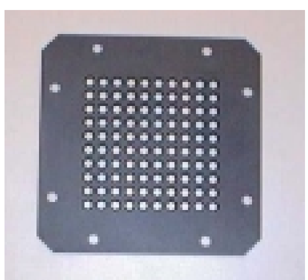

Fig.13 A 100-hole square-array screen.

The setup of the wavefront-error measurement at the Photon Factory is shown in Fig. 14. With this setup, if we measure the dot positions of the Hartmann pattern on the observation plane with 0.1mm resolution, we can measure the wavefront with $\lambda/6$ (in here, λ is 633nm) precision.

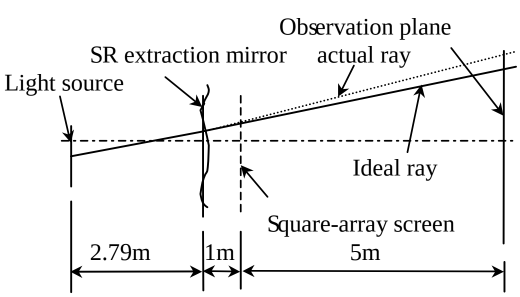

Fig. 14 Measurement setup.

A typical Hartmann pattern observed in the Photon Factory is shown in Fig. 15. Reconstructed wavefront-error is also shown in Fig. 15. To determine the true separation between the two rays at the location of double slit, we use a single-hole screen as shown in Fig. 16. The paths of two ideal rays are probed by scanning the single-hole screen in the plane which perpendicular to the optical axis.

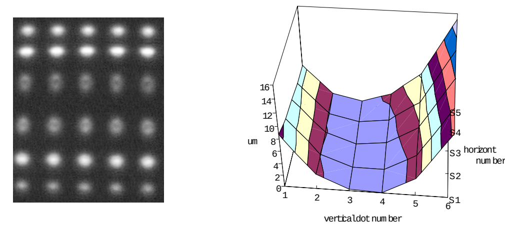

Fig. 15 Typical Hartmann pattern observed in the Photon Factory and reconstructed wavefront.

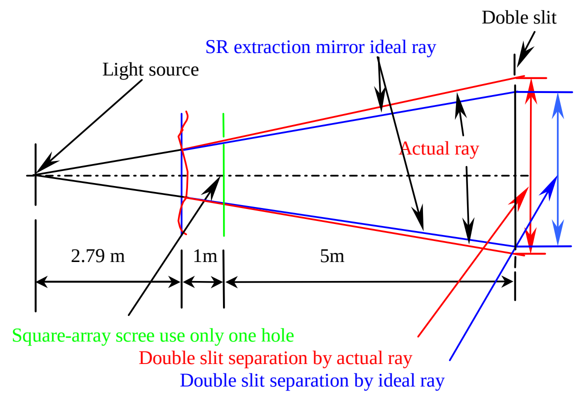

Fig. 16 Setup of determination of true double slit separation by scanning a single-hole screen.

7 CONCLUSIONS

The SR interferometer was developed to measure the spatial coherency of the visible region of the SR beam, and we demonstrated that this method is able to measure the beam profile based on the van Cittert-Zernike theorem. Using a Gaussian beam profile approximation, we can measure μm range very small beam size with the resolution less than 1μm. With automatic analysis system, the SR interferometer is conveniently used as a beam size monitor. The measuring interval is about 1sec.

REFERENCES

[1] T. Mitsuhashi and M. Katoh, Proc. 5th European Particle Accelerator Conference, 1669, (1996), Sitges (Barcelona).
[2] H. Fizeau, C.R.Acd.Sci. Paris, 66, 934 (1868).
[3] P.H.van Cittert, Phisica, 1, 201(1934) and also see M. Born and E. Wolf, "Principles of Optics", chapter 10, P491, Pergamon press. (1980).
[4] A.A. Michelson, Astrophsyc.J51,257 (1920).
[5] T. Mitsuhashi, Proc. of 1997 Particle Accelerator Conference, 766, (1997) ,Vancouver(Canada).
[6] T. Mitsuhashi,“ Beam Profile andSize Measurement by SR Interferometer ” in Beam measurement, Ed. By S. Kurokawa et.al., pp399-427, World Scientific(1999).
[7] J.W. Flanagan, S. Hiramatsu and T.Mitsuhashi, Proc. 7th European Particle Accelerator Conference,1714 , (2000),Vienna(Austria).
[8] I.Ghozeil “ Hartmann and other screen tests” in Optical shop testing, Ed. By D. Malacara ,pp367-396,Wiley-International (1992).

ACCELERATOR PHYSICS EXPERIMENTS WITH BEAM LOSS MONITORS AT BESSY

P. Kuske, BESSY, Berlin, Germany

Abstract

The extended use of beam loss monitoring has led to a better understanding of the linear and non-linear physics involved in the single and multiple particle dynamics at BESSY. This knowledge has been used for improving the performance of the light source in terms of lifetime, beam stability, and stability of the energy.

The key to these experiments are loss monitors placed at strategic locations of the ring with high sensitivity to Touschek or Coulomb scattered particles.

Coulomb-scattering depends strongly on the transverse dynamics which is determined by the magnetic guiding fields. Losses occur primarily at the vertical aperture restrictions imposed by the flat insertion device vacuum chambers. Tune scan measurements clearly show resonances produced by the lattice magnets and by some of the insertion devices.

Touschek scattering depends on the 3-dimensional electron density and the spins of the colliding particles. In transfer function type experiments these dependencies have been used to observe the effect of resonant transverse and longitudinal beam excitations. Loss monitors allow to detect excited head-tail and higher longitudinal modes which are invisible in the center of mass motion. Another application is the detection of the resonant destruction of the spin polarization of the ensemble of electrons. This is used routinely in order to determine the beam energy with high accuracy.

1 INTRODUCTION

The lifetime of the stored beam current, or its inverse, the decay rate of the intensity, is a very convenient measure of global particle losses. However, a fast and accurate determination of this quantity is difficult. The limited resolution of current monitors require long time intervals, Δt, in order to detect significant changes of the intensity, ΔI, especially if the lifetime, τ, is large since $\Delta I/I=-\Delta t/\tau$.

The alternative is the direct local detection of lost particles. When high energy particles are hitting the vacuum chamber, they produce a shower of many particles with low energy like photons, electrons, and positrons. These fragments are emitted into a small cone in the forward direction and they are easy to observe with different types of detectors[1]. With beam loss monitors (BLM) placed close to the vacuum chamber each lost electron at that location can be detected. Particles hit the chamber at specific locations depending on the loss mechanisms involved. With a system of strategically distributed loss monitors the detection is sensitive to the mechanisms causing the loss.

The high speed of the measurements and the information on the loss mechanisms have been exploited by correlating beam losses with parameters like external transverse and longitudinal excitations, the working point, different settings of machine parameters, the beam current, and further more.

2 PARTICLE LOSS MECHANISMS

Experiments have been performed at the second generation light source BESSY I, an 800 MeV electron storage ring, and the third generation source BESSY II operating at energies between 900 MeV and 1.9 GeV[2]. Dominating, unavoidable particle losses in this energy range stem from the electron-electron interactions within one bunch, the so called Touschek effect, and interactions of electrons with residual gas molecules, like elastic and inelastic Coulomb scattering[3]. Particle losses can occur just downstream the collision point at the next transverse or longitudinal aperture restriction or at any other location if particles are scattered close to, but not exceeding the aperture limits. This introduces a background of losses which can not clearly be attributed to a specific loss mechanism.

2.1 Detection of Touschek Scattered Particles

Good locations for the detection of Touschek scattered particles are in the achromatic sections with the highest value of the dispersion function just behind straight sections where a high particle density is reached. Since the two colliding particles loose and gain an equal amount of momentum, they will hit the in- and outside wall of the vacuum chamber. In principle the selectivity of the detection to Touschek events can be improved by counting losses at these locations in coincidence.

2.2 Detection of Coulomb Scattered Particles

Losses from elastic Coulomb scattering occur at locations where the beta functions are large and where apertures are small. Aperture restrictions are introduced either intentionally, like in the case of small gap insertion device (ID) vacuum chambers, in-vacuum IDs, the septum magnet, and by mechanical scrapers or unintentionally by burned RF fingers and other obstructions.

If, in an inelastic Coulomb collision, the energy carried away by the emitted photon is too large, the particle gets lost behind the following bending magnet on the inside wall of the vacuum chamber.

3 DETECTION OF LOST PARTICLES

Over the years different detectors were tested at BESSY. The choice right now are plastic scintillation counters. A 3x3 cm^2 piece of the fast NE100 material is used. The light is coupled through a light pipe to the photo multiplier. Up to 42 of these beam loss monitors (BLM) can be distributed around the storage ring. The high voltage power supplies, the pulse shaping-electronics, and the discriminators are located on the gallery above the ring.

So far 12 detectors have been installed. 4 monitors are placed where a large contribution from particles lost due to the Touschek effect are expected. The remaining monitors are more sensitive to losses from elastic Coulomb scattering: 6 BLMs have been mounted at the end of the straight sections, on top of the small gap insertion device vacuum chambers and 2 BLMs are installed at the horizontal physical aperture limitation behind the injection septum magnet. With these 12 detectors a few percent of all lost electrons can be counted.

With this distribution a very good sensitivity for detecting Touschek losses is obtained, even without coincidence techniques. The selectivity for observing elastically Coulomb scattered particles is sufficient. Until now, no attempts were made to achieve selective detection of inelastic Coulomb scattered electrons.

4 EXPERIMENTS WITH LOSS MONITORS SENSITIVE TO COULOMB LOSSES

In the ideal case, the 3-dimensional distribution of particles in an electron storage ring is Gaussian. Coulomb scattering increases the population of the tails of the distribution. Any modification of the phase space will have an impact on the number of lost electrons. By observing losses related to elastically scattered particles as a function of the working point, the beam-beam interaction and the lattice related phase space were investigated[4]. At BESSY the non-linearity of the storage ring lattice as well as the one introduced by the IDs were analyzed with this technique.

4.1 Impact of Insertion Devices

The APPLE II type undulators UE56 show a dramatic impact on the lifetime of the stored beam at BESSY II[5]. In Fig. 1. two loss rates are shown as a function of the vertical tune for open and closed undulator gaps: vertical losses at one of the ID chambers and horizontal losses at the septum magnet. Loss rates and lifetime show the same tune dependence and exhibit very similar resonance-like features. Even though the upstream (red) and the

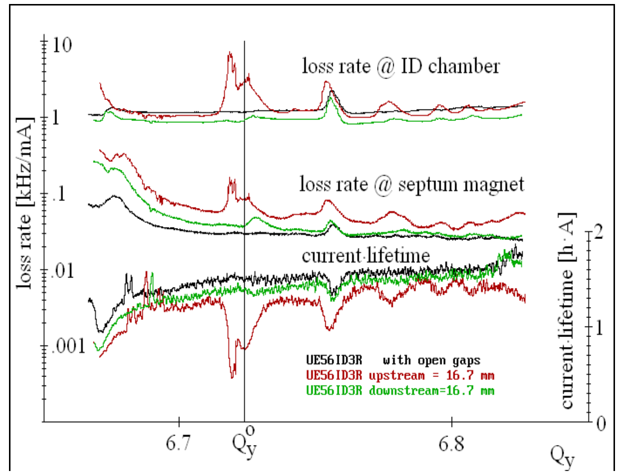

Fig. 1: Impact of two nominally identical IDs on beam dynamics. Lifetime and loss rates as a function of the vertical tune exhibit the same resonance-like features.

downstream (green) part of the ID are nominally identical only the upstream part leads to severe losses at the nominal working point. This has to be attributed to statistical field errors of the ID and is not a systematic effect.

The high speed of loss rate detection even allows to perform tune scans as a function of other parameters. Tune scans as a function of the magnetic gap of the IDs show, how resonances get stronger and stronger the more the gap is closed. The UE56 is intended to produce light with variable polarization. By shifting the magnet poles longitudinally the electron beam wiggles either in the horizontal, the vertical plane, or, in between, it moves on a helical orbit. Tune scans as a function of the shift parameter show, that this parameter has no strong impact on the beam dynamics.

Two dimensional tune scans close to the nominal working point were performed in order to find out which resonance was responsible for the dramatic impact of the upstream part of the ID on the lifetime. Since there is a one to one relationship between the resonances and the multipole field component driving the resonance in lowest order this allows to pinpoint the harmful field components. The result is shown in Fig. 2. It is the $Q_x+3{\cdot}Q_y$-resonance which is driven by a skew octupole component. Many other resonances are excited by this ID. Better shimming should improve the situation considerably. For the time being, the working point was moved slightly away from the most harmful resonance.

4.2 Lattice Non-Linearity

Since the loss rates are high tune scans can be performed at lower beam currents where instabilities do not occur. Fig. 3 shows the losses at the vertical aperture limitation and Touschek losses as a function of the vertical tune with only 1 mA stored in a single bunch. All IDs are open and the resonances are excited by the lattice.

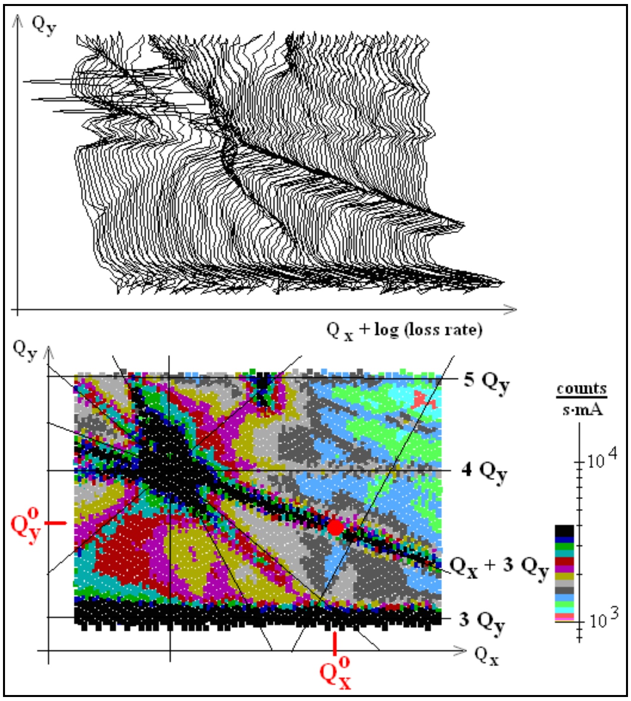

Fig. 2: 2-dimensional tune scan close to the nominal working point: Q_y=6.72 and Q_x=17.84. The magnetic gap of the upstream part of the UE56ID3R is closed to 16.7 mm and the 6 Tesla WLS is running.

The lattice contains strong sextupole magnets, a few skew quadrupole magnets, and obviously the lattice symmetry is broken. The octupole component driving the $4{\cdot}Q_y$-resonance is probably the result of a feed-down from the decapole of the dipole magnets and not a quadrupole fringe field effect. In the Coulomb loss rate the Q_x-Q_y-resonance is only visible because the large horizontal emittance of Coulomb scattered particles is coupled on the resonance into the vertical plane, where the particles get lost on the aperture restriction. Generally, because of the tune shift with amplitude, Coulomb losses show strong asymmetries and hysteresis effects.

In the loss rate related to Touschek scattered particles 3 difference coupling resonances show up. On a coupling resonance the horizontal emittance is coupled to the vertical plane, the particle density drops, and the loss rate goes down. The Q_x-Q_y-resonance is the most dominating one. The reduction of the Touschek losses on this resonance, where the Coulomb loss rate increases, demonstrates nicely how these BLMs discriminate the loss mechanisms. Also on the nominal working point, Touschek scattered particles are not primarily lost in the vertical plane opposite to what was observed at the ESRF[6].

Tune scans and the observation of loss rates are very helpful in order to investigate the impact of non-linearities on beam dynamics. Interpretation of the results is simplified if a good selectivity of the beam loss monitors to the different loss mechanisms can be achieved. In certain cases the dominating loss mechanism can be found and the effect of counter measures can be verified easily with BLMs.

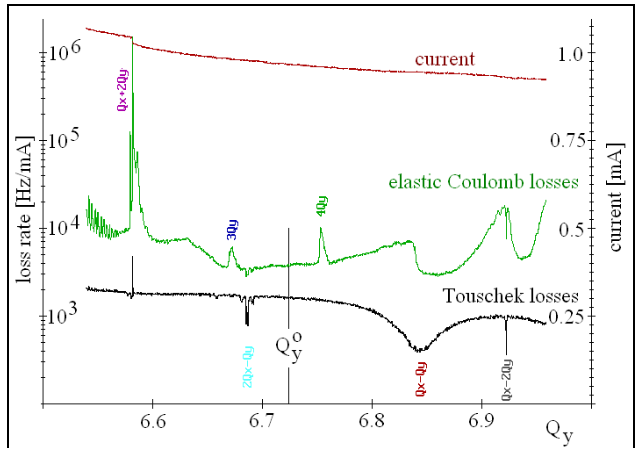

Fig. 3: Comparison of Coulomb and Touschek scattering related losses measured with 1mA stored in a single bunch. The horizontal tune was kept fixed at its nominal value and the vertical tune was varied.

5 EXPERIMENTS WITH LOSS MONITORS SENSITIVE TO TOUSCHEK LOSSES

Touschek scattering and the rate of related losses depend on the density of particles in the transverse and longitudinal phase space and depend in addition on the spin orientation of the colliding particles. Transfer function type experiments have been performed which exploit these sensitivities of the Touschek effect.

In these experiments, the beam is excited by a sinusoidal, time varying external force and the loss rates are monitored as a function of the frequency which is swept slowly back and forth over the region of interest. The observed resonant effects have been used for the determination of the energy, the investigation of the mechanisms which turn the coherent excitation into an incoherent and sometimes desired blow-up of the beam, and the detection of coherent head-tail modes.

5.1 Accurate Determination of the Energy

Historically, at BESSY, the spin sensitivity of Touschek scattering was used very early for the energy measurement of the stored electron beam[7]. In the experiment, BLMs tailored for a high sensitivity to Touschek scattered particles, are used as polarimeter. An increase of the loss rates is observed if the ensemble of electrons is depolarized. This occurs resonantly at a certain frequency of the radial field and from the resonance frequency the average energy of the beam can be determined with high accuracy.

Lately the energy was measured routinely during the normal user runs in order to investigate the intrinsic

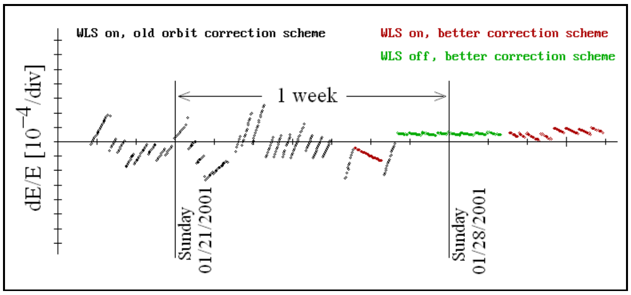

Fig. 4: Relative variations of the energy of the stored beam over 2 weeks measured with the help of BLMs. The automated slow orbit correction is running and for the colored traces a modified algorithm was used.

energy stability of the storage ring[8]. As seen in Fig. 4, the modification of the automated closed orbit correction algorithm has improved the stability of the energy further[9]. Nevertheless, the superconducting wavelength shifter (WLS), running in the so called persistent current mode, still introduces larger drifts of the energy.

The determination of the energy based on the technique of resonant spin depolarization in combination with spin sensitive beam loss monitoring can be applied at most synchrotron light sources if fast vertical feedback kicker magnets are available in order to depolarize the beam. This was done at the ALS and has been used to measure the momentum compaction factor[10].

5.2 *Emittance Dilution*

Third generation light sources, with their low natural emittance and their small emittance coupling ratio, especially operating with high currents per bunch, suffer from high Touschek scattering loss rates and the resulting lifetimes are rather short. Under these circumstances it is quite common to reduce the particle density and sacrifice brilliance in order to gain longer lifetimes. At BESSY the mechanisms of density reduction have been investigated with BLMs. In this study different ways were found how an external coherent excitation can be used for blowing up the beam[11].

There are other possibilities to dilute the emittance. Often the coupling is increased by skew quadrupole magnets or tunes are chosen close to the Q_x-Q_y-coupling resonance. A similar type of resonance can be created by an external time varying skew quadrupole field with a corresponding resonance condition. This was observed in the Touschek loss rates during the spin depolarization experiments indicating that the depolarizing radial field contains an additional skew quadrupole field component. The four striplines, two on the top and two on the bottom of the vacuum chamber, form an ensemble which can create this field component quite naturally.

5.3 *Coherent Head-Tail Modes*

In collaboration with E. Plouviez from the ESRF an attempt was made to selectively excite and detect, with the help of beam loss monitors, the lowest head-tail modes, where head and tail of the bunch move, for example vertically, 180° out of phase. This mode of oscillation can be created if the beam is excited resonantly over many turns such that head and tail always experience kicks in opposite directions. Stripline kickers will do this, if driven by an amplitude modulated high frequency voltage at 250 MHz, locked to the RF master oscillator. The phase of the excitation can be chosen such, that either all particles inside the bunch experience the same kick and dominantly the rigid dipole mode, m=0, is excited, or, with the phase shifted by 90°, the head and the tail of the bunch are kicked in opposite directions and preferentially the m=±1-modes are excited. According to simulations of the latter case, the particle density inside the bunch should be reduced on average if the coherent head-tail mode is excited. The resonant density reduction leads to a smaller Touschek scattering rate which can be detected easily.

In Fig. 5 the effect of a selective excitation of the head-tail modes in the vertical plane on the loss rates, the vertical beam size, as measured with the X-ray pinhole camera[12], and the beam current is shown. The head-tail modes show up very clearly in the Touschek loss rates and the vertical beam size. Not shown here is the trace recorded on the spectrum analyzer whose tracking generator was producing the frequency ramp. No signs of the head-tail modes can be seen in the center of mass motion of the ensemble of particles since the vertical chromaticity was set to zero.

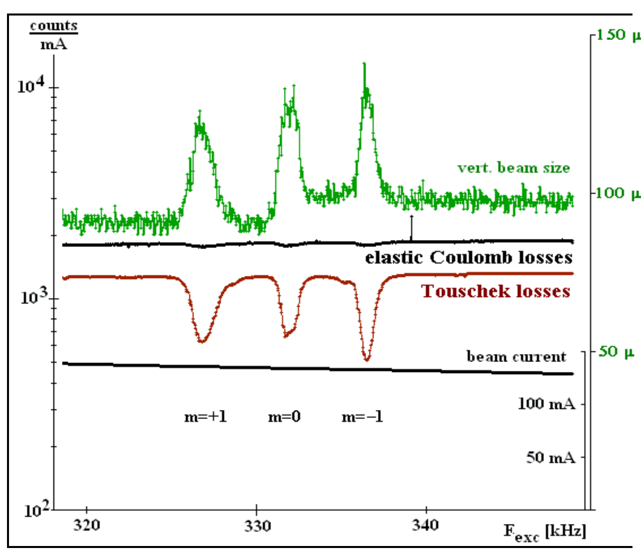

Fig. 5: Touschek (red), elastic Coulomb (black) loss rates, and vertical beam size (green) measured as a function of the frequency used for the modulation of the amplitude of the beam exciting 250 MHz voltage. Dominantly the head-tail modes m=±1 are excited.

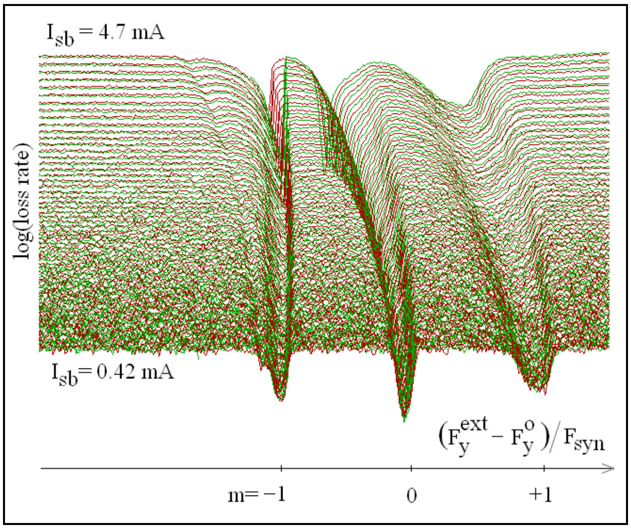

Fig. 6: Head-tail modes as a function of current in a single bunch at zero chromaticity. The head-tail modes were excited with the technique described in the text. Note the strong broadening of the m=+1-mode, the small line emerging from the m=-1-mode, and the hysteresis effects of this mode between up- and down-scans (green and red curves) at higher beam currents.

This technique was used in order to investigate the current dependence of these modes as a function of single bunch beam current at zero chromaticity. The result is shown in Fig 6. Under these conditions a clear observation of the coherent head-tail modes is not possible with the conventional approach of looking at the center of mass motion and without strong coupling of the head-tail modes to the rigid dipole mode. However, these exper-iments are relevant for a better understanding of the head-tail instability and the role played by the longitudinal dynamics in this, often current limiting, instability.

The selective excitation and beam loss monitoring as a means to detect coherent head-tail modes should be applied on other storage rings in order to find out whether the observations are similar to BESSY II: Strong broadening of the m=+1-mode, the small line emerging from the m=-1-mode at rather low single bunch beam current, and the non-linearity which shows up in the hysteresis between the up- and down scans. These observations are unexpected and theory does not yet give an explanation.

6 CONCLUSION

The use of beam loss monitors in storage rings opens a wide field of challenging experiments. Tune scans and Coulomb related loss rate detection leads to a better understanding of the lattice or insertion device induced non-linearity. Transfer function type experiments in combination with monitoring the Touschek related losses opens a new field of experiments especially if more complex ways for the excitation of the beam are chosen.

The observation of the head-tail modes with beam loss monitors will hopefully improve the understanding of the related instabilities.

7 ACKNOWLEDGEMENT

The use of BLM was initiated by the Physikalisch Technische Bundesanstalt (PTB), who require a reliable accurate energy measurement of the stored electron beam at BESSY. I thank G. Ulm, R. Klein, and R. Thornagel.

The instrumentation was realised by the diagnostics group at BESSY: J. Kuszynski, R. Goergen, T. Mayer, and F. Falkenstern. This work was supported by the members of the RF-group, the fast feedback group, the control system group and the ID-group.

I thank our guests, E. Plouviez, J.-L. Revol, and P. Elleaume from the ESRF for the fun of many discussions.

REFERENCES

[1] K. Wittenburg, “Beam Loss Detection“, DIPAC’93, Montreux, May, 1993, CERN SL/93-35 (BI), p. 11
[2] D. Krämer, “BESSY II: Exceeding Design Parameters - the First Year of User Service“, EPAC’00, Vienna, p. 640
[3] J. Le Duff,“Current and Current Density Limitations in Existing Electron Storage Rings“, Nucl. Instr. and Meth. A239 (1985) 83-101
[4] D.V. Pestrikov, “Detection and Correction of Non-Linear Resonances“ in Beam Measurement, Eds: S-i. Kurokawa, S.Y. Lee, E. Perevedentsev, S. Turner, 1999, World Scientific, p. 312 and
D. Robin, et al., “Enhanced Performance of the Advanced Light Source Through Periodicity Restoration of the Linear Lattice“, EPAC’00, Vienna, p. 136
[5] P. Kuske, J. Kuszynski, “Investigation of Non-Linear Beam Dynamics with APPLE-type Undulators at BESSY II“, to be published, PAC’01, Chicago
[6] J.M. Filhol, et al., “Mastering of Beam Losses at the ESRF“, EPAC’98, Stockholm, p. 1374
[7] Ya.S. Derbenev, et al., “Accurate Calibration of the Beam Energy in a Storage Ring Based on Measurement of Spin Precession Frequency of Polarized Particles“, Particle Accel. **10**, 177(1989)
[8] P. Kuske, et.al,, “High Precision Determination of the Energy at BESSY II“, EPAC’00, Vienna, June, 2000, p. 1771
[9] R. Müller, et al. “Orbit Drift Correction with Ultra-High DAC Resolution“, to be published, PAC’01, Chicago
[10] C. Steier, et al., “Energy Calibration of the Electron Beam of the ALS Using Resonant Depolarization“, PAC’00, Vienna, p. 1566
[11] P. Kuske, “Emittance Manipulations at BESSY I“, EPAC’98, Stockholm, p. 1297
[12] K. Holldack, et al., „Review of Emittance and Stability Monitoring Using Synchrotron Radiation Monitors“, these proceedings

BREAKING NEW GROUND WITH HIGH RESOLUTION TURN-BY-TURN BPMS AT THE ESRF

L.Farvacque, R.Nagaoka, K.Scheidt, ESRF, Grenoble France

Abstract

This High-Resolution, Turn-by-Turn BPM system is a low-cost extension to the existing BPM system, based on the RF-multiplexing concept, used for slow Closed-Orbit measurements. With this extension Beam Position measurements in both planes, at all (224) BPMs in the 844 m ESRF Storage Ring, for up to 2048 Orbit Turns with 1 micrometer resolution are performed.

The data acquisition is synchronised to a single, flat 1 uS, transverse deflection kick to the 1µs beamfill in the 2.8µs revolution period. The high quality of this synchronisation, together with the good reproducibility of the deflection kick and the overall stability of the Closed Orbit beam allows to repeat the kick & acquisition in many cycles. The subsequent averaging of the data obtained in these cycles yields the 1um resolution.

The latter allows lattice measurements with high precision such as the localisation of very small focussing errors and modulation in Beta values and phase advances. It also finds an unique application to measure, model, and correct the (H to V) Betatron coupling which recently showed successfully the reduction of coupling and vertical emittance below respectively 0.3% and 12picometer.rad. This method takes full benefit from 64 BPM stations situated around 32 straight-sections (no focussing elements) of 6m length allowing the phase-space measurements in their centers.

1 EXTENSION TO THE EXISTING CLOSED-ORBIT BPM SYSTEM

1.1 The 'slow' BPM system for Closed Orbit

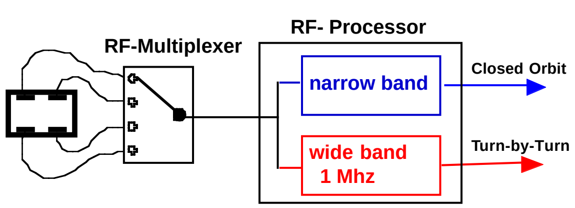

fig.1 the BPM RF-Mux concept with fast & slow output

The C.O. BPM system measures the electron beam Closed Orbit position in the Storage Ring at a slow rate of 1Hz at 224 individual BPM stations evenly distributed in the Storage Ring. This measurement is an average of many turns and taken on all the beam filling i.e. all bunches & electrons. This C.O. BPM system is at the heart of the slow Global Orbit correction scheme that attains the objective of serving the beamlines with a stable positioned beam over time periods of a few seconds to hours, days, weeks and longer [1].

The requirements of notably high reproducibility, low drift and low dependency on beam fill were fulfilled using the concept of RF-Multiplexing. [2,3] Each BPM station scans the 4 signals from the electrode buttons by an RF-Multiplexer device and performs all the signal conditioning operations (filtering, amplification, detection, digitization) on the 4 time-multiplexed signals by a single RF Processor. (see fig.1) This offers the advantage of high immunity to variations of characteristics (gain, linearity, offset) of the Processor electronics (since it affects the 4 signals equally). However, the drawback is that the slow scanning (millisec) does not allow to measure a beam position on a single beam turn (microsec).

Nevertheless, the Processor possesses 2 channels of signal conditioning : 1) a narrow band, low noise channel, and 2) a wide band (1MHz) for fast signals (1µs). With the latter a single turn can be detected, but only on one electrode at a time. Consequently a position measurement needs 4 separate cycles. It is in this way that First-Turn BPM measurements after injection have been performed to satisfaction with the existing system.

After careful analysis of the applications that the Turn-by-Turn BPM system would fulfil it was concluded that in a similar way the position data on a large number of turns could be obtained.

1.2 a 'pseudo' Turn-by-Turn beam position measurement system

A wealth of information can be obtained on the beam characteristics and machine parameters by measuring the beam position on a turn-by-turn basis after the application of a single deflection kick. [4-15]

Note that the measurement is to be synchronised with this deflection kick. If this synchronisation is precise and if this kick is of good reproducibility then the measurement can be performed in 4 distinct cycles (1 for each of the 4 electrodes). Moreover, each cycle may itself be repeated a large number of times. The individual measurements can be averaged which then improves the resolution of the results. It is essential that the beam is otherwise stable during the whole measurement sequence. It is obvious that the system is a 'pseudo' turn-by-turn system since the data is acquired over many cycles during a time much longer then N x revolution time. However, this has no effect on the information that the system yields, i.e. turn-by-turn beam position after an applied beam excitation, since the beam excitation and the data acquisition are intimately synchronised, and therefor reproducible & repeatable.

1.3 Hardware & Software additions :

The extension had to be realised without interfering with the existing BPM system that permanently serves the slow orbit correction. Since the RF electronics would be untouched the main hardware additions are :
- a data acquisition card (32 units) that digitises pulsed signals at 355Khz rate (upto 2048 turns) and performs an internal averaging (up to 4096).
- a synchronisation / timing network between the beam, the kick and 32 data-acquisition cards.

The software for driving and reading these devices was added with full compatibility with the existing system. A user-level application permits the setting of the parameters like number of turns and averaging.

The quality (stability) of the synchronisation is about 50ns. Also, due to difference in RF cable lengths, relative time delays (up to 120ns) exist between the 7 BPMs in one cell (digitised by the same card). Avoiding the slightest impact on the precision (and resolution) of the system by these time differences and timing (in-)stability implied the following conditions :
a) The beam-fill is partial up to a maximum duration of 1µs. b) The beam-kick is flat and uniform over the whole of the beam-fill. c) The data acquisition card incorporates a track & hold function of the peak input signal.

1.4 The Beam Deflection Kick

For the deflection kick in the horizontal plane one of the four injection kickers could readily be used. They offer the advantage of delivering a flat & clean single kick of 1µs that is adjustable in strength with a maximum >10mm rms. These kickers have a negligibly small component in the vertical plane and equally negligible parasitic kick on the next beam passage (2.8µs). The injection kickers however are limited in repetition frequency to 10Hz.

For kicks in the vertical plane a HV pulser was implemented to an existing fast ferrite shaker (used for tune measurements). Its kick amplitude is limited to 0.5mm rms but the repetition frequency can be > 100Hz.

2 RESULTS : HIGH RESOLUTION

2.1 Resolution vs. acquisition-time and current

The measurement time of the system is obtained by multiplying the number of averages with 4 (for the 4 electrodes) and dividing by the repetition frequency. For a beam current of 10mA (in 1µs beamfill) a resolution of 2µm is reached for an averaging of 256 (typically used). This value can easily be assesed by analysing the standard deviation of the position measurements on a number of turns (typically 16) before the kick is applied to the beam. The measurement time here is 103sec for a 10Hz repetition freq. (with injection kicker) or 10sec at 100Hz (with vertical shaker device).

The resolution varies square-root with the number of averaging and the beam current. Because of the use of switchable attenuators in the RF processors the resolution in the 0.5mA to 10mA beam current range is about the same as for the 10 to 200mA range.

However, this assesment only quantifies the noise (or resolution) of the data acquisition system, and not the contribution of fluctuations or imperfections of the beam deflection kicker. A way to estimate the resolution of the whole system is to construct phase-space diagrams and to compare the individual measurement points to a fitted phase-space ellips. The BPM distribution in the Storage Ring has 64 BPMs situated at the extreme ends of the 32 straight-sections (see figure 3). Separated 6.1meters they offer the possibility of drawing phase-space plots in the middle of these sections and to compute the optical functions. If the Storage Ring is operated at low chromaticity then a sufficient number of turns (e.g. >30) can be measured at a practically constant oscillation amplitude (i.e. negligible damping). The figure 2 here below shows a typical example in one of these straight sections of 70 phase-space points obtained with a 10µm vertical kick at 100Hz with an averaging of 1024.

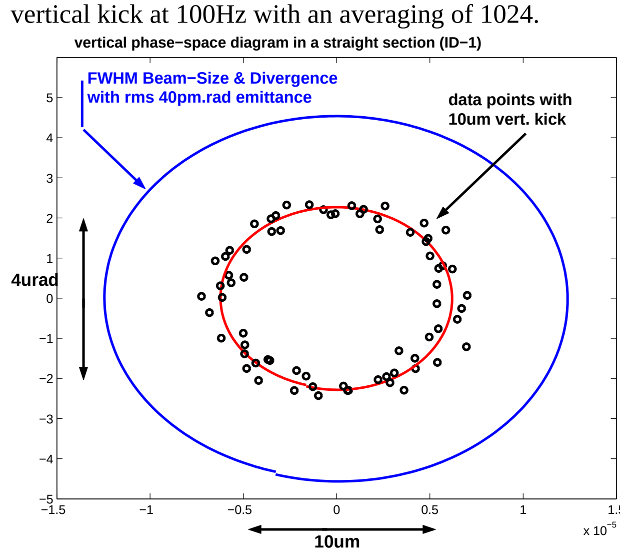

The comparison of these points to the (red) ellips fitting indicates a resolution of about 1µm. Note that the large (blue) ellips represents the ESRF vertical beam-emittance (FWHM) with the standard operation of 1% coupling (40pm rms). This clearly shows that the system is capable of measuring phase-space plots that are a fraction of the ESRF's small vertical beam emittance.

The calibration errors of the BPMs was assesed by comparing the 32 invariants that can be computed in the straight sections, and found to be less than 2%.

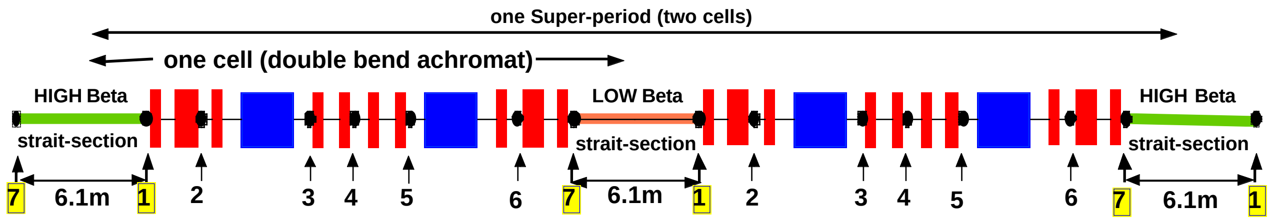

fig.3: the position of 14 BPMS in a 2-cell super-period with 2 BPMs at the extreme ends of all the straight-sections

3 APPLICATIONS AND RESULTS

3.1 Linear Optics

The first use of the Turn-by-Turn BPM system is to study the linear optics of the machine. This requires a small excitation of the beam so that the non-linearities of the motion are negligible. Given the resolution of ~2 µm of the BPMs, this is usually done with an rms. beam excitation of 200 to 300 µm.

Phase advance

The phase advance φ between BPMs is obtained by computing for each BPM the spectral amplitude and phase of the motion on the tune frequency. The average phase advance $\overline{\varphi}$ is computed by taking the average of the phase advances per superperiod. and the phase modulation is defined as $\Delta\varphi = \varphi - \overline{\varphi}$.

β-functions

The layout of the BPMs is such that in the 32 straight sections of the Storage Ring, we have 2 monitors, separated by 6.1 m without any intermediate magnetic element (fig.3). In such conditions, we can obviously get a phase-space plot of the beam trajectory in the middle of the straight section, from which we extract the Twiss parameters α and β, and the invariant of the motion of the kicked beam. This is independent of any calibration of the BPMs and kicker. The comparison of the 32 invariant values from the different straight sections shows the calibration errors in the different monitors. [16] Another method for extracting the β-functions is to scale the spectral amplitude of the motion on the tune frequency. This may be applied on each BPM. Combining both methods by adjusting the scaling factor to match the phase-space values gives the β-function on each BPM. The β-modulation is defined as $\Delta\beta = \left(\beta - \overline{\beta}\right)/\overline{\beta}$, with $\overline{\beta}$ is the average over all superperiods.

Focusing errors.

Focusing errors such as quadrupole length or gradient errors, or sextupole horizontal misalignment result in a modulation of the phase advances and β-functions. This appears on the results of MT-BPM analysis. [17] The method was tested by introducing arbitrarily a single focusing error with a quadrupole corrector magnet. The resulting tune shift was 0.006, and the error represents 2.10^{-3} of gradient error in the strongest quadrupole. Fig.4 shows the difference in phase advance with and without the error: such an error is well within the sensitivity of the method.

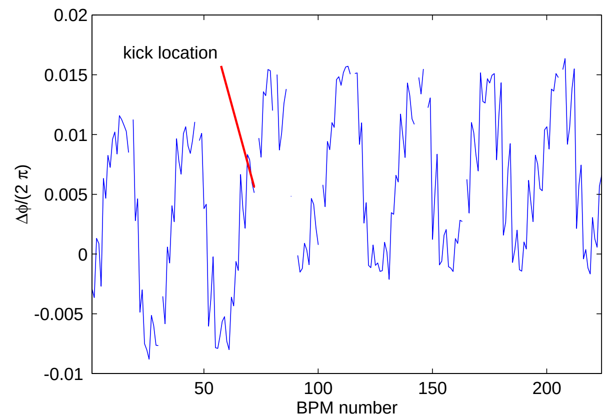

Fig.4: difference in phase-advance with a single focusing error

This was applied to draw the phase modulation with and without the resonance correction applied: Fig.5 shows that the resonance correction is indeed effective. The comparison with a similar data coming from the analysis of the response matrix of the Storage Ring shows an excellent agreement.

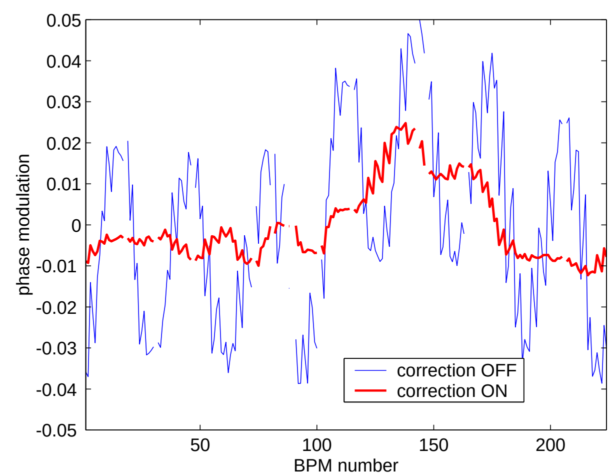

Fig. 5: phase modulation with and without correction

This was also used to try and identify the sources of multibunch detuning as a function of beam current.

Betatron coupling

By making full use of the excellent measuring accuracy provided by the system, an attempt was made to measure the betatron coupling through the normal mode decomposition [18]. The advantage of this method is clearly in its comprehensive description of the betatron coupling as opposed to those due to particular resonances, which has been found to be of great importance at the ESRF in achieving ultimately low couplings [19]. Although the quantity of interest for a light source such as the ESRF is the emittance coupling rather than the betatron coupling, it has been found that the latter counts for the major part of the former at the ESRF. The developed steps for the decomposition are as follows: For each straight section that has no focusing element in between two BPMs, 1) Construct the phase space (x, x', z, z'). 2) Fit the phase space data to extract a 4×4 one turn matrix. 3) Perform the normal mode decomposition to obtain the normal modes as well as the rotation matrix that transforms the geometric modes to the former.

The second step was found to be the most non-trivial, especially as the number of available turns is severely limited by the strong decoherence of the beam, which comes from tune shifts with amplitude, with momentum (chromatic modulation), as well as from the head-tail damping. To minimise them, measurements were made with a low beam current in 1/3 filling, a small oscillation amplitude given by a horizontal injection kicker, and a sextupole setting that gives zero chromaticities and minimal tune shift with amplitude. It turned out nevertheless that measured readings are sufficiently free from the decoherence effects only in the first few tens of turns. Since the matrix can be obtained using only 4 independent turns, the data over the first 20 turns were used to increase the precision through averaging. It was also found important in many cases to impose the symplectic condition to be fulfilled by the one turn matrix, to extract more ambiguous off-diagonal elements due to smallness of the vertical amplitudes.

The correctness of the results can be readily seen in the decoupling of the two normal modes (Figs. 6), as well as in constancy of the normal mode ellipses around the machine. The application was successful over the entire range of coupling, surprisingly down to the lowest coupling, where the vertical emittance of 8 pm.rad (~0.2% emittance coupling) was measured with a pinhole camera. Note that the corresponding normal mode phase space ellipse (Figs. 6 lower) measured has even a smaller magnitude than the vertical emittance. In fact, it was found that the decomposition at the ultimately low coupling requires a perfect machine stability and fails as soon as the beam is perturbed by external noises.

Although the ratio of the two normal mode ellipses in most cases closely followed the measured emittance coupling, it depends on the initial condition. The magnitude of off-diagonal elements in the rotation matrix, instead, represents the local coupling of the machine. The present scheme thus opened a new possibility of coupling correction with two advantages, one that the coupling can be measured at all ranges, and the other that it enables a global correction. At the ESRF, the response matrix approach, despite offering an accurate model of the coupling, could only measure the initial large coupling, and smaller couplings had to be measured with pinholes, which are located at only two positions in the ring. The first tests showed positive results, managing corrections in both high and low coupling regimes.

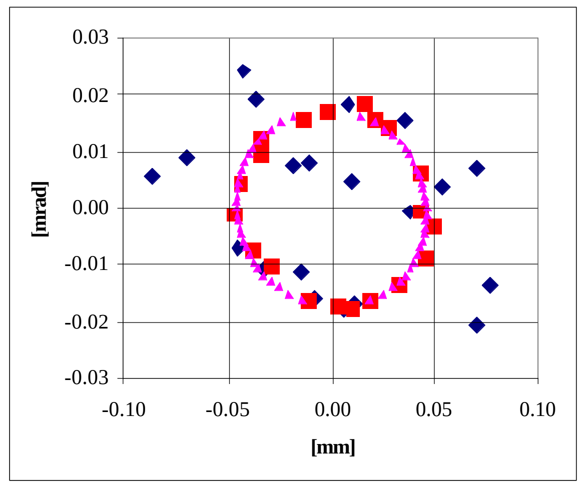

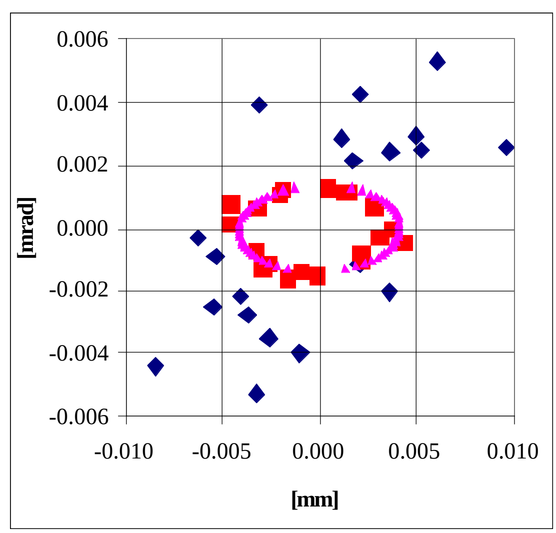

Fig.6: Two examples of decomposition showing the transformation from the vertical phase space (blue) to the normal mode (red), and triangles (pink), the fit of the normal mode. Upper: The standard operation setting (30 pm.rad vertical emittance). Lower: The lowest coupling (8 pm.rad vertical emittance).

3.2 Non-linear optics

The MT-BPM system was also used to measure tune shifts with amplitude [20]. We need here larger kicker excitations. The oscillation is then damped in a shorter time because of the decoherence resulting from the tune dependence with amplitude within the bunch. The amplitude is measured by the invariant coming from phase-space analysis, the tune is given by the spectral analysis, both being taken over the first 20 turns only. The figure 7 shows a typical measurement for 3 different sextupole tunings.

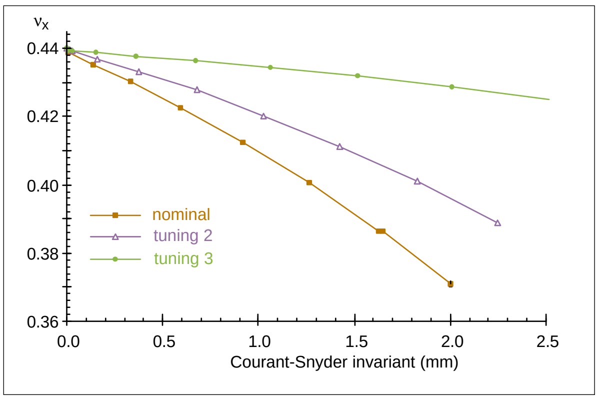

Figure 7: tune shifts with amplitude

4 CONCLUSION & FUTURE

The high resolution Turn-by-Turn extension has been implemented at a minimum cost and without any interference with the existing Closed Orbit BPM system. The system concept takes full advantage of the good reproducibility of the beam deflection kick and the stable synchronisation between this kick, the beam and the data acquisition system, allowing to repeat individual measurement cycles and to achieve micrometer resolution by averaging.

This has been used to study with precision and in detail the linear optics of the SR Machine and to model the betatron coupling to very small values. It is also a valuable tool for measurements of non-linear optics and the studies of injected beam conditions for which its application is planned in the near future.

ACKNOWLEDGEMENTS

The authors would like to thank J.Cerrai and Ph.Chappelet for the digital hardware developments and M.C.Dominquez and J.L.Pons for the writing of the device-servers and application software.

REFERENCES

[1] L.Farvacque "Beam Stability" CERN Accel. School on synchrotron radiation source and FELs, Grenoble 1996
[2] K.Scheidt, F.Loyer "Electron Beam Position Monitors : Performance Considerations", DIPAC-93, Montreux, May 1993
[3] G.Vismara "The Comparison of Signal-Processing for Beam Position Monitors", DIPAC-99, Chester UK, May 1999
[4] A.Hofmann "beam diagnostics and applications", BIW-98, Stanford,C.A. May 1998
[5] J.Borer et al.,"Harmonic Analysis of Coherent Beam Oscillations in LEP", EPAC-92, Berlin 1992
[6] A.Burns et al., "Betatron Function Measurment at LEP using the BOM 1000 Turns Facility", PAC-93, Washington D.C. 1993
[7] G.Morpugo, "The BOM 1000 Turn Display : a tool to visualise transverse Phase-Space Topology at LEP", EPAC-98, Stockholm
[8] P.Castro, "Applications of the 1000-turns Orbit Measurement System at LEP", PAC-99, New-York, 1999
[9] J.Klem et al., "Multiturn measurements at the CERN SPS", EPAC-2000, Vienna, June-2000
[10] J.Klem and G.Morpugo "a method to measure the Beta-beating in a 90 deg. phase-advance lattice", EPAC-2000, Vienna, June-2000
[11] K.T.Hsu et al., "functionality enhancement of the multiplexing BPM system in the storage ring of SRRC", this DIPAC-2001 proceedings Grenoble May-2001
[12] M.Lamont, G.Morpugo, H.Schmickler "Practical Diagnostic Measurements" Beam-Measurement Joint-CERN Accelerator School, Montreux May 1998
[13] F.Zimmerman, "Measurement and Correction of Accelerator Optics", Beam-Measurement Joint-CERN Accelerator School, Montreux May 1998
[14] K.Scheidt, "Diagnostics : Mille-Tours BPM system", ESRF-Machine Workshop Sassenage, Jan-2000
[15] R.Nagaoka, "Beam Studies with 1000-Turns BPMs", ESRF-Machine Workshop Sassenage, Jan-2001
[16] L.Farvacque, ESRF-Machine tech.note 1-00/Theory, Jan.2000, "Processing of 1000-Turn BPM system"
[17] L.Farvacque, "Modélisation des erreurs de couplage et de focalisation", Journées Accélérateurs de la SFP Roscoff, March-2000
[18] D. Edwards and L. Teng, "Parameterization of Linear Coupled Motion in Periodic Systems", IEEE Transactions on Nuclear Science, NS-20, No. 3, June 1973.
[19] R.Nagaoka, "Work carried-out at the ESRF to Characterise and Correct the Coupling", EPAC-2000, Vienna, June-2000
[20] A.Ropert, "Measurements of the Lattice Characteristics with the 1000-Turn BPM system", ESRF-Machine tech.note 08-00/theory, May-2000.

OVERVIEW OF RHIC BEAM INSTRUMENTATION AND FIRST EXPERIENCE FROM OPERATION *

P. Cameron, P. Cerniglia, R. Connolly, J. Cupolo, C. Degen, K. A. Drees,
D. Gassner, M. Kesselmann, R. Lee, T. Satogata, B. Sikora, R. Witkover
Brookhaven National Laboratory, Upton, NY, USA

Abstract

A summary of the beam instrumentation tools in place during the year 2000 commissioning run is given including the technical layout and the appearance on the user level, here mainly the RHIC control room. Experience from first usage is reported as well as the lessons we have learned during RHIC operation so far. Upgrades and changes compared to the year 2000 systems are outlined. Described tools include beam position monitors (BPM), ionization profile monitors (IPM), beam loss monitors (BLM), bunch current measurements, luminosity monitors, tune meters and Schottky monitors.

1 INTRODUCTION

The **R**elativistic **H**eavy **I**on **C**ollider (RHIC) is the new accelerator flagship at Brookhaven National Laboratory on Long Island, NY (USA). The two super-conducting rings are built in the 3.8 km long tunnel originally constructed for the ISABELLE project. RHIC has 6 interaction regions where the two beams - “blue” circulating clockwise and “yellow” counter-clockwise - collide with zero crossing angle. Four are equipped with experiments. Table 1 summarizes some of the major collider parameters.

One of the major goals of the RHIC project is to discover and study the quark-gluon plasma, a very hot and dense state of matter believed to have existed a fraction of a second after the Big Bang. For this purpose, RHIC is designed to operate with various ions, from gold to lighter species such as copper, oxygen or silicon. In addition RHIC can accelerate polarized proton beams. The combination of polarization, luminosity, and beam energy to be found in RHIC will open exploration of a new and theoretically interesting regime in high energy spin physics.

RHIC instrumentation systems [1, 2] monitor diverse beams of up to 60(120) bunches in each of the two collider rings. Intensities range from low-intensity commissioning and pilot bunches to 10^{11} protons/bunch at 250 GeV and 10^9 Au^{+79} ions/bunch at 100 GeV/nucleon.

The major challenge to Instrumentation during the year 2000 commissioning run was to provide adequate diagnostic information during the acceleration ramp. While the main dipole and quad bus power supplies were well behaved, there were regulation problems in the shunt supplies (these problems grew out of late vendor deliveries, and are

Parameter	Value	Unit
Circumference	3833.845	m
Beam energy (Au)	10.2 - 70 (100)	GeV/u
Beam energy (p)	28.3 - (250)	GeV
Revolution Frequency	78	kHz
Revolution Time	12.8	μs
RF frequency	28 (200)	MHz
# of filled buckets	60	
Bunch separation	220	ns
Luminosity	0.2 (2) 10^{26}	$cm^{-2}sec^{-1}$
Betatron tunes (x/y)	0.22/0.23 (0.19/0.18)	
horiz. ϵ_{nor} (*)	10-20	π mm mrad
vert. ϵ_{nor} (*)	10-15	π mm mrad
β^*	3,8 (1,10)	m
Number of ions/bunch	5 10^8 (1 10^9)	

Table 1: *Basic RHIC parameters during the year 2000 commissioning run. Design values, if different from commissioning run values, are added in brackets.((*): measured)*

corrected for the year 2001 run) that caused tune and orbit to drift up the ramp. The effect of orbit drift at the beginning of the ramp was aggravated by poor sextupole power supply regulation at the extreme low currents required at injection, as well as by the compensation required for snapback. In addition, during acceleration of Gold the beam must pass thru transition. Transition crossing was complicated by the absence of power supplies for the gamma jump, which led to the use of a radial jump for transition crossing, and tune shifts proportionate to chromaticity. All of the above suffered the additional complication that the machine was not fully repeatable, that ramps with apparently identical initial conditions often produced radically different results. Despite these difficulties, but not without considerable effort, the machine was successfully commissioned and good experimental physics data was gathered.

2 BEAM POSITION MONITORS

The BPM electrode assemblies [3] operate at 4.2 K. The collider ring contains 480 BPM assemblies plus additional units for spin rotators, Siberian snakes, and beam dumps. Tight constraints on orbit relative to quadrupole centers are imposed during polarized proton acceleration, to minimize the strength of spin resonances. The relative locations of BPM electrical centers and quadrupole magnetic centers

* Work performed under the auspices of the U.S. Department of Energy

was measured for all BPMs with an estimated accuracy of approximately 100 μm RMS, and beam positions are corrected with this database.

2.1 BPM Electronics

Each channel of BPM electronics employs a broadband sampler [4]. The basic design is depicted in Figure 1. All measurement planes are treated independently; dual-plane assemblies are connected to two independent electronic channels. Two channels are contained within each BPM integrated front-end (IFE) module. Channels in the ring insertion regions, injection area, and dump area are cabled to accessible equipment buildings in up to 150-meter runs. All other ring modules are located in cryogenic areas of the tunnel and cabled to the appropriate electrodes with shorter, 2-meter cables. The low vacuum minimizes beam-gas scattering and the resulting radiation field at the electronics.

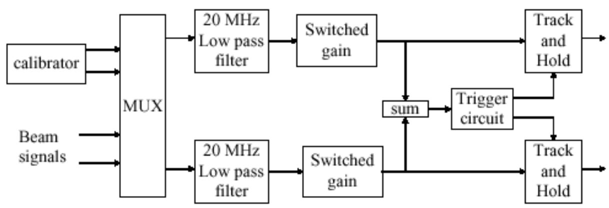

Figure 1: BPM electronics sampler design

Variable gain of 0, 20 or 40 dB is available. A high-impedance sum circuit provides the input to a self-trigger circuit. The trigger threshold is adjustable and self-trigger can be completely disabled to allow external clocking. In RHIC a selected bunch is sampled turn-by-turn at the revolution frequency of 78 kHz. There is no provision for simultaneous multi-bunch acquisition with a single BPM plane. Each sampler resides on a circuit board that also contains an FPGA-based timing decoder, DSP-based signal processing, and IEEE-1394 interface. [5]. The control system communicates with the channels via shared memory in a VME/Firewire [6] interface board. Up to 12 channels are connected to each interface board. The channels can operate in different modes. During injection, a turn-by-turn record of 128 turns for each injected bunch was collected. For the rest of the collider cycle, the channels periodically sent a turn-by-turn record for a particular bunch, and simultaneously streamed 10-kiloturn averaged and RMS position data at 0.25 Hz. For the next run the turn-by-turn record is upgraded to 1024 turns. Depending on gain setting and beam intensity, the BPM single measurements with a resolution of $1\mu m$ yield an accuracy of $20 - 50\mu m$ while the average orbit accuracy is of the order of $5\mu m$.

Among other things, data from the BPM system was used to accomplish remarkably good measurements of betatron functions[7], and in and in the orbit correction system[8].

3 BEAM LOSS MONITORS

3.1 Ion Chambers

The primary function of the RHIC ring BLM system[9, 10] is to prevent a beam loss induced quench of the superconducting magnets. BLMs also provide quantitative loss data for tuning and loss history in the event of a beam abort[11]. Due to the various magnet quench scenarios, RHIC BLMs have to cope with a range of signal currents from 5.5 mA for the injection fast loss level to 17.6 nA for a slow loss quench at full energy. This results in a dynamic range of 8 decades in detector current. The amplified signal is continuously compared to programmable fast and slow loss levels that can cause a beam abort, when data acquisition is halted to provide a 10 second history of the pre-abort losses. BLM parameters are adjusted during injection, magnet ramp, and storage phases to set gains, fast and slow loss thresholds, and abort mask bits on specific RHIC event codes.

The Detectors The BLMs are modified Tevatron ion chambers [12] with improved radiation hardness. The ion chamber [13] consists of a 113-cc glass bulb filled with argon. Half of the ion chambers are mounted between the two RHIC rings on the quadrupole cryostats. 96 BLMs are placed at insertion region quads. In the warm regions, 68 detectors are mounted on the beam pipe at expected sensitive loss points. In addition, 38 BLMs are available as movable monitors. In 1999 the BLM system could successfully be used to locate aperture limits (such as broken bellows shield fingers).

Electronics and Data Acquisition The electronics are located in service buildings, allowing access during beam storage. Since the ring BLM system is used for quench prevention, redundancy is provided by separate HV power supplies. In addition the power supplies are monitored by the RHIC alarm system. Readings can be taken at additional times as required for specific applications. Different gain settings compensate for the increased magnet quench sensitivity with current. Signals are directed to respective fast or slow loss comparators with independent programmable references. Each comparator can be masked to prevent a bad BLM from inhibiting the beam or to allow special conditions. The gains, mask bits and trip levels may be changed by events on the RHIC Event Link. A micro-controller [14] allows the BLM system to continue to provide beam loss quench protection even in the event of a controls failure.

3.2 PIN Diodes

A total of 16 PIN diodes [15, 16] are employed as fast, sensitive, cheap and easy to install loss monitors in the vicinity of the collimators in both rings. Arrays of 4 diodes surrounding the beampipe are installed downstream of the blue and yellow beam scrapers. In the yellow ring an additional array of 8 diodes is installed upstream of the scrapers, approximately 5m downstream of the crystal collimator. All diodes are readout by VME based scaler boards situated outside the ring.

4 BEAM INTENSITY MONITORS

4.1 DCCT

A DCCT for each ring was purchased from Bergoz. The unit has remotely switchable 50 and 500 mA maximum current ranges. The unit was specified with 75-meter long cables to allow front-end electronics to be removed from the RHIC tunnel. However, preliminary tests indicate that the modulator noise is more than an order of magnitude greater than with the standard 3-meter cables. This noise is not a problem when viewed on the electronics low-pass output, or when the wide-band output is integrated over 30 msec or more, but higher frequency measurements are affected. Because the modulation is regular, the high oversampling makes it possible to digitally filter much of this noise. The BCMs are located in the warm region of the 2 o'clock sector, which will be baked to 130 C. The BCM housing has been designed to insulate the transformer core from the heated beam pipe and prevent it from exceeding 60 C. Thermocouples on the detector are used to interlock the heater blanket. The outer shell of the housing provides the bypass path for the wall current around the transformer. Beam intensity information is used in a number of ways which set different requirements on the data.

4.2 Wall Current Monitor

The wall current monitor system [17]incorporates ferrite-loaded pickups based on the design by Weber [23]. One pickup is installed in each ring. The ferrite has been selected to attain flat frequency response down to 3 kHz with a transfer impedance of 1 Ω. The response extends to 6 GHz, which is well above pipe cutoff. Microwave absorber installed on either side of the pickup attenuates interfering modes. A LeCroy scope with a bandwidth of 1 GHz digitizes in 8 Gsa/s bursts with trigger rates up to 30 kHz. The scope is controlled and read out over GPIB by a computer running LabVIEW. The RHIC control system communicates with this application via shared memory on a VME/MXI interface board. The entire system is event-driven and synchronized by the RHIC beam synch clock. The two basic functions provided by the WCM are bunch fill pattern and bunch profile. In fill pattern mode the WCM delivers integrated charge per bucket (360 buckets at injection, 2520 at store) and total charge. In bunch profile mode it delivers longitudinal profile of a single bunch as well as centroid relative to the bucket, typically in a waterfall display with 3 turn minimum interval, and calculated parameters such as bunch length and peak current. Since the WCM is sensitive to bunched beam only while the DCCT monitors the total circulating current, the difference between the two devices is used to detect and monitor debunched beam currents in RHIC.

The DCCT and WCM were useful for measurements of beam lifetime and emittance growth [18, 20], intra-beam scattering [19], and non-linear momentum compaction [21]. The WCM was particularly useful for transition studies.

5 IONIZATION PROFILE MONITORS

The ionization profile monitors (IPM) collect electrons that are produced as a result of beam-gas interactions [24]. Two monitors are installed in each ring, one horizontal and one vertical.

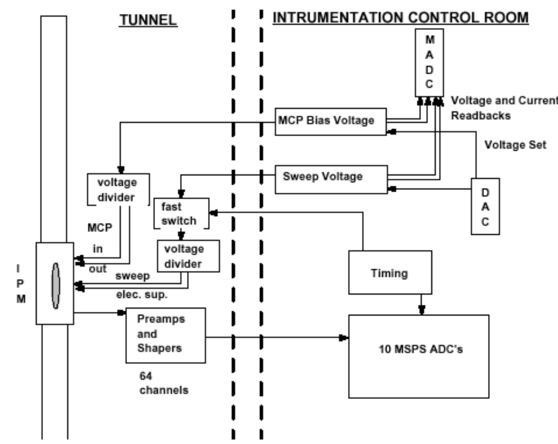

Figure 2: Block diagram of the IPM system

With 10^9 Au^{+79} ions/bunch, beam width measurements were expected to be accurate to 3%, and with a single bunch in RHIC good profiles were obtained. However, ringing caused by image current effects made the IPMs practically useless for operations. The addition of shielding and modified grounding should remedy this problem for the year 2001 run [22].

The system block diagram is shown in Figure 2. All timing is controlled by the beam synchronous event system. The 10 Msample/s, 12 bit ADCs consist of 8 channel VME boards with 128 ksamples of memory behind each channel. These digitizer boards and the timing board reside in the control system front-end computer.

Data gathered by the IPM was used for injection matching and in emittance growth measurements [18, 20]

6 TUNE METER

6.1 ARTUS

At RHIC the first generation tune measurement device, ARTUS [25, 26], consists of a fast horizontal and vertical kicker magnet and one dual-plane BPM per ring. To measure the machine tunes, betatron oscillations are excited with a fast transverse kicker magnet [27] and transverse beam positions are recorded from the BPM. The fractional tunes are extracted from the position data by performing a FFT analysis. The capability of multiple turn-by-turn kicks ensures decent signal amplitude at all beam energy settings. The readout electronic developed for the dedicated BPM and the control system is installed in a VME crate outside the ring.

The Transverse Kicker Each ring has two kicker modules with four 2-m stainless steel striplines, allowing both horizontal and vertical kicks. The two kickers are connected in series to provide 4 m of stripline kickers. Each stripline subtends an angle of 70°at an aperture of 7 cm. Single pulses can power each of the four planes independently. The kick pulses are generated by fast FET switches [28] producing an approximately 140 ns long pulse. Single bunch excitation is possible with even up to 120 bunches per ring. All switches for all striplines in both rings are charged by one 5kV/2A power supply.

Trigger and Data Acquisition The FET switches are triggered by a TTL pulse of 200 ns width from a numerically-controlled oscillator (NCO) board. The two opposing kicker striplines for each plane are driven by one NCO channel. Thus both striplines are fired in accordance with the set frequency resulting in kicks with positive and negative signs. By selecting a NCO frequency close to the horizontal and vertical betatron frequency the beam is kicked resonantly enhancing the effect on the beam significantly if compared with a single kick. The enhancement factor was estimated to be of the order of 10 for a limited number of kick pulses. However, a set point equal or very close to the betatron frequency was shown to kick the beam out of the ring if the number of turns was too high. Tune measurements with ARTUS along the ramp have been successfully used as a feed forward correction to compensate for the large tune swings in RHIC.

6.2 Phase Locked Loop

During the year 2000 run a prototype Phase Locked Loop tune measurement system was operated. During beam store tune was continuously tracked with a precision of a few parts in 10^{-4}. The beam was excited with about 50 microwatts of power driving the tune kicker mentioned above. Emittance was monitored with good sensitivity by observing the power in the transverse Schottky signal. There was no observable emittance growth. The pickup was a movable BPM [29]resonated in difference mode with a Q of about 100 at a frequency of 230MHz. Schottky signals were also observable with this pickup. Using a resonant pickup above the coherent spectrum (acceleration RF is 28MHz) permits the low kicker power, and removes the beam-synchronous timing requirement. This system is evolving from prototype to operational status. It is hoped that after the PLL is operational the measured tunes can be used to drive the RHIC quadrupole buses [30], keeping the tunes at desired values all the way up the ramp.

7 LUMINOSITY MONITORS

Luminosity is monitored using a sampling Zero Degree Calorimeter (ZDC) [31] with two arms, one on either side of IR2, IR6, IR8 and IR10. The calorimeters are designed to measure neutrons emitted from nuclear fragments from Au+Au collisions that missed the actual interaction zone. The inclusive correlated emission in each beam direction is used to suppress many kinds of backgrounds and corresponds to a large cross section in the order of 10 b [32, 33].

The ZDC with a total length of about 0.7 m consists of alternating absorber and Cerenkov fiber layers. Crossing particles within a limited angular cone produce Cerenkov radiation which is channeled in the fiber ribbons to a photo multiplier tube (PMT). The detector arms are located at about +/- 18 m from each of the four equipped interaction points subtending an angle of about 2.5 mrad of the forward direction. The warm section between the DX and D0 magnets allows the installation of the ZDC modules between the two beampipes limiting the transverse size of the calorimeter to about 11 cm. The detector location is illustrated in Fig. 3.

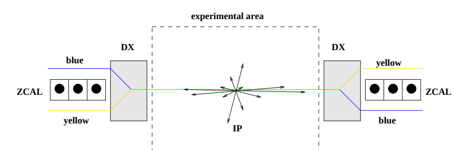

Figure 3: Geometry of the interaction region showing the beam splitting dipoles (DX) and the ZDC position.

At RHIC the ZDCs are both, monitors of the the collision rates at the four IRs and part of the experimental detectors, mainly the trigger system. Having the same design in each experiment the ZDCs are especially well suited to give comparable results everywhere. To guarantee comparability the readout electronics is identical in all IRs and split into two paths: one is leading to RHIC control system, the other is input to the experimental trigger.

8 SCHOTTKY

With the 17dB advantage in signal-to-noise ratio enjoyed with Au beams relative to protons, the Schottky spectrum is an extremely valuable source of information at RHIC. Two high-frequency cavities from Lawrence Berkeley National Laboratory [34] are used to detect longitudinal and transverse Schottky signals from both beams. The transverse modes of interest are the TM210 and the TM120 at about 2.1 GHz. These two modes have a measured Q of about 4700 and are separated by 4 MHz. A longitudinal mode is at 2.7 GHz. The signals are down-converted to 2 MHz and amplified in the tunnel, then transported on 7/8” solid shield coax to a 10 MHz bandwidth FFT analyzer outside the ring.

Data is provided to the control system through LabVIEW communicating with the FFT analyzer via TCP, as well as through a remote Xterm scope application. During the year 2000 run this was primarily a specialist system. Considerable effort is being devoted to making the system more operator accessible, and to improving the interface to the control system.

During the beam run the Schottky system was useful for measuring tune and chromaticity up the ramp, and particularly at transition. In addition, non-linear momentum compaction was calculated [21] from the measurement of small variations in the frequency of synchrotron satellites near transition. Despite the comparatively poor S/N ratio relative to Au, during polarized proton running the Schottky system provided stripchart displays of tune, chromaticity, momentum spread, and transverse emittance during beam stores. [35]

9 REFERENCES

[1] "RHIC Design Manual", April 1998.

[2] T.J. Shea and R.L. Witkover, "RHIC Instrumentation", *Proc. 98 Beam Instrumentation Workshop*, 1998.

[3] P. R. Cameron, et al., "RHIC Beam Position Monitor Characterization", *Proc. 95 Particle Accel. Conf.*, 1995, p. 2458, IEEE Cat. No. 95CH35843.

[4] W. A. Ryan and T. J. Shea, "A Sampling Detector for the RHIC BPM Electronics", *Proc. 95 Particle Accel. Conf.*, 1995, p. 2455, IEEE Cat. No. 95CH35843.

[5] T.J. Shea, J. Mead, C.M. Degen , "DSP Based Data Acquisition for RHIC", *Proc. 95 Particle Accel. Conf.*, 1995, p. 2448, IEEE Cat. No. 95CH35843.

[6] T. J. Shea, et al., "Evaluation of IEEE 1394 Serial Bus for Distributed Data Acquisition", presented at the 1997 Particle Accelerator Conference, Vancouver, BC, May 1997.

[7] D. Trbojevic et al., "Measurements of the Betatron Functions in RHIC", to be published in PAC 2001.

[8] V. Ptitsyn et al., "The RHIC Orbit Correction System", to be published in PAC 2001.

[9] "RHIC Beam Loss Monitor System Commissioning in RHIC Year 0 Run", P. Thompson, M. Bai, T D'Ottavio, D. Gassner, R. Michnoff, T. Russo, D. Shea, R. Witkover, Proceedings of the BIW2000 Workshop, Cambridge, p 313-321.

[10] R.L. Witkover et al., "RHIC Beam Loss Monitor System Initial Operation", Proc 1999 PAC p 2247.

[11] L. Ahrens et al., "Performance of the RHIC Abort System during the Year 2000 Beam Run", to be published in PAC 2001.

[12] R. E. Shafer, et al., "The Tevatron Beam Position and Beam Loss Monitoring Systems", *Proc. 12th International Conference on High-Energy Accel.*, Aug 1983, p. 609.

[13] Troy-Ionic Inc., 88 Dell Ave, PO BOx 494, Kenvil, NJ 07847.

[14] R. Michnoff, "V118 RHIC Loss Monitor Controller Module System Specification", http://www.rhichome.bnl.gov/Hardware/lossmon1.htm, September 1996.

[15] W.Bialowons, K. Wittenburg, F.Ridoutt, "Electron Beam Loss Monitors for HERA", Proc. EPAC 1994, LONDON.

[16] K. Wittenburg, "Preservation of beam loss induced quenches, beam lifetime and beam loss measurements with the HERAp beam loss monitor system", NIM A 345 (1994) 226-229.

[17] P.R. Cameron et al., "The RHIC Wall Current Monitor System", *Proc. 99 Particle Accel. Conf.*, 1999, p. 2146, IEEE Cat. No. 99CH36366.

[18] W. Fischer et al., "Beam Growth Measurements in RHIC with Gold at Injection", BNL Accelerator Physics Note C-A/AP/44, Mar 2001.

[19] W. Fischer et al., "Beam Lifetime and Emittance Growth Measurements of Gold Beams in RHIC at Storage", to be published in PAC 2001.

[20] W. Fischer et al., "Measurement of Intra-Beam Scattering Growth Times with Gold Beam below Transition in RHIC", to be published in PAC 2001.

[21] M. Blaskiewicz et al., "Measuring Nonlinear Momentum Compaction in RHIC", to be published in PAC 2001.

[22] R. Connolly et al., "Performance of the RHIC IPM", to be published in PAC 2001.

[23] R.C. Weber, "Longitudinal Emittance: An Introduction to the Concept and Survey of Measurement Techniques Including the Design of a Wall Current Monitor", *AIP Conf. Proc.* **212**, 1989, p. 85.

[24] R. Connolly, P. Cameron, W. Ryan, T.J. Shea, R. Sikora, N. Tsoupas, "The RHIC Ionization Beam Profile Monitor", *Proc. 99 Particle Accel. Conf.*, 1999, p. 2114, IEEE Cat. No. 99CH36366.

[25] A. Drees et al., "ARTUS: The Tune Measurement System at RHIC", Proceedings of the Ninth Beam Instrumentation Workshop, Cambridge, 2000 (p. 341).

[26] A. Drees et al., "ARTUS: A Rhic TUne Measurement System", RHIC/AP/98-125, internal note.

[27] J. Xu et al., "The Transverse Damper System for RHIC", Proceedings of the Particle Accelerator Conference (PAC) in San Francisco, 1991.

[28] Behlke Electronic GmbH, http://www.euretek.com/

[29] M. Kesselman et al., "Resonant BPM for Continuous Tune Measurement in RHIC", to be published in PAC 2001.

[30] P. Cameron et al., "Tune Feedback at RHIC", to be published in PAC 2001.

[31] C. Adler et al., nucl-ex/0008005.

[32] A. Baltz et al., Nucl. Instr. and Method, A417 (1998) 1

[33] A. Drees, Zhangbu Xu, "Luminosity Scans at RHIC during the Year 2000 Run", RHIC/AP/01-43, internal note.

[34] W. Barry et al., "Design of A Schottky Detector for Use at RHIC", Proc. EPAC 1998, Stockholm, p 1514.

[35] P.R. Cameron et al., "Schottky Measurements During RHIC 2000", to be published in PAC 2001.

6-D ELECTRON BEAM CHARACTERISATION USING OPTICAL TRANSITION RADIATION AND COHERENT DIFFRACTION RADIATION

M. Castellano, V. Verzilov, INFN-LNF, Italy
L. Catani, A. Cianchi, INFN-Roma2, Italy
G. D'Auria, M. Ferianis, C. Rossi, Sincrotrone Trieste, Italy

Abstract

The development of non-intercepting diagnostics for high charge density and high energy electron beams is one of the main challenge of beam instrumentation.

Diffraction Radiation based diagnostics, being non-intercepting, are among the possible candidates for the measurements of beam properties for the new generation linacs.

At the 1 GeV Sincrotrone Trieste linac, we are performing the first measurements of beam transverse parameters using Diffraction Radiation emitted by the electron beam passing through a 1 mm slit opened on a screen made of aluminium deposited on a silicon substrate.

The analysis of the angular distribution of the Diffraction Radiation for a given wavelength, slit aperture and beam energy gives information about the beam size and its angular divergence.

1 INTRODUCTION

The usefulness of Optical Transition Radiation (OTR) for electron beam diagnostics was demonstrated in 1975 by L. Wartski [1], but it took more than ten years before becoming a real instrument usable for beam measurement [2]. For the first time, in the design of the TESLA Test Facility (TTF) linac, OTR was considered as the main beam diagnostics tool, with the intent of fully exploit its many properties. In these years, we have used OTR to measure all the 6D phase space beam parameters. Some of the most interesting measurements will be described in this paper. More recently we started some experiments with the Diffraction Radiation (DR), that is emitted when the beam crosses a hole in a metallic screen. This radiation open the possibility of a non-intercepting diagnostics, required for high power beams or strongly focalised ones, as those designed for short wavelength FELs or Linear Colliders. On the TTF beam we have proved that coherent DR can give the same result as coherent Transition Radiation for bunch length measurement, while on the Sincrotrone Trieste linac an experiment is running to demonstrate the possibility of measuring beam size and angular spread with near-infrared DR.

Transition Radiation has many advantages over more traditional imaging devices, being completely linear and free from source saturation, but its spatial resolution has some peculiar aspects that can create some limits in the details that can be extracted from an image. So a very brief presentation of the space resolution of OTR will precede the illustration of the experimental results.

2 OTR RESOLUTION

Few years ago, some concern aroused about the spatial resolution reachable with OTR, especially at very high energy. The reason was the collimating of the radiation, with its peak cone at an angle of $1/\gamma$, that could produce an auto-diffraction limit increasing with the energy. This argument has been fully studied in [3-5], and now we know that the only real limitation arises from the collection optics diffraction, independently from energy, but with peculiar features due to the nature of this radiation. In particular, the radial polarisation produces a zero in the centre of the image, resulting in a FWHM larger than that of a standard scalar point source. On the other hand, the extension of the source (the e.m. field of the particle) increases with energy, and this produces a long tail which contain most of the optical intensity. This means that some caution must be used in defining the OTR spatial resolution, depending on how this long tail is managed. Figure 1, taken from Ref. [4], shows the normalised radial distribution for a single particle OTR image with different angular acceptance.

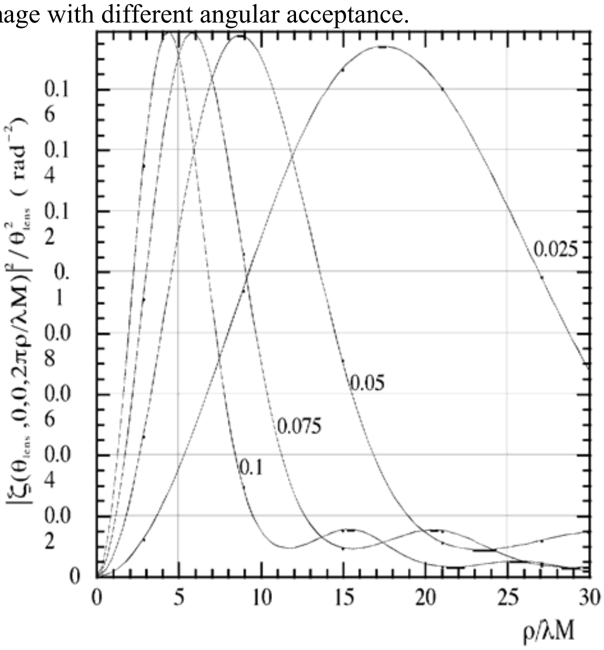

Figure 1: Normalised OTR angular distribution for different acceptance of the collection optics.

The 3D image is shown in Figure 2, together with its projection on one axis. The tail has been cut at the 0.5% of the maximum.

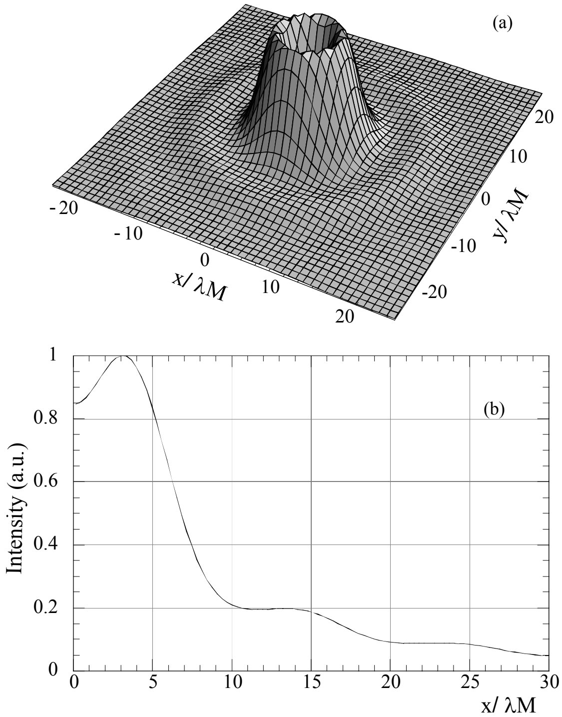

Fig. 2 – 3D OTR distribution and its projection on a plane. Tails are cut at .5% of the peak intensity

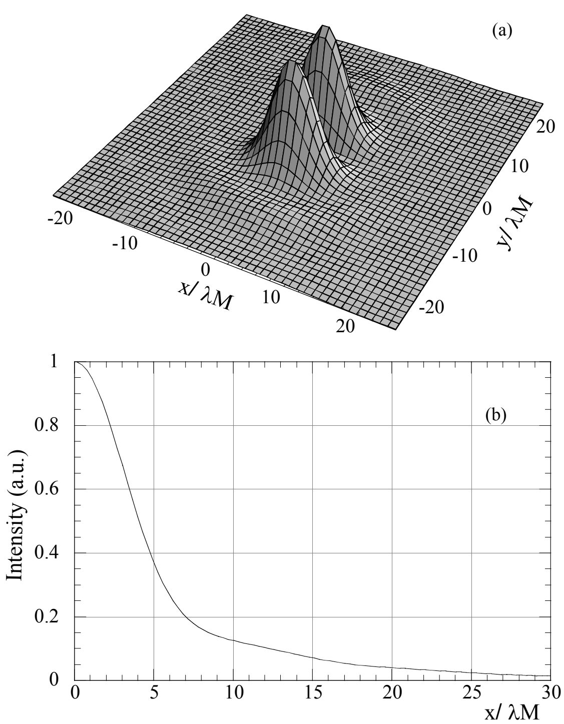

Fig. 3 – 3D OTR selected by a polarizer and its projection on the plane normal to the polarisation vector

From this picture it is possible to see that the FWHM is of the order of 12 λ, i.e. much larger than a standard point source with the same angular acceptance.

A better resolution can be obtained by the use of a polarizer. In this case, as shown in Figure 3, a FWHM of about 6 λ can be reached.

3 OTR MEASUREMENTS

In this paragraph we will illustrate some of the measurements performed on TTF. We will not mention the more standard measures, as the emittance measurement by the quadrupole scan or the beam size evolution along the macropulse taken by a gated camera, that were already presented at a previous Conference [3]. Instead, we will give space to measurements where the image details are important.

3.1 Pepper Pot measurement

At the injector level we have a beam of 16 MeV, and with a charge per microbunch of 1-4 nC, the standard emittance measurement by quadrupole scanning is rather inaccurate, requiring a space charge effect correction, which is by necessity based on not well known beam parameters. We are routinely using a pepper pot technique. The beam passes through a system of 100 μm wide slits cut in 1 mm stainless steel target. Two sets of slit are present: with .5 mm and 1 mm spacing. An OTR screen, at 45 degree, is mounted on the same actuator allowing the beam dimension being measured. The beamlet sizes and relative positions are measured on an OTR screen some 60 cm downstream.

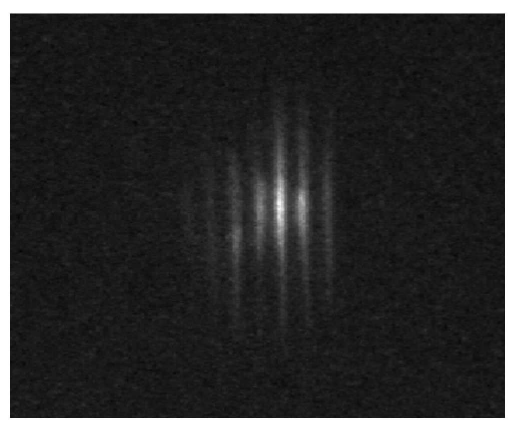

Fig. 4 – OTR image of the beam through the slits

Figures 4 show a typical OTR image of the beam through the slits. From the projection on the horizontal axis the emittance is derived on-line (figure 5).

This technique is fast enough to allow the optimisation of the gun and capture section settings.

In this case the advantage of OTR over other fluorescent screen is its absolute linearity.

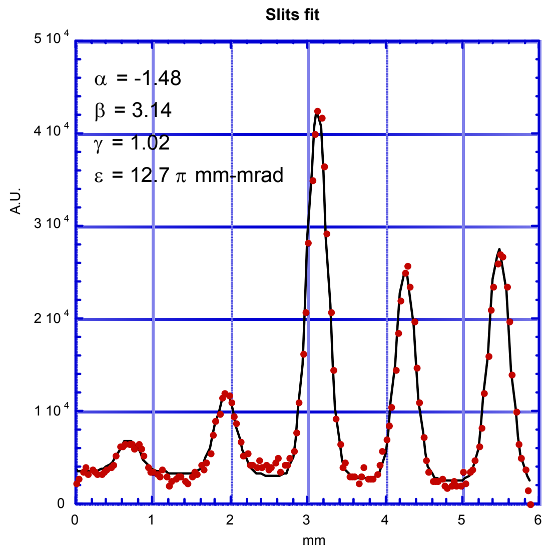

Fig. 5 - Emittance reconstruction from the slit image

3.2 *Longitudinal phase space tomography*

Measuring the energy spread in a dispersive section after a bending magnet by means of OTR is not often considered necessary or even advantageous. The reason is that in this case the beam is spread over a rather large surface, giving a very low OTR intensity, and in many cases small details are not considered important. There are also effects, in using OTR for imaging large objects, that must be carefully evaluated and considered in the design stage. One of the main problem is the possible different radiation collection efficiency from the centre or the border of the image. To evaluate this effect and design an appropriate optical system, it must be remembered that it is true that OTR has a peak at an angle of $1/\gamma$, but most of the intensity is carried by the tail at much larger angles.

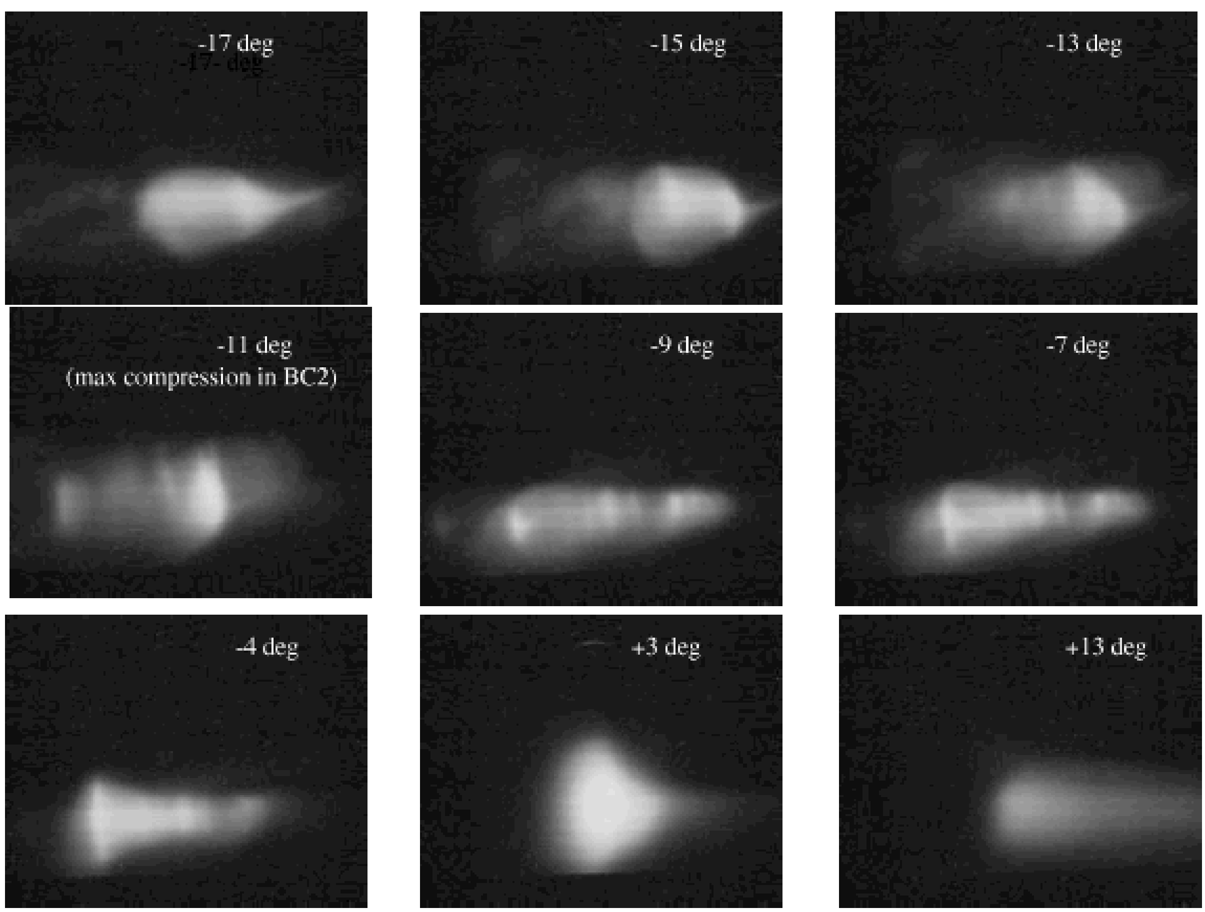

Fig. 6 - Energy spread at the end of the TTF linac as function of the off-phase angle in the first accelerating module

There are measurements for which the details that only OTR can give are absolutely required. One of these is the tomographic reconstruction of the longitudinal phase space.

To reduce the bunch length and increase the peak current for the FEL experiment, in TTF there is a magnetic compressor after the first accelerating module. Driving the beam off-crest in this module, a correlated energy spread is introduced, and the compressor rotates the longitudinal phase space, resulting in a shorter bunch. This process introduces unwanted, and not completely predicted, energy modulations. To study this effect, a measure of the energy spread at the end of the linac for different compression factors can be used for a tomographic reconstruction of the longitudinal phase space. In Figure 6 the measured energy spread for different phases in the first module, corresponding to different compression values, is shown.

More information can be found in the talk of M. Hüning at this conference [4].

3.3 Energy stability along the macrobunch

A more traditional use of OTR is the measurement of its angular distribution, of which an example is shown in Figure 7. From a line profile through the centre of this image, the beam energy and angular spread can be obtained

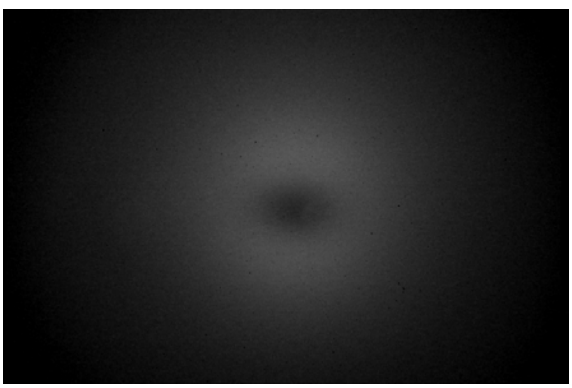

Fig. 7 - OTR angular distribution

In Figure 8 is shown the line profile obtained from the previous image.

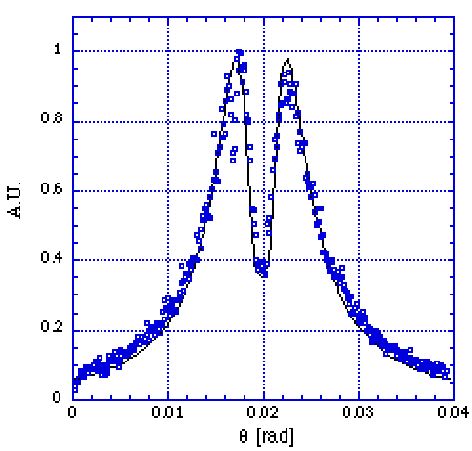

Fig. 8 – OTR angular distribution profile with a fit giving beam energy and angular spread

Our main interest was in this case on the energy value, that is obtained in absence of any dispersive section, and thus in any place along the linac. Using a gated camera, the energy for each single micropulse along the macropulse can be measured. Figure 9 show the result obtained at two different acceleration gradient during the set up of the RF feedback system.

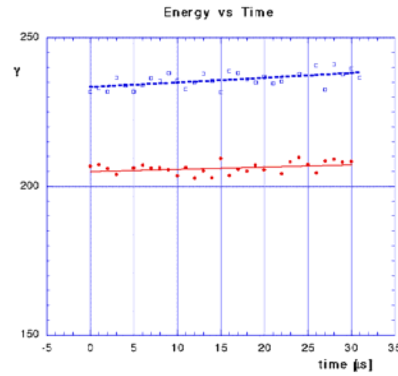

Fig. 9 - Energy stability along macropulse

4 DIFFRACTION RADIATION

OTR is very useful foe many aspects, as we have shown, but it is an intercepting device, directly hit by the beam. Like all intercepting devices, there is a limit in beam density that can be supported. For the new generation of beams for both Linear Colliders and FELs this limit is easily reached. A new generation of non-intercepting diagnostics is thus needed.

Diffraction Radiation (DR), i.e. the radiation produced when a particle goes through a hole or passes near the border of a screen, can be a possible solution. This radiation is only a special case of Transition Radiation, when only part of the e.m. field of the particle hits the screen, and diffraction aspects arise. For this to happen, the transverse extension $\lambda\gamma$ of the e.m. field of the particle must be larger than the hole radius

At the energy of less than 300 Mev, as actually available on TTF, the only way to exploit DR is through the coherent emission at wavelength equal or longer than the bunch length. It is well known that from the coherent spectrum it is possible to reconstruct the bunch length itself, and this technique has been widely used with transition or synchrotron radiation. We have used for the first time in a clear way the coherent DR.

For this experiment we have mounted a variable aperture slit, that allowed us to compare the intensity of DR with that of TR in the same experimental conditions.

The complete description of the experiment can be found in [5], here we will only show that to exactly evaluate the CDR spectrum, the effects of the finite dimension of the screen, analysed in [6], and the relatively short distance of the detector from the source that does not allow the use of asymptotic formulae, must be taken into account.

In Figure 10 the total CDR intensity as function of the slit aperture is shown together with the behaviour expected using the far field analytic expressions presented in [7] for a slit in an infinite screen.

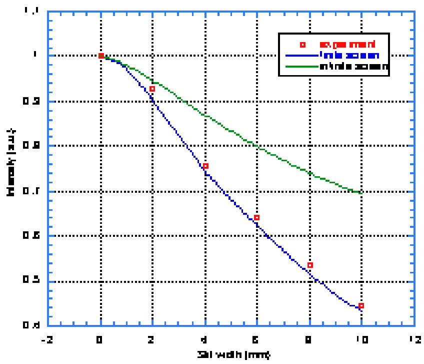

Fig. 10 – CDR total intensity as function of the slit aperture and theoretical curves based on different assumptions

It is evident that to account for the experimental results, a more realistic description, taking into account both the finite screen effect and the source dimension, is required.

The bunch length has been obtained from the interferograms in a simple way, assuming a single cut-off frequency, and the results, as function of the slit aperture, are shown in Figure 11.

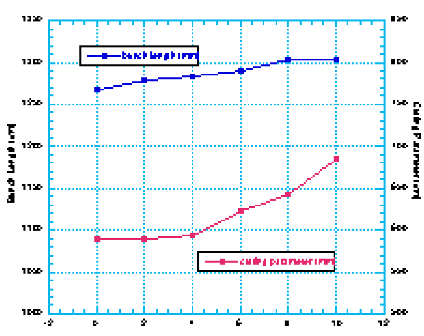

Fig. 11 – Bunch length and cutting frequency as function of slit aperture

We have demonstrated that CDR, even with rather large slit aperture, gives a bunch length equivalent, within the errors, to that obtained for CTR, but in a non-intercepting way.

Diffraction Radiation, at larger energies, gives also the possibility of measuring the beam size and angular distribution, as was suggested in [8].

An experiment is in progress at the 1 GeV linac of the Sincrotrone Trieste. In this case a fixed slit of 1 mm aperture is used, but the available energy requires to work with infrared radiation (1.6 mm) making the measurement much more difficult.

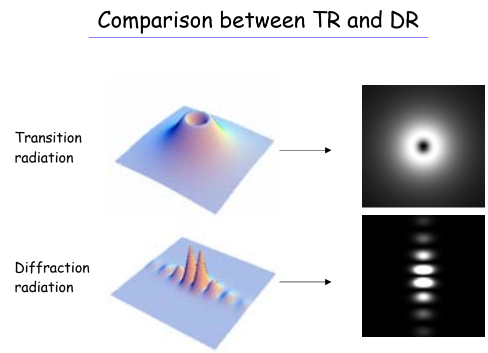

Fig. 12 – TR and DR angular distribution

In Figure 12 is shown the difference between the angular distribution of OTR and that expected for DR. The fringes visibility is a function of the beam size.

We will also test the possibility of changing the relative phase of the two half plane, in order to modify the angular distribution of the radiation, as shown in Figure 13. Many interesting applications can be obtained by a clever use of the phase control.

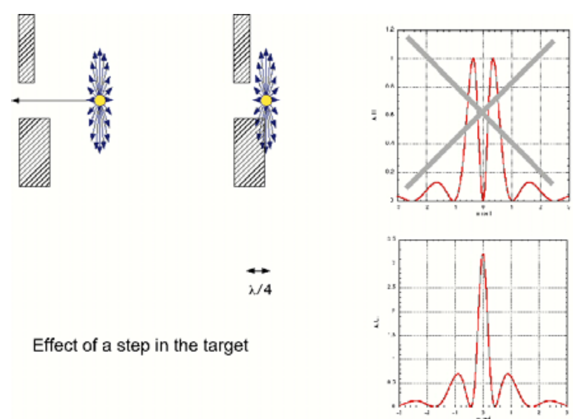

Fig. 13 – Effect of phase control in DR

REFERENCES

[1] L. Wartski et al, J. Appl. Phys. **46**, 3644 (1975).
[2] X.K. Maruyama et al, Nucl. Inst. And Meth. Phys. Res. A272, 237 (1988)
[3] M. Castellano et al, Proc. Of DIPAC97, 195 (1997)
[4] M Hüning, These Proceedings
[5] M. Castellano et al, Phys. Rev.E **63**, 056501 (2001)
[6] M. Castellano et al, Nucl. Inst. And Meth. Phys. Res. **A435**, 297 (1999)
[7] Ter Mikaelian, High Energy Electromagnetic Processes in Condensed Media, Wiley-Interscience 1972
[8] M. Castellano, Nucl. Inst. And Meth. Phys. Res A394, 275 (1997)

POSSIBLE SPIN-OFFS FROM LHC PHYSICS EXPERIMENTS FOR BEAM INSTRUMENTATION

R. Jones, CERN, Geneva, Switzerland

Abstract

This paper aims to introduce some of the new technology and materials used in the construction of the LHC physics experiments into the domain of the beam instrumentalist. The development of radiation hard fibre-optic technology, for example, can equally well be applied to beam instrumentation systems for the direct transmission of analogue or digital signals from high to low radiation environments. Many electronics techniques such as a system developed for the fast integration of photomultiplier signals could also prove very useful in the construction of new beam diagnostic instruments for bunch-to-bunch measurements. Other topics covered will include a fast beam synchronous timing system based on laser technology and a look at pixel detectors as a possible replacement for CCD cameras in imaging applications.

1 INTRODUCTION

The Accelerator and High Energy Physics (HEP) Experiment domains of large laboratories are often separated, with very little interaction taking place between the two. Accelerators are generally maintained by on-site staff, while the HEP Experiments are designed and built by a multitude of world-wide institutions. This makes it difficult to exchange ideas and foresee common applications for any development work. However, many of the new techniques investigated by the HEP Experiments can equally well be applied to beam instrumentation. With the ever-increasing demands on beam diagnostics requiring new and innovative solutions, coupled with decreasing staff numbers, such collaborations can prove to be very useful. In the following sections I will highlight a few techniques derived from the LHC Physics Experiments that are already being investigated for beam instrumentation purposes.

2 RADIATION HARD FIBRE-OPTIC TECHNOLOGY

Acquiring data in the front-end systems of HEP experiments necessitates the use of radiation resistant electronics. The detector itself is also crowded with equipment, severely limiting the amount of space available. Hence, in order to minimise the amount of electronics located in these high radiation regions, the LHC experiments have been investigating ways to transmit the data as soon as possible to the outside world. Described in this section is a way in which analogue signals can be extracted with limited very-front-end electronics.

2.1 CMS Analogue Signal Transmission

The CMS tracker is comprised of pixel, silicon and gas microstrip detectors, located in the centre of the experiment, right next to the beam pipe [1,2]. The silicon and gas microstrip detectors are read-out by charge sensitive amplifiers. The resulting signal, from some 12 million detector channels, has to be transmitted to the counting room on the outside of the CMS detector. The requirements for this link is as follows:

- Full scale dynamic range ~ 200:1 (46dB)
- < 2% deviation from linearity
- Overall rms link noise < 0.2% of full scale.
- Operation in magnetic field of up to 4T
- ~10kGy/year integrated radiation dose and 10^{13} (1Mev neutron equivalent)/cm^2 hadronic fluence.

The solution adopted by the CMS tracker team[1] makes use of analogue fibre-optic transmission [3,4]. A 1310nm, edge emitting, MQW semiconductor laser diode is directly modulated by a transconductance amplifier, with the light produced passing into a single-mode optical fibre. This fibre, some 150m in length, carries the analogue signal to the digitisers in the counting room, where it is converted back into an electrical signal by PIN photodiodes. Using this technique, the requested linearity was obtained, with a link noise of less than 0.2%. The overall bandwidth was limited by the laser driver to 172MHz.

Since radiation hardness was of great concern, many tests were carried out on the influence of radiation on the laser characteristics [5,6,7] and on the fibre-optic cable [8]. In conclusion, it was found that a variety of commercially available 1310nm lasers and single-mode fibres could meet the stringent radiation requirements for operation in the CMS tracker environment.

2.2 Example Application for Beam Instrumentation

This type of fibre-optic transmission is already being investigated for possible use in beam instrumentation. In

[1] http://cms-tk-opto.web.cern.ch/cms-tk-opto/default.htm

the original design of the LHC beam position system it was envisaged that all of the front-end electronics would remain in the tunnel. It soon became apparent, however, that qualifying all components for a high radiation environment would prove to be very difficult. Hence an alternative solution was sought.

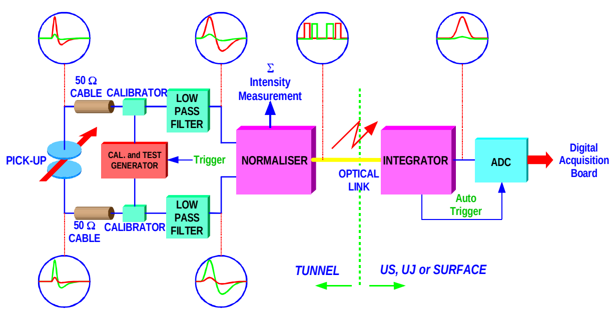

Figure 1: The LHC beam position measurement system

A schematic of the new system is shown in Fig. 1. The acquisition is based on a wide band time normaliser [9], which encodes position as a pulse modulation. This pulse modulated signal, originally transported electrically between the normaliser and integrator, will now be transmitted from one to the other using a 2km fibre-optic link. Only the very front-end analogue electronics and the radiation-hard laser transmitter will remain in the tunnel, with the integrator, ADC and subsequent digital electronics installed in surface buildings.

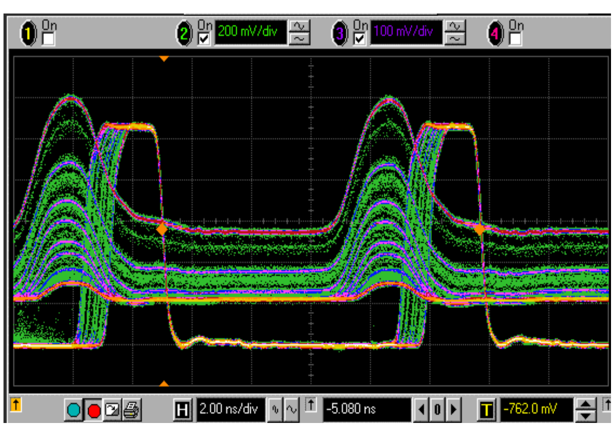

Figure 2: Output response of the LHC beam position monitor fibre-optic link.

Fig. 2 shows the final ECL output pulses (rectangles) as a function of the PIN photodiode amplitude response. The position is encoded in the time between the two falling edges (10ns ± 1.5ns). It was not possible to accurately measure the overall jitter in the link, since it was less than the 11ps jitter of the oscilloscope itself. To give some idea of its influence, a 15ps jitter would introduce noise into the system at the 1% level. This system is being tested at CERN this year and, if successful, will be adopted for the LHC beam position measurement system.

3 FAST TIMING SYSTEMS

Most beam instrumentation relies on an accurate timing system. This is particularly true for applications requiring bunch-to-bunch measurements. In this section I will describe the timing system developed for the LHC Experiments, which has now also been adopted to provide the fast timing signals for the LHC beam instrumentation.

3.1 The Timing, Trigger and Control System for the LHC

The Timing, Trigger and Control (TTC) system [10] for the LHC Experiments is being developed as part of the CERN-RD12 Project[2], which was initially a common project for ALICE, ATLAS, CMS and LHCb. The usefulness of the system has now become apparent for many other users, transforming the project into an LHC Common Project financed by both the CERN Experiment and Accelerator sectors.

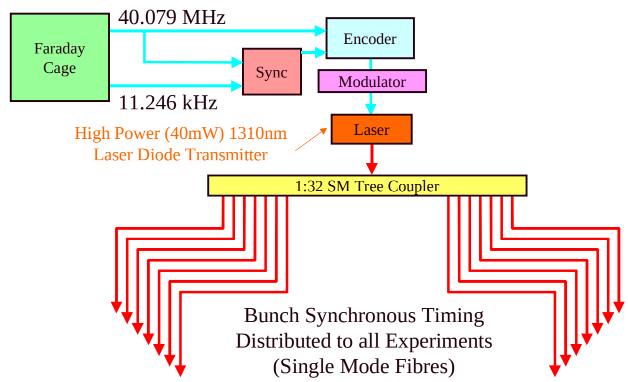

Figure 3: Schematic of the TTC distribution chain.

The TTC system is designed to provide bunch synchronous timing, a level-1 trigger (or revolution frequency for beam instrumentation), and the ability to send broadcast and individually-addressed control signals to front-end equipment. A schematic of the TTC distribution chain is shown in Fig. 3.

The 11.246kHz LHC revolution frequency and the 40.08MHz LHC bunch frequency are derived from the 400MHz RF acceleration frequency. These are used via a PLL to provide the 160.32MHz clock required for the 160.32MBaud biphase mark encoding shown in Fig. 4. Encoding at four times the bunch frequency allows two data streams (Channels A and B) to be sent in addition to this frequency. Channel A is used to provide the revolution frequency (for beam instrumentation) or the

[2] http://ttc.web.cern.ch/TTC/intro.html

level-1 trigger (for the experiments), while Channel B can be used to encode formatted commands and data. These messages can be used to synchronise acquisitions on a given turn and to send data such as the current beam type, energy, intensity etc. to the front-end controllers. All this is carried out using the TTCvi encoding VME interface [11].

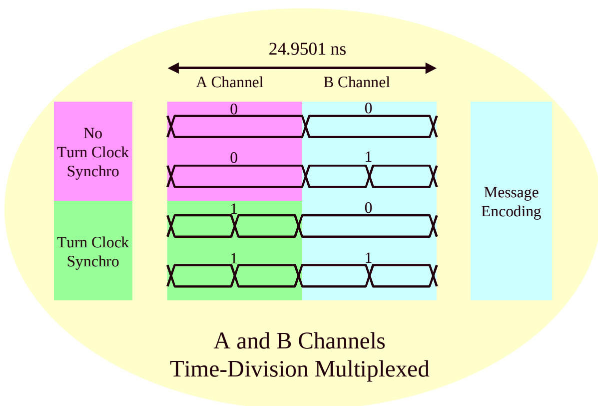

Figure 4: TTC encoding

Once encoded, the signal will be transmitted via a high power (40mW) 1310nm diode laser, though single-mode fibre optic cables to all the LHC access points. At each point, the signal will be redistributed via multi-mode fibres either to the experiments, where it is re-encoded with experiment specific information, or to the beam instrumentation.

A radiation hard receiver ASIC, the TTCrx [12], will be used to decode the transmitted data. Each receiver chip can be individually addressed and has programmable coarse and fine delays to adjust for bunch time-of-flight and varying fibre lengths around the ring. The overall jitter at the output of the TTCrx is ~100ps.

The TTC system provides a 'ready made' solution for the fast timing requirements of the LHC beam instrumentation. In addition, the ability to encode messages will provide users with the possibility of receiving relevant machine parameters in their front-end systems. Another advantage is the fact that the receiver chip is radiation hard, so allowing its use inside the tunnel. The TTC system has therefore been adopted to provide all beam synchronous timing for the LHC.

4 ELECTRONIC CHIP DESIGN

The fact that HEP experiments are at the forefront of technology, combined with the stringent space requirements inside the detectors themselves, often leads to the design of specialised ASICs on which many complex functions are integrated. One example of such an ASIC, the TTCrx, was described in the previous section. Here we will look at a further example with a more general functionality, which could prove very useful for several beam instrumentation applications.

4.1 Fast Integration ASICs

The LHCb experiment[3] is equipped with three types of calorimeter [13]. The pre-shower and scintillator pad detector contain some 12000 channels in total, with each channel constructed of coils of optical fibre embedded in a scintillator material. Their function is to separate electrons and pions or photons and minimum ionising particles (MIPs), for the level-0 trigger of the experiment. This is followed by the 6000 channel, lead/scintillator electron calorimeter, and the 1500 channel, steel/scintillator hadron calorimeter. The light from all these scintillators will be detected using photomultiplier tubes.

Each photomultiplier signal has to be integrated at a rate of 40MHz, requiring a very fast integrator. Two separate developments are being undertaken by the LHCb collaboration to achieve such performance. The Laboratoire de Physique Corpusculaire (Université Blaise Pascal, Clermont-Ferrand, France) is developing a multiplexed differential integrator, capable of providing 10-bit resolution after digitisation at 40MHz [14]. This is intended for use with the pre-shower calorimeter, to produce the level 0 trigger. For the electron and hadronic calorimeters, the Laboratoire de l'Accélérateur Linéaire (Orsay, France) is producing an integrator with a 12-bit resolution that works at 20MHz [15]. It is this second integrator that I will describe in more detail in this section.

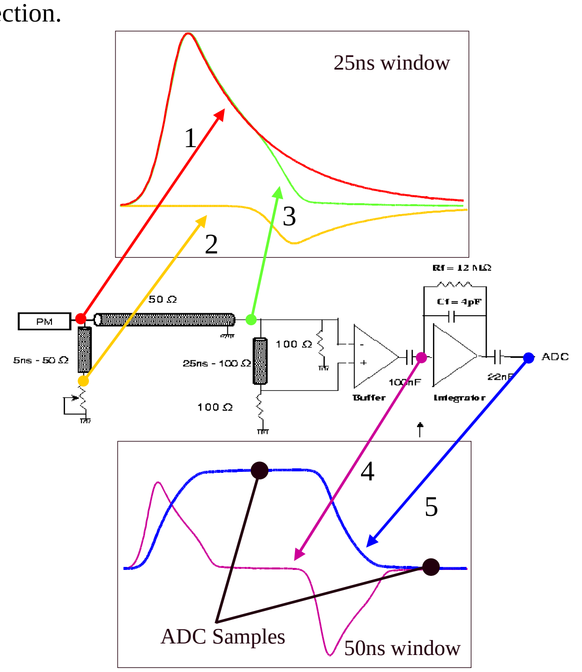

Figure 5: Schematic of the front-end electronics for the LHCb electron and hadronic calorimeters.

[3] http://lhcb.web.cern.ch/lhcb/

The general layout of the front-end electronics is shown in Fig. 5. At the exit of the photomultiplier (trace 1), the signal needs to be shaped to avoid an electronic pile-up at the next bunch crossing after 25ns. This is done using a clipping circuit, which inverts and returns part of the signal (trace 2), to pull the photomultiplier signal to zero after ~10ns.

The integration repetition rate for such signals is limited by the finite discharge time of the integrating capacitor. One way to reduce this dead-time is by using two integrators and a multiplexor, allowing one to integrate while the other discharges. This is the technique being applied to the pre-shower calorimeter. However, the inevitable injection of charge from the discharge switches of such an integrator generates pedestals that can be sources of drifts at the 0.1% level. The alternative possibility, adopted for the electron and hadronic calorimeters, is to subtract the signal from itself in a linear way during the integration process. This is achieved by delaying half of the signal by 25ns before combining it with the original signal via a differential buffer. The buffer and the integrator are AC coupled to remove any DC offsets, so that the integrator finally sees a signal similar to that shown in trace 4. The 12-bit ADC samples the integrated signal (trace 5) at 40MHz with one sample for the signal and one for the background, giving a 20MHz overall signal integration rate.

Both the multiplexed and signal subtraction integrators have been developed as analogue ASICs, and are currently under test by the institutions involved.

4.2 Possible Applications for Beam Instrumentation

There are several possible candidates that spring immediately to mind, when looking for applications of such integrators in beam instrumentation. The most obvious is for the integration of similar photomultiplier signals, for example from beam loss monitors or from the multi-anode photomultipliers used for bunch-to-bunch beam size measurements. Another application, which is currently under investigation at CERN, is their use for the integration of fast BCT signals. The current method of providing bunch-to-bunch intensity measurements takes the difference of the peak and valley of the signal using two 40MHz ADCs. There are, however, several drawbacks to this technique, namely that it is very sensitive to bunch length variations and also to the bunch synchronous timing. A fast integrator would overcome both of these difficulties. Similar signals can also be obtained from luminosity monitors and numerous other instruments, which could all benefit from the development of such fast integrator ASICs for their signal treatment.

5 IMAGING

In this section I will describe the development of a hybrid pixel detector, an exciting spin-off from HEP experiments, which I am sure will find many applications in all kinds of imaging instrumentation.

5.1 Hybrid Pixel Detectors

Hybrid pixel detectors were first used successfully in the WA97 experiment at CERN [16] following the developments in the CERN-RD19 collaboration [17]. Since that time many particle physics experiments are developing sub-detectors based on this new technology, which can detect both particles and γ-radiation. The readout requirements for HEP detectors, however, differ from those for imaging. The detected signals are generally delayed and require an external trigger before recording one image. Moreover, the shape of the pixel is a narrow rectangle, favouring a high spatial resolution in one dimension, usually corresponding to the direction of the magnetic field in the experiment. The CERN-MEDIPIX project[4] was therefore launched as a spin-off from the CERN-RD19 collaboration, to apply such hybrid pixel technology specifically to imaging applications.

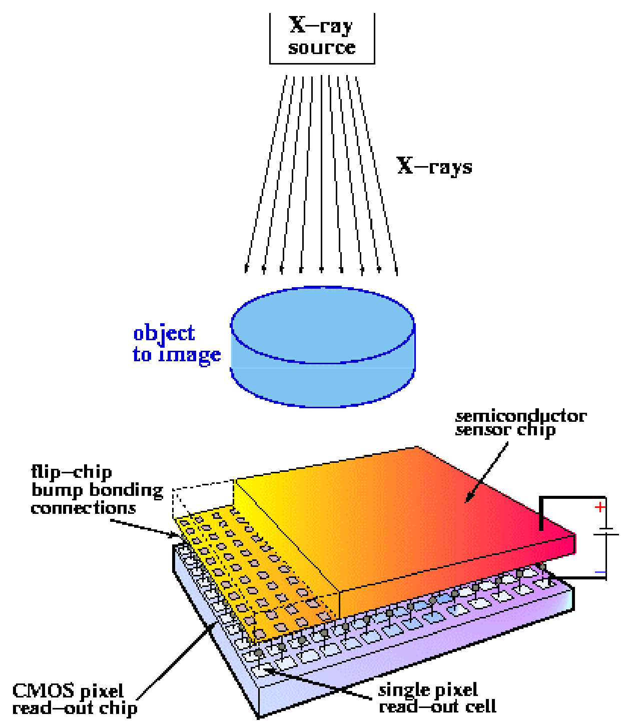

Figure 6: Hybrid pixel detector layout

Hybrid pixel detectors consist of one or several ASICs, each containing a 2-dimensional matrix of readout electronics which are bump-bonded to an equally segmented semiconductor detector (see Fig. 6). This has the advantage that the underlying readout electronics is

[4] http://medipix.web.cern.ch/MEDIPIX/

independent of the choice of pixel detector. The material used (e.g. Si, GaAs, CdTe) can therefore be chosen according to the requirements of each individual application, depending on their response to a certain photon or particle energy range.

The Medipix1 chip consists of a 2D diode array of monolithic semiconductor containing 4096, 170μm square pixels, giving an active area of ~1.2 cm^2. This is bump-bonded to an equally segmented array of readout electronics. Each individual pixel has a read-out chip containing a pre-ampifier, comparator, global threshold setting, 3-bit threshold fine-tune (addressable on each pixel), elements for masking and testing, and a 15-bit counter giving a maximum count of 32768 photons per pixel. This means that in total each cell is made up of ~400 transistors.

In terms of its operation, the maximum count rate is 1MHz per pixel, with a dead-time between acquisitions of 384μs, which is the time taken by the 10MHz clock to read out a complete frame.

The advantage of such a system over conventional CCD imaging is the fact that it makes use of single photon counting as opposed to charge integration. This means that noise is suppressed and that detector leakage current and electronics mismatch can be compensated, leading to a dynamic range that is ultimately limited by the size of counter implemented behind each pixel. Its insensitivity to dark currents also allows for long exposure times under very low intensity illumination. The other great advantage is that the whole readout system is purely digital.

A second-generation chip, the Medipix2, is currently under development, and will contain 256 × 256 square pixels each 55μm^2 in size, giving a total active area ~2cm^2. On this new chip it will also be possible to select a window in energy over which the device is sensitive.

5.2 Possible Applications for Beam Instrumentation

It is clear that hybrid pixel detectors could very soon become real candidates as replacements for CCD cameras and other imaging detectors. In fact, the Medipix1 detector has already been tested on instruments in the experimental zones of several synchrotron light sources (see e.g. [20]). Studies are also in progress for their use in future projects such as DIAMOND and CLIC. The current detectors are probably not sufficiently radiation resistant for use in general accelerator environments. However, the fact that very radiation resistant examples exist for HEP applications, will hopefully mean that such models will, before long, be available as an alternative for CCD cameras for beam imaging applications.

REFERENCES

[1] CMS Collaboration, "CMS, the Tracker System Project : Technical Design Report", CERN LHCC 98-6, CMS-TDR-5, CERN-Geneva, 1998.

[2] CMS Collaboration, "Addendum to CMS Tracker Technical Design Report", CERN LHCC 2000-16, CERN-Geneva, 2000.

[3] F. Vasey *et al.*, "Development of Radiation-Hard Optical Links for the CMS Tracker at CERN", IEEE Trans. Nucl. Sci., Vol. 45, No. 3, pp.331-337, 1998.

[4] V. Arbet-Engels *et al.*, "Analogue optical links for the CMS tracker readout system", Nucl. Instr. and Meth. A, Vol 409, pp. 634-638, 1998.

[5] K. Gill *et al.*, "Comparative Study of Radiation Hardness of Optoelectronic Components for the CMS Tracker Optical Links", RADECS conference, Oxford, 1998.

[6] K. Gill *et al.*, "Radiation damage studies of optical link components for applications in future high energy physics experiments", Photonics for Space Environments, SPIE Vol. 3440, 1998.

[7] F.B.H. Jensen *et al.*, "Characterization of laser diodes for analog parallel optical links", Testing, packaging, reliability and applications of semiconductor lasers IV, SPIE Vol. 3626B, pp. 202-207, 1999.

[8] J. Troska *et al.*, "Radiation effects in commercial off-the-shelf single-mode optical fibres", Photonics for Space Environments, SPIE Vol. 3440, 1998.

[9] D.Cocq, "The Wide Band Normaliser : a New Circuit to Measure Transverse Bunch Position in Accelerators and Colliders", Nucl. Instrum. Methods Phys. Res., A : 416, no.1, pp.1, 1998.

[10] B.G. Taylor, "TTC Distribution for LHC Detectors", IEEE Trans. Nuclear Science, Vol. 45, No. 3, pp. 821-828, 1998.

[11] P. Gällnö, "Modules development for the TTC system", in: 5th Conference on Electronics for LHC Experiments, Snowmass, CO, USA, 1999, Ed. by Decosse, CERN-OPEN-2000-076.

[12] J. Christiansen *et al.*, "Receiver ASIC for Timing, Trigger and Control Distribution in LHC Experiments", IEEE Trans. Nuclear Science, Vol. 43, 1996.

[13] LHCb Collaboration, "LHCb calorimeters: Technical Design report", CERN-LHCC-2000-036, LHCb-TDR-2, CERN, 2000.

[14] G. Bohner *et al.*, "Very front-end electronics for the LHCb preshower", LHCb-2000-047, CERN, 2000.

[15] C. Beigbeder *et al.*, "The front-end electronics for LHCb calorimeters", LHCb-2000-028, CERN, 2000.

[16] F. Antinori *et al.*, "First results from the 1994 Lead Beam run of WA97", Nucl. Phys. A590, pp 139c-146c, 1995.

[17] E. H. M. Heijne *et al.*, "Development of hybrid and monolithic silicon micropattern detectors", CERN DRDC/90-81, CERN, 1990.

[18] M. Campbell *at al*, "Readout for a 64 × 64 pixel matrix with 15-bit single photon counting", IEEE Trans.Nucl.Sci. 45 (3), pp. 751-753, 1998.

[19] M. Chmeissani *at al*, "Performance limits of a single photon counting pixel system", Nucl. Instr. and Meth. in Phys. Res. A 460, pp. 81-90, 2001.

[20] J. Watt *et al*, "Applications of pixellated GaAs X-ray detectors in a synchrotron radiation beam", Nucl. Instr. and Meth. in Phys. Res. A 460, pp. 185-190, 2001.

INVESTIGATIONS OF THE LONGITUDINAL CHARGE DISTRIBUTION IN VERY SHORT ELECTRON-BUNCHES

Markus Hüning, III. Phys Inst RWTH Aachen, Sommerfeldstrasse 26-28, 52056 Aachen, Germany
current address: DESY, Notkestrasse 85, 22603 Hamburg, Germany

Abstract

Electro-optical-sampling is a powerful technique to measure the longitudinal charge distribution of very short electron bunches. The electrical field moving with the bunch induces an optical anisitropy in a ZnTe crystal which is probed by a polarized laser pulse. Two measurement principles are possible. In the first one a short laser pulse of lengths < 50 fs is used directly to scan the time varying optical properties of the crystal. In the second method the laser pulse is frequency chirped and the temporal information is encoded into the time ordered frequency spectrum, which can be recovered by an optical grating and a CCD camera.

A resolution in the 100 fs regime can also be achieved with longitudinal phase space tomography. Acceleration on the slope of the rf wave at different phases and measurements of the energy profiles are sufficient for a reconstruction algorithm based on maximum entropy methods. The longitudinal phase space distribution can be obtained without artefacts due to the limited angular range of the projections.

1 INTRODUCTION

Linear electron positron colliders or free electron lasers (FEL) require electron bunches of subpicosecond bunch length. Measurement techniques have been developed in recent years to provide diagnostics in this parameter regime.

One possibility is to measure the coherent radiation emitted by the bunches under certain circumstances: Coherent transition radiation (CTR), diffraction radiation, or synchrotron radiation (CSR). By analysis of the radiation spectrum one can determine the longitudinal bunch profile. In most cases the phase information is lost and has to be reconstructed for example with the Kramers-Kronig-Relation. This kind of analysis can be considered as well established [3][4][5] and will be used as a reference in this paper.

The development of Ti:sapphire lasers with ultra-short pulses of FWHM < 50 fs led to the concept of electro-optic sampling and imaging in THz-spectroscopy [17][20]. At the FEL Laboratory for Infrared Experiments (FELIX) in Rijnhuizen near Utrecht, NL electro-optic sampling (EOS) has been successfully applied to measure bunch lengths [19][7]. Similar measurements are being prepared at several accelerators and as well at the TESLA Test Facility (TTF)[2][8].

Many experiments have been carried out to measure longitudinal beam profiles by means of the rf acceleration in the linac themself [3][16]. Using off-crest acceleration in the rf cavities an energy deviation is induced depending on the longitudinal position of the electrons in the bunch. This can be measured with a spectrometer dipole. One of the problems with this kind of measurement is the entanglement with the initial energy spread, which often is in the same order of magnitude. Using magnetic chicanes followed by an acceleration section, it is possible to rotate the phase space by $90°$ so that the longitudinal position is projected onto the energy [13][4]. In general tomographic methods can be used to get a reconstruction of the full longitudinal phase space.

2 ELECTRO-OPTIC METHODS

Exposed to a strong electric field some optical crystals exhibit the Pockels effect: The electric field distorts the lattice of the crystal and the material becomes birefringent. Linearly polarized light with its polarisation oriented $45°$ to the optical axis is transformed into elliptically polarised light with the fraction of circularly polarized light proportional to the strength of the electrical field.

Compared to the oszillation of the laser even THz-fields can be considered as slowly varying and so the Pockels Effect can be applied to measure the electric field strength in THz pulses with a resolution governed by the width of the laser pulse used to sample. There are Ti:Sapphire lasers available which deliver pulses shorter than 20 fs FWHM. For the EOS often ZnTe is used because it provides good sensitivity and good optical properties for THz frequencies as well as for the light from Ti:sapphire lasers. The Phonon resonances with the lowest frequency in ZnTe can be found at 5.6 THz, but their influence on the measurement can be modelled precisely. Electro-optical Sampling has been demonstrated with ZnTe up to frequencies of 37 THz [18].

In contrast to many applications in THz-Spectroscopy where the same laser pulse is utilized for generation of the THz-pulse as well as for probing the electrical field, in a linac the bunches and the ultra-short laser pulses are generated by different sources. A demanding task in the adaption of EOS to accelerator diagnostics is therefore the synchronisation of the Ti:Sapphire laser to the master clock of the accelerator. This can be accomplished by building a phase locked loop which synchronizes a harmonic of a photodiode signal from the laser with the rf-reference from the master clock. In this way phase noise can be reduced by a factor of 10. The residual noise translates into a timing

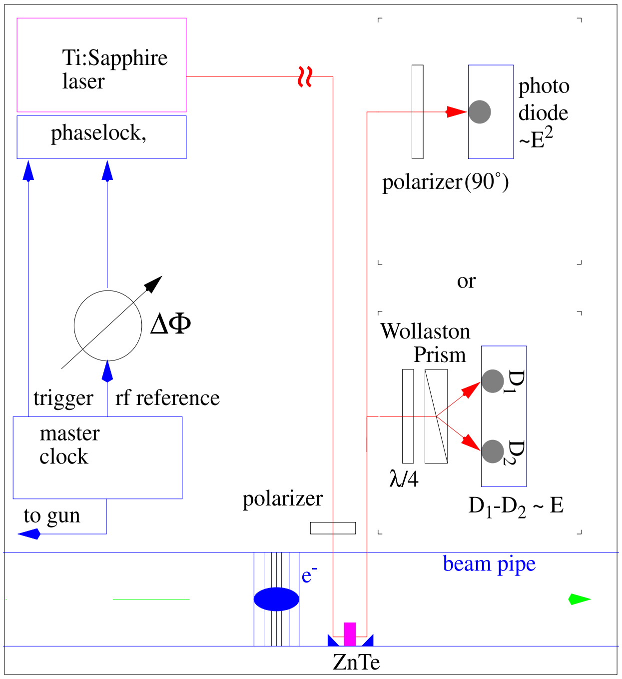

Figure 1: Possible setup for the Electro Optic Sampling

jitter of 100 fs within 1 ms respectively 1 ps over 1 second. This dominates the achievable resolution in a direct sampling of the electron bunches.

The ZnTe crystal can be mounted directly inside the vacuum chamber to probe the electrical field travelling together with the bunch. Due to the Lorentz contraction of the field the electrical field lines of each electron are concentrated in a disk with opening $1/\gamma$ orthogonal on the trajectory of the electrons. Thus the longitudinal charge distribution can directly be measured by scanning the copropagating fields. The design of the vacuum system has to be done carefully to minimize distortions of the measurement by wakefields.

2.1 Setting up the Timing

There are several ways to resolve the time information. The first attempt one would do to start this kind of measurement is to scan the laser pulse across the electron bunches. With a variable delay each laser pulse overlaps with a different part of the electron bunches. As can be seen from the previous section the time jitter and thereby the achievable resolution depends on the velocity of scanning. With an electronic phaseshifter a full scan can be performed within milliseconds to achieve the best resolution of

$$\Delta T = \sqrt{T_0^2 + (T_{jitter})^2}\,. \qquad (1)$$

At FELIX this kind of measurement has been established. Results can be seen in figure 2. Instead of shifting the laser pulse with respect to the beam at FELIX the frequency of the whole accelerator was shifted. The resolution achieved in these experiments is reported to be 440 fs, a full discussion of the experiment can be found in [7][19].

It is possible to take advantage of the timing jitter by using a technique called differential optical gating. In this method the THz-pulses are sampled by two laser pulses with a fixed time delay between them. The pair of pulses is allowed to jitter with respect to the THz-pulses so that statistically they cover them totally. With each measurement one obtains a value for the instantaneous intensity I and its time derivative $\dot{I}$. The resulting distribution can be represented by a function

$$F(I) = \frac{dI}{dt}. \qquad (2)$$

The time information can be obtained by integration, yielding

$$t(I_1) = t(I_0) + \int_{I_0}^{I_1} \frac{dI}{F(I)}. \qquad (3)$$

The integral can only be performed where $F(I) \neq 0$, which creates problems at the maximum of the pulse where the derivative is zero. Using only equation 3, one can reconstruct the rising and the falling edge separately. This leaves some uncertainty about the length of the plateau at maximum. One can reconstruct this information from the density of data points where $F(I) = 0$ in comparison to other parts of the curve. A more detailed description can be found in [12].

Another method to become independent from timing jitter is a technique called electro-optical imaging. This method also offers the possibility for single pulse measurements. Before interacting with the THz-radiation the laser pulse is chirped, i.e. stretched by sorting its wavelengths in time. In this way the time axis is marked by the corresponding wavelength inside the pulse. For single shot measurements the resulting pulse length has to be longer than the expected bunch length plus some margin for the jitter, typically 10 ps. Each part of the laser pulse interacts with the corresponding part of the THz-pulse. The longitudinal profile can then be obtained using a monochromator.
The achievable time resolution is given by

$$\tau = \sqrt{T_0 \cdot T_c}\,, \qquad (4)$$

with T_0 being the initial length of the laser pulse and T_c the length of the chirped pulse [17]. A measurement of this kind has been successfully performed at FELIX [11].

2.2 Sensitivity

The sensitivity of the setup increases with the thickness of the non-linear crystal. On the other hand dispersion effects inside the material lead to divergence of the pulses in the crystal. So one has to find a trade-off between sensitivity and time resolution. For picosecond THz-pulses generated from biased semiconductors a signal-to-noise ratio of $S/N = 60$ has been demonstrated for single THz-pulses with $E = 1$ kV/cm [1].

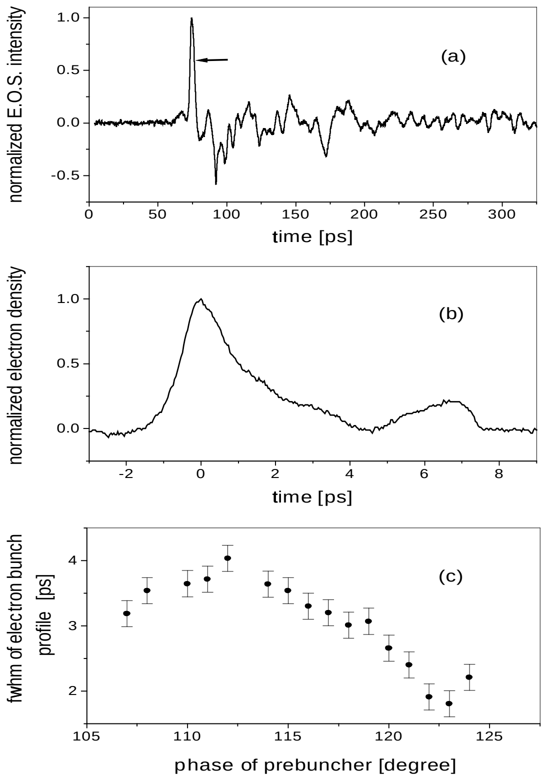

Figure 2: Logitudinal charge profile in the FELIX accelerator measured with the method of electro-optical sampling. The head of the bunch is shown left. The upper part (a) shows the bunch together with wakefields travelling along the beamline. The second part (b) shows the shortest bunch achieved, the third (c) the dependence of the RMS bunchlength on the phase of some buncher cavity in the injector.

At FELIX the sensitivity in the measurement shown in figure 2 was estimated to be $E = 1$ kV/cm with a signal to noise ratio of $S/N = 1$. The maximum field strength was estimated to be 12 kV/cm at the crystal.

3 TOMOGRAPHY

By means of computerized tomography it is possible to reconstruct a multi-dimensional distribution from a series of projections. In case of phase-space tomography a 2-dimensional distribution is reconstructed from 1-dimensional projections. Most of the reconstruction algorithms have been developed under the assumption that the different projections were obtained by rotation of the object. The most popular algorithms require a set of projections that cover 180° for the projection angles. If the projection data do not fulfill this requirement, the reconstruction produces severe artefacts [10], peaks are broadened and streaks are produced. In this way the achievable resolution is dilluted and sometimes the whole reconstruction becomes meaningless.

In a linear accelerator in most cases the only possibility to create different projections of the longitudinal phase space is off-crest acceleration, i.e. acceleration at different phases between bunch and rf wave. But this method does not induce a rotation of the phase space but only a shearing, so that the required rotation of 180° can never be accomplished.

To circumvent this problem at the TESLA Test Facility the reconstruction is done in a different way [6]. By defining the entropy of the phase space distribution f one finds a criterion to minimize artefacts

$$\eta(f) = -\iint_{\mathcal{D}} \mathrm{d}s\mathrm{d}t\, f(s,t) \ln\left(f(s,t)A\right), \qquad (5)$$

where A is the area of $\mathcal{D}$, s the energy and t the time. Every streak or broadening of peaks is additional information to the necessary minimum information. By maximizing the entropy the additional information is suppressed. The distribution with the least additional data that can still reproduce the projections is considered to be the most probable candidate for the real distribution. This can be seen

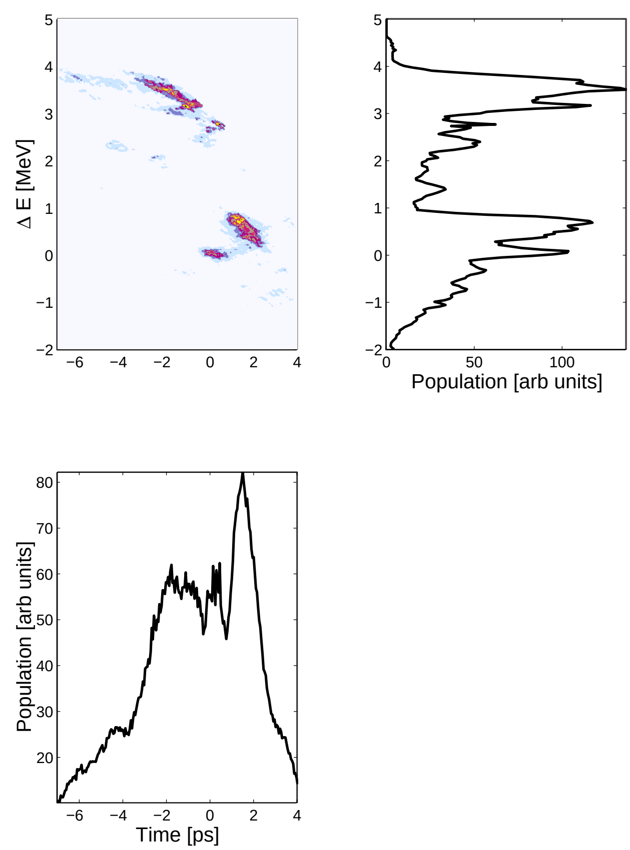

Figure 3: Result from longitudinal tomography in the TESLA Test Facility. In the TTF a splitting of the energy distribution has been observed and the tomography is one of the techniques to study this effect. The upper left part shows the 2-dimensional distribution whilst the upper right and lower left show the projection onto the energy axis respectively the time axis. Note: the head of the bunch is on the right.

in analogy to statistical thermodynamics where the distribution with the least order, i.e. the least information, is realized with highes probability. The corresponding algorithm was named by the author Maximum Entropy Algorithm (MENT) [9][14].

The shearing of the phase space can be written as

$$\triangle s = a_j + b_j \cdot t + c_j \cdot t^2, \tag{6}$$

where a_j is the energy shift of the centroid, b_j is the linear shearing, and c_j takes care for the nonlinear curvature of the rf. Each projection may have its own binning s_{jm}. Let G_{jm}, $j = 1 \ldots J$, $m = 1 \ldots M$ be the contents of the m^{th} bin of the j^{th} projection. Then this data can be calculated from the phase space distribution via

$$G_{jm} = \iint \mathrm{d}s\mathrm{d}t f(s,t)\chi_{jm}(s + a_j + b_j t + c_j t^2), \tag{7}$$

with χ_{jm} being the characteristic function of the interval $[s_{jm}, sjm + 1)$

$$\chi_{jm} = \begin{cases} 1, & s_{jm} \leq s < s_{jm+1} \\ 0, & \text{otherwise.} \end{cases} \tag{8}$$

The task is now to find a distribution $f(s,t)$ which satisfies all boundary conditions (7) and maximises the entropy (5). This problem can be solved by introducing Lagrange multipliers. After some manipulations the solution is

$$f(s,t) = A^{-1} \prod_j \sum_m H_{jm}\chi_{jm}(s + a_j + b_j t + c_j t^2). \tag{9}$$

The value of H_{jm} is found in an iterative process, the nonlinear Gauss-Seidel method

$$\begin{aligned} H_{jm}^{i+1} &= \frac{AG_{jm}}{\iint \prod_k \sum_n H_{kn}^i \chi_{kn}(s + a_{jk} + b_{jk}t + c_{jk}t^2)}, \\ & \qquad m = 1 \ldots M, \quad j = i \bmod J + 1, \\ H_{jm}^{i+1} &= H_{jm}^i, \quad m = 1 \ldots M, \quad j \neq i \bmod J + 1, \\ a_{jk} &= a_j - a_k, \quad b_{jk}, c_{jk} \text{ similar.} \end{aligned} \tag{10}$$

Note that it is not necessary to calculate any logarithm or exponential. Reasonable results can be expected after 3 turns of iteration.

3.1 Resolution

The resolution expected depends on the layout of the accelerator and its mode of operation. In the TTF there are two accelerating modules each delivering the same energy gain, by the time of the experiment ≈ 100 MeV. There is a magnetic chicane for bunch compression between the two modules. The goal was to measure the longitudinal phase space at the entrance of the second acceleration module. By various reasons the phase offset of the second module was limited to $\pm 45°$. Together with the operating frequency of 1.3 GHz and the energy gain this results in a shearing parameter

$$b(45°) \approx 570 \text{ keV/ps}. \tag{11}$$

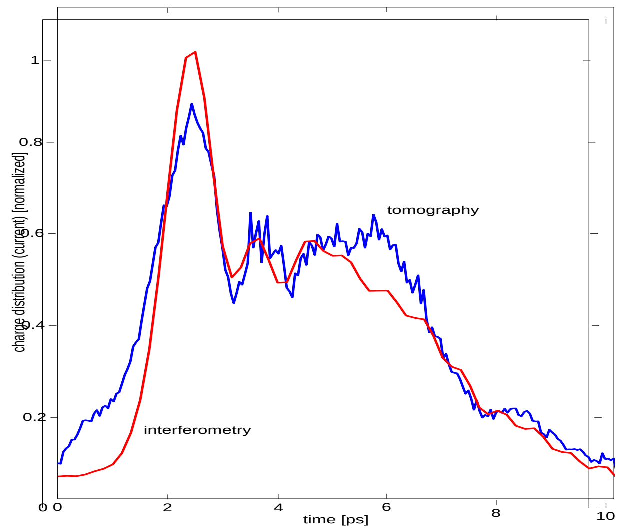

Figure 4: Longitudinal profile as reconstructed with tomography in comparison with a result from CTR interferometry.

The energy resolution of the spectrometer is estimated to be $\delta_E \approx 60$ keV. From these two numbers it is possible to calculate the minimum separation in time one can allow for two gaussian peaks. Due to the shearing the peaks are shifted against each other by $\triangle E = b \cdot \triangle t$ and their variance increases to

$$\sigma_E' = \sqrt{\sigma_E^2 + b^2\sigma_t^2}. \tag{12}$$

This means a loss of resolution. This implies that two peaks have to be separated by 3σ in time to achieve a separation of 2σ in the projection onto the energy. Then the achievable resolution is

$$\delta_t = \frac{3}{\sqrt{5}b}\delta_E. \tag{13}$$

For the case of the TTF this yields a resolution of $\delta_t = 150$ fs. Tests with the reconstruction algorithm showed that there is no significant contribution from the reconstruction algorithm.

The longitudinal tomography has been implemented in the TESLA Test Facility to study effects in the longitudinal phase space. The figure 3 shows experimental results from a measurement of that kind. It is remarkable that the phase space distribution is broken up especially in energy. Investigations are in progress whether this is caused by short range wakefields or coherent synchrotron radiation. The timeprofile measured with tomography has been compared to the result of interferometry of coherent transition radiation (CTR) analysed with the help of the Kramers-Kronig Relation. The (CTR)-interferometry suffers from a cutoff for low frequencies which had to be extrapolated in the reconstruction. Except for that uncertainty the agreement is good as can be seen in figure 4.

4 CONCLUSION

Diagnostics for bunch length measurements are being developed aiming at resolutions in the 100 fs regime. In this paper two promising techniques are described. First the electro optic methods measuring the fields of the bunches directly. The potential of this method in terms of achievable time resolution has to be explored, the limit is not reached yet by far. The method has the opportunity for single bunch diagnostic with the results delivered online and noninterceptive. It is possible to measure wakefields inside the accelerator as well.

The longitudinal tomography can only be performed with dedicated machine operation but it only relies on standard diagnostics and delivers very high resolution depending on the setting of the accelerator. It can reconstruct the two dimensional longitudinal phase space and therefore offers the possibility to study wakefields, coherent synchrotron radiation, and similar effects directly on the bunches themselves.

5 REFERENCES

[1] M. van Exeter, D. Grischkowsky, *Characterization of an optoelectric terahertz beam system*, IEEE Trans. Microwave theory and techniques 38, 1684 (1990)

[2] M.J. Fitch, *Electro-Optic Sampling of Transient Electric Fields from Charged Particle Beams*, ph.D.-thesis at the University of Rochester, Rochester, New York

[3] M.A. Geitz, *Bunch Length Measurements*, Proceedings of DIPAC 99

[4] M.A. Geitz, *Investigation of the Transverse and Longitudinal Beam Parameters at the TESLA Test Facility Linac*, DESY-THESIS-1999-033

[5] C.J. Hirschmugl et al., Phys. Rev. A, Vol. 44, No. 2, (1991)

[6] M. Hüning, *Dissertation*, Universität Hamburg, to be published

[7] G.M.H. Knippels, X. Yan, A.M. McLeod, W.A. Gillespie, M. Yasumoto, D. Oepts, A.F.G. van der Meer, *Generation and Complete Electric-Field Characterization of Intense Ultrashort Tunable Far-Infrared Laser Pulses*, Phys. Rev. Lett. Vol. 83, pp. 1578-1581

[8] H. Loos, *Dissertation*, TU Darmstadt, to be published

[9] G. Minerbo, *MENT: A Maximum Entropy Algorithm for Reconstructing a Source from Projection Data*, Computer Graphics and Image Processing 10, 48-68 (1979)

[10] F. Natterer, *The Mathematics of Computerized Tomography*, John Wiley & Sons and B. G. Teubner, 1986

[11] D. Oepts, Giel Berden *private communication*

[12] C.W. Rella, G.M.H. Knippels, D.V. Palanker, H.A. Schwettman, *Pulse shape measurements using differential optical gating of a picosecond free elecron laser source with an unsynchronized femtosecond Ti:sapphire gate* Optics Communications 157 (1998) 335-342

[13] K. N. Ricci, T. I. Smith, *Logitudinal electron beam and free electron laser microbunch measurements using off-phase rf acceleration*, Phys. Rev. ST - Accelerators and Beams, Vol. 3, 032801 (2000)

[14] U. Rohrer, W. Joho, *Introduction of 2-dimensional Tomography for monitoring the transverse beam emittance at SIN*, SIN Annual Report 1982, NL 5-6, Paul Scherrer Institut

[15] A.A. Starostenko et al., *Nondestructive singlepass bunch length monitor*, EPAC 2000, Viena, 2000

[16] X.J. Wang, Proc. of PAC 99 Conference, New York, 1999

[17] Q. Wu and X.-C. Zhang, *Ultrafast electro-optic field sensors* Appl. Phys. Lett. 68(1996), 1604-1606

[18] Q. Wu, X.-C. Zhang, Appl. Phys. lett., 67, 3523-3525 (1995)

[19] X. Yan, A.M. MacLeod, W.A. Gillespie, G.M.H. Knippels, D. Oepts, A.F.G. van der Meer, W. Seidel, *Subpicosecond Electro-Optic Measurement of Relativistic Electron Pulses*, Phys. Rev. Lett. Vol. 85, (16 Oct 2000), pp. 3404-3407

[20] Y. Yiang and X.-C. Zhang, Appl. Phys. Lett. 72(1998), 1945-1947

BPM READ-OUT ELECTRONICS BASED ON THE BROADBAND AM/PM NORMALISATION SCHEME

M. Wendt, DESY, Hamburg, Germany

Abstract

Recently developed circuit modules, used for the processing of position signals of electrostatic (“button”-type) pickups are presented. The concept is based on the broadband (“monopulse”) AM/PM normalisation technique. The short integration time (≈ 10 ns) makes this read-out electronics suitable for single-bunch position measurements nearby interaction areas and in linear accelerators. Details on circuit design and technology, as well as the practical realization are shown. The results discussed include beam position and orbit measurements made with a set of 40 units at the FEL-undulator sections of the TESLA Test Facility (TTF) linac.

1 INTRODUCTION

Each *beam position monitor* (BPM) (Figure 1) basically consists out of a *pickup* station for the signal detection and a set of *read-out electronics* (often 2 channels for horizontal and vertical plane) for signal processing and *normalisation*.

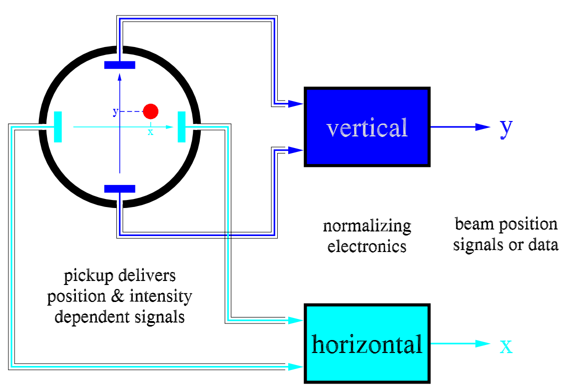

Figure 1: BPM principle.

A single electrode of a BPM pickup delivers a signal voltage

$$V_{\text{elec}}(\omega, x, y) = s(x, y)\, Z(\omega)\, I_{\text{beam}}(\omega) \tag{1}$$

which is proportional to the beam intensity $I_{\text{beam}}(\omega)$ (e.g. bunch charge) and to the beam-to-electrode distance (x, y) (e.g. tranverse beam displacement) or coupling which is covered by a sensitivity function $s(x, y)$. In case of high energy electron accelerators the frequency spectra of $I_{\text{beam}}(\omega)$ is of no concern; for the BPM system the bunches behave like dirac impulse excitation signals. The transfer impedance $Z(\omega)$ of the pickup electrode (centred beam) depends on the type of BPM pickup (e.g. button, stripline, cavity-BPM, etc.) and its geometry. It also fixes (roughly) the frequency range of the following signal processing system.

The BPM read-out electronics extracts the beam position (displacement) information from the analogue signals of the pickup electrodes. In order to simplify the normalisation procedure and to reduce the nonlinearities of $s(x, y)$ two symmetrically arranged electrode are sensed in each plane (see Figure 1). The read-out electronics *normalises* the electrode signals and therefore performs a beam intensity independent beam position measurement.

For each plane (horizontal or vertical) the corresponding BPM pickup electrodes supplies two signals (A and B). For symmetry reasons the *amplitude-ratio* $\hat{a}/\hat{b}$ is a beam-intensity independent function of the beam displacement:

$$\text{beam-position} = f(\frac{\hat{a}}{\hat{b}}) \tag{2}$$

which is processed by the presented broadband AM/PM technique [1]. The read-out system outputs an analogue pulse signal, from which the flat peak value is proportional to the beam displacement. Further data acquisition techniques are required to digitise the signal for use in the control system.

2 THE AM/PM PRINCIPLE

The amplitude-ratio, and such the beam-position, is measured with the *AM/PM signal processor* by converting the ratio into a phase-difference – the *amplitude modulation* (AM) converts into a *phase modulation* (PM). Practically the conversion is realized by a 90^0 hybrid junction, which is extended at one output port with a 90^0 delay-line.

For the analysis it is sufficient to simplify the two sine-wave burst (“ringing”) shaped input signals of the pickup electrodes to stationary sine-wave voltage functions v_A and v_B:

$$v_A(t) = \hat{a}\, e^{j\omega t} \tag{3}$$
$$v_B(t) = \hat{b}\, e^{j\omega t} \tag{4}$$

They have same frequency and are in phase, but the amplitudes $\hat{a}$ and $\hat{b}$ differ due to the beam displacement and are bunch charge dependent. At the outputs C and D of the hybrid-with-delay circuit the signals:

$$v_C(t) = \sqrt{\frac{\hat{a}^2 + \hat{b}^2}{2}} \arctan\left[\frac{\hat{a}\sin(\omega t) + \hat{b}\cos(\omega t)}{\hat{a}\cos(\omega t) - \hat{b}\sin(\omega t)}\right] \tag{5}$$

$$v_D(t) = \sqrt{\frac{\hat{a}^2 + \hat{b}^2}{2}} \arctan\left[\frac{\hat{a}\sin(\omega t) - \hat{b}\cos(\omega t)}{\hat{a}\cos(\omega t) + \hat{b}\sin(\omega t)}\right] \tag{6}$$

[1] For an overview of normalisation schemes see [1, 2]

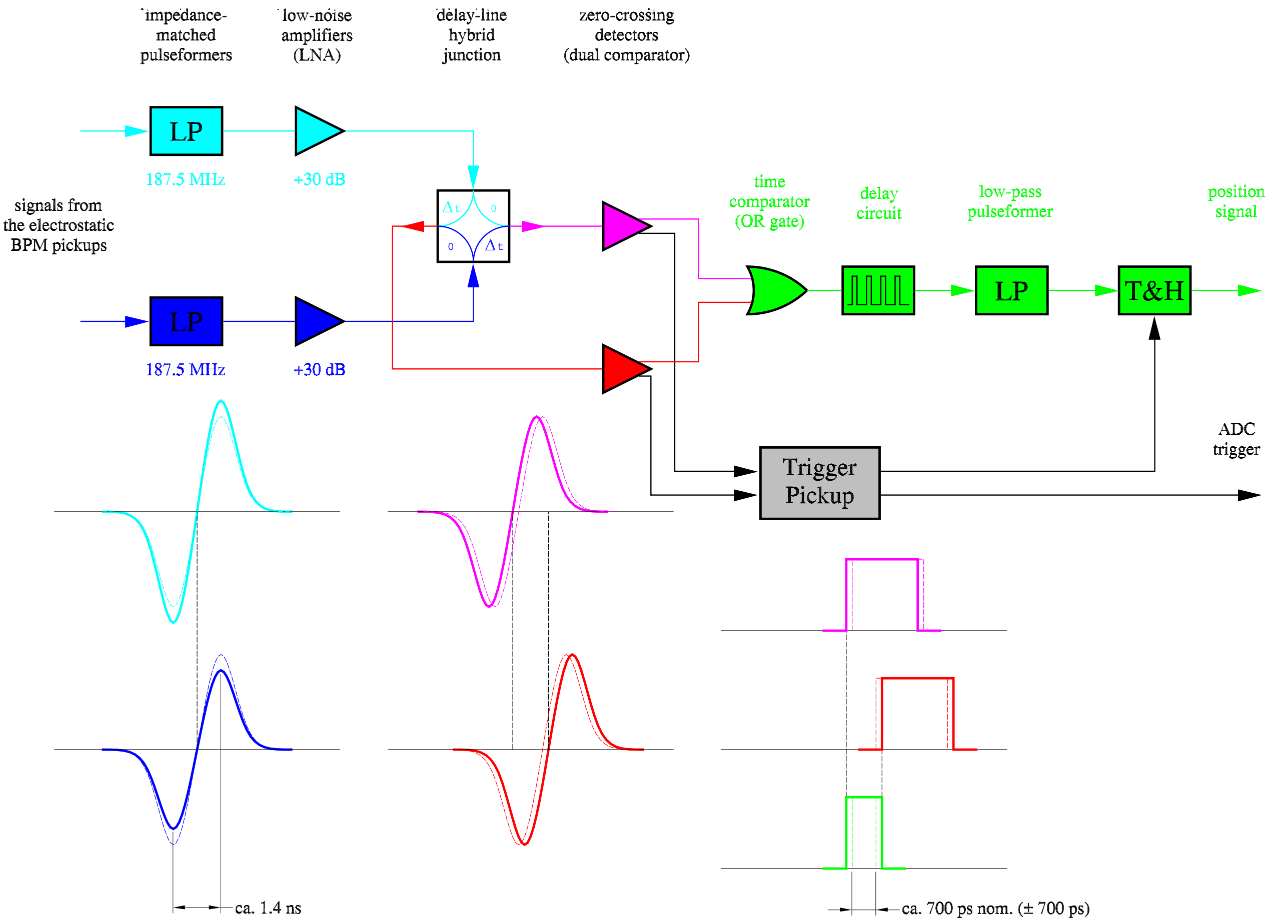

Figure 2: Monopulse AM/PM read-out electronics.

have the same amplitude, but the amplitude-ratio of A and B is converted into a phase-difference:

$$\Psi_{C-D} = 2\,\mathrm{arccot}\left(\frac{\hat{a}}{\hat{b}}\right) \tag{7}$$

The AM/PM BPM signal processing was introduced first in the *Tevatron* (FNAL) as narrow bandwidth system [3]. The single bunch capability was added in the installations at *LEP* (CERN) [4] and *HERA-p* (DESY) [5]. The successful operation in those large scale, high energy particle accelerators are due to some major advantages of the AM/PM BPM read-out method:

- The full beam displacement range is covered, including a large dynamic range (> 40 dB) of beam/bunch intensities, without attenuator/amplifier switching or feedback circuits.
- The AM/PM method offers a reliable beam position measurement, also at small beam displacements, when subtraction methods (e.g. Δ/Σ signal processing) may fail.
- The AM/PM BPM electronics can be devided into a few simple basic subcircuits: passive networks, linear amplifiers, digital gate functions and analogue comparators. There is no manufactur dependence for high integrated and/or specialized semiconductor circuits.
- All the needed semiconductors and parts are available in radiation resistant (!) bipolar process technology.

3 MONOPULSE AM/PM READ-OUT ELECTRONICS

Instead of operating – time-consuming – a burst of RF sine-wave oscillations, the *monopulse* AM/PM scheme processes the beam position from a single pulse, which is the slightly "integrated" – by lowpass pulseformers – pickup signal. The technique was proposed by D. Cocq (CERN) as analogue signal processor for the LHC BPM-system [6]. It offers a couple of additional features:

- Direct processing of the button or stripline BPM pulse signals through simple lowpass pulseformers.
- Short integration (measurement) time for single bunch position measurements with little intra-bunchspacing.
- Relaxed tolerances for matching the input filters.
- Improved sensitivity for low intense bunch signals.

A set of 40 monopulse BPM units where developed for the read-out of 20 electrostatic ("button"-type) pickups, which are located inside the FEL-undulator sections of the TTF linac. The BPM electronics are realized by subdividing each BPM unit into "rf-block" modules mounted on a VXI C-size PCB. Figure 2 gives an overview on the schematics and the principle of operation.

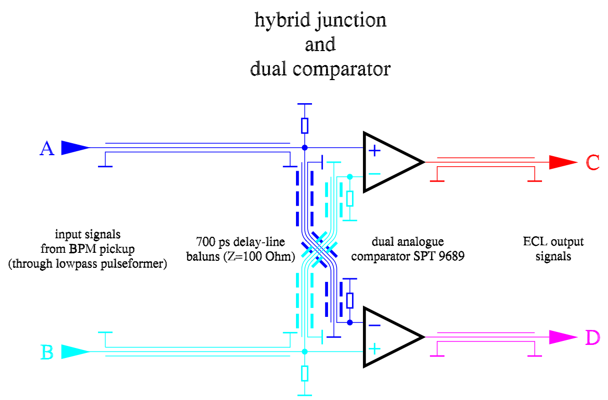

Figure 3: Monopulse AM/PM conversion circuit.

Basic part is the delay-line balun based hybrid-junction and the following pair of zero-crossing detectors (dual comparator) (see Figure 3). Here the amplitude-varying signals from the two pickup electrodes – after passing impedance-matched (absorbing) lowpass pulseformers and 30 dB low-noise amplifiers – are converted into time-varying signals. The analogue comparators act on the zero-crossings of their difference-input signals and outputs bunch charge independent digital ECL-level signals.

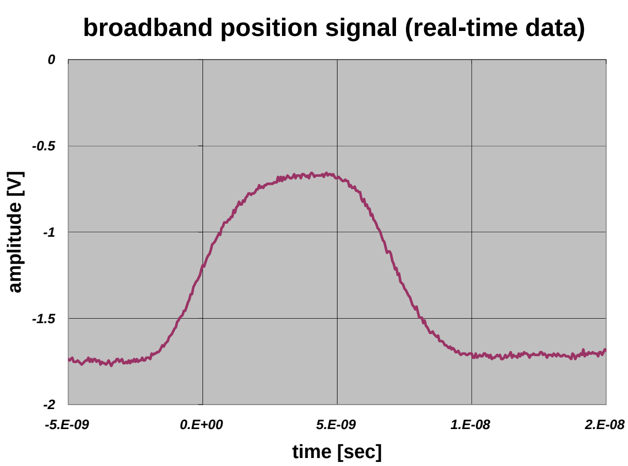

Figure 4: Processed beam position (displacement) signal.

The following time comparator (OR gate) compares both signals to a short ECL pulse (nominal width ca. 700 ps); it's width, respectively area is proportional to the beam displacement. For a simplified integration this pulse signal is "lined-up" four times by use of programmable digital delay circuits. Figure 4 shows the lowpass-integrated, ≈ 10 ns long beam position signal. For adapting to the data acquisition system at TTF a high-speed track&hold amplifier is used to freeze the peak value of this displacement signal for an adequate amout of time.

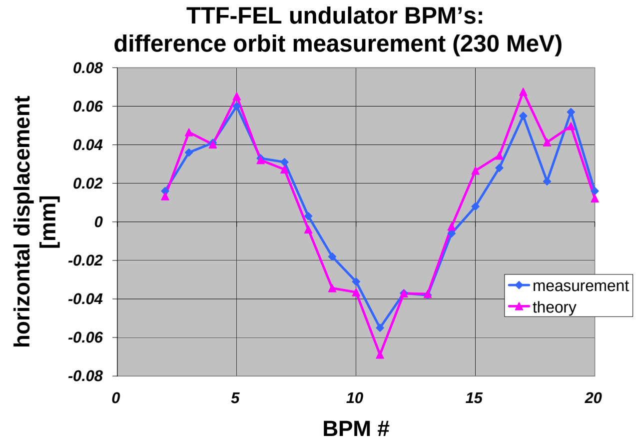

Figure 5: Orbit in the FEL-undulator sections of TTF.

The TTF FEL-undulator BPM system operates since spring 2000 (see Figure 5). With the *Onsemi* ECLinPS Plus family gates and the SPT 9689 dual comparator used in the electronics hardware a **single-bunch, single-pass resolution** $< \mathbf{10}\ \mu\mathbf{m}$ (10 mm dia. beam pipe) was achieved, while the **integration (measurement) time keeps within** $\approx$ **10 ns**.

Several modifications and re-developements are underway to improve the displacement range limitations (only ≈ 70 %), as well as the rather limited intensity range (5...10). The moderate linearity of the read-out electronics can be corrected by applying an automatized calibration routine to each individual BPM unit.

4 REFERENCES

[1] G. Vismara, "The Comparision of Signal Processing Systems for Beam Position Monitors", Proceedings of the 4^{th} European Workshop on Diagnostics and Instrumentation for Particle Accelerators DIPAC 99, Chester, UK ; May 16 - 18, 1999.

[2] G. Vismara, "Signal Processing for Beam Position Monitors", 9^{th} Beam Instrumentation Workshop BIW '00, MIT Bates, Cambridge, MA, USA ; May 8 - 11, 2000.

[3] R. E. Shafer, et. al., "The Tevatron Beam Position and Beam Loss Monitoring System", Proc. of the International Conference of High Energy Accelerators HEACC 88, FNAL Batavia, IL, USA; 1988.

[4] J. Bosser, L. Burnod, G. Feroili, "Beam Position Measurements by Use of 90^{0} Hybrids (Proposal for LEP)", CERN SPS/ABM/83-01/00586, January 1983.

[5] A. Jacob, et. al., "The HERA-p BPM Readout System", Proc. of the 2^{th} European Particle Accelerator Conference EPAC 90, Nice, France; August 16 - 18, 1990.

[6] D. Cocq, "The wide band normalizer – a new circuit to measure transverse bunch position in accelerators and colliders", Nulcear Instruments & Methods in Physics Research A 416 (1998) 1 - 8.

FIRST COMMISSIONING RESULTS OF THE ELETTRA TRANSVERSE MULTI-BUNCH FEEDBACK

D. Bulfone, C. J. Bocchetta, R. Bressanutti, A. Carniel, G. Cautero, A. Fabris, A. Gambitta, D. Giuressi, G. Loda, M. Lonza, F. Mazzolini, G. Mian, N. Pangos, R. Sergo, V. Smaluk, R. Tommasini, L. Tosi, L. Zambon, Sincrotrone Trieste, Trieste, Italy
M. Dehler, R. Ursic, Paul Scherrer Institut, Villigen, Switzerland

Abstract

A wide-band bunch-by-bunch Transverse Multi-Bunch Feedback, developed in collaboration with the Swiss Light Source (SLS), has been installed at ELETTRA. After a description of the main hardware/software components, the first commissioning results and the present status of the system are given.

1 INTRODUCTION

The ELETTRA Transverse Multi-Bunch Feedback (TMBF) [1] consists of a wide-band bunch-by-bunch system where the positions of the 432 bunches, separated by 2 ns, are individually corrected. After combining and demodulating the wide-band signals from a standard ELETTRA electron Beam Position Monitor (BPM), the X (Y) baseband signal (0-250 MHz) is sampled by an eight-bit 500 Msample/s Analog-to-Digital Converter (ADC). The resulting 500 Mbyte/s data flux is first de-multiplexed into six 32 bit FDPD (Front Panel Data Port) channels. The data from each of them is then distributed by means of a programmable switch to the four TI-TMS320C6201 programmable Digital Signal Processors (DSP) housed in one VME board. In the present configuration all of the data coming from one FPDP channel, which correspond to 72 bunches, are passed to one DSP for on-line diagnostics and concurrently split over the remaining three DSPs for the execution of the feedback algorithm. A detailed description of the digital processing electronics is given in [2]. The calculated corrective kick values are recombined following a symmetric multiplexing scheme and transmitted to an eight-bit 500 Msample/s Digital-to-Analog Converter (DAC), amplified by an RF power amplifier and applied to the beam by a stripline kicker. A flexible timing system provides the necessary synchronization signals.

2 CLOSED-LOOP RESULTS

Commissioning has focussed on the vertical plane since the instabilities are stronger and users are more sensitive to vertical emittance. The TMBF loop has been characterized and successfully closed on beams of increasing current and energy, up to 320mA@2GeV and 130mA@2.4GeV, which are the typical target values during users' shifts. Figure 1 shows the effect of the TMBF as seen on the synchrotron radiation profile monitor image of a 200 mA stored beam affected by vertical transverse coupled-bunch instabilities.

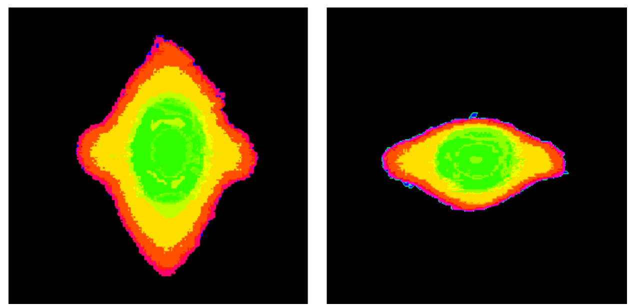

Figure 1: Synchrotron radiation profile monitor images of a 200 mA beam affected by vertical transverse coupled-bunch instabilities with TMBF off (left) and on (right).

The developed DSP software allows the adoption of Finite Impulse Response (FIR) filters with up to 5 taps for the feedback algorithm. However, the presently used filter is a 3-tap FIR that provides rejection of the closed orbit signal while ensuring the right phase and gain at the betatron frequency. The total closed-loop delay is four revolution periods plus the BPM-to-kicker delay. One RF amplifier per plane powers the downstream port of a single kicker stripline.

3 DIAGNOSTIC TOOLS

In parallel to the closed loop functionality, the digital implementation of the TMBF system opens the way for additional diagnostic features that can be built by appropriate programming of the system. A number of them have been developed starting from the commissioning phase.

3.1 Bunch-by-Bunch Data Acquisition

As already mentioned, one of the four DSPs on each VME board is dedicated to data acquisition for on-line diagnostics and 16 Mbytes of Synchronous Dynamic RAM are available for this purpose. The whole system made up of six boards allows 96 Mbytes of bunch-by-bunch continuous data at 500 Msample/s, corresponding to 192 ms, to be recorded in parallel during normal feedback operation.

A VME OS/9 based host computer acts as the TMBF system supervisor and communicates with the DSP boards via the VME bus. It triggers the recording and collects the stored data from the DSPs. Two Mbytes of Global Static RAM, which is accessible both from the VME bus and from the DSPs, are used as a communication buffer.

3.2 Change of the Digital Filter Coefficients

The values of the coefficients used by the 5-tap FIR filters can be changed on the fly while the feedback is running. This feature is implemented using the TMS320C6201 Host Port Interface (HPI), which is an additional 16-bit wide parallel port through which the VME bus host computer can read/write the DSP internal memory locations where the coefficients are stored without interfering with the currently executed code. The complete operation of changing the 90 filter coefficients on all of the 18 DSPs involved in the feedback loop is carried out in 150 µs.

3.3 Integration with the Matlab Environment

Beside managing the DSPs' operation as described above, the VME host computer is used to interface all of the TMBF system components (timing, ADC, DAC and RF amplifier) to the ELETTRA control system through the Remote Procedure Call (RPC) protocol running over the Ethernet network.

A set of newly developed Matlab commands, implemented as M/Mex-files on top of RPC, also allows to access the TMBF equipment from any Matlab session running on the control room workstations (Figure 2). This provides a powerful unified platform for both commissioning operations and machine physics studies as it merges TMBF system control, on-line analysis of the acquired data and graphical visualisation of the results.

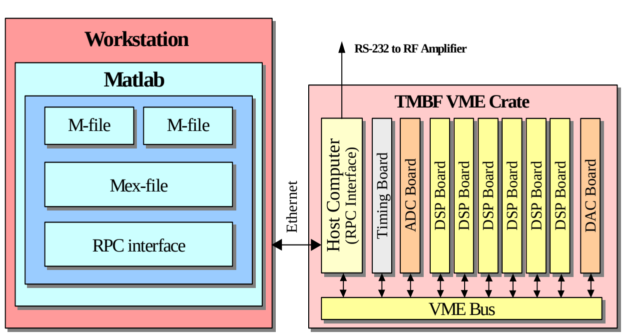

Figure 2: Block diagram of the hardware/software TMBF system architecture.

The following are some of the developed Matlab commands:

get_all(): acquires an array of bunch-by-bunch position samples of all the bunches. An option allows to reject the DC closed orbit component from each bunch as well as the spurious low frequency components due to longitudinal coupled-bunch modes.

get_bunch(): acquires an array of turn-by-turn position samples of a chosen bunch.

set_filter(): sets the digital filter coefficients.

set_filter_sync(): changes the digital filter coefficients in time according to a specified sequence of intervals and contemporarily records the position data containing the transients generated by the filter changes.

4 DIAGNOSTICS MEASUREMENTS

During the commissioning period several measurements have been carried out to test the TMBF system and evaluate its performance and effect on the beam. The most significant of them are reported here.

4.1 Frequency Domain Analysis

The data acquisition features make the feedback system a powerful tool for spectrum analysis. 250MHz-wide spectra for complete multi-bunch mode analysis with 1 kHz resolution can be obtained in the control room at a repetition rate of about 0.5 Hz. Figure 3 is an example of such a measurement and shows the base-band (0-250MHz) open/closed loop amplitude spectra of a beam with vertical coupled-bunch instabilities.

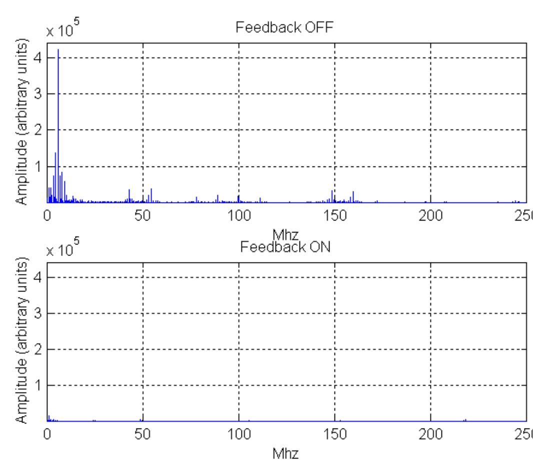

Figure 3: Feedback off/on base-band (0-250MHz) multi-bunch amplitude spectra (with rejected DC closed orbit component) of a 210 mA vertically unstable beam.

4.2 Growth/Damp Transients

Figure 4 shows the spontaneous growth of the oscillation amplitudes of the bunch train of a vertically unstable beam when the feedback is switched off and the subsequent damping effect when the feedback is switched back on. This time domain transient has been obtained using the Matlab routine *set_filter_sync()*, which sets the filter coefficients to zero and restores them back to their original value after a specified 2.3 ms interval.

The same transient can be analysed also on a 3D plot where the evolution of the entire beam spectrum is plotted vs. time. Figure 5 illustrates how the amplitude of the vertical modes sidebands grows and the effect of the feedback when it is switched on.

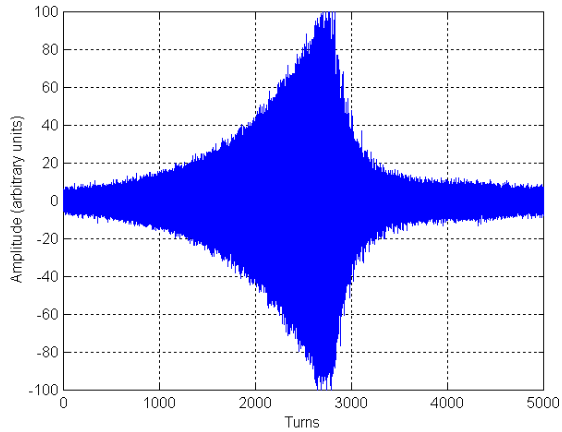

Figure 4: Vertical growth/damp transient generated by switching off/on the feedback.

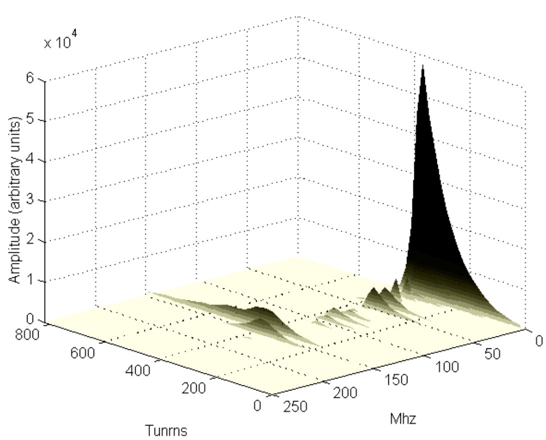

Figure 5: Base-band spectra vs. time showing the growth of unstable vertical modes when the feedback is turned off and the damping effect when the feedback is turned back on.

4.3 *Betatron Tune Measurements*

Accurate betatron tune measurements can be performed using the TMBF system. The spectrum of the motion of a single bunch clearly reveals the betatron tune line at the fractional tune frequency when an unstable mode is excited. If no multi-bunch instabilities are present, changing the FIR filter taps in order to produce an anti-damping effect with a positive feedback can artificially excite transverse oscillations. The Matlab routine *set_filter_sync()* is used to create anti-damping/damping transients during which betatron oscillations can be detected and measured.

In particular, the filter coefficients can be changed only for those 24 bunches managed by one selected DSP. The feedback can therefore be switched off/on on some bunches while it continues to run on the rest of them. This technique allows performing tune measurements in parallel to TMBF operation with no effect on the stored beam.

5 CONCLUSIONS

A bunch-by-bunch TMBF system based on programmable DSPs for the processing of the position data coming from all of the 432 2ns-spaced bunches has been installed at ELETTRA and is finishing its commissioning phase. As of today, commissioning has been done on the vertical plane. Vertical coupled-bunch instabilities have been completely damped on beams of different energies/currents that correspond to the ELETTRA standard operational values during users' shifts.

In addition to the verification of the main hardware components, a number of software based diagnostic tools that can run in parallel to feedback operation have been tested and used since the first phases of commissioning. Such tools allow an effective characterization of both the TMBF system hardware and beam behaviour.

The availability and integration of beam diagnostics routines in the Matlab environment make the TMBF system a valuable tool also for general machine physics studies.

In order to improve the usable dynamic range at the input of the ADC and simplify machine operations by relaxing the present constraints on the closed orbit whose offsets has to be minimized at the TMBF BPM location, a dedicated DC signal rejection electronic circuit is under development.

The TMBF system has been developed as a collaboration project with the Swiss Light Source, where it will be installed during the next summer. The necessary DSP software changes to deal with 480 2-ns spaced bunches are in progress.

A Longitudinal Multi-Bunch Feedback is also being designed for both the accelerators and will use the already developed digital processing hardware, running the appropriate software.

REFERENCES

[1] D. Bulfone et al., “Design Considerations for the ELETTRA Transverse Multi-Bunch Feedback”, PAC’99, New York, March 1999.
[2] M. Lonza et al., “Digital Processing Electronics for the ELETTRA Transverse Multi-Bunch Feedback System”, ICALEPCS’99, Trieste, October 1999.

PERFORMANCE OF THE DIGITAL BPM SYSTEM FOR THE SWISS LIGHT SOURCE

V. Schlott, M. Dach, M. Dehler, R. Kramert, P. Pollet, T. Schilcher, PSI, Villigen, Switzerland;
M. Ferianis, R. DeMonte, Sincrotrone Trieste, Italy;
A. Kosicek, R. Ursic, Intrumentation Technologies, Slovenia.

Abstract

The accelerator complex of the Swiss Light Source (SLS) is presently under commissioning at the Paul Scherrer Institute (PSI) in Villigen, Switzerland. The newly developed digital beam position monitor (DBPM) system has been successfully used to determine beam positions in the pre-injector LINAC, the transfer lines, the booster synchrotron and the storage ring. Instant and free selection of operation modes through the EPICS-based SLS control system allows to choose between single turn, turn-by-turn and closed orbit measurements. The operational experience and performance of the DBPM system is presented, based on measurements, taken during SLS commissioning. A monitoring system (POMS), which measures the horizontal and vertical mechanical positions of each BPM block in reference to the adjacent quadrupole magnets has been installed and first results, indicating transverse movements of the BPM blocks as a function of current in the storage ring will be presented.

1 INTRODUCTION

The DBPM system played a vital role during the commissioning of the SLS accelerator complex, which started in March 2000 and is still continuing until August 2001 [1]. The implementation of all available operation modes [2] from the beginning delivered beam position measurements in the LINAC, the transfer lines, the booster synchrotron and in the storage ring. In addition to simply visualizing the positions in the control room, the DBPM system is constantly delivering data to SLS beam dynamics applications [3]. This data transfer is arranged through a batch process consisting of up to 8192 x- and y-position and intensity readings, synchronized to the 3 Hz repetition rate of the SLS injector. The full programmability of the quad digital receiver (QDR) [2] as well as the complete integration of the DBPM electronics in the EPICS based control system, allows remote switching of operation modes for each sector of the booster synchrotron and storage ring individually. Optimization of injection and beam optics studies like measurement of tunes and chromaticities as well as “beta scans” have been performed in the high speed / medium resolution *turn-by-turn mode*. For determination of closed orbits, the system has been switched to lower bandwidth and therefore higher resolution. The application of a pilot signal in the RF front end [2] provides calibration of the electronics for any chosen gain setting. A self test mode can be applied to exclude mal-functioning of BPM stations and therefore improves reliability. Using the features and flexibility of the DBPM system resulted in a fast and efficient commissioning and provided complete understanding of the SLS accelerator optics.

2 PERFORMANCE CHARACTERISTICS

The following measurements have been taken in the laboratory and during SLS commissioning to determine the DBPM systems performance, to demonstrate first operational experience and to present some results from the SLS accelerators.

2.1 Resolution and Beam Current Dependence

While an AGC loop is presently not yet implemented, the full dynamic range of the DBPM system is covered through downloading of specific sets of pre-calibrated gain levels which correspond to pre-defined beam current ranges. These ranges are large enough to guarantee standard storage ring operation between adjacent injection (re-filling) cycles. The gain settings are chosen in such a way that the signal levels in the RF front end are always kept within the linear regimes of all electronics components and that the RF front end output is not exceeding 70% of the QDRs analog-to-digital converters input range (1 Vpp for presently used 12 bit AD9042 from Analog Devices). Minimum *turn-by-turn* resolution, which corresponds in case of SLS to 1 MS/s, has been measured to be in the order of 20 μm over a dynamic range of 5 mA to 700 mA. The minimum resolution at 15 kHz bandwidth corresponding to a so called "*ramp-250 ms*" mode, which was especially implemented for the booster synchrotron, has been determined to be < 3 μm and the resolution in the *closed orbit / feedback* mode, which operates at 4 kS/s, is < 1.2 μm. The increase of resolution from *turn-by-turn* mode over the "*ramp-250ms*" mode to the *closed orbit / feedback* mode goes - as can be expected - with the square root of bandwidth. In the latter two modes however, some low bandwidth noise floor can still be observed, which may be caused by phase noise in the RF front end. This issue needs be addressed (and solved) before the global closed orbit feedback [4] will be implemented. The sudden decreases of resolution whenever the gain levels of DBPM system are changed is a systematic effect and will be minimized as soon as the AGC loop is operational.

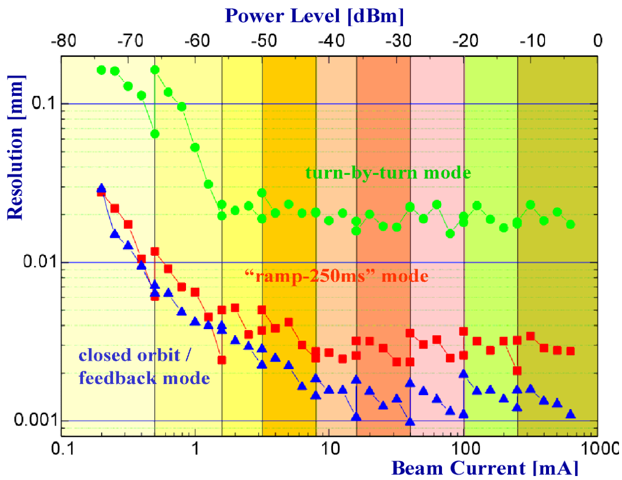

Figure 1: Measurement of DBPM resolution for different bandwidths: 500 kHz (green dots), 15 kHz (red squares) 2 kHz (blue triangles). Gain levels of the system are kept constant for the marked beam current ranges.

Beam current dependence has been measured in the lab for a centered beam by performing several measurement cycles over the whole dynamic range of the system with the same (constant) pre-calibrated gain settings as above. It was determined to be ⌖ 5 µm within ranges of constant gain levels. At low signal intensities, position jumps occur, whenever a new gain setting is loaded. In these cases, the calibration routine still needs to be improved. Drifts of < ⌖ 5 µm, in a beam current range between 7 mA and 700 mA, are within specifications of SLS.

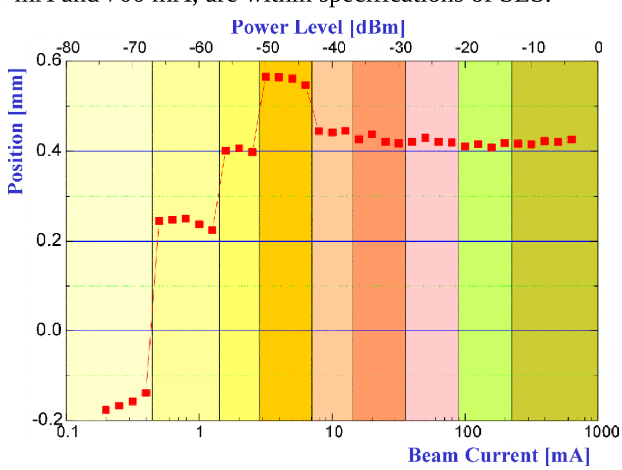

Figure 2: Beam current dependence over the whole dynamic range of the DBPM system in *closed orbit / feedback* mode.

2.2 Long Term Stability

Measurement of long term stability of DBPM electronics has been performed in the SLS technical gallery with a constant input power level of –12 dBm and a constant DBPM gain setting at the carrier frequency of 499.654 MHz over a time period of 24 hours. It resulted to be within ⌖ 1 µm.

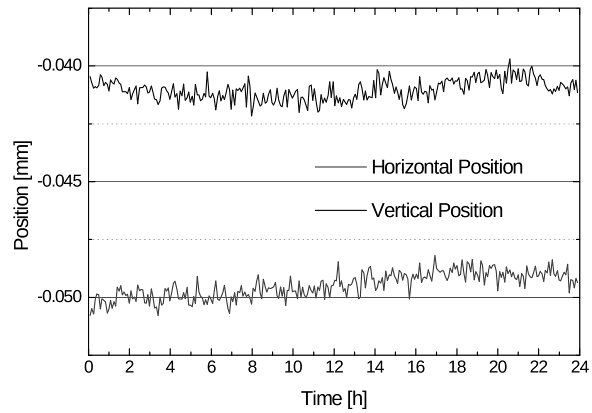

Figure 3: Long term stability of the SLS DBPM system was measured to be within ± 1 µm over a time period of 24 hours.

2.3 Measurements on SLS Booster Synchrotron

The SLS booster synchrotron which ramps up the energy of the electrons from 100 MeV to 2.4 GeV, is placed in the same tunnel as the storage ring (magnets are fixed at the inner wall of the tunnel). With its circumference of 270 m, it allows the use of quite small combined function magnets, which leave only space for a 20 by 30 mm elliptical vacuum chamber [5]. Therefore, the requirements for beam positioning as well as orbit and tune control in order to obtain good injection rates into the storage ring are quite challenging. Low injection losses and knowledge about beam parameters are especially important in the anticipated *top-up injection mode*, which should keep the beam current in the storage ring constant to a level of 10^{-4} of the nominal 400 mA. In this respect, the flexibility of the DBPM system is extremely helpful and all available operation modes have been extensively used during commissioning. The first turn(s) and turn-by-turn capabilities allowed optimization of injection, built-up of the ramp and single turn extraction. Tunes (predominantly the horizontal tune) have been determined and corrected throughout the acceleration cycle by continuously adjusting the trigger delay of the DBPM system, operating in tune mode. Orbits have been measured and could be corrected along the ramp down to rms values of about 400 µm, which is especially important at low energies, where emittances and therefore electron beam sizes are still rather large.

Figures 4a and b show horizontal and vertical beam orbits at booster BPM station ABODI-BPM-6C over a complete ramp for nominal injection with 0.5 mA beam current and for the future top-up injection with beam currents as low as 5 µA. For the small SLS booster vacuum chamber geometry, resolutions of 1.5 µm and 100 µm have been achieved applying equal gain settings.

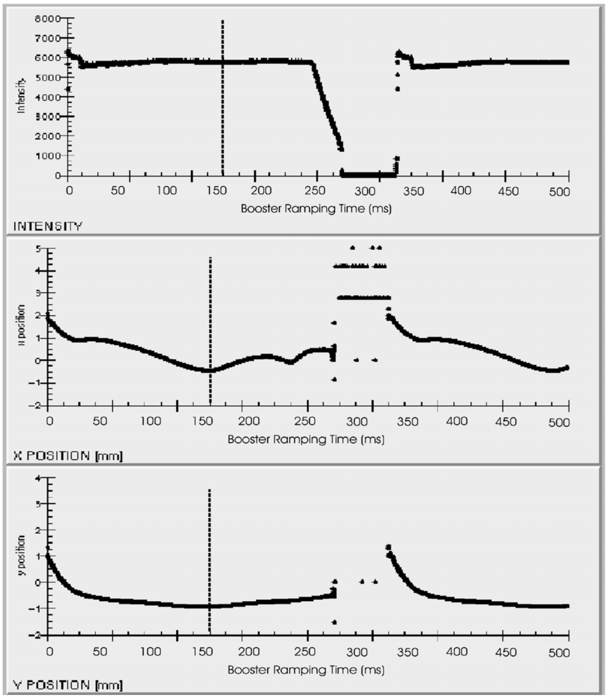

Figure 4a: Display of electron beam orbit along booster synchrotron ramp at BPM station ABODI-BPM-6C for nominal injection current of 0.5 mA. 1/E-damping of initial orbit correction is clearly visible in the vertical for not ramped correctors. Only during commissioning, the ramp was exceeded to 270 ms duration, corresponding to a deceleration of the beam down to about 300 MeV in order to minimize radiation losses.

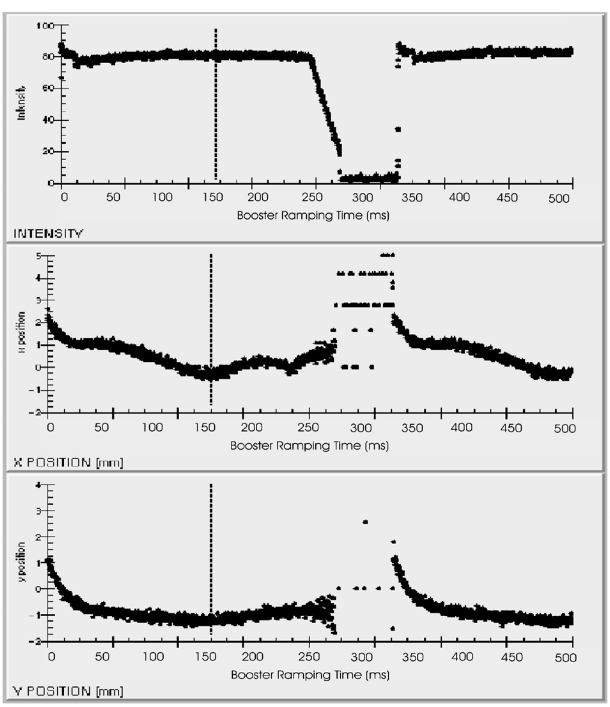

Figure 4b: Same measurement as above for low top-up injection current of 5 µA.

2.4 SLS Storage Ring Measurements

Likewise in the booster synchrotron, first turn(s) and turn-by-turn modes supported a fast and well optimized injection in the SLS storage ring. As already mentioned in the introduction, the direct connection of the DBPM system with the SLS beam dynamics applications over the EPICS based control system allowed automated tune, chromaticities and beta scans for good understanding of storage ring optics. Therefore, the machine modeling is extremely close to reality, which results in closed orbit corrections as low as 7 µm rms in the horizontal and 1 µm rms in the vertical! Displays of the corrected orbits are shown in figure 5.

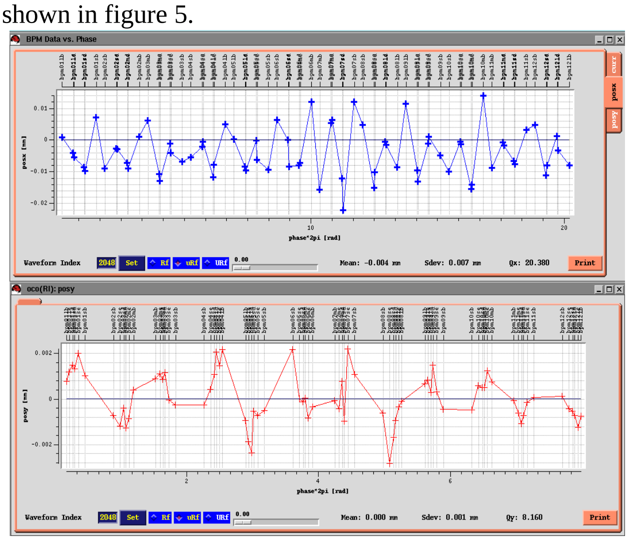

Figure 5: Horizontal (top) and vertical (button) orbit in SLS storage ring corrected to 7 µm rms respectively 1 µm rms.

3 MONITORING OF THE BPM'S MECHANICAL POSITIONS

At SLS, the final alignment of the BPM block positions will be performed by the method of beam based alignment (BBA). Since each quadrupole has its own power supply, it is expected to reach an accuracy of < 2 µm in reference to the magnetic axis of the storage ring. However, finite element analyses (FEA) show, that thermal loads or gradients, caused by changing beam currents in the machine, lead to a strong deformation of the vacuum chamber, resulting in position changes of the BPM stations in the order of 2 µm/°K. Figure 6 shows an example of such a FEA-simulation for a measured temperature distribution along sector 06 of the SLS storage ring. It is clearly visible, that the vacuum chamber is strongly bent between the BPM supports but still not touching the storage ring magnets, which leave 0.7 mm space to each side. The BPM supports, which are designed for stiffness in the transverse plane, move up to 3 mm in the longitudinal direction, while horizontal and vertical displacements are in the order of a few tens of microns.

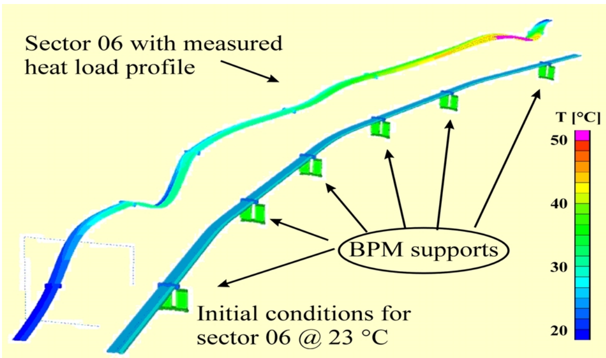

Figure 6: Finite element analysis of vacuum chamber movement in SLS storage ring for measured temperature profile along sector 06.

The mechanical drifts of the BPM supports in the SLS storage ring are constantly measured by a so called mechanical position monitoring system (POMS). It uses two linear encoders of the Renishaw RGH24Z50A00A type with 0.5 µm resolution for each BPM station. The sensors, which are rigidly attached to the adjacent quadrupole magnets, serve as dial gauges in the horizontal and vertical directions. The raw data from 12 encoders per sector are transferred via a SSI-serial interface electronics to a 32 channel VME-card, where the data can be read and written through memory mapping into the EPICS control system.

A snapshot during SLS storage ring commissioning is shown in figure 7, where daytime activities concentrate on injection and RF studies while the nightshift performed vacuum system laundry. The BPM blocks movements, which are measured by the POMS system, can be nicely correlated to the beam current (respectively heat load) in the storage ring and agree well with the FEA-simulations. Even with a well corrected orbit, movements are in the order of several tens of microns (maximum of 50 µm with 150 mA current change) are measured in the horizontal.

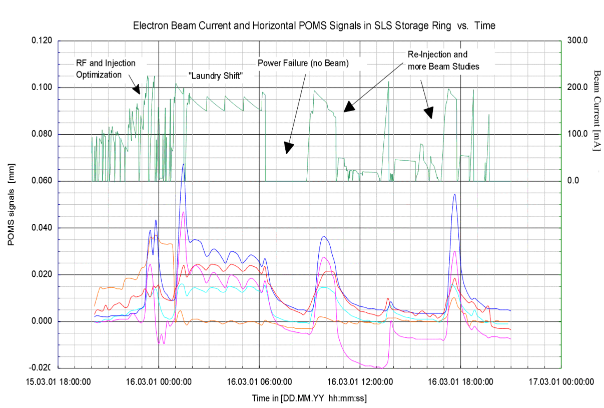

Figure 7: Horizontal BPM block movements and beam current in SLS storage ring during commissioning.

Since BPM readings are always relative measurements between electrode (BPM block) positions and electron beam positions, the POMS data will be taken in account for the final determination of "real" beam positions in the DSP part of the DBPM electronics. With this de-coupling of mechanical movements and electron beam motion, it is anticipated to keep a "golden" orbit throughout a machine run without any re-calibration of BPM centers by BBA. This approach should improve the reproducibility and stability of the SLS as a light source for the users.

4 CONCLUSIONS AND OUTLOOK

The DBPM system has reached and even exceeded the design specifications in all available operation modes and supported the successful and efficient commissioning of the SLS accelerator complex. Its complete integration into the EPICS based control system allows online re-programmability (e.g.: selection of operation mode) by the operators in the control room through a BPM control panel. Mechanical movements of the BPM blocks in the order of some tens of microns have been observed with the POMS system as a function of beam current in the storage ring.

TABLE 1. SLS DBPM system parameters

Parameter	Requirements	Achievements
Resolution turn-by-turn mode feedback mode	 < 20 ✪m < 1 ✪m	 < 20 ✪m <1.2 ✪m
Beam Current Dep. 5 - 400 mA const. gain ranges	 < ⌖ 50 ✪m < ⌖ 2.5 ✪m	 ⌖ 20 ✪m ⌖ 5 ✪m
24 h stability	⌖ 2.5 ✪m	⌖ 1 ✪m

DBPM features like an AGC loop and real time data transfer for the SLS closed orbit feedback still have to be implemented in the next few months in order to support SLS user operation, starting in August 2001.

REFERENCES

[1] A.Streun, et al. "Commissioning of the Swiss Light Source", to be presented at PAC'01, Chicago, June 2001.
[2] V. Schlott, et al. "Digital BPM System for the Swiss Light Source - First Operational Results", AIP Conf. Proc. 546, of BIW'00, Cambridge, May 2000, p 572.
[3] M. Böge, et al. "Commissioning of the SLS using CORBA based Beam Dynamics Applications", to be presented at PAC'01, Chicago, June 2001.
[4] M. Böge, et al. "Fast Closed Orbit Control in the SLS Storage Ring" PAC'99, New York, June 1999.
[5] W. Joho, et al. "The SLS Booster Synchrotron", EPAC'98, Stockholm, June 1998.

FIBRE OPTICAL RADIATION SENSING SYSTEM FOR TESLA

H. Henschel, Fraunhofer-INT, Euskirchen, Germany
M. Körfer, DESY, Hamburg, Germany
F.Wulf, HMI, Berlin, Germany

Abstract

High energy accelerators generate ionising radiation along the beam-line and at target places. This radiation is related to beam losses or dark currents. The in-situ measurement of this ionising dose that is distributed over long distances or large areas requires a new monitor system. This paper presents first results and the concept of such a monitor system at the Tesla Test Facility.

1 MOTIVATION

Field emission electrons are coming out of the RF laser gun and accelerator cavities. Particles based on this dark current can leave the cavity when they are emitted in a proper phase and will be accelerated together with the bunched beam. The dark current is not well-matched to the magneto optics so that most of it will hit the vacuum chamber, cavities and collimators in front of the undulators/detectors. This mechanism produces high energetic X-rays and electromagnetic showers. The regular bunched beam can also be lost during the accelerator commissioning or standard beam operation due to power supply failures. For a long and complex accelerator system like TESLA [1] it will be advantageous to monitor and measure on-line the local dose in sections of interest, especially at radiation sensitive equipment like fast signal processing units (PCs), superconducting components, collimators and permanent undulator magnets . A new in-situ sensing system could be realised by optical fibres combined with an Optical Time Domain Reflectometer (OTDR).

2 MEASUREMENT

2.1 General Layout

The most obvious effect of ionising radiation in optical fibres is an increase of light attenuation. The radiation penetrates the fibre and creates additional colour-centres which cause a wavelength-dependent attenuation that can be measured with an OTDR (Fig.1). A short laser pulse is launched into the fibre. A fraction of the signal reaches the photo-detector by Rayleigh back-scattering and Fresnel-reflections. The light coming from fibre sections behind the exposed fibre part suffers absorption leading to an attenuation step on the OTDR trace. The height of the step is proportional to the radiation dose. Differentiation of the OTDR curve results in peaks with dose-proportional height.

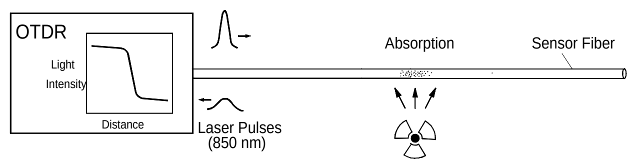

Figure 1: Principle of radiation dose measurement with optical fibres: OTDR-solution (= "distributed" sensor with local resolution). The radiation produces absorbing "colour centers". Propagation time and intensity of the back-scattered laser pulses allow determination of radiation intensity (= dose) and location of the radiation exposure.

With the known speed of light (~ 0.66 c), the measured pulse propagation time can be converted into distance, allowing the localisation of dose deposition. The shorter the laser pulse length, the better the local resolution. But reducing the pulse length leads to a reduction of the light intensity and thus of the dynamic range of the OTDR. As a consequence, the maximum sensor fibre length and/or the maximum measurable dose are reduced. The multimode fibre module of the chosen OTDR (Tektronix TFP2A) is equipped with a 850 nm laser of pulse widths (PWs) ≥ 1 ns as well as a 1300 nm laser (PWs ≥ 10 ns). Due to the wavelength dependence of the radiation-induced attenuation, the dynamic range at 1300 nm is about a factor of five higher than at 850 nm. The local resolution is also limited by the pulse broadening (= mode dispersion) that reduces the bandwidth (BW) of the selected multimode gradient-index (MM GI) fibre of 50 µm core diameter. The table below shows the broadening of laser pulses of different width by fibres with different BW along fibre sections with a length of 0.33, 1 and 5 km, respectively. To avoid excessive pulse broadening, the BW for the Tesla Test Facility (TTF; [2]) should be at least 800 MHz.

BW [MHz·km]	Fibre Length [km]	Pulse Width, FWHM [ns] with initial light pulse width of 0.2 ns	1 ns	3 ns
250	0.33	0.62	1.16	3.06
	1.00	1.77	2.02	3.48
	5.00	8.80	8.86	9.30
800	0.33	0.27	1.02	3.01
	1.00	0.59	1.14	3.05
	5.00	2.76	2.93	4.07
1500	0.33	0.22	1.00	3.00
	1.00	0.35	1.04	3.01
	5.00	1.48	1.78	3.34

The fibre that was purchased for TTF has a BW of 1100 MHz·km at 850 nm, but only 500 MHz·km at 1300 nm. The lower BW at 1300 nm is tolerable since the minimal laser pulse width of the OTDR at 1300 nm is only 10 ns, anyhow.

2.2 Radiation Effects on Optical Fibres

The amount of attenuation during irradiation is determined by the fibre properties as well as by the irradiation conditions, e.g. the radiation dose, dose rate and fibre temperature. The high purity of the modern fibre raw materials has reduced their radiation sensitivity. However, if the core material of Germanium (Ge)-doped MM GI fibres is co-doped with Phosphorus (P), their radiation-induced attenuation increases significantly so that these fibres are suitable for dosimetry purposes.

The precondition that an optical fibre can be used for dosimetry is that it shows a high increase of attenuation with dose and very slow annealing (= fading) of this radiation-induced attenuation after the end of irradiation (at "normal" conditions). Such fibres show *nearly* linear increase of attenuation (A) with Dose (D)

$$A = c \cdot D^f, \qquad \text{(c = constant, in dB/m·Gy)}$$

i.e., exponent f is not far below "1". Fig. 2 shows the increase of attenuation of such a fibre (in dB/m) as a function of dose, measured at 850 nm with OTDR pulse lengths of 1ns and 3ns, respectively. Exponent f is equal to 0.875, i.e. nearly 1. Usual MM GI fibres show relatively fast attenuation annealing and therefore distinctly lower radiation sensitivity and an exponent f far below 1. As a consequence their increase of attenuation (or measured dose) strongly depends on the dose rate (i.e. the time to reach a certain dose).

2.3 Results

The data presented here originate from a TTF operation period of 17 days. The measurements were done with a laser wavelength of 850 nm and 3 ns pulse length. The accumulated dose versus fibre length is shown in Fig.3.

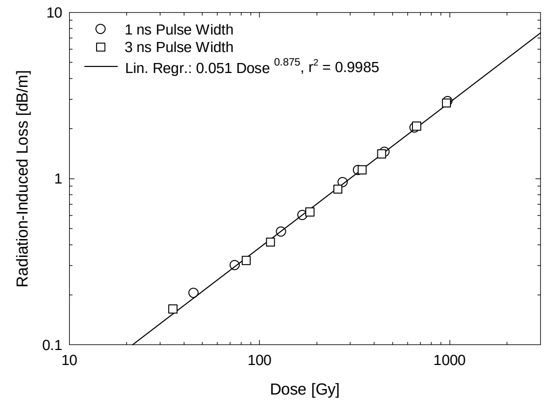

Figure 2: Loss increase with dose of the (Ge+P)-doped MM GI fibre FiberCore N2900107GA during ^{60}Co gamma irradiation. Measurements were made with the 850 nm multi-mode module of the OTDR and pulse lengths of 1 ns and 3 ns, respectively.

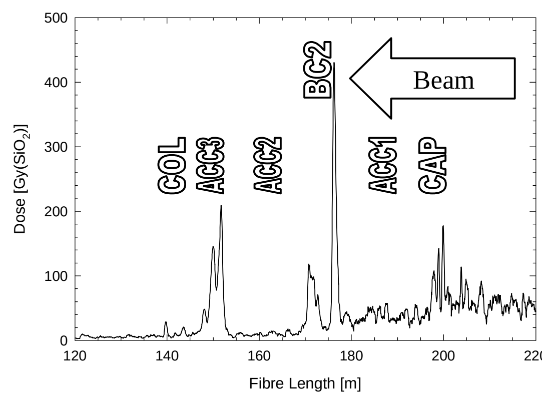

Figure 3: Dose versus fibre length at TTF. The direction of the beam is opposite to the fibre scaling. The beam passes through the capture cavity CAP, the accelerator modules ACC #, the bunch compressor BC2 and the collimator in front of the undulators.

The highest dose deposition was located at bunch compressor BC2, whereas the accelerator modules ACC1 and ACC2 have relatively low radiation levels due to the shielding by the cryogenic tanks. The dose at the temporary beam-line ACC3 (without cryogenic tank) is significantly higher, because the fibre was lying directly on the vacuum pipe. The minim um detectable dose is less than 3 Gy with a distance resolution of 0.6 m. Above 180 m the back-reflected light intensity reached the noise level, i.e. the end of the dynamic range of the OTDR.

2.4 Fibre Regeneration

For the present investigations at TTF the fibre cables are laid directly on or near to the beam pipe. Therefore, the dose rate at some places will be orders of magnitude higher, especially at BC2, than at electronic equipment one or two meters away. A dose > 1 kGy could be reached within unwanted short operation periods. Since it would be inconvenient or even impossible to replace the fibres by new ones every few months, it should be carefully investigated whether they could be regenerated, e.g. by bleaching out the colour-centres with laser light of high intensity, as described by Gaebler et al. [3]. Some first efforts with the fibre used for the measurements of Fig. 2 have shown that regeneration of this fibre type would be very difficult in the accelerator environment. The reason is that fibres that are suitable for dosimeter must have very stable colour-centres. One meter of that fibre was irradiated up to 4000 Gy(SiO_2). The residual attenuation about one hour after the end of irradiation, when the regeneration tests began, was 11.2 dB. Injection of 830 nm and 670 nm laser light with intensities up to about 100 mW and 200 mW, respectively, only led to a loss reduction to about 7.7 dB. Only a temperature increase up to 150 °C, together with injection of the 830 nm laser light, led to a final loss of only about 2.3 dB.

After cooling down, the fibre was irradiated a second time and showed (after subtraction of the residual loss of 2.3 dB) the same loss increase as during the first irradiation (Fig. 4). This is quite encouraging, but on the other hand it is obvious that it would be impossible to heat up all dosimeter fibres along TESLA up to 150 °C. These investigations will be continued with laser light of shorter wavelength and higher intensity.

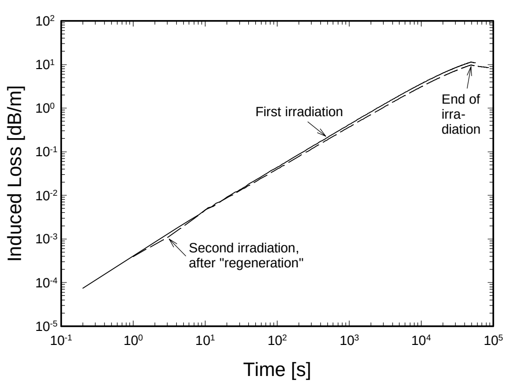

Figure 4: Behaviour of a fibre "regenerated" by heating and high power laser light during a second identical irradiation.

CONCLUSIONS

A new in situ sensing system that observes the local origin of radiation in accelerator sections of interest can be realised by optical fibres. The advantages of optical fibre dosimeters are:

- they enable the operator to control radiation emission at very lengthy objects or in spacious areas.
- they show identical properties (i.e. radiation sensitivity) over greater sensor lengths and of different sensor sections because of the identical composition and high quality of modern fibres.
- the dosimeter sensitivity can be adjusted to the dose or dose rate of interest by selection of fibre type or measuring wavelength. The radiation-induced attenuation increases from a minimum around 1100 nm towards about 670 nm or 450 nm by orders of magnitude.
- the dose can be measured in inaccessible, narrow slits due to very small dosimeter dimensions. Bare (i.e. uncabled) fibres usually have a diameter of only 250 µm.
- the length of each fibre section can exceed several kilometres. Therefore, only a few sensors are needed for the whole accelerator, even with a position resolution of several meters.

A complete OTDR-based fibre optic radiation detection and measuring system covering all parts of TESLA could help to find locations with an unexpected high dose as well as places with lower dose levels where the signal processing electronics could be installed. One could get an estimate of the lifetime of these electronic systems from the measured dose rate, and could optimise the accelerator control.

Permanent dose measurements, with a different sensor type, at the undulator magnets are desirable because they are made of radiation sensitive alloys. Here we need no local resolution (i.e. an OTDR) since the measurements are made at known position(s).

A separate fast radiation detection system is needed in cases of dangerous high radiation emission somewhere along the beam line. It shall be based on the generation of luminescence light in optical fibres and could be used for rapid accelerator switch-off and fast beam loss detection.

REFERENCES

[1] R.Brinkmann et al., (Editors), TESLA Technical-Design-Report, Tesla-Report 2001-23, March2001

[2] D. A. Edwards et al., TTF Conceptual Design Report, TESLA-Report 95-01.

[3] W. Gaebler, G. Sulz, D. Bräunig, "Radiation Effects Testing of Optical Fiber Waveguides", SPIE Vol. 404: Optical Fibers in Adverse Environments, pp. 132-140, 1983.

BEAM-PROFILE INSTRUMENTATION FOR A BEAM-HALO MEASUREMENT: OVERALL DESCRIPTION, OPERATION, AND BEAM DATA•

J. D. Gilpatrick, D. Barr, L. Day, D. Kerstiens, M. Stettler, R. Valdiviez, Los Alamos National Laboratory
M. Gruchalla, J. O'Hara, Honeywell Corporation
J. Kamperschroer, General Atomics Corporation

Abstract

The halo experiment presently being conducted at the Low Energy Demonstration Accelerator (LEDA) at Los Alamos National Laboratory (LANL) has specific instruments that acquire horizontally and vertically projected particle-density beam distributions out to greater than 105:1 dynamic range. We measure the core of the distributions using traditional wire scanners, and the tails of the distribution using water-cooled graphite scraping devices. The wire scanner and halo scrapers are mounted on the same moving frame whose location is controlled with stepper motors. A sequence within the Experimental Physics and Industrial Control System (EPICS) software communicates with a National Instrument LabVIEW virtual instrument to control the movement and location of the scanner/scraper assembly. Secondary electrons from the wire scanner 33-μm carbon wire and protons impinging on the scraper are both detected with a lossy-integrator electronic circuit. Algorithms implemented within EPICS and in Research Systems' Interactive Data Language (IDL) subroutines analyse and plot the acquired distributions. This paper describes the beam profile instrument, describes our experience with its operation, compares acquired profile data with simulations, and discusses various beam profile phenomenon specific to the halo experiment.

1 HALO INSTRUMENTATION

At LEDA a 100-mA, 6.7-MeV beam is injected into a 52-quadrupole magnet lattice (see fig. 1). Within this 11-m FODO lattice, there are nine wire scanner/halo scraper/wire scanner (WS/HS) stations, five pairs of steering magnets and beam position monitors, five loss monitors, three pulsed-beam current monitors, and two image-current monitors for monitoring beam energy (2). The WS/HS instrument's purpose is to measure the beam's transverse projected distribution. These measured distributions must have sufficient detail to understand beam halo resulting from upstream lattice mismatches. The first WS/HS station, located after the fourth quadrupole magnet, verifies the beam's transverse characteristics after the RFQ exit. A cluster of four HS/WS located after magnets #20, #22, #24, and #26 provides phase space information after the beam has debunched. After magnets #45, #47, #49, and #51 reside the final four WS/HS stations. These four WS/HS acquire projected beam distributions under both matched and mismatched conditions. These conditions are generated by adjusting the first four quadrupole magnets fields so that the RFQ output beam is matched or mismatched in a known fashion to the rest of the lattice. Because the halo takes many lattice periods to fully develop, this final cluster of WS/HS are positioned to be most sensitive to halo generation.

Figure 1. The 11-m, 52-magnet FODO lattice includes nine WS/HS stations that measure the beam's transverse projected distributions.

As the RFQ output beam is mismatched to the lattice, the WS/HS actually observe a variety of distortions to a properly matched gaussian-like distribution (1,3). These distortions appear as distribution tails or backgrounds. It is the size, shape, and extent of these tails that predicts specific type of halo. However, not every lattice WS/HS observes the halo generated in phase space because the resultant distribution tails may be hidden from the projection's view. Therefore, multiple WS/HS are used to observe the various distribution tails.

2 WS/HS DESCRIPTION

Each station consists of a horizontal and vertical actuator assembly (see fig. 2) that can move a 33-μm-carbon monofilament and two graphite/copper scraper subassemblies (4). The carbon wire and scrapers are connected to the same movable frame. Attached to this movable frame is a linear encoder that provides the wire and scraper edges' relative position to within 5 μm, an additional linear potentiometer provides an absolute approximate position for LEDA's run permit systems. A stepper motor and ball lead screw drive the actuated moveable frame, and microswitches and motor brakes limit the wire and scraper movement.

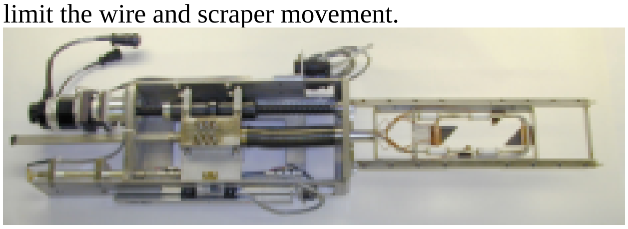

Figure 2. The WS/HS assembly contains a movable frame on which a 0.03-mm carbon wire resides between two water-cooled graphite scrapers.

The carbon wire, which senses the beam's core, is cooled by thermal radiation. If the beam macropulse is too long, the wire temperature continues above 1800 K resulting in the onset of thermionic emission. Thermionic emission gives the distribution an inaccurate appearance of a larger distribution core current density. To eliminate these effects for the halo experiment, the maximum pulse length and repetition rate is limited to approximately 30 ms and 1 Hz, respectively.

The halo scrapers are composed of a 1.5-mm thick graphite plate brazed to a water-cooled 1.5-mm thick copper plate. Since 6.7-MeV protons average range in carbon is approximate 0.3 mm, the beam is completely stopped within the graphite plate. Cooling via conduction lowers the average temperature of scraper sub-assembly and allows the scraper to be cooled more rapidly than the wire. The lower average temperature and faster cooling allows the scraper to be driven in as far as 2 rms widths from the beam distribution peak without the peak temperature increasing above 1800 K.

The movement and positioning of each wire and scraper pair is controlled by a movement control system that contains a stepper motor, stepper motor controller, a linear encoder, and an electronic driver amplifier. The controller's digital PID loop controls the speed and accuracy at which the assembly is moved and placed.

The target position, as defined by the WS/HS operator, is relayed from the EPICS control screen via a database process variable to a National Instruments LabVIEW Virtual Instrument (VI). The VI also calibrates the relative position of the linear encoders based on the measured position of the limit switches, and provides some error feedback information. The total error between the target wire position and the actual position attained are <+/-2% of a 1-mm width beam (see fig. 3).

beam's energy is imparted to the wire causing secondary electron emission to occur. The secondary electrons leaving the wire are replaced by negative charge flowing from the electronics. This current flow for both axes is connected through a bias battery to an electronic lossy integrator circuit and followed by an amplification stage.

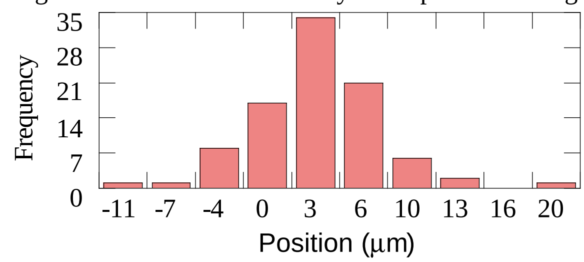

Figure 3. The above histogram shows a typical distribution of wire/scraper movement errors.

The integrator capacitance and amplifier gain are set to allow a very wide range of values of accumulated charge. Data are acquired by digitising the accumulated charge through the lossy integrator at two different times within the beam pulse. This charge difference acquired by subtracting the two values of charge provides a low noise method of relative beam charge acquisition. The wire and scraper accumulated charge signals are digitised using 12-bit digitisers. The analogue noise floor has been measured to be 0.03 pC, a noise level slightly lower than the scraper digital LSB noise level of 0.6 pC using the highest gain settings within the detection electronics.

The front-end electronic circuitry, mounted on a daughter printed circuit board, is connected to a motherboard that has all of the necessary interface electronics to communicate with EPICS via a controller module and within the same electronics crate. A software state machine sequence was written within EPICS to control and operate WS/HS instrumentation (5). The state machine instructs the VI to move the wire and scraper to a specific location, acquire synchronous distribution data from either the wire or scraper, and triggers the IDL routine to normalise the acquired charge with a nearby toroidal current measurement, graph the normalised data, and write the distribution to a file. The sequence also instructs IDL to calculate the first through fourth moments, fit a gaussian distribution to the wire scanner data, and calculate the point at which the beam distribution disappears into the distribution background noise.

To plot the complete beam distribution for each axis, the wire scanner and two scraper data sets must be joined. To accomplish this joining, several analysis tasks are performed on the wire and scraper data including,

1) scraper data are spatially differentiated,
2) wire and scraper data are acquired with sufficient spatial overlap, and

The scraper data need only be normalised in the relative charge axis since the distances between each wire and scraper edge are known to within 0.25-mm. In addition, the first four moments and the point at which the beam distribution disappears into the noise are also calculated for the combined distribution data.

3 ACQUIRED DISTRIBUTIONS

Fig. 4 shows data from WS/HS #26 with some slight mismatch generated by increasing the field above nominal by 5% in the first matching quadrupole magnet. These typical WS/HS profiles show distributions with a dynamic range of > 10^5:1 and provide distribution information to > 5X to 7X times typical rms widths of the beam. The calculated rms widths are 1.10 and 1.13 mm for the horizontal and vertical distributions, respectively. The points at which the distributions rises out of the noise are 5.9 and –8.2 mm for the horizontal axis and 5.8 and –6.7 mm for the vertical axis.

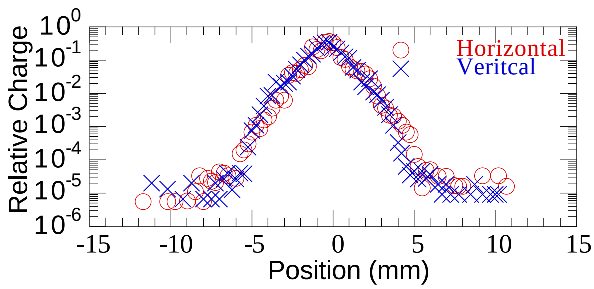

Figure 4. WS/HS distributions, such as #26 shown here, have a typical dynamic range of > 10^5:1.

4 WIRE AND SCRAPER PHYSICS

The choice of bias potential was determined by measuring the wire and scraper currents as a function of bias potential. The resulting data, displayed in fig. 5, show that the wire is optimally biased at -6 to -12 V and the scraper is optimally biased at +20 to +30 V.

The net wire current near the 0 V potential is approximately 15% higher than at either +6 V or –10 V. One proposed cause of the elevated net wire current is the interception of electrons and ions from off-energy protons ionising residual background gas - both of these ionised species creating further secondary emission. As the wire is biased negatively, the intercepted electrons are rejected causing a reduction in secondary emission, and as the wire is biased positively, the intercepted ions are rejected causing a reduction in secondary emission. If the intercepted electron-ion pairs are the mechanism for the elevated net current, the wire should be biased to not include this additional 15% net current component. Also note that as the wire bias is positively increased from 0 V to > +100 V, the wire secondary electron emission is inhibited and the net wire current reduces to very near collects positive ions with < -25 V bias potentials well after the beam pulse. This ion collection additionally limits the amount of negative bias that is applied to the wire for proper secondary emission operation.

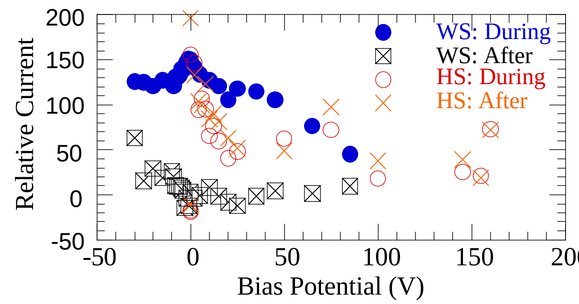

Figure 5. The above graph displays the wire scanner and halo scraper net current during and after the macropulse as a function of applied bias potential.

The scraper detection goal is to inhibit secondary emission and detect only 6.7-MeV protons. With 0 V applied to the scraper, the scraper net current is elevated by a factor of X3, likely from secondary emission. With approximately +25 V bias applied to the scraper, the secondary emission is almost entirely inhibited and the net current reduces to the nominal proton current. Also, note that with this +25 V bias, the data show that no ions appear to be collected after beam pulse.

5 SUMMARY

A wire scanner and halo scraper have been integrated into a beam profile instrument capable of 10^5:1 dynamic range. The scanner and scraper V-I curves show that the wire and scraper are optimally biased at –12 V and +25 V, respectively. We are presently acquiring halo data with these instruments and comparing these data to simulation halo models.

REFERENCES

[1] P. L. Colestock, et al., “The Beam Halo Experiment at the LEDA Facility: a First Test of the Core-Halo Model,” LINAC2000 Proceedings, SLAC-R-561, pp. 806-809.

[2] J. D. Gilpatrick, et al., "Beam Diagnostics Instrumentation for a 6.7-MeV Proton Beam Halo Experiment”, LINAC2000 Proceedings, SLAC-R-561, pp. 184-186.

[3] T. Wangler, et al., “Beam Halo in Proton Linac Beams,” LINAC2000 Proceedings, SLAC-R-561, pp. 341-345.

[4] R. Valdiviez, et al., “Intense Proton Core And Halo Beam Profile Measurement: Beam Line Component Mechanical Design”, LINAC2000 Proceedings, SLAC-R-561, pp. 181-183.

[5] L. Day, et al., “Control System for the LEDA 6.7-MeV Proton Beam Halo Experiment”, LINAC2000

THE MEASUREMENT OF Q' AND Q'' IN THE CERN-SPS BY HEAD-TAIL PHASE SHIFT ANALYSIS

R. Jones, H. Schmickler, CERN, Geneva, Switzerland

Abstract

A so-called "Head-Tail" chromaticity measurement system has recently been installed in the CERN-SPS, which allows the chromaticity (Q') to be calculated from several hundred turns of data after transverse excitation. The measurement relies on the periodic dephasing and rephasing that occurs between the head and tail of a single bunch for non-zero chromaticity. By measuring the turn-by-turn position data from two longitudinal positions in a bunch it is possible to extract the relative dephasing of the head and the tail, and so to determine the chromaticity. In addition, by changing the orbit of the circulating beam this technique allows the variation of chromaticity with radial position (Q") to be measured with a much higher resolution than is currently possible using RF modulation. This paper describes this "Head-Tail" measurement technique and discusses some recent results obtained using prototype LHC beam (25ns spacing) in the CERN-SPS.

1 INTRODUCTION

The tight tolerances on beam parameters required for successful LHC operation implies a good knowledge of the chromaticity throughout the cycle. However, many of the methods currently used to measure chromaticity in circular machines (see [1] and references therein) are likely to be incompatible with LHC high intensity running. For example, the most common method, of measuring the betatron tune as a function of beam energy, might be difficult to implement due to the tight tolerances imposed on the betatron tune itself and the limited momentum acceptance of the LHC. Chromaticity can also be calculated from the amplitude of the synchrotron side-bands observed in the transverse frequency spectrum. This method, however, suffers from resonant behaviour not linked to chromaticity and the fact that the low synchrotron tune of the LHC would make it difficult to distinguish these side-bands from the main betatron tune peak. The width of the betatron tune peak itself, or the phase response of the beam transfer function also give a measure of chromaticity, but require a knowledge of how the momentum spread in the beam changes with energy.

In this paper we describe the first results from an alternative method, tested during 2000 on the CERN-SPS. This so-called "Head-Tail" chromaticity technique does not rely on an accurate knowledge of the fractional part of the betatron tune and, for a machine operating well above transition, the calculated chromaticity is virtually independent of beam energy.

2 THE HEAD-TAIL PRINCIPLE

Assuming longitudinal stability, a single particle will rotate in longitudinal phase-space at a frequency equal to the synchrotron frequency. During this longitudinal motion the particle also undergoes transverse motion, which can be described by the change in the betatron phase, $\theta(t)$, along the synchrotron orbit. If the whole bunch is kicked transversely, then the resulting transverse oscillations for a given longitudinal position within the bunch can be shown to be given by

$$y(n) = A\cos[2\pi nQ_0 + \omega_\xi \hat{\tau}(\cos(2\pi nQ_S) - 1)] \qquad \textbf{(1)}$$

where n is the number of turns since the kick, Q_0 is the betatron tune, Q_S is the synchrotron tune, $\hat{\tau}$ is the longitudinal position with respect to the centre of the bunch, and ω_ξ is the chromatic frequency and is given by

$$\omega_\xi = Q'\omega_0 \frac{1}{\eta} \qquad \textbf{(2)}$$

Here Q' is the chromaticity, ω_0 is the revolution frequency and $\eta = 1/\gamma^2 - 1/\gamma_{tr}^2$. If we now consider the evolution of two longitudinal positions within a single bunch separated in time by $\Delta\tau$, then from Eq. 1 it follows that the phase difference in the transverse oscillation of these two positions is given by

$$\Delta\Psi(n) = -\omega_\xi \Delta\tau(\cos(2\pi nQ_S) - 1) \qquad \textbf{(3)}$$

This phase difference is a maximum when nQ_S = ½, i.e. after half a synchrotron period, giving

$$\Delta\Psi_{MAX} = -2\,\omega_\xi\,\Delta\tau \qquad \textbf{(4)}$$

The chromaticity can therefore be written as

$$Q' = \frac{-\eta\ \Delta\psi(n)}{\omega_0\,\Delta\tau(\cos(2\pi nQ_s) - 1)}$$
$$Q' = \frac{\eta\ \Delta\Psi_{MAX}}{2\,\omega_0\ \Delta\tau} \qquad \textbf{(5)}$$

3 THE SPS HEAD-TAIL MONITOR

A schematic layout of the SPS Head-Tail monitor set-up is shown in Fig. 1. A straight stripline coupler followed by a 180° hybrid is used to provide the sum and difference signals for a given measurement plane. These signals are fed into a fast-sampling (2GS/s on each channel), high bandwidth (2GHz) digital oscilloscope. A VME front-end acquisition crate then retrieves the data via a GPIB link. All the oscilloscope and acquisition parameters are accessible from the SPS control room through a UNIX graphical interface.

The oscilloscope is triggered using bunch synchronous

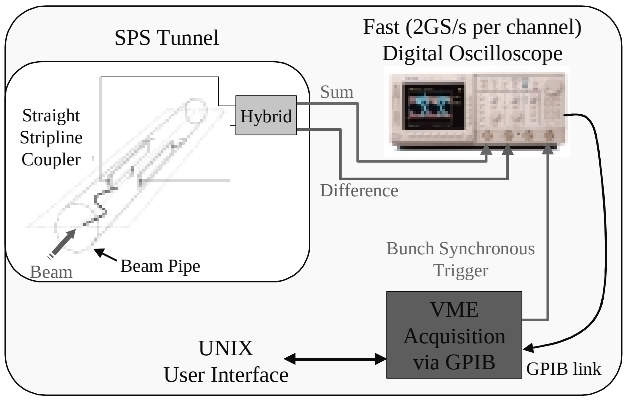

Figure 1: Layout of the SPS Head-Tail Monitor

timing. Using the "Fast-Frame" capabilities of the oscilloscope allows 25ns of data (corresponding to the LHC bunch spacing) to be captured on each SPS revolution. In this way the evolution of the signal from a single, specific bunch can be tracked over 372 turns (the memory limit of the oscilloscope). Since the bunch synchronous timing has a peak-peak jitter of 12ns, the sum signal is used to re-align the difference signal for each turn. In this way, the timing jitter is reduced to well below the sampling frequency.

Fig. 2 shows some typical signals obtained from the

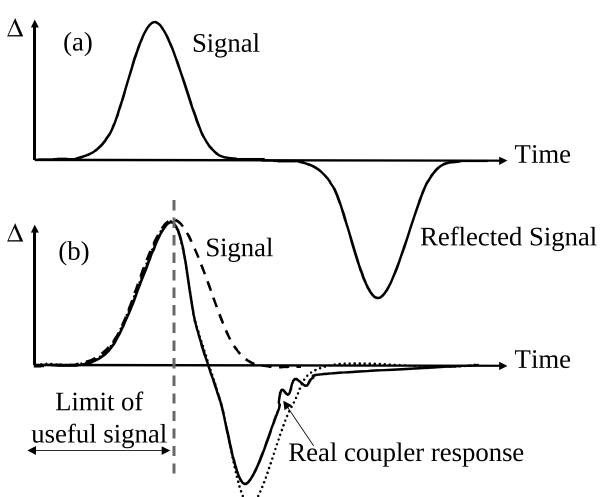

Figure 2: Typical coupler response.
a) total bunch length < 2 × coupler length.
b) total bunch length > 2 × coupler length.

coupler. If the total bunch length is less than twice the coupler stripline length, Fig 2(a), then the signal from the bunch and its reflection from the opposite end of the stripline are well separated in time. If, however, the bunch is longer than twice the stripline length then the signal and reflection are no longer separated, Fig. 2(b), and the useful part of the signal is limited. This latter case was true for the SPS set-up during 2000, where the typical bunch length was ~4ns and twice the coupler length corresponded to 2.5ns. Hence measurements on the tail of the bunch were not possible, and therefore all the results shown are for measurements of the head and centre of the bunch.

All measurements were performed using an LHC batch of 84 bunches with 25ns bunch spacing, a bunch intensity of ~ 2×10^{10} protons, accelerated from 26GeV to 450GeV. Each measurement was performed on-line on one bunch after the application of a single transverse kick using an SPS Q-kicker.

4 RESULTS

An example of a Head-Tail monitor acquisition is shown in Fig 3. Fig. 3(a) and 3(b) show the transverse evolution of the head and tail (or more precisely the head and centre) of the bunch after the application of a single kick. By performing phase demodulation using a Hilbert transformation on this data, the relative phase difference (Fig. 3(c)) of the head and tail of the bunch can be extracted. The periodic phasing and dephasing between head and tail, at a frequency corresponding to the synchrotron tune, is clearly visible. In this case it is only the head that changes its relative phase, since the tail corresponds to the centre of the bunch, which does not undergo a dephasing with respect to the betatron tune. Using the head-tail phase difference and Eq. 5 it is possible to calculate the chromaticity. The result is shown in Fig. 3(d). Due to cosine term in the denominator of Eq. 5, the error in the calculation is large around multiples of the synchrotron tune. Hence only the points around the maximum of the dephasing are used to obtain the final, average value for the chromaticity.

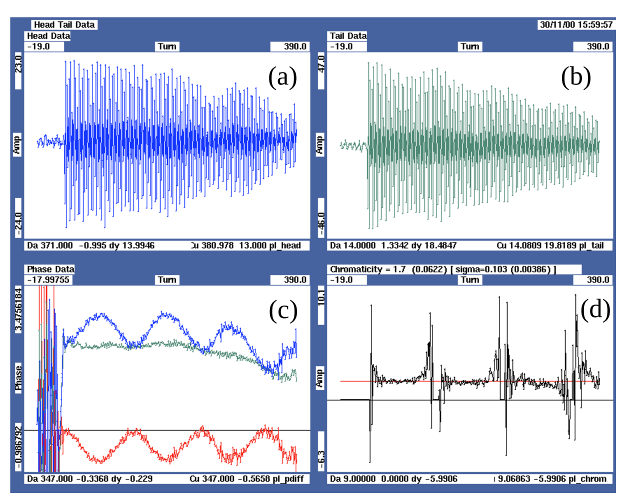

Figure 3: CERN-SPS Head-Tail monitor acquisition.
a) head oscillations; b) tail oscillations;
c) head-tail phase difference; d) chromaticity

The usual way in which to measure chromaticity in the SPS is by changing the RF frequency, and hence the beam momentum, and measuring the corresponding change in the betatron tune. In practice, this implies three measurements performed for three different RF settings, taking place over several SPS supercycles. Due to the momentum change imposed by each RF setting, the beam has different transverse positions, hence the term "radial steering" chomaticity measurement.

Fig. 4 shows the results obtained from this traditional technique compared to those using the head-tail method, as a function of chromaticity. For each chromaticity setting, several measurements were performed using the radial steering technique, each implying three different RF frequency settings corresponding to three different transverse positions. The head-tail measurement was acquired for all RF settings.

A very good linearity is seen to exist between the head-tail and radial steering techniques when the measurement is performed for the same transverse beam position. However, the absolute value of the chromaticity measured via the head-tail technique is approximately a factor of two smaller than would be expected. Measurements carried out for several different energies between 26Gev and 400GeV all showed this good linearity, but required correction factors ranging from 1.6 to 2.4. No firm explanation can be put forward at the moment to explain this missing factor, however this could be caused by bandwidth limitations in the acquisition electronics or the fact that the theoretical model relies on single particle dynamics, and therefore does not take into account any collective effects.

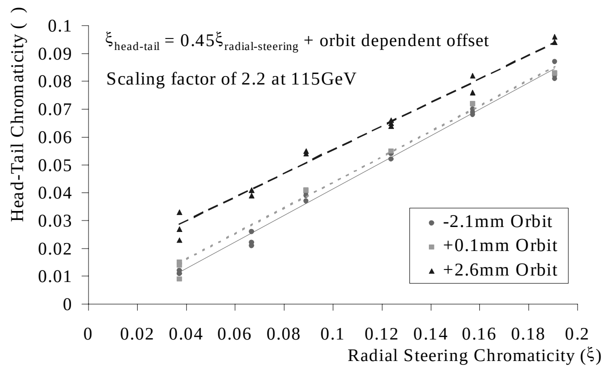

Figure 4: Comparison of chromaticity measured by radial steering and the head-tail technique.

Another thing that can be remarked from Fig. 4 is the fact that the head-tail measurement is able to distinguish the chromaticity for different radial positions of the beam. This makes it possible to use this technique measure the variation of chromaticity with position, or Q'', of the machine. The results from such a measurement is shown in Fig. 5. Here the RF frequency was changed in much smaller steps than for a traditional chromaticity measurement, so as to build up a picture of the Q'' of the SPS. The results from radial steering measurements are included for completeness, but have very large error bars due to the nearly immeasurable changes in betatron tune induced by such small RF changes. The head-tail measurements were scaled by the appropriate factor to allow a comparison with the radial steering, and can be seen to give a very accurate picture of the variation of chromaticity with radial position.

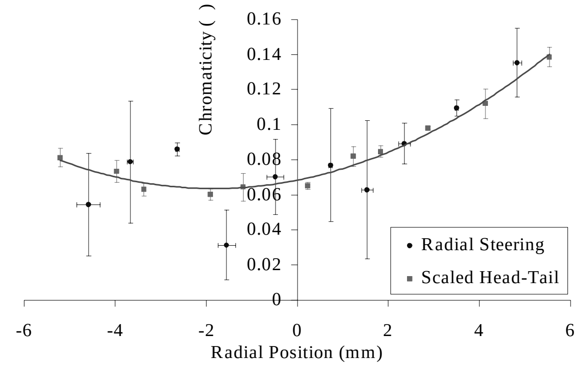

Figure 5: The measurement of second order chromaticity (Q'') using head-tail phase shift analysis.

A further advantage of the head-tail technique is that the whole measurement can be performed during a single synchrotron period, which in the SPS corresponds to between 100-300 turns. This means that it is possible to measure the chromaticity throughout the cycle, with the only limitation being the emittance blow-up induced by each applied kick. Measurement at 0.5Hz has been achieved at the SPS, a rate which is determined solely by the GPIB data transfer rate and re-arm time of the oscilloscope.

5 CONCLUSIONS

It has been demonstrated that the chromaticity of a proton synchrotron can be measured in an operational way from the evolution of the phase difference between the head and tail of a single bunch after the application of a transverse kick. In addition this head-tail technique provides an accurate method for investigating the second order chromaticity of such a machine. Further studies are planned to pursue the origins of the scaling factor, the effects of higher order fields, transverse coupling, and also to determine the signal to noise ratio required for accurate measurements.

6 REFERENCES

[1] Schmickler, H., "Diagnostics and Control of the Time Evolution of Beam Parameters" (CERN-SL-97-68), presented at the 3rd European Workshop on Beam diagnostics and Instrumentation for Particle Accelerators (DIPAC 97), Frascati, Italy, October 1997.

[2] D. Cocq, O. R. Jones, H. Schmickler, "The Measurement of Chromaticity via a Head-Tail Phase Shift", 8th Beam Instrumentation Workshop BIW '98, Stanford, CA, USA, May 1998.

Excitation of Large Transverse Beam Oscillations Without Emittance Blow-up Using the AC-Dipole Principle

O. Berrig, W. Hofle, R. Jones, J. Koopman, J.P. Koutchouk, H. Schmickler, F. Schmidt,
CERN, Geneva, Switzerland

Abstract

The so-called “AC-Dipole” principle allows the excitation of transverse oscillations to large (several σ) excursions without emittance blow-up. The idea was originally proposed and tested at BNL for resonance crossing with polarized beams, using an orbit corrector dipole with an excitation frequency close to the betatron tune, hence “AC-Dipole”. This method of beam excitation has several potential applications in the LHC, such as phase advance and β-measurements, dynamic aperture studies and the investigation of resonance strengths. The technique was recently tested in the CERN SPS using the transverse damper as an “AC-Dipole” providing the fixed frequency excitation. results from this experiment are presented, along with an explanation of the underlying principle.

1 INTRODUCTION

The measurement of transverse beam parameters requires either kicking the beam or exciting a coherent oscillation. In both cases the emittance of hadron beams increases in the absence of a significant radiation damping. Furthermore the decoherence due to the incoherent betatron tune spread and head-tail damping perturbs the measurement in a complicated way in the presence of non-linearities.

In LHC, the latter are expected to be significant, requiring corrections of the geometric and chromatic sextupole, octupole, decapole and dodecapole field perturbations. The emittance budget for nominal performance is only 7%. The blow-up due to beam measurements integrated over a machine cycle should therefore be limited to $\approx 1\%$.

Another requirement is the understanding of the non-linearity. If it is significant, the transverse signal due to a kick decoheres very rapidly. The number of possible sources is too large for an empirical optimization. The emittance blow-up can be tolerated at injection energy as the machine can be refilled rapidly. At collision energy, however, the measurement of the non-linearity by kicking the beam would become very costly in time, on top of being very delicate if quenching the machine is to be avoided.

There is therefore a strong motivation to explore other means of transverse beam measurements for small and large transverse amplitudes.

2 PRINCIPLE OF THE AC DIPOLE EXCITATION

The emittance-conserving beam excitation was studied at BNL for adiabatic resonance crossing with polarized hadron beams [1]. It was realized that the same principle can be used to diagnose the linear and non-linear transverse beam dynamics [2] [4] [3]. The principle is as follows: the beam is excited coherently at a frequency close but outside its eigenfrequencies by an oscillating dipolar field. Hence the name of AC dipole given to the excitor. In the simplified model of a linear oscillator, the beam is expected to oscillate at the excitor frequency with a phase shift of $\pi/2$. The energy of the coherent oscillation does not couple with the incoherent oscillations of the individual beam particles. There is therefore no change of the beam emittance. The amplitude of the forced oscillation is given by, e.g. [2]:

$$z(s) \approx \frac{1}{4\pi|Q_z - Q_e|}\frac{B_e l}{B\rho}\sqrt{\beta(s)\beta_e} \qquad (1)$$

where z stands for x or y, Q_z the eigentune of the z-mode, Q_e the tune of the excitor (frequency divided by the revolution frequency), $B_e l/B\rho$ the kick angle and β the usual focusing function.

There is no constraint which would prevent selecting a rational excitor frequency of the form $Q_e = n/p$. The beam can then be seen to circulate on a dc closed orbit which closes after p turns.

3 ADIABATICITY CONDITION

The field of the AC dipole must be turned on and off in such a way that no beam blow-up occurs during these phases. The adiabaticity condition can be calculated by integrating the equation of the motion for a simple linear ramp. The results (Figure 1) show that a ramp duration in the few ms range is enough to guarantee a blow-up less than 1% up to amplitudes of the order of 100σ. This adiabaticity condition may be understood qualitatively in two ways:

- Considering that the beam circulates on a p-turn closed orbit, the usual criterion of bumping the beam closed orbit can be used. The orbit increment on each turn shall be small compared to the beam size, giving a blow-up of the order of this increment. This criterion explains why the ramp rate must be reduced when the tune difference $|Q_z - Q_e|$ decreases. The orbit increment per turn indeed increases like $1/|Q_z - Q_e|$.

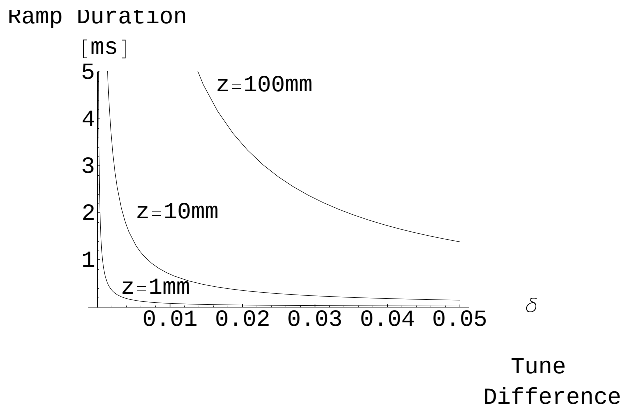

Figure 1: Minimum rise time of the field versus tune split

- The spectrum of the ramping excitor is the convolution of the excitor pure frequency with the Fourier transform of the ramp envelope. The convolution simply shifts the ramp envelope spectrum towards the beam eigenfrequencies. A proper shaping of the ramp envelope and the choice of its duration minimizes the overlap between the excitor and beam spectra.

4 EXPERIMENT AT THE SPS

4.1 Experimental Set-up

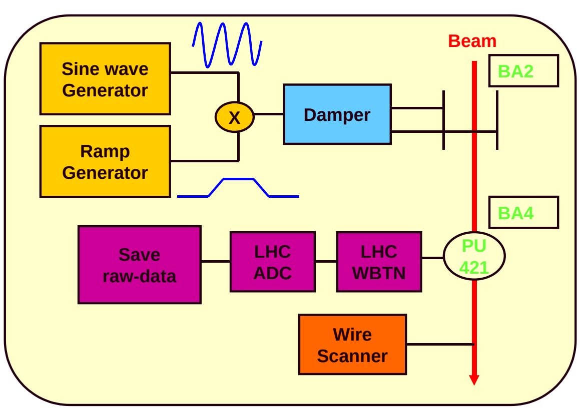

Figure 2: Experimental set-up in the SPS

The feasibility of emittance-free excitation has already been verified at the AGS [2]. It was noted that a careful tuning of the chromaticity is important. We therefore checked this feasibility on the SPS under conditions closer to that of LHC. The experimental set-up is shown on figure 2. The machine was operated at 26 GeV with the LHC bunch pattern, 72 bunches spaced by 25 ns, with a bunch intensity of 1.5 10^{10} protons. The transverse damper was used as an AC-dipole. Two signal generators were used to produce the excitation, one for the 15-20 kHz sine excitation and another to generate a $\cos^2$ ramp up and down. The durations were set to 25ms for the ramp up or down and 50ms for the flat top (5000 turns) scalable by a factor of 2 or 4. The maximum deflection $B_e l/B\rho$ was 4.2μrad. The prototype LHC orbit system was used to record the transverse beam oscillation (figure 3). It is capable of recording up to 30000 turns. The beam size was measured before and after excitation with a wire scanner but had to be performed on consecutive cycles. The error bars (figure 4) arise mostly from the beam reproducibility over several injections and much less from the instrumentation. The chromaticity was corrected to a value close to zero. The tune spread (FWHM) was measured to be 0.009, mostly due to the space charge. A single kick was applied to the beam after the AC-dipole excitation to measure the tunes. It appears on the right of figure 3.

4.2 Results

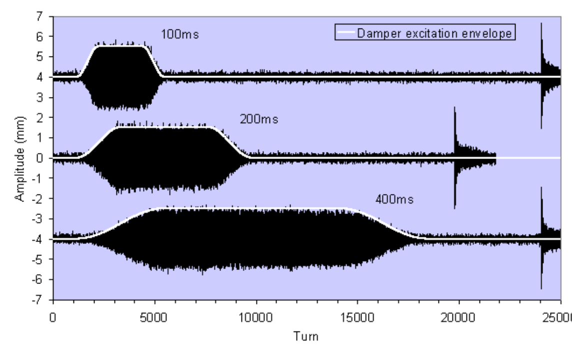

Figure 3: Transverse amplitude versus time

Outside of the beam eigenfrequencies, the beam response is indeed well modelled by that of a linear oscillator (figure 4) and reaches an amplitude of about 1mm, i.e. 1σ. The beam blow-up remains insignificant in this domain. Figure 5 shows that a response at the beam eigenfrequencies is observed under conditions causing a blow-up. The small left-right asymmetry of the blow-up curve on figure 4 is not understood, but is at the limit of significance. The frequency analysis (figure 5) shows indeed no activity within the beam eigen-frequencies for $Q_z - Q_e = \pm.014$. A variation in emittance of the injected beam seems the most plausible explanation. The duration of the large coherent oscillations was about 100 times longer than after a kick (figure 3), allowing potentially a significantly improved accuracy of beam measurements.

5 CONCLUSIONS

The SPS beam could indeed sustain a coherent oscillation of about 1σ amplitude for a large number of turns without measurable beam blow-up. The limit on the duration of the excitation was not explored, but the gain is already at least an order of magnitude larger than a kick excitation. As expected, the shortest ramp time of 25 ms did not violate the adiabaticity criterion. These results appear sufficient

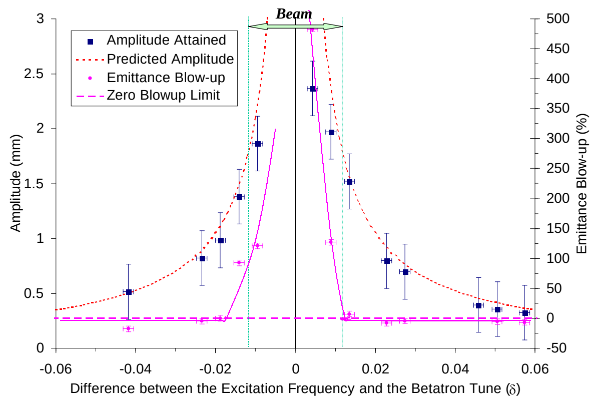

Figure 4: Amplitude response and emittance blow-up versus tune split

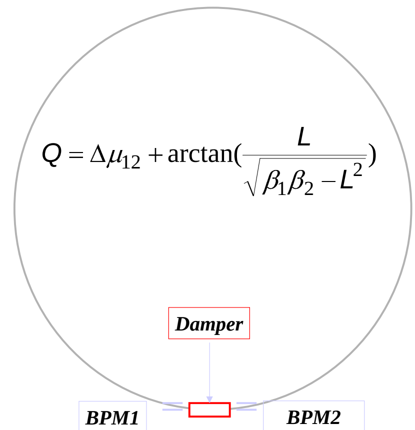

Figure 6: LHC set-up for the tune measurement

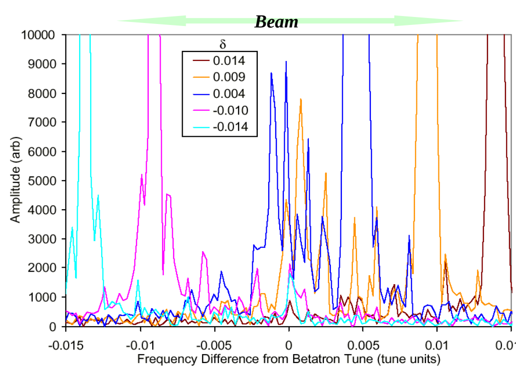

Figure 5: Frequency response versus tune split

to establish the interest of this excitation method for the LHC. The experiment will be repeated in view of exploring the parameter space more precisely (adiabaticity condition, length of the excitation plateau) and the capability in measuring linear and non-linear optics parameters (linear optics functions, chromatic and amplitude detunings, resonance strengths,...). In spite of the forced oscillation outside the beam eigenfrequencies, a measurement of the betatron tunes seems at hand with a set-up as indicated on figure 6. This opens the possibility of harmless continuous tune/chromaticity measurements. The additional BPM's required for this measurement have been added to the LHC layout.

6 REFERENCES

[1] M. Bai *et al.*, 'Overcoming intrinsic spin resonances with an RF dipole', BNL-65149.

[2] M. Bai *et al.*, Experimental test of Coherent Resonance Excitations', Phys. Rev. E, Vol56, No 5, Nov 1997, pp. 6002-6007.

[3] S. Peggs, IEEE Part. Acc. Conf., New York, 1999.

[4] S. Peggs, C. Tang, 'Nonlinear Diagnostics using an AC Dipole', RHIC/AP/159, 1998.

MEASURING BETA-FUNCTIONS WITH K-MODULATION

O. Berrig, C. Fischer, H. Schmickler CERN, Geneva, Switzerland

Abstract

The precise measurement of the local value of the beta-function at the place of a beam size monitor is necessary for the precise determination of the beam emittance. We developed a new method for the measurement of the beta-function by using of continuous square-wave modulation of the force of the quadrupole and by continuous tune tracking. Measurements were performed at LEP in order to evaluate the precision that can be achieved with this method in the LHC.
The paper describes the method and discusses in details the results obtained at LEP for colliding and non-colliding beams.

1 EMITTANCE MEASUREMENT

The emittance can be obtained from the measurement of the beam size from the following formula:

$$\sigma(s) = \sqrt{\varepsilon\beta(s)}$$

where $\sigma(s)$ is the transverse beam size, ε is the emittance, $\beta(s)$ is the beta-function and s is the longitudinal distance.

Therefore, in order to determine the emittance with high precision, the beta-function must also be known to high precision. We aim at a precision of 1%.

2 BETA-FUNCTION MEASUREMENT

The general principle of the beta-function measurement can be seen in fig.1. By changing the strength (k) of the quadrupole, the accelerator optics change, and therefore the tune change. The bigger the change of the strength, the bigger the tune change. The two are linked via the average value of the beta-function in the quadrupole:

$$\beta_{average} \approx 4\pi \frac{\Delta Q}{\Delta k \cdot l}$$

where ΔQ is the tune change, Δk is the change in quadrupole strength and l is the length of the quadrupole. The measurement of the tune is done by a PLL [1]. We could also have measured the tune with a continuous FFT, but chose not to, because a FFT has a quantization error of 1/(NΔT).

Apart from the internal noise in the PLL, the measurement of ΔQ is subjected to noise from various sources, like:

- A change in the closed orbit.
- Beam-beam interactions.

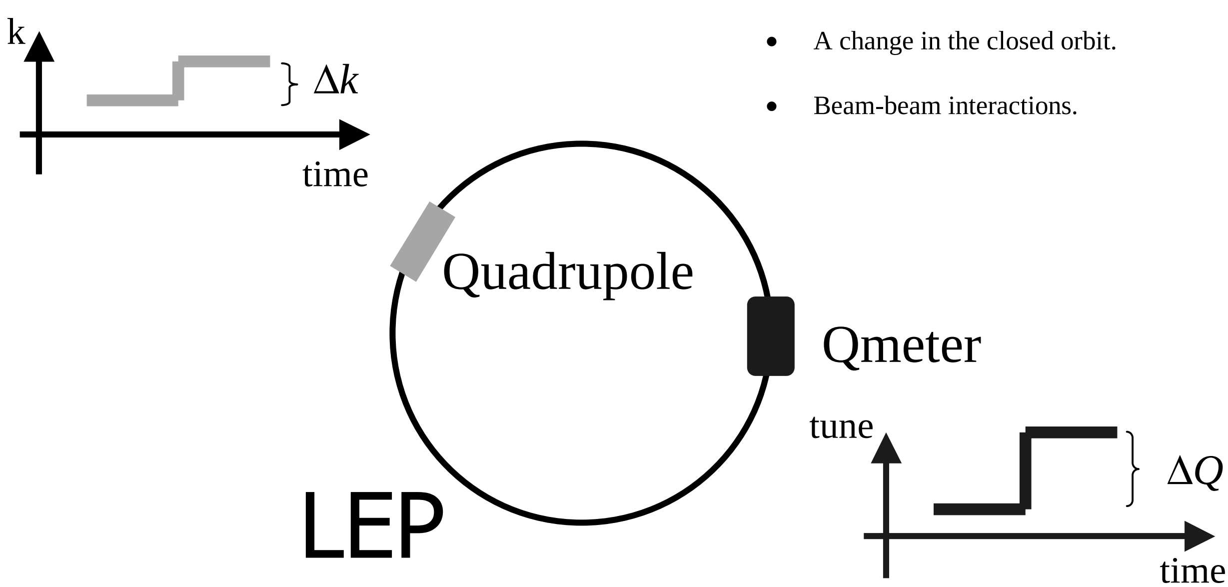

Figure 1: Static-k measurement. By changing the strength (=Δk) of the quadrupole, the tune (=ΔQ) change. The ratio between them is determined by the value of the beta-function at the place of the quadrupole.

3 K-MODULATION

3.1 Difference of static-k and k-modulation

K-modulation was introduced to gain precision due to averaging over many measurements, thereby removing random errors. K-modulation consists of a repeated change in the quadrupole strength.:

Static-k measurement:

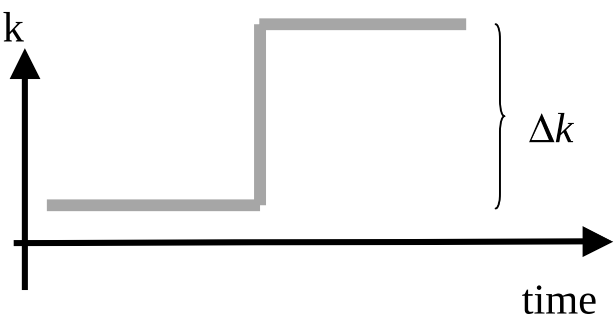

Measurement with k-modulation:

Figure 2: Difference between static-k and k-modulation.

The error reduction resulting from the averaging is so big that we can afford to reduce the step size (= Δk). This makes the method less perturbing. K-modulation can even be used during physics with colliding beam.

Advantages of k-modulation:

- Many measurements => increase precision
- Use small Δk => use during physics

Disadvantages of k-modulation:

- Compensate for dynamic effects (see chapter *3.2*)
- Requires high (10^{-5}) precision in tune measurement

3.2 Compensation of dynamic effects

A change in the quadrupole strength will create a transient response. Many different equipment are part of the transient response:

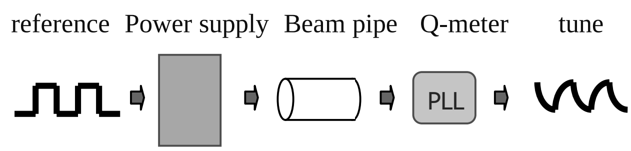

In the static-k measurement, such transients could be ignored because datataking would only be done when the transients had died out. When using k-modulation , the transients might not have died out before the quadrupole strength changes again. Our tests used a k-modulation frequency of 0.25 Hz i.e. a time between up and down in quadrupole strength of 2 seconds. Since the transients takes ~ 1.5 seconds to die out, this left us ~ 0.5 seconds to measure the stable response of the tune. In figure 3 is shown the response of the tune to a k-modulation cycle (this cycle is the average of very many cycles). The blue curve is the tune response and the pink curve is the Fourier component of the fundamental frequency. From this curve we established the ratio between the Fourier component and the stable response of the tune. This ratio we called the form factor (here 1.27544). When measuring shorter series of k-modulations with different amplitudes of Δk, we could then calculate the stable response by dividing the Fourier coefficient of the fundamental frequency with the form factor.

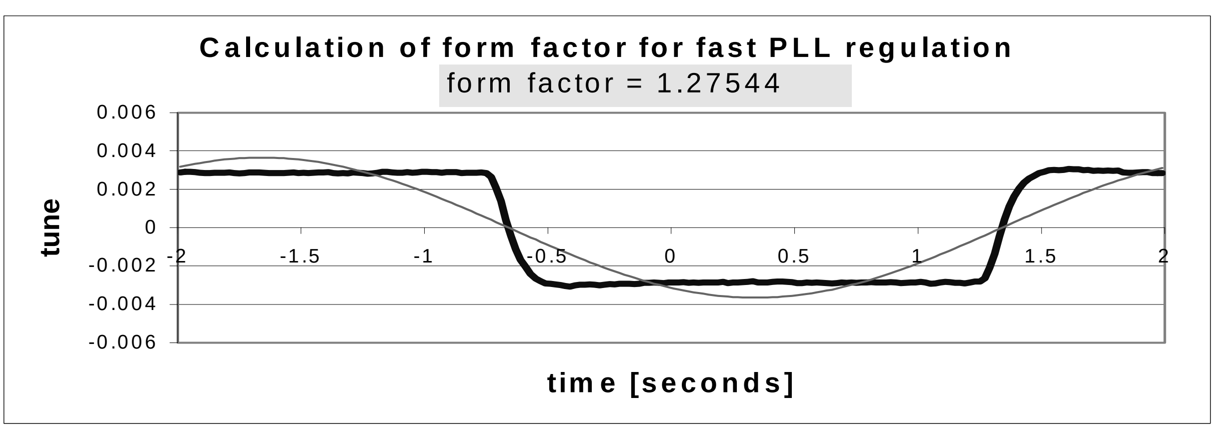

Figure 3: The tune response to k-modulation. The pink curve is the fundamental frequency of the tune response.

3.3 Obtained resolution in tune measurement

In order to disturb physics the least possible, the value of ΔQ is minimised. We characteristically used values of ΔQ of 0.005. Because we aimed at a measurement precision of 1%, the amplitude of the tune-noise should be less than 0.01% i.e. $5\ 10^{-5}$ in tune. Fig. 4 shows the Fourier spectrum of the noise of the PLL, which tracks a constant tune:

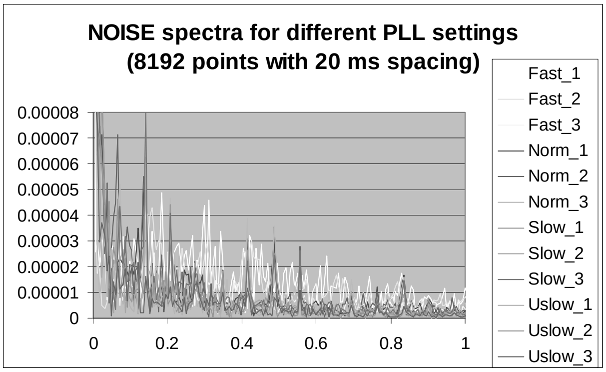

Figure 4: Fourier components of noise

The noise at 0.25 Hz (the k-modulation frequency) was always less than 0.00005 for any mode (Fast, Normal, Slow or Ultraslow) of the PLL.

4 RESULTS

The following table shows results from an machine development (MD). The theoretical value comes from MAD. The MD started with two series of k-modulation, then followed three 1000 turns [2] measurement (The 1000 turns measurement is the bench mark for beta-function measurements), then followed 4 static-k measurements, and finally -after many hours- came two series of k-modulation:

Table 1: MD results

Method	β value	σ
Theory (QS249)	181.7 m	
k-modulation before	161.1 m	0.43
1000 turns	166.5 m	2.86
static-k	164.4 m	5.62
k-modulation after	162.0 m	0.06

All four measurements agrees to each other within 2σ.

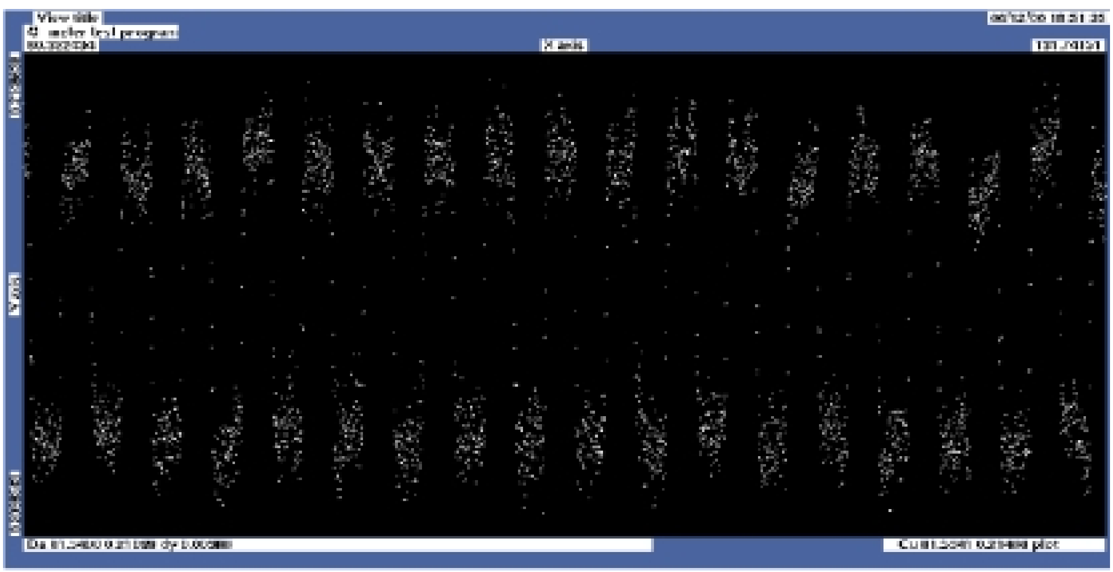

Figure 5: An example of raw tune measurements with k-modulation

5 CONCLUSION

β-function measurement with k-modulation is precise to better than 1%. It is a robust method that measures as well during collisions as with a single beam. The values of the beta-function from k-modulation measurements compare to within 4% to the 1000 turns measurements. We propose to measure β-functions with k-modulation in LHC. We expect to get even better precision by increasing the k-modulation frequency. An increased frequency will increase the number of averages and be further away from the noise of the slow tune drifting.

6 ACKNOWLEDGEMENTS

Thanks to all the members of the CERN SL operations group for adapting their schedule to our measurements. Thanks also to A.Burns for his enlightning ideas.

7 REFERENCES

[1] Buur G., Collier P., Lohmann K. D. & Schmickler H., Dynamic tune and chromaticity measurements in LEP. CERN SL 92-15 DI

[2] Applications of the 1000-turns Orbit Measurement System at LEP. P.Castro

X-RAY INTERFERENCE METHODS OF ELECTRON BEAM DIAGNOSTICS

O.Chubar, A.Snigirev, S.Kuznetsov, T.Weitkamp, ESRF, Grenoble, France
V.Kohn, Russian Research Center “Kurchatov Institute”, Moscow

Abstract

Electron beam diagnostics methods based on interference and diffraction of synchrotron radiation (SR) in hard X-ray range will be discussed. Two simple optical schemes providing X-ray interference patterns highly sensitive to transverse size of the emitting electron beam, will be considered. For each scheme, the visibility of fringes in the pattern depends on transverse size of the electron beam. However, the pattern is also determined by the scheme geometry, shape and material of diffracting bodies. Therefore, for correct interpretation of the experimental results, high-accuracy computation of SR emission and propagation in the framework of physical optics should be used. Examples of practical measurements and processing of the results are presented.

1 INTRODUCTION

Visible light interference methods have proved to be very efficient for diagnostics of relativistic charged particle beams emitting synchrotron radiation in magnetic fields of accelerators [1-6]. Nevertheless, since 3rd-generation SR sources are mainly dedicated for X-rays, the use of X-rays for electron beam diagnostics in these accelerators can be advantageous. Such diagnostics can be based on the same equipment that is used in other experiments; besides, it may offer higher resolution.

A number of X-ray experimental techniques benefiting from high spatial coherence of the SR, e.g. phase-contrast imaging, holography, interferometry, have been developed [7-11]. These techniques require characterisation and “in-place” control of the source coherence, which makes the X-rays based beam diagnostics further important.

This paper considers two very simple diffraction/ interference schemes, which can be readily used for beam diagnostics at any X-ray beamline (not necessarily fully dedicated for the diagnostics). One is the well-known Fresnel diffraction at a slit, and the other is a wavefront-splitting interference scheme where a thin fiber is used as an obstacle and phase-shifting object. As different from previous considerations made for isotropic source with finite transverse size [12-14], the current paper takes into account peculiarities of synchrotron (undulator) radiation emitted by an electron beam with finite transverse emittance (i.e., not only with the size, but also with angular divergence).

2 BASICS OF THE METHODS

2.1 Isotropic Source with Finite Transverse Size

Let us recall that in the case when a source has finite transverse size, and different points of the source emit incoherently, the resulting intensity of the radiation passed through an optical system to a detector plane is obtained by summing up intensities of emission from all points of the source [15]:

$$I(x,y) = \iint I_0(x,y;x_s,y_s)\, B(x_s,y_s)\, dx_s dy_s\ , \qquad (1)$$

where (x,y) are transverse coordinates in the detector plane, (x_s,y_s) transverse coordinates at the source, I_0 intensity from a point source (referenced below as point-source intensity), and B the source brightness.

For many simple diffraction and interference schemes with a source emitting spherical waves, in small-angle approximation, Eq. (1) is a convolution-type integral, i.e.:

$$I_0(x,y;x_s,y_s) \approx \tilde{I}_0(x - mx_s, y - my_s)\,, \qquad (2)$$

where $m = -r_d/r_s$ is a “magnification” factor, with r_s being distance from the source to an obstacle, and r_d distance from the obstacle to the detector (see Fig. 1). We note that this effect is used in pinhole cameras (which are successfully applied for electron beam diagnostics [16]).

If Eq. (2) is valid, $\tilde{I}_0(x,y)$ is known, and the resulting intensity $I(x,y)$ is measured to a sufficient accuracy, one can try to reconstruct $B(x_s,y_s)$ using the Wiener filtering [17] or a regularization technique [18].

The resolution of an optical scheme at the source size measurement depends on the point-source intensity $\tilde{I}_0(x,y)$. In the case of Fresnel diffraction at a slit, $\tilde{I}_0$ possesses fringes with the widths on the order of $\lambda r_d/a$, where λ is the radiation wavelength and a the slit size. This can be compared with the source image size $\sigma r_d/r_s$. However, the resolution of this scheme can be much better, because $\tilde{I}_0$ has also smaller details originating from “interaction” of the slit edges (see Fig. 2).

Figure 1: Interference pattern formation from a source with finite transverse size.

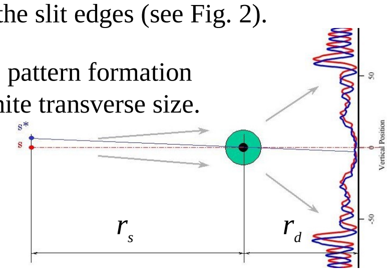

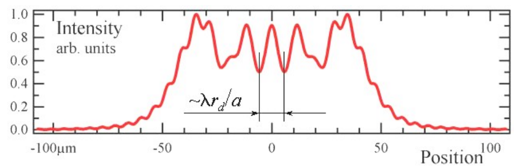

Figure 2: Point-source intensity distribution at the Fresnel diffraction at a slit.

2.2 Finite-Emittance Electron Beam

This section describes how a more accurate computation of the SR emitted by an electron beam and propagated through an optical system, can be performed. Such a computation allows to verify whether a particular approximation corresponds to realistic experimental conditions, and thus to choose an adequate simplified model and method for processing the experimental results.

Starting from Fourier transformations of the retarded potentials, one can obtain the following expression for the frequency-domain electric field of radiation emitted by a relativistic electron (Gaussian System) [19]:

$$\vec{E} = iek \int_{-\infty}^{+\infty} [\vec{\beta} - \vec{n}\,[1 + i\,(kR)^{-1}]]\, R^{-1} \exp[ik(c\tau + R)]\, d\tau\,, \quad (3)$$

where k is a wave number, $\vec{\beta} = \vec{\beta}(\tau)$ instant relative velocity of electron, $\vec{n} = \vec{n}(\tau)$ unit vector directed from instant electron position to an observation point, $R = R(\tau)$ distance from the electron to the observation point, c speed of light, e charge of electron. Eq.(3) describes practically all kinds of single-electron emission in the near- and far-field observation regions. It allows to compute SR electric field at some longitudinal position, e.g. before the first optical element of a beamline. Typically, only transverse components of the electric field (3) need to be considered.

The wavefront propagation through transmission optical elements can be simulated by multiplication of the transverse electric field by a complex transmission function of transverse position, which can take into account both attenuation and phase shift of the wave field.

Assuming small angles and distances considerably larger than wavelength, the transverse component of the electric field propagated through a drift space $\vec{E}_{\perp 2}$ can be computed from the electric field $\vec{E}_{\perp 1}$ before the drift space by the well-known Huygens-Fresnel principle

$$\vec{E}_{\perp 2} = -ik(2\pi)^{-1} \iint_{\Sigma} \vec{E}_{\perp 1}\, S^{-1} \exp(ikS)\, d\Sigma\,, \quad (4)$$

where S is a distance from a point on this surface to an observation point. If the integration surface Σ is (a part of) a plane perpendicular to the optical axis, and the observation points belong to another plane perpendicular to the optical axis, then Eq. (4) is a convolution-type integral that can be quickly computed by applying the convolution theorem and 2D FFT.

To obtain intensity distribution of the SR emitted by the finite-emittance electron beam, one needs to sum-up intensities obtained after propagation of electric fields from individual electrons. In general case, the single-electron intensity I_0 depends on transverse coordinates, angles and energy of the electron $(x_s, y_s, x'_s, y'_s, E_s)$, so that the final intensity is derived by integration with respect to all these variables:

$$I(x,y) = \int I_0(x,y; x_s, y_s, x'_s, y'_s, E_s) \times n(x_s, y_s, x'_s, y'_s, E_s)\, dx_s dy_s dx'_s dy'_s dE_s \quad (5)$$

where n is particle distribution in the beam phase space.

For different types of SR and different optical schemes, the single-electron intensity I_0 may not strongly depend on some of the phase-space variables. In each particular case, this dependence, as well as the validity of the convolution approximation (e.g. Eq.(2)), can be checked numerically, by making single-electron wavefront propagations for different values of $(x_s, y_s, x'_s, y'_s, E_s)$.

When performed for the Fresnel diffraction of undulator radiation (UR) at a slit, this test showed that if angular aperture of the slit is comparable to the opening angle of the single-electron UR, and to the electron beam angular divergence, then the latter can contribute to the final intensity distribution of the diffracted radiation. This contribution is typically smaller than that of the beam transverse size, however it should be taken into account at the process of results, of the beam diagnostics measurements.

The numerical methods based on Eqs.(3)-(5) are implemented in the SRW, a physical optics computer code for synchrotron radiation [20].

3 MEASUREMENTS

The measurements of Fresnel diffraction and the interference from a fiber were carried out at ID22 beamline of ESRF, using the radiation from a planar undulator (38 periods of 42 mm) at 11 keV photon energy. After the undulator, the radiation was deflected horizontally by a mirror (in order to suppress high-energy part of the UR spectrum), and then passed through a double-crystal monochromator.

In the Fresnel diffraction scheme, a 100 μm x100 μm rectangular slit was located at 37.6 m distance from the middle of the undulator, and the distance from the slit to detector was 5.5 m.

In another scheme, a cylindrical boron fiber was placed at a distance of 40.6 m from the undulator, and the detector was located at 1.85 m after the fiber. The diameter of the fiber was 100 μm; the fiber possessed a tungsten core with a diameter of ~15 μm.

The intensity distributions in the two schemes were registered by a 2D coordinate-sensitive detector consisted of a 1 μm thick YAG scintillator coupled by a visible light microscope to a CCD camera. The re-focused CCD pixel size was 0.24 μm, and the resolution, estimated as FWHM size of the point-spread function, was on the order of1 μm. The intensity distributions registered in the two schemes are shown in Fig. 3 on the left.

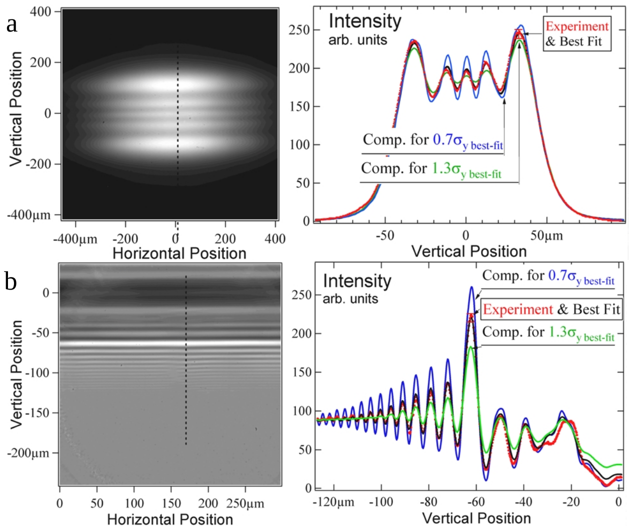

Figure 3: Measured intensity distributions and results of the fitting procedure for the Fresnel diffraction at a slit (a) and interference from a boron fiber (b).

The right-hand plots in Fig. 3 illustrate the fitting of vertical slices of the measured intensity by distributions computed for different values of vertical electron beam emittance ε_y, using a numerical procedure based on Eqs. (3)-(5). At the fitting, the vertical beam size and divergence were re-calculated for the middle of the straight section via:

$$\sigma_y = (\varepsilon_y \beta_y)^{1/2}; \; \sigma'_y = (\varepsilon_y / \beta_y)^{1/2}, \tag{6}$$

with the value of the vertical beta function assumed to be known: β_y = 2.5 m [21]. The particle distribution in the electron beam was assumed Gaussian over vertical position and angle. The detector point-spread function was approximated by the Gaussian as well.

The vertical RMS beam size value obtained from the Fresnel diffraction measurements is: $\sigma_y = 22 \pm 4$ µm, and from the interference at the fiber: $\sigma_y = 24 \pm 5$ µm. These values are larger than the vertical beam size value in the middle of a straight section which follows from the ESRF pinhole camera measurements performed at larger β_y [21]. The most probable reason for this discrepancy is the presence of the mirror and the vertically reflecting crystal monochromator in the optical scheme. These two optical components were not taken into account at processing of the experimental results, however, each of them could reduce the transverse coherence of the wavefront, due to imperfections of the mirror surface and possible contribution of the crystal transfer function, respectively.

5 CONCLUSIONS

X-ray diffraction and interference schemes can be used for beam diagnostics in 3rd-generation SR sources. The schemes are very simple and can be applied nearly at any X-ray beamline. This diagnostic has a very high theoretical resolution: on the order of microns. However, it is also very sensitive to the quality of optics. Therefore, to avoid systematic errors, transfer functions of the optical elements should be known to a reasonable accuracy; the use of transmission X-ray optics is preferable.

On the other hand, this type of measurements and data processing can be applied to characterize the transverse coherence properties of an entire X-ray beamline, including both the source and the optics in use.

REFERENCES

[1] T.Shintake et.al., “Experiments of nanometer spot size monitor at FFTB using laser interferometry”, Proc. of IEEE PAC-95, p.2444

[2] O.Chubar, “Transverse electron beam size measurements using the Lloyd's mirror scheme of synchrotron light interference”, Proc. of IEEE PAC-95, p.2447.

[3] Å.Andersson, M.Eriksson and O.Chubar, “Beam profile measurements with visible synchrotron light on MAX-II”, Proc. of EPAC-96, p.1689.

[4] T.Mitsuhashi, “Spatial coherency of the synchrotron radiation at the visible light region and its application for the electron beam profile measurement”, Proc. of IEEE PAC-97, p.766.

[5] S.Hiramatsu et. al., “Measurement of small beam size by the use of SR interferometer”, Proc. of IEEE PAC-99, p.492.

[6] N.V.Smolyakov, “Interference diagnostics for storage ring electron beam”, Nucl. Instr. and Meth., 1998, vol.A405, p.229.

[7] A.Snigirev, I.Snigireva, V.Kohn, S.Kuznetsov and I.Schelokov, “On the possibilities of X-ray phase contrast micro-imaging by coherent high-energy synchrotron radiation”, Rev. Sci. Instrum., 1995, vol.66(12), p.5486.

[8] A.Snigirev, “Hard X-ray microscopy with coherent light: holography, phase contrast and interferometry”, ICFA Workshop on 4th Generation Light Sources, Jan. 22-25 1996, ESRF, Grenoble.

[9] C.Raven, A.Snigirev, I.Snigireva, P.Spanne, A.Souvorov and V.Kohn, Appl. Phys. Lett., 1996, vol.69, p.1826.

[10] P.Cloetens, R.Barret, J.Baruchel, J.P.Guigay and M.Schlenker, J.Phys. D: Appl. Phys., 1996, vol.29, p.133.

[11] T.E.Gureyev, C.Raven, A.Snigirev, I.Snigireva and S.W.Wilkins, J.Phys. D: Appl. Phys., 1999, vol. 32, p.563.

[12] A.Snigirev, V.Kohn, I.Snigireva, “Fresnel diffraction by slits”, in “ESRF Highlights 1996/1997”, Nov.1997, p.91.

[13] V.Kohn, I.Snigireva and A.Snigirev, “Direct measurement of transverse coherence length of hard X-rays from interference fringes”, Phys. Rev. Lett., 2000, vol.85(13), p.2745.

[14] V.Kohn, I.Snigireva, A.Snigirev, “Interferometric characterization of spatial coherence of high energy synchrotron X-rays”, submitted to Elsevier Preprint.

[15] M.Born, E.Wolf, Principles of Optics, 4th ed., Pergamon Press, 1970.

[16] P.Elleaume et. al., “Measuring beam size using X-ray pinhole camera”, J. Synchrotron Rad., 1995, vol.2, p.209.

[17] L.R.Rabiner, B.Gold, Theory and application of digital signal processing, EnglewoodCliffs, N.J.: Prentice-Hall, 1975.

[18] AN.Tikhonov, A.V.Goncharsky, V.V.Stepanov, “Inverse problems in image processing”, in Ill-posed problems in natural sciences, Moscow: Mir Publishers, 1987.

[19] O.Chubar, "Precise Computation of Electron Beam Radiation in Non-uniform Magnetic Fields as a Tool for the Beam Diagnostics", Rev. Sci. Instrum., 1995, vol.66 (2), p.1872.

[20] Synchrotron Radiation Workshop (SRW) computer code is available from: http://www.esrf.fr/machine/support/ids/Public/Codes/software.html

[21] P.Elleaume, http://www.esrf.fr/machine/support/ids/Public/Sizes/sizes.html

This work was supported by INTAS Project No. 99-0469

Beam Charge Asymmetry Monitors for Low Intensity Continuous Electron Beam*

Chris Cuevas, Jean-Claude Denard, Arne P. Freyberger, Youri Sharabian
Jefferson Lab, 12000 Jefferson Avenue, Virginia, 23606 USA

Abstract

Experimental Hall B at Jefferson Lab (JLAB) typically operates with CW electron beam currents in the range of 1 - 10 nA. This low beam current coupled with a 30 Hz flip rate of the beam helicity required the development of new devices to measure and monitor the beam charge asymmetry. We have developed four independent devices with sufficient bandwidth for readout at 30 Hz rate: a synchrotron light monitor (SLM), two backward optical transition radiation monitors (OTR) and a Faraday Cup. We present the results from the successful operation of these devices during the fall 2000 physics program. The reliability and the bandwidth of the devices allowed the control of the current asymmetry at the source laser by means of a feedback loop.

1 POLARIZED BEAM AT JLAB AND HALL B REQUIREMENTS

The JLAB polarized source generates three CW electron beams for the experimental halls (A, B & C). Two of these halls, A & C, house two-arm spectrometers and operate with beam currents between 50μA and 100μA. Hall B houses a large acceptance spectrometer which is luminosity limited to beam currents of 1 to 10nA. This small CW beam current is a challenge for beam diagnostics.

The electron beam polarization is toggled between the h^+ helicity state and the h^- helicity state at a 30Hz rate. The relative beam charge for each state must be accurately measured in order to correctly extract the physics cross sections. The measured physics asymmetries are of the order of a few percent, which was used to place a desired limit on the beam charge asymmetry; $A_Q = \frac{N^+_{e^-} - N^-_{e^-}}{N^+_{e^-} + N^-_{e^-}} < 0.1\%$.

2 BEAM CHARGE ASYMMETRY MONITORS

To monitor the relative amount of beam charge in each helicity state requires devices that are linear with respect to beam current, fast enough to be recorded at the 30Hz time scale and independent of other possible helicity dependent effects (like beam motion).

Prior to fall 2000, the Hall-B beam current instrumentation consisted of the Faraday Cup and beam position/current RF cavities. Both were of insufficient bandwidth to measure the beam charge at a 30Hz rate. Three new devices were installed along the beam-line, a synchrotron light monitor (SLM) and two backward optical transition radiation monitors (OTR), prior to the fall 2000 physics run. The Faraday Cup electronics was upgraded to work at a higher bandwidth at this time as well. The following sections describe these developments.

2.1 Synchrotron Light Monitor

The electron beam is transported from the “switch-yard” to Hall-B via a vertical “S” bend. The bending radius of the last dipole is 33m. Downstream of this dipole a mirror reflects the synchrotron light through an optical port. From there the synchrotron light goes through an aperture and is split, with one half of the light incident on a CCD camera and the other half is focussed via a lens onto a photomultiplier tube (PMT). The PMT current output is proportional to the beam current and is used to measure A_Q. The lens is used to focus the light onto the photo-cathode so that the synchrotron light position on the photo-cathode is independent of beam position. Beam motion in the bend plane changes the geometrical acceptance. Details of the PMT and electronics chain is found in a later section.

2.2 Optical Transition Radiation Monitors

Two OTR monitors were installed; each use 0.8μm Al foils[1] as the source of OTR. OTR-1 consists of a foil 2.54cm in diameter mounted at a 45^0 angle with respect to the beam and an optical port. OTR-1 is installed just upstream of the Hall-B Møller polarimeter target and is used only during Møller runs. OTR-2 consists of a foil mounted at 60^0 with respect to the beam. The foil resides just inside of an integrating sphere[2], and uniformly illuminates the photo-cathode. The integrating sphere is used to minimize reflective variations in the OTR foil and to minimize the position dependence of the light on the photo-cathode. OTR-2 is located $\sim$5m upstream of the experimental target. The electron beam in this region is rastered in a spiral pattern approximately 1.5cm in diameter.

2.3 Faraday Cup

After the electron beam traverses the experimental target it is transported to the Faraday Cup. With a capacitance of

* Work supported the Southeastern Universities Research Association (SURA) which operates the Thomas Jefferson National Accelerator Facility (JLAB) for the United States Department of Energy under contract DE-AC05-84ER40150

[1] Goodfellow Cambridge Limited, Cambridge, CB4 4DJ, England

[2] Oriel Instruments, 150 Long Beach Boulevard, Stratford, CT 06615-0872

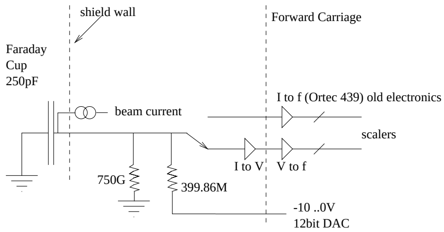

Figure 1: Schematic of the F-Cup electronics, including the old electronics as well as the calibration circuit

250 pF, the RC time constant is small enough to measure the beam current on a 30Hz time scale.

3 LIGHT DETECTION AND ELECTRONICS

Both the OTR and SLM devices produce light in the visual region of the EM spectrum. Phillips XP2262[3] photomultiplier tubes are used to detect both SLM and OTR light. These PMT's are used extensively throughout the Hall-B instrumentation. Their use in a CW light detection environment meant that the electronics would have to be different than the nominal discriminator-scaler setup. In order to avoid statistical fluctuations of detecting single photons, the PMT's are operating in current mode. The PMT output current is proportional to the number of photons incident on the photo-cathode.

The PMT's operating in current mode are a current source similar to the Faraday Cup. Measuring the current from these devices while retaining correlation with the beam helicity state is done with the following electronics chain; current to voltage amplifiers (ItoV) [4] are placed as close to the PMT's/F-CUP as possible to keep the RC time constant small. The voltage output is fed into a voltage to frequency converter (Vtof)[5] followed by a VME scaler [6]. Figure 1 is a schematic of the F-Cup circuit, including the previous electronics and the calibration circuitry.

4 LINEARITY AND POSITION DEPENDENCE

Figure 2 shows the response of the SLM and OTR's versus the beam current as measured by the Faraday Cup. Both OTR's saturated their electronics at large beam currents, this was fixed by changing the gain of the ItoV amplifier after the test. The beam position varied by $\pm 100\mu$m during this portion of the test. The non-linearity of each device is measured by determining the slope at each beam current cluster (at 0.5,1,2,5,8,10nA) The results of this comparison

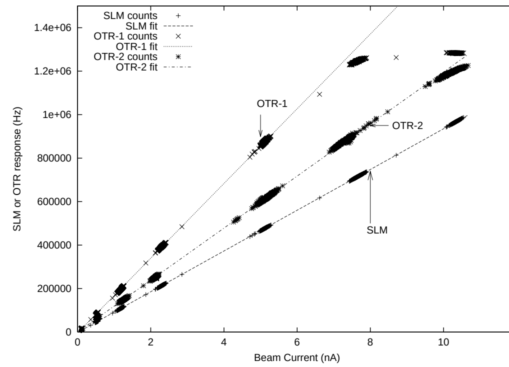

Figure 2: SLM, OTR-1 and OTR-2 light yield as a function of the beam current as measured by the Faraday Cup. The line drawn is the result of a linear fit to the data; data where the electronics on OTR-1 and OTR-2 are saturating are excluded from the fit.

are a 1%, 3% and 1% non-linearity for the SLM, OTR-1 and OTR-2 respectively. This non-linearity includes the effect $\pm 100\mu$m of beam motion and the improved response of OTR-2 compared to that of OTR-1 is presumably due to the integrating sphere reducing the effects of beam motion.

The effects of beam motion on the SLM and OTR responses was investigated by steering the beam off axis in 0.5mm steps in both x and y directions. The SLM and OTR-1 are $\sim$50m from the F-Cup and these beam motions led to beam loss as observed in the beam halo monitors. Unable to perform a direct comparison to the F-Cup, the measured asymmetry at the SLM and OTR's was compared to the F-Cup asymmetry. This is done by measuring the "double-asymmetry"; $\Delta A_{SLM-FCu} = \frac{N^{+}_{e^-}(SLM)N^{-}_{e^-p}(FCu)-N^{-}_{e^-}(SLM)N^{+}_{e^-p}(FCu)}{\Sigma}$. The top plot in Figure 3 shows the double-asymmetry for OTR-2 and the F-Cup and the bottom plot shows the beam position during this measurement. The double-asymmetry is fit to a Gaussian function, resulting in a mean of $(-0.6 \pm 2.2) * 10^{-5}$ demonstrating that the two devices are measuring the same asymmetry within statistics. Similar comparisons for SLM and OTR-1 showed that the measured asymmetry in all devices is independent of the beam position. While a zero double-asymmetry does not demonstrate the SLM and OTR responses are independent of position, it does show that the beam motion occurs on a slow enough time scale (compared to the helicity flip rate) that the measured A_Q is independent of beam motion.

5 SLM AND OTR LIGHT YIELDS

The PMT gain can be determined by measuring the widths of the ratio groups [SLM/F-Cup, OTR-1/F-Cup, SLM/OTR-1] and [SLM/F-Cup, OTR-2/F-Cup, SLM/OTR-2][7] and comparing with the calculated widths

[3]Phillips Photonics, BP 520, F-19106 BRIVE, France

[4]PMT5-R,Advanced Research Instruments Corporation, 1pA to 1μA sensitivity, gain selected via 3 TTL lines. Bandwidth at 1nA is 1kHz.

[5]8400series VtoF, 0.001% FS linearity, 1V input produces 100kHz output, Dymec, 27 Katrina Road, Chelmsford, MA 01824

[6]SIS3801, SIS GmbH, Moorhof 2d, 22399 Hamburg, Germany

[7]Only one OTR could be inserted at a time due to control issues. This led to two datasets, one with SLM, OTR-1 and F-Cup data and the other

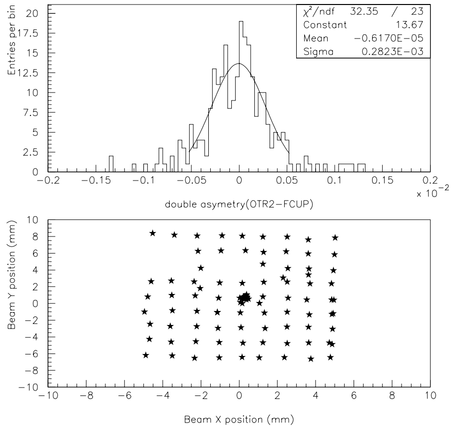

Figure 3: The top plot shows the double-asymmetry for OTR-2 and F-Cup and the bottom plot shows the x and y beam position during the measurement.

	Coefficient	$\frac{n_\gamma}{e^-_{beam}}(mea.)$	$\frac{n_\gamma}{e^-_{beam}}(cal.)$ [1, 2]
SLM	5.28(set 1) 5.18 (set 2)	$0.32 * 10^{-3}$	$0.64 * 10^{-3}$
OTR-1	11.1	$1.2 * 10^{-3}$	$5.6 * 10^{-3}$
OTR-2	5.91	$0.44 * 10^{-3}$	$1.9 * 10^{-3}$

Table 1: Table listing the results of constraining the $(measuredwidth)/(calculatedwidth) = 1$ at the 1nA data point. Using 0.25 for the photo-cathode efficiency the number of photons per electron of beam is determined.

based on Poisson statistics. Each group of ratios results in three equations with three unknowns at each beam current point. The coefficients for the 1nA data are listed in Table 1.

As expected OTR-2 looses some light as compared to OTR-1 due to the integrating sphere. The discrepancy between the calculated light yield and the measured yield for the OTR's suggests that there is an additional noise term contributing to the measured width. This discrepancy increases as a function of beam current and might be due to the presence of UV light on the photo-cathode[3]. The SLM light yields for all beam currents are constant. The light splitter in the SLM optics does not transmit in the UV region ($\lambda < 350n$m) so this PMT is protected from UV light.

6 SUMMARY

Using the results in the previous section the time needed to measure the beam charge asymmetry with 0.05% error at 1nA of beam current are determined to be (1.4, 8, 2, and 6s) for the (F-Cup, SLM, OTR-1 and OTR-2). The limiting factor on the F-Cup is the *digital* error as the F-Cup count

with SLM, OTR-2, F-Cup data.

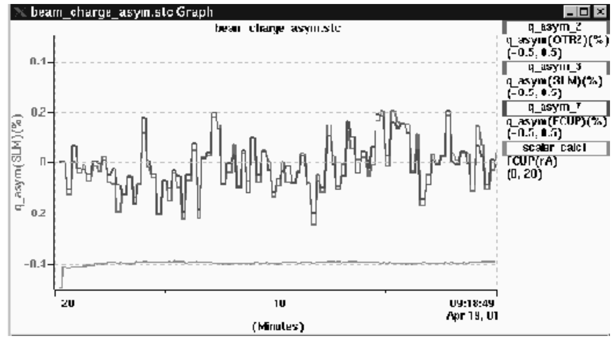

Figure 4: Screen capture of a real-time plot of A_Q as measured by the F-Cup and SLM as a function of time. A_Q was calculated using 10s worth of data. The lower trace (not fluctuating) is the beam current as measured by the F-Cup.

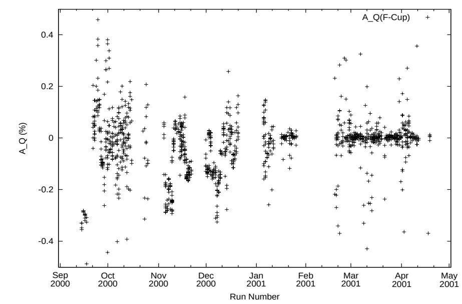

Figure 5: Beam charge asymmetries, one hour samples, corresponding to a data run in the hall. One can easily see the improvement when the feedback loop was enabled in Jan. 2001.

rate is only 309 pulses per helicity bin. Real-time plot of A_Q as a function of time for the SLM and F-Cup are shown in Figure 4. Actual fluctuations of the beam charge asymmetry are measured accurately within a 10s time frame as shown by the agreement between the F-Cup and SLM measurements. The helicity uncorrelated noise of the injector is the likely source of these fluctuations.

All these devices have been reliably used since Sept. 2000. Starting in Jan. 2001 the measured asymmetry is used to control the laser power at the injector to constrain the charge asymmetry to the Hall's requirements (see Figure 5).

7 REFERENCES

[1] Helmut Wiedemann, "Particle Accelerator Physics", Springer-Verlag, 1993.

[2] V.L. Ginzburg and V.N. Tsitovich, "Transition Radiation and Transition Scattering", Adam Hilger, 1990.

[3] "Photomultiplier Tubes, Principles & Applications", Phillips Photonics, 1994.

NEW DEVELOPMENT OF A RADIATION-HARD POLYCRYSTALLINE CdTe DETECTOR FOR LHC LUMINOSITY MONITORING

E. Rossa, H. Schmickler, CERN, Geneva, Switzerland,
A. Brambilla, L. Verger, F. Mongellaz, LETI, Grenoble, France

Abstract

Detectors presently considered for monitoring and control of the LHC luminosity will sample the hadronic/electromagnetic showers produced by neutrons and photons in copper absorbers designed to protect the superconducting magnets from quenching. At this location the detectors will have to withstand extreme radiation levels and their long term operation will have to be assured without requiring human intervention. For this application we have successfully tested thick polycrystalline-CdTe detectors. The paper summarizes the results obtained on rise-times, sensitivity and resistance to neutron irradiation up to a dose of $10^{15}/cm^{2}$.

1 - INTRODUCTION

The requirements on the LHC luminosity monitors can be summarised as:

- Possible counting rate of 40 MHz, i.e. rise and fall times below 10 ns
- Resistance to radiation damage up to doses of 10^{18} neutrons/cm^2 and 10^{16} protons/cm^2
- Good signal to noise ratio even for single minimum ionisation particles, such that in the shower sample statistically multiple events per bunch crossing can be destinguished from single events.

Cadmium telluride (CdTe) photo-conductor material used for nuclear radiation detectors and opto-electronic devices. A single Minimum Ionising Particle (MIP) creates about 50 000 electron-hole pairs in a 300 µm thick CdTe layer. In comparison about 53 000 pairs will be created in GaAs, but only 32 200 in Si and 11 850 in diamond [1].
The CdTe samples used for our tests have been produced by LETI (part of CEA) in Grenoble. These prototype detectors consist of discs of polycrystalline-CdTe about 16-mm in diameter with gold electrodes of 7 by 7 mm on both sides.

An ionisation chamber is currently as well under study to meet the above requirements [2]. References on the luminosity project are given in [3] and some others applications of CdTe are in [4-5].

2 - SPEED TESTS

2.1 Tests with a picosecond laser

The speed tests of the polycrystalline-CdTe output signal were undertaken at the Laboratoire de Sciences et Ingénierie des surfaces at the Université Claude Bernard-Lyon 1, [7]. A laser pulse (35 ps FWHM, 1060 nm wavelength) was onto one of the gold plated electrodes. The electrodes are porous enough to allow photons to reach the main bulk of the photoconductor. The photon transmission through the 0.5 mm thick sample was close to 50% at 1060 nm. Such a pulse is a good simulation of the ionisation track produced by a high energy particle going through the detector parallel to the electric field.

The signal produced by the laser pulse was very large and easy to measure on a single shot, fast-sampling oscilloscope. The measured rise time was limited to a fraction of nanosecond by the oscilloscope bandwidth.

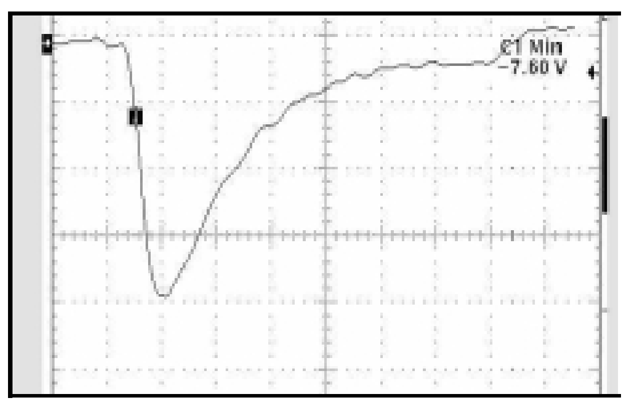

Figure 1: Example of a CdTe output signal terminated directly into 50Ω on the oscilloscope. The vertical scale is 2 Volts/division and the horizontal 2.5 ns/division. The applied bias voltage was 100 Volts.

3 - TESTS WITH MIP

The sensitivity was measured using a charge sensitive amplifier with a shaping time of 2 µs. The set-up used is described in reference [8]. The sample was irradiated by a radioactive source (^{90}Sr) and the particles traversing the sample were detected by a diode and triggered the acquisition of a digital oscilloscope. With a bias voltage of 200 Volts the collected charge reached 10000 electrons (see Fig.2)

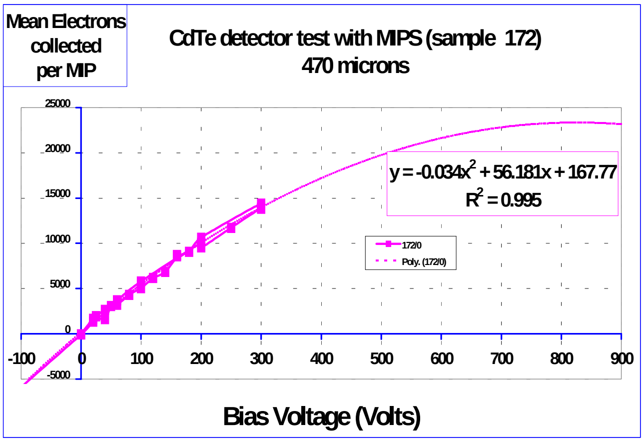

Figure 2: Average number of electrons per incident particle collected by the charge amplifier connected to the CdTe electrode

4 - IRRADIATION TESTS

The irradiation of the sample was carried out both at CERN and at a nuclear reactor in Valduc (France) where a high neutron flux was made available for our tests.

a) The set-up used at CERN is described in references [9,10]. After a total flux of $1.18\ 10^{14}$ n/cm^2 with neutron energies above 1 keV no significant change in the sample sensitivity was measured. The beam provided a flux in excess of $9\ 10^{13}$ n/cm^2 with energies above 100 keV.

b) In the Valduc reactor the samples were irradiated up to 10^{15} n/cm^2 at energies up to 1 MeV for about 2 weeks. No appreciable change in the sensitivity of the CdTe sample could be observed within the 5% precision of the measurement.

4.1-Time response measurement after neutron irradiation (laser stimulation of CdTe)

The speed test after neutron irradiation was carried out at CERN with a fast laser (1047 nm, 60 ps FWHM) using a similar technique as outlined in section 2.

Figure 3 shows the comparison of the time response measurement before and after irradiation to 10^{15} n/cm^2

4.2 Time response measurement after neutron irradiation (radioactive source stimulation of CdTe)

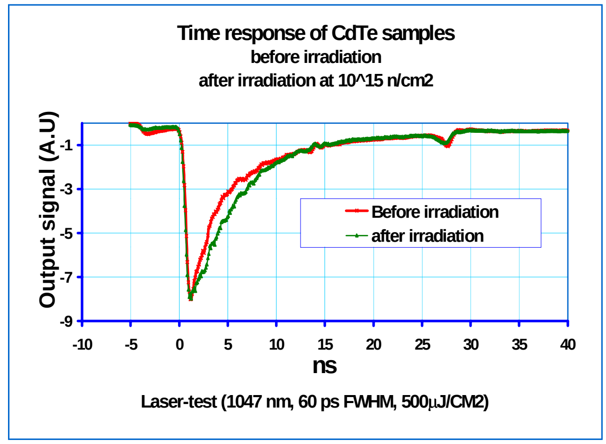

Figure 3: Time Response of CdTe detector before and after neutron irradiation

For this measurement the CdTe was exposed to the radiation of a ^{90}Sr source. The small signal produced by the minimum ionising radiation of the source had to be amplified before a signal spectrum could be measured. A digital oscilloscope Lecroy 9354 and a fast preamplifier(DBA) [11] developed in GSI (Germany) were chosen for the test. The amplified signal was analysed by using the facilities of the scope software.

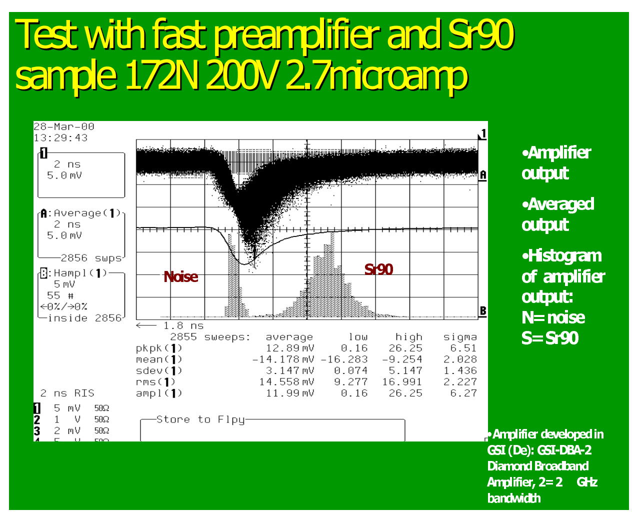

Figure 4: Real time analysis of the preamplified output signal using a Lecroy 9354 oscilloscope.

This preliminary result confirms the speed tests with the infrared laser.

6 - FUTURE PLANS

Irradiation tests at very high doses of up to 10^{18}n/cm2, during a reasonable exposure time of a few weeks are available at a research nuclear reactor facility in Ljubljana. These tests are scheduled to take place in autumn 2001 in order to fully qualify the detectors for the expected irradiation levels in the LHC.

One of the major problems with these tests is that the detector itself will become highly activated, such that later tests on its functionality in a laboratory are excluded.

We are planning to install a set of detectors connected via radiation resistant coaxial cables to the outside of the reactor core. A coincidence circuit of several detectors will be used to register online the pulse height spectrum of cosmic ray minimum ionising radiation.

7 - CONCLUSIONS

We have successfully tested thick polycrystalline-CdTe detectors for a potential use as LHC luminosity monitors. The following results were obtained:

- The signal response of the 300 µm thick detectors (16 mm diameter) is largely sufficient for a 40 MHz event rate measurement.
- The sensitivity is in excess of 10 000 electrons/MIP in combination with fast 50 ohms-preamplifier deliver a signal, which has an excellent signal to noise ratio and which allows statistically to distinguish single proton-proton interactions from multiple interactions.allows for a simple design.
- No significant loss in sensitivity or speed has been measured after irradiation tests up to 10^{15} n/cm^2.
- Beam tests confirmed the preliminary results obtained with a fast laser and a ^{90}SR source.
- New experiments after irradiation up to 10^{18} n/cm^2 are in preparation.

ACKNOWLEDGEMENT

The authors would like to thank A. Million, O. Peyret, G. Rumen from LETI, E. Berdermann, P. Moritz from GSI and P. Legros, S. Hutchins, G. Burtin and J-P. Bindi from CERN. The help of Karl Gill during the neutron irradiation tests is acknowledged as well as Rhodri Jones for his collaboration all along this development.

REFERENCES

[1] E. Rossa, C. Bovet, D. Meier, H. SchmicklerL. Verger, F. Mongellaz, G. Rumen, CdTe photoconductors for LHC luminosity monitoring, http://documents.cern.ch/archive/electronic/cern/preprints/sl/sl-2000-068.pdf

[2] W.C Turner, M.T. Burks, P.S. Datte, P.F. Manfredi, J.E. Millaud, N.V. Mokhov, M. Placidi, L. Ratti, V. Re, H Schmickler, V. Speziali, "Development of a detector for bunch by bunch measurement and optimization of luminosity in the LHC", LBNL-45774. CBP Note 337.

[3] H. Schmickler, "Summary Comments" in Proc. Of Tools for Luminosity Optimisation in LHC, 15-16 Apr. 1999, CERN, Geneva. Proceedings at http://www.cern.ch/CERN/Divisions/SL/groups/bi

[4] E. Rossa, " Picosecond diagnostics", in Opt. Eng. : 34 (1995) pp.2353-2360

[5] M.Placidi, E.Rossa, H.Schmickler, "A CdTe Detector for Muon Transverse Profile Measurements" http://documents.cern.ch/archive/electronic/cern/preprints/open/open-2001-034.pdf

[6] LETI (CEA-Technologies Avancées) -17 Rue des Martyrs-F38054 Grenoble Cedex 9- France

[7] With the help of Jean-Pierre Girardeau-Montaut and Bélà Kiraly at the Laboratoire de Sciences et Ingénierie des surfaces at the Université Claude Bernard-Lyon 1.

[8] Dirk Meier thesis: “CVD Diamond Sensors for Particle Detection and Tracking” Fig.3.27 page 92 http://atlasinfo.cern.ch/Atlas/documentation/thesis/thesis.html

[9 M. Glaser, RADEC99, 5th European Conference on Radiation and its Effects on Components and Systems. by Sharp, Richard ed. ; Publ. Ref.: IEEE Trans. Nucl. Sci. : 47 (2000) no.3, 13 - 17 Sep 1999

[10] M. Glaser, L. Durieu, F. Lemeilleur, M. Tavlet, C. Leroy, P. Roy," New irradiation zones at the CERN-PS " - ROSE Collaboration. In: Nucl. Instrum. Methods Phys. Res., A : 426 (1999) no.1, pp.72-77

[11] The DBA amplifier are developed by Peter Moritz in GSI (Germany) **email**: p.moritz@gsi.de

REAL-TIME TUNE MEASUREMENTS ON THE CERN ANTIPROTON DECELERATOR

M.E. Angoletta, M. Ludwig, N. Madsen, O. Marqversen[#] and F. Pedersen,
CERN, Geneva, Switzerland

Abstract

A novel system for real-time tune measurement during deceleration of a low-intensity particle beam is presented. The CERN Antiproton Decelerator decelerates low intensity (2 x 10^7) antiproton beams from 3.5 GeV/c to 100 MeV/c. Because of the eddy-currents in the magnets, a tune-measurement during a pause in the deceleration would not be representative. One must thus be able to measure the tune in real time during the deceleration. The low intensity of the antiproton beam prevents the use of standard Schottky techniques, and swept Beam Transfer Function (BTF) measurements are too slow. A system was therefore developed which uses an M-shaped power spectrum, exciting the beam in a band around the expected frequency of a betatron side-band. Excitation at the betatron frequency, where beam response is highest, is thus minimized and measurements of BTF, and therefore the tune, can be made with much reduced emittance blow-up.

1 INTRODUCTION

The CERN Antiproton Decelerator (AD) decelerates low intensity (15 µA to 0.2 µA) antiproton beams from 3.5 GeV/c to 100 MeV/c. The low intensity in the AD results in very weak transverse Schottky signals from 0.5 pA/√Hz at 3.5 GeV/c down to 0.025 pA/√Hz for an uncooled beam at 100 MeV/c measured around 5.6 MHz (The resonance frequency of the pick-up (PU)). The Schottky signals are not large enough to measure the tune, so it is therefore necessary to use BTF-measurements. To measure the AD tune during deceleration without pausing (due to eddy-currents in the magnets, a paused measurement will not be representative) we needed a technique faster than a swept BTF (although swept BTF on plateaux has been used during the start up phase). A system was therefore developed which uses an M-shaped power spectrum, exciting the beam in a band around the expected frequency of a betatron side-band.

2 THE TUNE MEASURING SYSTEM

The system, see Figure 1, consists of the Schottky system, which measures the beam response, and the M-shaping filters that generate the stimulation. The Schottky system consists of a resonant PU and an ultra- low-noise pre-amplifier followed by a level adaptation system (to lift the signal over the quantization noise of the digital system). The amplified signal enters a Digital Receiver Board (DRX) after being analog to digital converted, where the data are hardware pre-processed in up to 8 Digital Down Converters (DDC). By this digital translation (down-mixing) the frequency window of interest is from DC and upwards. This will enable a Digital Signal Processor (DSP) perform the processing i.e. find the BTF. This is then passed on to the control system. The control system sets up the wanted analysis including the hardware control. The stimulation centre frequency is set as a factor n±q of the revolution frequency, where n is

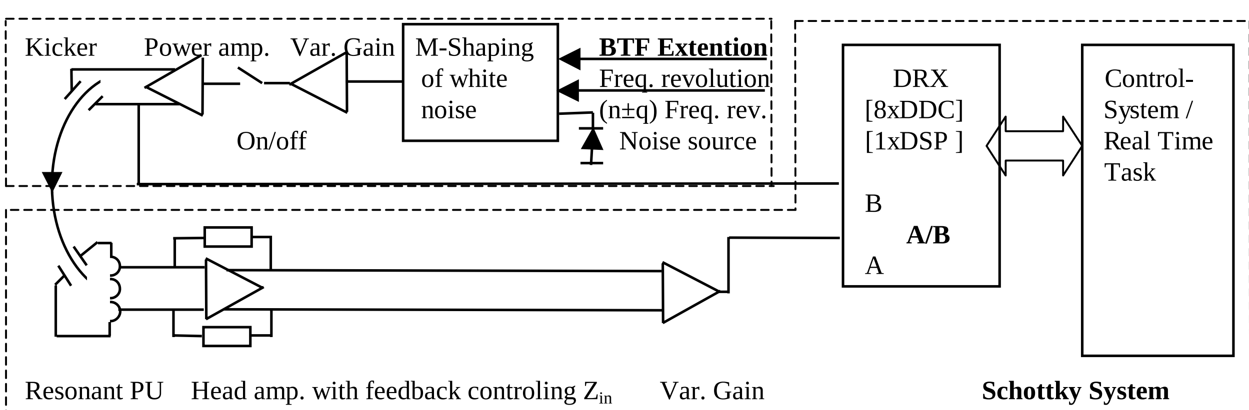

Figure 1: System block diagram.

the harmonic number chosen such that the frequency lies in the resonant range of the PU and q is the fractional part of the tune. The stimulation thus follows the expected betatron frequency during deceleration.

2.1 The Pick-up System

In order to avoid overlap of adjacent betatron side-bands at low momentum, the 1m long electrostatic PU is resonant at 5.6 MHz. The pre-amplifier has been designed so that, in a band around the resonance frequency, the Johnson noise from the losses in the coil is the dominant noise source of the system. To achieve the highest possible Q (low losses) of the resonant circuit, the PU has been designed with the coil inside the vacuum chamber. The total system noise density achieved is 0.9 pA/√Hz.

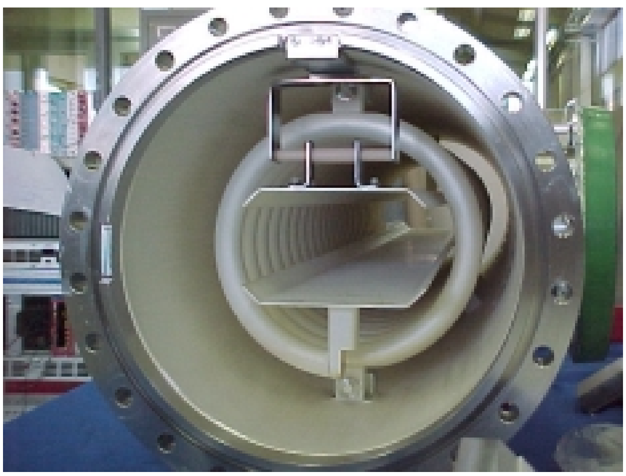

Figure 2: The resonant PU

The high Q resonant circuit is detuned by a feedback around the pre-amplifier, making the input impedance appear like a 350 Ω resistor working at a temperature of less then 13 K. Detuning the resonant circuit makes the PU broad-banded enough to always have a betatron sideband in the low noise part of the response from 5.3 MHz to 6.2 MHz. The details of the feedback and noise calculation can be found in ref. [1], describing the longitudinal Schottky system with which this system was developed in parallel.

Since the coil ends are fixed to the PU plates at opposite ends, a relatively big signal compared to the Schottky signal (max. of a few mV for the AD intensity) is generated at the beam revolution frequency. This is due to the beam time of flight through the PU. Therefore a high dynamic range of the system is needed.

2.2 The BTF Stimulation

A betatron sideband is like a parallel LCR-resonant circuit, in the way that it is most sensitive to stimulation at the exact resonant frequency and that it will make a 180° phase shift when passing through the resonance. To see the whole of the response the stimulation has to be increased more and more as one moves away from resonance. The blow-up of the beam emittance is given mainly by the stimulation power at the beam resonance frequency [1]. The blow-up rate is given by:

$$\frac{d\varepsilon}{dt} = \frac{\beta_0 \omega_0^2}{4\pi} \left(\frac{eL}{2md(\beta c)^2} \right)^2 \frac{S_p(f_n)}{2\pi} \qquad (1)$$

Here β_0 is the beta function at the kicker, ω_0 the angular revolution frequency, L the length of the kicker, d the distance between the kicker plates, m the particle mass, βc particle speed and $S_p(f_n)$ the power density at the betatron frequency.

Table 1: The expected blow-up rates for the AD, with β_0 =7.55 m, L=1 m and d = 0.15 m.

Momentum [GeV/c]	$S_p(f_n)$ [V^2/Hz]	$S_p(f_n)$ [dBm]	β	ω_0 [rad/s]	dε/dt [μm/sec]
2.0	$5x10^{-4}$	-20	0.905	$9.35x10^6$	0.08
0.1	$5x10^{-6}$	-40	0.106	$1.09x10^6$	0.06

Table 2: The measured blow up in the AD due to a 50 kHz wide M-shaped (6 dB depth) noise of density S_p.

Momentum [GeV/c]	$S_p(f_n)$ [V^2/Hz]	$S_p(f_n)$ [dBm]	β	ω_0 [rad/s]	dε/dt [μm/sec]
2.0	$5x10^{-4}$	-20	0.905	$9.35x10^6$	0.14
2.0	$5x10^{-3}$	-16	0.905	$9.35x10^6$	0.30
2.0	$5x10^{-3}$	-10	0.905	$9.35x10^6$	0.82

Table 1 and 2 show respectively calculated and measured blow-up rates in the AD. The measured blow-up at 2 GeV/c agrees within a factor 2 the calculated value.

Using an M-shaped power spectral density gives a blow-up corresponding to the power in the centre of the M, while it still gives a good beam response over a broad spectrum. See Figure 3.

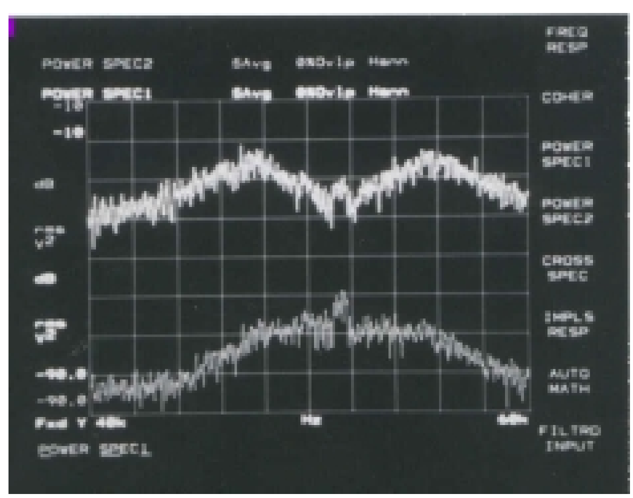

Figure 3: An M-shaped power spectrum (upper trace) and the corresponding flat beam response.

Dividing these two complex spectra gives the BFT, shown in Figure 4. From this, the resonant frequency is found and the tune is calculated.

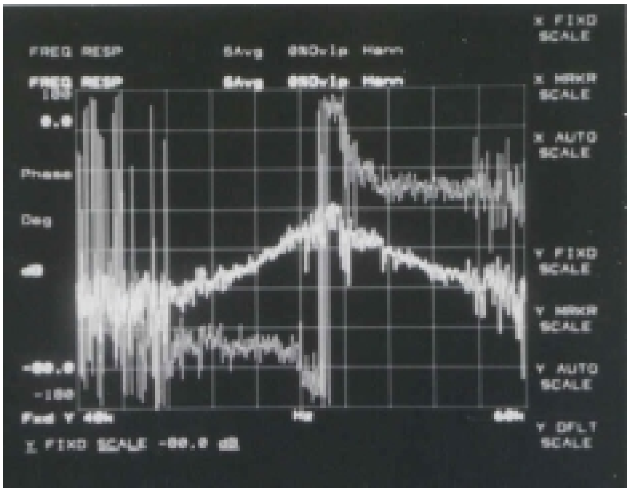

Figure 4: The BTF magnitude (centre trace) and phase.

The frequency range in which the measurement is valid is seen from the noise levels of the signals on the magnitude and phase plots in figure 4. A correlation calculation performed in the DSP will extract this as well:

$$\gamma^2 = \frac{G_{xy} \cdot G_{xy}^*}{G_{xx} \cdot G_{yy}} \qquad (2)$$

$G_{xy} = F_y \cdot F_x^*$ is the cross spectrum, F_x is the stimuli frequency spectrum and F_y the beam response spectrum, * marks the complex conjugate, G_{xx} is the stimuli power spectrum and G_{yy} the beam response power spectrum.

If there is a good correlation in the measurement, the correlation coefficient γ will be 1, if not it will be 0 se Figure 5. The usable frequency range can be changed by changing the M-width and keeping the power level constant at the centre. The data processing to be implemented is in preparation [3].

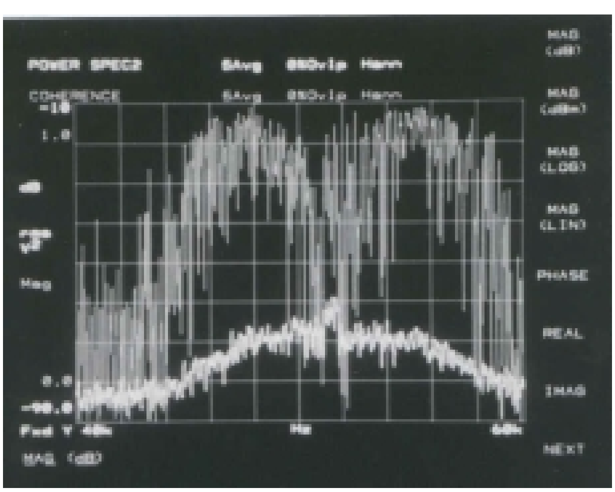

Figure 5: Top curve is the calculated γ i.e. correlation.

The measurements in Figure 3, 4 and 5 were done, as a proof of principle using analog down-mixing and a commercial FFT analyser at 2 GeV/c with 2×10^7 antiprotons, an M-width of 10 kHz with a power spectral density of -30dBm at the M-centre. Each spectrum is an average of 5 beam stimulations of 40 ms. The ramp of the M is 6 dB/octave from the shoulder frequency of 5 kHz and down towards the centre to at depth of -24 dB. The small spike in the centre (Fig. 3 upper trace) is due to an imperfection in the prototype M-shaping circuit. The duration of each measurement was given by the FFT analyser frequency resolution. As can be seen from formula (1) the blow-up rate that is a product of the stimulation is proportional to the power given to the beam; thus if less frequency resolution is needed, one can stimulate in a shorter time, with more power, to get the same beam response. It is essential to be fast when measuring during deceleration, since the duration of the measurement defines the time resolution on the q value.

2.2.1 The M-shaping

The M-shaping is made using switched capacitor filters [4] in order to make the M-width a fixed fraction of the revolution frequency that changes during deceleration. The cut-off frequencies are made 1/20 of the filter control frequency, and additionally a divider is introduced in order to get smaller fractions of the revolution frequency when needed.

White noise is filtered by a low-pass filter and by a band-pass filter (2^{nd} order giving the 6 dB/octave on the inner ramp of the M). The two parts are then added with a switchable gain for the low-pass filtered signal to determine the depth of the M. The shaped noise is then mixed up to the expected betatron frequency, where the positive and negative image makes up the M.

During set-up of the accelerator the M will be kept wide to allow measuring tunes deviating a lot from those expected. When the accelerator has been set up, the tunes will correspond to the expected ones and the system can monitor the tune without causing significant beam blow-up.

3 SYSTEM STATUS

The Schottky part of the tune measurement system is ready, but the S/N is too poor to measure the tune. The BTF analysis is expected integrated in the system during the summer of 2001.

REFERENCES

[1] C.Gonzalez and F.Pedersen, PAC'99, New York, USA, March 1999.
[2] V.A.Lebedev, in Proc. Accelerator Physics at the Superconducting Super Collider, Dallas (AIP Conf. Proc. 326), 396 (1995)
[3] M.E.Angoletta, Private communication
[4] Linear Technology, Datasheet for LTC1068.

BENCH TEST OF A RESIDUAL GAS IONIZATION PROFILE MONITOR (RGIPM)[1].

W. C. Sellyey, J. D. Gilpatrick, LANL, Los Alamos NM, USA
Ralph Senior, General Atomics, San Diego CA, USA

Abstract

An RGIPM has been designed[1], constructed and bench tested to verify that all components are functioning properly and that the desired resolution of about 50 μm rms can be achieved. This paper will describe some system details and it will compare observed results to detailed numerical calculations of expected detector response.

1 BEAMLINE COMPONENTS

Figure 1 shows a top view horizontal cross section of the primary beam line components. It is set up to measure a vertical beam profile. The magnet (1) is a split H configuration with a gap of 24.6 cm. The coils (2) can produce a 0.12 T field at the center of the magnet. The electrostatic vacuum box (3) contains an 8 mm thick high voltage (HV) plate (4) 39 by 38 cm. One cm above the plate (towards the bottom of the page) is a set of 100 μm gold coated wires (not seen) running across the page. These are separated by 30 mm. High voltage feedthrough (5) is used to supply up to -15 kV to the plate and (6) supplies voltage to the grid wires. The vacuum box is at ground potential. Not seen is a 100 μW Krypton light and collimator on the top of the box. It shines a 5° wide beam on the wires near the center of the box. Its spectrum consists of 20% 10.64 eV photons and 80% 10.03 eV photons. On the left and right side of the box are flanges (not shown) to connect to 10 cm diameter beam tubes.

A removable "hat" (7) contains a mechanism that moves a scintillation detector (8) across the wires (in and out of the page). A quartz fibre (9) carries scintillation photons through an optical vacuum feedthrough (10). A motion feed through under the hat (not visible) connects the moving mechanism to a worm gear driven by a stepper motor. The worm gear shaft was rigidly connected to an LVDT.

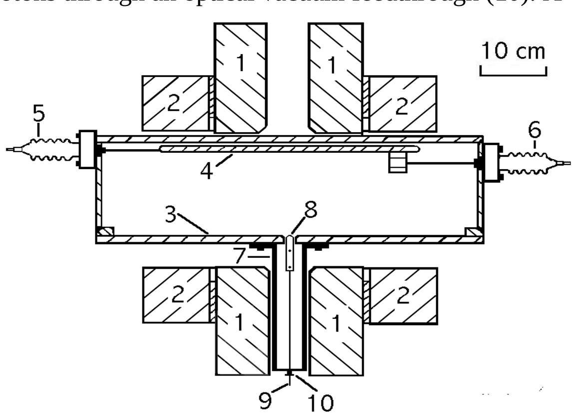

Figure 1. Major Beam Line Components

Some details of the scintillation detector are shown in figure 2. The limiting aperture (1) was a 125 μm hole in a 1 mm thick Aluminum piece. The electrons that pass through this hit a 0.5 mm thick, 2X2 mm square scintillator (2). A 500 μm gold coated quartz optical fibre (3) caries some of the resulting photons to a photomultiplier (PM) tube outside the vacuum. The detector moves in a 1.8 cm by 10 cm slot in the top of the vacuum box. The total distance from the HV plate to the scintillator is 14 cm.

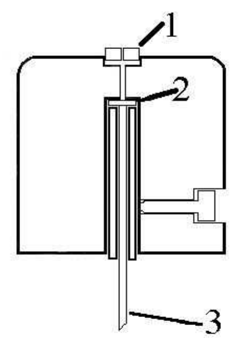

Figure 2. Scintillation Detector

2 DATA ACQUISITION SYSTEM

The single photon PM output pulses are amplified, shaped and sent as TTL pulses to a counter/timer on a National Instruments (NI) PCI-MIO-16XE-10 board. This board is installed in a Micron PC. A/D's and D/A's on the NI board are used for controlling and measuring most voltages and currents in the system.

High voltages are generated by analogue control of Glassman MJ series power supplies. A high precision resistive high voltage divider system is used to produce a stable ratio of voltages to the plate and grid. The exact ratio of the grid to plate voltage is fine tuned by a manually controlled potentiometer.

The stepper motor is controlled by a set of output bits on the NI board. The LVDT electronics is interfaced to the PC by a serial port. Software closes the loop between the stepper motor and the LVDT. The detector position is reproducible to about 3 μm on a short term basis (hours

[1] This work supported by U.S. Department of Energy.

and a few degrees C temperature change). All control and display software is written in LabVIEW.

3 DATA

Photoelectrons are guided to the detector by the parallel electric and magnetic fields. The detector is scanned across this distribution and this results in a count rate distribution that is a convolution of the detector aperture and the electron distribution. Figure 3 shows a typical scan with a magnetic field of 0.12 T, a plate high voltage of 9 kV and grid potentiometer setting of 50 kΩ. The figure shows two sets of data. One is the actual scan and the second is background correction data. The background correction data was taken by moving the detector back to the starting position of the scan after every third data point. Data set acquisition time was typically several hours.

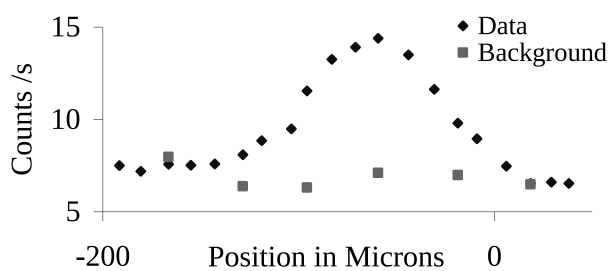

Figure 3. A Profile. B field =0.1 T, E field =64.5k V/m, grid potentiometer=50 k.

Figure 4 shows all the (scaled) background corrected measured areas for scans taken at a 0.12 T magnetic field, 9 kV plate voltage while varying the grid potentiometer. The potentiometer rate of change is 12.85 divisions per volt. The actual grid voltage is to be defined below and is initially treated as unknown.

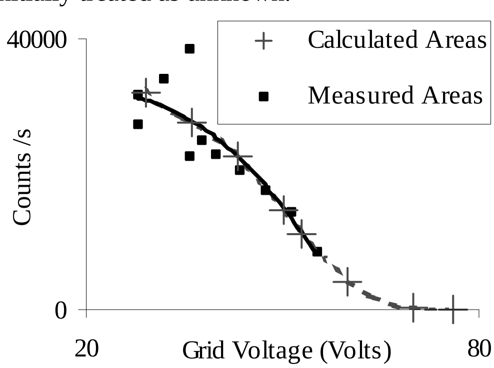

Figure 4. Grid Voltage Results.

4 THEORY

Software was written to describe the process that the photoelectrons go through from the time they absorb the energy of a photon, to when they arrive at the GSO scintillator. The first part of the program traces the electrons in the gold of the 100 μm wire and is Monte Carlo based[2]. The photons arrive at the wire with random positions across (up and down the page in figure 1) the wire. The photon penetration depth was calculated as -30.3ln(x) Å where x is a random number between 0 and 1. A single electron in the Fermi sea absorbs the full energy of the photon and moves off in a random direction determined by three random direction cosines and the restriction that it started out in the Fermi sea. The bottom of the Fermi well is taken at 8.22 eV, and the depth of the Fermi distribution is 3.4 eV. The density of states of the electrons is assumed to vary as $E^{1/2}$. The electron moves through the metal, loosing energy through collisions with other electrons and phonons. The energy loss process due to phonon collisions is taken to be the same as that experienced by electrons at the top of the Fermi distribution during the electrical conduction process[3]. This is characterised by a relaxation length l=410 Å and the electron velocity decays as exp(-x/l) where x is the distance the electron travelled.

The average separation of the conduction electrons is 2.57 Å. Thus the moving electron is always interacting with many electrons. To simulate this, the electron is taken as undergoing a collision every -2.57ln(x) Å, where x is a random number. The collision is treated as Rutherford scattering in the center of mass of the two electrons with two quantum mechanical restrictions. The first is that both of the electrons after the collision have to be above the Fermi level. The second sets a limit on the minimum size of the impact parameter[4] $b=\hbar/p$ where p is the initial momentum in the relative frame. The electron with the larger energy after the collision is taken as the scattered incoming electron. The electron is stepped through the gold until either its kinetic energy drops below the well potential depth value of 8.22 eV, or it reaches the surface with enough of a kinetic energy component perpendicular to the surface to escape.

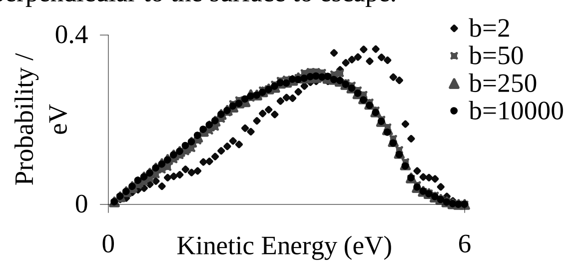

Figure 5. Energy Distribution as a Function of Impact Parameter b.

Figure 5 shows the energy distribution of electrons for different upper limits on the impact parameter in units of average electron separation. It can be seen that at 50 and above, the value of the maximum impact parameter does not matter. Most calculations were done using a maximum impact parameter of 250.

Once an electron leaves the metal, its motion is determined by the uniform magnetic field, and an initially rapidly changing electric field. The path of the electrons is traced to the detector using F=ma in 0.1 ps steps.

The electric field can be well approximated by considering it as being made up of two independent components. The first component is calculated by considering the wire as being in a uniform electric field perpendicular to its axis. The uniform field is calculated by dividing the plate voltage by the plate to detector distance. The second component is obtained by considering the cylindrical wire with an applied voltage 1 cm above the grounded (infinite) plate. If the wires were not present, the electrons would see a linear voltage change as they moved through the plate to the detector gap. If now the wires are introduced at 1 cm from the plate, and their potential is adjusted so that it is the same as the potential that existed at their location before they were introduced, the electric field near the wires will be described by only the first term. The second term is determined by the deviation from this potential and results in a field outside the wire described by two line charges: one located at the center of the wire and an equal and opposite sign charge one cm inside the plate. This potential deviation will be referred to as the grid voltage. In principle, this can be calculated from the resistor values in the voltage divider and detailed knowledge of the geometry. However it more accurately measured as described below.

For every plate voltage there is a minimum positive grid voltage that stops all the electrons leaving the wire. This can be calculate numerically by requiring the highest kinetic energy electrons velocity drop to zero at the same location the electric field becomes zero along a line perpendicular to the plate and passing through the wire center. For a 9 kV plate voltage this is 77.9 V and the stopping point is 200 μm from the wire centrer.

Another way to do this is to use the program described above to calculate the number of electrons that reach the detector for 10^7 photoelectrons. This is shown in figure 3 along with a 6th order fit. A 2nd order fit to the scaled measured count rates for various grid voltages is also shown. When these were first plotted on the graph, they did not coincide with the calculated numbers. To obtain the relation between grid voltage and potentiometer setting the experimental count rate line is scaled vertically (this is the same as changing the UV light intensity) and displaced horizontally until it overlaps the calculated curve. This process produces a grid voltage for every measurement on the graph.

5 DATA ANALYSIS

The position distribution obtained with the software described above was convolved with the expected shape of the collimator in front of the GSO scintillator. The obvious initial choice for this shape is a d=125 μm radius circle. However this does not produce acceptable results.

The construction of the moving mechanism is such that it could readily be tilted in the direction of motion. This is simulated by two overlapping circles with their centers displaced with respect to each other. The aperture is the overlapping part of the circles. Shown in figure 6 is the data of figure 3 and fitted to it is a (normalised) convolution of this type for a grid voltage of 36 V with the centers displaced by 0.9d in the direction parallel to the detector motion. The fit parameter χ^2=.0.2. Also shown is an additional set of data taken at the same grid voltage with a fitted convolution using a displacement of 0.4d (χ^2=.0.7). The area under this second set of data with circle separation of .4d should be much larger than for .9d. At this time this is an unexplained discrepancy.

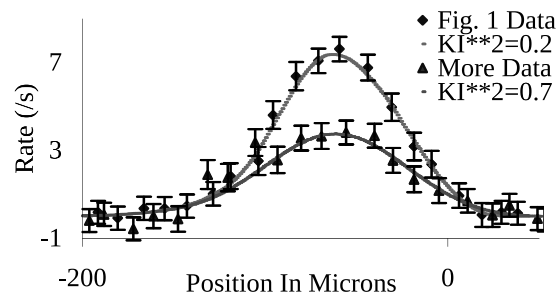

Figure 6. Fit To Two Profiles.

The statistical errors in the count rates are typically about 0.1 count per second. A straight line fit to the background data of figure 3 results in average deviations from the line of 0.5/s. This was added in quadrature for all data and is presumably due to things like photomultiplier dark current, electronic drift, and cosmic radiation. The detector assembly is guided by two linear bearings on two parallel shafts. The assembly is attached to the linear drive mechanism at a point midway between these bearings and 2.5 cm from the scintillator. The bearings are lose enough so the assembly can wobble in the direction of motion. This results in two correlated errors. The first is caused by a change in the separation in the overlapping circles. The other happens only on the leading and trailing edge of a profile. As the detector assembly pivots around the point where it is attached to the drive, the scintillator moves at the end of a 2.5 cm arm. This will case a count rate variation that adds to the first on one side of a profile, and subtracts on the other side. It was assumed that addition occurs on the leading edge because most of the data shows more scatter here. An rms wobble of .01° was assumed for the analysis in figure 6.

All profile measurements done with B=0.12 T, E=64.5 kV/m resulted in rms resolutions of between 27 and 44 μm

REFERENCES

[1] W C. Sellyey, J. D. Gilpatrick, “A Compact Residual Gas Ionization Profile Monitor System”, Proceedings of the 1999 PAC, 2152.

[2] M. Kotera, Y. Kamiya, “Computer Simulation of Light by High Energy Electrons in YAG Single Crystals”, Ultramicroscopy, 54 (1994) 293.

[3] M. A. Omar, “Elementary Solid State Physics: Principles And Applications”, Addison-Wesley, 1975, 157.

[4] J. D. Jackson, “Classical Electrodynamics”, John Wiley & Sons, 1963, 440.

OPTICAL BUNCH-BY-BUNCH BEAM DIAGNOSTIC SYSTEM IN KEK-PF

T. Kasuga, A. Mochihashi, T. Obina, Y. Tanimoto
High Energy Accelerator Research Organization (KEK), Japan

Abstract

An optical bunch-by-bunch beam diagnostic system, which can detect oscillations of individual bunches in a multi-bunch operation, has been developed. The system is composed of a high-speed light shutter and an optical beam-oscillation detector. The shutter that consists of a pockels cell and polarizers can be opened or closed in a bunch spacing time (2ns in KEK-PF) and it can select a light pulse corresponding to a certain bunch in a bunch train. The beam oscillation detector can detect oscillations of the picked-out bunch with a spectral analysis method. The diagnostic system has been installed in KEK-PF Beamline-21, and observed vertical oscillation of individual bunches due to an instability in the multi-bunch operation.

1 INTRODUCTION

An analog switch method is usually adopted for a bunch-by-bunch beam diagnostic system. In the method, a pulse corresponding to a certain bunch in a pulse train from a beam monitor (a button type electrode is usually chosen) is selected by a fast electronic switch [1]. A bunch-by-bunch and turn-by-turn beam diagnostics with a digital memory system has also been developed [2]. However, ringing that commonly occurs in a fast electronics degraded the detection capability. Moreover, the electronic detection has an unavoidable problem that the BPMs detect not only the beam signal but also wake fields. To avoid these problems, we have adopted an optical beam detection method and developed an optical switch called a "high-speed light shutter"[3]. One of its merits is that the optical system is free from harmful effect caused by ringing, and has an excellent tolerance to electronic noise. Moreover, it is the most important strong point that the system is not affected by wake fields propagating in vacuum ducts. We have developed an optical bunch-by-bunch beam diagnostic system with the shutter, and have been observing vertical oscillation of individual bunches due to an instability in a multi-bunch operation in KEK-PF with the system.

2 OPTICAL BEAM DIAGNOSTIC SYSTEM

2.1 High-Speed Light Shutter

Basically, the shutter system is composed of a pair of polarization filters and a pockels cell [3]. The pockels cell (Fast-pulse Technology, 1044-FW) is placed between the polarization filters whose polarization angles are perpendicular to each other. The incident light can pass through the shutter while a high voltage pulse is applied to the cell because the cell rotates the polarization plane. Since the time response of the cell is fast enough, the operation speed of the shutter is mainly determined by the rise and fall time of the pulser. We have used the pulser whose output pulse has a width (FWHM) of 1.7 ns, which is shorter than the bunch spacing of 2 ns, and a height of 550 V. We operate the shutter with a repetition rate of $f_{shutter}$= 534 kHz which is one third of a revolution frequency (f_{rev}=1.60 MHz in the KEK-PF) because of the limitation of the repetition rate of the high voltage pulser (max. 600 kHz) and a reason described below.

2.2 Operation of High Speed Light Shutter

In order to observe the time structure of the shutter we made use of a photon counting method [4] and used a CW-laser (Spectra Physics, $\lambda = 488$ nm) as a light source. A block diagram of the shutter, including the optical setup, is shown in Fig. 1. To improve the polarization of the incident light on the cell we used a couple of polarizers. A signal generator generates a signal with a frequency equal to the RF acceleration frequency (f_{RF}=500 MHz in the KEK-PF). A divider generates a signal with a repetition frequency of $f_{rev}/3$. We used the divided signal as a trigger for the high voltage pulser. To eliminate electronic noise caused by the high voltage pulse, we carefully shielded the whole of the cell and cables that feed the pulse to the cell.

The light from the shutter passes through a pair of lenses. To eliminate stray light due to multiple scattering between optical devices, an iris diaphragm is set at the focal position of the first lens of the pair. The light from the lenses is attenuated by a neutral density filter (ND filter) and a slit, and detected by a microchannel-plate type photomultiplier (MCP-PMT, Hamamatsu Photonics, R3809U-52), which has an excellent time resolution (rise time of 0.15 ns, transit time spread of 25 ps). The output signal of the MCP-PMT is processed by a constant fraction discriminator (CFD, TENNELEC, TC454) to generate the start signal of the time-to-amplitude converter (TAC, ORTEC 467). On the other hand, a signal synchronized with the trigger for the pulser is used as a stop signal for the TAC. The output signals of the TAC are amplified and analyzed with a multichannel analyzer (MCA, Laboratory Equipment). An extinction ratio, which is defined as the ratio of intensity of singled-out light by the shutter to that of the leaked one, sensitively depends on a direction of an axis of the cell. Therefore, it is important to align the axis of the cell precisely with the direction of the light to operate the shutter system properly. To adjust the angle of the cell minutely we mounted the cell on a triaxial goniometer and adjusted within $\sim 0.5°$ for all the directions.

The time structure of the shutter is shown in Fig. 2. The ordinate and the abscissa in the figure correspond to the counting rate of the photons and the time, respectively. FWHM of 1.0 ns and the extinction ratio of 800 are obtained. Because the bunch spacing of the KEK-PF is 2 ns, it is possible to single out light from one particular bunch in the multi-bunch operation with the shutter system.

We installed the shutter system in Beamline 21 (BL-21) in the KEK-PF and tried to pick out a light pulse from a certain bunch in the the multi-bunch operation. For the observation we used visible light component of SR from a bending section. In the experiment we used the RF signal of the KEK-PF as a signal source of the shutter system instead of the signal generator in Fig. 1. Figure 3 shows the time structure of the light passing through the shutter measured by the photon counting method. The three peaks in the figure show the count rates of the photons from 3 successive bunches. The count rate of the central peak, which corresponds to the picked-out bunch, is about 300 times as large as those of the others although the electron number in each bunch is almost equal; that is, the shutter system which has the extinction ratio of 300 is obtained. The ratio is about one third as compared to the experiment with CW-laser. One of the reasons is that the rotation of the polarization in the cell depends on the wavelength of the incident light; therefore, it is difficult to single out the SR as clearly as monochromatic light, like laser light, because the SR has a wide wavelength range. The other is that SR propagating in a direction with a certain angle from the median plane has elliptic poralization component and the polarizers cannot eliminate the elliptic polarization component completely.

2.3 Detection of Beam Oscillation of Individual Bunches

In order to detect vertical betatron oscillation of individual bunches in the bunch train, we have developed an optical betatron oscillation detection system which is composed of the high-speed light shutter and an optical betatron oscillation detector. A lens system is set behind the shutter and an image of the beam is put on a horizontal edge [5]. Because half of the image is cut off by the edge, the intensity of the light through the edge varies in response to the vertical motion of the beam. We used a photomultiplier tube (PMT, Hamamatsu Photonics, H2431-50) to measure the intensity. The change in amplitude of the signal selected by the shutter is analyzed with a spectrum analyzer (ADVANTEST, R3361D). Figure 4 shows a photograph of the beam diagnostic system in the beamline.

Because 280 in the 312 RF-buckets are filled in the multi-bunch operation in the KEK-PF, the contribution of leaked light pulses through the shutter during the closing time is not negligible even though the light shutter has the extinction ratio of 300. The spectral lines corresponding to the betatron oscillations of all bunches appear as side-

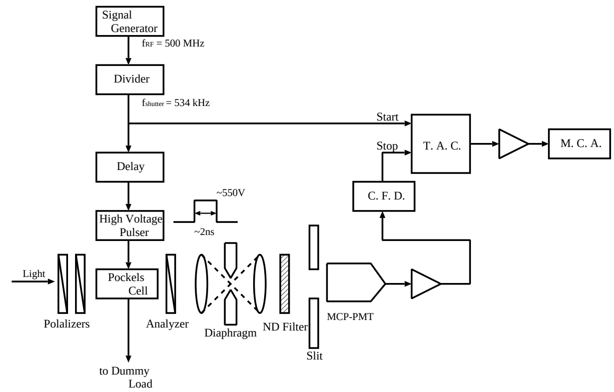

Figure 1: Block diagram, including the optical setup, of the high-speed light shutter.

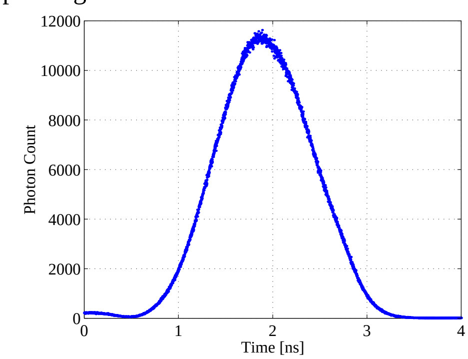

Figure 2: Time structure of the singled-out light pulse from the CW-laser.

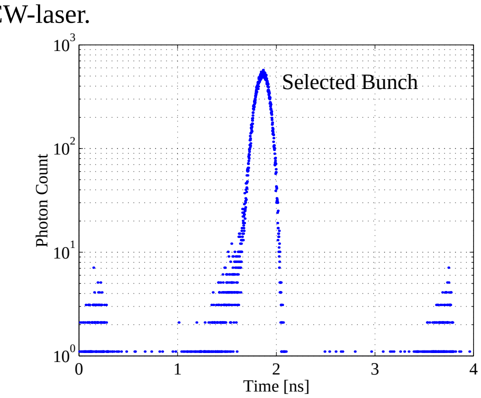

Figure 3: Time structure of the transmitted light. The SR of BL-21 in the KEK-PF at the multi-bunch mode was used as the light source.

bands of the harmonics of the revolution frequency. Meanwhile, those corresponding to the singled-out bunch appear on both sides of the harmonics of the shutter frequency. Therefore, we can distinguish the betatron oscillation of the selected bunch from the contributions of the other bunches by detecting the betatron sidebands (f_{obs}) of the spectral lines that are not harmonics of the revolution frequency (f_{rev}) but of the shutter frequency ($f_{shutter} = \frac{1}{3} f_{rev}$), i.e.,

$$f_{obs} = \frac{n}{3} f_{rev} \pm q f_{rev} \qquad \left(\frac{n}{3} \neq \text{integer} \right), \qquad (1)$$

where q is the decimal part of the vertical tune (0.29).

We have tried to observe a vertical instability observed in the multi-bunch condition in the KEK-PF with the system and the spectral method, and measured vertical tunes of individual bunches. The result shows that the vertical tunes depend on a position of bunches in a bunch train, and we were able to show that the phenomenon is caused by a modulation of ion density due to periodic passage of the bunch train. Detailed discussions are referred in Ref. [5].

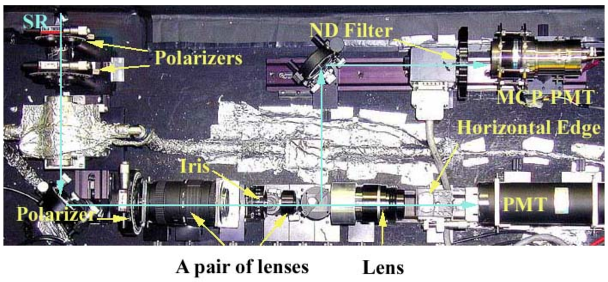

Figure 4: Photograph of the beam diagnostic system, including the high-speed light shutter, the photon counting system and the beam oscillation detection system.

3 SUMMARY AND DISCUSSION

We have developed an optical bunch-by-bunch beam diagnostic system which can detect betatron tunes of individual bunches in a multi-bunch condition in KEK-PF. We have adopted an optical method with an optical analog switch called “high-speed light shutter”. The diagnostic system composed of the light shutter and an optical beam-oscillation detector can distinguish betatron oscillation of a selected bunch from contribution of the other bunches by a spectral method.

We can indicate some remarkable merits of the diagnostic system;

- A ringing, that usually occurs in electronic detection with button electrodes and causes a bad effect that each bunch-signal is affected by preceding bunches, does not occur in the optical system.
- It detects the beam signal only, in contrast to a button type electrode that detect not only the beam signal but also wake fields.
- It can be used for visible light, which can treat easily and safely in the atmosphere.
- In relation to above, most of optical devices that compose the system are not special-ordered but commercial ones.

The system also has a demerit; because we use an edge to detect the oscillation of the light in the diagnostic system, it is difficult to measure oscillation amplitude of the beam when that the amplitude is larger than a spot size on the edge. Now we plan to develop a new detection system using a fast-response position sensitive detector which has a good time response and good spatial resolution.

We built the detector on a beamline for a photon counting system that requires merely weak light; therefore, the intensity of light provided by the beamline was insufficient for the beam diagnostics in our present experiment and the S/N ratio of the measurement was unsatisfactory. We have improved the beamline to increase photon flux in the March 2001 and some adjustments for the beamline are now under way.

4 ACKNOWLEDGMENTS

One of the authors (A.M) thanks to Research Fellowships of the Japan Society for the Promotion of Science for Young Scientists for its financial support.

5 REFERENCES

[1] A. Mochihashi et al., “Observation of Transverse Instability Using Bunch- by-Bunch Beam Diagnostic System in KEK-PF”, EPAC 2000, Vienna, Austria, June 2000.

[2] M. Tobiyama and E. Kikutani, “Development of A High-Speed Digital Signal Process System for Bunch-by-Bunch Feedback Systems”, PR-ST AB **3**, 012801 (2000).

[3] A. Mochihashi et al., “Bunch by Bunch Beam Diagnostics Using A Fast Light Shutter”, APAC'98, KEK, Tsukuba, Japan, March 1998.

[4] T. Obina, T. Kasuga, M. Tobiyama, T. Katsura, K. Tamura, “Measurement of the Longitudinal Bunch Structure in the Photon Factory Positron Storage Ring with a Photon Counting Method”,
Nucl. Instr. and Meth. A **354**, 204 (1995).

[5] A. Mochihashi et al., “Vertical Instability with Transient Characteristics in KEK-Photon Factory Electron Storage Ring”, PR-ST AB **4** , 022802 (2001).

DESIGN OF A MAGNETIC QUADRUPOLE PICK-UP FOR THE CERN PS

A. Jansson, L. Søby and D.J. Williams, CERN, Geneva, Switzerland

Abstract

A quadrupole pick-up is sensitive to the quantity $\sigma_x^2 - \sigma_y^2$, where σ_x and σ_y are the horizontal and vertical r.m.s. beam sizes. Since it is a non-invasive device, it is potentially very useful for matching and emittance measurements. A magnetic quadrupole pick-up has been developed for the CERN PS. By coupling to the radial component of the magnetic field around the beam, it was possible to eliminate the common-mode problem, which is usually a limiting factor in the use of quadrupole pick-ups. This paper presents the final pick-up design, which is the result of a series of simulations and test prototypes. The performance of the pick-up and its associated electronics is discussed. Preliminary results from the two pick-ups recently installed in the PS machine are also presented.

1 INTRODUCTION

A quadrupole pick-up measures the quadrupole moment of the transverse beam distribution

$$\kappa = \sigma_x^2 - \sigma_y^2 + \bar{x}^2 - \bar{y}^2, \tag{1}$$

by probing the quadrupole component of the field that the beam induces inside the vacuum chamber. Here, σ_x and σ_y are the r.m.s. beam dimensions in the x and y directions, while $\bar{x}$ and $\bar{y}$ denote the beam position.

An electrostatic pick-up measures the charge collected on electrodes around the beam. The charge is proportional to the electric field in the radial direction, which in polar coordinates (r, θ) is

$$E_r \propto \frac{i_b}{r}\left(1 + 2\left[\frac{\bar{x}}{r}\cos\theta + \frac{\bar{y}}{r}\sin\theta + \frac{\kappa}{r^2}\cos 2\theta + \dots\right]\right) \tag{2}$$

if the pick-up is round. Here, i_b is the beam current. To measure the κ component, four electrodes at $0°$, $90°$, $180°$ and $270°$ are used. A problem with this setup is that the κ component is a very small part of the signal on each electrode, which requires extremely good common-mode rejection and a large dynamic range in the electronics. To bypass this problem, a new design was proposed [1], where the radial magnetic field is measured instead. If the conducting boundary is at r_0, this field is

$$B_r \propto \frac{i_b}{r}\left[\left(\frac{\bar{x}}{r}\sin\theta - \frac{\bar{y}}{r}\cos\theta\right)\left(1 - \frac{r^2}{r_0^2}\right) + \right.$$
$$\left. + \frac{\kappa}{r^2}\sin 2\theta\left(1 - \frac{r^4}{r_0^4}\right) + \dots\right] \tag{3}$$

where there is no constant term causing a common-mode signal. For such a pick-up, four antenna loops at $45°$, $135°$, $225°$ and $315°$ are needed to measure the quadrupole field component (see Fig. 1). A prototype tested in the machine produced encouraging results [2]. Based on the prototype experience, laboratory tests and simulations, a final design has been produced [3].

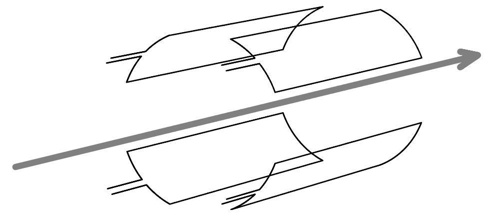

Figure 1: Schematic quadrupole pick-up measuring radial magnetic field. The arrow symbolises the beam.

2 PICK-UP DESIGN

2.1 Bandwidth and Transfer Impedances

The bunch spectrum at injection into the PS normally covers about 20 MHz, with the lowest interesting frequency component at about 75 kHz (betatron frequency). The pick-up was therefore built with a low-frequency cut-off at 75 kHz. On the high frequency end, the usefulness of the pick-up is limited by reduced common-mode rejection at frequencies above 25 MHz (due to standing waves in the loop). The transfer impedances of the pick-up have a flat frequency characteristic in the pass-band and are 35 $\mu\Omega$/mm^2 for the quadrupole signal and 1.5 mΩ/mm for the position signals. These values are for a single antenna loop.

The final pick-up has a length of 508 mm, and a (circular) aperture of 145 mm diameter.

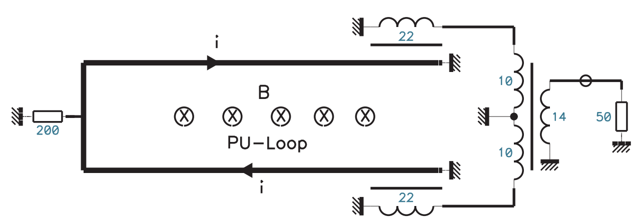

Figure 2: Schematic layout of one antenna loop

2.2 Common-Mode Rejection

Although theoretically a pick-up measuring the radial magnetic field has a perfect common-mode rejection, in practice the common-mode rejection is finite due to misalignments and parasitic couplings. Misalignments cause constant offsets of the measured signals, and can therefore relatively easily be calibrated away, if these offsets are known from reference measurements. Other parasitic couplings can, however, distort the measured bunch shape, and a lot of effort was therefore made to reduce them. The key issue was the design of the current read-out from the antenna loop. It had to be strictly symmetric to avoid path length differences for the signals. Also, the grounding of the loop had to be close to the read-out transformer, in order to avoid capacitive coupling across the transformer. The thickness of the rod forming the loop restricted the primary winding on the read-out transformer to one turn. Two transformers were therefore used, one on each side of the ground point. A third transformer was then used to combine the two signals. This arrangement, shown in Fig. 2 gave the best common-mode rejection.

2.3 Longitudinal Impedance

In order to obtain reasonable transfer impedances, the conducting boundary had to be moved away from the loops (see Eq. 3), forming a cavity-like structure. To reduce the longitudinal impedance of the pick-up, four metal vanes were introduced in the cavity. By placing these in the symmetry planes of the quadrupole field, they did not reduce the quadrupole transfer impedance of the pick-up. Several sharp peaks in the impedance spectrum due to standing waves in the antenna loops were removed using suitably chosen termination resistors. For high frequencies, an effective screening was produced by a thin resistive layer deposited on the ceramic vacuum tube, which effectively damped all cavity resonances. Therefore, the pick-up has an impedance Z/n of less than 80 mΩ in the entire spectrum.

3 ELECTRONIC SIGNAL TREATMENT

The analog signal chain is shown in Fig. 3. The outputs of the four loops are connected to the hybrid via 0.5 m semi-rigid cables. The output signals from the hybrid are

$$\Delta H = \frac{(A+D)-(B+C)}{2} \tag{4}$$

$$\Delta V = \frac{(A+B)-(C+D)}{2} \tag{5}$$

$$\Delta Q = \frac{(A+C)-(B+D)}{2} \tag{6}$$

so the transfer impedances for the combined signals after the hybrid are twice the transfer impedances for a single loop. The reason why the horizontal and vertical signals appear interchanged (with respect to a standard pick-up) can be understood by comparing Eqns. 2 and 3.

The amplifiers have four channels, each with two different gains: one standard gain for proton beams (peak currents up to 4 A) and a special high gain, low noise mode

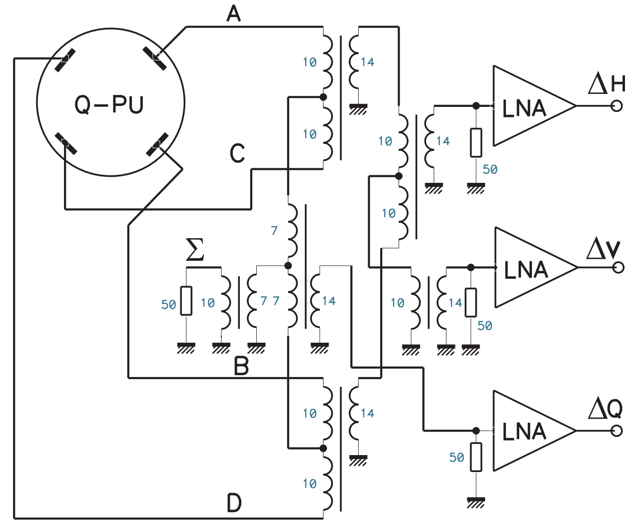

Figure 3: Analog signal chain.

intended for lead ions (peak currents as low as 20 mA). The performance with the high gain is summarised in Table 1.

Three channels are used for the pick-up signals, and the fourth for a reference signal from a nearby wall-current monitor. This is because the pick-up itself cannot measure the beam current, which is needed for normalisation. To make an in-situ measurement of the gain on different channels (including cable attenuation), an external calibration signal can be applied to the inputs. This enables the correction for aging of the electronics, due for example to radiation. After amplification, the combined signals are transmitted to the control room where they are digitised at 500 MS/s by oscilloscopes.

Table 1: Quadrupole PU performance for a 20mA beam.

Channel	ΔQ	ΔH & ΔV
Gain	65 dB	52 dB
Input noise	5.6 μV r.m.s.	5.6μV r.m.s.
Hybrid output	5.6 μV @ 40 mm^2	6 μV @ 0.1 mm

4 DIGITAL SIGNAL TREATMENT

The data is transferred from the scope to a PC via the GPIB interface, and the analysis is made in a LabView program. In order to resolve single bunches, the data is treated in the time domain. If it is assumed that the quadrupole pick-up and the wall current monitor have the same frequency response, the shape of the pulses is the same in all signals (for a given bunch passage). The problem therefore consists in determining the scaling factor between a pulse on the beam current signal and the corresponding pulse on the pick-up outputs.

First, any timing differences between signals are corrected for (this is presently done by digital re-sampling, but would be better done by adding short lengths of cable). Then, time slices of about one RF period (centred on the bunch passage) are selected. Each selected slice is an N-vector (consisting of N samples), and under the above assumption, corresponding slices are proportional to each other, apart from noise effects and a possible baseline difference. The scaling factor c for the quadrupole signal, for example, is found from the least squares solution of the equation

$$\begin{pmatrix} i_1 & 1 \\ i_2 & 1 \\ \vdots & \vdots \\ i_N & 1 \end{pmatrix} \cdot \begin{pmatrix} c \\ b \end{pmatrix} = \begin{pmatrix} q_1 \\ q_2 \\ \vdots \\ q_N \end{pmatrix}, \qquad (7)$$

and the quadrupole moment κ is then calculated from c, using the transfer impedances for the two signals. The same is done for the position signals. This treatment suppresses noise and parasitic signals, and also automatically corrects for amplifier offsets and drifts in the base-line due the lack of DC response.

Notice that differences in the frequency response of the two instruments can be corrected by filtering the signals, if these responses are known. For the moment, however, such sophisticated corrections have not been attempted.

When the position and quadrupole moment at each bunch passage have been calculated, the contribution of the beam position to the quadrupole moment is subtracted using Eq. 1.

5 MEASUREMENT SYSTEM

There are several frequency components in the signal (see Table 2. If these were well separated, they could be distinguished in the signal from a single pick-up using a Fourier transform. However, for the normal PS working points, the frequency separation is usually small. Because of rapid filamentation of the beam size due to the incoherent space charge tune shift, the different frequencies cannot be resolved. Therefore, two pick-ups have been installed in the machine. By installing one pick-up in a location with large horizontal and small vertical beta, and the other in a location where the opposite applies, the known dependence of the amplitudes of the different components on the beta functions can be used to distinguish components that cannot be resolved in frequency. It is also possible to measure the beam emittance with this system[4].

6 MEASUREMENTS WITH BEAM

The measurement system is currently being commissioned, but has already produced interesting signals. The first real signals obtained (see Fig. 4) showed a very large oscillation of the beam widths, signalling a big mismatch. The cause for this was found later to be that some of the quadrupole magnets in the transfer line had wrong currents programmed.

Table 2: Quadrupole signal components due to different kinds of injection errors δ.

Parameter	Frequency	Amplitude
Horizontal Matching	$f_{\rm rev}(n \pm 2q_h)$	$\beta_h\ \delta_{\beta_h}$
Vertical Matching	$f_{\rm rev}(n \pm 2q_v)$	$\beta_v\ \delta_{\beta_v}$
Horizontal Dispersion	$f_{\rm rev}(n \pm q_h)$ $f_{\rm rev}(n \pm 2q_h)$	$2D_h\sqrt{\beta_h}\ \delta_{D_h}$ $\beta_h\ \delta^2_{D_h}$
Vertical Dispersion	$f_{\rm rev}(n \pm 2q_v)$	$\beta_v\ \delta_{D_v}$

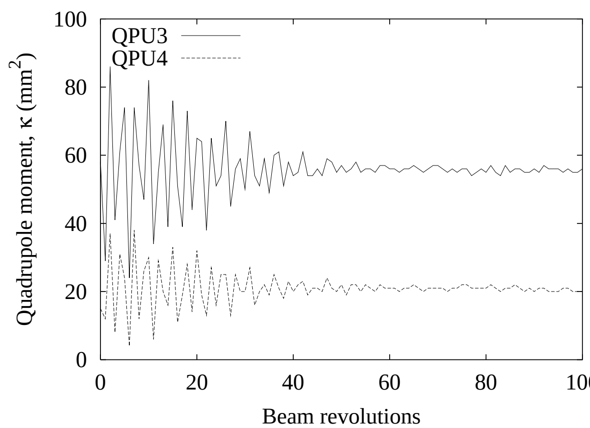

Figure 4: First measurement with the new quadrupole pick-ups, showing large beam size oscillations at injection.

7 SUMMARY AND CONCLUSIONS

A magnetic quadrupole pick-up have been designed for the CERN PS. Three pick-ups have been built and two are now installed in the machine; they are currently being commissioned with proton beams. Used with special low-noise amplifiers, the pick-ups should also be able to detect injection oscillations on the future beam of stacked lead ions from LEIR for the LHC.

8 REFERENCES

[1] A. Chapman-Hatchett, A. Jansson, D.J. Williams, "A magnetic quadrupole pick-up for the CERN PS", proceedings of PAC99, New York, 1999.

[2] A. Jansson, M. Lindroos, L. Søby, D.J. Williams, "Measurements with the magnetic quadrupole pick-up in the CERN PS", proceedings of EPAC2000, Vienna, 2000.

[3] A. Jansson, D.J. Williams, "A new optimised quadrupole pick-up design using magnetic coupling", accepted for publication in Nucl. Instr. Meth. in Phys. Res. A.

[4] A. Jansson, "Non-invasive measurement of emittance and optical parameters for high-brightness beams in a synchrotron". Dissertation, Stockholm University, 2001.

MEASUREMENT OF THE TIME-STRUCTURE OF THE 72 MEV PROTON BEAM IN THE PSI INJECTOR-2 CYCLOTRON

R. Dölling, Paul Scherrer Institut, Villigen, Switzerland

Abstract

The time-structure monitor at the last turn of the 72 MeV Injector-2 cyclotron has been improved in order to meet the stringent time-resolution requirement imposed by the short bunch length. Protons scattered by a thin carbon-fibre target pass through a first scintillator-photomultiplier detector and are stopped in a second one. The longitudinal bunch shape is given by the distribution of arrival times measured with respect to the 50 MHz reference signal from the acceleration cavities. From a coincidence measurement, the time resolution of the detectors has been determined to be 51 ps and 31 ps fwhm. Longitudinal and horizontal bunch shapes have been measured at beam currents from 25 µA to 1700 µA. Approximately circular bunches were observed with diameter increasing with current. The shortest observed proton bunch length was 38 ps fwhm.

1 INTRODUCTION

Time-structure measurement has been used at PSI since 1974 and has delivered valuable information during the commissioning of Injector 2 and at the introduction of the buncher in the injection line to Injector 2 [1 - 6]. Due to the buncher, the bunch length inside the cyclotron was reduced from ~15° fwhm of RF period to below 5° and it was not clear if the resolution of the time-structure monitor was still sufficient to resolve the bunch shape. In the end of 2000 a new double detector set-up based on NE111 scintillators and Hamamatsu R7400 metal package PMTs with custom divider circuits was tested, which allowed for the determination of the time resolution.

2 EXPERIMENTAL SET-UP

The monitor is located half a turn in front of the beam extraction in the space between two sector magnets. A carbon fibre of 30 µm diameter is moved transversally through the beam by a motorised feedthrough (Fig. 1). The detectors are located above, behind a 0.5 mm stainless steel window and a stainless steel aperture of 4.5 mm diameter. Scintillator A (a 8x8x16 mm^3 piece of NE111) is separated from scintillator B (8x8x40 mm^3 from the same piece of raw material) by a 12 µm aluminium foil which also covers the surface opposite to PMT A in order to enhance light collection. Both PMTs are coupled to the scintillators by silicon grease.

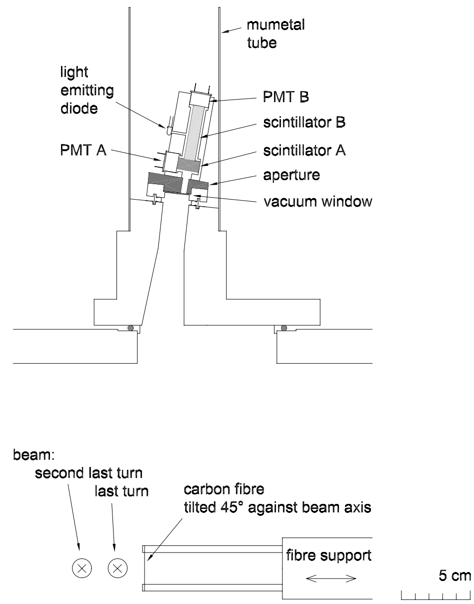

Fig. 1: Detector geometry.

An overview of the electronic set-up and modes of operation is given in Fig. 2. The output signals from the PMTs are transmitted through approximately 80 m of 50 Ω Cellflex LCF ½” cable to the control room. After passing an ohmic divider, one part of the signal is fed to an Elscint STD-N-1 snap-off timing discriminator (SOD) [7] and the other part is used for pulse height discrimination. Besides the elastically scattered protons, there are protons with lower energy from inelastic scattering at the carbon fibre and from scattering at the aperture, which arrive later. Hence, only the highest pulses at PMT B correspond to the correct timing information, and pulse height discrimination is necessary. This is provided by a SIN-FDD100 leading edge discriminator (LED). For a time-structure measurement with PMT B, the fast timing signal of SOD B is allowed to proceed as the start signal to a Canberra 2043 time-to-amplitude converter (TAC) if the pulse height of PMT B surpasses a defined high level. Gating is provided by a SIN-FC107B logic module. The stop signal is derived from the 50 MHz RF-reference signal by a SIN ZCD100A zero-crossing detector and gated in the same way. If the probe is positioned at the centre of a 1600 µA beam, the rate of accepted pulses is of the order of 250 cps.

If the time structure is measured with PMT A, pulse height discrimination is done also with the PMT B signal.

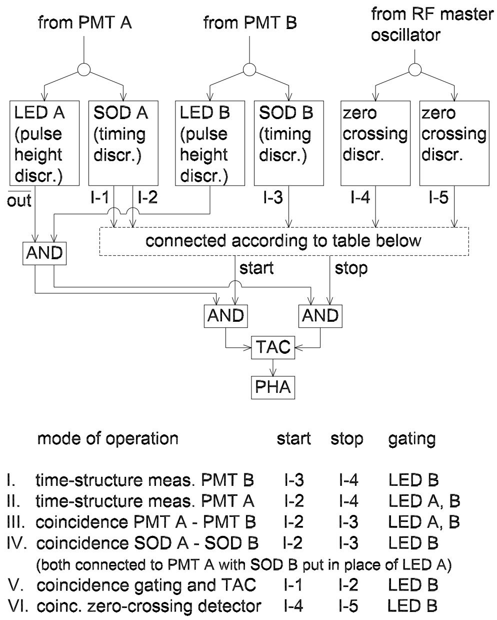

Fig. 2: Block diagram of the timing system.

The TAC-output is connected to a Northern-Econ-2 pulse height analyser (PHA). The overall conversion gain was determined to be 8.7 ps/channel by introducing known delays. Usually, the fwhm and full-width-20%-maximum values of the time spectra were recorded, and its ratios corresponded well with a gaussian shape of the spectra. All times given below are fwhm.

Time structure as well as coincidence measurements were performed with the carbon fibre positioned near the centre of the beam. Transversal beam profiles were determined by measuring the rate of accepted pulses at several beam positions.

3 RESULTS AND DISCUSSION

3.1 Non-linearity of pulse height and charge

The height and shape of the highest PMT output pulses, corresponding to elastically scattered protons, were measured with a fast oscilloscope. The dependency of pulse height and pulse charge Q_{pulse} on the PMT supply voltage U_{PMT} is given in Fig. 3. The non-linear behaviour at higher supply voltages can probably be attributed to space-charge forces resulting from the high pulse current density at the last dynodes. No dependency of pulse height on pulse rate was observed.

3.2 Estimation of the number of photoelectrons

The gain of the individual PMT is determined from the ratio of anode and cathode luminous sensitivities provided by the manufacturer. The quantities of photoelectrons generated at the photocathodes of the individual PMTs 1 and 2 at positions A and B in response to elastically scattered protons were determined according to Fig. 3. This was repeated after interchanging the PMTs (Table 1). The higher numbers with PMT 2 reflect its higher quantum efficiency.

Table 1: Quantities of generated photoelectrons.

	PMT 1	**PMT 2**
serial number	AD7126	AD7266
cathode lumin. sens.* [μA/lm] [9]	56.9	65.6
anode luminous sens.* [A/lm] [9]	33.3	21.2
individual gain*	585000	323000
N_{PE} at position A	1927	2173
N_{PE} at position B	4900	5500

* at U_{PMT} = -800 V

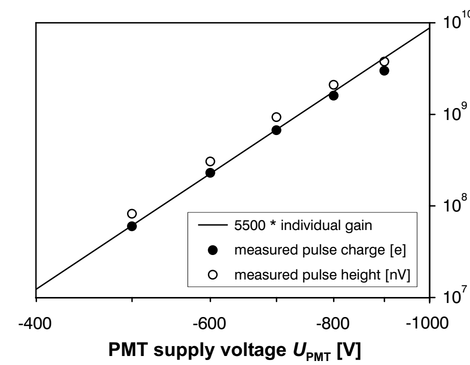

Fig. 3: Pulse height and charge of output pulses of PMT 2 at position B. The straight line represents the dependency of the gain on the supply voltage for this type of PMT [8] normalized to the gain of the individual tube (Table 1) and fitted by a factor (5500) to the measured pulse charge at lower supply voltages. This factor corresponds to the number of photoelectrons N_{PE} generated at the photocathode: $N_{\mathrm{PE}} = Q_{\mathrm{pulse}} / (e * gain)$ with e the electron charge.

3.3 Estimation of time resolution

The time resolution of detectors A and B can be deduced from the width t_{AvsB} = 60 ps of the coincidence spectrum measured according to Fig. 2, mode III. From the separation

$$t_{\mathrm{AvsB}}^2 = t_{\mathrm{loc,A}}^2 + t_{\mathrm{det,A}}^2 + t_{\mathrm{det,B}}^2 + t_{\mathrm{elo}}^2 \quad (1)$$

$t_{\mathrm{det,A}}$, $t_{\mathrm{det,B}}$ the time jitter of the detectors (scintillator and PMT) at positions A and B

$t_{\mathrm{loc,A}}$ = 16 ps the time jitter introduced by the variety of distances between individual proton paths and PMT A which is allowed by the aperture

t_{elo} = 21 ps the time jitter of the electronics measured according to Fig. 2, modes IV, V, VI

and the known fact that the time jitter of the detectors scales with the inverse square root of the number of photoelectrons generated at the photocathode [10, 11]

$$t_{\mathrm{det,A}}^2 \big/ t_{\mathrm{det,B}}^2 = N_{\mathrm{PE,B}} \big/ N_{\mathrm{PE,A}} \quad (2)$$

follows with $N_{\mathrm{PE,A}}$, $N_{\mathrm{PE,B}}$ from Table 1 (PMT 1 at position A, PMT 2 at position B)

$$t_{\mathrm{det,B}} = \sqrt{\frac{t^2_{\mathrm{AvsB}} - t^2_{\mathrm{loc,A}} - t^2_{\mathrm{elo}}}{1 + N_{\mathrm{PE,B}} / N_{\mathrm{PE,A}}}} = 27\ \mathrm{ps} \qquad (3)$$

$$t_{\mathrm{det,A}} = 46\ \mathrm{ps}$$

as well as the time jitter of the detectors including the contribution of electronic jitter and path variety

$$t_{\mathrm{total,B}} = \sqrt{t^2_{\mathrm{det,B}} + t^2_{\mathrm{elo}}/2} = 31\ \mathrm{ps} \qquad (4)$$

$$t_{\mathrm{total,A}} = \sqrt{t^2_{\mathrm{det,A}} + t^2_{\mathrm{loc,A}} + t^2_{\mathrm{elo}}/2} = 51\ \mathrm{ps} \quad .$$

The resolution of the time-structure measurement with detector A or B can be calculated according to

$$t_{\mathrm{resol,B}} = \sqrt{t^2_{\mathrm{det,B}} + t^2_{\mathrm{elo}} + t^2_{\mathrm{ref}}} \approx 35\ \mathrm{ps} \qquad (5)$$

$$t_{\mathrm{resol,A}} = \sqrt{t^2_{\mathrm{det,A}} + t^2_{\mathrm{loc,A}} + t^2_{\mathrm{elo}} + t^2_{\mathrm{ref}}} \approx 53\ \mathrm{ps}$$

with t_{ref}, the jitter of the RF-reference signal, assumed to be negligible.

Similarly, the width t_{TS} of a time spectrum measured according to Fig. 2, mode I or II is separable as

$$t^2_{\mathrm{TS}} = t^2_{\mathrm{bunch}} + t^2_{\mathrm{resol}} \quad . \qquad (6a)$$

The bunch length t_{bunch} can be derived by Eq. (6a) from the measured t_{TS} and known t_{resol} (6b). Alternatively, t_{resol} can be deduced from the measured t_{TS} and the known t_{bunch} (6c).

Short bunch lengths measured according to Eq. (6b) with detectors A and B agree well, thereby corroborating the above derived values of time resolution.

Fig. 4 compares the derived time resolution, according to Eq. (4), to that of other experiments. Also the performance of the former set-ups of the time-structure monitor at Injector 2 is estimated from Eq. (6c) using t_{bunch} determined with the present set-up. The inferior time resolution is probably mainly due to the electronic components used at that time.

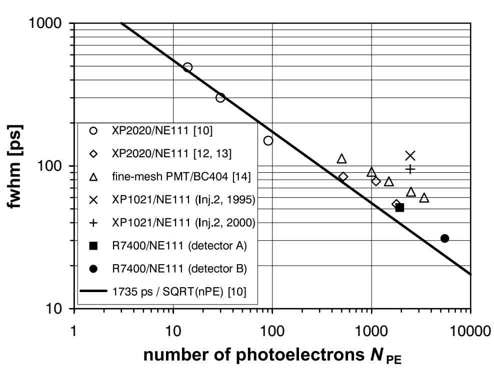

Fig. 4: Resolution of single scintillator-PMT detectors.

3.3 Bunch length and transverse width

To demonstrate the capability of the monitor, the dependency of the bunch length on proton beam current is depicted in Fig. 5 together with the transverse beam width. The bunch width is about 2/3 of the length. The bunch size decreases at lower currents with the relative dimensions approximately unchanged.

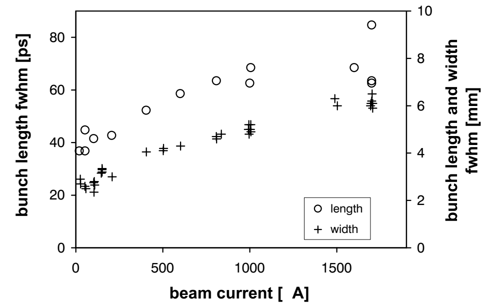

Fig. 5: Bunch length (accord. to Eq. (6b)), and width at the last turn of the Injector-2 cyclotron. (PMT 2 at position B was used. U_{PMT} in the range -700 V … -850 V.)

4 CONCLUSION

The time resolution of the time-structure monitor has been determined by a coincidence measurement. It has been improved significantly by using a set-up with enhanced light-collection efficiency, an advanced PMT (and divider circuit) and improved electronics. The detector is compact and the PMT offers an enhanced immunity to magnetic fields. Hence, a moving detector covering nearly all turns of Injector 2 seems feasible.

REFERENCES

[1] M. Olivo, "Beam diagnostic equipment for cyclotrons", Proc. 7th Int. Conf. on Cyclotrons and their Applications, Zürich (1975) p. 331

[2] W. Joho, "High intensity beam acceleration with the SIN cyclotron facility", Proc. 11th Int. Conf. on Cyclotrons and their Applications, Tokyo (1986) p. 31

[3] S. Adam, M. Humbel, "Integration of compute-bound tasks in the SIN control system", ibid. p. 418

[4] J. Stetson et al., "The commissioning of PSI Injector 2 for high intensity, high quality beams", Proc. 13th Int. Conf. on Cyclotrons and their Applications, Vancouver, Canada (1992) p. 36

[5] T. Stammbach, "Experience with high current operation of the PSI cyclotron facility", ibid. p. 28

[6] T. Stammbach et al., "The feasibility of high power cyclotrons", Nucl. Instr. & Meth. B 113 (1996) 1

[7] Manual STD-N-1, Elscint Ltd., Haifa (1973)

[8] Hamamatsu PMT R7400U data sheet TPMH1204E05 (Apr. 2000), Hamamatsu Photonics K.K.

[9] Hamamatsu PMT R7400U final test sheet (24 Oct. 2000), Hamamatsu Photonics K.K.

[10] J. Pouthas et al., "Intrinsic time resolution of detectors in a time-of-flight spectrometer", Nucl. Instr. & Meth. 145 (1977) 445

[11] P. J. Carlson, "Prospects of scintillator time-of-flight systems", Physica Scripta 23 (1981) 393

[12] M. Moszynski et al., "Timing study with R 1294 U microchannel plate photomultipliers", Nucl. Instr. & Meth. 204 (1983) 471

[13] M. Moszynski, "Prospects for new fast photomultipliers", Nucl. Instr. & Meth. A 337 (1993) 154

[14] T. Mashimo, International Center for Elementary Particle Physics, Univ. of Tokyo, private communication

LASER PROFILE MEASUREMENTS OF AN H⁻ BEAM

R. Connolly, P. Cameron, J. Cupolo, M. Grau, M. Kesselman,
C-J. Liaw, and R. Sikora
Brookhaven National Lab, Upton, NY, USA

Abstract

A non-intercepting beam profile monitor for H^- beams is being developed at Brookhaven National Lab. An H^- ion has a first ionization potential of 0.75eV. Electrons can be removed from an H^- beam by passing light from a near-infrared laser through it. Experiments have been performed on the BNL linac to measure the transverse profile of a 750keV beam by using a Nd:YAG laser to photoneutralize narrow slices of the beam. The laser beam is scanned across the ion beam neutralizing the portion of the beam struck by the laser. The electrons are removed from the ion beam and the beam current notch is measured.

.1. INTRODUCTION

The Spallation Neutron Source (SNS) under construction at Oak Ridge National Lab consists of a 1GeV H^- linear accelerator (linac), a storage ring, target, and connecting beam-transport lines [1]. The linac delivers a 1.04 ms macropulse which is chopped into 10^3 pulses of 10^{11} protons each. As this pulse enters the storage ring from the linac each chopped pulse lines up longitudinally with all proceeding pulses forming a single 550-ns bunch and a 250-ns gap. After stacking beam in the storage ring for 1000 turns the proton beam is dumped onto a metal target producing a 550 ns pulse of neutrons.

Profiles of the H^- beam will be measured in the medium energy transport line (MEBT) between the radio frequency quadrupole (rfq) and the linac entrance, along the linac, and in the linac-ring transport line. Stepped carbon-wire scanners are the primary profile diagnostic. However beam heating will limit wire scanners to tuning and matching applications with either the beam pulses shortened or the current reduced. Also there are concerns about placing wires near the superconducting cavities where wire failure can cause cavity damage.

We are developing a laser beam profile monitor (LPM) which is non-invasive and suitable for continuous profile monitoring. The technique selects a transverse slice of an H^- beam by photoneutralization by a laser beam [2,3]. An H^- ion has a first ionization potential of 0.75eV and can be neutralized by interacting with a photon with wavelength<1500 nm, fig.1. The 1064-nm light from a Nd:YAG laser is very near the peak of the cross section.

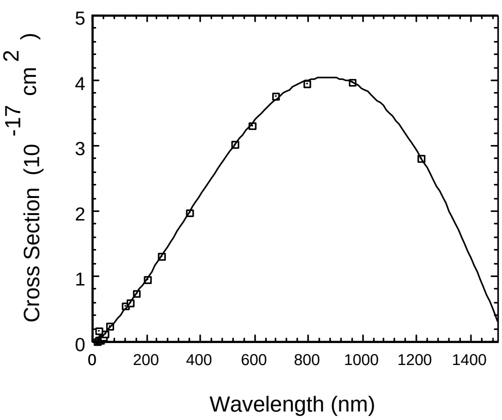

Figure 1: Calculated cross section for H^- photoneutralization as a function of photon wavelength. Data are from a table in ref. [4].

2. LINAC EXPERIMENT

Figure 2 shows the experiment on the BNL linac. A light pulse from a Q-switched Nd:YAG passes through the 750 keV H^- beam from the linac rfq neutralizing most of the beam the light passes through. A downstream current transformer measures a dip in the beam current which is proportional to the fraction of the beam hit with the light, fig. 3. The laser beam is stepped across the ion beam and the profile is constructed by plotting the depth of the current notch vs. laser beam position.

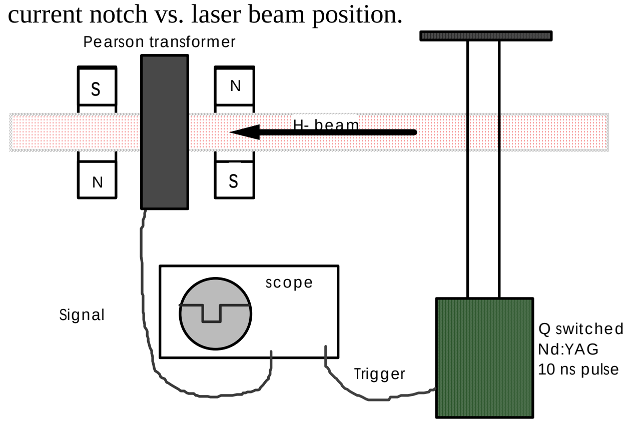

Figure 2: Laser scanner experiment on BNL linac. The first of two 10 Gm dipole magnets removes the free

electrons from the beam and the second straightens the beam.

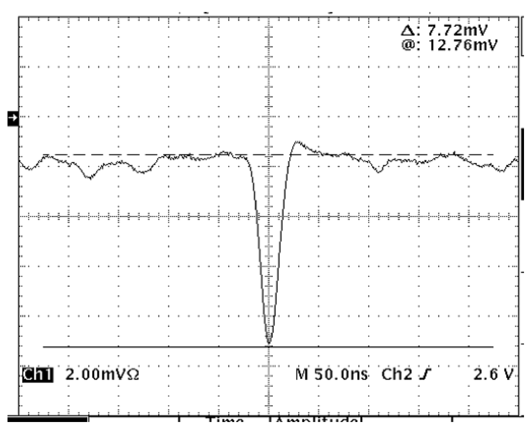

Figure 3: Scope trace of the current transformer signal showing notch created by the laser pulse.

The arrangement of the laser and optics on the linac beamline is shown in fig. 4. A CFR200 laser from Big Sky Laser [5] is mounted on a shelf at the top left. Three 45° mirrors are mounted inside the vacuum on linear motion feedthroughs. The top-left mirror is used to switch between vertical and horizontal scans and the other two do the scanning. The top-right mirror scans horizontally and the bottom-left mirror scans vertically. Both scanning mirrors are shown with arms to hold lenses. In this experiment the lenses were not installed.

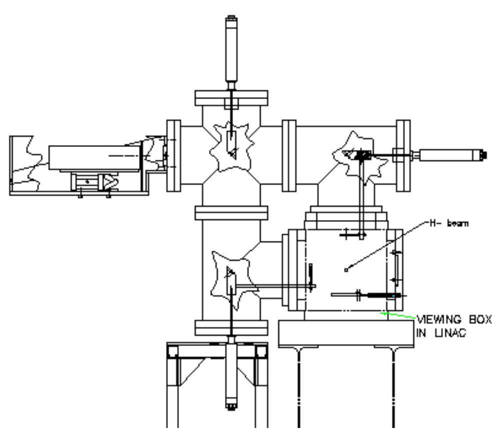

Figure 4: Laser scanning assembly installed on linac beamline. View is looking up beamline.

The CFR200 puts out 200 mJ pulses that are about 10 ns long. Without lenses the beam diameter is about 0.6 cm giving a photon flux of 3.5 x 10^{26}/cm^{2}s. The neutralization fraction f_{neut} is calculated from,

$$f_{neut} = 1 - e^{-\sigma(E)Ft} \qquad (1)$$

where $\sigma(E)$=3.7 x 10^{-17}cm^2 is the cross section from fig. 1, F is the photon flux and t is the flight time of the ion beam through the laser beam. The flight time of 750keV ions through the 0.6cm diameter beam is 420ps. Using these numbers we calculate that over 99% of the ions passing through the center of the laser beam were neutralized.

When an ion is neutralized the free electron continues to move along with the beam. These electrons have to be removed from the beam to measure a current drop. In an accelerator installation this is accomplished by either rf cavities or quadrupoles but in the experiment the current transformer had to be placed in the same vacuum chamber as the laser optics. For this reason we placed two weak permanent-magnet dipoles on either side of the transformer. The pole tips are 2.5cm square and 5cm apart and the field is about 400 G. The first magnet deflects the electrons from the beam and the second one straightens out the beam.

3. MEASURED PROFILES

Figure 5 shows the measured horizontal and vertical profiles. In each plot the measured points are indicated by markers and the curve is a gaussian fit to the data.

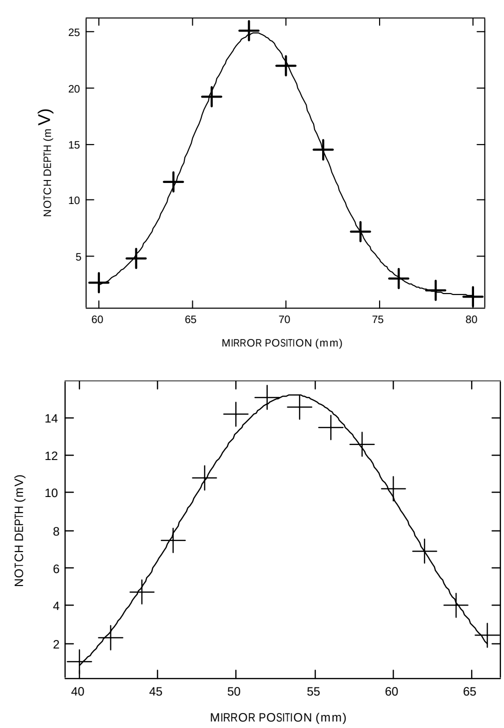

Figure 5: Measured horizontal (top) and vertical beam profiles.

The rms widths of the two fitted curves are σ_x=3.32±0.05 mm and σ_y=7.3±0.6 mm. These values agree with expectations from previous measurements at this location, however for this experiment there was no profile measurement by another method.

These data were taken by moving the mirrors manually and measuring the notch depth on an oscilloscope set to average 15 shots. We measured a maximum notch depth of about 40% on the horizontal scan. If the laser beam power was uniformly distributed over the spot the maximum notch depth should have been closer to 60%. Based on this we conclude the laser power is not uniform over the spot.

4. DISCUSSION

Beam profiles of an H- beam can be measured by laser photodetachment followed by current measurement. To automate the data collection we are going to use a gated boxcar integrator triggered by the Q-switch timing output of the laser. The output of the integrator will be digitized and averaged over several laser bursts to accommodate shot-to-shot variations in the laser power output and the ion beam current.

A compact laser scanning station, fig. 6, is being built for measuring profiles in the SNS medium energy transport line between the rfq and the linac entrance. This will use a 50mJ/pulse laser and all of the optical components will be mounted on a 35x20 cm plate. The plate will attach to tapped holes on the viewports of the wire-scanner chamber.

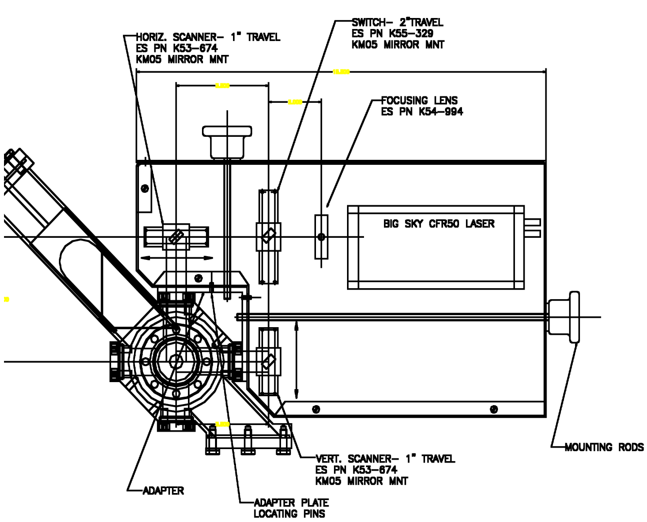

Figure 6: Laser profile scanner plate that will be tested on the SNS beamline between the rfq and linac entrance. It is shown mounted to the wire-scanner chamber.

ACKNOWLEDGEMENTS

We thank Vincent Lo Destro and Brian Briscoe for their help in setting up the experiment and for providing support at the linac. Robert Shafer at LANL has done calculations and picked out the laser. This work was performed under the auspices of the United States Department of Energy.

REFERENCES

[1] http://www.sns.gov/

[2] R.C. Connolly, K.F. Johnson, D.P. Sandoval and V. Yuan, "A transverse phase-space measurement technique for high-brightness H^- beams", Nucl. Instr. and Meth. A132 (1992) 415-419.

[3] V.W. Yuan, R.C. Connolly, R.C. Garcia, K.F. Johnson, K. Saadatmand, O.R. Sander, D.P. Sandoval and M.A. Shinas, "Measurement of longitudinal phase space in an accelerated H^- beam using a laser-induced neutralized method", Nucl. Instr. and Meth. A329 (1993) 381-392.

[4] J.T. Broad and W.P. Reinhardt, Phys. Rev. A14 (6) (1976) 2159.

[5] Big Sky Laser Technologies, Inc., Bozeman, MT 59715.

NEW SCHOTTKY- PICKUP FOR COSY - JÜLICH

I.Mohos, J. Bojowald, J. Dietrich and F.Klehr
Forschungszentrum Jülich GmbH, Germany

Abstract

A new Schottky-pickup for the Cooler Synchrotron COSY [1] at the Forschungszentrum Jülich was developed, tested and installed. The new pickup with four diagonally arranged plates replaces the two 1 m long Schottky–pickups used until now in COSY. The previous ones were removed mainly to gain space for new installations (e.g. rf-cavity, experimental devices), but also to increase the horizontal aperture. The available space for the new pickup is only 0.8 m. The pickup plates can be combined by means of relays to measure either in the horizontal or in the vertical plane. The pickup can also be used either as a sensitive broadband beam position monitor or as a tuneable narrowband pickup for Schottky-noise analysis with ultahigh sensitivity. A new method for resonant tuning of the Schottky-pickups for transversal measurements was developed. The differentially excited resonant circuitry enhances the sensitivity by about a factor of 30. The pickups are also used for dynamical tune measurements (tune meter) in the acceleration ramp [2].

1 INTRODUCTION

The Schottky-noise is preferably measured in the 10 to 60 MHz frequency range. This is due to the fact that the line widths in the Schottky-noise spectrum are proportional to the harmonic number with equal noise power per line. The narrow longitudinal lines are measured in the upper part of this frequency range, but the generally much broader transversal lines at lower frequencies because here the line structures do not yet overlap and, in particular at higher frequencies, the amplitudes can vanish in the noise level.

Because of the low power of the transversal signals an especially sensitive monitor is required whose sensitivity will be enhanced further by resonant tuning. Despite of the gain of 20 to 30 dB by resonant tuning, the sensitivity itself is very important and also its frequency dependence. Both sensitivity and frequency dependence are influenced by the layout and the mode of operation.

Three monitor types are at disposal: inductive, capacitive and stripline monitors. In the frequency range of 10 to 60 MHz the capacitive monitor is well suited, but the inductive monitor less so. This is due to the fact that the azimuthal magnetic field of the beam and hence the induced signal power is proportional to $ß^2$, and Schottky-noise measurements at COSY also must be performed at low ß-values. The stripline monitor can be operated at high frequencies and it is able to separate the signals of particles travelling opposite to each other (directivity), a very useful feature in storage rings. This cannot be used at COSY, however, the great disadvantage is the sinusoidal frequency dependence. The maximal sensitivity, obtained at frequencies with $\lambda/4$ corresponding to the monitor length, would be with 0.8m length at 94 MHz. In the 10 to 60 MHz range the sensitivity diminish drastically.

The amplitudes of the transversal Schottky signals are dependent on the square root of the ß-function. A suitable position in COSY with high ß-function values should therefore be chosen. In monitor design, attention must be payed to save the total aperture. For this reason the electrodes must be arranged far outside, at best with beam tube diameter.

2 MONITOR DESIGN AND TRANSFER IMPEDANCE

The capacitive monitor with high impedance preamplifier has the particular advantage of a flat frequency response within a pass band. The lower cut-off frequency is determined by the electrode capacity and the preamplifier input impedance, and can be realized to 10kHz. The upper cut-off frequency is determined by the bandwidth of the preamplifier and is larger than 100MHz, the proper frequency range.

The sensitivity or transfer impedance of one electrode with beam centred is given by

$$Z_{tr} = \frac{A_{el}}{2\pi r} \cdot \frac{1}{\beta c \cdot C_{el}} = \frac{\alpha_{el}}{2\pi} \cdot \frac{L}{\beta c \cdot C_{el}}$$

where: A_{el} = electrode plane, r = beam tube radius, L = monitor length and α = azimuthal angle of electrode. The first term is a geometrical factor, corresponding to the ratio of electrode plane to total monitor cylinder plane. The transfer impedance is maximized if all electrodes together entirely enclose the beam, i.e. if $\Sigma\alpha_{el} = 2\pi$. For high sensitivity the electrode capacity C_{el} must be small, i.e. the distance to the beam tube cannot be too small.

Therefore the vacuum tube should be enlarged and the electrodes positioned in extension of the beam tube.

For the longitudinal or Σ- signal follows: $\Sigma(t) = n \cdot Z_{tr} \cdot i(t)$ where: n = number of electrodes and i(t) = beam current. Important for the transversal or Δ- signals is the coupling capacity C_c between the electrodes that reduces the amplitude, because

$$\Delta(t) = \frac{\Sigma(t)}{a/2} \cdot \frac{C_{el}}{C_{el} + 2C_c} \cdot \left(x - x_0\right)$$

where: a = electrode distance, x = displacement of beam from centre and x_0 = monitor displacement from optical axis. The coupling capacity must be small in comparison to the electrode capacity. This also means, that the electrode capacity cannot be made as small as possible.

The geometry of the new Schottky-pickup has the schematic layout as shown in Fig.1. The apertures in horizontal (150mm diameter) and in vertical (60mm, rectangular) directions remain free, if the pickup diameter is made slightly larger.

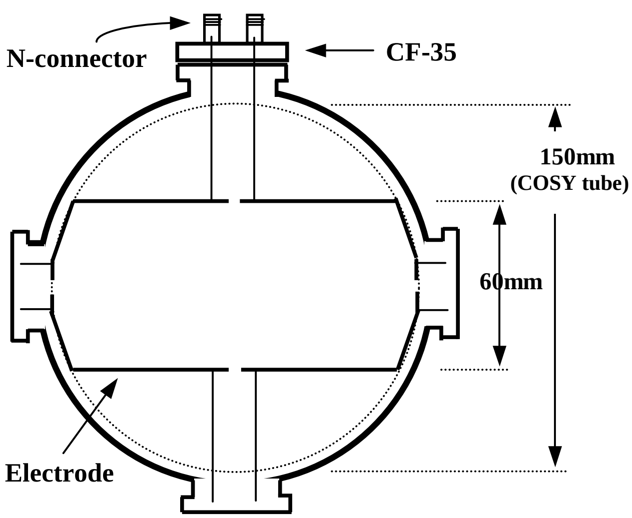

Figure : Layout of the new Schottky-pickup for measurements in horizontal and vertical plane (after proper switching of coax-relays).

The structure is split into four electrodes that together surround the beam. By proper switching of coax-relays, Schottky-noise measurements become possible both in horizontal and vertical planes. To achieve a small coupling capacity (e.g. $C_c < C_{el} / 10$), the separating slits cannot be made too narrow, thus an azimuthal range of about 95% must be tolerated.

Before installation, measurements of the pickup sensitivity (also called transfer impedance) were carried out using a special test set-up. A well defined RF-current is coupled into a matched inner conductor (diameter 1 mm) for simulation of the beam current. The response in the time domain of the Schottky- pickup is shown in Fig. 2. The output signal is attenuated because of damping in the matching networks.

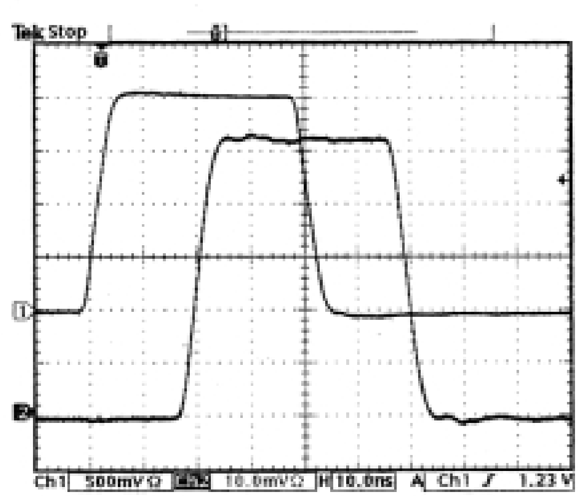

Figure 2: Time response of the Schottky-pickup (Ch1: input; Ch2: output, BW = 70 MHz).

The pickup electrodes can be combined by means of relays for horizontal, vertical or longitudinal broadband measurements as is shown in Fig. 3. An example for broadband measurements is shown in Fig. 4.

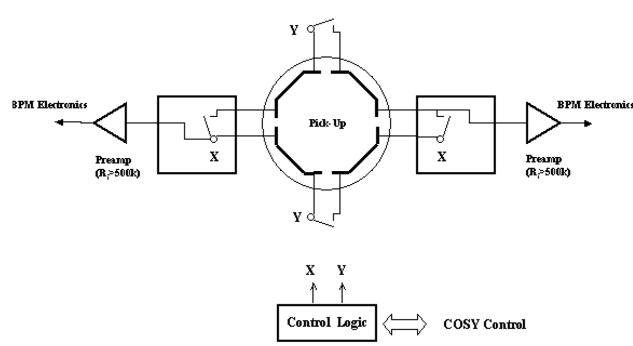

Figure 3: Broadband application of the Schottky-pickups.

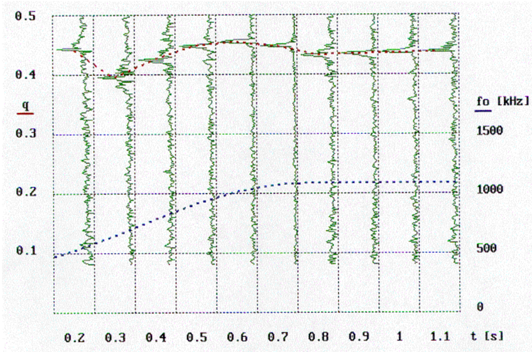

Figure 4: Display of a tune measurement in the acceleration ramp consisting of ten FFT-spectra. The sideband lines are clearly seen. In the lower part (dashed curve) the frequency ramp is shown [2].

3 RESONANT TUNING

For Schottky-noise analysis, special narrowband electronics consisting of two critically coupled LC resonant circuits were developed (Fig. 5.). The first one is connected between two sectors of the properly combined electrode pairs. In this configuration the resonant circuitry will be excited only by the differential current, i.e. by the transversal component of the beam charge. With a coupled additional resonant circuit a band bass filter was formed. To avoid unwanted tuning effects by the strong magnetic fields at COSY, ironless coils with fixed inductivity were used. The centre frequency of the filter and the coupling factor can be tuned by means of double-diode aviators. Three Dace's operated from the control room of COSY generate the tuning voltages using stored arrays for centre frequencies between 8 and 13 MHz and coupling factors for flat pass band response. The bandwidth is about 200 kHz.

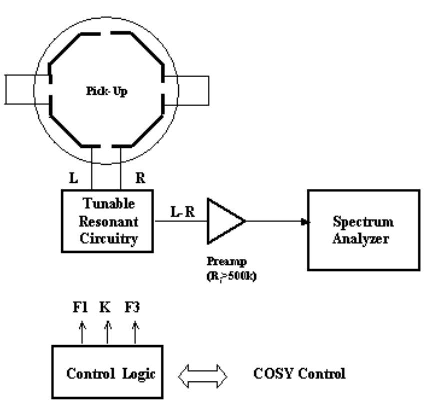

Figure 5: Schottky- pickups with resonant circuitry for horizontal transversal measurements.

The output of the band pass filter corresponds to the transversal beam current. No further subtracting (hybrid) circuitries are necessary for extracting the differential signal component. The filter enhances the pass band sensitivity of the Schottky-pickup and thus it the signal to noise ratio by about a factor of 30 in comparison to the broadband configuration. The small signals of the pickup are amplified by a programmable gain broadband amplifier.

REFERENCES

[1] Maier, R., "Cooler synchrotron COSY – performance and perspectives," Nucl. Instrum. and Methods A **390**, 1- 8 (1997).

[2] Dietrich, J. et al, "Real-time betatron tune measurement in the acceleration ramp at COSY- Jülich", DIPAC, Chester (1999).

CURRENT TRANSFORMERS FOR GSI'S KEV/U TO GEV/U ION BEAMS - AN OVERVIEW

H. Reeg, N. Schneider
Gesellschaft fuer Schwerionenforschung (GSI), Darmstadt, Germany

Abstract

At GSI's accelerator facilities ion beam intensities usually are observed and measured with various types of current transformers (CT), matched to the special requirements at their location in the machines.

In the universal linear accelerator (UNILAC), and the high charge state injector (HLI) as well, active transformers with 2nd-order feedback are used, while passive pulse CTs and two DC-CTs based on the magnetic modulator principle are implemented in the heavy ion synchrotron (SIS) and the experimental storage ring (ESR). In the high energy beam transfer lines (HEBT) the particle bunch extraction/reinjection is monitored with resonant charge-integrating types.

Since more than 10 years number and significance of beam current transformers for operating GSI's accelerators have grown constantly. Due to increased beam intensities following the last UNILAC upgrade, transmission monitoring and beam loss supervision with CTs have become the main tools for machine protection and radiation security purposes.

All CTs have been constructed and developed at GSI, since no commercial products or were available, when solutions were needed.

1 INTRODUCTION

In GSI's various accelerators a large range of ion species are handled, from protons to uranium, including a lot of isotopes and nearly all possible charge states. The peak beam currents in the SIS in the meantime have grown up to nearly 1 Ampere, reaching the space charge limit with Ne^{+10}, while still experiments with less than one μA are performed with low energy beams in the UNILAC. The time structures of the different beams spread from 10^{-9} to more than 10 seconds, and often have to be resolved and displayed.

CTs built from high permeability tape-wound ring cores have replaced most of the faraday cups in the UNILAC, because they do not destroy or even influence the beam, and do not suffer from beam power load. Their output exhibits no dependence to the beam's position or extent.

Their most important characteristic feature is their inherent and reliable calibration, if careful design and construction are applied.

2 LINAC TRANSFORMERS

2.1 Electronic and magnetic layout

Up to 15 different machine settings with respect to ion energy or species can be treated in a periodically pulsed sequence. Typical macropulse duration of the ion sources and linacs between 50 μs and 8 ms demand rise times about 1 μs, and negligible pulse droop losses to guarantee accurate measurements. The RF cavities are operated at 36 and 108 MHz, with bunch widths of about 1 ns FWHM, respectively. As this would require more than 1 GHz bandwidth, beam energy (Time-Of-Flight), energy spread, longitudinal emittance and beam position measurements are performed with a system of capacitive pick-ups installed along the machines, so transformer bandwidth can be kept around 500 kHz. At present 38 CTs are installed in the linac sections and the low energy experimental areas.

Each CT's crossed-differential winding is connected to the front electronics, mounted as close as possible to the beam pipe. By those means excessive noise or hum pickup is reduced. A current-to-voltage converter with a second-order current feedback network [1], range selection and a switched clamp for baseline restoration are installed in the front box. The analogue output signals are then transmitted via differential and terminated twisted pair lines to their associated integrating digitizers [2]. These again are installed in a central control station outside the linac tunnel, keeping the cable lengths below 100 meters. Via special interfaces, a multiplexer and a PC equipped with an ADC plug-in, 2 of 64 CT pulse signals can be selected for display on the PC screen.

This feature enables the machine operators to observe any modulations on the macropulse, like plasma fluctuations in the ion source, or settling problems of the RF cavity amplitude controllers induced by beam loading.

A/D-conversion of the CT signals is performed by an U/F-converter with 8 MHz maximum frequency, feeding a 16-bit digital counter. In the lowest current range one count equals a charge amount of 0.6 pC. By gating the counter with a trigger interval congruent to the beam pulse, the pulse charge can be read as the counter end value. This is transferred to the control system together with the gate length value (measured simultaneously), and a simple calculation returns the average beam current and the number of particles in the CTs for all sequential beam pulses. The results are displayed as bar graphs or trend plots in the operating programs.

Tab. 1: Main specifications of linac CTs

Ranges	5, 10 µA ..... 100mA full scale
Resolution	200nA rms, full BW
Risetime	< 2 µs
max. pulse length	6ms for droop error < .5%

When the upgraded UNILAC is operated at highest intensity level, the pulse power for Uranium-Ions accelerated to 11.4 MeV/u will exceed 1 MW. Under this conditions, a single beam pulse of 100 µs will destroy the wires of a profile harp or even will melt the beam tube wall. As a consequence, a beam loss controlled protection system was installed.

Starting after the injector section, all CT front electronics are equipped with an additional analogue output with a fixed transimpedance. The signals of two consecutive CTs at each case are fed into a dual-U/F-converter. Each pulse from the first converter channel triggers an up-counter, the corresponding down-counter is driven by the pulses from the successive CT. When this action is started and reset with a signal congruent to the desired time interval, the counter's value represents the instantaneous beam charge lost between the CT pair. If the value exceeds a threshold preset by the control system for each machine setup and monitor location, an interlock line is activated and the beam pulse length is shortened automatically with the beam chopper. This protective state is kept until the loss falls below the threshold again, whether by operator's intervention or by chance. With respect to electronic response times and the distance between the chopper and the respective transformer pair reaction times ≤10 µs are achieved.

Tape-wound ring-cores made from crystalline Supermalloy® or amorphous VITROVAC® are used for all CTs. These alloys exhibit highest initial permeability μ_i, improving signal-to-noise ratio in combination with a negligible magnetostriction coefficient λ_s, which helps to reduce microphonic noise produced by mechanical vibrations. Nevertheless, the cores fabricated from crystalline material had to undergo an initial demagnetization process. In most cases the noise, mostly induced by line-asynchronous motors of the vacuum pumps, could be reduced below 1 µA rms.

2.2 Mechanics, shielding and vacuum

A standard type with 48mm aperture diameter, an overall length of 100mm, and with DN100CF flanges commonly used in the linacs, was the first development. Some special versions with apertures up to 100mm or reduced length followed, solving problems with beam envelope clipping in the injector sections, or due to limited installation space between the RF cavities.

All transformer housings are fabricated from a ferritic stainless Cr-based steel. This material combines reasonable magnetic shielding efficiency with good surface properties for high vacuum usage and mechanical strength. A drawback has to be mentioned - it is not suitable for welding or brazing processes. Thus a single O-Ring breaks the wall mirror currents, and acts as a vacuum seal. The ring core is supported inside the housing by rad-hard foam strips, whereas mechanical stresses and vibrations are avoided.

3 TRANSFORMERS FOR SIS AND ESR

In the SIS the CTs have to solve two tasks. A fast CT [3] is used for multiturn-injection observation, while DC-CTs [4] based on the well-known fluxgate principle measure the accelerating ramp, the interval with a coasting beam, and while the intensity decays during slow extraction. The regular acquisition times are below 15 s, but can rise to minutes or even hours, if beam is accumulated and stored in the ESR, or lifetime measurements during e^--capture are performed in the SIS.

The cores for all versions are made from VITROVAC® with an inner diameter of 260mm and 10 mm^2 cross section.

3.1 Fast CT

The fast CT is a passive type with 100Ω termination, followed by a gain switchable amp and a fixed-rate ADC. As usual the signals from the front electronics are transmitted via differential lines to the control rooms Neglecting eddy current time constant τ_E and the secondary stray inductance, the output response equals

$$U(t) = I_b R/n * \exp(-t/\tau_L) \quad \text{if} \quad \tau_E << \tau_L \quad (1)$$

with
I_b = beam current
R = termination impedance
N = number of secondary turns
L = secondary inductance
τ_L = L/R = inductive time constant
τ_E = eddy current time constant

Tab.2: Main specifications for fast CTs

ranges	8, 100 µA ..... 300 mA f. s.
resolution	5 µA rms, BW = 1MHz
risetime	~500 ns
max. pulse length	100 µs for droop error < 10%

3.2 DC-CT

SIS and ESR each are equipped with a DC-CT [5], based on an identical design, but with some appropriate modifications.

The SIS type has been trimmed for fast response and low noise by adding a ripple reduction technique with an ADC/RAM/DAC-system. The ESR type was optimized for DC stability by a selected core pair and limiting the bandwidth with a sampling filter. Both CTs recently were extended with a voltage-to-frequency converter, providing a range-independent output.

The DC-CT core stacks are mounted in a bakeable and shielded housing, which is also used for the fast CT in the SIS. A 19" rack close to the beam tube contains the analogue station, equipped with differential signal transmission and processing.

Tab. 3: Main specification for DC-CT (SIS)

ranges	8, 300 µA .... 1 A f. s.
resolution	2 µA rms, BW = 20 kHz
risetime	< 20 µs
offset stability	±2 µA @ auto zero mode, <15µA/day
temp. coeff.	~1.6 µA/°C
mod. ripple	≤5 µA pp @ 2 kHz

4 HEBT TRANSFORMERS

4.1 Principle and Electronics

If particle bunches are extracted from SIS or ESR in the fast mode, their ionic charge as well as the transmission efficiency in the beam lines are monitored with CTs based on a parallel-resonant working principle [6]. After one to four bunches have passed, the circuit behaves as an exponentially damped oscillator. The circuit's terminal voltage at the first extremum is approximately:

$$U(\tau)= Q/nC*(1- \omega^2\tau^2/24) \quad \text{if } \tau < .1*T \qquad (2)$$
$$= Q/nC*(1- 1.6\ (\tau/T)^2)$$

with
Q = primary pulse charge
$\omega = 2\pi/T$ resonance frequency
τ = pulse duration, independent on time structure
n = number of secondary turns (100)
C = effective parallel capacitance

The transformer core is equipped with a crossed-differential winding, forming the inductor of the resonant circuit. A ferrite ring with μ_i=2200 and an inner diameter of 165 mm to fit over the DN100 beam pipe was chosen because of it's low parallel loss impedance at the frequencies of interest, and lower costs. The circuit is tuned to ~18 kHz, resulting in an integration error less than .2 %.

The CT's signal is routed to a front electronic block as close as possible to the core housing. It consists of an instrumentation amplifier, a 1...70 kHz bandpass, a gain programmable amp and a peak detector (PD), which was chosen for circuit simplicity (no bunch-synchronous timing necessary, averaging techniques not adequate for transmission monitoring). It's noise rectification characteristic turned out to be insignificant. Signal transmission via differential line drivers is as usual, range switching and PD reset are done from control electronics located far from the beam lines; the measured values are displayed by bar graphs in the control room.

Tab. 4: Main specification for HEBT CTs

ranges	4, 1 nC .... 1 µC
resolution	10 pC rms, or <1% f.s.
max. bunch width	1.5 µs total

4.2 Mechanics, shielding and vacuum

All HEBT CTs are operated under UHV conditions, which required appropriate materials and fabrication processes. A ceramic wall gap as well as metallic seals and baking jackets are implemented. The core is surrounded by a double µ-metal shield against magnetic interference.

5 ACKNOWLEDGEMENTS

The authors like to thank K. Unser (formerly CERN) for his helpful publications and private communications about CTs in general, R. Steiner for continuos help and discussions on the HEBT CTs, G. Froehlich and V. Schaa from the GSI operating software group, and a lot of people from the GSI beam diagnostic group for support and fruitful discussions.

6 REFERENCES

[1] N. Schneider, H. Walter, "Beam Current Measurements", GSI Scientific Report '90, Darmstadt, March1991
[2] N. Schneider, "Beam Current Monitors at the UNILAC", BIW '98, San Francisco, May 1998
[3] H. Reeg, N. Schneider, GSI 86-1, Darmstadt, March 1986
[4] K. B. Unser, "A Toroidal DC Beam Current Transformer ...", IEEE Trans. Nucl. Sci., NS-28, June 1981
[5] H. Reeg, N. Schneider; S. Steinhaeuser, "The Beam Current Transformers at SIS and ESR", GSI Scientific Report '90, Darmstadt, March 1991
[6] R. Steiner, Diploma Thesis, Inst. F. Kernphysik, Univ. Mainz, 1973

TRANSVERSE BEAM PROFILE MEASUREMENTS USING OPTICAL METHODS

A. Peters, P. Forck, A. Weiss, A. Bank
Gesellschaft für Schwerionenforschung (GSI), Darmstadt, Germany
e-mail: A.Peters@gsi.de

Abstract

Two different systems are currently under development at GSI's heavy ion facility to measure transverse beam profiles using optical emitters.
At the GSI-LINAC for energies up to 15 MeV/u residual gas fluorescence is investigated for pulsed high current beams. The fluorescence of N_2 is monitored by an image intensified CCD camera.
For all ion species with energies above 50 MeV/u slowly extracted from the synchrotron SIS a classical viewing screen system is used. Three different target materials have been investigated and their behavior concerning efficiency, saturation and timing performance is evaluated.
Both systems (will) use CCD cameras with a digital readout using the IEEE 1394 standard.

1 RESIDUAL GAS FLUORESCENCE MONITORS

The traditional determination of transverse beam profiles by secondary emission grids can not be applied at the high current heavy ion LINAC at GSI [1] due to the high beam power. Alternatively a non-intersecting residual gas monitor can be used or the fluorescence of the residual gas can be detected. The latter has the advantage that no mechanical parts and therefore no extra apertures are installed in the vacuum pipe, leading to a compact and cost efficient design. The method of residual gas fluorescence was applied to a proton LINAC [2] and recently also at a synchrotron [3]. Here a first test at a pulsed heavy ion LINAC is done.

The residual gas at the LINAC has a typical pressure of 10^{-7} mbar containing mainly Nitrogen. We use an additional gas inlet to increase the pressure up to 10^{-4} mbar. The N_2 is excited by the accelerated ions and the fluorescence from neutral or ionized molecules at wavelengths between 350 and 470 nm is dominant [2, 4]. The excited states have lifetimes of 40 ns and 60 ns, short enough to prevent broadening due to the movement of N_2^+ in the space charge potential of the beam.

For the detection we used an intensified camera (Proxitronics NANOCAM HF4 [5]), yet with a video signal output which is digitized using a PC frame-grabber. The photo-cathode is made of S20/Quartz, having a quantum-efficiency of $10 - 15\%$ at the interesting wavelength interval and a low dark current. A two-fold MCP amplified the photo-electrons with a gain of 10^6 and a P46 fast phosphor screen is used. The gating of the camera is done by switching the voltage between photo-cathode and the MCP within 5 ns.

A first test was performed with an 5.8 MeV/u Ar^{11+} beam with an electrical current of 700 μA and a pulse length of 200 μs. This corresponds to $\sim 10^{11}$ particles per macro-pulse passing the 35 mm diameter view-port for the camera. An example is given in Fig. 1 for one macro-pulse recorded at a pressure of 10^{-5} mbar having a relatively large vertical width of 13.6 mm FWHM. The projection of the 2-dim. plot with the 'single photon counting' pixels onto the axis of interest shows sufficient statistics. This can by easily improved by binning, in particular for a large width. The measurement is background-free, even without using any optical filters.

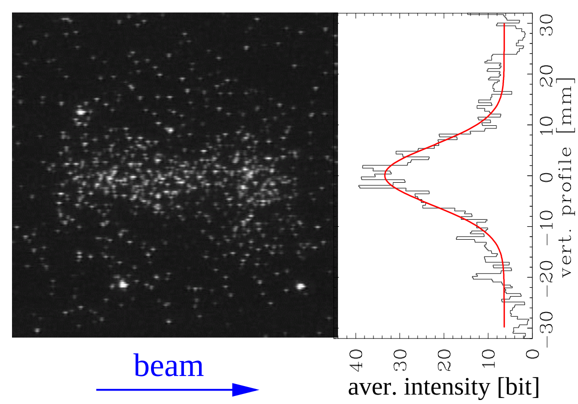

Figure 1: Fluorescence image and projection of a 5.8 MeV/u Ar^{11+} beam

It is shown, that for beams behind the stripper, like tested here, the method can be applied with a moderate pressure bump. While for beams at the first section of the LINAC, before the stripper, the particle current is an order of magnitude higher as well as the energy deposition, therefore a pressure bump is not needed. Using the switching of the photo cathode voltage, movement of the beam within the macro-pulse can be detected easily.

2 IMPROVEMENT OF VIEWING SCREEN SYSTEM

Up to now the viewing screens used at GSI to observe the slowly extracted ion beams from the heavy ion synchrotron are equipped with Chromox targets [6], which have a good sensitivity, a high radiation hardness and are UHV-compatible as well. But a major disadvantage is their longlasting afterglow up to some minutes. Therefore they can not be used for exact measurements of beam movements in the millisecond region as well as changings of beam profile widths from spill to spill. Because of these facts multi-wire proportional chambers (MWPCs) are mainly used when precision measurements are necessary. But these MWPC systems are rather expensive due to the large number of analog electronics. Especially for a commercial therapy facility planned at the university clinicum in Heidelberg [7] an improvement of the GSI viewing screen was aspired leading to an inexpensive alternative to MWPCs.

In addition to the modernization of the image acquistion system (see next section) the main task was to test more suitable target materials. A comprehensive study [8] showed that commercially available phosphor screens [5] - prepared by sedimentation of phosphor grains on a glass or metal substrate - should have the right parameters. Therefore, the following two screens were chosen and compared to Chromox.

Name	Composition	Max. Light Emission	Decay Time (90% to 10%)	Decay Time (10% to 1%)
Chromox	Al_2O_3:Cr	700 nm	some ten ms	$\sim$ min.
P43	Gd_2O_2S:Tb	545 nm	1 ms	1.6 ms
P46	$Y_3Al_5O_{12}$:Ce	530 nm	300 ns	90 μs

Both phosphor screens have reasonable decay times as well as their maximum light output lies in the green region (about 540 nm) which fits ideally to the sensitivity of monochrome CCD sensors.

All screens were tested in two short beam times with protons and carbon ions, the main beam species foreseen for the cancer therapy facility.

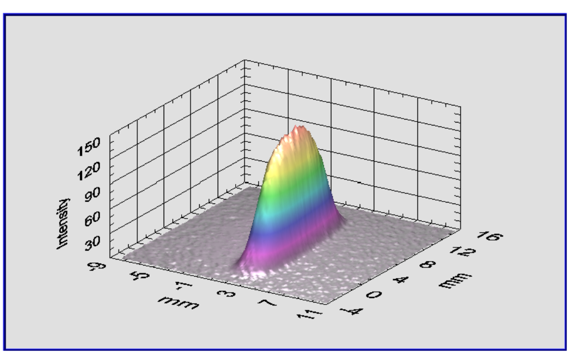

Figure 2: 3D profile of a 356 Mev/u $^{12}C^{6+}$-beam on a P43 target

Fig. 2 shows a typical example of a beam spot image. No differences in size are observed due to the target material, but the yield of light differs by a factor of about 7. The following table shows the values of the summarized surface luminosity relative to Chromox. All measurements were taken with the same camera settings with a 356 MeV/u $^{12}C^{6+}$-beam, a proton beam of 200 MeV shows similar results.

Target material	Rel. yield of light
Chromox	1.0
P43	1.46
P46	0.2

In Fig. 3 the summarized surface luminosity of the target images is compared to a current measurement with an ionization chamber (the last 200 ms of the spill were not measured due to a wrong camera setup). The data are not directly correlated because of the necessary target changes but P43 and P46 show the same time distribution with fluctuations in the ms as the IC. The different yield of light corresponds to the above given table. Differing is the offset and the smaller slope of the Chromox curve which shows directly the longer decay times of this target material.

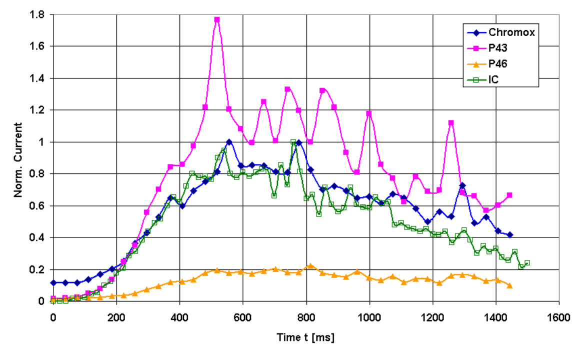

Figure 3: Summarized surface luminosity of the three different targets in comparison to a current measurement with an ionization chamber

No saturation was found in our experiments with up to 4×10^8 carbon ions per second, even at lower energies (80 MeV/u), which lead to higher energy loss in the target. But further studies have to be carried out.

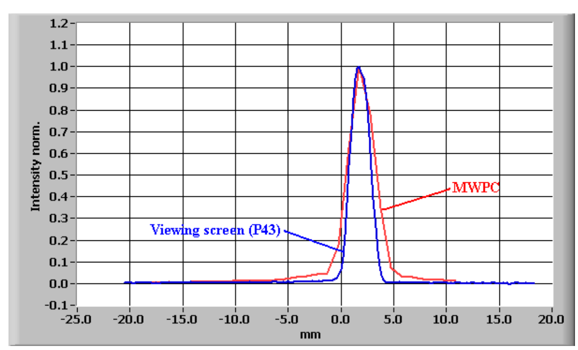

Figure 4: Horizontal profile of a 356 Mev/u $^{12}C^{6+}$-beam on a P43 target in comparison to a MWPC measurement

In comparison to MWPCs smaller profile widths are found by using viewing screens, see Fig. 4. This effect was yet observed by irradiation of films to verify the homogenity of area scans for therapy [9]. From these measurements it can be deduced that viewing screen images generate a more realistic picture of the beam spot size.

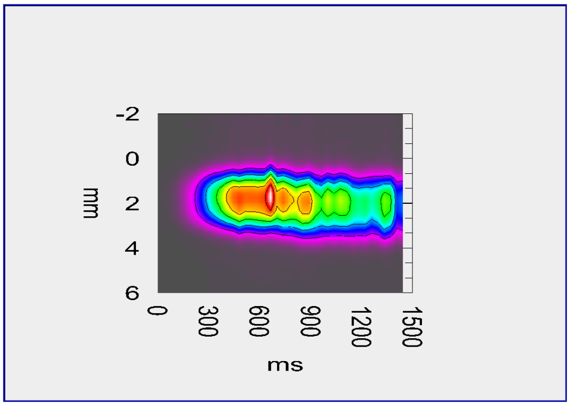

Figure 5: Evolution of the horizontal profile of a 356 Mev/u $^{12}C^{6+}$-beam on a P43 target during the spill

The contour plot in Fig. 5 shows the beam profile evolution during one spill. Even with a frame rate of only 30 images per second the good stability of the beam position - independently from the fluctuating intensity - is verified.

Recapitulating the first results of the target improvements one can state that with restricted parameters in ion species, energy and intensity as foreseen for therapy project viewing screens seem to be a good alternative to MWPCs with the same or even better properties for beam profile measurements.

3 DIGITAL IMAGE DATA ACQUISITION USING IEEE 1394

Until today most CCD cameras transmit the captured images as an analog TV-signal which is digitized afterwards with a framegrabber. This technique has two main disadvantages: the multiple AD-conversions and vice versa and the signal-loss due to noise and reflections on the analog cables. Direct digital readout of CCD cameras came up in the last years, but mostly each company uses its own protocol on different hardware, the cable length between camera and interface is limited to some meters or only point-to-point solutions are offered like “Channel Link”.

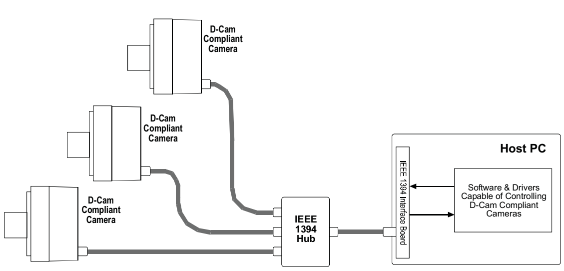

Figure 6: An example of an IEEE 1394 camera network

A new approach in industrial automation is to use the IEEE 1394 high-speed serial bus [10, 11], also known as “FireWire (Apple)” or “i.link (Sony)”. Unlike normal camcorders, which send highly compressed video data, industrial digital cameras for image processing must deliver uncompressed data. For this purposes the DCAM specification [12] was set up. This standard has several advantages for beam diagnostic measurement systems:

- a complete digital data path without any loss of image quality,
- a single bus with up to 63 nodes (see Fig.6 as an example), which can be brigded to other segments,
- multiple cameras with different properties, e.g. resolutions on the same bus,
- isochronous and asynchronous data transfer, with a throughput up to 400 Mb/s (and up to 3.2 Gb/s in the future),
- standardized and inexpensive PC interfaces, cables, hubs and repeaters for the bus infrastructure.

Up to now the cable length is limited to 4.5 meters between the individual nodes without repeaters, but bus extenders using glass optical fibers for longer distances exist [13], and the next IEEE 1394b specification will include standards for longer cable lengths.

For the above mentioned target measurements a prototype camera (type A302fs from Basler, [14]) was used which is capable to take 30 frames per second (maximum) with exposure times of up to 80 ms. The software package was written in LabVIEW using the IEEE 1394 driver for IMAQ to acquire the images and IMAQ Vision for image processing. For the viewing screen tests the camera works reliable and with the pronounced parameters. An intensified version of a similar camera will be built in the next months together with Proxitronic (see more information on [5]) for the residual gas fluorescence monitors.

4 REFERENCES

[1] W. Barth, *Proc. 20th LINAC Conference, Monterey*, p. 1033 (2000)

[2] D.P. Sandoval et al., 5th *BIW, Santa Fe, AIP Conference Proceedings 319*, pp. 273-282(1993)

[3] G. Burtin et al., *Proc.* 6th *Euro. Part. Acc. Conf. EPAC, Vienna*, p. 256 (2000).

[4] L.W. Dotchin et al., *J. Chem. Phys.* **59**, 3960 (1973).

[5] http://www.proxitronic.de

[6] R. Jung, *Proceedings of the* 1st *DIPAC, Montreux, Switzerland*, pp. 54-63 (1993)

[7] A. Peters, P. Forck, 9th *BIW, Boston, AIP Conference Proceedings 546*, pp. 519-526 (2000)

[8] A. Weiss, *“Neues Leuchtschirm-System für hochenergetische Ionenstrahlen”*, diploma thesis, to be published

[9] Th. Haberer, U. Weber, priv.comm.

[10] D. Aderson, *“FireWire systems architecture: IEEE1394a”*, www.mindshare.com

[11] Basler Vision Technolgies, *“IEEE 1394 Technology Brief”*, March 2001, www.basler-mvc.com

[12] 1394 Trade Association, *“IIDC 1394-based Digital Camera Specification, Version 1.30”*, www.1394ta.org

[13] NEC MX/GF4 IEEE 1394 Network Adapter, see http://www.1stt.at

[14] Basler Vision Technolgies, *“Basler A302fs camera manual”*, Nov. 2000, www.basler-mvc.com

CONTROL AND DATA ANALYSIS FOR EMITTANCE MEASURING DEVICES

T. Hoffmann, D.A. Liakin[1]
Gesellschaft für Schwerionenforschung (GSI), Planckstr. 1, 64291 Darmstadt, Germany
E-Mail: T.Hoffmann@gsi.de, Liakin@vitep5.itep.ru

Abstract

Due to the wide range of heavy ion beam intensities and energies in the GSI linac and the associated transfer channel to the synchrotron, several different types of emittance measurement systems have been established. Many common devices such as slit/grid or dipole-sweep systems are integrated into the GSI control system. Other systems like the single shot pepper pot method using CCD-cameras or stand-alone slit/grid set-ups are connected to personal computers. An overview is given about the various systems and their software integration. Main interest is directed on the software development for emittance front-end control and data analysis such as evaluation algorithms or graphical presentation of the results. In addition, special features for improved usability of the software such as data export, project databases and automatic report generation will be presented. An outlook on a unified evaluation procedure for all different types of emittance measurement is given.

1. INTRODUCTION

The GSI linear accelerator provides ion acceleration of all chemical elements from p up to U and allows various energies in a range from 120 keV/u to 15 MeV/u[1]. Therefore in ion source development, ion type changing activities, regular beam optimisation and for commissioning purposes emittance measurement is required. Since the foundation of the GSI facility in 1970 a lot of different types of emittance measurement devices have been installed. Slit/grid systems, dipole-sweep systems but also slit/sandwich systems, a special type of detector using 32 isolated layers with a thickness of 0.15 mm are operated with the GSI control system. However, different types of control software are used within the control system leading to manifold data outputs and evaluation processes. Newer emittance measurement systems like the pepper pot [2,3] or the stand-alone slit/grid device are operated with personal computers and are based on various types of Windows and DOS control and evaluation software. All types of the emittance soft- and hardware components are working properly but reorganisation to a unitary graphical user interface (GUI) and evaluation procedure is mandatory due to improved usability and comparability of the results.

2. STRUCTURE OF THE SOFTWARE

The new designed control and evaluation software, first used for pepper pot emittance measurement, is a bundle of subprograms, which are combined together using unified data structures and Windows Component Object Model (COM) technology. Due to this not only pepper pot emittance measurement devices but also other types could

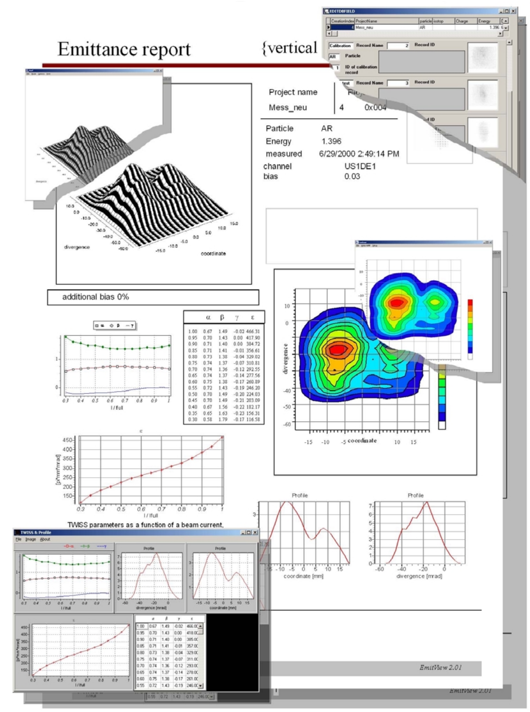

Fig.1. All ‘independent’ software parts are merged into the hardcopy report generation.

be connected without code recompilation. To provide flexibility in data computation few output data formats are realized. Independent data analysis algorithms may be used if they are available as special dynamic libraries.

The software consists of data acquisition, evaluation and visualization tools.

An extensive description of the software on the basis of the pepper pot method is given in [2]. The possibilities of the visualisation part of the software are shown in fig.1. The calculated emittance data is illustrated with various visualisation tools such as contour plot and three-

[1] ITEP-Moscow, work done at GSI.

dimensional surfaces. These tools are implemented as autonomous subprograms and may be run independently. The data like images, tables and graphs produced by these tools are merged into the final printable report.

3. SPECIAL ALGORITHMS

The software includes a set of algorithms. Most of the mathematical routines as grid placement algorithm, data re-sampling, coordinate system recalculating etc. has been evaluated and tested in MATLAB environment before they were implemented in C++ code. Some of them, like grid placement, are used specifically for the pepper pot system, others (noise cancellation, data re-sampling) are necessary to solve common problems. For instance two procedures are briefly described below.

One plane data analysis.

RMS parameter calculation. The root-mean-square phase space distribution parameters are calculated as a normalized sum of matrices elements.

$$V = \sum_{ix}\sum_{iy}\hat{E}; \qquad \hat{e} = \hat{E}\cdot 1/V$$

$$x_0 = \sum\left\{\hat{e}\bullet\vec{X}\right\} \qquad y_0 = \sum\left\{\hat{e}^T\bullet\vec{Y}\right\}$$

$$\sigma_x = \sqrt{\sum_{ix}\sum_{iy}\left\{e_{ix,iy}\cdot(x_{ix}-x_0)^2\right\}}$$

$$\sigma_y = \sqrt{\sum_{ix}\sum_{iy}\left\{e_{ix,iy}\cdot(y_{iy}-y_0)^2\right\}}$$

E and e are original and normalized rectangular intensity matrices in the space-divergence coordinate system.

Obtained statistical values are used for rms twiss coefficients calculation.

To improve accuracy the initial data set may be re-sampled. The improvement is achieved due to the fact that the summation means rectangular rule integration while the re-sampling uses cubic interpolation method.

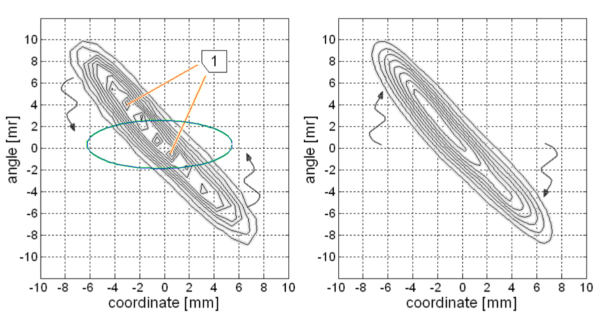

Fig.2. Re-sampling in canonical coordinates allows removing the 'islands' (1) on experimental data.

Geometric emittance. The contour data is used to calculate the geometric emittance dependence of the current. The contours are being calculated using linear data approximation, which leads to better results rather than simple summation. Data re-sampling also improves accuracy of this algorithm.

Re-sampling. To improve accuracy of calculations the data may be re-sampled with smaller steps in both x and x' directions. If usual interpolating routines are applied to convergent or divergent beam data, 'islands' may be produced. To remove these 'islands' the re-sampling is executed in rms emittance ellipse canonical coordinate system. The result of this operation is shown in fig.2.

Data reduction

One of the disadvantages of the pepper pot measurement method is the limited number of beam slices. The number of the slices depends on spot sizes and CCD matrix resolution. When the spacing of the pepper pot mask holes is too small or drift length from the mask to the scintillation screen is too large the spots may overlap each other. Then a different technique can be used

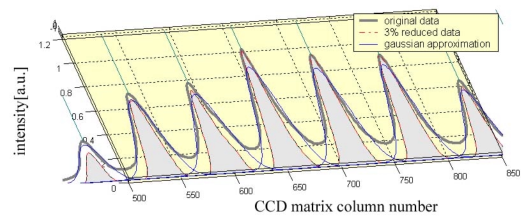

Fig.3. Plot of real profile data evaluated with approximation and offset applying methods.

to improve the device performance. Typical measured two-dimensional emittance data is shown on fig.3. This data is obtained as the integral of a two-dimensional data array along vertical direction (horizontal profile). Each peak represents one slice of the two-dimensional emittance or compared with the slit/grid method every peak would correspond to one slit position.

As it can be seen in fig. 3, the peaks from adjacent 'slits' are significantly overlapped. There are two possibilities for effective peak separation. The first is the data approximation by Gaussian (normal) distribution. In fig. 3 this case is shown thin lined. This variant should be used for noisy data, but some information may be lost. The data acquisition software supports the opportunity to apply an offset value to the initial 2D data and not only to the profile. The result of applying a 3% offset is shown in fig. 3 as a grey highlighted graph. A significant difference between the approximation and the offset applying method is recognizable. It was found that the second method leads to results, which are much closer to the slit-grid measurement than the first one.

4. VISUALIZATION POSSIBILITIES

The results of measurements may be presented in different ways. Due to human mind limitation it is more native to have a few parameters, which values can be easily compared with the others. As a basis the rms TWISS parameters were chosen. To give additional possibilities in beam analysis the contour plot and 3D

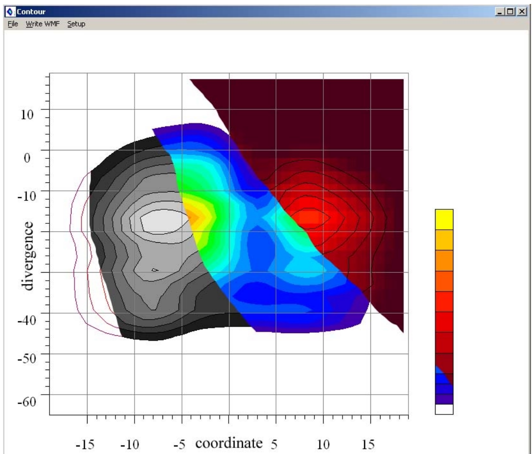

Fig.4. Different types of contour plots are available.

graph are also available for analysing purposes. The operator has several alternatives in selecting the shape of the graphs: contours, bricks or filled contours with different colour palettes in two-dimensional graphs, surfaces, bars or wire frames and standard OpenGL effects like the fog and lighting in three-dimensional case. The twiss parameters are given in table style and as graphs as a function of beam percentage. On the same window the beam profiles in space and angular directions are shown. Each image or graph may be saved in form of Windows bitmap or metafile.

5. DATA IMPORT

The data evaluation part of the software was initially developed to manage the pepper pot system. Meanwhile, this part of software may be used independently to calculate data obtained by other emittance measurement devices.

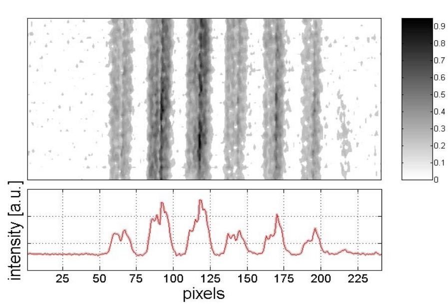

Fig.5. Data from the TWAC injector emittance measurement device had been calculated with the presented evaluation tools.

For example this tool is used with data from a one plane multislit CCD based device, which is used in emittance measurements for ITEP's ISTRA (protons) and TWAC (heavy ions) projects [4], see fig. 5.

6. DATA EXPORT

The software provides the possibility to export raw or evaluated data. The export may be executed on different stages of data evaluation:

- Original data, obtained from CCD camera, or parts to be stored as bitmap file or as a text table in ASCII format.
- ASCII or binary file with vertical and horizontal profiles of modulated beam.
- Beam density distribution in two dimensional phase spaces.
- Four-dimensional beam density distribution as a set of equal charged macro particles.

Data presentation as a row of randomly scattered particles gives possibility to realize the advantages of the pepper pot method due to real four dimensional emittance measurement, which is not available for slit-grid techniques. An obtained array of macro particles can be natively used in beam dynamics simulation programs. A simple real measured data evaluation over a drift space executed and painted in MATLAB is shown on fig.6.

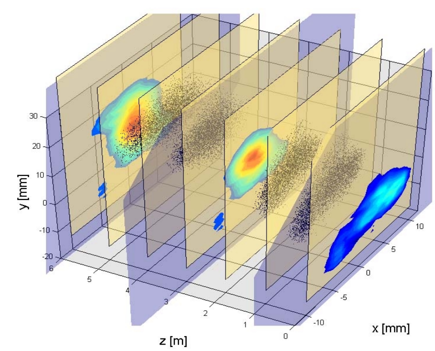

Fig.6. Data, exported as random distributed macro particles allow realizing advantages of the pepper pot method.

7. REFERENCES

[1] P. Forck, P. Strehl, Proc. 4th DIPAC 1999, Chester, UK, pp.42-46.
[2] T. Hoffmann, W. Barth, P. Forck, A. Peters, P. Strehl, D. A. Liakin, Proc. 9th BIW 2000, Cambridge, USA, pp. 432-439
[3] D.A.Liakin, T. Hoffmann, P. Strehl, et. al., Proc. 4th DIPAC 1999, Chester, UK, pp. 161-163
[4] Kozodaev A.M. et. al. Proc. *PAC97*, pp.3848 (1997).

TEST OF DIFFERENT BEAM LOSS DETECTORS AT THE GSI HEAVY ION SYNCHROTRON

P. Forck and T. Hoffmann
Gesellschaft für Schwerionenforschung GSI, Darmstadt, Germany.
e-mail: p.forck@gsi.de

Abstract

For the sensitive process of slow extraction from a synchrotron a reliable control of the beam losses is needed. We have tested several types of particle detectors mounted at the extraction path of the SIS: A BF_3-tube for pure neutron detection, a liquid and a plastic scintillator detecting neutrons, gammas and charged particles and an Ar filled ionization chamber mainly sensitive to charged particles. While the count rate is quite different, the time evolution of all detector signals during the spill are similar, but the plastic scintillator has the highest dynamic range. This type is going to be used for beam alignment.

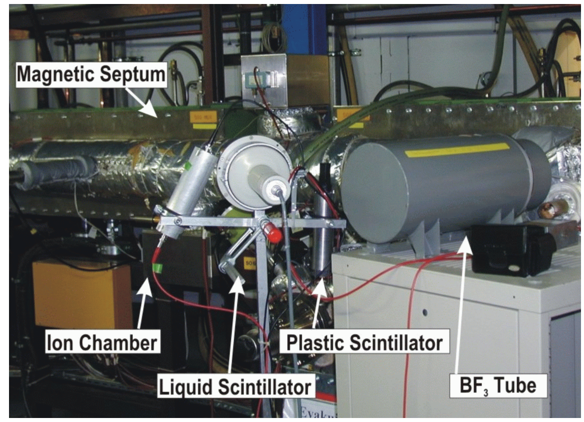

Figure 1: The detectors installed at the SIS-extraction.

1 DEMAND FOR LOSS MONITORS

To control the beam losses during the beam alignment and operation of an accelerator it is an important issue to prevent permanent activation. At the GSI heavy ion synchrotron SIS all heavy ions can be accelerated from 11.4 MeV/u to a variable final energy up to $\sim$ 1.5 GeV/u. During the last years a large increase of beam current up to a factor of 100 in particular for heavy specious was possible due to the installation of an electron cooler and an upgrade of the LINAC [1]. Most of the experiments are using third order resonance extraction having an extraction time of several seconds. Most of the losses occur during this extraction, some of them are unavoidable, others should be minimized by careful setting of the accelerator parameters like tune changes, focusing, steering angles, in particular of the septa etc. The highest activation is measured around the electrostatic septum (mostly due to 'unavoidable' losses for slow extraction), the following dipole magnet inside the SIS and the magnetic septa due to their small acceptance (here the right orientation of the transverse emittance is needed). Compared to other large accelerators there are some differences concerning the loss: Firstly the currents in terms of particles per second are relatively low due to the long cycle time using slow extraction. Secondly different ions with a wide span of current and final energy are accelerated. Thirdly the detectors should be used for the alignment procedure and not for creating an emergency interlock (like used elsewhere for quench-protection of superconduction magnets).

The cross section of the production of secondary particles is not well known for heavy ions. The energy of the colliding nuclear system is comparable to the energy of it constituents leading to a more complex reaction mechanism, as used e.g. for high energy protons [2]. Moreover, the penetration depth is in the order of several cm, and the assumption of a 'thick target' can not be applied for particles hitting the vacuum chamber. Some investigations using heavy ions have been made to measure the cross section, scaling laws and angular distribution [3], but not all needed parameters (ion specious and energy) are covered. In addition the charged primary or secondary particles loose a noticeable amount of energy in the target due to electronic stopping. Therefore the main secondary particles reaching the detector are expected to be neutrons from fragmentation and spallation processes. The angular distribution is peaked in forward direction inside a cone having an opening angle of several degrees with a strong depending on the primary ion's energy [3]. Due to all these dependences, an absolute dose cannot be generated from the data.

2 TYPES OF DETECTORS

Different detectors have been tested at the SIS in a distance of $\sim$3 m and an angle of $\sim 20^o$ from the magnetic septa, see Fig. 1. One of them is only sensitive to neutrons, while the others have different sensitivity to other secondary particles, see below. For the purpose of beam alignment, a high dynamic range i.e. large count-rate capability and a background free operation is needed. General demands are an easy and hazard-free installation and a stable operation.
Liquid scintillator: An older device form Nuclear Enterprise containing NE 213 liquid scintillator (decay time 3.2 ns [4]) in a cylinder container of 1 l was installed. The light generation is based on collisions of the neutrons with hydrogen atoms of the polymers (elastic n+p-reaction), the

proton's electronic stopping leads the scintillation. For other charged particles the electronic stopping creates directly the scintillation [4]. To have the possibility of pulse shape discrimination (i.e. the discrimination between γ and neutrons) an integrating pre-amp is attached to the photomultiplier output, restricting the maximum count-rate to $\sim$ 30 kHz. This discrimination is not used here. The material is sensitive to γ, n, e^- and charged hadrons. Care has to be taken due to the flamability of the solvent.

Plastic scintillator: Like in the liquid scintillator, the elastic n+p-reaction creates the scintillation light for neutrons, and direct energy loss is measured for charged particles. We use a block of $20 \times 20 \times 50\,\mathrm{mm}^3$ BC400 standard plastic material (decay time 2.4 ns [4]) coupled to a fast photomultiplier (Philips XP2972) having a voltage of 1500 V. A counting mode is used via standard discriminators (LeCroy 4608C) to get high dynamic range up to several MHz. The material is sensitive to γ, n, e^- and charged hadrons. The pulse height distribution shows a broad distribution due to the different detected particles and their energy deposition.

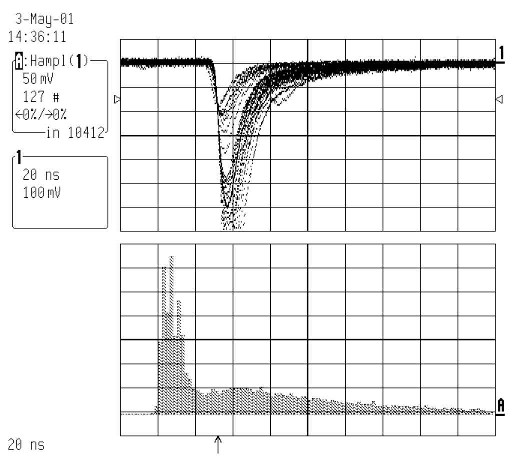

Figure 2: Typical pulses from the plastic scintillator (top, 100 mV/div and 20 ns/div) and their pulse height distribution (bottom, 50 mV/div).

BF_3 proportional tubes: To have the possibility to measure only neutrons a cylindrical proportional tube (diameter 15 mm, length 400 mm) filled with BF_3 is installed. For thermal neutrons the reaction B+n $\rightarrow$ Li + α has a high cross section ($\sim$ 1 kbarn) and is exothermic (Q-value of 2.3 MeV) [4]. To slow down the fast neutrons form the primary beam interaction concentric layers of polyethylene with an outer diameter of 220 mm surround the proportional tube. Special precaution are done to get a flat detection efficiency as a function of the angle. Normally these detectors are used at nuclear power plants for neutrons with energy up to 10 MeV, but the thermalization yield of the neutrons can be extrapolated at least up to 100 MeV.

Ionization chamber: In contradiction to the BF_3-tube, an IC is not sensitive to neutrons and has a low efficiency for γ, only charged hadrons and electrons are detected. A type of IC routinely used at Brookhaven RHIC [5] is build of

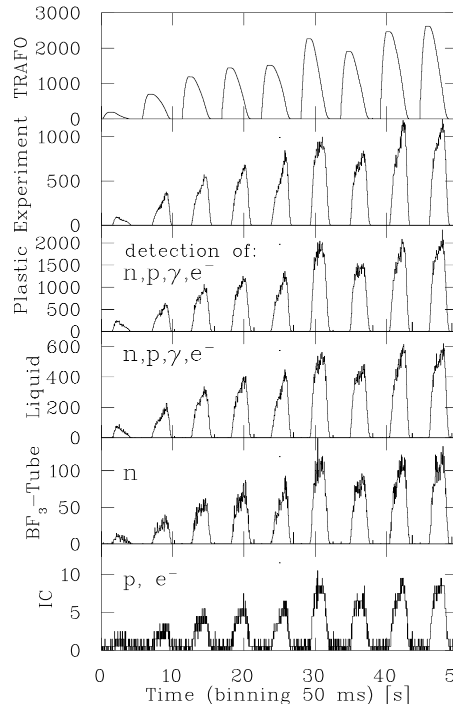

Figure 3: Typical example from different beam loss monitors for a O^{8+} beam at 800 MeV/u with up to 4×10^{10} particles per spill.

a sealed 100 mm long cylinder with outer diameter of 38 mm filled with pure Ar at $\sim$ 970 mbar. The readout is done in the current mode using a current-to-frequency converter with the range of 100fA equals one count, i.e. a resolution of 1 pA for the current is reached [6]. This current is directly proportional to the absorbed dose.

Solid state detector: At the most accelerators PIN-diodes are used [7]. We installed a PIN-diode of size $10 \times 10\,\mathrm{mm}^2$ and a thickness of 300 μm. An integrating pre-amp and a spectroscopy-amp is used for a good energy resolution. But the measured pulse height distribution is a comparable to the one of the plastic scintillator. This type is sensitive only to charged hadrons. For the application of beam alignment, the count-rate of this small active volume is too low.

3 COMPARISON OF THE DETECTORS

To fulfill the requirements described above test with typical beam parameter were taken with the detectors installed at the magnetic extraction septum at the SIS. A typical example is shown in Fig. 3 for a O^{8+} beam accelerated from 11.4 MeV/u to 800 MeV/u and then extracted slowly within 3 s. The maximum number of stored particles was 4×10^{10}, which is close to the incoherent space charge limit. The signal as a function of time seen at the figure is displayed together with the signal for the synchrotron dc-transformer (top, arbitrary units) and a signal proportional to the extracted current measured at the experiment location (second plot, using a secondary electron monitor in arbitrary units [8]). The general feature is, that the signals for the different loss monitors are showing the same time behavior. This is not directly evident due to the different detection mechanisms. This shows the predominant role of the 'prompt' radiation (prompt within a time scale of ms) what ever the type of secondary radiation consists of. The signals of all detectors are background-free, showing the minor role of permanent activation compared to the signals induced during the spill.

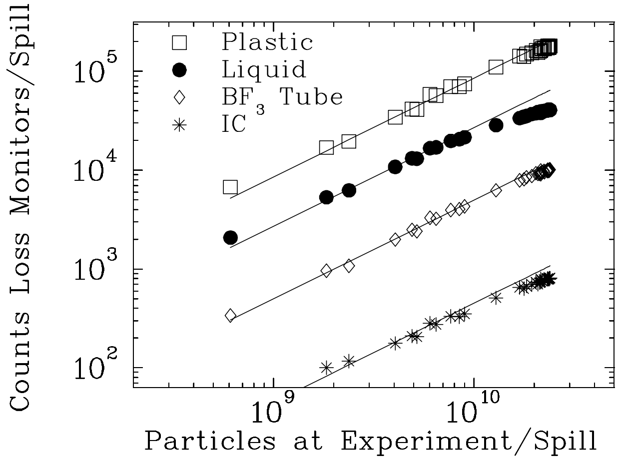

Figure 4: Linearity of the loss monitors as a function of the current at the experiment, with the beam parameters as Fig 3. The lines are linear fits.

The linearity of the different detectors is better seen in Fig. 4 where the total counts for one spill are shown as a function of the current detected at the experiment. The count-rate is quite different: The plastic scintillator shows the maximum rate, about a factor of 30 more than the BF_3-tube, due to the detection of more categories of secondary particles. The liquid scintillator shows a lower rate; the saturation for the highest rate is due to the slow integrating per-amp. The IC is lower by a factor of 200 as compared to the plastic scintillator. The dynamic range needed for the optimization procedure is highest at the plastic scintillator, making this type a preferable choice for our application. With this high rate the losses during the spill can be reduced e.g. by changing the extraction angle during the spill.

More tests were done using other primary ions from d to U having different final energies. The count-rate varies much with the ion specious, but no significant change in the ratio of the detector's count-rate has been seen as a function of the ions nuclear charge. The radiation hardness of the plastic scintillator was not yet investigated.

4 BEAM ALIGNMENT USING THE PLASTIC SCINTILLATORS

Using the plastic scintillator a first test has been done to minimize the losses close to the septa. We installed them each left and right close to the extraction devices at five different places to examine the capability for the alignment. As an example, Fig. 5 shows the rate for a d beam at 250

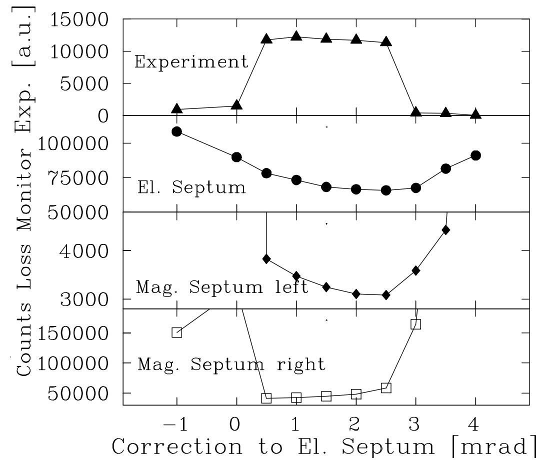

Figure 5: Counts per spill from three loss monitor locations and the current at the experiment averaged over 10 spills as a function of the angle electrostatic septum for a 250 MeV/u d beam.

MeV/u with 2×10^{11} particles. The voltage on the electrostatic septum is varied yielding a slightly different extraction angle. The losses varied due to this correction at the sensitive locations, while the current measured at the experiment shows no significant change. To monitor the losses instead of the transmitted current is a more sensitive method due to the direct determination. In addition, the installation of several devices at the sensitive location can be done easily. The large dynamic range of plastic scintillators guarantee a linear signal behavior even in the case of large differences in the left/right count-rate. More investigations have to be done to proof the capability for the alignment for the operating of the SIS.

Acknowledgment: We like to thank D. Gassner for the release of the IC used at RHIC.

5 REFERENCES

[1] W. Barth, *Proc. 20^{th} LINAC Conf., Monterey*, p. 1033 (2000), M. Steck et al., *Proc.* 6^{th} *Euro. Part. Acc. Conf. EPAC, Stockholm*, p. 550 (1998) and references therein.

[2] A.H. Sullivan, *A Guide to Radiation and Radioactivity Level near high Energy Particle Accelerators*, Nuclear Technology Publishing, Ashford (1992).

[3] S. Menard et al., *Phys. Rev. ST-AB, 033501* (1999). S. Agosteo et al., *Nucl. Instrum. Meth.* **A 459**, p. 58 (2001).

[4] G. Knoll, *Radiation Detection and Measurement*, John Wiley, New York (1999).

[5] R.E. Shafer et al., *Proc. 12^{th} intern. Conf. High Energy Acc., Batavia*, p. 609 (1983). D. Gassner et al., *9^{th} Beam Instrum. Workshop BIW, Cambridge*, p. 392 (2000).

[6] H. Reeg, *Proc. 4^{th} Workshop on Diagn. Instrum. Part. Acc. DIPAC, Chester*, p. 140 (1999).

[7] K. Wittenburg, *9^{th} Beam Instrum. Workshop BIW, Cambridge*, p. 3 (2000).

[8] P. Forck et al., *Proc. 3^{th} Workshop on Diagn. Instrum. Part. Acc. DIPAC, Frascati*, p. 165 (1997).

SOURCE IMAGING WITH COMPOUND REFRACTIVE LENSES

O. Chubar, e-mail: chubar@esrf.fr
M. Drakopoulos, A. Snigirev, T. Weitkamp
ESRF, European Synchrotron Radiation Facility, Grenoble, France

NO PAPER SUBMITTED

References

B. Lengeler, C. Schroer, J. Tümmer, B. Benner, M. Richwin, A. Snigirev, I. Snigireva & M. Drakopoulos, "Imaging by parabolic refractive lenses in the hard X-ray range", J. Synchrotron Rad., 1999, vol.6, p. 1153.

T. Weitkamp, M. Drakopoulos, A. Souvorov, I. Snigireva, A. Snigirev, F. Günzler, C. Schroer & B. Lengeler, "Direct imaging of high-energy synchrotron radiation sources using X-ray lenses", in Free Electron Lasers 1999, edited by J. Feldhaus and H. Weise, 2000 Elsevier Science B.V., p. II-117.

T. Weitkamp, O. Chubar, M. Drakopoulos, I. Snigireva, A. Snigirev, C. Schroer, F. Günzler & B. Lengeler, "Electron beam size and profile measurements with refractive X-ray lenses", Proc. of EPAC 2000, p. 1824.

T. Weitkamp, O. Chubar, M. Drakopoulos, A. Souvorov, I. Snigireva, A. Snigirev, F. Günzler, C. Schroer & B. Lengeler, "Refractive lenses as a beam diagnostic tool for high-energy synchrotron radiation", to appear in NIMA (Proc. of SRI 2000).

A ZONE PLATE BASED BEAM MONITOR FOR THE SWISS LIGHT SOURCE

C. David, Laboratory for Micro- and Nanotechnology, Paul Scherrer Institute, CH-5232 Villigen

V. Schlott, A. Jaggi, Swiss Light Source, Paul Scherrer Institute, CH-5232 Villigen, Switzerland

Abstract

At the Swiss Light Source, a source imaging set-up is planned on a dedicated dipole magnet beam-line. A transmission Fresnel Zone Plate will be used to generate a demagnified image of the source at a photon energy in the 1.8 keV range. The image will be acquired by scanning a pinhole in the image plane. A diffraction limited spatial resolution of approximately 2 microns can be anticipated. The concept has the advantage of having no components operated in reflection, and no components inside the front-end.

1 PRINCIPLE OF OPERATION

Source imaging can provide valuable information about the size, shape, position, and stability of 3rd generation synchrotron radiation sources, and allows for an optimisation of the brilliance by minimizing the coupling parameter [1-3]. At SLS, a bending magnet beamline (12-B) is reserved for diagnostics purposes. At this location electron beam size, emittance and coupling measurements are planned. Apart from that, bunch purity and bunch length measurements have to be performed at the same beamline using visible synchrotron radiation. For beam size measurements we are expecting 1-sigma horizontal beam size of 45 µm and 1-sigma vertical beam size of 40 µm for 1% emittance coupling. The horizontal emittance is expected to be 4.8 nmrad at 2.4 GeV beam energy. However, the storage ring design allows much smaller coupling values for different lattice modes. Emittance coupling of 0.1% would already lead to vertical 1-sigma beam size of 13 µm. Thus, a resolution in the micron range is necessary.

Apart from the required resolution, some practical constraints have to be taken into account. Firstly, it is desirable to have no reflective components in the imaging system that could introduce aberrations and thus affect the source size measurements. Secondly, it is advantageous to have no components inside the beamline's front end. This allows for easier access and alignment and it is possible to remove the set-up from the beam without complications to use the beamline for other experiments. In our case this means, that the first component of the monitor has a distance from the source of at least g=10 m. Generating a magnified image of the source would thus require a very long, potentially unstable set-up. To keep the set-up short, we chose a demagnifying geometry.

The separation of two distant point sources that can be distinguished according to the Rayleigh-criterion is generally limited by the diffraction of the optics aperture [4]. This means that the distance between the images of two distinguishable source points is limited to: $B= 0.61\cdot\lambda\cdot f/r \approx 0.61\cdot\lambda\cdot b/r$, where λ is the light wavelength, f the focal length, and b the image distance. This corresponds to a source size that could be resolved of $G = B \cdot g/b = 0.61 \cdot\lambda\cdot g/r$. If we introduce the solid angle α = 2r/g collected by the optics, we see that

$$G=1.22\cdot\lambda/\alpha. \quad (1.0)$$

The angular divergence of the bending-magnet beam line 12-B is in the order of 0.5 mrad, which limits the useful optics diameter to 5 mm at 10 m source distance. According to eq. (1.0) this results in a resolution of 1.7 µm at 1.8 keV photon energy (0.7 nm wavelength). However, it should be noted that the resolution criterion applied in this calculation is very conservative. The size of a source which is larger than the diffraction limit of the set-up can be determined with much better accuracy by deconvolution with the point spread function of the optical system. This is especially true if the function describing the source profile is known and e.g. only the position and width of a gaussian have to be determined.

Fresnel zone plates have been successfully applied for focusing and high resolution imaging in the x-ray range. As a good approximation the radius r_n of the n^{th} ring follows the law

$$r_n = \sqrt{n\cdot\lambda\cdot f} \quad (1.1)$$

where f is the first order focal length. The outermost (smallest) zone width dr_n the total zone number n and the total radius r are linked by the following equations:

$$dr_n = r/2n \quad (1.2)$$

$$f = 2r\cdot dr_n/\lambda \quad (1.3)$$

$$f = r^2/(n\cdot\lambda) \quad (1.4)$$

The following properties of zone plates are of importance in the context of the presented set-up:

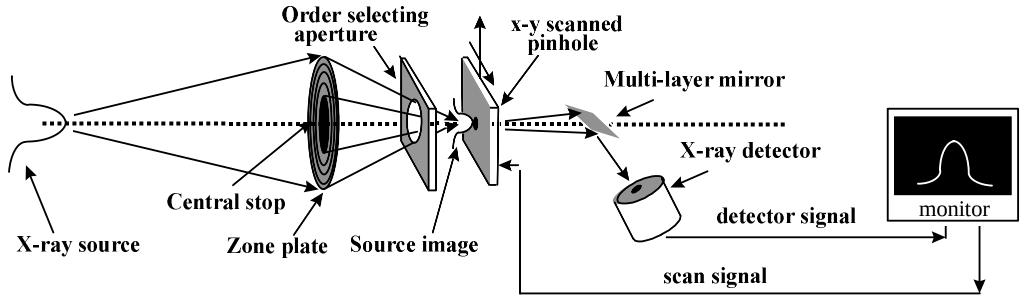

Fig. 1: scanning type set-up for beam monitoring planned for the SLS

- A zone plate's focal spot size δ is limited by its outermost zone width dr_n: $\delta = 1.22 \cdot dr_n$.
- Due to the high chromatic error according to (1.4), the bandwidth $\lambda/\delta\lambda$ has to be greater than the zone number n. For smaller bandwidth, the obtainable resolution gradually decreases. It has been calculated [5] that the resolution is reduced only by a few percent for $\lambda/\delta\lambda = 1/4 \cdot n$.
- For reasons of diffraction efficiency only the first focusing order is used in most cases. Other diffraction orders (especially the zeroth order) can be eliminated by a central stop near the zone plate plane and an order selecting aperture (see figure 1).

From Eq. 1.0 it is clear that for a given wavelength and source distance, the resolution in the source G depends on the optics diameter, but not on the outermost zone width dr_n. One has the freedom to choose this parameter within certain limits. A small outermost zone width only gives the advantage of a shorter focal length and thus a shorter optical set-up. On the other hand, such zone plates are more difficult to produce, and the image is more strongly demagnified which requires a smaller pinhole to avoid an additional loss in resolution. However, the most important consequence of a small dr_n is that a narrower band width is required to produce a diffraction limited image due to the larger zone number. This decreases the total signal, since for optimum resolution all intensity outside the allowed band has to be filtered out, and it increases the demands on the band pass filter. Thus, zone plates with larger dr_n and longer focal lengths should be preferred for beam monitoring purposes.

There are two principal ways of imaging a synchrotron source. Either the source image is collected by a spatially resolving detector like a phosphorous screen and a CCD camera. In this case, the granularity of the detector which is at least in the order of several microns requires a 1:1 or even a magnifying set-up. Under the constraint that the first optical element should be outside the shielding wall of the beam line, i.e. at least 10 m away from the source, this would result in an undesirably long set-up. This could be overcome by a two step imaging set-up, where the (demagnified) intermediate source image is strongly magnified by a second lens. Such a set-up is very similar to that of the imaging type x-ray microscopes. Indeed these microscopes are capable of imaging the source. The set-up is, however, complicated, difficult to align, and it requires a costly, spatially resolving detector system. Furthermore, the source image contains contributions of defocused wavelengths if no monochromator is used. The use of such a (reflective) device has the inherent problem that one does not directly image the source but a possibly distorted image from the monochromator.

To avoid these difficulties we chose the principle based on scanning a pinhole through the image plane of a zone plate as shown in figure 1. The source is imaged by a single zone plate, the (demagnified) image is recorded by scanning a pin-hole in the image plane and detecting the transmitted flux. An order selecting aperture (OSA) and a central stop remove all radiation from other diffraction orders. Since the zone plate is highly chromatic, the focused source image for the wavelength corresponding to the distance between zone plate and pinhole is superimposed by the defocused images of other wavelengths. To suppress these defocused contributions, a multilayer mirror or a crystal can be used as a band-pass filter. This filter can be very small in size, furthermore it does not have to meet any further demands with respect to its flatness etc. As a detector a simple photo-diode can be applied. The set-up is easy to align, since all optical components except for the detector are on the optical axis.

2 OPTIMUM PHOTON ENERGY

The most important decision that has to be taken is the one about the used wavelength. Although the diffraction limit of the obtainable resolution becomes more favourable for shorter wavelengths, we propose to use radiation in the 0.8 nm wavelength range (1.8 keV photon energy) for a number of practical reasons: Firstly, this energy range is very favourable for the fabrication of zone plate optics with the required dimensions and high diffraction efficiency. Especially silicon, a material easy to pattern by reactive ion etching, has a very favourable ratio of phase shift and absorption. This means that phase zone plates with efficiencies up to 35% can be fabricated (see Fig. 2).

Secondly, the proposed method requires a pinhole for image formation with a sub-micron diameter. For hard x-rays such pinholes are extremely difficult to obtain with high optical contrast. For 0.7 nm radiation, the transmission of a 1 µm thick Ta layer is already below $1{\cdot}10^{-3}$, which allows for the application of thin film pinholes fabricated by Focused Ion Beam technology [6].

Compared to lower energies, 1.8 keV radiation has the advantage of a higher transmission for filters and support membranes (93% transmission for 1 µm thick Si). As a result of the above considerations, the planned layout of the beam monitor is given in Table 1.

Table 1: Parameters of a beam monitor for SLS

Wavelength	0.7 nm
distance source – zone plate	10 m
zone plate diameter	4 mm
central stop diameter	2 mm
diffraction limit of resolution	2.1 µm
outermost zone width	0.35 µm
focal length	2 m
distance zone plate - source image	2.5 m
demagnification factor	4
number of unobstructed zones	1700
required bandwidth $\lambda/\delta\lambda$	500
pinhole diameter	0.4 µm
field of view (3× expected FWHM)	300 µm
range of pinhole scanner	75 µm
Number of pixels	256 x 256

3 EXPECTED SIGNAL

The proposed layout is the basis for an estimation of the expected photon flux. The spectral flux density at the beamline 12 B has been calculated to be $3{\cdot}10^{11}$ photons/sec/0.1%BW/mm^2 on the optical axis at 0.7 nm wavelength and 10 m distance from the source. By moving in the direction of the radiation, we can estimate the signal at the detector.

First element in the beam will be a transmission filter membrane to reflect most of the visible and UV spectrum. Its transmission is estimated to be 0.5. The zone plate has an area of about 12 mm^2 of which about 3 mm^2 is obstructed by the central stop. The effective collecting area is thus 9 mm^2. If we assume a diffraction efficiency of a binary Si zone plate including support membrane absorption of 20%, we are left with a spectral flux of approximately $3{\cdot}10^{11}$ photons/sec/0.1%BW behind the zone plate. In the focal plane the spectral flux is drastically increased: assuming a source size of 100 µm x 20 µm (i.e. 0.1% coupling), the demagnfied image will be 25 µm x 5 µm in size, which means that the flux will go into an area of about 10^{-4} mm^2. This gives a spectral flux density of about $3{\cdot}10^{15}$ photons/sec/0.1%BW/mm^2 in the focal spot.

The area of the pinhole is about 0.1 µm^2 = 10^{-7} mm^2. This yields a spectral flux of $3{\cdot}10^{8}$ photons/sec/0.1%BW behind the pinhole. Assuming a band width of the multilayer band pass of $\lambda/\delta\lambda = 500$ and a reflectivity of 10%, we end up with $6{\cdot}10^{7}$ photons/sec at the detector. For a quantum efficiency of 20% this would mean a count rate in the order of $1{\cdot}10^{7}$ Hz in the center of the source image. As indicated in the table above, two dimensional scans should have in the order of $5{\cdot}10^{4}$ pixels. For an image acquisition time of 10 seconds this would still give 2000 counts per pixel. Taking into account a shot-noise of $n^{1/2}$ this would correspond to an image with 5-6 bit depth. Line scans to determine the source size and position in horizontal or vertical direction could of course be taken with scan frequencies of many Hertz.

REFERENCES

[1] P. Elleaume, C. Fortgang, C. Penel, E. Tarazona, ”Measuring Beam Sizes and Ultra Small Emittances Using an X-Ray Pinhole Camera”, J. Synchr. Rad. Vol. 2 (1995), p. 209.

[2] W.B. Peatman, K. Holldack, “Diagnostic front end for BESSY II”, J. Synchrotron Rad. 5 (1998) p.639.

[3] Z. Cai, B. Lai, W. Yun, E. Gluskin, D. Legnini, P. Illinski, G. Srajer, “Beam Size Measurement of the Stored Electron Beam at the APS Storage Ring Using Pinhole Optics” Rev. Sci. Instr. 67 (1996) p.1.

[4] M. Born, E. Wolf, “Principles of Optics”, Pergamon Press (1980) p. 459.

[5] J. Thieme: “Beugungstheoretische rechnungen zu den Abbildungseigenschaften von Zonenplatten in der Röntgenmikroskopie', PhD-Thesis, University of Göttingen (1988)

[6] C. David, C. Musil, A. Souvorov, B. Kaulich: ”Nanofabrication of custom x-ray optical components”, in: X-ray microscopy, Proceedings of the sixth international conference, Eds.: W. Meyer-Ilse, T. Warwick, and D. Attwood, American Institute of Physics (2000) p. 704

MICROWAVE PICKUPS FOR THE OBSERVATION OF MULTI GHZ SIGNALS INDUCED BY THE ESRF STORAGE RING ELECTRON BUNCHES

E. Plouviez, ESRF, Grenoble, France

Abstract

The length of the bunches stored in ESRF lies in the 30 ps to 120 ps range (FWHM). The observation of single bunch phenomena like transverse or longitudinal oscillations or bunch length variation requires the acquisition and analysis of signals at frequencies higher than 10 GHz. A set of microwave cavity pick ups operating at 10 GHz and 16 GHz together with the appropriate electronics has been implemented on the ESRF storage ring; it detects the wall currents on the vacuum chamber due to the electron beams circulation. We describe the design of these cavities, give the result and analysis of measurements performed with the pick ups and indicate how we plan to use these devices as beam diagnostics

1 SINGLE BUNCH SIGNALS

Some examples of single bunch oscillation simulations are shown in the figure 1 (longitudinal oscillation) and 2 (transverse oscillation).

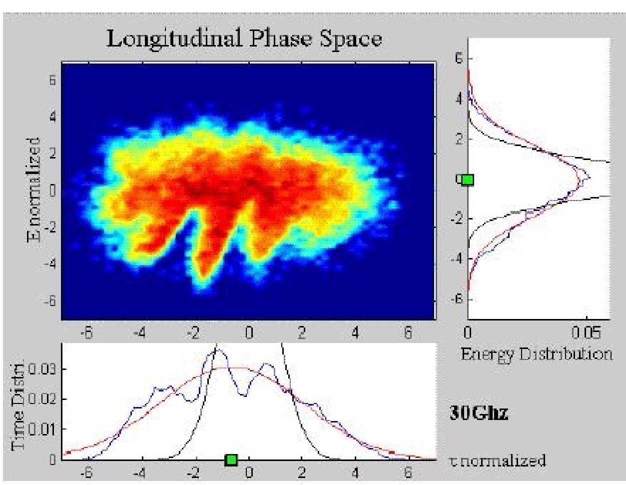

Figure 1: simulation of a microwave longitudinal instability caused by a 30 GHz broadband impedance [1]

For bunch lengths in the 30 ps to 120 ps range, the spectrum of the image currents of the bunch on the vacuum chamber will extend up to tens of gigahertz. However, especially in single bunch filling, the pattern of this spectrum is very repetitive: the parameters of interest are usually the frequency offset of the side bands of the harmonics of the revolution frequency ; So the analyze of an oscillation will only require the study of a narrow span of the total spectrum, in a part of the spectrum where the line amplitudes will be sufficient to be properly detected. An advantage of detecting the beam signal in a narrow span of its total spectrum is also to reduce the large peak/average level of a single bunch signal, avoiding the saturation of the detection electronics. In order to acquire this narrow bandwidth signals, we have developed and implemented dedicated pick ups on the ESRF storage ring

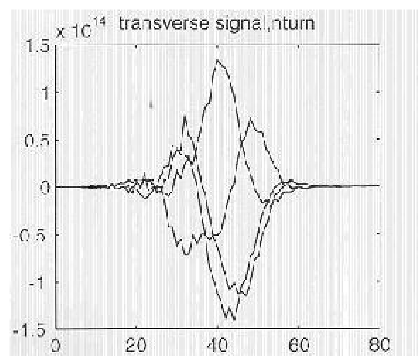

Figure 2: time domain simulation of a short rise time single bunch vertical instability [2] (horizontal scale:1ps/div)

2 PICK UP DESIGN

2.1 General Layout

The pick up principle and mechanical design is shown in the figure 3. The pick up is a 7mm diameter-2mm thick vacuum tight cylindrical iris filled with ceramic. The iris couples the beam image current to the TM010 mode of a pill box cavity. The frequency of this mode is the Nth harmonic of f_{rev}=352.2 MHz, revolution frequency of the beam. The iris diameter and thickness sets the coupling of the cavity to the image current. Two sets have been designed with TM010 mode frequency equal to 29 X f_{RF} = 10.213 GHz and 45 and 45 X f_{RF} = 16.2 GHz. The choice of these frequencies is consistent with the spectrum expected of signals induced by bunches with lengths ranging from 30 ps to 120 ps. The design was optimised using the Agilent HFSS high frequency electromagnetic simulator. By using cavities with different resonating frequencies, we expected to be also able to monitor the variation of the bunch length as function of the bunch charge. The two sets of cavities have been installed on the storage ring. (the set up would allow the mounting of three sets of cavities). The bandwidth of the cavities is 20 MHz for the 10.2 GHz cavity and 30 MHz for the 16.2 GHz cavity.

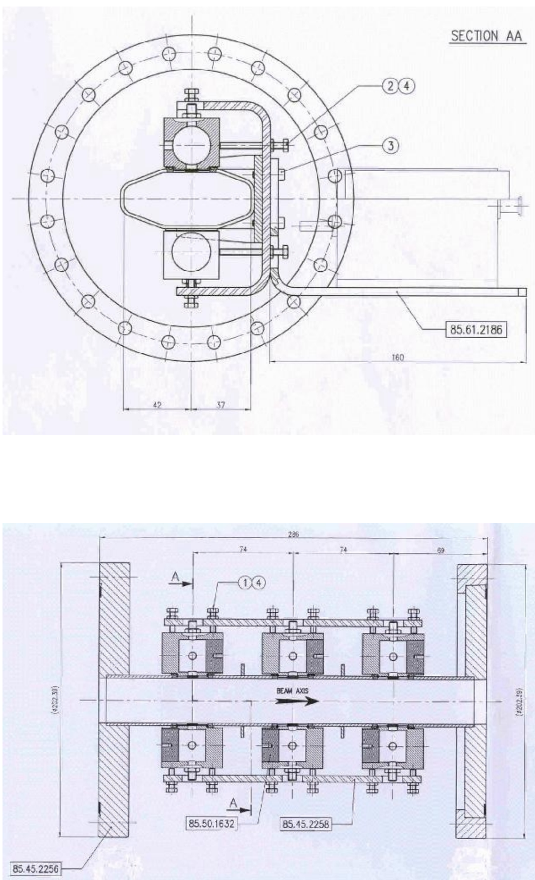

Figure 3:Pick ups front and side view

3 CAVITY SIGNALS DETECTION

The signal from the upper and lower cavity are combined using passive HF combiners to get their sum Σ signal or difference Δ signal. The Σ signal will be used to study the single bunch longitudinal parameters and oscillations of the beam and the Δ signal to study the transverse oscillations. The HF combiner output signals are detected using a 2 stage receiver scheme. The figure 4 shows the layout of the 10.2GHz cavities receiver; the 16.2 GHz cavities receiver is similar. The first stage components are implemented very close to the cavity, on the support visible on the right side of the front view, in order to reduce loses in the connections: The N X f_{RF} signals from the cavities are mixed with a local oscillator signal at (N-1) X f_{rev} to produce a signal at an intermediate frequency IF = f_{rev}. The phase of this (N-1) X f_{RF} signal can be adjusted in order to have its maximum in synchronism, in the mixer, with the signal induced by the center of mass of the bunch, in order to detect the transverse bunch center of mass motion, or in quadrature, in order to detect signals induced by differential head-tail oscillations. The 352.2 MHz output signals of the first stage are sent to the technical gallery, 20 m away, to an homodyne receiver. The 352.2 MHz signal is mixed with a f_{RF} reference signal to perform a vector detection: the in phase detection is used to perform a bipolar detection of the transverse vertical oscillation signal (on the Δ signals) or a detection of the amplitude modulation due for instance to a quadrupolar longitudinal oscillation (on the Σ signals). The quadrature detection is used to study the phase oscillations (on the Σ signal).

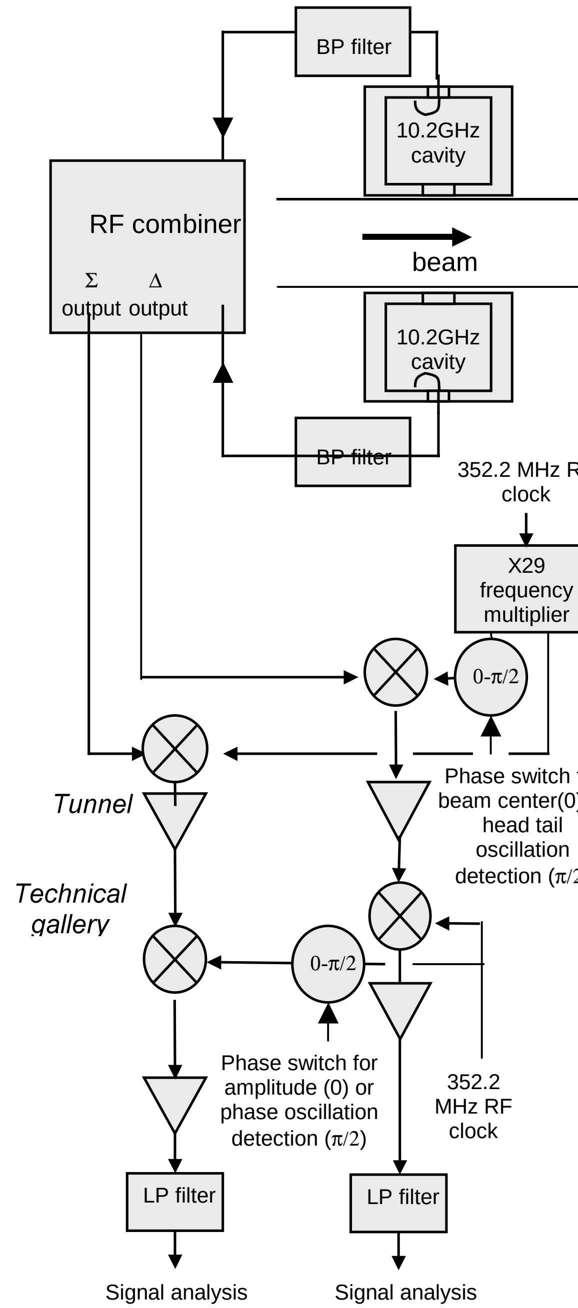

Figure 4: layout of the cavity signals detection electronics (10.2 GHz cavities)

4 SIGNALS MEASURED ON THE ESRF BEAM.

2.1 Longitudinal oscillations

Figure 5a, 5b and 5c shows the spectrums of the 16.2 GHz cavities Σ signal for 5 mA, 10 mA and 16 mA in single bunch filling. The transition from a regime with an incoherent bunch lengthening when the current increases, below 8 mA, to a regime of coherent microwave instability at 10 mA and 16 mA is clearly observable. The synchrotron frequency f_{sync} at ESRF is about 1.6 KHz. The satellites line spacing is 3 X f_{sync} , which seems to indicate a sextupolar mode of oscillation. The signal displayed by the streak camera for the same filling is shown on the figure 5c

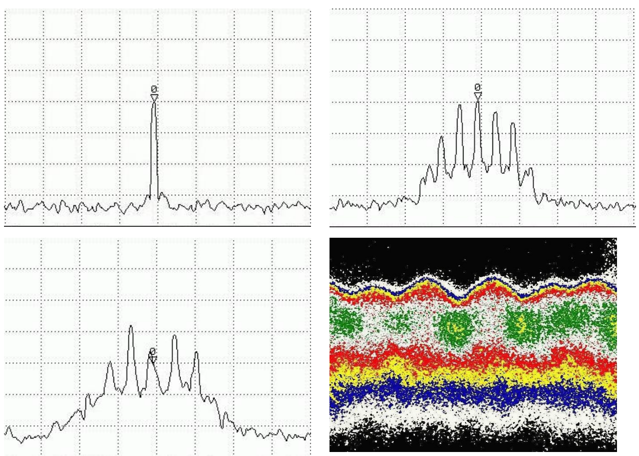

Figure 5a, b, c, d: Spectrums of the Σ signal detected on the 16.2 GHz cavity at 5mA, 10mA, 16mA in single bunch (scale 10 KHz/div-10dB/div) and streak camera image at 16mA (scale: 1000 turns X 150ps).

2.2 Vertical oscillations

Figures 6a and 6b show the signals observed with a 16 X 5 mA filling of the storage ring, with vertical bunch oscillations induced by a 1 MHz BW noise signal applied on a vertical kicker. Figure 6 right shows, for comparison, the spectrum of the signal displayed by the storage ring tune monitor which analyses the modulation of Δ signals coming from 13 mm diameter capacitive electrodes tuned at 352.2 MHz with an RF matching transformer. The figure 6 left shows the spectrums of the product of the Δ HF signal from the 10.2 GHz cavity set, with and without excitation. Though the signal to noise ratio is presently lower with the microwave cavity signals than with the tune monitor signals, the relative sensitivity of the detection of the -1 mode versus 0 mode, with the cavity pick up is much better than with the 352.2 MHz tuned electrodes of the tune monitor, which was the goal of this design. In the future the coupling to the beam of the 10.2 GHz cavities, used to produce the Δ HF signals, will be increased in order to achieve a better signal to noise ratio.

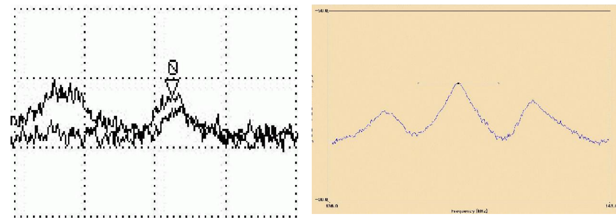

Figure 6: Spectrum of the Δ signal detected on the 10.2 GHz cavity set (left) and spectrum of the signal of the tune monitor (right). Scale:10 dB/div, 1KHz /div

5 CONCLUSION

Following the encouraging results obtained so far, we will implement a remote control of the phases of the different reference oscillator signals in order to provide an easier control of this diagnostic for the accelerator physics studies at ESRF. We plan also to use it in combination with a stripline kicker for single bunch instability feedback experiments [3].

5 CONCLUSION

- The acquisition of signals induced by the image current of the beam the 10 to 16 GHz region of the spectrum with frequency selective cavities allows the study of single bunch phenomenon not easily observable with others type of pick ups.
- This type of pick up is a good complement to the streak camera, particularly for the accurate study of the spectrum of the single bunch signals.

ACKNOWLEDGMENTS

I wish to acknowledge the contribution of Bernard Plan and Bernard Ogier. of the mechanical engineering group for their contribution to the cavity design, and Philippe Arnoux for the implementation of the RF receivers. Discussions with P. Kernel, R. Nagaoka, J.L. Revol helped me a lot to understand the issues of single bunch measurements.

REFERENCES

[1] C. Limborg, “Longitudinal beam dynamic in high intensity/bunch”, Beam Instability Workshop, ESRF, March 2000.

[2] P. Kernel,”Instabilités transverses a fort courant du mode mono paquet des anneaux de stockage: une nouvelle approche mettant en évidence un mécanisme post-synchrotronique”, Ph D thesis, ESRF, October 2000.

[3] E. Plouviez “Can we build a single bunch feedback”, Beam Instability Workshop, ESRF, March 2000.

A NEW WIRESCANNER CONTROL UNIT

M. Werner, K. Wittenburg, DESY, Hamburg, Germany

Abstract

Wires scanners are standard instruments for beam size measurements in storage rings: A wire is crossing the beam at a given speed and the secondary emission current of the wire and/or the photomultiplier signals produced from Bremsstrahlung or particles scattered at the wire are recorded together with the wire positions. The control unit described here is based on a previous CERN design [1]. It now has additional features:

- Triggered fast scans (1m/s) with a trigger uncertainty below ± 30µs (mechanics + electronics) used at the TTF Linac and at the proton synchrotron DESY III,
- Slow scans (e.g. 50µm/s) for the TTF Linac,
- Positioning of the wire within ± 3µm for tail scans at the storage rings PETRA and HERA,
- A 10.5MHz data acquisition rate for bunch-by-bunch acquisitions in the accelerators at DESY.

Another important design goal was the compatibility with CERN scanners; it is foreseen to operate them at LHC with the new control unit. First measurements with the new control unit at TTF and HERA will be presented.

1 OVERVIEW

The system is based on a special 19” 6HE VME crate controlled by a Motorola CPU running VxWorks. One crate controls 4 Wirescanners, one at a time. The concept is based on an earlier wire scanner control unit designed by J. Koopman, CERN and redesigned for new demands.

2 NEW FEATURES

2.1 Fast Scan with delayed Trigger

A scan can be triggered in synchrotrons (to get a profile for a certain energy) or linacs (to cross the beam exactly while it is present) during a “Fast scan”. A trigger delay up to 4 sec can be selected and the real time between trigger and reaching the desired acquisition start position is measured internally. So all time relations between trigger and acquisition data are defined. For storage rings the scan trigger can be disabled. The average trigger uncertainty is below ± 30µs (mechanics + electronics).

2.2 Slow Scan and Tail scans

Slow scans are useful for linacs: a data array (all bunches, all photo multiplier signals) is recorded for each linac pulse while the wire is moving slowly (e.g. 20..100µ/sec) across the beam. For tail scans in circular accelerators the wire can be moved to a given position within ± 3µm. In this mode (useful for the range 3..6σ around the beam) the “statistical” low rate photo multiplier pulses are counted during several seconds per position point.

2.3 Data acquisition

The 8-channel data acquisition for the photo multiplier signals or secondary emission signals from the wire now work up to 10.5 Msample/sec with 14 bits with a maximum of 128k datasets, using a low cost VME ADC card from DESY/Zeuthen.

2.4 Other improvements

The position resolution was improved to 1µm. The positions of all wires are remote accessible at any time. Hardware trimming is no longer necessary. The wire motion is now controlled by a programmable function generator, allowing any movement, only limited by the maximum acceleration. The four-channel system fits into a single crate now.

3 HARDWARE CONFIGURATION

3.1 General

The main system components are:

- The Motorola VME CPU with 4 IP Module sockets, one is occupied by an IP module (TIP570, 8-channel ADC + 8-channel DAC) to control voltage and current of up to 4 high voltage supplies for the photo multipliers
- The photo multiplier signal integration card
- The VME 8-channel 14 bit ADC card (designed by F. Tonisch, DESY/Zeuthen)
- The VME “motion control card” (in-house)
- The “motor driver” module and the ±48V/12A power supply (in-house)

3.2 Motion control card

The motion control card contains:

- A quadrature decoder to read out the 4 optical position encoders including error recognition, connected to a memory for fast position recording
- A delay unit for delayed fast scans
- A time / frequency measurement unit for remote tests of the external clock signals and to check the time between scan trigger and reaching of a given position
- A programmable function generator to generate any motion function

- A Test LED output for remote photo multiplier tests
- A programmable clock processing unit to control synchronised acquisition of photo multiplier signals and positions for the different modes
- An isolated serial link to the motor driver module

3.3 Motor driver module

The 4-channel motor driver module contains:

- Precision readout of the 4 position potentiometers
- Digital position control with position feedback by position potentiometer or optical encoder
- Motor driver amplifier (40V/12A)
- Safety pullout and safety switch off for dangerous conditions
- Interlock interface to inhibit scans for accelerator conditions dangerous to the wire
- Remote readout of power supplies, potentiometer positions, motor voltage and current
- Isolated serial link to the motion control module

The motor driver has its own power supply and communicates with the CPU and the motion control module only over the isolated serial link. So the high power part is totally electrically separated from the VME part to avoid cross talk into the ADC.

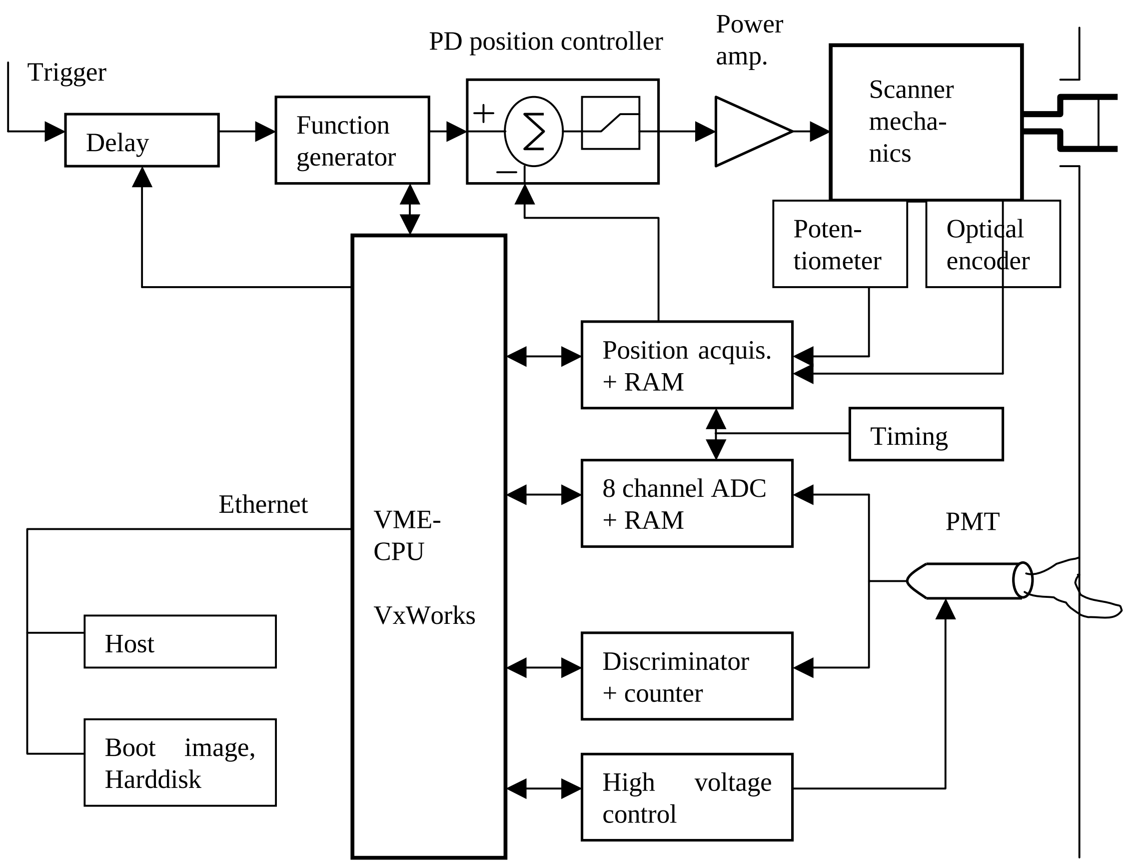

Figure 1: Functional block diagram of the control unit in its environment

4 SCAN EXAMPLES

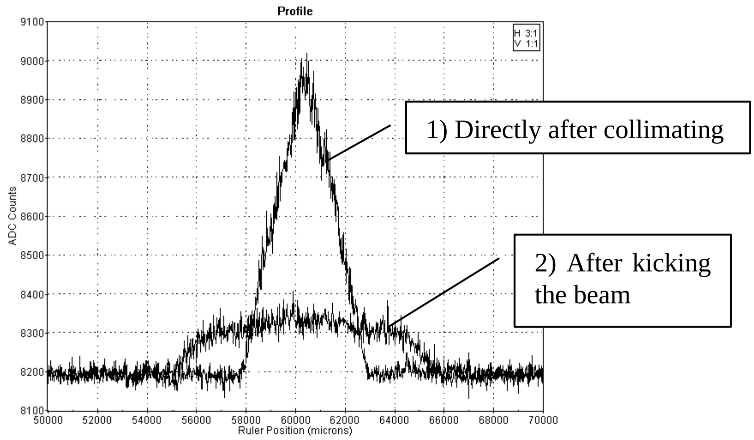

Figure 2: Fast proton scan at HERA (one bunch selected)

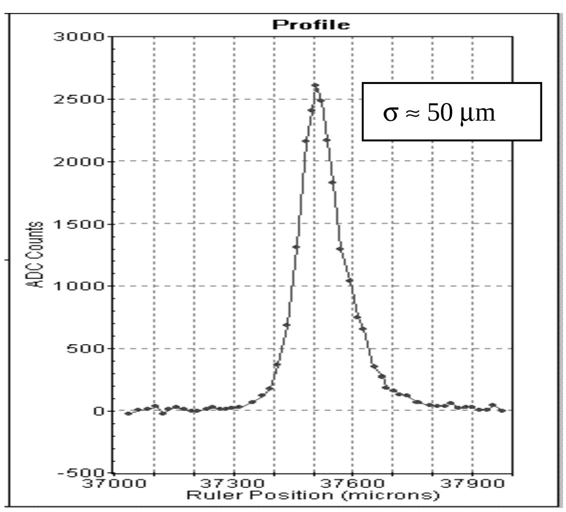

Figure 3: Slow scan at TTF (approx. gaussian beam)

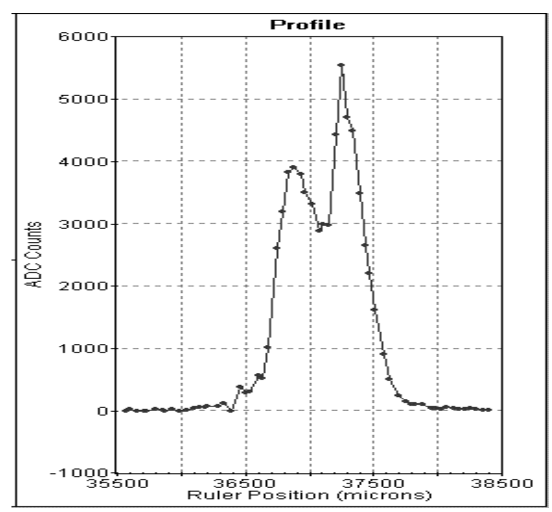

Figure 4: Slow scan at TTF (double peaked beam)

5 CONCLUSION

The unit was commissioned successfully at TTF and HERA-p. The commissioning for HERA-e, PETRA and DESY3 will be done as soon as possible. With a modified mechanical design and an additional new high power motor driver (4 kW power, not yet existing) a maximum speed of 2 m/s could be possible in the future.

REFERENCES

[1] Wire Scanners at LEP, By B. Bouchet, et al.. CERN-SL-91-20-DI. IEEE PAC San Francisco, CA, 6 - 9 May 1991., p. 1186-1188

ACKNOWLEDGEMENTS

I want to thank M. Seebach for his support and ideas during design and realisation, J. Koopman for documentation and support on the “original” control unit, F. Tonisch for support with his new ADC card, J. Davydenko, P. Duval and M. Lomperski for software support and the other colleagues who helped with hardware, software and ideas.

BEAM SIZE MEASUREMENT OF THE SPRING-8 STORAGE RING BY TWO-DIMENSIONAL INTERFEROMETER

M. Masaki and S. Takano
Japan Synchrotron Radiation Research Institute, SPring-8, Hyogo 679-5198, Japan

Abstract

Two-dimensional interferometer using visible synchrotron radiation was developed in order to measure beam sizes at a source point in a bending magnet of the SPring-8 storage ring. The theoretical background of this method is described in the framework of wave-optics. Assuming designed optics parameters, transverse emittance was evaluated from measured beam size.

1 INTRODUCTION

Electron beam imaging using visible synchrotron radiation (SR) is a conventional method of beam size measurement. In the case of SPring-8 storage ring, the resolution of vertical beam imaging is limited by diffraction effect [1] due to collimation of SR in a narrow vertical divergence angle. Interferometric technique has superior resolution than beam imaging. A visible SR interferometer with a double slit was first applied to KEK-PF and a small vertical beam size was successfully measured [2]. The similar technique was applied to the SPring-8 storage ring in order to measure the vertical beam size [3]. As an improvement of the interferometer, we newly developed a two-dimensional interferometer with a quad slit having four apertures, which has an advantage that horizontal and vertical beam sizes can be simultaneously measured by observing visibility of a two-dimensional interference pattern.

2 TWO-DIMENSIONAL SR INTERFEROMETER

2.1 Principle

When a monochromatic light is diffracted by a quad slit with four apertures located rectangularly, a two-dimensional interference pattern appears on an observation screen. The interference pattern of a spherical wave from a point source can be calculated by Rayleigh-Sommerfeld diffraction formula using a paraxial approximation. If the source is a group of incoherent point sources distributed in Gaussian shape with width σ_x and σ_y (1σ), the interference pattern is expressed as,

$$I(x_s, y_s) = I_0 \left[\frac{\sin\left(\frac{\pi x_s a}{2\lambda L}\right)}{\frac{\pi x_s a}{2\lambda L}}\right]^2 \left[\frac{\sin\left(\frac{\pi y_s b}{2\lambda L}\right)}{\frac{\pi y_s b}{2\lambda L}}\right]^2 \left[1 + V_x \cos\left(\frac{4\pi x_a x_s}{\lambda L}\right)\right]\left[1 + V_y \cos\left(\frac{4\pi y_a y_s}{\lambda L}\right)\right] \tag{1}$$

where L, a, b and λ are distance from the source to quad-slit, horizontal and vertical slit aperture sizes and wavelength of light, respectively. Parameters V_x and V_y are called as visibility. We have approximated that a are Gaussian convolution integral of envelope expressed by a sinc function can be neglected when the envelope width becomes far larger than the light source size by the use of a quad-slit with small aperture sizes. The relationships between the source size, namely electron beam size, and the visibility expressed by,

$$\sigma_x = \frac{\lambda}{2\pi\theta_x}\sqrt{-2\ln\left(V_x\right)}, \quad \sigma_y = \frac{\lambda}{2\pi\theta_y}\sqrt{-2\ln\left(V_y\right)} \quad . \tag{2}$$

2.2 Effect of aspherical features of SR wavefront

The wavefront of SR from an orbiting electron is not spherical in a strict sense. The relative phase relation of SR at each aperture of the quad-slit depends on the electron orbit angle, and an interference fringe shifts with respect to the overall envelope depending on the orbit angle. Therefore, a visibility generally depends not only on electron beam size but also on beam angular divergence. Deviation of SR phase from that of spherical wave on the transverse plane of the quad-slit of the SPring-8 interferometer is shown in Fig.1, which was calculated by Fourier transforming a radiation field derived from Lienard-Wiechart potentials of an electron orbiting in a bending magnet [1]. Wavelength λ is 441.6nm. The aspherical feature of SR is apparent in the horizontal direction, however the deviation of SR phase

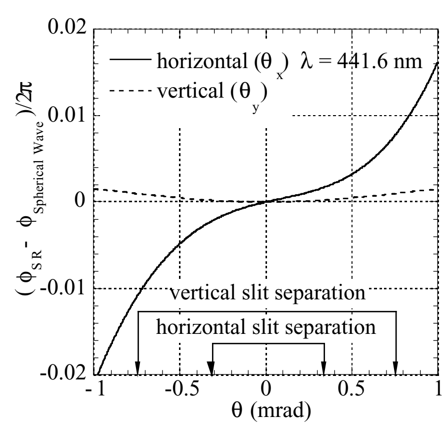

Figure 1:Difference of phase distributions between an ideal spherical wave and realistic radiation field derived from Lienard-Wiechart potentials of an electron orbiting in a bending magnet. Wavelength is 441.6nm.

from that of spherical wave is at most λ/500 at the apertures of the quad-slit, and spherical wavefront is still a good approximation to SR. The horizontal and vertical angular divergences of the electron beam at the source point are about 100μrad and 0.5μrad, respectively. By convolution of beam divergence, the degradation of visibility is evaluated to amount to resolution of 1.4μm and 0.013μm in horizontal and vertical directions, respectively.

2.3 Optimization of interferometer

It is advisable to measure a beam size in condition of visibility range that an accuracy of the measurement is tolerable to various instrumental errors. If we consider a simplified case in which a slit size is zero, visibility V and average intensity I of an interference fringe are expressed by the peak $I_{\max}$ and the bottom $I_{\min}$ intensity as follows,

$$V = \frac{I_{\max} - I_{\min}}{I_{\max} + I_{\min}}, \qquad I = \frac{I_{\max} + I_{\min}}{2}. \tag{3}$$

If we assume that fluctuations of $I_{\max}$ and $I_{\min}$ are $\Delta I_{\max}= \Delta I_{\min}= \Delta I$, from error propagation using equations 2 and 3, the error of beam size becomes as,

$$\frac{\Delta\sigma}{\sigma} = -\frac{\sqrt{1+V^2}}{2\sqrt{2}\,V\ln(V)}\frac{\Delta I}{I}. \tag{4}$$

Fig.2 shows that the error of measured beam size is insensitive to the intensity error ΔI in the range of visibility from 0.1 to 0.6. It is necessary to optimize the wavelength and the slit separation in order to measure in condition of the suitable visibility. Fig.3 shows relationships between the wavelength and the slit angular separation giving visibility 0.6 for specified beam sizes. The vertical slit separation is limited by finite extent of SR. In the case of our interferometer, a narrow aperture of photon beam transport line prevents us from selecting the appropriate vertical slit separation.

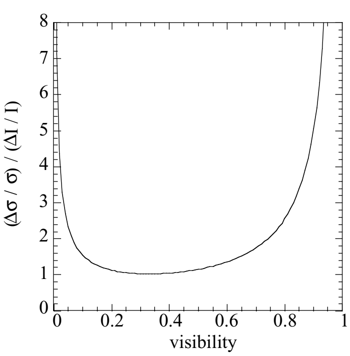

Figure 2: Visibility dependence of beam size error. Curve is Δσ/σ normarized by $\Delta I/I$. It is advisable to measure beam size in condition of visibility range from 0.1~0.6.

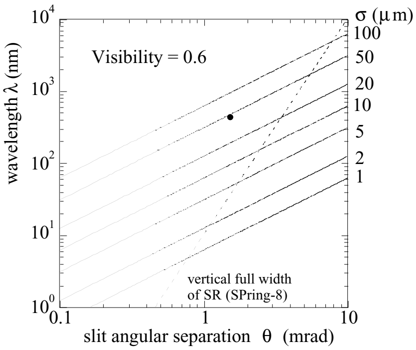

Figure 3: Solid lines show relations between wavelength and slit angular separation giving visibility 0.6 for various beam sizes. Broken line shows full width of vertical divergence of SR from SPring-8 bending magnet. Dot shows combination of θy and λ of interferometer of SPring-8.

3 EXPERIMENT

An experimental set-up of the two-dimensional interferometer of the SPring-8 storage ring is shown in Fig.4. All the instruments are installed in the accelerator tunnel. Visible SR is steered to the optical system of interferometer by two plane mirrors. The 1st mirror is located in vacuum at 18m downstream from the source point. X-ray heat load is protected by water-cooled x-ray absorber in front of the 1st mirror. A quad slit is located at 19.6m downstream from the source point. The size of each square aperture is 3mm*3mm and the horizontal and vertical angular separations are 0.65mrad and 1.51mrad, respectively. The position accuracy of each aperture is about ±0.2mm, which corresponds to the ambiguity of angular separation of about ±0.02mrad. Two-dimensional interference pattern is imaged on a CCD camera with pixel size 7.6μm*7.6μm by two achromatic doublet lenses behind the quad slit. The magnification is adjusted to one by moving the 2nd lens and the CCD camera axially. The CCD camera has electrical shutter and the exposure time is adjustable from 0.06ms to 31.7ms. Typical exposure time is 1.71ms. A polarizer with extinction ratio $5*10^{-4}$ is located in front of the camera in order to select σ-polarization. Center wavelength and bandwidth of a bandpass filter are 441.6nm and 10nm(FWHM), respectively. It is attached to the camera.

The interference pattern observed by the CCD camera is captured into a picture processing system. The captured data is analysed by making horizontal and vertical projections after subtracting the background which is measured by closing a photon shutter located at the photon beam transport line. A typical measured two-dimensional interference pattern is shown in Fig.5. A following model function is fitted to the projected data corrected for linearity of the CCD camera,

$$f(z) = I_0\left[\frac{\sin\left(a\left[z-z_0\right]\right)}{a\left[z-z_0\right]}\right]^2\left[1 + V\cos\left(kz+\phi\right)\right] \tag{5}$$

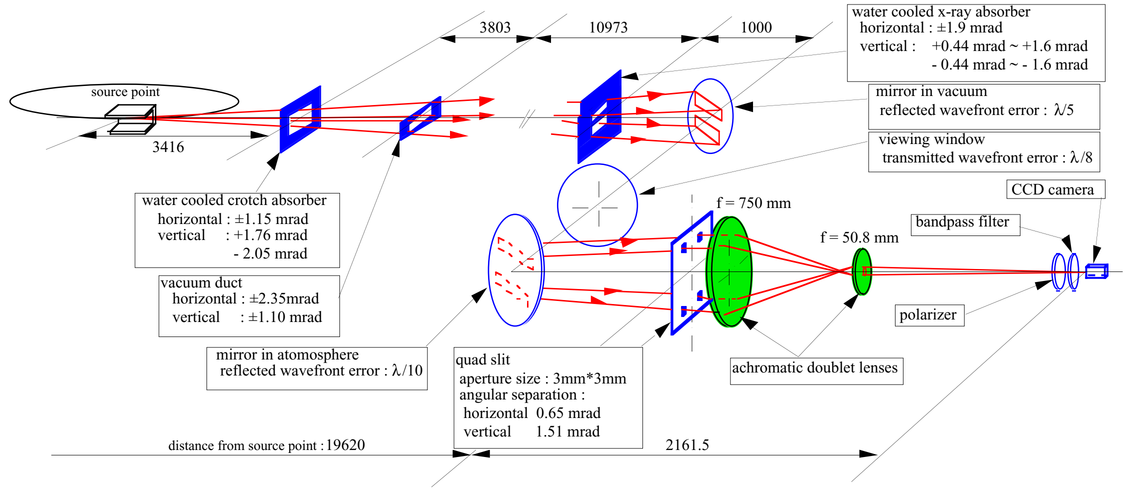

Figure 4 Experimental setup of two-dimensional interferometer of the SPring-8 storage ring

where I_0, a, z_0, V, k and ϕ are free parameters.

It is necessary to deconvolute the instrumental resolutions from the measured values in order to obtain real beam sizes. We evaluated as 7.4µm in the both horizontal and vertical directions by taking into account the effects of following instrumental factors on visibility.

- Imbalance of photon intensity among four apertures of quad slit
- Wavefront distortion by optical components
- Electron beam angular divergence
- Bandwidth of bandpass filter
- Extinction ratio of polarizer
- Pixel size of CCD camera

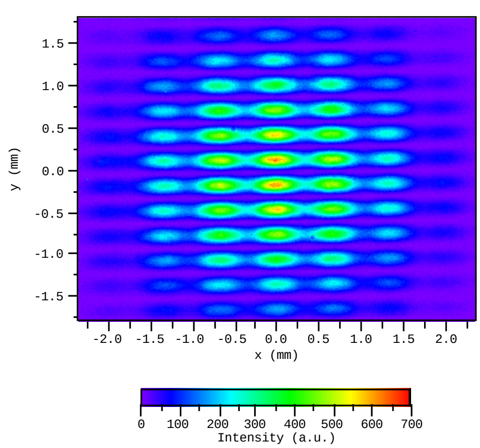

Figure 5: Typical two-dimensional interference pattern observed.

4 RESULTS

We measured beam sizes after improvement of the storage ring with four magnet-free 30m-long straight sections. Beam conditions of the storage ring are as follows, betatron tunes of the operating point are ν_x= 40.142 and ν_y= 18.359 which are used in ordinary user time operations, distribution of the vertical dispersion along the circumference of the ring is corrected as small as 1.2mm (r.m.s.), stored beam current is 100mA, gaps of all insertion devices are completely opened. We obtained the beam sizes as,

horizontal beam size (1σ) : 153.7±5.1 µm

vertical beam size (1σ) : 19.5±1.8 µm.

The beam size errors caused by ambiguity of slit angular separations are ±4.0µm and ±0.3µm in the horizontal and vertical directions, respectively. The accuracy of linearity correction of the CCD camera introduces errors of ±0.4µm (horizontal) and ±1.1µm (vertical). The statistical errors are estimated as ±0.7µm (horizontal) and ±0.4µm (vertical).

If we assume designed values of optics parameters at the source point and beam energy spread, the horizontal and vertical emittance ε_x, ε_y and the coupling ratio κ are evaluated as follows,

$$\varepsilon_x = 7.3 \pm 0.8 \text{ (nm•rad)}$$

$$\varepsilon_y = 14.2 \pm 2.7 \text{ (pm•rad)}$$

$$\kappa = \varepsilon_y / \varepsilon_x = 0.0019 \pm 0.0006.$$

The estimated transverse emittance of the storage ring is consistent with the designed value of 6.6 (nm•rad) within the error. It is necessary to estimate various systematic errors carefully in order to obtain an absolute beam size with higher accuracy. We consider that the resolution of the present interferometer is limited by using visible light in principle. It is planned to use X-ray in order to measure beam size with the resolution of 1µm.

REFERENCES

[1] M. Masaki and S. Takano, SPring-8 Annual Report 1997, p169

[2] T. Mitsuhashi, Proceedings of the 1997 Particle Accelerator Conference, Vancouver, Canada, p.766

[3] M. Masaki, S. Takano, H. Tanaka, K. Soutome, M. Takao, M. Oishi, K. Tamura, M. Shoji, S. Sasaki and H. Ohkuma, Proceedings of the 12th Symposium on Accelerator Science and Technology, Wako, Japan 1999, p.525

PLANNED X-RAY IMAGING OF THE ELECTRON BEAM AT THE SPRING-8 DIAGNOSTICS BEAMLINE BL38B2

M. Masaki, H. Ohkuma, S. Sasaki, M. Shoji, S. Takano*, and K. Tamura
Japan Synchrotron Radiation Research Institute, SPring-8, Hyogo 679-5198, Japan

Abstract

X-ray imaging observation of the electron beam is planned at the SPring-8 storage ring diagnostics beamline BL38B2 to evaluate small vertical emittance. The resolution target is 1 micron of electron beam size (1σ). The synchrotron radiation from a dipole magnet source will be imaged by a single phase zone plate. Monochromatic X-ray with energy of 8keV will be selected by a double crystal monochromator. The magnification factor of the zoneplate is 0.27, and an X-ray zooming tube will be used as a detector to compensate for demagnification.

1 INTRODUCTION

Measurement of small vertical size of electron beam is among the most challenging subjects of accelerator beam diagnostics of low emittance synchrotron radiation sources. At the SPring-8 storage ring, the high energy of electrons, 8 GeV, collimates synchrotron radiation in a narrow vertical divergence angle, and diffraction effect severely limits the resolution of conventional electron beam imaging with visible light[1].

The resolution is significantly improved by utilizing synchrotron radiation in shorter wavelength regions. X-ray imaging observation of the electron beam is planned at the SPring-8 storage ring diagnostics beamline BL38B2 to evaluate small vertical emittance.

2 DIAGNOSTICS BEAMLINE BL38B2

The beamline BL38B2 is dedicated for accelerator beam diagnostics and R&D of accelerator components. It has a bending magnet light source, and wide band spectral availability including visible/UV light, and soft and hard X-rays is anticipated. The beamline consists of a front end in the accelerator tunnel, an optics hutch in the experiment hall, a visible light transport line transporting visible/UV light from the optics hutch to a dark room, and an X-ray transport line in the optics hutch. The visible light transport line was completed in 2000, and longitudinal diagnostics of the electron beam such as bunch length and single bunch impurity are available.

Installation of the X-ray transport line is now under way. It has a double crystal monochromator, which can be moved off the beam axis when use is made of white, including both soft and hard, X-rays. Electron beam imaging with monochromatic X-ray is planned to evaluate small vertical emittance of the SPring-8 storage ring. The X-ray transport line as well as the front end has no windows, which potentially could distort wavefront and degrade imaging resolution, or obstructs soft X-ray and visible/UV light.

3 BEAM IMAGING WITH X-RAY

3.1 Why Phase Zone Plate ?

The resolution target of the beam size measurement is 1 micron (1σ). Assuming the vertical betatron function β_y of 30m at the source point, it corresponds to the resolution of vertical emittance ε_y of 33 fm•rad.

In the initial stage of the design study of the diagnostics beamline BL38B2, an X-ray pinhole camera was proposed. The positions of the pinhole and the camera were 17.2m (front end) and 34.4 m (X-ray transport line), respectively, from the source point. In order to optimize the observing photon energy and the size of the pinhole, we calculated an image of a single electron numerically and concluded that the diffraction limited resolution of the X-ray pinhole camera is no smaller than 10 μm (Fig. 1).

The alternative is to use an imaging optical element. If the electron beam is imaged by utilizing full vertical divergence of synchrotron radiation, it is necessary to

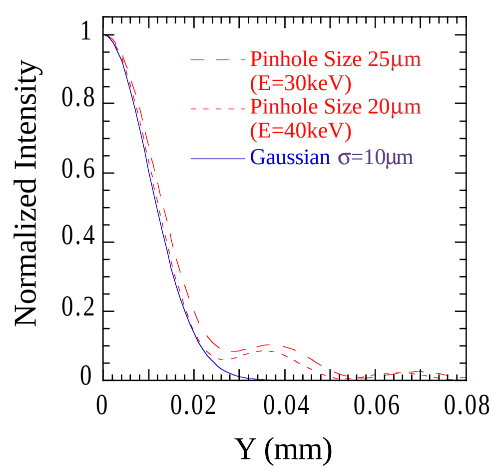

Figure 1: Computed intensity distributions of a single electron imaged by X-ray pinhole camera. The magnification factor is one.

---
* Email:takano@spring8.or.jp

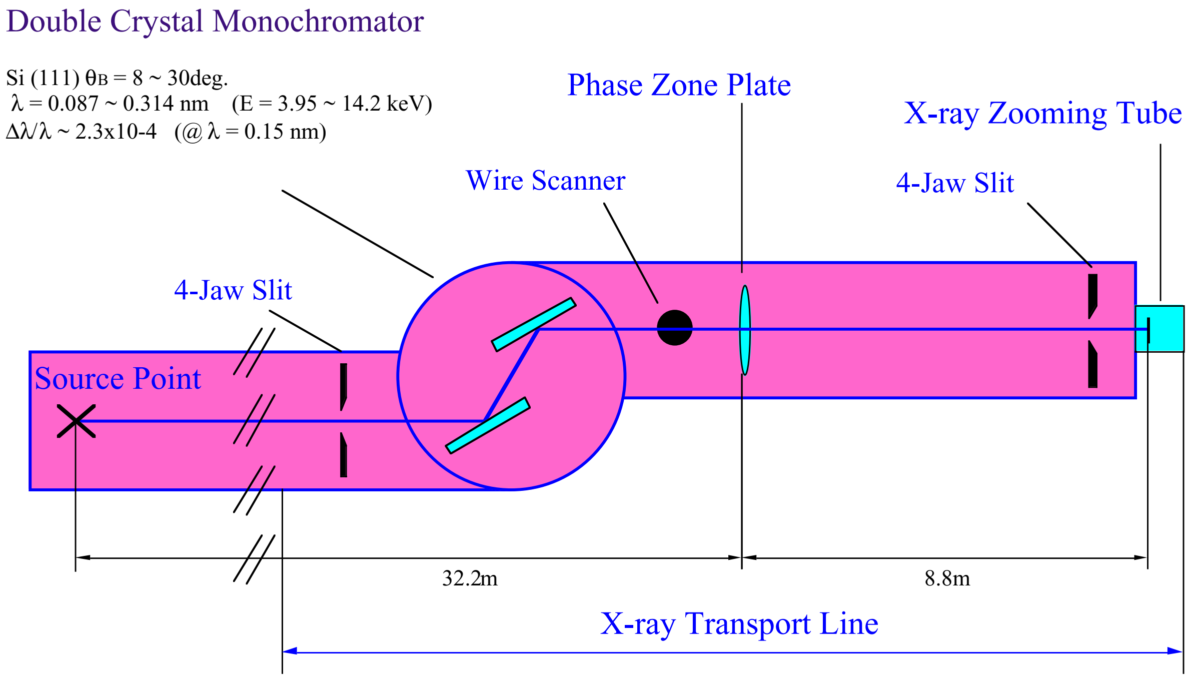

Figure 2: The optical system of the X-ray beam size monitor. All the components are installed in the optics hutch.

observe at photon energies higher than 1 keV to achieve resolution better than 1µm. If we observe at higher photon energies around 10 keV, necessary numerical aperture is much smaller than the vertical divergence of synchrotron radiation, and degradation of resolution caused by contamination of π polarized component can be ignored. In the hard X-ray region, a phase zone plate achieves superior spatial resolution.

3.2 Optical System

The optical system of the X-ray beam size monitor is shown in Fig. 2. Monochromatic X-ray is selected by a double crystal monochromator. A single phase zone plate images the electron beam on the input photocathode of an X-ray zooming tube. The magnification factor is 0.27.

Table 1: Parameters of the phase zone plate

Diameter	1.4 mm
Number of zones	468
Outermost zone width	0.75 µm
Zone material	Tantalum
Zone thickness	2.0 µm
Focal length*	6.92 m
Diffraction Efficiency *	32 %
Spatial Resolution* (1σ)	1.5 µm

*Calculated Value at E = 8.2 keV (λ = 0.15 nm).

The phase zone plate was fabricated by NTT Advanced Technology Co. The characteristics of the zone plate is summarized in table 1. The thickness of the zone material was optimized to obtain maximum diffraction efficiency. The X-ray zooming tube (Hamamatsu Photonics K. K., C5333) has resolution better than 0.5 µm (FWHM) at the input photocathode which is sensitive to X-rays below 10keV.

3.3 Imaging Properties of the Phase Zone Plate

The spatial resolution of the phase zone plate was calculated based on wave optics. A point source of spherical wave was assumed at the bending magnet

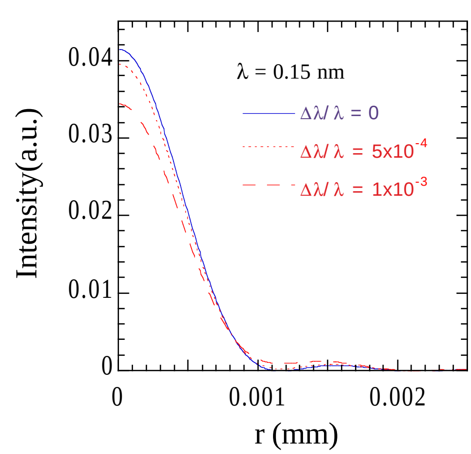

Figure 3: Computed intensity distributions of a point source imaged by the phase zone plate at the tuned and detuned wavelengths. The magnification factor is 0.27.

source point. The focusing of the zone plate was simulated by multiplying a complex factor which takes into account both phase shift and attenuation of the electric field in the zone material, and propagation of light to the photocathode of the X-ray zooming tube was calculated by diffraction formula. Figure 3 shows intensity distributions of diffraction limited image of the point source at the tuned and detuned wavelengths. At the tuned wavelength, the diffraction limited image is in good agreement with that obtained by an ideal lens, and best fitted Gaussian curve has a width (1σ) of 1.5 µm in the source coordinates. The images at detuned wavelengths show chromatic aberration of the zone plate. It is necessary to use monochromatic light with bandwidth narrower than $1*10^{-3}$, which is attainable by the double crystal monochromator.

3.4 Effects of Electron Beam Divergence

An electron moving in magnetic field of a bending magnet is not a point source of light in a strict sense. Therefore synchrotron radiation emitted by a single electron is not an ideal spherical wave. Figure 4 shows

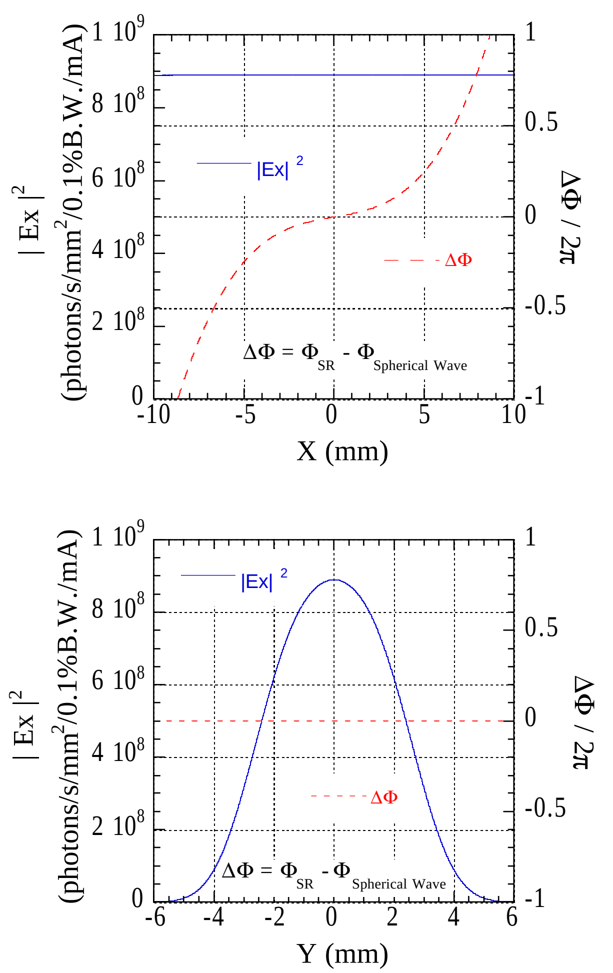

Figure 4: Electric field of synchrotron radiation at the position of the phase zone plate (σ polarized component).

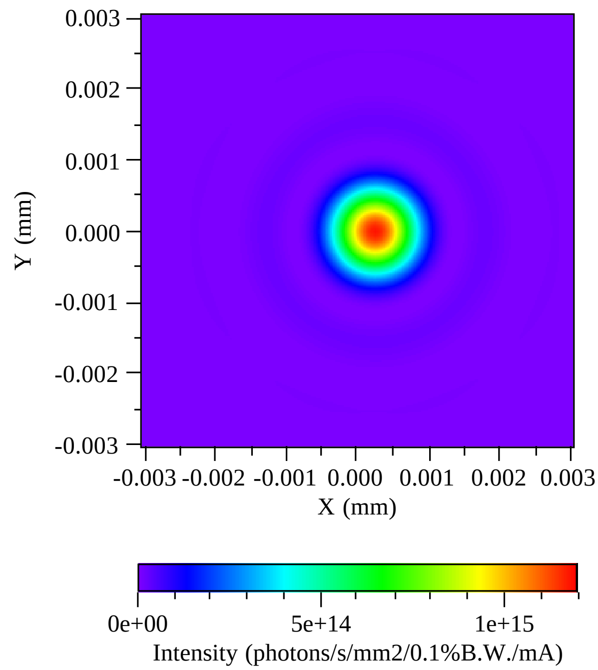

Figure 5: Image of a single electron moving on an orbit with angles at the source point ($\Delta\theta_x$ = 0.2 mrad, $\Delta\theta_y$ = 1.0 µrad, see text). Magnification is 0.27.

electric field of synchrotron radiation at the position of the zone plate, which was calculated from Lienard-Wiechart potentials of an electron moving on ideal orbit in a bending magnet. In the horizontal direction, distribution of phase of synchrotron radiation is different from that of ideal spherical wave. If the orbit has an angle at the source point, it will affect the image of the electron. In the vertical direction, distribution of phase of synchrotron radiation is in good agreement with that of ideal spherical wave. It is anticipated that an angle of the orbit will not affect the image.

In order to evaluate effects of angular divergence of electron beam on imaging, we calculated an image of a single electron moving on an orbit which has angles at the source point (Fig. 5**)**. The horizontal angle $\Delta\theta_x$ and the vertical angle $\Delta\theta_y$ are 0.2 mrad and 1.0 µrad, respectively, which approximate 2σ of designed angular divergences of the electron beam. The size of the image in Fig. 5 is in good agreement with that of a point source shown in Fig. 3. However , the position of the image is apparently shifted in the horizontal direction. Thus convolution of beam angular divergence could degrade resolution of horizontal imaging. However, degradation of horizontal imaging resolution by beam angular divergence amounts to at most 0.5 µm, which is still negligibly smaller than the measured horizontal beam size σ_x of about 150 µm.

REFERENCES

[1] M. Masaki and S. Takano, "Diffraction Limited Resolution of a Synchrotron Radiation Beam Profile Monitor", SPring-8 Annual Report 1997, p169.

STATUS OF THE DELTA SYNCHROTRON LIGHT-MONITORING-SYSTEM

U. Berges, K. Wille, DELTA, Institute for Accelerator Physics and Synchrotron Radiation,
University of Dortmund, 44221 Dortmund, Germany

Abstract

Synchrotron radiation sources like DELTA need an optical monitoring system to measure the beam size at different points of the ring with high resolution and accuracy. An investigation of the emittance of the storage ring can also be done by these measurements.

Scope of this paper is the investigation of the resolution limit of the different types of optical synchrotron light monitors [1] at DELTA, a third generation synchrotron radiation source. At first the normal synchrotron light monitor is analysed. The minimum measurable electron beamsize at DELTA is about 80 µm. Emphasis is then put on a special synchrotron light interferometer, developed for DELTA, which has been built up and tested. This interferometer uses the same beamline and can measure beamsizes down to about 8 µm. So its resolution is about ten times better and sufficient for the expected small vertical beamsizes at DELTA. Measurements of the electron beamsize and emittance were done with both (synchrotron light monitor and interferometer) at different energies.

The image processing system based on a PC Framegrabber generates a gaussian fit to the images from different synchrotron light-monitors and calculates the beamsizes and positions.

An investigation of possible reasons of beam movements will be appended, because the theoretical values of the present optics are smaller than the measured emittance.

1 INTRODUCTION

The **D**ortmund **El**ectron **T**est **A**ccelerator facility DELTA consists of a 35 – 100 MeV LINAC, the 35 – 1500 MeV ramped storage ring called **Bo**oster **Do**rtmund (BoDo) and the electron storage ring called Delta (300 – 1500 MeV) [2].

Both transverse beamsizes of the electron storage ring Delta are measured by optical monitoring using synchrotron radiation from bending magnets and commercial CCD-cameras. We installed two optical synchrotron radiation monitors at different points of the ring (see Figure 1). One monitor is completely inside the radiation shielding. The other one allows use of synchrotron radiation outside the shielding, but not during injection time. We are able to measure the horizontal beamsize down to about 80 µm with a normal optical synchrotron light monitor. Because of the not optimal orbit due to not optimal alignment of the magnets at the moment the measured beamsize and emittance is larger than the theoretical values. Another reason are high frequent beam oscillations. Therefore the better resolution of a synchrotron light interferometer, which has been built up and tested, is not necessary at the moment, but will be used in near future.

2 OPTICAL SYNCHROTRON LIGHT MONITORING SYSTEM

The design of the optical synchrotron light monitors inside and outside the shielding at Delta have been described in DIPAC 1999 [3]. These monitors work reliable in a routine way. The video signal of the CCD-cameras can permanently be displayed on TV screens in the control room. The image processing system has been changed to a PC frame grabber DT 3155 and a new graphical surface, adapted from DESY software [4]. This allows a faster analysis of the beamsize by a gaussian fit to a chosen part of the image and determination of the position of the beam center than our old system [5]. The software enables subtraction of a background image.

Necessary corrections of the calculated beamsize are done by this software due to diffraction, curvature, depth of field and resolution of the CCD-chip. The experimental setups of the monitors are equipped with apertures to minimize the necessary corrections of the measured beamsize. This limits the achievable resolution to about 80 µm @ 500 nm with even an optimised horizontal or vertical opening angle.

The correction due to diffraction has been measured in an experimental setup (see Figure 2). A Siemensstar is illuminated by monochromatic light (LED with 660 nm) and used as a source instead of the electron beam. The image is digitized and analysed to determine the resolution. The experiment gives $\sigma = (34 \pm 2)$ µm as minimal measurable beam size due to diffraction only in this setup. The result is in good agreement with the theoretical value ($\sigma = 0.61 * \lambda / \Theta = 33.55$ µm).

The influence of the opening angle of the synchrotron radiation concerning the measured beam size has been investigated at DELTA synchrotron light monitors by variation of the horizontal and vertical aperture. After subtraction of the necessary corrections due to different opening angles, the real beam size was in good agreement at the different opening angles (see Figure 3).

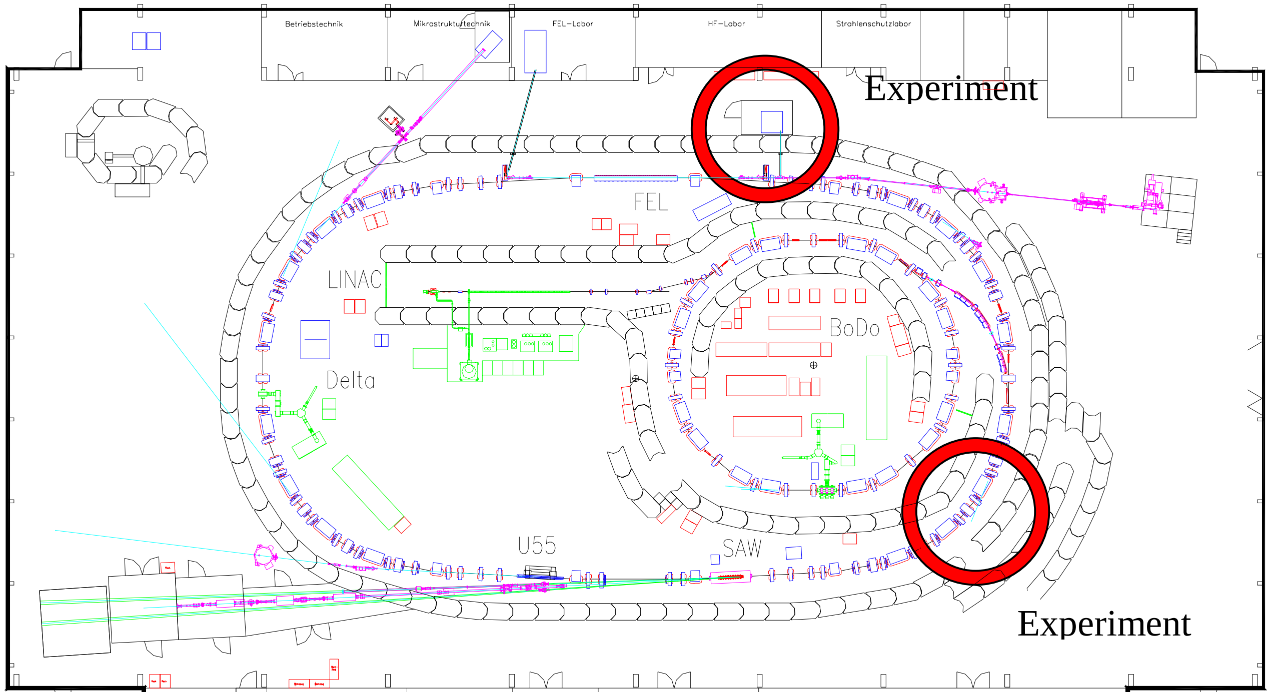

Figure 1: The Accelerator facility DELTA with the two positions of the storage ring synchrotron light monitors.

3 OPTICAL SYNCHROTRON LIGHT INTERFEROMETER

A synchrotron light interferometer according to the theory of T. Mitsuhashi [6] using also the visible part of the synchrotron radiation has been build up at the same beamline at Delta as the normal optical synchrotron light monitor. The advantage is that no separate or new beamline using X-rays is needed to improve the achievable resolution of the monitor by a factor of 10. The visibility allows an easy and direct arrangement of the components and cheap diagnostics with a normal CCD-camera. The layout of the interferometer is shown in Figure 4. It consists of a double slit (diameter 1 mm) with different slit distances D (between 2 and 8 mm) at the distance s = 1410 mm from the source point, followed by a linear polarisator, a bandwidthfilter (λ = 500 ± 3 nm) and an achromat with f = 1500 mm. The visibility V = $(I_{max} - I_{min}) / (I_{max} + I_{min})$ of the digitized interferogramm is determined in order to achieve the beam size σ:

$$\sigma = \frac{\lambda s}{\sqrt{2}\,\pi D}\sqrt{\ln\frac{1}{V}}$$

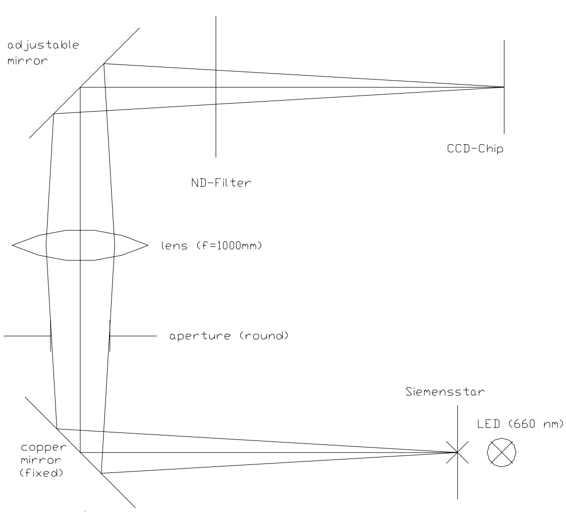

Figure 2: Experimental setup to determine the necessary correction due to diffraction at DELTA.

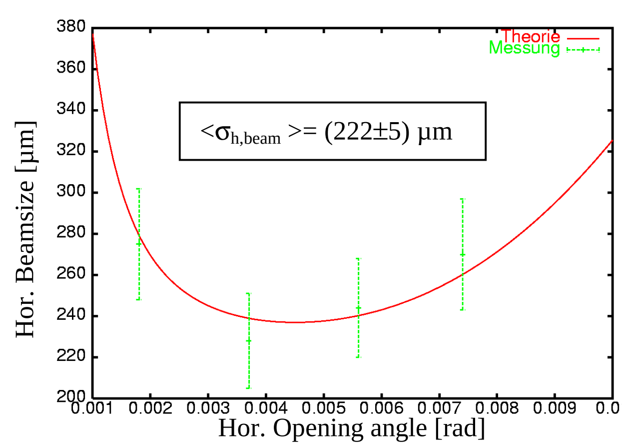

Figure 3: Measured beamsize after correction vs. opening angle of synchrotron radiation.

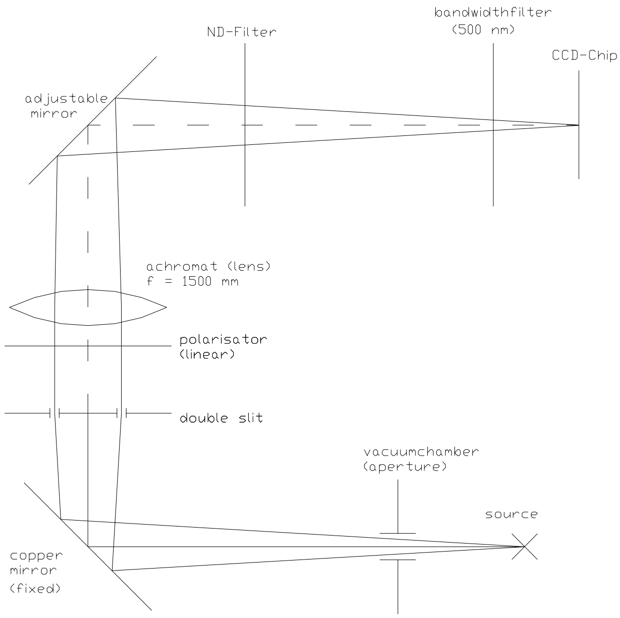

Figure 4: Layout of the optical synchrotron light interferometer at DELTA.

The resolution of the synchrotron light interferometer has been measured in an experimental setup. A Siemensstar illuminated by monochromatic light (LED with 660 nm) is used as source instead of the electron beam. The experiment gives σ = (10.3 ± 3.4) μm. The resolution limit for the measurable electron beamsize at Delta is therefore σ = (7.8 ± 2.5) μm for λ = 500 nm.

The electron beamsize of Delta at 960 MeV has been determined to σ = (159 ± 15) μm by the optical synchrotron light monitor and to σ = (160 ± 5) μm by the interferometer. So both methods are in good agreement.

4 RESULTS OF EMITTANCE MEASUREMENTS AT DELTA

The transverse emittance of the electron beam at Delta at different energies has been measured with both types of optical synchrotron light monitors, the interferometer and the normal optical synchrotron light monitor. They are in good agreement, but about a factor of 5 larger than the theoretical values @ 10% coupling [1]. The reasons are beam oscillations due to a missing feedback system and a not optimal orbit due to the not optimal alignment of magnets at the moment, which will be realigned in this summershutdown.

The time dependence of the measured electron beam sizes has been investigated. They are not varying very much in the time range between 20 ms and 10 μs. This has been measured by a CCD-camera with variable and adjustable shutter time and by analysis of BPM-Data [7]. Therefore fast beam movements, especially betatron oscillations, have to be reduced by a necessary feedback system to improve beam stability and to reduce beam size.

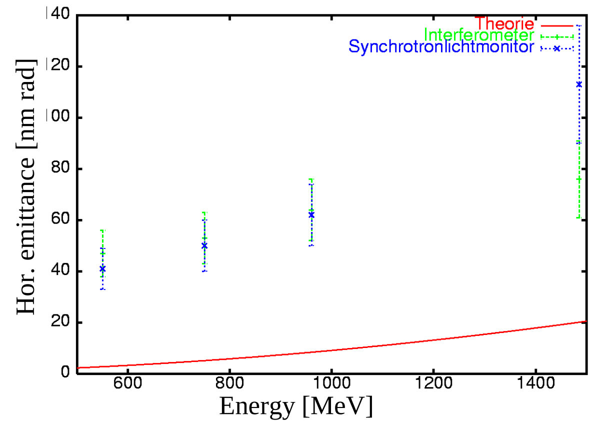

Figure 5: Results of emittance measurements at Delta. Theory is based on calculations of the ideal machine without any corrections.

5 CONCLUSIONS

The normal optical synchrotron light monitors at Delta work routinely down to their resolution limit σ ≈ 80 μm.

A suitable optical synchrotron light interferometer to determine beamsizes down to σ ≈ 8 μm at Delta has been developed, build up and tested. The results of both types of optical synchrotron light monitors are in good agreement in their common range (σ > 100 μm).

6 ACKNOWLEDGEMENTS

Thanks to Kay Wittenburg and Fedor Solodovnik from DESY, Hamburg, Germany for their support concerning the frame grabber software and to Rainer Fisher from DESY for his technical help concerning the normal optical synchrotron light monitor setup.

I also want to thank Mario Ferianis from Elettra, Italy, and Alan Fisher from SLAC, Stanford, USA for their help, support and advice concerning the interferometer.

REFERENCES

[1] U. Berges, “Hochauflösende optische Strahldiagnose mittels Synchrotronstrahlung am Beispiel der Synchrotronstrahlungsquelle DELTA”, PhD Thesis, University of Dortmund, Germany, 2000
[2] J. Friedl, “Recent results of the commissioning of the DELTA facility”, PAC 97, Vancouver, Canada, 1997
[3] U. Berges, “Status of the DELTA Synchrotron Light-Monitoring-System”, DIPAC 99, Chester, GB
[4] F. Solodovnik, “DT3155 sample programm: Principles of operation”, DESY, Hamburg, Germany
[5] M. Preuß, “Integration der Strahldiagnose mittels Synchrotronlicht in das Kontrollsystem von DELTA”, Diploma Thesis, University of Dortmund, Germany, 1997
[6] T. Mitsuhashi, “Beam Profile and Size Measurement by SR Interferometers”, SR Beam Measurements, Proceedings Joint US-CERN-Japan-Russia school on Particle Accelerators, Montreux, Switzerland, 1998
[7] P. Hartmann, private communication, DELTA, University of Dortmund, Germany, 2001

BEAM DIAGNOSTIC FOR THE NEXT LINEAR COLLIDER

Stephen R. Smith, Stanford Linear Accelerator Center, Stanford, CA 94309, USA

Abstract

The Next Linear Collider (NLC) is proposed to study e+ e- collisions in the TeV energy region. The small beam spot size at the interaction point of the NLC makes its luminosity sensitive to beam jitter. A mechanism for aligning the beams to each other which acts during the bunch-train crossing time has been proposed to maintain luminosity in the presence of pulse-pulse beam jitter[1]. We describe a beam-beam deflection feedback system which responds quickly enough to correct beam misalignments within the 265 ns long crossing time. The components of this system allow for a novel beam diagnostic, beam-beam deflection scans acquired in a single machine pulse.

1. INTRODUCTION

The beam-beam deflection feedback consists of a fast position monitor, kicker, and feedback regulator which properly compensates for the round-trip time-of-flight to the interaction point (Figure 1). A system consisting of conventional components may be effective at reducing the loss of NLC luminosity in the presence of vertical beam jitter many times larger than the vertical beam size.

Table 1: Beam Parameters at the IP

Parameter	Value	Comments
CM Energy	490 GeV	Stage 1
Bunch Charge	0.75×10^{10}	$e^{+/-}$ / bunch
Bunches / train	95 / 190	
Bunch Spacing	2.8 / 1.4 ns	
Repetition rate	120 Hz	
σ_y / σ_x	2.7 nm / 245 nm	At IP
σ_z	110 µm	
D_y	14	Disruption
Deflection slope	20 x 10^{-6} /nm	Head-on

2. POSITION MONITOR

2.1. Transducer

We propose a stripline-type position monitor pickup, located about 4 meters from the IP. The strips are 50 Ohm lines and are assumed to be 10 cm long, peaking the response at the 714 MHz bunch spacing frequency. A 20 mm diameter BPM diameter is modelled here. Care must be taken to minimize radiation hitting the BPM, and to keep RF from propagating into the BPM duct.

Table 2: Beam Position Monitor Parameters

Parameter	Value	Comments
Distance to IP	4 m	
Duct diameter	2 cm	
Stripline length	10 cm	
Impedance	50 Ohms	
Frequency	714 MHz	Center
Bandwidth	360 MHz	
Input filter	4-pole bandpass	Bessel
Bandwidth	200 MHz	Base band
Base band filter	3-pole low pass	Bessel
Rise time	3 ns	0-60%

2.2. Processor

The position processor produces an analog output proportional to beam position. This signal must be fast to be useful in intra-pulse feedback. We propose to demodulate a 360 MHz band width around the 714 MHz BPM center frequency. The processor consists of an RF hybrid, band pass filter, and mixer driven by 714 MHz from the timing system, followed by a low pass filter. See Figure 2. This produces an amplitude proportional to the product of beam position and beam current.

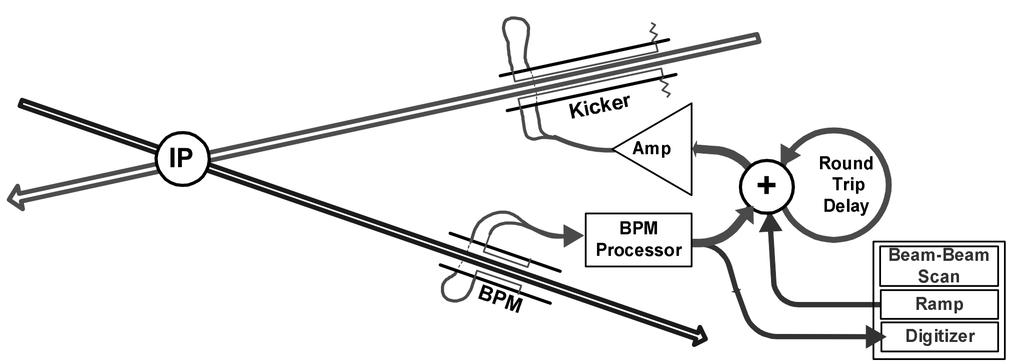

Figure 1: Intrapulse Feedback Block Diagram

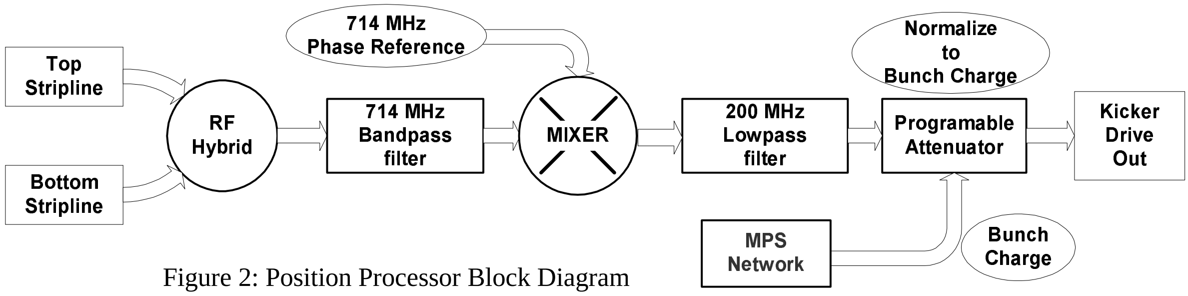

Figure 2: Position Processor Block Diagram

A variable attenuator scales the output inversely proportional to the beam intensity to recover the position signal. This scaling is set up before the pulse, either with charge information from the damping rings, or from slow feedback based on the charge of recent pulses. Using common RF parts we can achieve output rise times less than 3 ns and position resolutions below a micron. Figure 3 shows simulation of the turn-on transient.

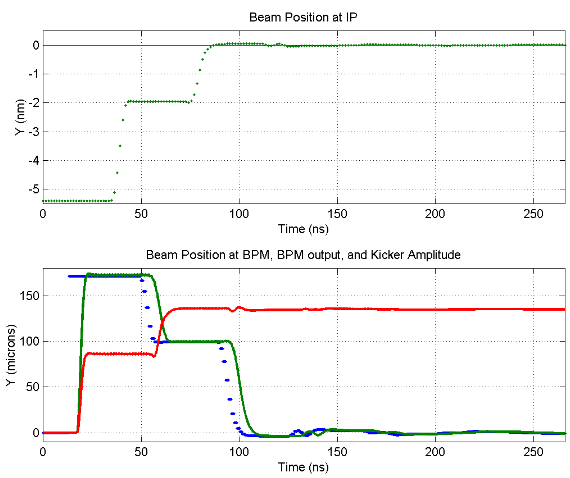

Figure 3: Capture transient for 2σ initial offset.

2.3. Noise

Intrinsic (thermal) resolution of such a BPM is less than 50 nm rms, This corresponds to a beam-beam offset resolution on the picometer scale, absent other error terms. The feedback system requires position resolution of only microns, so this is an excellent start.

Absorption of charged particles and secondary emission from the strip lines is another potential source of position noise. This design is sensitive at the level of about 3 pm per secondary electron knocked off the strip lines, and somewhat less for those knocked off the walls of the walls inside the BPM. Imbalances of intercepted spray of 10^5 particles per bunch would be a problem for this BPM.

The near-IR region is likely to be a rich source of RF power. These fields propagating into the BPM give rise to position errors. The proposed BPM diameter has cut off frequency well above the processing frequency so external RF fields are excluded.

3. KICKER

Our model for the kicker has curved strip lines at 12 mm diameter and a length of 75 cm. Each stripline subtends 120° from the beam. Such a kicker will have an impedance of 50 Ohms if its enclosed in a beam duct of radius about 10 mm. The kicker is to be operated at base band, so that several bunches may be propagating concurrently through it. The impulse response of the kicker is a rectangular pulse of 5 ns width. The step response is a linear ramp with this rise time. In the present system model, this represents the slowest rise-time in the system. Faster response may be obtained by shortening the stripline, with power required for a given deflection increasing quadratically.

4. FEEDBACK REGULATOR

The feedback regulator must converge rapidly to the optimal beam position. There are three major issues here. The lag in loop response due to the roundtrip time-of-flight to the IP must be compensated to get rapid, stable convergence. The beam-beam deflection response has a non-linear character which slows convergence for large initial beam-beam offsets. Finally, angle jitter in the incoming beam contributes to an error in estimation of the beam-beam deflection angle.

4.1. Compensating Loop Delay

The IP round-trip delay, about 30 ns for BPM and kicker 4 meters from the IP is 10% of the entire bunch train length, making a conventional PID regulator work poorly; the gain on the integral term must be kept small to avoid oscillation due to round-trip lag. Low gain leads to slow convergence[1]. A higher-order regulator allows for improved convergence. We assume a comb-filter integration of the response from one full loop delay time earlier. The physical implementation is a cable transmitting the output of the kicker driver back to the summing node. The length of this cable is adjusted to the loop propagation delay, including the round-trip to the IP and electronics delays. This lets the feedback compare the kicker amplitude from the time when it was relevant to the beam deflection now being measured. Critical tuning is not required for convergence or stability. Compensation for the kicker fill time is warranted; a simple RC is adequate. Loop compensation is an electrical model of the response of the system, composed of cable delay, and shaper with the rise time of the kicker.

4.2. Deflection Curve Non-Linearity

Deflection is linear in displacement for small vertical displacements, but the slope flattens when the beam-beam offset is greater than a few σ of the vertical beam size[2]. Hence the overall gain of the feedback loop drops like 1/δ for large offsets. A linear regulator will then take many loop propagation delays to reach the linear part of the deflection curve, where it converges rapidly. Figure 4 shows a simulated capture transient from an initial beam-beam offset of 27 nm. This shows restoration of full luminosity in about 130 ns, so a little more than 50% of nominal luminosity is recovered when the beams start out missing each other by 10 σ.

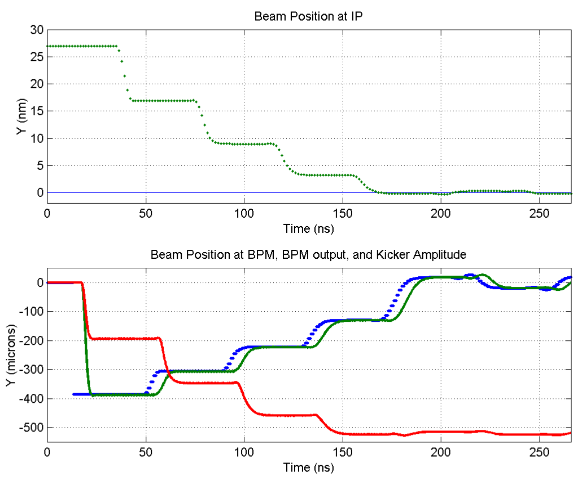

Figure 4. Capture transient from 10σ initial offset

Convergence speed from far off is improved by increasing loop gain, at the cost of slowing convergence from small initial offsets[3]. The optimal loop gain then depends on average jitter conditions. At sufficiently large initial offsets, convergence is too slow to recover luminosity before the end of the train.

4.3. Incoming Angle Compensation

Jitter in the interaction-point angle of the incoming beams has two consequences. The high aspect ratio of the beam spots in the y-z plane means bunches must be aligned precisely to get luminosity. If the incoming angle jitter is of the order of σ_y/σ_z, then incoming angle feedback, not considered here, must be implemented.

Second, the incoming angle of the beam heading to the feedback BPM contributes to the position signal at that BPM. If not compensated, this angle is interpreted as beam-beam deflection signal and is incorporated, in error, in the intra-pulse feedback. This may be compensated within the beam crossing time if another fast BPM is installed on the incoming beam, on the other side of the IP, and its analog output brought through the detector in some timely fashion.

5. DIAGNOSTIC BEAM-BEAM SCANS

The existence of the fast BPM and kicker allows for a novel beam diagnostic. One can program the kicker with a ramp, open the feedback, and record beam-beam deflection throughout a single machine pulse. This provides initial beam-beam alignment and beam spot size information, free of pulse-to-pulse machine jitter.

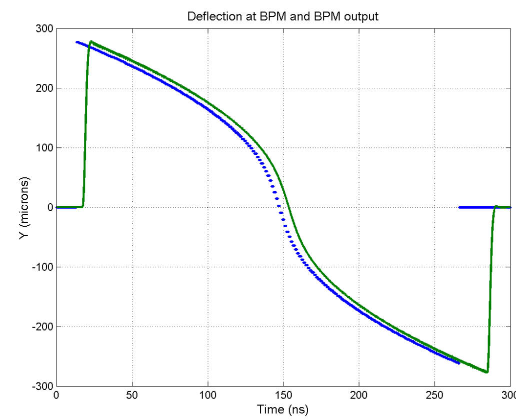

Figure 5. Beam-beam scan simulation.

6. CONCLUSIONS

We've presented a conceptual design of an intra-pulse beam-beam feedback for the Next Linear Collider interaction point. Principle components have been sketched in sufficient detail to model the system, including beam-beam effects, BPM and processor, feedback regulator and kicker. Simulink was used to perform the simulations; its output shows rapid convergence from initial offsets of a few beam σ. With these tools, beam-beam alignment and spot sizes may be measured in a single pulse.

REFERENCES

[1] Daniel Shulte, "Simulations of and Intra-Pulse Interaction Point Feedback for the NLC", Sep. 1999, LCC-Note-0026 on web at http://www-project.slac.stanford.edu/lc/nlc-tech.html.

[2] K.Yokoya and P.Chen, "Frontiers of Particle Beams: Intensity Limitations", M.Month and S.Turner eds**.,** **Lecture Notes in Physics Vol. 400** (Springer-Verlag, Berlin, 1990),pp.415-445.

[3] O. Napoly, N. Tesch, I. Reyzl, "Interaction Region Layout, Feedback, and Background Issues for TESLA", **Proceedings of the World-Wide Study on Physics and Experiments with Future Linear e+e- Colliders Vol. 2,** April 28 – May 5, 1999, ed. E. Fernandez and A. Pacheco, Sitges, Barcelona, Spain, p. 663.

DIAGNOSTICS FOR THE PHOTOINJECTOR TEST FACILITY IN DESY ZEUTHEN

J. Bähr*, I. Bohnet, D. Lipka, H. Lüdecke, F. Stephan, Q. Zhao, DESY, Zeuthen, Germany
K. Flöttmann, DESY, Hamburg, Germany
I. Tsakov, Inst. for Nucl. Res. and Nucl. Energy of the Bulgarian Acad. of Sci. (NRNE), Sofia

Abstract

A **P**hoto **I**njector **T**est facility (PITZ) is under construction at DESY-**Z**euthen. The aim is to develop and operate an optimized photo injector for future free electron lasers and linear accelerators. This concerns especially minimal transverse emittances and proper longitudinal phase space. The commissioning of the photo injector will take place in summer 2001. In the first phase the energy of the produced electrons is about 5 MeV. A short description of the setup and beam parameters are given. Optimization of an electron gun is only possible based on an extended diagnostics system. The diagnostics system for the analysis of the transversal and longitudinal phase space will be described. It consists of a measurement system of the transversal emittance, a TV-based image measurement system, a streak-camera measurement facility, a spectrometer using a dipole magnet and further detectors. Problems of the measurement of the longitudinal phase space are discussed in detail.

1 INTRODUCTION

A Photo Injector Test Facility (PITZ) is under construction in DESY Zeuthen and will be commissioned in summer of 2001. The project was originated by a collaboration of the following institutions: BESSY (Berlin), DESY (Hamburg and Zeuthen), Max-Born Institut Berlin, Technical University (Darmstadt) and is funded partially by the HGF-Vernetzungsfonds.

The goal of PITZ is to operate a test facility for laser driven RF guns and to optimize photo injectors for the operation of Free Electron Lasers (FEL) and the TESLA linear collider. Comparisons of detailed experimental results with simulations are foressen. The setup will be used for conditioning of optimized cavity resonators for subsequent operation at the TESLA Test Facility - FEL. New developed components (for example lasers, cathodes) will be tested under realistic conditions. Later questions related to the production of flat beams for linear colliders and the development of polarized electron sources will be addressed.

At present, the mounting and commissioning of different subsystems (laser, interlock systems, control system, diagnostics systems) is going on. The vacuum system including cathode section, cavity section and diagnostics section is under vacuum. The commissioning of the RF system and conditioning of the cavity are the next steps. First photoelectrons will be produced in autumn 2001 followed by the commissioning of the full setup. An upgrade with a booster cavity is foreseen in the next years.

2 DESCRIPTION OF PITZ

The schematic layout of the PITZ facility is seen in Fig. 1. It consists of the following main components:

- the photo cathode based on Cs_2Te [1])
- the copper cavity with a 1.5 cell geometry
- the laser system with output wavelength 263 nm
- the 1.3 Ghz RF-system with a klystron of 5 MW (later 10 MW)
- the control system based on DOOCS (Distributed Object-Oriented Control System)
- the diagnostics section

One of the main complex parameters and development goal is the time structure of the laser beam shown in Fig. 2.

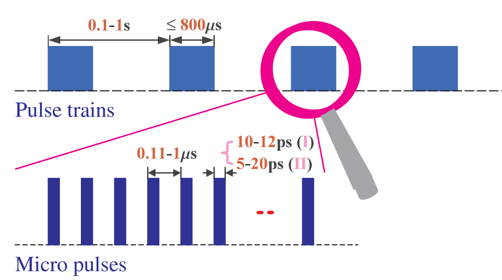

Figure 2: Schematic of the time structure of the laser beam. I) Phase I: GAUSSian-shape $\sigma \sim 6$ ps, II) Phase II: Rectangular shape with rise and fail time < 1 ps.

3 DIAGNOSTICS AT PITZ

3.1 Diagnostics of Laser Beam

- Time resolved bunch analysis of the laser beam by means of streak cameras.

  Two types of streak cameras (both from Hamamatsu)): FESCA-200 (time resolution > 200 fs), which is running only in single shot mode and C5680, running in single shot mode and synchroscan (time resolution > 2 ps) are available to analyse the time structure of

* baehr@ifh.de

[1] INFN Milano

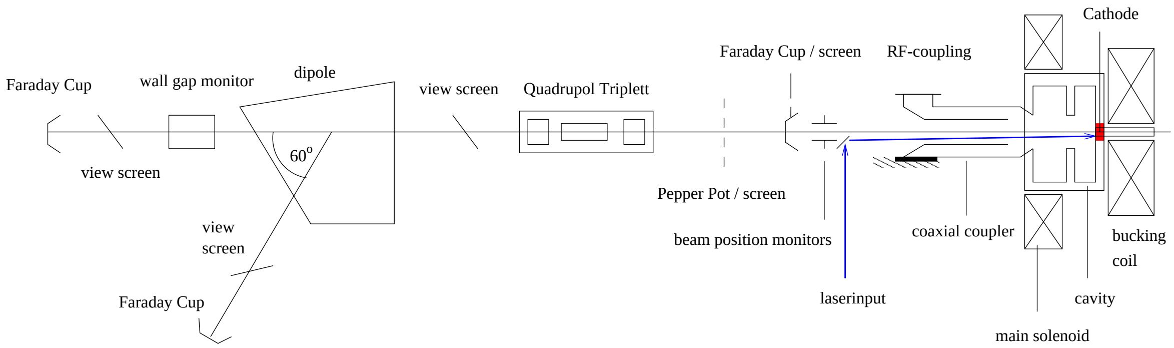

Figure 1: Schematic of the setup of the PITZ facility.

the laser beam. There are no restrictions concerning light level or aperture.

- Laser power measurement

  It is foreseen to measure the time-resolved laser power. A small fraction of the laser beam could be used for the time resolved measurement using a simple setup based on a photodiode. An alternative is the use of a commercially available laser power meter.

- Virtual cathode

  The virtual cathode simulates the cathode. Especially, the position, the shape and the energy distribution of the laser spot in a plane corresponding to the cathode plane will be measured. Either a plastic scintillator or an evaporated YAG (Yttrium-Aluminium-granate) screen will be used as converter of the UV laser light to visible light, both in transmission.

3.2 *Diagnostics of Electron Beam*

- EMSY - Emittance Measurement SYstem for measurement of transverse emittance.[2]

  The goal is to measure the transverse emittance of the electron beam by means of slit masks and/or hole masks (pepperpot), see Fig. 3. It is aimed to reach a tranverse emittance of 1 π mm mrad. The beam pattern behind one of the slit or hole masks is detected about one meter downstream using screens and the TV system and is analysed later.

- TV diagnostics system

  It is the goal to measure and to analyse the position and the profile of the electron beam at different positions along the beam line.The resolution is aimed to be 1...10 μm, optionally a view camera geometry is used to overcome the depth-of-field problem.

- Time resolved bunch analysis of the electron beam using streak camera

[2] Institute for Nuclear Research and Nuclear Energy the Bulgarian Academy of Sciences (NRNE) Sofia

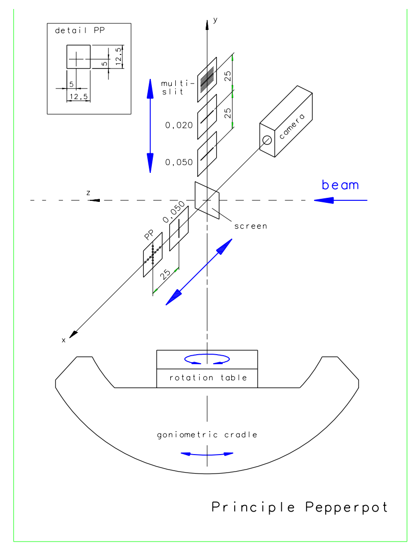

Figure 3: Transverse emittance measurement system.

Two types of streak cameras (see above) are available to analyse the time structure of the electron beam. The electron beam hits radiators based on Cherenkov effect or transition radiation. The light is transported using an optical beam-line to the streak camera lab. This 25 m long beam-line is under construction considering a high light collection efficiency, low photon losses and insignificant time dispersion to be realized.

- Measurement of magnetic field on cathode

  The magnetic field will be measured using the electron beam. The beam goes through a slit mask. In the case of a non-zero field on the cathode, the pattern of the beam on a screen behind the slit mask is rotated. The calibration is done using a laser. The laser beam is expanded and projected onto the slit mask. The orientation of the slit images gives the zero field position. The method has to be optimized so, that the calibration is not limited by diffraction of the laser beam at the mask.

- Dipole spectrometer

  A dipole is used to measure the momentum spectrum of the beam.

- FARADAY cup

  A water-cooled copper absorber insulated from ground is used to measure the beam charge.

- Wall gap monitor

  This monitor is used to measure the beam current using the image current on the vacuum pipes.

- Beam position monitor

  Beam position and charge are measured by a button monitor.

4 DIAGNOSTICS FOR LONGITUDINAL PHASE SPACE

The measurement of the longitudinal phase space will be done in three steps:

- Measurement of momentum

  The electron beam will be deflected by a dipole and its particle distribution will be measured with a YAG-screen.

- Measurement of bunch length

  The electron beam will be transformed by a radiator into photons which are measured by a streak camera. The temporal length of the photon bunch gives the electron bunch length.

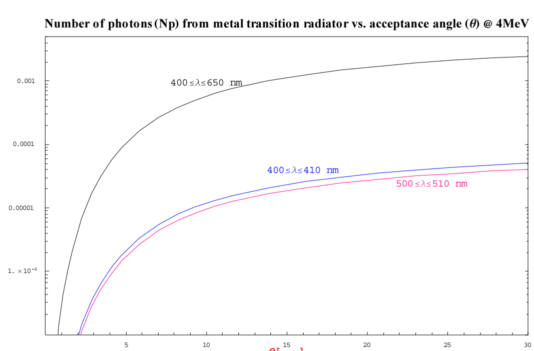

Figure 4: Number of photons from a metallic transition radiator in the acceptance angle produced by a 4 MeV electron.

Possible radiators are Optical Transition Radiator (OTR) and Cherenkov radiators. OTR produces only few photo electrons for electron energies of about

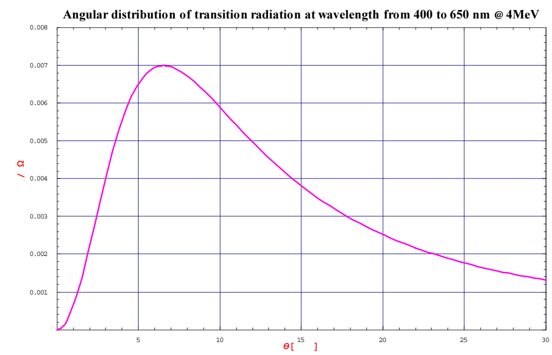

Figure 5: The angular distribution of the photons (from 400 nm to 650 nm) per solid angle produced by a metal transition radiator with 4 MeV electron beam.

4 MeV (Fig. 4) and with a broad angular distribution (Fig. 5). At the same energy Cherenkov radiators produce much more photons (Fig. 6), but the time dispersion is higher. This distribution can be improved by a special machined quartz.

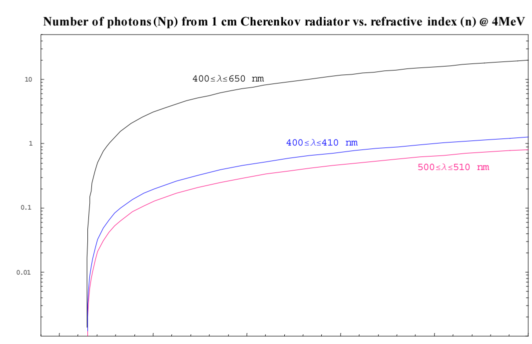

Figure 6: Number of photons from a 1 cm thick Cherenkov radiator with refrative index (n) produced by a 4 MeV electron.

- Measurement of longitudinal phase space

  A simultaneous measurement momentum and bunch length measurement gives the longitudinal phase space. This could be done by a dipole and a slit to separate the momentum and using a radiator. The streak camera measures the temporal distribution of photons. By repetition with different slit position the whole momentum distribution and temporal distribution of the electron bunch are reconstructed.

POSITION MONITORING OF ACCELERATOR COMPONENTS AS MAGNETS AND BEAM POSITION MONITORS

G. Schmidt, E. Kasel, D. Schirmer, D. Zimoch, K. Wille

DELTA, University of Dortmund, Germany

Abstract

In third generation light sources a large amount of heat load from synchrotron radiation must be dissipated from the vacuum chamber. The synchrotron radiation hits the outer chamber wall and leads to a bending of the vacuum chamber.

Due to the fact that very often beam position monitors are included into the vacuum chamber, they start to move with increased heat load onto the vacuum chamber.

An inexpensive and precise method to monitor this movement has been tested at the Dortmunder Electron Test Accelerator (DELTA). Commercially available Linear Variable Differential Transformers (LVDTs) have been used.

In addition it was possible to demonstrate that due to the vacuum chamber contact to quadrupole magnets the quadrupoles were moving with increasing beam current leading to a significant orbit drift.

1 DELTA STORAGE RING

The DELTA Storage Ring is a 1.5 GeV 3rd generation storage ring for synchrotron radiation production [1].

The stability and reproducibility of the storage ring, especially the beam orbit, is crucial for the operation as synchrotron light source. The stability of the measured beam orbit itself depends on the position of the beam position monitors and the focusing magnets. Therefore the position of quadrupole magnets and beam position monitors was measured.

2 POSITION SENSORS

To allow the monitoring of the large amount of components with sufficient resolution an inexpensive commercially available solution was searched, which allows the direct position measurement of the components. As a good compromise between cost, sensitivity and ease of use, Linear Variable Differential Transformers (LVDTs) were chosen. For the time being 5 sensors from Schlumberger [2] and TWK [3] have been used to make first tests. The next step will be the installation of 25 sensors to monitor quadrupoles and BPMs in one fourth of the DELTA storage ring. This will allow to study, survey and improve the mechanical stability of the components. After an efficient reduction of the movement of components the sensors will be mounted permanently on important BPMs to allow the correction of the BPM reading by the measured BPM position movement.

3 LINEAR VARIABLE DIFFERENTIAL TRANSFORMERS (LVDTS)

The position sensor works as an inductive half bridge. A position change of a Mu-Metall cylinder inside two solenoids induces an inductance change inside the two solenoids, which is transferred into a position proportional electrical signal (see Fig. 1). A standard measurement range of 5 mm was used. The sensor has a linearity of 0.25 % (10 μm).

The output signal is connected to the DELTA control system via standard ADC boards.

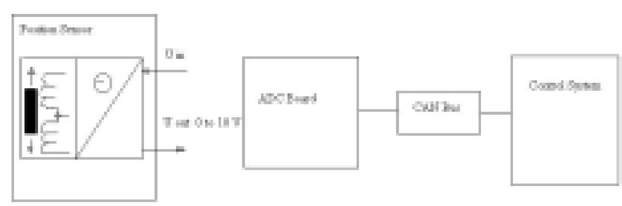

Fig. 1: Working principle of the Linear Variable Differential Transformer (LVDT).

4 FIRST MEASUREMENTS AND RESULTS

DELTA is only operated during the week from Monday morning to Friday afternoon. Especially on Mondays the reproducibility of the machine was difficult. The position monitoring of magnets showed a large movement of magnets during the Monday morning shift (see Fig. 2).

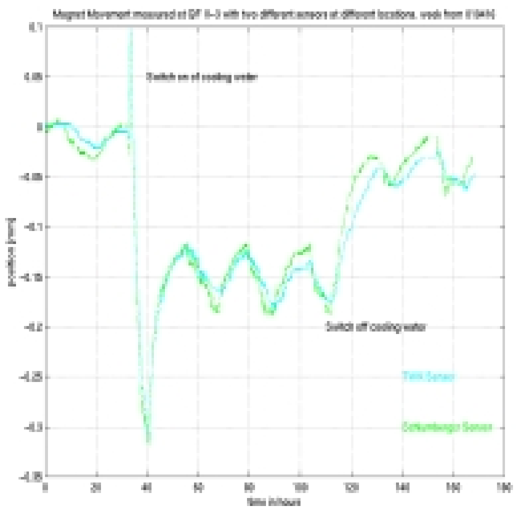

Fig. 2: Quadrupole Position measured during one week with beam stored at low energy (750 MeV) (no influence due to synchrotron radiation). Startup of the machine and daily changes are visible.

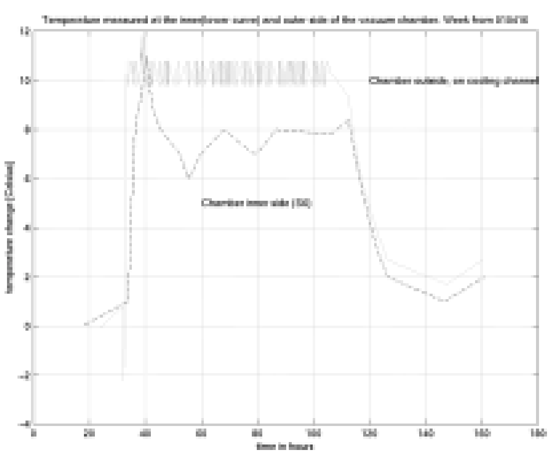

Fig. 3: Temperature development during the same week with low beam energy (750 MeV) (no heat load due to synchrotron radiation).

The effect can be explained by the rise of the cooling water temperature during the startup of the machine (see Fig. 3). The cooling channel is welded to the outside of the stainless steel vacuum chamber to dissipate the heat load from synchrotron radiation. During the start-up of DELTA the cooling water temperature increases. The outside of the vacuum chamber in the cooling channel becomes more than 10 degree Celsius warmer. This leads to a bending of the chamber because the inner chamber part follows with a delay. The temperature sensor reading shows that it takes more than 4 hours to establish an equilibrium between inner and outer side of the chamber. The position of the quadrupoles follows this bending of the chamber (see Fig. 2 and 3).
The vacuum chamber very often has contact to the quadrupole magnets and therefore moves them with the bending of the chamber.

In addition a daily change of the temperature in the hall leads to a temperature change at the inner side of the chamber whereas the outer chamber temperature due to the cooling stays constant. This leads to a bending of the chamber and to a movement of quadrupole magnets (see Figure 2 and 3). The data were recorded during a low energy run of DELTA so that the influence of synchrotron radiation can be neglected.

The third thermal effect is the heat load from synchrotron radiation. As a function of beam current and the cooling water temperature changes. This again bends the chamber and moves quadrupole magnets as visible in Figure 4 and 5.

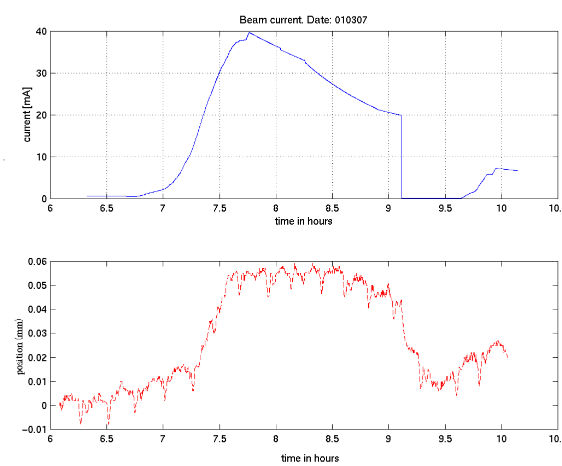

Fig.4: Magnet movement with increasing the beam current at 1.5 GeV beam energy.

The influence of a quadrupole magnet onto the equilibrium beam orbit depends on the position movement and the local betatron function. As a conclusion of the measurement especially some quadrupoles show a strong effect. To stabilise the beam orbit these quadrupoles will be disconnected from the vacuum chamber.

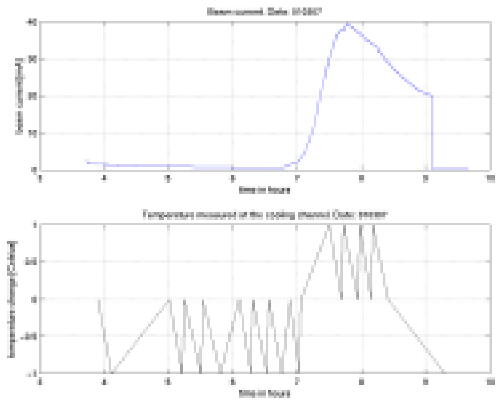

Fig.5: Chamber temperature as function of the beam current at 1.5 GeV beam energy. Synchrotron radiation changes the cooling water temperature.

5 CONCLUSION

The use of position sensors in combination with temperature sensors has allowed to understand the behaviour of the DELTA orbit stability problems. Some quadrupoles have already been located which have a significant position movement and influence on the equilibrium beam orbit. The next step will be to stabilise these quadrupoles.

The low cost and industrial availability of the used sensors will allow to use an increased number of sensors to study the effect of different improvements and changes in the chamber support, chamber design or cooling system.

Finally the position sensors will be used to monitor the position of BPMs and to include this information into the orbit correction scheme.

ACKNOWLEGEMENT

Thanks to O. Kaul, B. Sarau, R. Fischer, M. Seebach from DESY Hamburg for their support and who made the Schlumberg sensors available to us.

REFERENCES

[1] J. Friedl et al.: Recent results of the commissioning of the DELTA facility', PAC 97, Vancouver, Canada, 1997
[2] TWK-Elektronik GMBH, Düsseldorf, Germany
[3] Schlumberger, West Sussex, England

SIGNAL PROCESSOR FOR SPring-8 LINAC BPM

K. Yanagida, T. Asaka, H. Dewa, H. Hanaki, T. Hori, T. Kobayashi, A. Mizuno,
S. Sasaki, S. Suzuki, T. Takashima, T. Taniuchi, H. Tomizawa,
Japan Synchrotron Radiation Research Institute, Mikazuki, Hyogo, 679-5198, Japan

Abstract

A signal processor of the single shot BPM system consists of a narrow-band BPF unit, a detector unit, a P/H circuit, an S/H IC and a 16-bit ADC. The BPF unit extracts a pure 2856-MHz RF signal component from a BPM and makes the pulse width longer than 100 ns. The detector unit that includes a demodulating logarithmic amplifier is used to detect an S-band RF amplitude. A wide dynamic range of beam current has been achieved; 0.01 $\sim$ 3.5 nC for below 100-ns input pulse width, or 0.06 $\sim$ 20 mA for above 100-ns input pulse width. The maximum acquisition rate with a VME system has been achieved up to 1 kHz.

1 INTRODUCTION

Beam operation of the SPring-8 linac began in 1996, but a BPM system was not equipped. Development of a BPM system started in 1990 and the conceptual design has been modified several times looking for the optimum BPM system for the SPring-8 linac. The guidelines for designing the BPM system were as follows.

- Bunch separation as short as 350 ps (2856 MHz).
- A wide range of beam pulse length; i.e., from a 1-ns (including a single bunch) beam to a 1-μs beam.
- A wide dynamic range of beam power; i.e., from a 1-ns - 10-mA (for the positron) beam to a 1-μs - 100-mA beam.
- Required resolution or beam-position measurement stability of < 0.1 mm (6 σ).
- A high acquisition rate of $\geq$ 60 Hz.
- Simple design and low cost manufacturing.

In the past decade, the conceptual design of the BPM system has been fixed. The detection frequency of 2856 MHz was determined in 1993. The electrostatic stripline pickup method for the BPM was chosen in 1998. Finally, a detection method based on a circuit using a demodulating logarithmic amplifier AD8313 (ANALOG DEVICES) was determined in 2000. After connection to the control system, the BPM system will be in operation in this year. The latest design of the BPM system was described in the previous paper [1].

2 SIGNAL PROCESSOR

The signal processor consists of two Nuclear Instrumentation Modules: the BPF (band pass filter) module, and the detector module. Both modules have four equivalent process channels. Figure 1 shows a block diagram of the signal processor.

There are two reasons to adopt the band pass filter. One is to extract a pure 2856-MHz RF signal component from the BPM or to eliminate noise (or higher harmonic) components. The other is to make the pulse width longer than 100 ns when an input pulse width is shorter than 100 ns. The pulse width of 100 ns was determined to match the response of the detector unit (the rise time of 40 ns).

A band pass filter is mounted in a case unit (the BPF unit), because characteristics of all BPF units cannot be adjusted precisely. This enables us to examine BPF units and to select four BPF units that have similar characteristics in order to get temperature stability. A component that includes the AD8313 is also mounted in a case unit (the detector unit) for the same reason.

2.1 BPF Module

The BPF unit is a second-order Butterworth cavity filter which has very flat transmission spectrum around center frequency. The center frequency is tuned to 2856 $\pm$ 0.01 MHz under the temperature of 33 $\pm$ 0.1 °C. These characteristics of the BPF unit are summarized in Table 1.

Table 1: Characteristics of the BPF unit

Type of Filter	Second-Order Butterworth Cavity Filter
Material	Brass
Center Frequency	2856 $\pm$ 0.01 MHz
Tuning Temperature	33 $\pm$ 0.1 °C
Temperature Drift of Frequency	$\sim$ 50 kHz/°C
Flatness	-0.01 dB at $\pm$ 300 kHz
Band Width	$\sim$ 10 MHz
Insertion Loss	$\sim$ 1.5 dB
VSWR	$\leq$ 1.5
Input/Output Impedance	50 Ω

2.2 Detector Module

The principal elements of the detector module are the detector unit that detects an S-band RF amplitude, a self-triggered peak hold (P/H) circuit, an externally triggered sample hold (S/H) IC and a 16-bit analog-to-digital converter (ADC). Although the signal processor needs an external trigger synchronizing with the input signal, the pulsed output (Detector Unit Output) can be used as the external trigger.

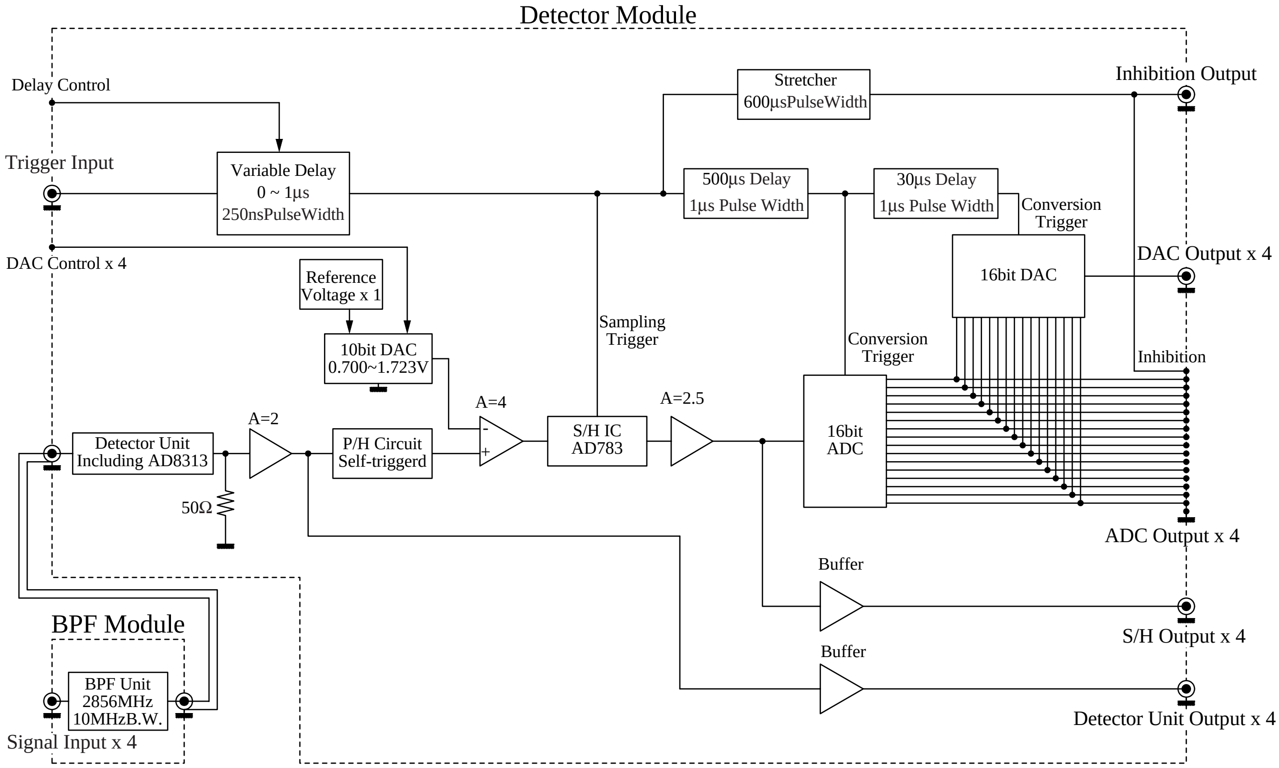

Figure 1: Block diagram of the signal processor.

Detector Unit The detector unit involves a protection circuit, the AD8313, a slope trimmer and an offset trimmer as shown in Fig. 2. Figure 3 and 4 show output and its slope of the detector unit, when CW RF power is input. The slope is adjusted to 10 mV/dBm between -45 dBm and -15 dBm. The offset voltage is adjusted to 535 mV at -45 dBm.

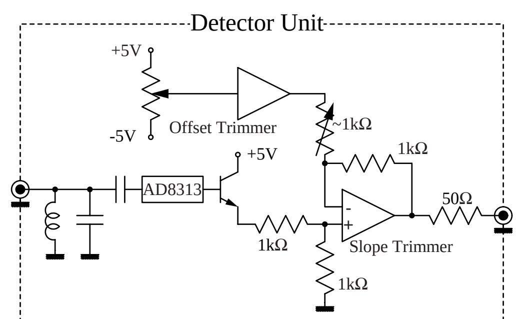

Figure 2: Block diagram of the detector unit.

If we define the dynamic range as the region above 7.5 mV/dBm of the slope, the dynamic range becomes $-52 \sim -2$ dBm of the input power. The dynamic range of the beam current corresponds to 0.01 $\sim$ 3.5 nC for below 100-ns input pulse width, or 0.06 $\sim$ 20mA for above 100-ns input pulse width as shown in Fig. 5. These characteristics of the detector unit are summarized in Table 2.

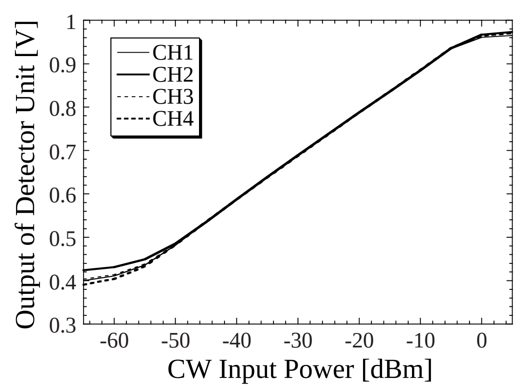

Figure 3: Output of the detector unit.

Stretcher and ADC The minimum input pulse width from the detector unit is 100 ns, while the conversion time of ADC ADS7807 (BURR BROWN) is 25 μs. This means a pulsed signal must be stretched to 25 μs.

There are two sequential stretchers. The first stretcher is the self-triggered P/H circuit as shown in Fig. 6. This P/H circuit has a low leak shottkey diode HSMS-282 (AGILENT TECHNOLOGIES) and a high impedance operational amplifier OPA655 (BURR BROWN). The response (the rise time of $<$ 20 ns) is faster than the response of the detector unit. The droop rate of < 2 μV/ns enables a small droop of $<$ 0.5 mV during the acquisition time of the second stretcher.

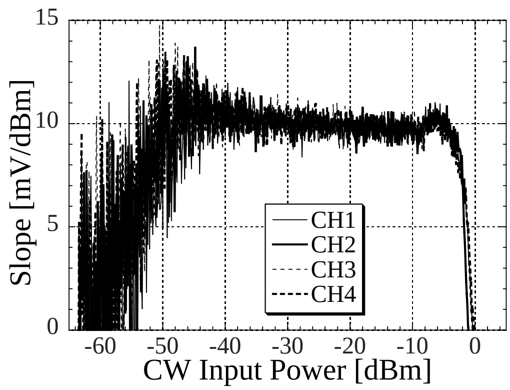

Figure 4: Slope of the output.

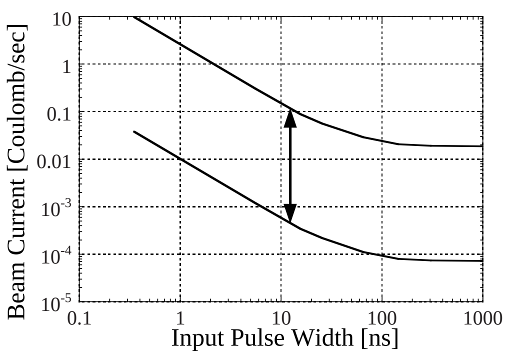

Figure 5: Dynamic range of the beam current (Area lies between lines).

The second stretcher is an S/H IC AD783 (ANALOG DEVICES) whose acquisition time and droop rate are $\leq$ 250 ns and $\leq$ 1 μV/μs. This droop rate enables a small droop of $\leq$ 25 μV during the conversion time of ADC.

Noise Level and Resolution The shot-by-shot resolution of beam position is determined by noise level. The major noise comes from the AD8313 or the S/H IC. Figure 7 gives the output noise level of the prototype detector module and a deduced resolution of the beam position when the smallest BPM (ϕ32mm) is used (calculated by log-ratio method [2]). This noise level was dominated by the S/H IC, therefore a low noise S/H IC AD783 is used in the latest design to improve the resolution.

Table 2: Characteristics of the detector unit

Detection Band	S-Band
VSWR	≤ 1.5
Slope	10 mV/dBm
Offset	535 mV at -45 dBm
Dynamic Range	$-52 \sim -2$ dBm
Rise Time	40 ns
Temperature Drift of Output	$-1 \sim -0.5$ mV/°C
Input/Output Impedance	50 Ω

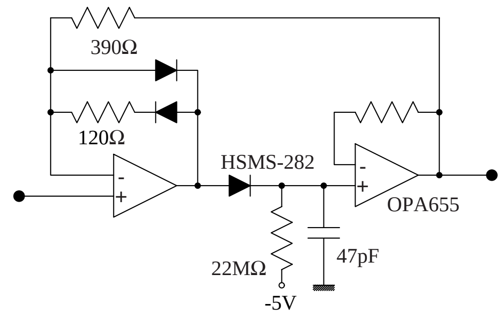

Figure 6: Block diagram of the P/H circuit.

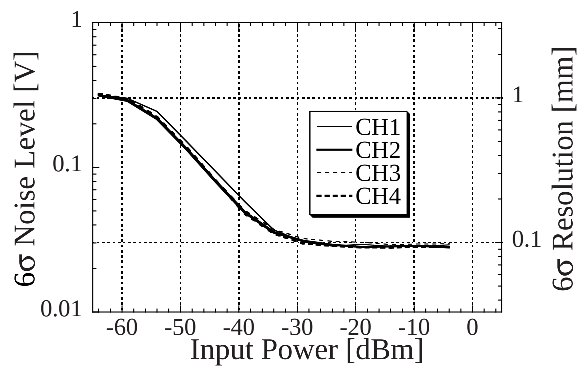

Figure 7: Output noise level of the prototype detector module and deduced resolution of the beam position.

3 DATA ACQUISITION

The signal processor prepares two kinds of signal output for every channel. One is an analog output, and the other is a 16-bit digital output. The range of both outputs is $\pm$10 V. For the digital output, an inhibition signal is sent when the ADC is converting. The computer system (we usually use a VME computer) detects the rise of the inhibition bit and then starts to acquire data after a delay of 0.6 ms. In this way, the maximum acquisition rate has been achieved to up 1 kHz.

4 ACKNOWLEDGMENT

The authors would like to thank J. Bergoz and K. Unser (BERGOZ INSTRUMENTATION) for the proposal of using a logarithmic amplifier and useful discussion.

5 REFERENCES

[1] K. Yanagida, et al., "A BPM SYSTEM FOR THE SPring-8 LINAC", Proc. of the 20th Int. Linac Conf., Monterey USA, Aug. 2000, pp. 190-192.

[2] F. D. Wells, et al. "LOG-RATIO CIRCUIT FOR BEAM POSITION MONITORING", AIP Conf. Proc. **229**, p. 308 (1991).

Accuracy of the LEP Spectrometer Beam Orbit Monitors

E. Barbero, B. Dehning, J. Prochnow, CERN, Geneva, Switzerland
J. Bergoz, K. Unser, Bergoz Instrumentation, 01630 St. Genis Pouilly, France
J. Matheson, Rutherford Appleton Laboratory, Chilton, UK
E. Torrence, University of Chicaco, Chicago, IL60637, USA

Abstract

At the LEP e+/e- collider, a spectrometer is used to determine the beam energy with a target accuracy of 10^{-4}. The spectrometer measures the lattice dipole bending angle of the beam using six beam position monitors (BPMs). The required calibration error imposes a BPM accuracy of 1 μm corresponding to a relative electrical signal variation of $2 \cdot 10^{-5}$. The operating parameters have been compared with beam simulator results and non-linear BPM response simulations. The relative beam current variations between 0.02 and 0.03 and position changes of 0.1 mm during the fills of last year lead to uncertainties in the orbit measurements of well below 1 μm. For accuracy tests absolute beam currents were varied by a factor of three. The environment magnetical field is introduced to correct orbit readings. The BPM linearity and calibration was checked using moveable supports and wire position sensors. The BPM triplet quantity is used to determine the orbit position monitors accuracy. The BPM triplet changed during the fills between 1 and 2 μm RMS, which indicates a single BPM orbit determination accuracy between 1 and 1.5 μm.

1 INTRODUCTION

The LEP energy calibration requires the determination of the beam energy ratio between 50 GeV and 93 GeV. The beam energy at 50 GeV is accurately calibrated using the spin polarization of the circulating electrons. Therefore only changes of the relevant quantities which occur during the calibration procedure have to be taken into account. The spectrometer measures the change in bending angle in a well-characterised dipole magnet as LEP is ramped [1, 2]. The beam trajectory is obtained using three beam position monitors (BPMs) on each side of the magnet. The BPMs used consist of an aluminium block with an elliptical aperture and four capacitive button pickup electrodes placed at the corners of a square with a length of 62 mm. The button signals are fed to customised electronics supplied by Bergoz Instrumentation. The electronics use time multiplexing of individual button signals through a single processing chain to optimise for long-term stability. The position of the BPM block is surveiled with wire position sensors [6]. Two independent wires are used to monitor the relative horizontal and vertical movements. The environmental magnetic field in the drift space is monitored with fluxgates.

The required BPM accuracy of 1 μm means that a orbit position determination at time t_1 and a second at t_2 should not differ more then 1 μm for the same beam position. In between of t_1 and t_2 the beam energy has to be changed from 50 to 93 GeV and several other parameters will change accordingly (for example: radiated synchrotron power, transverse and longitudinal beam size). A unobserved BPM support movement of 1 μm in between of t_1 and t_2 for the same beam position would be not acceptable.

An estimate of the influence of changing measurement conditions on the orbit determination accuracy is given in section 2 and 3. The absolute calibration of the BPMs with wire position sensors is explained in section 4. The orbit determination accuracy is estimated by using a beam position independent quantity (BPM triplet) and by calculating the difference of measurements taken at t_1 and t_2 (see section 5).

2 BEAM CURRENT AND BEAM ORBIT

During the operation, differences in the beam current in a fill were observed with a mean value of 55 μA and a RMS of 44.4 μA. The average beam current in a fill was 2050 μA. Estimating the position changes due to current variations, using the beam simulator results [3], an upper limit of position changes of 0.3 μm is calculated. The difference and the absolute value of the beam current during a fill as function of the fill number are shown in figure 1. The absolute beam currents in fill 7833, 8223 and 8443 were on purpose reduced.

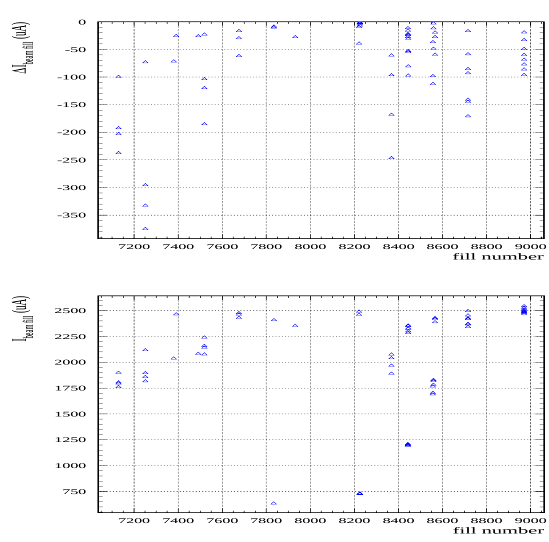

Figure 1: The beam current changes (top) and the absolute beam current (bottom) during a fill throughout the year.

Beam position changes have been minimized during operation (see Fig. 2) to avoid position errors caused by the non-linear response of the monitors [4, 5]. The non-

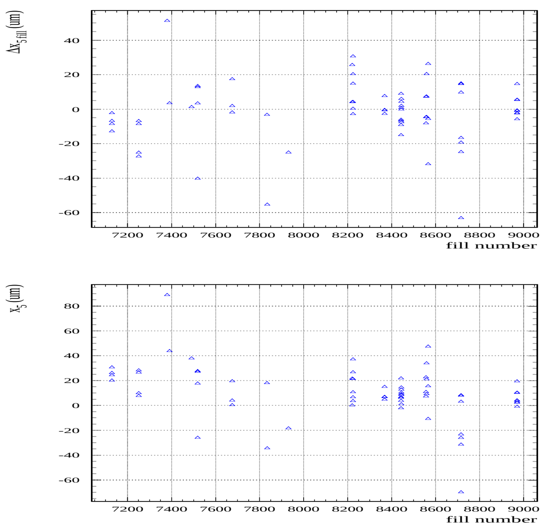

Figure 2: The variation of the horizontal beam position change (top) and the absolute beam position (bottom) during a fill throughout the year.

linear simulations predict systematic position errors below 0.3 μm due to the beam position changes during a fill. For all BPMs the position variations are shown in table 1.

Table 1: Mean and RMS beam position in the horizontal plane for all BPMs in μm

	1x	2x	3x	4x	5x	6x
Mean	0.8	2.79	-3.21	3.03	1.06	4.19
RMS	23.9	33.5	29.5	19.2	32.2	22.1

3 ENVIRONMENTAL MAGNETIC FIELD

The environmental magnetic field requires a significant beam position measurement correction. The environmental field is caused by the earth magnetic field, power cables placed near to the beam line and some vacuum pumps. Fig. 3, top, shows the vertical field component of the environmental field for different operation conditions along the drift space of the spectrometer. The BPMs are placed at $\pm$ 2,6 and 10 m. The large field increases at $\pm$ 3.25 m are due to the permanent magnets of vacuum ion pumps. The horizontal beam orbit at the left and right side of the magnet for two different operating conditions is shown in figure 3, bottom. The relevant orbit correction for the spectrometer is given by the difference between the two curves. The correction is mainly caused by the non zero field and not by the large field changes due to ion pumps. The largest correction of 3 μm has to be applied at the left/right extreme

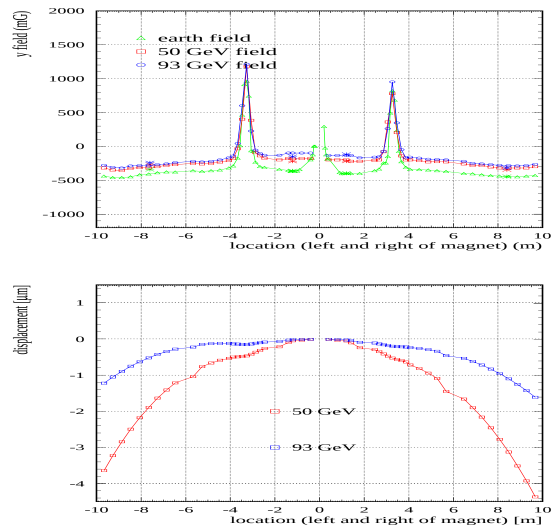

Figure 3: Top: The vertical environmental magnetic field in the region left and right of the spectrometer bending magnet. Different fields are caused by different excitations of the main magnets. Bottom: The calculated horizontal bending of the beam due to the environmental field for two different beam energies.

BPMs.

4 MOVEABLE BPMS AND GAIN CALIBRATION

The absolute gain calibration of the BPM was done by moving the BPM support and measuring the movement with wire position sensors [6]. All 6 BPM supports were mounted on translation stages and driven with stepping motors. The position was measured using the wire position sensors (WPS) installed for surveillance purpose. The BPM position reading is corrected for orbit changes during the 20 min operation by using the BPM triplet (see next section). Fig. 4, top, shows the BPM triplet versus the wire position measurement. The difference between BPM triplet and parametrisation shows no systematic effect (see Fig. 4, bottom) and has a RMS value of 0.8 μm.

5 ORBIT POSITION AND BPM TRIPLET

The monitor orbit reading has to be corrected for possible movements of the BPM support. A system of wire position sensors [6] is used to monitor support position changes (wps_{corr}). The bending effect of the environmental field is another correction applied ($b_{fieldcorr}$). The relative gains ($g_{r\,i}$) of BPMs are determined by orbit bumps before every measuring period [4]. The absolute gains are determined using the wire position sensors ($g_{a\,i}$).

The evaluated orbit position reads:

$$x_i = g_{r\,i} \cdot < g_a > \cdot bpm_i + offset_i - wps_{corr\,i} - b_{field\,corr\,i} \quad (1)$$

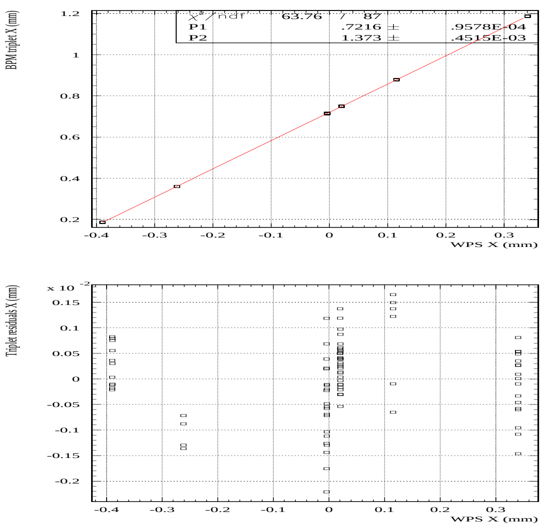

Figure 4: Top: The BPM position measurement as function of the wire position readings over a range of 1 mm. A straight line parametrization is applied to the measurements. The parameter P2 expresses the gain ratio between the two monitors. Bottom: The residuals between data and parametrization as function of wire position readings.

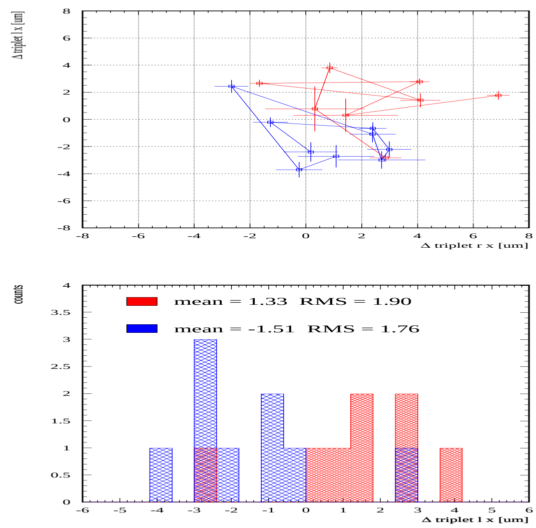

Figure 5: Top: The difference of the left BPM triplet vs the difference of the right BPM triplet for different energies (50 and 93 GeV). The colours (different lines) indicate measurements done using different beam optics. Bottom: The histogram shows the frequency distribution of the left triplet differences with mean and RMS value for the the different optics.

The alignment and electronic offset is summarised in the formula by the term offset.

To study the relative accuracy of the BPM monitors three position signals are combined to the BPM triplet:

$$Triplet = \frac{x_1 + x_3}{2} - x_2 \qquad (2)$$

The BPM triplet response is independent of beam orbit changes. The difference of BPM triplets of different orbit measuements allows to test the relative accuracy of BPMs by changing beam positions. A change of the accuracy of one BPM lead to a non zero BPM triplet difference and a change of the accuracy of 2 or 3 BPMs will likely lead to a difference. The BPM triplet difference is composed of an orbit measurement at a beam energy of 50 GeV and 93 GeV. Figure 5, top, shows the BPM triplet difference of the 3 BPMs on the left side of the magnet versus the 3 BPMs on the right side. Measurement were done using two different optics (different lines and colours) The left BPM triplet (see Fig. 5,bottom) shows significantly different mean values for the two different beam optics (mean: 1.3 and -1.5 μm with a RMS of 1.9 and 1.8 μm, number of measurements: 8 and 9). This systematic difference is not yet explainable. The BPM triplet difference mean value and RMS value result in a single BPM orbit determination accuracy between 1 and 1.5 μm.

6 CONCLUSION

The influence of changing measurement conditions on the orbit determination accuracy (beam current variation, beam position variation) was kept well below 1 μm and is not limiting the accuracy. The orbit position measurements are corrected for BPM block movements and environmental magnetic field influences. A relative BPM calibration procedure using orbit bumps and an absolute procedure using wire position sensors have been applied. The BPM triplet quantity was used to estimate the single BPM orbit determination accuracy.

7 REFERENCES

[1] B. Dehning et al., “Status of the LEP2 Spectrometer Project”, CERN-SL-2000-038-BI, 7th European Particle Accelerator Conference, Vienna, Austria, 24 Jul 2000.

[2] B. Dehning, “The LEP Spectrometer”, CERN-OPEN-99-112, 9th LEP-SPS Performance Workshop, Chamonix, France, 5 Jan 1999.

[3] E Barbero et al., “Performance of BPM Electronics for the LEP Spectrometer”, CERN-SL-2000-054-BI, 9th Beam Instrumentation Workshop, Cambridge, MA, USA, 8 May 2000.

[4] R. Assmann et al., “Nonlinearities in the Response of Beam Position Monitors”, CERN-SL-2000-055-BI, 9th Beam Instrumentation Workshop, Cambridge, MA, USA, 8 May 2000.

[5] R. Assmann et al., “Nonlinear Response of Orbit Monitors”, CERN-SL-2000-030-BI, 7th European Particle Accelerator Conference, Vienna, Austria, 24 Jul 2000.

[6] W. Coosemans et al., “Determination of the Accuracy of Wire Position Sensors”, CERN-SL-2000-029-BI, 7th European Particle Accelerator Conference, Vienna, Austria, 24 Jul 2000.

STRIPLINE BEAM POSITION MONITORS FOR "ELBE"

P.Evtushenko, A.Büchner, H.Büttig, P.Michel, R.Schurig, B.Wustmann, FZR, Germany
K. Jordan TJNAF, USA

Abstract

At the Forschungszentrum Rossendorf (FZR), the superconducting electron linear accelerator ELBE is under construction. It will deliver an electron beam with an energy of up to 40 MeV at an average beam current of up to 1mA. The accelerator uses standing wave DESY type RF cavities operating at 1.3 GHz. A non-destructive system for the measurement of the beam position at about 30 locations is needed. To obtain the required resolution of 100 µm, a system of stripline beam position monitors (BPM) is under design.

1 INTRODUCTION

There are some different applications of the electron beam of the ELBE accelerator. It will be used for experiments in radiation physics, nuclear physics and neutron physics. It also will be the driver for the infra red free electron laser (FEL). Obviously an accelerator needs a system for the beam position measurements. Also the position of the electron beam has to be controlled at the target in any experiment and inside the undulator of the FEL. In the case of the ELBE accelerator, the required resolution of the beam position measurements is about 100 µm. We decided to use stripline BPM, since it is well known that with the BPM one can easily achieve the resolution.

2 MECHANICAL DESIGN OF THE BPM

2.1 3λ/4 version of the ELBE BPM

Two versions of the BPMs were designed. The BPM of the JLab FEL machine was the prototype for our first BPMs. The BPM is electron beam welded and it has four SMA feedthroughs which are also welded to the BPM. The transmission line which is formed by the strip and external pipe of the BPM has on impedance of 50 Ω. The length of the strip is an important item for BPM sensitivity and for the calibration of the whole BPM system. Usually the length is optimized so that the BPM has maximum sensitivity at the fundamental frequency of the accelerator, which leads to a strip length $(\lambda/4)\times(2n+1)$, where n is 0,1,2,… That means 57 mm, 173 mm and so on at 1.3 GHz. But because of the calibration procedure which we want to use the length of the strip of the BPM is 144 mm, instead of 173 mm.

2.2 Calibration of the BPM system

For the calibration and verification of the BPM system we will use the procedure familiar with the JLab BPM system [1]. Before we explain the idea of the calibration we want to note, that during machining and welding of the BPM the X plane electrodes can be a little shifted in the X direction, but not in the Y direction. The procedure of the calibration is the following, if we want to calibrate, for instance, the Y plane of a BPM, we can inject a 1.3 GHz signal to the X plane electrode of the BPM. In this case the position which will be displayed in the corresponding BPM software is a result of two facts. First is the difference between the mechanical and electrical center of the BPM and second is that electrical chains of the two opposite channels can have slightly different gain and offset. All these facts can be taken in to account in the calibration. There is one more important item in the calibration. To enable such a method of calibration the S_{21} from the X channel to a Y electrode has to be big enough. To increase the S_{21} the strip length was reduced from 173 mm to 144 mm. Important is that such calibration can be done when the BPM detectors are already installed on the beam line.

2.3 Compact version of the BPM

During the manufacturing of the first BPMs we faced some technological problems. For instance, some feedthroughs

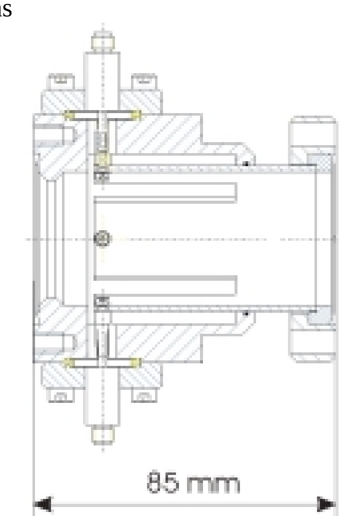

Figure 1: Compact BPM with strip length 40 mm

were broken under welding of the BPM or during the baking of the beam line. Sometimes it was not possible to put the BPM at the desirable position on the beam line because of its length. All these reasons pushed us to design another BPM. The main idea was to reduce the strip length from 3λ/4 to λ/4. The cutaway view of the compact BPM is in figure 1. On the BPM another kind of the SMA feedthrough is used. The feedthroughs are not welded to the BPM but sealed to it with the CF flanges. This make possible changing the feedthrough on the BPM without removing it from the beam line. The BPM is done with the help of hard soldering, but not with electron beam welding, which makes it significantly cheaper. The strip length is 40 mm, this enable the calibration described above. The total length of the BPM is 85 mm.

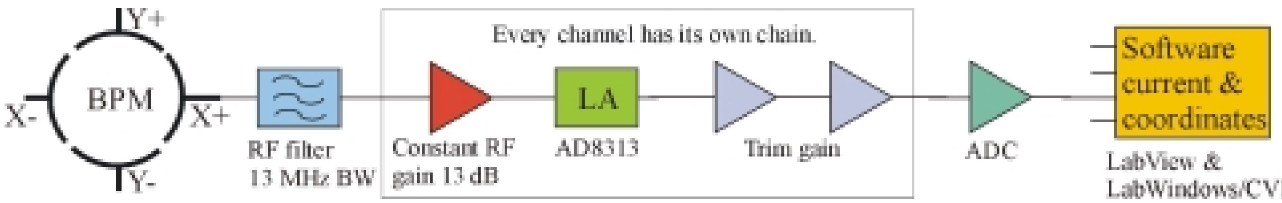

Figure 2: Principle scheme of the BPM electronics

3 THE BPM ELECTRONICS

The BPM electronics is based on the logarithmic amplifier AD8313 from Analog Devices [2], which is a direct RF to DC converter rated up to 2.5 GHz. This fact give us the possibility building the BPM electronics without mixing down the RF signal of the BPM. Thus the electronics operate at the fundamental frequency of the accelerator, which is 1.3 GHz, and have a rise time of about 10 µs. The BPM signal goes through the bypass filter with 13 MHz bandwidth. Then it is amplified with constant RF gain 13 dB to be matched to the extra linear range of the AD8313. The range goes from –65 dBm up to –5 dBm. The output of the logarithmic amplifier is matched to the ADC working range with the trim gain. One digit of the ADC corresponds to 8 µm beam displacement.

4 MEASUREMENTS ON THE WIRE TEST BENCH

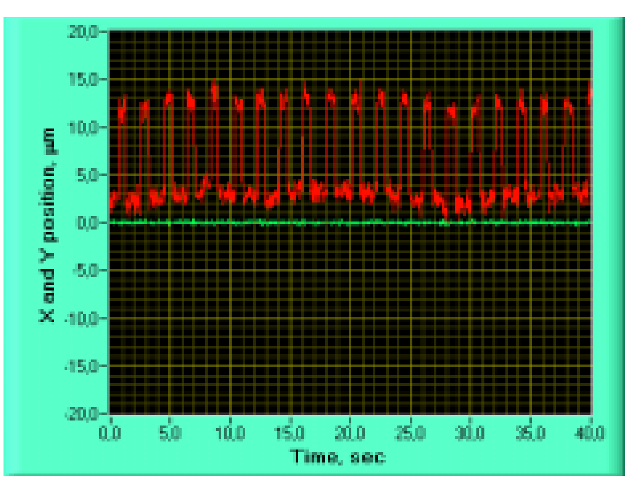

Figure 3: One result from the wire test bench.

All new BPMs and the BPM electronic units are tested on the "wire test bench”. The BPM is mounted on the linear motor stage, which can move the BPM in steps of 2.5 mm. A well aligned wire is stretched through the BPM. All this equipment is mounted on the optical table to prevent wire oscillations. The wire is driven by an RF generator at 1.3 GHz and excites TEM waves in the BPM thus simulating the electron beam. One of the tests we perform with the wire is a modulation of the wire position with a very small amplitude. Decreasing the amplitude of the modulation we can see the minimum of the wire (beam) displacement which we can detect with the BPM and electronics. The result of one of the tests is shown in figure 3. During the test, the position of the wire was modulated with an amplitude of 10µm. Another test concerned the linearity of the BPM. This way we proved that the BPMs are linear enough in the required range of ±5mm.

5 MEASUREMENTS ON THE ELBE INJECTOR

Finally, the real BPM resolution has to be measured with the beam. Up to now we were able to make such measurements with the ELBE injector with the 250 keV electron beam and current of up to 1 mA. To estimate the BPM resolution, the beam position was measured with a 5 µs rate over several milliseconds. The average position of the beam was calculated, as well as the standard deviation of the beam position distribution. The standard deviation is naturally the accuracy of the position measurements in the case when the measurement time has the same order of magnitude as the sampling time which is 5 µs in our case. In fact the minimum of the macro pulse length of the accelerator has to be 100 µs. That means that with the help of the averaging we have accuracy even better than the measured standard deviation.

Results of the measurements at different currents are presented below.

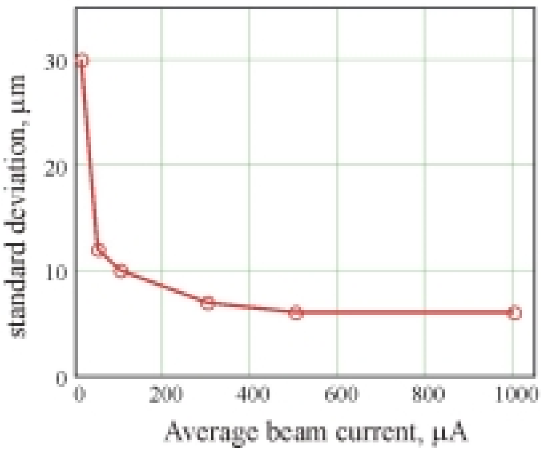

Figure 4:Standard deviation of the position measurements.

6 BUNCH LENGTH MINIMIZATION IN THE INJECTOR

For proper operation of the accelerator it is very important to minimize the length of the bunch entering the RF cavity. The injector of the ELBE accelerator consists of the pulsed thermionic electron gun and two buncher cavities. The gun is producing pulses with a repetition rate of 13 MHz or 260 MHz with a length of about 500 ps. The bunchers are used to compress the bunch so that its length is about 10 ps at the entrance of the first RF cavity. The first subharmonic buncher operates at 260 MHz and second fundamental buncher operates at 1.3 GHz. To make the correct bunch compression we must set the right phase and gradient of both bunchers. Thus we have to be able to measure the bunch length in the range from 500 ps down to 10 ps. One of the BPMs is installed upstream of the accelerating module. Since the spectrum of a beam depends on the bunch length, measurements in the frequency domain can give information about the bunch length. The idea is used successfully on the accelerator. To do this we just need to connect the BPM output directly to the spectrum analyzer and to maximize the signal amplitude by changing the power and phase of the bunchers. During the test phase of the injector we did the cross check measurements of the bunch length with the help of the kicker cavity. Measurements done with the kicker cavity and with the BPM are in good agreement. In figures 5 and 6 there are results of the measurements of the BPM signal at 1.3 GHz as a function of the subharmonic buncher power and phase. Thus we can see that optimal power and phase are 500 W and 5° respectively.

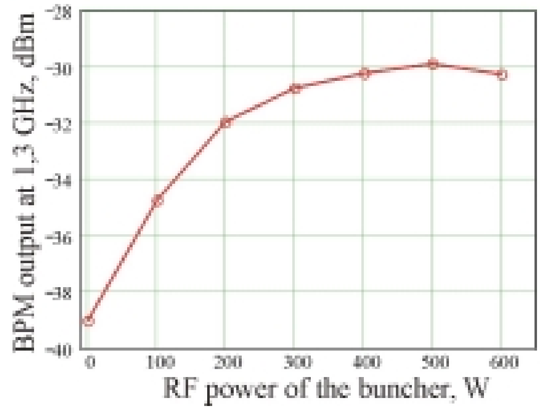

Figure 5:The BPM signal vs. the buncher power.

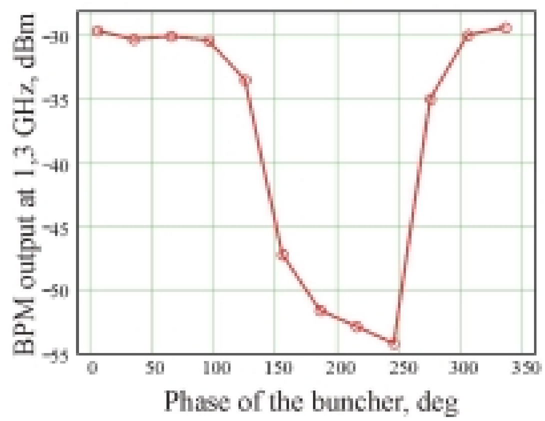

Figure 6:The BPM signal vs. the buncher phase.

REFERENCES

[1] T. Powers et al., "Design, Commissioning and Operational Results of Wide Dynamic Range BPM Switched Electrode Electronics", BIW'96, Chicago, May 1996.

[2] http://www.analog.com/

FUNCTIONALITY ENHANCEMENT OF THE MULTIPLEXING BPM SYSTEM IN THE STORAGE OF SRRC

Jenny Chen, C. S. Chen, K. H. Hu, K. T. Hsu, C. H. Kuo, Demi Lee, K. K. Lin
Synchrotron Radiation Research Center, Hsinchu, Taiwan, R. O. C.

Abstract

An extension of existing multiplex BPM electronics to provide capability for turn-by-turn beam position and phase advance measurement is implemented. The system can be configured as turn-by-turn beam position measurement or phase advance and coupling measurement. For turn-by-turn mode, the system performed four consecutive measurements of four BPM buttons. Data acquisition is synchronize with beam excitation. Turn-by-turn beam position is reconstructed by these four independent measurements. This system was named as pseudo-turn-by-turn beam position monitor system (PTTBPM). Resonance excitation of the stored beam and adopting lock-in techniques can measure betatron phase and local coupling. Design considerations of the system and preliminary beam test results are presented in this report.

1 INTRODUCTION

Measured betatron function and phase advance information is essential for precision beam-based machine modelling and is helpful to achieve ultimate machine performance. The BPM system of SRRC is a multiplexing system for precision closed-orbit measurement [1]. Using all BPMs for machine optics measurement is highly desirable. However, at present stage, only a couple of BPMs are equipped with log-ratio processor for turn-by-turn beam position measurement. Based upon the ideas of ESRF's "Mille-Tour" BPM system [2], we made a simple functional extension of the SRRC BPM system. A log-amplifier video detector mezzanine is implementing and installing at all BPMs electronic. Accompany with beam excitation and data acquisition system, turn-by-turn beam position at all BPMs site can be acquired. The data from four measurement of individual button can be reconstructed as pseudo-turn-by-turn beam position. Averaging out time dependent information is its drawback. Using lock-in amplifier to detect coherent oscillation with resonance excitation can support fast betatron phase measurement. PTTBPM system can acquire a lot of information for various beam physics study. However, the data analysis is tedious. On the other hand, the lock-in detection techniques accompany with resonance excitation can also be used for betatron phase measurement, betatron functions measurement, local coupling parameter measurement, and determines the errors of the lattice.

2 MEZZANINE MODULE

The multiplexing BPM electronics is a commercial units (Bergoz's MX-BPM). It is designed for averaged beam position measurement with micron resolution. The electronics composed of low pass filter, GaAs RF switch, band pass filter, high performance mixer and IF amplifier, quasi-synchronous detector, analog de-multiplexer and position computation circuitry. To observe betatron oscillation, wide bandwidth detector is needed. The IF bandwidth of MX-BPM before quasi-synchronous detector is larger than 5 MHz which is sufficient for betatron oscillation observation. This simple log amplifier detector was implemented due to its simplicity, no need of gain control, and small component counts. This mezzanine supports more than 50 dB dynamic range. When mezzanine module is engaged, AGC function of MX-BPM is disabled and single button is enable. The mezzanine is installed near the IF amplifier and detector circuitry. Small signal sensitivity is limited to about – 60 dBm that is due to deteriorate of the operation of PLL in synchronous detector. The functional block diagram of the mezzanine is shown in Figure 1. The mezzanine demodulates bunches signal at IF frequency (21.4 MHz). Position error of reconstructed position due to log conformance is acceptable for small oscillation amplitude.

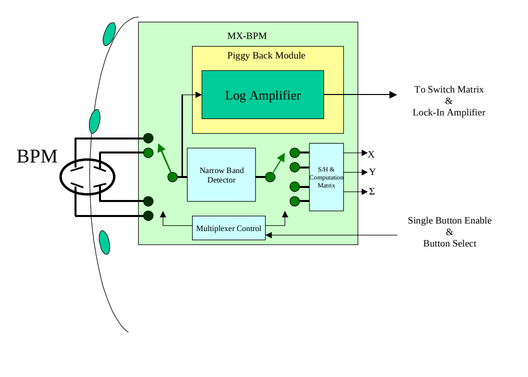

Figure 1. Functional block diagram of BPM processing electronics.

3 PTTBPM SYSTEM

The idea of PTTBPM is shown in Figure 2. Four measurements of individual BPM button signal can be reconstructed to obtain the turn-by-turn beam position.

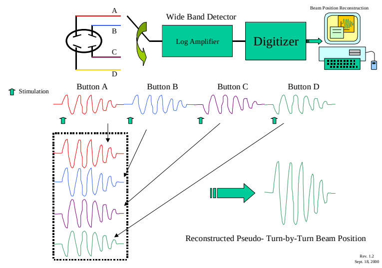

Figure 2. Concepts of PTTBPM

Reconstruction is based upon log-ratio normalization technique and is done by computer. Data acquisition is synchronized with beam excitation and controlled by VME crate. Figure 3 shows the system implementation. Matlab scripts running at control console arranges the sequence of data acquisition, data construction and analysis. Data reconstruction is done by the relationship

$$x = K_x\left[\log(\frac{A}{C}) - \log(\frac{B}{D})\right]\cos\alpha$$
$$y = K_y\left[\log(\frac{A}{C}) + \log(\frac{B}{D})\right]\sin\alpha \text{-----------------------..(1)}$$

where, α is the effective button skew angle of BPM, K_x and K_y are the sensitivity of BPM and A,B,C,D are the button signal strengths.

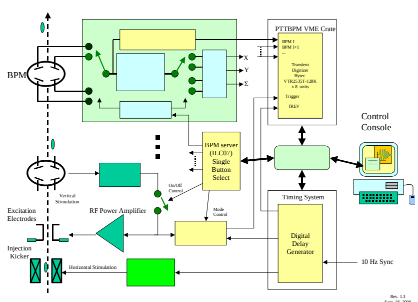

Figure 3. Functional block diagram of PTTBPM system.

4 BETATRON PHASE AND COUPLING MEASUREMENT

Resonance excitations of the stored beam and measure the betatron phase are adopted by several experiments [3]. We use the MX-BPM mezzanine to detector betatron oscillation. An RF lock-in amplifier is used to measure the amplitude and phase of the coherent oscillation. Basic concept of the operation is shown in Fig. 4. Resonance excitation is done by phase locked loop. The loop has functions of search and tracking. Coherent signal is detected by a commercial log-ratio BPM electronics (Bergoz's LR-BPM) [4]. On each MX-BPM, a log video detector is installed. RF multiplexer and single button select circuitry are used to select single button signal. Measured revolution harmonic phase shift are used to compensate the cable and detector circuitry delay. Since the betatron oscillation of the storage ring is between 300 kHz and 800 kHz and is out of the working frequency range of a low frequency lock-in amplifier. Consequently, an RF lock-in amplifier is selected.

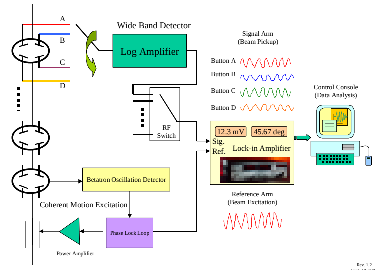

Figure 4. Concepts of betatron phase and local coupling measurement.

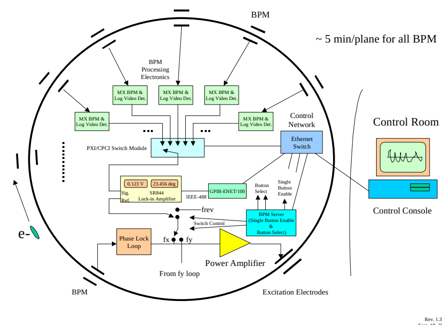

Figure 5. Block diagram of the experimental set-up.

The measured betatron phase can be used to extract betatron function by the relationship of $1/\beta_{x,y} = d\phi_{x,y}/ds$. Concept of the implementation is shown in Figure 4.

The coupling can be parameterised by using $\bar{C}$ matrix [3]. Based on the weak coupling assumption, the motion of the horizontal normal mode at the detector is given by equation (2). For the vertical normal mode, the $\bar{C}_{11}$,giving the in-phase component of the horizontal normal mode at the detector, is described by equation (3).

$$x = A_x\sqrt{\beta_x}\cos(n\omega_x)$$
$$y = -A_x\sqrt{\beta_y}\left[\bar{C}_{22}\cos(n\omega_x) + \bar{C}_{12}\sin(n\omega_x)\right] \text{------------(2)}$$

$$x = A_y\sqrt{\beta_x}\left[\bar{C}_{11}\cos(n\omega_y) - \bar{C}_{12}\sin(n\omega_y)\right]$$
$$y = A_y\sqrt{\beta_y}\cos(n\omega_y) \text{-----------------------(3)}$$

where A_x is the overall amplitude, β_x and β_y are the beta functions, ω_x is the mode tune, and n is the turn number, $\bar{C}_{22}$ is the normalized amplitude of the vertical component of the motion that is in phase with the horizontal motion, and $\bar{C}_{12}$ is the normalized amplitude of the out-of-phase component of the vertical component of the motion.

The $\bar{C}_{ij}$ is a measure of the coupling with $\bar{C}_{ij}$ ~1 corresponding to full coupling. $\bar{C}_{11}$, $\bar{C}_{12}$, and $\bar{C}_{22}$ are calculated from measurement using above equations. $\bar{C}_{21}$ is not a direct measurable parameter. It can be measured if the transverse momentum, x' and y', are measurable. The $\bar{C}_{12}$ data have a better signal-to-noise ratio than the $\bar{C}_{11}$

or $\bar{C}_{22}$ data from experimental viewpoint. This is due to the fact that any cross talk from the reference signal into the beam signal will tend to pollute the in-phase component but not the out-of-phase component. Also, any twisting of the beam pipe will result in changes in the in-phase $\bar{C}_{11}$ and $\bar{C}_{22}$ components but not in $\bar{C}_{21}$.

Figure 5 shows the functional block diagram of the betatron phase and local coupling measurement system. Experimental procedures for betatron phase advance and local coupling measurement is to excite coherent betatron oscillation firstly. Selecting signal source, acquire phase and amplitude data by lock-in amplifier is the second step. Repeating the procedure until all button data are acquired. Performed analysis is the last step.

5. PRILIMINARY BEAM TEST AND DISCUSSION

Two out of six super-periods of MX-BPM are installed with log video mezzanines at this stage. The storage ring does not have vertical kicker. Only limited vertical betatron oscillation can be excited by applying vertical betatron frequency burst to excite the system. Preliminary beam test was done recently. The horizontal betatron oscillation is excited by one of the injection kicker with ~ 1 mrad kick strength. Figure 6 shows the data of a BPM with horizontal kick. Betatron oscillation is clearly observed by the output of the log video demodulator.

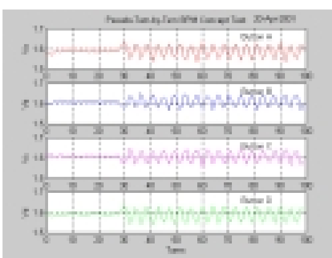

Figure 6. Concept of beam test of the PTTBPM. These four subplots are the raw data acquired from four consecutive measurements of BPM's four buttons.

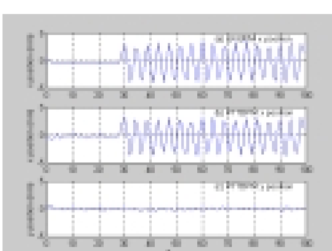

Figure 7. Comparison of single turn beam position and reconstructed beam position. Top figure is the x position reading of single turn log-ratio processor. Middle and bottom subplot shown the reconstructed x and y position.

The reconstructed beam position is shown in Figure 7(b) and (c). Figure 7(a) is the signal of a log-ratio BPM [5] that is paralleled connected to the same BPM with high isolated four divides by two power splitters. It shows that both results are consistent.

Measuring the phase advance in comparison with model calculation is shown in Figure 8. It shows that the discrepancy is small. A systematic study will be started after all BPM are equipped with log amplifier mezzanine.

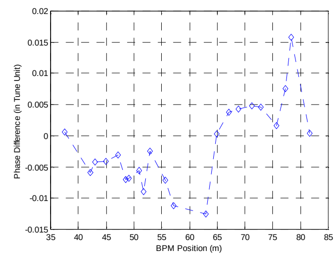

Figure 8. Phase advance difference between measured phase data and model phase advance of two super-period.

System integration and preliminary beam test is on going. The beam test results show that the basic operation principle is working properly. Remaining work includes integrating the system and develops Matlab scripts to support data acquisition and analysis.

6. ACKNOWLEDGEMENT

The authors appreciate brainstorming discussion with Jim Hinkson and Julien Bergoz. Information provided by Kees Scheidt is helpful. David Sagan's explanation of the ideas of betatron phase measurement is beneficial for this works.

REFERENCES

[1] Beam Position Monitor User's Manual, Rev. 1.5.3, BERGOZ Instrumentation.

[2] K. Scheidt, "Measuring Thousand Turns of the ESRF's closed orbit with a simple extension to the existing BPM system, DIPAC97, LNF-97/048 (IR), Dec. 19, 1997.

[3] D. Sagan, R. Meller, R. Littauer, and D. Rubin, "Betatron phase and coupling measurements at the Cornell Electron/Positron Storage Ring", Published 5 Sept. 2000, E092801 Phys. Rev. ST Accel. Beams and reference therein.

[4] Log-ratio Beam Position Monitor User's Manual, Rev. 0.1, BERGOZ Instrumentation.

[5] K. H. Hu, et al., "Turn-by-Turn BPM Electronics Based on 500 MHz Log-Ratio Amplifier", Proceeding of PAC99, 2069 (1999).

THE LOW GAP BPM SYSTEM AT ELETTRA: COMMISSIONING RESULTS

M.Ferianis, R. De Monte, Sincrotrone Trieste, Trieste, Italy

Abstract

Two Low Gap BPMs have been successfully installed at ELETTRA and have now completed the commissioning phase. The main purpose of these new devices is to provide stable beam position measurement, at sub-micron level, to monitor the stability of the light delivered to the Users. The improvements with respect to the normal BPM system have been obtained adopting both a new Low Gap BPM sensor and a new non-multiplexed BPM detector, the latter being developed in co-operation with the SLS diagnostic group at the PSI. Beside the Closed Orbit mode, thanks to the digitally selectable bandwidth, the new BPM detector can be operated also in the Turn-by-Turn mode and provide the position signal to feedback loops.

In this paper we first briefly review the system architecture, describing its mechanical and electronic parts. Then, we present the digital BPM detector set-up used at ELETTRA and the associated firmware required by the four-channel BPM detector to guarantee performance over the full dynamic range. The BPM-position monitoring system is also described and its integration in the BPM system presented. Laboratory tests confirmed sub-micron resolution at 10kHz data rate. A series of beam based measurements have been performed in order to test this system and to verify the improvement in performance. The system is presently used in the control room as a powerful beam quality monitor; its extension to other Storage Ring straight sections is under evaluation.

1 SYSTEM OVERVIEW

To provide a stable photon source point is a well-known challenge in third-generation synchrotron light sources. The stabilization over long time periods, typically 24-hours, of the position of the electron beam can be achieved only using high- resolution, high-stability beam position monitoring systems in feedback loops, high meaning here at the sub-micron level.

The Low Gap Beam Position Monitor (LG-BPM) system at ELETTRA [1] has been developed to provide both high resolution and high accuracy beam position measurements. Two main developments have been completed to satisfy the requirements: the new digital programmable detector and the new sensor with its dedicated support system. The new digital detector has been jointly developed between the Swiss Light Source (SLS) Diagnostic group, the Instrumentation Technology Company [2] and the ELETTRA diagnostic group. This is a completely new four-channel system using parallel processing of the four button signals, to avoid errors due to multiplexingand to improve read out rate. Furthermore, thanks to direct IF signal under-sampling and digital filtering, the receiver bandwidth can be tuned to any of the operation modes: closed orbit, feedback mode or turn-by-turn [3].

The new Low Gap BPM sensor has been developed at ELETTRA [4] and it has been designed taking full advantage of the 14mm, low gap, new aluminum ID chamber installed at ELETTRA. Furthermore, this new sensor is fitted with bellows on each side to reduce mechanical coupling to the vacuum chamber.

Two sensors have been located in straight section 2, close to the undulator, using a dedicated support system. The position of each sensor is monitored in real time with respect to a reference column made of carbon fiber. The absolute position of the electron beam is therefore measured at sub-micron accuracy with a suitable resolution.

2 DIGITAL DETECTOR AT ELETTRA

2.1 System configuration

The Digital Detector system installed at ELETTRA relies on the Quad Digital Receiver (QDR) VME board and on the Front-End (FE) VME board. Both units are four channel devices for non-multiplexed acquisition of the button electrode signals and have been described in [3]. At ELETTRA two pairs of QDR+FE have been installed to acquire the signals of the LG-BPM.

2.2 Software Configuration

Two different software environments have been created. The first one runs under the Windows operating system and it is written in ‘C’ language using National Instruments CVI. With this software it is possible to perform all the hardware settings and tests on the Digital Receiver VME boards. The results are graphically displayed in real-time. The second environment has a completely different architecture and is used for field operation with the same hardware. The requirements for field operation are: continuous real time data acquisition, network (Ethernet) connectivity, data reliability and compatibility with the Elettra Control System, remote control access capability (telnet). To meet all these requirements, Linux with real time extensions (RTAI) has

been chosen and implemented. The code has been written in 'C' language with the GNU Gcc Compiler.
The software is structured in multiple parts. The core of the system is a Real Time kernel module that acquires continuously the data from the VME Digital Receiver boards and performs the X and Y position calculations. The core module is synchronised by an interrupt generated by the DDC boards at 4, 8, 16 and 32kHz. It writes the acquired data in a common memory area that can be accessed by other non real-time user processes. This area is also used to pass all of the calibration factors and settings to the Digital Receiver boards. The user processes are the following. MEAN calculates all the average and rms values triggered by the acquisition core every 500 acquisitions via a RT FIFO. RS_RCV receives and manages the mechanical movements of the LG-BPM sensors. BEAM_INFO_CL reads the current beam parameters. ACQUI collects all the data and stores them in log files. AUTOAGC manages automatically the gains of the RF front ends. MONITOR simply displays the internal acquisition system data and allows setting some parameters. The real-time data pass to the Pentek 'C40' DSP for the Elettra local feedback system. The delay introduced by the acquisition system when delivering the XY position to the DSP via the VME bus has been measured to be equal 30 µSec.

2.3 Laboratory measurements

Multiple laboratory measurements have been performed to optimize the system for the required accuracy, resolution and long term stability. In fig. 1 the longterm stability test is shown: the acquisition rate was 10kHz.

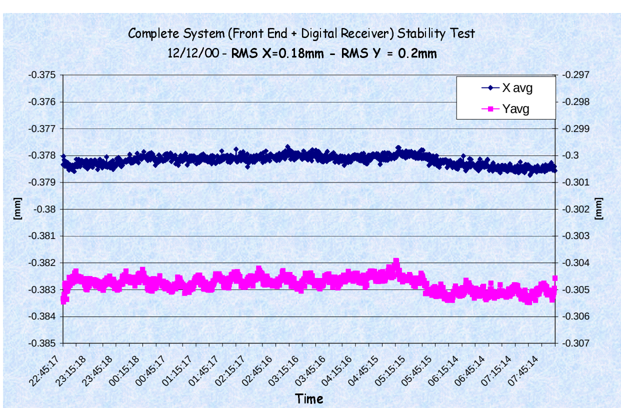

Fig. 1: 10-hour, long-term stability measurements performed in the laboratory on a complete system: Front End plus Digital Receiver. X_{rms}=0.18µm Y_{rms}=0.20µm.

3 THE BPM MONITORING SYSTEM

3.1 System description

The BPM monitoring system [1] is in operation since fall 1999. It is used to monitor in real-time the actual horizontal and vertical position of each Low Gap BPM with respect to a reference column installed adjacent to each LG-BPM. The temperatures are also monitored.

Movements of the LG-BPM body are measured using Capacitive Sensors by Physik Instrumente [5], which proved to be ideally suited for this task. The Capacitive Sensor provides an output voltage that is linearly related to the distance between its capacitor plates, with <50nm resolution in the 400µm range. Preliminary measurements have been made in the ELETTRA tunnel [1] before adopting this solution. No vibrations of significant (>200nm) amplitude were recorded while the tunnel air temperature was stable to within ±0.5°C. Under these assumptions, a column made of Carbon Epoxy Laminate (CTE=-0.1µm/°Km) and free from any mechanical load, can be considered as a reference for the position measurement of the LG-BPM.

3.2 Model of the support system

To gain a deeper knowledge on the position and temperature measurements, a simple model has been derived for the LG-BPM support system both for the vertical and horizontal axis (see fig.2).

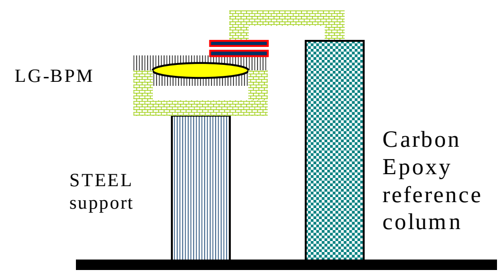

Fig. 2: drawing (not to scale) of the model of the LG-BPM support system, vertical axis. *Vertical lines*=steel, *bricks*=aluminum, *squares*=Carbon Epoxy laminate and *solid*=capacitive sensors.

The measured position drifts are in good agreement (see fig.3) with the computed one, obtained with following formula, which holds for the vertical axis.

$$\Delta L_y = \alpha_{steel}\Delta T_{air} L_{steel} + \Delta T_{LG-BPM} * \left(\alpha_{steel} L_{LG-BPM} + \alpha_{alu} L_{eq}\right)$$

with:

$\alpha_{steel,\,alu}$ Coeff. of Therm. Exp. of steel and aluminum
$\Delta L_{y,x}$ the computed drift along Y or X
ΔT_{air} the measured tunnel air temperature variation
L_{steel} the length of the LG-BPM support
$\Delta T_{LG\text{-}BPM}$ the measured LG-BPM temperature variation
$L_{LG\text{-}BPM}$ the size of the LG-BPM along Y or X
L_{eq} the length of the aluminum LG-BPM holder

3.3 Integration into the LG-BPM system

A Peripheral Intelligent Node (PIN) is fitted to each LG-BPM installed in the storage ring tunnel.

A PIN is a micro-controller [6] based unit, which acquire the position and temperature signals and send them to a Master Unit via CAN-bus.

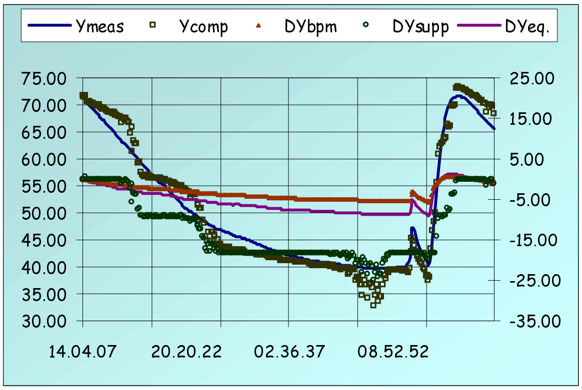

Fig.3: plots of measured and computed vertical position drift of the LG-BPM; vertical scales: 5µm/div

The acquisition runs continuously at 1Hz. In normal operation mode, the Master Unit collects the data from the PINs and at regular, user-definable time intervals (typically equal to 1 minute) computes the average and root mean square values for each PIN buffer and sends them the LG-BPM Linux CPU via a serial line. Vibration measurements are possible running the acquisition at 4kHz as the maximum output bandwidth of the Capacitive Sensor readout electronic is 3kHz.

4 THE COMMISSIONING RESULTS

4.1 Long term measurements

The electron beam position has been measured with the LG-BPM system over a 5-hour period (see fig.4). The SLOW Feedback process was running for the first two hours while it was OFF for the rest of the time. The SLOW Feedback process relies on the readings from the standard e-BPM of ELETTRA.

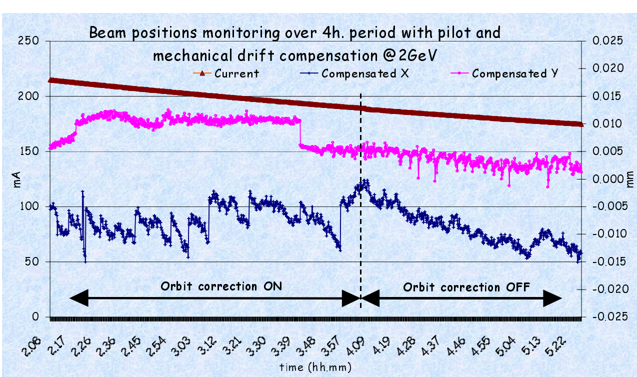

Fig.4: beam position measurement over 5 hour time; vertical scale:5µm/div.

Two main considerations can be drawn from fig.4:

- the vertical beam position is stable within few microns over many hours
- the sub-micron resolution of the Digital Detector, measured in the laboratory, is confirmed here by the granularity of the beam position reading.

4.2 Fast acquisitions and turn-by-turn

The Digital Receiver is fully programmable by the User; the bandwidth of the position readings can be tuned to the different operation modes, like close orbit, feedback or turn-by-turn. Thanks to turn-by-turn mode a parassitic tune measurement can be performed on line (fig.5). In the close orbit and feedback mode, the lower frequency beam spectrum can be measured and proper error signal can be delivered to a feedback system.

Fig.5: tune measurement with turn-by-turn acquisition.

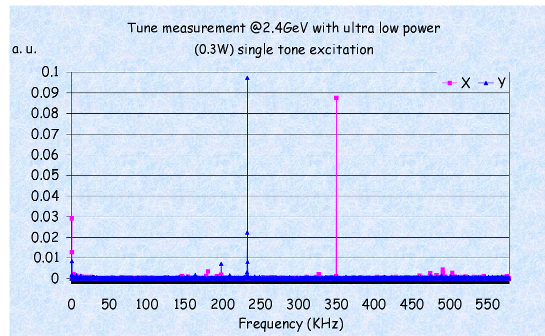

5 CONCLUSIONS

The LG-BPM system has proved sub-micron resolution and accuracy; it is therefore suitable for driving a feedback system at ELETTRA.

6 ACKNOWLEDGMENTS

The authors acknowledge V. Schlott and P. Pollet of the SLS, R. Ursic of Instrumentation Technologies for the efforts spent in the commom development of the Digital Receiver. C. Scafuri for the ELETTRA control system integration. D. Novak for the CAN bus work.

REFERENCES

[1] M. Ferianis et al., “The New Low Gap BPM System at ELETTRA: Description and Prototype Tests”, BIW’00, Cambridge, May 2000
[2] Instrumentation Technologies, Solkan SI-5250 SLO
[3] M. Dehler et al.;”Digital BPM System for the Swiss Light Source- First operational Results”, BIW’00, Cambridge, May 2000
[4] P.Craievich et al., ”Electromagnetic Modeling and simulation results for the ELETTRA Low Gap Beam Position Monitor”, ICAP 2000, Darmstadt (D), Sept 2000
[5] Physik Instrumente D-76337 Waldbronn, www.physikinstrumente.com
[6] Kit-CON 167 Evaluation Board, Phytec D-55129 Mainz, www.phytec.com

ORBIT CONTROL AT THE ADVANCED PHOTON SOURCE*

Glenn Decker, Argonne National Laboratory, Argonne, Illinois 60439 USA

Abstract

The Advanced Photon Source (APS) began operation in 1995 with the objective of providing ultra-stable high-brightness hard x-rays to its user community. This paper will be a review of the instrumentation and software presently in use for orbit stabilization. Broad-band and narrow-band rf beam position monitors as well as x-ray beam position monitors supporting bending magnet and insertion device source points are used in an integrated system. Status and upgrade plans for the system will be discussed.

1 INTRODUCTION

Since the commissioning of the APS, there has been significant progress in the understanding of beam stabilization, with the result that a first round of hardware upgrades is near completion. The goal is ultimately to achieve better than 1 micron rms beam stability at all x-ray source points in a frequency band up to 30 Hz and extending at the low frequency end to 24 hours or longer, and to be able to prove it.

2 HARDWARE DESCRIPTION

The APS beam position monitor (BPM) systems consist of approximately 360 stations employing broad-band (monopulse) rf receivers [1], 48 narrow-band receivers [2] distributed among the 24 insertion device vacuum chambers, and 86 front-end x-ray BPMs [3,4].

Data from each of these BPM systems are provided to a distributed array of digital signal processors (DSPs) that have real-time (1.534 kHz) connections to as many as 317 combined function horizontal/vertical steering corrector magnet power supplies. For normal operation, this real-time feedback system [5] employs 160 broad-band rf BPMs and uses a singular value decomposition (SVD) algorithm to compute set points for writing to 38 corrector magnet power supplies.

The 38 corrector magnets employed by the real-time feedback system are mounted at spool piece locations and thus have faster response times than the other 279 units, which are mounted at locations with thick aluminum vacuum chamber walls that are subject to large eddy current effects. Each corrector is powered by an identical pulse-width-modulated power supply, which is interfaced both to the Experimental Physics and Industrial Control System (EPICS) network and the real-time feedback dedicated network. EPICS also reads the BPMs at up to a -Hz rate, after de-aliasing, for use in a separate DC correction algorithm.

* Work supported by U.S. Department of Energy, Office of Basic Energy Sciences under Contract No. W-31-109-ENG-38.

3 SYSTEMATIC EFFECTS

Virtually all of the orbit correction technique can be reduced to the study and compensation of systematic effects of one form or another. While space does not allow a detailed study of the many known effects, a listing of them should give some idea of the depth of this area. With regard to orbit correction, there are both intrinsic and extrinsic systematic effects. The extrinsic effects are those for which the BPM system was built to correct in the first place. The challenge in putting together an effective orbit correction strategy is to reduce the size of the intrinsic systematic effects to such a degree that the extrinsic perturbations can be reduced to an acceptable level.

3.1 Rf BPM systematic effects

- Timing/trigger stability
- Intensity dependence
- Bunch pattern dependence
- The “rogue” microwave chamber modes [6]
- Electronics thermal drift

3.2 X-ray BPM systematic effects

- Stray radiation striking X-BPM blade pickups [7]
- X-BPM blade misalignment
- Electronics thermal drift
- Gap-dependent effects (e.g., sensitivity, steering)

3.3 Extrinsic systematic effects (noise sources)

- Magnet power supply noise/ripple
- Rf system high-voltage power supply ripple
- Mechanical vibration
- Thermal effects (tunnel air/water temperature)
- Earth tides
- Insertion device gap changes

Each of these systematic effects has its own spectrum, ranging from long-term drift effects of hours to days, up to motions of several kHz. Ultimately, one can speak of stabilizing turn-by-turn motions using rf frequency broad-band feedback systems, however this can be considered to impact beam size for most x-ray experiments that average over many turns, and is beyond the scope of the present discussion. Ultimately, however, the goal is to stabilize the flux striking the user's sample, and plans are being made to correct for multipole-induced beam size changes associated with insertion device gap changes using feed forward.

4 SOFTWARE DESCRIPTION

The EPICS control system provides a convenient and reliable framework upon which all orbit correction algorithms are based. The EPICS low-level "engineering screens" allow access to individual "process variables" for troubleshooting purposes. A higher level library of programs known as the self-describing data set (SDDS) toolkit [8] allows the development of very high-level scripts and graphical user interfaces, which typically use the tool command language (Tcl) scripting environment.

In addition to the real-time orbit feedback system, workstation-based (DC) orbit correction [9] takes place nominally with a 2.5-second update period. A Tcl application is used for orbit correction configuration and allows the generation of response matrices, which are inverted using singular value decomposition (SVD). Any combination of rf and x-ray BPMs together with the selection of any of the 317 corrector magnets in each plane is allowed.

Additionally, the weighting of BPMs provides the possibility of building quasi-local bumps. For example, the x-ray BPMs are considered to be more reliable than the rf BPMs for the determination of angles due to their lever arm advantage gained from their being located further from the x-ray source points. A popular algorithm is to use two upstream and two downstream corrector magnets, with all rf BPMs having weight 1 and one of the two x-ray BPMs associated with that source point having a weight of 5. Thus the source position is held stable by the best-fit line through several rf BPMs straddling the source point, while the source angle is fixed by the single x-ray BPM. The second x-ray BPM is used as a check on the performance of the first unit.

Because the new x-ray BPM data acquisition system is just recently coming online, primarily only rf BPMs have been used to date during normal user beam operation. The configuration found most robust has been to use as many rf BPMs as possible (i.e., functioning units), with two corrector magnets per sector-a total of eighty in each plane. This provides a smooth fit and minimizes the effects of unit-to-unit variation among the different BPMs. Quasi-local control as described above has been used in a few cases during machine operation, in one case vertically on a bending magnet beamline, and in both planes at fixed gap on three separate insertion device beamlines. The local control is integrated together with the two-corrector-per-sector pattern into a single response matrix.

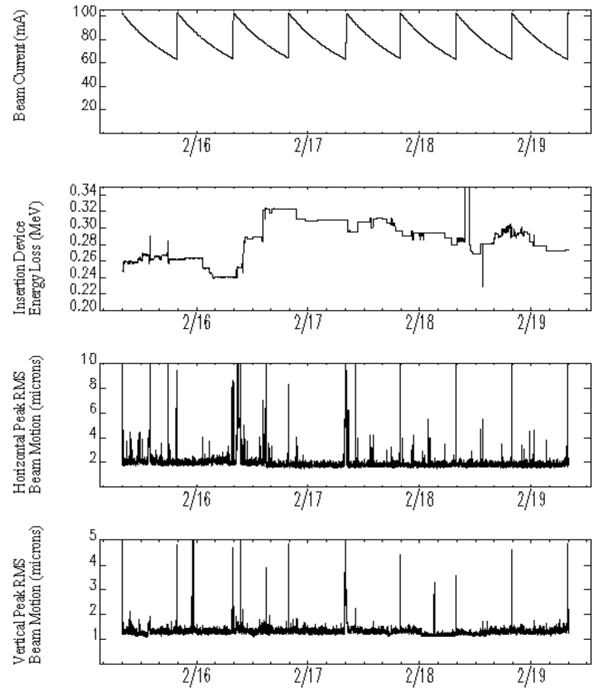

Figure 1: APS beam stability over a 96-hour period.

5 STATUS AND PLANS

Figure 1 is a representative data set showing beam stability in the frequency band from 0.1 Hz up to 30 Hz. The top frame shows stored beam current as a function of time over a four-day period during February of 2001. The second frame shows the total radiative energy loss resulting from insertion device radiation and thus indicates individual gap changes anywhere around the ring as steps in the data. The two bottom frames show the "peak rms" beam motion averaged over approximately 80 beam position monitors located near the insertion device source points. This data is computed by the real-time feedback system.

At 1.5 kHz, data for each BPM has a 0.01 Hz input high-pass digital filter applied to reject DC, followed by a

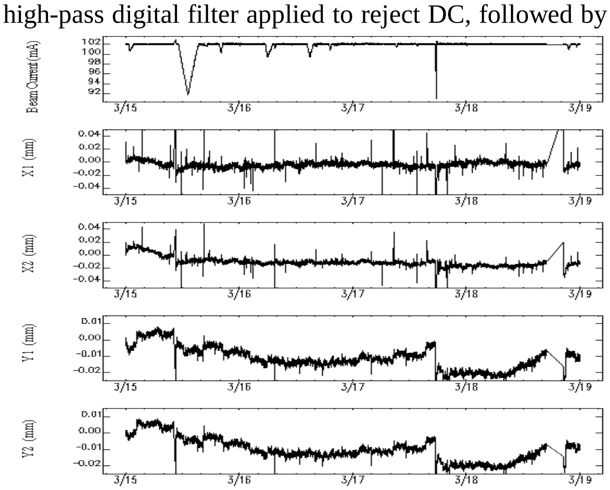

Figure 2: X-BPM drift over a 96-hour period.

30 Hz low-pass filter, squaring, exponential averaging, and finally a square root operation, resulting in a de-aliased "noise" signal. Noise data from approximately 80 BPMs is averaged, with a 0.1 Hz low-pass filter applied to the result. Since the data logger collects data every 60 seconds, this signal is peak detected over a 60-second buffer period in order that the logger not "miss" any orbit transients, nor de-emphasise them by averaging. Thus the data of Figure 1 is robust, i.e., unforgiving, and provides an unadulterated view of the beam stability in this band.

Generally speaking, the stability sits near 1.3 microns rms vertically and 2.0 microns in the horizontal from 0.1 to 30 Hz. Most of the transients seen vertically are correlated with injection. Many of the remaining transients, especially horizontally, are correlated with insertion device gap changes, which are controlled by users. An aggressive effort is taking place to reduce these 5-to-15 micron rms transients by using feed forward algorithms in the real-time feedback system processors. Please note that the beam size at insertion device source points is 300 microns rms horizontally and approximately 20 microns rms vertically.

Shown in Figure 2 are horizontal (X1, X2) and vertical (Y1, Y2) X-BPM data from insertion device beamline 34-ID with a fixed, 20-mm gap, over a four-day period during top-up operation mode. Top-up entails injection of a single injector shot every two minutes with x-ray user shutters open to maintain a constant 102 mA [10]. The data of Figure 2 is digitally filtered with a 20-second time constant and is logged every two minutes.

The detectors represented in Figure 2 are located 16 and 20 meters, respectively, downstream from the insertion device source point and are sensitive primarily to source angle, e.g., 20 microns corresponds to about 1 micro-radian. Neither detector was included in the DC or real-time orbit-correction algorithm. So these data indicate our performance to date without X-BPM feedback. The common mode signal where two detectors in the same front end agree with one another is an indication of the "true" beam motion and gives some idea of the level of improvement that can be expected once these systems are folded into the correction algorithm.

As can be seen from the figures, the immediate improvements needed toward the goal of submicron beam stability are feed forward on insertion device gap changes plus the incorporation of the recently upgraded X-BPMs into the DC correction algorithm. Additionally, the recently completed upgrade to the timing/triggering of the monopulse BPMs from beam-derived to low-level-rf-derived will reduce intensity dependence to 10 microns or less while allowing closer bunch spacing. New software has been tested that integrates the DC and real-time correction, reducing a "dead band," and this will be commissioned soon. Integration of X-BPM data into the real-time system is a further planned upgrade.

6 CONCLUSIONS

Orbit correction techniques at the APS have matured significantly during its five-year operating history. The latest round of hardware and software upgrades should lead the way toward true submicron rms beam stability. Robert Lill, Om Singh, John Carwardine, Frank Lenkszus, John Galayda, Michael Borland, and Louis Emery have all been instrumental in the success of this effort.

REFERENCES

[1] E. Kahana, "Design of Beam Position Monitor Electronics for the APS Storage Ring," Proceedings of the 3rd Accelerator Beam Instrumentation Workshop, AIP Conference Proceedings 252, pp. 235-240 (1992).

[2] O. Singh, C. Doose, J. Carwardine, G. Decker, F. Lenkszus, R. Merl, "Commissioning Results of the Narrow-band Beam Position Monitor System Upgrade in the APS Storage Ring," Proc. of the 1999 Particle Accelerator Conference, New York City, New York, IEEE 99CH36366, pp. 2093-2095 (1999).

[3] D. Shu, B. Rodricks, J. Barraza, T. Sanchez, and T. M. Kuzay, Nucl. Instrum. Methods Phys. Res., Sect. A 319, 56 (1992).

[4] O. Singh, L. Erwin, G. Decker, R. Laird, F. Lenkszus, "X-ray BPM-Based Feedback System at the APS Storage Ring," 2000 Beam Instrumentation Workshop, Cambridge, MA, May 8-11, 2000.

[5] J. Carwardine, F. Lenkszus, "Real-Time Orbit Feedback at the APS," 1998 Beam Instrumentation Workshop, AIP Conference Proceedings 451, pp. 125-144 (1998).

[6] Y. Kang, G. Decker, J. Song, "Damping Spurious Harmonic Resonances in the APS Storage Ring Beam Chamber," Proc. of the 1999 Particle Accelerator Conference, New York City, New York, IEEE 99CH36366, pp. 3092-3094 (1999).

[7] Glenn Decker and Om Singh, "Method for reducing x-ray background signals from insertion device x-ray beam position monitors," Phys. Rev. St Accel. Beams 2, 112801 (1999).

[8] M. Borland, "Applications Toolkit for Accelerator Control and Analysis," Proc. of the 1997 Particle Accelerator Conference, Vancouver, BC, Canada, IEEE 97CH36167, pp. 2487-2489 (1997).

[9] Louis Emery, Michael Borland, "Advances in Orbit Drift Correction in the Advanced Photon Source Storage Ring," Proc. of the 1997 Particle Accelerator Conference, Vancouver, BC, Canada, IEEE 97CH36167, pp. 742-744 (1997)

[10] L. Emery, M. Borland, "Top-up Operation Experience at the Advanced Photon Source," Proc. of the 1999 Particle Accelerator Conference, New York City, New York, IEEE 99CH36366, pp. 200-202 (1999).

ADVANCED PHOTON SOURCE RF BEAM POSITION MONITOR SYSTEM UPGRADE DESIGN AND COMMISSIONING

R. Lill, G. Decker, O. Singh
Advanced Photon Source, Argonne National Laboratory,
9700 South Cass Avenue, Argonne IL 60439 USA

Abstract

This paper describes the Advanced Photon Source (APS) storage ring monopulse rf beam position monitor (BPM) system upgrade. The present rf BPM system requires a large dead time of 400 ns between the measured bunch and upstream bunch. The bunch pattern is also constrained by the required target cluster of six bunches of 7 mA minimum necessary to operate the receiver near the top end of the dynamic range. The upgrade design objectives involve resolving bunches spaced as closely as 100 ns. These design objectives require us to reduce receiver front-end losses and reflections. An improved trigger scheme that minimizes systematic errors is also required. The upgrade is in the final phases of installation and commissioning at this time. The latest experimental and commissioning data and results will be presented.

1 INTRODUCTION

The measurement of the APS storage ring beam position is accomplished by 360 rf BPMs located approximately every degree around the 1104-m circumference ring [1]. The rf BPM signal processing topology used is a monopulse amplitude-to-phase (AM/PM) technique for measuring the beam position in the x and y axes. A logarithmic amplifier channel measures the beam intensity. The rf BPM upgrade was proposed at BIW 1998 [2].

2 SYSTEM DESIGN

Figure 1 is the block diagram for the monopulse rf BPM receiver front end. The matching networks are attached directly to 10-mm-diameter button electrodes [3]. The button matching network was designed to match the capacitively reactive button (0.25–j75 ohm) into 50 ohms in a 100-MHz, 3-dB bandwidth centered at 352 MHz. This matching network circuit has the response characteristics of a bandpass filter with the button's capacitance (4.8 pf) integrated as part of the filter design. To match the button's impedance, an inductor and resistor are placed in parallel with the capacitive electrode and the beam current source. The matching network circuit also includes a 3-pole, low-pass filter that attenuates the second harmonic (704 MHz) by 46 dB. The matching network typically improves the in-band signal strength by 5 dB. They also provide >25 dB return loss source match, in a 10-MHz bandwidth centered at 352 MHz.

The filter comparator (Figure 1) is to be located 42 inches away from the buttons via matched silicon dioxide cables. The system is matched in phase and amplitude to insure the vector addition and subtraction of the input signals. The 180-degree hybrid comparator network described in Figure 1 has been implemented using a rat race hybrid topology. The rat race hybrid consists of three $\lambda/4$ and one $3\lambda/4$ lengths of 70.7-ohm mini coax. The four lengths are connected together in a ring configuration yielding 50-ohm inputs and outputs. The bandwidth is extended from 20% to 30% by using a ferrite reversing coil on the $3\lambda/4$ leg of the bridge. The hybrid network provides a low loss sum of all four inputs and excellent return loss on all ports.

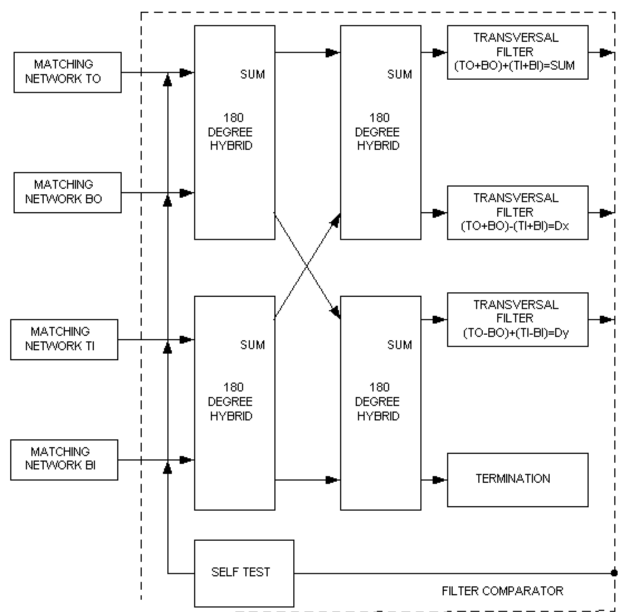

Figure 1: BPM receiver front-end block diagram.

The self-test input provides an input signal to test the comparator during maintenance periods. The input signal is split four ways and fed into the coupling arm of 15-dB directional couplers in each of the inputs. The new comparator can be operated with one input offset by 6 dB or with all inputs balanced. Resolving bunches spaced as closely as 100 ns and minimizing associated systematic errors required designing a bandpass filter that had nearly a rectangular time domain response. This $[\mathrm{SIN\ F/F}]^2$ frequency response was realized using the technique illustrated in Figure 2. The transversal filter is best explained in the time domain. The transversal filter processes the input signal by splitting the signal and passing it though a series of delays and then recombining the outputs. The delays are chosen such that some frequencies will add (passband) and some frequencies will cancel (rejection band), thus establishing the filtering function. The 4-dB bandwidth (BW) can be calculated by taking the inverse of the total filter delay. Our design used delay multiples of 2.84 ns or 1/351.93 MHz, the storage ring rf frequency. The filter design has 24 delay paths and is centered at 351.93 MHz. The 4-dB bandwidth is equal to 24×2.84 ns = 68.2 ns or 14.7 MHz. In the frequency domain shown in Figure 3, the first side lobe is down 13 dB from the main lobe. The nulls will occur at a frequency interval of 14.7 MHz.

The time domain response to six adjacent storage ring buckets filled with a total of 4 mA is shown in Figure 4. The time domain response is a rectangular burst with a side lobe rejection of 50 dB. The response has a flat top or constant input power into the receiver for the measurement. This is accomplished in our design by using unequal Wilkinson power dividers to compensate for the variation in delay loss. The construction of a single 24-pulse transversal filter requires forty-six two-way unequal power dividers. The total length of the delay line is just less than 30 meters. The filter was designed and built using stripline laid out on Rogers RO4003/4403 laminate microwave board materials. The dielectric constant of the composite ceramic/glass material is 3.53 and the loss tangent is 0.004. This material has an excellent temperature stability rating and meets the gamma radiation requirements necessary to install them in the tunnel. The new filter comparator using the transversal filters has an overall insertion loss of 7.0 dB, which is an improvement of 8 dB over the existing system.

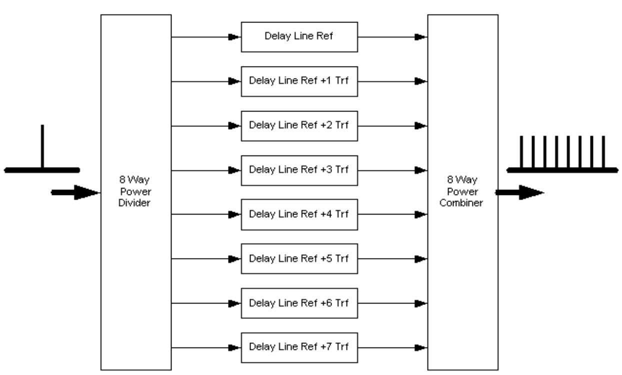

Figure 2: Transversal filter illustration.

The filter comparator output is fed through the tunnel penetration with 1/4-inch-diameter heliax cables and provides the mono pulse receiver inputs. The receiver is an integral part of the signal conditioning and digitizing unit (SCDU) with the receiver physically mounted on the VXI board [1].

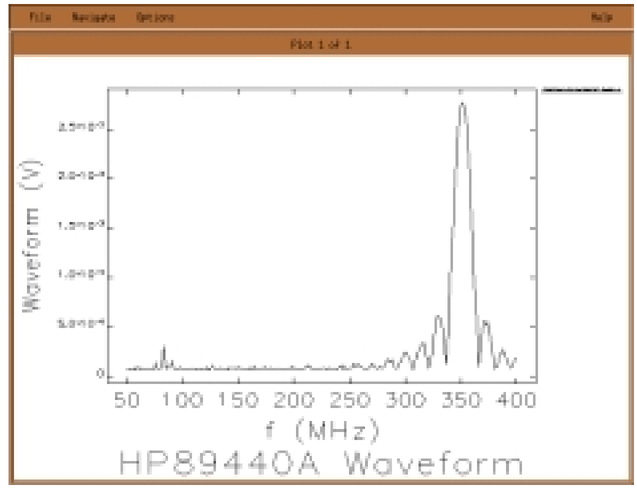

Figure 3: Transversal filter frequency response to single bunch with 8 mA.

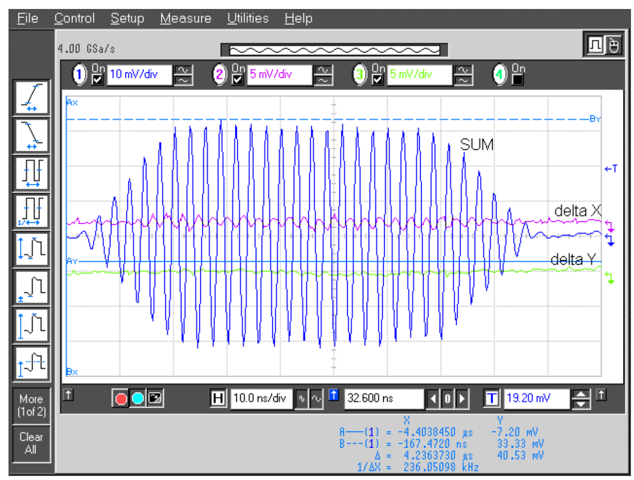

Figure 4: Transversal filter time domain response (10-dB coupler).

The sum data is peak detected, and the normalized position data is integrated on the SCDU shown in Figure 5. Both signals are digitized, and the data from the SCDU is then stored in registers. The upgrade also involved replacing the sum and position registers. The original register chip had a chronic failure mode that ranged from burning up completely to corrupting the data at certain bit patterns. The underling problem was related to the SCDU board layout. The I/O and clock lines were going negative or below the ground level (-1.5 volts for about 20 ns), which caused the chip to latch-up and/or overheat. The replacement register chip has a 2.5-volt undershoot rating and is a pin-for-pin replacement. This part of the upgrade has been operational for almost two years with good results. The registers are read periodically by the memory scanner in the same VXI crate via the local bus. The memory scanner then conditions the digital data and sends it to the appropriate systems.

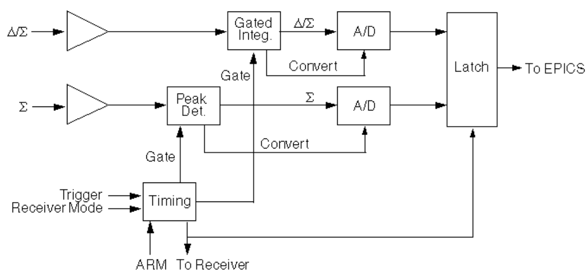

Figure 5: Signal conditioning and digitizing unit block diagram.

The BPM timing was also improved as part of the BPM upgrade. The original system utilized a beam-based trigger that was derived from the sum video signal. The external arm signal was used to select the bunch to be measured, and the threshold of the SCDU log video sum signal triggered the event. This timing scheme is susceptible to trigger walk and bunch-to-bunch spacing, which could change the shape of the trigger edge. The upgrade design leverages off an existing timing module called Bunch Clock Generator (BCG) [4] to generate the BPM trigger. The BCG loads the bunch pattern into RAM at injection and then shifts out the data one bit at a time at 352 MHz. The shifting is synchronized with the revolution clock such that the bit sequence starts over at each revolution. The upgrade was designed to operate with the original beam based trigger or the external BCG signal.

3 STATUS AND RESULTS

Presently one of the 40 APS sectors (nine BPMs) have been implemented with the full upgrade. The results shown in Figure 6 indicate typical crosstalk between bunches as a function of bunch spacing. First 5 mA were injected into a single bunch and the orbit corrected using all but the upgraded BPMs. Then a second bunch was injected on the opposite side of the ring and the timing for the upgraded units was set to trigger at that point. Finally, while measuring the beam position of this second bunch, a third bunch was injected at a fixed time preceding the second bunch. The variation of the position readback was then recorded as a function of charge in the third bunch. This experiment was repeated seven more times using different delay values for the third bunch, as indicated by the legend in Figure 6. While the crosstalk for the upgrade electronics is acceptable, it was discovered that the upgrade of the timing alone improved performance significantly in comparison to the beam-based trigger in use to date. It appears that the trigger walk is a more important factor for bunch-to-bunch crosstalk than the long decay time of the bandpass filter, as originally theorized.

The timing system upgrade is complete and is being commissioned during the May 2001 operating period. The new filter comparator unit upgrade is on hold pending commissioning of the new timing system and further studies.

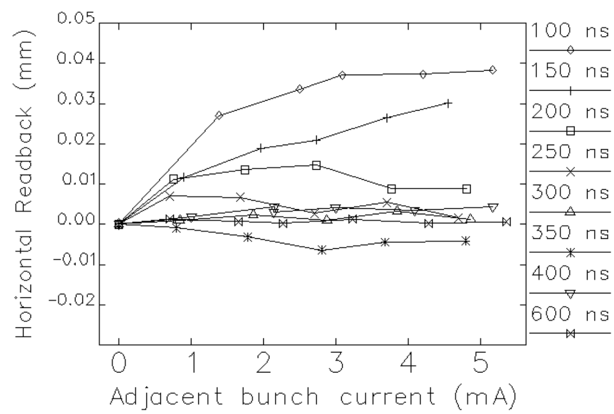

Figure 6: Bunch spacing systematic errors.

ACKNOWLEDGEMENTS

The authors would like to acknowledge the contribution and leadership that John Galayda provided. This work is supported by U.S. Department of Energy, Office of Basic Energy Science under Contract No. W-31-109-ENG-38.

REFERENCES

[1] E. Kahana, “Design of Beam Position Monitor Electronics for the APS Storage Ring,” Proceedings of the 3rd Accelerator Beam Instrumentation Workshop, AIP Conference Proceedings 252, pp. 235-240 (1992).

[2] R. Lill, G. Decker, “Advanced Photon Source Monopulse RF Beam Position Monitor Front-end Upgrade,” Proceedings of the 8th Accelerator Beam Instrumentation Workshop, AIP Conference Proceedings 451, pp. 318-324 (1998).

[3] E. Plouviez, S. Eandi, “A Fast Global Feedback System to Correct the Beam Position Deviation in the ESRF Storage Ring,” Proceedings of the 3rd European Workshop, DIPAC 97 Conference Proceedings, pp. 79-81 (1997).

[4] F. Lenkszus, R. Laird, “A Bunch Clock for the Advanced Photon Source,” Proceedings of the 1997 Particle Accelerator Conference, Volume 2, pp. 2490-2492 (1997).

DESIGN OF A MULTI-BUNCH BPM FOR THE NEXT LINEAR COLLIDER[1]

Andrew Young, Scott D. Anderson, Douglas McCormick, Janice Nelson, Marc Ross, Stephen R. Smith, Tonee J. Smith, SLAC, Stanford, CA. USA,
Hayano, T. Naito, N. Terunuma, S. Araki, KEK, Ibaraki, Japan

Abstract

The Next Linear Collider (NLC) design requires precise control of colliding trains of high-intensity (1.4×10^{10} particles/bunch) and low-emittance beams. High-resolution multi-bunch beam position monitors (BPMs) are required to ensure uniformity across the bunch trains with bunch spacing of 1.4ns. A high bandwidth (~350 MHz) multi-bunch BPM has been designed based on a custom-made stripline sum and difference hybrid on a Teflon-based material. High bandwidth RF couplers were included to allow injection of a calibration tone. Three prototype BPMs were fabricated at SLAC and tested in the Accelerator Test Facility at KEK and in the PEP-II ring at SLAC. Tone calibration data and single-bunch and multi-bunch beam data were taken with high-speed (5Gsa/s) digitisers. Offline analysis determined the deconvolution of individual bunches in the multi-bunch mode by using the measured single bunch response. The results of these measurements are presented in this paper.

1. OVERVIEW

The multi-bunch (MB) BPMs were designed to operate over a wide range of conditions (Table 1) allowing for testing to be performed at SLAC and KEK. The MB BPMs are used by the sub-train feedback, which applies a shaped pulse to a set of stripline kickers to straighten out a bunch train. These are qualitatively different from the quad (Q) and feedback (FB) BPMs due to their high bandwidth and relatively relaxed stability requirements. The primary requirement on the MB BPMs is a bunch train that generates a BPM signal, which is straight.

Table 1: BPM Specifications

Parameters	Value	Comments
Resolution	300 nm rms at 0.6×10^{10} e^- /bunch	For bunch-bunch displacements freq. Below 300 MHz
Position range	$\pm$2mm	
Bunch spacing	2.8 or 1.4 ns	
No. of bunches	1-95 1-190	2.8ns 1.4ns
Beam current	1×10^{9} 1.4×10^{10}	Particles per bunch
No. of BPMs	278	

2. IMPLEMENTATION

Figure 1 shows a simplified block diagram of the multi-bunch front-end chassis. The BPM chassis contains directional couplers, non-reflective switches for transfer function measurements, sum and difference hybrid, bandpass filters for noise rejection, and sold-state amplifies. The BPM chassis takes the two x or y inputs from the BPM buttons and takes the sum and difference. The BPM signal is then amplified in order to run it on a long cable to a digitiser outside the radiation area. The front-end has a feature where a single tone can be injected into the inputs of the sum and difference hybrid for calibration. Thus allowing the operators to perform a transfer function.

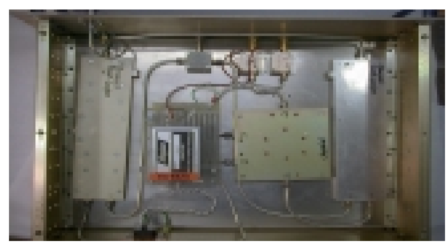

Figure 1 Block diagram of the BPM front-electronics

To obtain the bandwidth and performance requirements, several custom components were designed at SLAC. The first component is the heart of the front-end chassis, a stripline 5/4λ sum and difference hybrid illustrated in figure 2. The hybrid operates at 600MHz with a 300MHz bandwidth. The phase variation at the output across the bandwidth is $\pm$5 degrees.

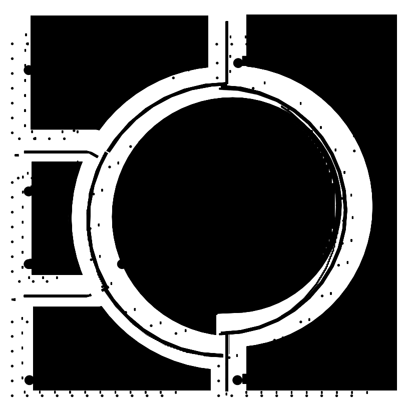

Figure 2 Stripline 5/4λ Hybrid

[1] Work supported by the Department of Energy, contract DE-AC03-76SF00515

The next custom component is a four-tap directional coupler that is shown in figure 3 and allows one to inject a single tone into the Hybrid and perform a transfer function calibration. The four-tap configuration allows the bandwidth to be stretched. This has the affect of a constant coupling ratio across the frequency band. This allows one to remove the phase variation in the hybrid and cable losses and insertion losses of other components. Also the calibration will allow one to remove any non-linearities in the digitiser that will be discussed later in the paper.

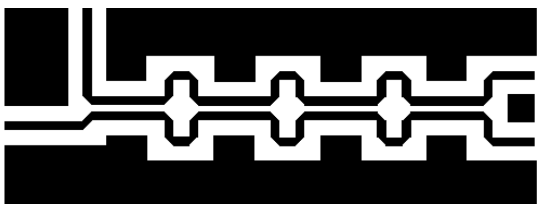

Figure 3 Stripline directional coupler

Other RF custom components such as amplifiers and switches were bought from manufactures and then integrated into a circuit board. Special care was taken to lower insertion losses by using low-loss dielectric materials.

The digitiser that was chosen for this experiment is a Tektronix 684. Analysis Tektronix 3054, which uses the same type of digitiser as the Tektronix 684, shows a phase noise problem with the digitiser. Figure 4 shows the baseband frequency spectrum of a Tektronix 3054 compared to an HP (Agilent) infinium scope. The figure illustrates that the Tektronix scope digitiser is dominated by low frequency in-band spurious noise while the Agilent infinium scope is dominated by noise at 284MHz.

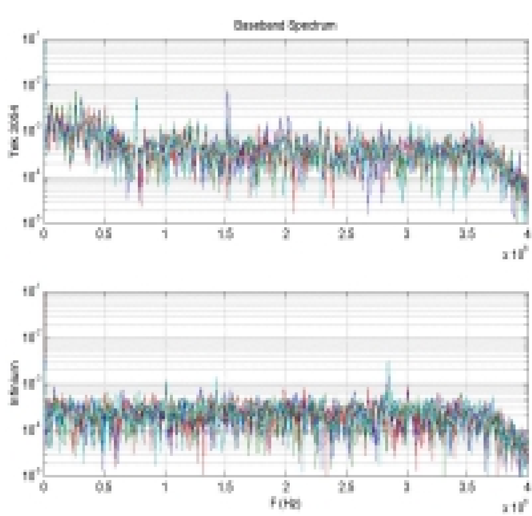

Figure 4. Baseband Frequency spectrum

This phase noise problem with the Tektronix scope will affect the resolution on the BPM as shown in Table 2. However, there is a significant cost differential between the Agilent and Tektronix scopes thus the Tektronix 684 was chosen for this test.

Table 2: BPM Digitisers Resolution Specifications

Bandwidth	50-MHz	100-MHz
HP (Agilent)	14µm 7.5 effective bits	10µm 8 effective bits
Tektronix	15µm 7.3 effective bits	12µm 7.7effective bits

3. RESULTS

Three Y-position BPMs chassis were installed in the KEK Accelerator Test Facility (ATF). The toroid current was recorded with each data set. The data presented in this paper is with toroid current of $1e^9$ particles per bunch. Figure 5 shows the results of a frequency spectrum of a single-bunch beam stimulus.

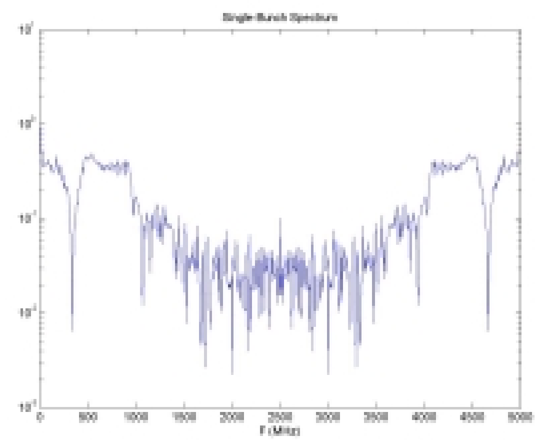

Figure 5. Frequency spectrum of a single bunch beam

Because the single bunch beam calibration data was digitised at separate times a phase error was injected into the signals illustrated in Figure 6. This phase error was corrected by writing a MATLAB script that ensured the digitisers started digitising at the same time.

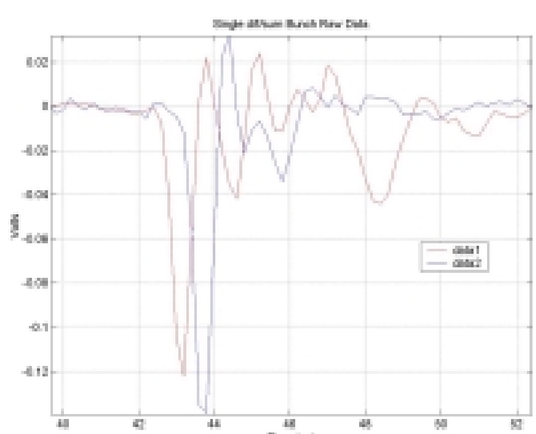

Figure 6. Single bunch raw beam data

The single bunch data was corrected using the tone calibration data that was taken at 600 MHz, which is the center frequency of the hybrid and RF coupler. Using the corrected single bunch data, an inverse matrix was generated that was used to correct the multi-bunch data.

The multi-bunch raw data is shown in Figure 7. In this figure, both the sum and difference signals are displayed. Examination of this data determined that there eighteen bunches in the accelerator. This figure shows that the difference signal comes before the sum signal. This delay can be removed with a MATLAB script.

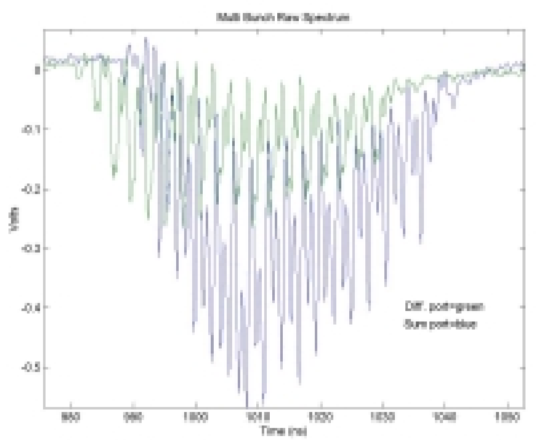

Figure 7. Multi-bunch raw beam data

Figure 8 shows the corrected multi-bunch data down-converted to baseband and low-pass filtered. The data illustrates that the same BPM has the same signal over seven turns of data. However, the data shows that there is only –15dB of isolation between the sum and difference ports. The RF simulations of the hybrid design predicted more than 20 dB of isolation over the bandwidth of the device.

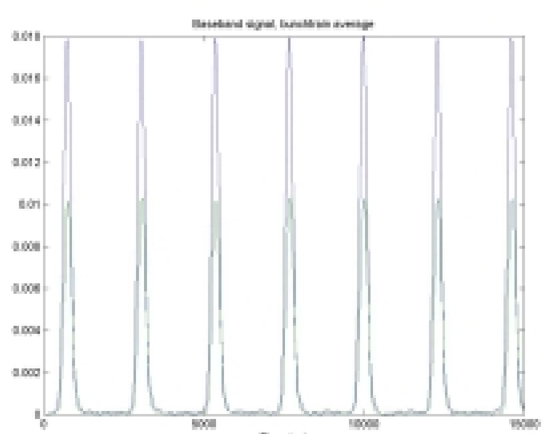

Figure 8. Multi-bunch baseband corrected beam train data

By sampling the maximum signal on the sum and difference ports, the position of the beam as a function of turns can be calculated. The equation for the Y-position is defined as:

$Y=R/2(\Delta/\Sigma)$ where,

R is the radius of the beam pipe,

$R/2=6000$microns

Δ is the difference signal from the BPM chassis,

Σ is the sum signal from the BPM chassis.

Figure 9 shows that the beam position varies 40 microns over seven turns. This is just one BPM however; all three BPMs have the same position resolution.

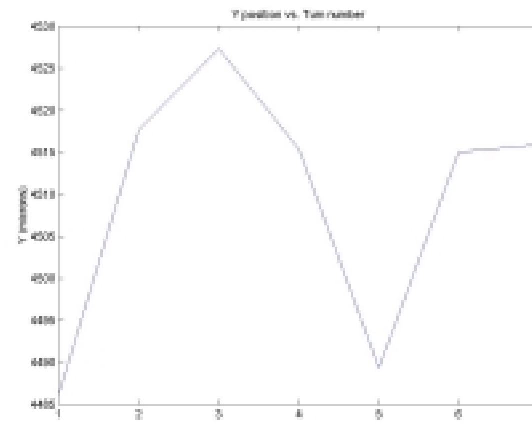

Figure 9. Multi-bunch Y-position over seven turns data

4. SUMMARY

A multi-bunch BPM was built at SLAC and tested at KEK. The BPM electronics can resolve both single and multi-bunch fills. The data clearly indicates that the multi-bunch BPM electronics can measure the beam to within 40 microns. However, the design goal of measuring the beam position within 1 micron was not achieved. The goals were not accomplished due to possible problems in the hybrid that had isolation between the sum and difference ports of –15dB. The timing jitters in the digitiser lead to the larger position resolution. When performing the tone calibration, we discovered that a single shot recording was needed to align the data. Because the tone calibration was done at SLAC, the data was taken at KEK did not use this recording technique.

Currently, a modified Y-position BPM chassis is being installed in PEP-II. Once this BPM is fully installed measurements will be taken to determine if the methodology used to gather data at KEK was flawed or the hardware needs to be improved.

Another solution to solve this problem of position resolution is to use a higher frequency 1428MHz and perform hardware downconversion thus operating at an IF frequency of 200-MHz. The advantage of this solution is a better signal to noise ratio, smaller components, and less sensitivity to phase noise in the digitisers.

A logarithmic processor for beam position measurements applied to a transfer line at CERN

H. Schmickler, G. Vismara, CERN, Geneva, Switzerland

Abstract

The transfer line from the CERN proton synchrotron (PS) to the super proton synchrotron (SPS) requires a new beam position measurement system in view of the LHC.

In this line, the single passage of various beam types (up to 7), induces signals with a global signal dynamics of more than 100 dB and with a wide frequency spectral distribution.

Logarithmic amplifiers, have been chosen as technical solution for the challenges described above.

The paper describes the details of the adopted solutions to make beam position measurements, with a resolution down to few 10^{-4} of the full pickup aperture over more than 50 dB of the total signal dynamics.

The reported performances has been measured on the series production cards, already installed into the machine and on one pickup in the transfer line.

1 BEAM PARAMETERS

1.1 Beam types

Here is a non-exhaustive list of the transfer line beams.

Table 1: Transfer line beam types

Beam Name	Number of bunches	Bunch width	Bunch spacing	Intensities (minimal)
Fix Target	2000	1.7	5	$1*10^9$
LHC	1 to 84	2.1	25	$5*10^9$
Special	1,8,16	4.8	262	$5*10^9$
Heavy Ions	16	6.2/15	131	$2.6*10^8$
		ns	ns	Charges/b

Due to the very low intensity of the heavy ions beams, long coupler pickups have been chosen. Their transfer impedance shows a maximum at about 100MHz, which is a good compromise for the various beams present in the transfer line. The position sensitivity corresponds to 0.54 dB/mm.

1.2 Signals spectral distribution

The signal spectra at the coupler's output are illustrated in fig. 1. In order to illustrate the large dynamic range, the most intense beams have been represented at their maximum intensity, while the weakest beams at their minimum intensity.

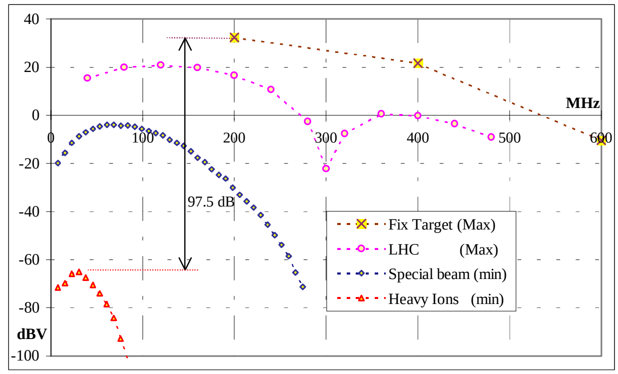

1.3 Global dynamic

The intensity dynamic corresponds to 97.5 dB, to which one should add a position dynamic of at least 25 dB.

Figure 1: Spectral distribution of various beam types

2 DESIGN CONSIDERATIONS

None of the existing electronic processors can cover the whole dynamic range.

Since the various beams are transferred at time interval in the range of seconds, it is acceptable to select a tailored processor to each individual beam. In practice, two processors can handle all the various situations.

The conditions associated to this choice are:

- No reliability reduction, hence no mechanical switching elements
- No significant power consumption increment
- Similar position resolution for the various beam
- Negligible costs increment

2.1 Beam grouping

2.1.1 Narrow Band

The most critical case corresponds to the "Heavy Ions" beam, which shows the largest spectral lines at 22.89 MHz. At this frequency, the "Special" beam is only 7 db below its maximum level and being over 40 dB larger, it can be treated by the same narrow band processor.

The bandwidth choice (BW = 1.3 MHz) is determined by the compromise between the time required to build up a stable signal level and the required long dumping time, to allow a proper measurement to be done, in the case of single LHC bunch.

2.1.2 Wide Band

The "Fix target" and "LHC" beams have respectively fundamental and 5th harmonics tuned at 200 MHz hence use the same processor. To avoid tuning problems the bandwidth can be as wide as 12 MHz.

They induce very large signals, which can be derived from the main path by a coupler or a voltage divider.

This way of grouping allows to compress by 40 db the required dynamic since the most intense beams are shifted in between "Special" and "Heavy Ions" beams.

The two processors can be identical but working at different frequencies.

The choice of a logarithmic processor [1] makes the realization quite simple.

It is reminded that the position is obtained by

$$\mathbf{P = K_{(h,v)}*[\log(R) - \log(L)]}$$

3 CIRCUIT DESCRIPTION

3.1 Splitter

The signal splitting is obtained by a 26 db resistive voltage divider to provide an accurate ratio and 50 Ω matching over the whole BW apart around 22.8 MHz caused by the BP filter tuning

3.2 Band-pass filters

3.2.1 Narrow band BP filter (f_o = 22.8 MHz)

It is made of a single L, C serial resonator. To obtain a relatively high Q, a 2:1 transformer is used to reduce the serial resistance.

The BP filters should be matched per pairs on two parameters: the central frequency and the BW.

The first condition is required to obtain an identical pedestal for the various beams the processor has to treat; in this case, a unique calibration is required.

The BW matching is important for single bunch measurement, in order to obtain a constant differential signal at least during the integration or digitalization time.

3.2.2 Wide band BP filter (f_0 = 200 MHz)

It's also a single resonator, where the Q is determined by the serial resistance of voltage divider (3.3 Ω) to produce a 12 MHz bandwidth. The logamp bandwidth (5MHz) is the limiting factor in the chain; rise time < 100 ns allows for a stable output during the integration time.

3.3 Logarithmic amplifier

The choice of the AD8306 logarithmic amplifier (logamp) has been determined by the following considerations:

- The non-conformance to the log transfer function and the resulting position measurement error.
- The dynamic range inside which this parameter is maintained.
- The standby facility of this chip allows a simple electronic switching between processors, while keeping the power consumption low and stable.
- The availability of a limiter signal output, to be used as auto-trigger facility.

Starting from 100 dB dynamic with a nominal ± 3 dB non-conformity, one ends up with at 66 dB (± 0.2 dB) dynamic range, in the frequency range 10 to 400 MHz.

One logamp for each BP filter is required.

The auto-trigger is obtained from the OR function of the two right channels; this signal has a very short pulse length (BW > 500 MHz), hence a retriggerable monostable drives the digitizer.

3.4 Control logic

The control logic allows the selection of:

- The most appropriate processor (enable function).
- Either the difference of the log (≡ Position) or individual log output (≡ Intensity * Position)
- The output bandwidth, according to the integration time, in the range .5 to 5 MHz.

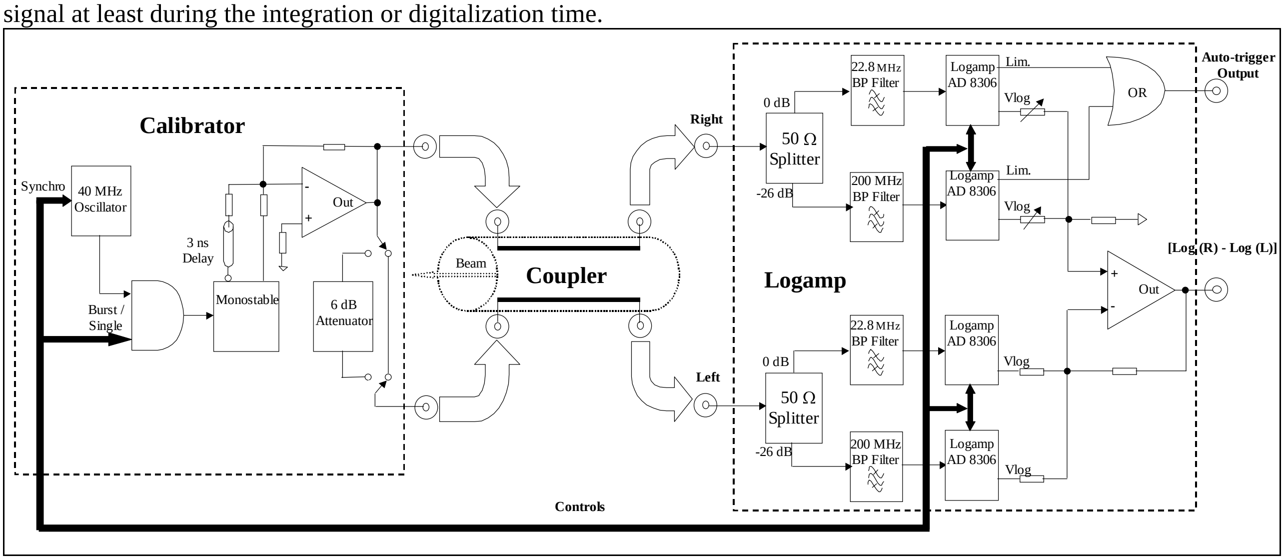

Figure 2: Calibrator - Coupler - Logamp Normalizer Block Diagram.

3.5 Output stage

The differential amplifier, capable to drive 50 Ω load, will produce an output signal proportional to the position, with a sensitivity of 10 mV/mm.

Two trimmings are required to adjust the slope of the logamps at 22.8 MHz and 200 MHz and maintain the central position in ± .2 mm over the whole dynamic range.

4 MEASUREMENTS

A 30 units serial production has been realized, tested and installed in the transfer tunnel. Each unit gives measurements of the horizontal and vertical beam positions. The logamps are housed in a shielded box of 140 x 70 x 40 mm.

4.1 Calibration Measurements

The BW dispersion is limited to 3% rms. for both filters and the NB filters are matched within 0.2 % rms.

The typical response of three different simulated positions is represented in fig.3.

It can be noticed that for a centred beam the stability is excellent; ±100 μm over > 70 dB dynamic. It becomes 3 times worst when the beam is offset by half the gain of an individual amplifier stage of the logamp (6 dB • 11 mm). The noise response versus input level, when measured by integrating over 1 μs tends asymptotically to 18 μm. For integration time of 100 ns this value rise to 50 μm.

In absence of input signal, the logamp has the maximum gain, hence the largest noise approaching the .9 mm rms.

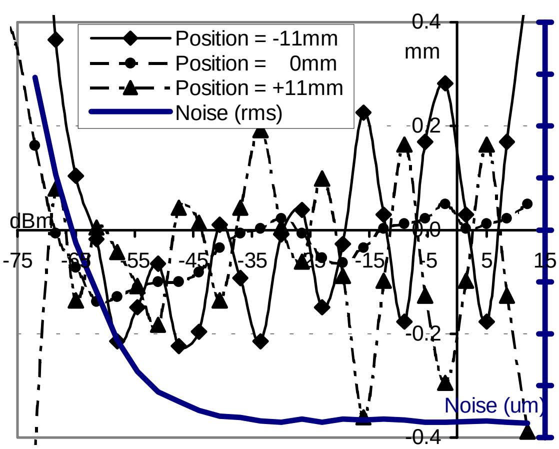

Figure 3: Position errors and noise versus input level

Figures 4, 5 show this, when looking at the difference output (U-D) just before the beam arrival.

4.2 Beam Measurements

Beam measurements have been done on one unit placed nearby the coupler.

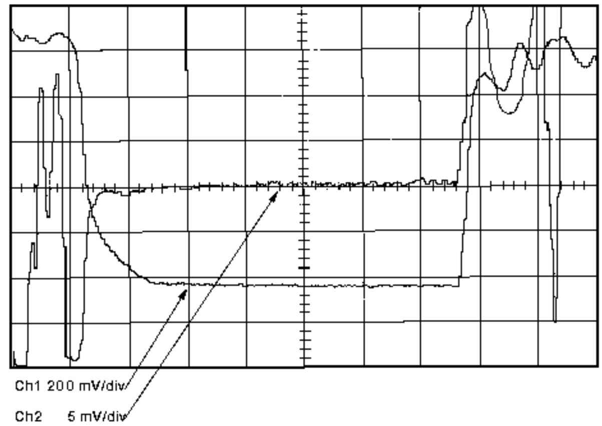

Fig. 4 Fix target beam response -D & [U-D]

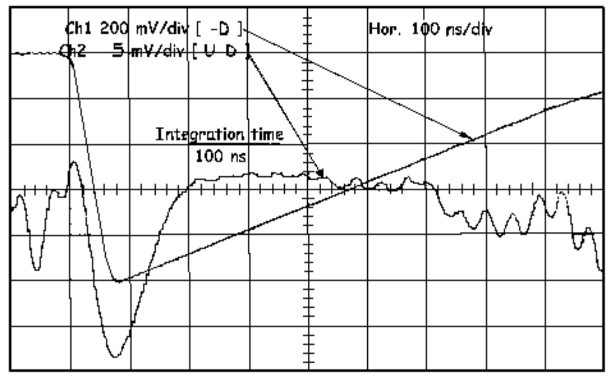

Fig. 5 Single LHC bunch beam response -D & [U-D]

Figure 4, 5 show the logamp processor response to a fix target beam (WB filter) and to a single LHC bunch (NB).

The position's sigma, including the beam jitter on the vertical plane, measured over 100 ejection cycles, is <50 μm for the fix target beam and <80 μm for the single LHC bunch.

It has to be noticed that settling time of the whole chain (NB), before a good measurement can be done, is ~200 ns, which corresponds to a 10 dB reduction on S/N.

The processor requires an accurate beam simulation, in order to correct for position offset and sensitivity.

5 CONCLUSIONS

When signals having a wide variety of frequency spectral contents has to be treated, the logamp appears to be the best choice.

The reasons are the total independence on the input frequency (up to >500MHz) and the true rms. detection. The processor allows single bunch or burst measurements and can resolve between bursts separate by >1 μs.

The system will be fully commissioned during the operations period of the year 2001.

REFERENCES

[1] G. Vismara, " Signal Processing for Beam Position Monitors", BIW 2000 pg 36 Cambridge, Ma AIP Conf. Proc. 546 Figure 3: Position errors and noise versus input level

INJECTION MATCHING STUDIES USING TURN BY TURN BEAM PROFILE MEASUREMENTS IN THE CERN PS

M. Benedikt, Ch. Carli, Ch. Dutriat, A. Jansson, M. Giovannozzi, M. Martini, U. Raich,
CERN, Geneva, Switzerland

Abstract

The very small emittance beam needed for the LHC requires that the emittance blow-up in its injector machines must be kept to a minimum. Mismatch upon the beam transfer from one machine to the next is a potential source of such blow-up.
The CERN PS ring is equipped with 3 Secondary Emission Grids (SEM-Grids) which are used for emittance measurement at injection. One of these has been converted to a multi-turn mode, in which several tens of consecutive beam passages can be observed. This allows the study of mismatch between the PS-Booster and the PS.
This paper describes the instrument and experimental results obtained during the last year.

1 MOTIVATION

Since the construction of the PS Booster (PSB) the transfer line between the PSB and the PS has been operated with a rather large dispersion mismatch. This was acceptable for beams with relatively large transverse emittance and small momentum spread. For LHC-type beams however, due to their low emittance requirements, it is essential to improve the dispersion matching.

The method described was used to measure this mismatch and to investigate new quadrupole settings in the transfer line in order to reduce it[1].

2 EXPERIMENTAL SETUP

Three SEM-Grids are installed in the PS ring in order to measure beam emittance at injection into the machine. After traversal of the detectors, the beam is normally stopped by an internal dump in order to prevent multiple passages, heating the SEM-Grid wires and destroying the detectors. Slow charge integrating electronics is used for the measurements.

However for the measurements reported here, one of the SEM-Grids has been equipped with a fast amplifier (100 ns rise-time) and 40 MHz Flash-ADC associated with 2 kbytes of memory for each SEM-Grid wire. The injection kicker is pulsed twice at 60 µs time interval. The second kick destroys the beam after 28 turns (revolution period in the PS at 1.4 GeV is 2.2 µs) in the machine, thus avoiding unnecessary heating of the SEM-Grid wires.

The ADCs are triggered a few µs before injection and the wire signals are converted and stored in memory at the ADC's internal clock frequency of 40 MHz.

An acquisition program reads out the ADC channels and saves the results onto a disk file for offline evaluation.

The beams used for the measurement had a bunch length of ~ 80ns, an intensity of 10^{11} protons and a small momentum spread in order to ease the evaluation of the betatron mismatch. The method has been first proposed in [2] and preliminary results presented in [3].

3 DATA EVALUATION

A *Mathematica* [4] program reads the disk file and evaluates the data.

3.1 The Raw Data

The raw data correspond to a copy of the ADC memory contents consisting of 2048 samples (one sample every 25 ns) for each of the 20 wires.
Figure 1 shows the signal seen on a single SEM-Grid wire in the centre of the SEM-Grid (wire 11).

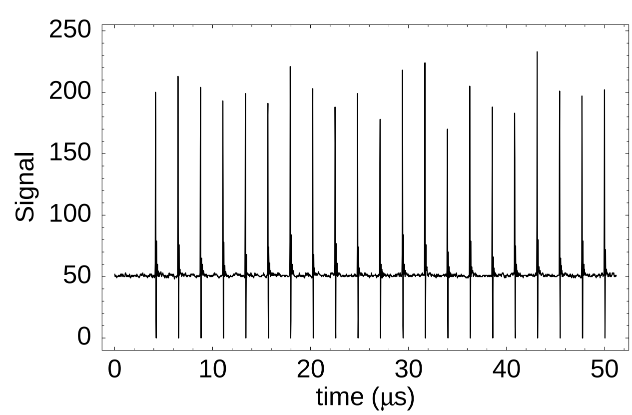

Figure 1: Raw data on a single wire

The raw data from 20 wires around a single beam passage is shown in fig. 2. Here 12 samples of the wire signals from all wires is plotted.

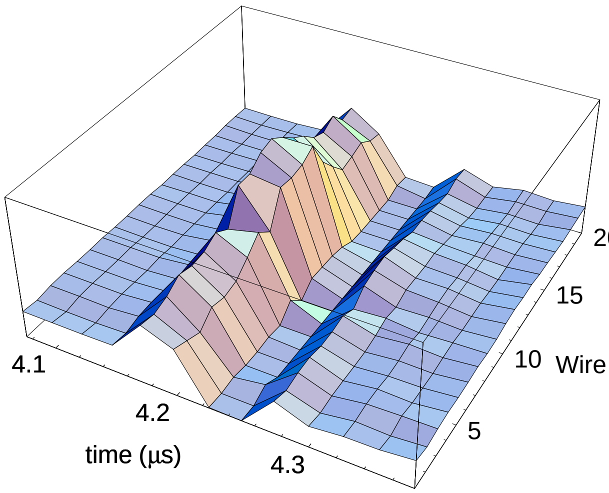

Figure 2: Raw data around 1 beam passage

The signal has 2 components:

- Signal induced on the wire by the charges of the beam (the outer wire see a signal) approximately proportional to the derivative of the longitudinal bunch shape, leading to a negative signal component.
- Signal created by secondary emission

Integration of the signal makes the first component vanish and keeps only the secondary emission part.
As can be seen from fig. 2 the ADC sampling rate is not high enough for the signal time-scale and a longer bunch-length would have been preferable.

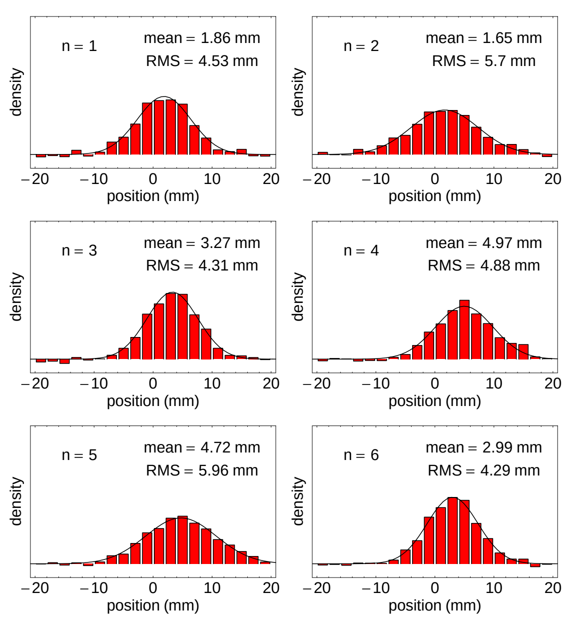

Figure 3: Turn-by-Turn Profile

The profiles obtained by integrating the signals from each wire can be seen in fig. 3 for the first 6 turns.

3.2 Trajectories and Dispersion Mismatch

The turn-by-turn profiles are fitted with a Gaussian and the mean position and beam width of are extracted from the fit parameters.

The mean position for a beam with a relative momentum offset of 4 ‰ is plotted in fig. 4. The solid curve is a fit from which the following parameters are extracted:

- The trajectory's mean position (<x>=3.5 mm). It is dominated by momentum offset via dispersion with a small contribution from the closed orbit.
- The amplitude (1.74 mm) with a main contribution from the dispersion mismatch and a small part due to mis-steering.
- The non-integral part of the tune (0.176). The method can be used to determine the tune to a precision of 0.001.
- The phase at the first passage (2.54 rad, phase=0 if the oscillation is at its maximum at the first passage)

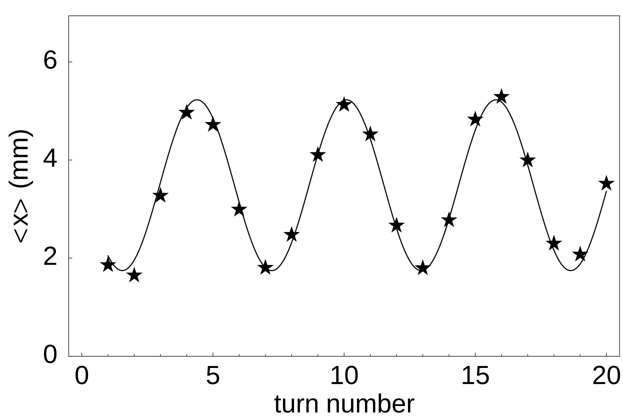

Figure 4: Square of the mean positions extracted from the profiles

From two acquisitions measured with different momentum offsets, the dispersion of the receiving synchrotron and the dispersion mismatch can be determined.
The data shown in fig. 4 are combined with an acquisition at the relative momentum offset of –1.4 ‰ leading to:

- Dispersion of the PS at the position of the SEM-Grid: 2.53 m
- Amplitude of the dispersion mismatch: 0.5 m
- Phase of the dispersion mismatch: 2.47 rad.

3.3 Width Oscillations and Betatron Mismatch

The variance of the beam distribution extracted from the fitted profiles is shown in fig. 5. This oscillation is determined by betatron mismatch, by dispersion mismatch, and from a very small contribution due to scattering on the SEM-Grid wires.

In addition to the dispersion parameters, which have been evaluated as described in section 3.2, the momentum spread is estimated from a longitudinal bunch-shape measurement and introduced into the calculations.

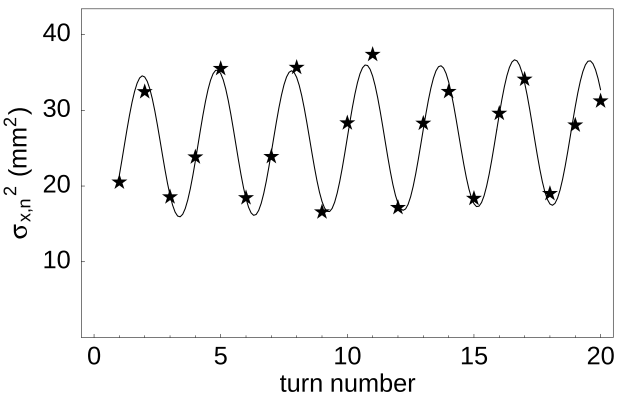

Figure 5: Beam width for each turn

The following parameters can be obtained by fitting the data points:

- The emittance of the injected beam (1.82 π μm). The advantage of this method, as compared to the standard 3-profile method, lies in the fact that only the beta function has to be taken into account and good statistics are obtained for the beam width due to multiple measurements on the same beam.
- Geometric betatron mismatch (~ 50 %) which leads to an RMS blow-up of 8 %.
- The contribution of the beam width due to scattering on the SEM-Grid wires is barely visible. The RMS scattering angle is estimated to 0.04 mrad per turn.

4 POSSIBLE IMPROVEMENTS

On the electronics side, several improvements can be considered:

- The ADC sampling rate should be increased by at least a factor 2 and its dynamic range improved. 10 bits resolution or better would simplify the adjustment of the beam intensity to the ADC range.
- The amplifier bandwidth should be extended in order to cope with the rather short bunches of a few tens of ns. Limits are the small momentum spread desired the minimum voltage of the PSB RF system and the fact that longitudinal scraping is used in order to adjust the beam intensity.

The injection of longer bunches would reduce the negative signal component. Limits are the small momentum spread desired, the minimum voltage of the PSB RF system and the fact that longitudinal scraping is used in order to adjust the beam intensity.

The CERN PS uses a pulse-to-pulse modulation scheme (ppm) that allows re-configuring the machine for 2 consecutive acceleration cycles in order to produce different types of beams for different users.

When performing the matching measurements, the accelerator must be dedicated to these studies and no other beams are allowed in order to protect the SEM-Grid. Improvements in the insertion mechanism such that the SEM-Grid can be inserted into the beam passage just before injection of the beam to be measured, and taken out before the next acceleration cycle, would allow using the scheme without blocking the accelerator for other users.

5 CONCLUSIONS

Machine experiments using multi-turn profile measurements have shown that valuable information on injection matching can be extracted.

It was possible to determine the mismatch in dispersion and in both transverse phase planes. In addition the tune, the emittance of the injected beam and the dispersion of the PS could be obtained.

REFERENCES

[1] M.Benedikt, C. Carli, C. Dutriat, M. Giovannozzi, A. Jansson, M. Martini, U. Raich, K. Schindl, “Study of a new PSB-PS transfer line Optics with Improved Dispersion Matching by means of turn-by-turn Beam Profile Acquisitions”, PS/AE Note 2001-003(MD)

[2] C. Bovet, R. Jung , “A New Diagnostic for Betatron Phase Space Matching at Injection into a Circular Accelerator”, LHC Project Report 3, Rev. , June 1996

[3] C. Bovet, R. Colchester C. Dutriat, G. Ferioli, J.J. Gras, R. Jung, P. Knaus, U. Raich, J.M. Voulliot , “First Results from Betatron Matching Monitors installed in the CERN PSB and the SPS”, EPAC’98

[4] Stephen Wolfram, ”Mathematica, A System for doing Mathematics by Computer”, Addison-Wesley,ISBN 0-201-51502-4

THE SPS INDIVIDUAL BUNCH MEASUREMENT SYSTEM

A. Guerrero, H. Jakob, R. Jones, J.J. Savioz.
SL Division CERN Laboratory - CH - 1211 Geneva 23

Abstract

The Individual Bunch Measurement System (IBMS) allows the intensity of each bunch in an LHC batch to be the measured both in the PS to SPS transfer lines and in the SPS ring itself. The method is based on measuring the peak and valley of the analogue signal supplied by a Fast Beam Current Transformer at a frequency of 40MHz. A 12 bit acquisition system is required to obtain a 1% resolution for the intensity range of 5×10^{9} to 1.7×10^{11} protons per bunch, corresponding to the pilot and ultimate LHC bunch intensities. The acquisition selection and external trigger adjustment system is driven by the 200MHz RF, which is distributed using a single-mode fibre-optic link. A local oscilloscope, controlled via a GPIB interface, allows the remote adjustment of the timing signals. The low-level software consists of a real-time task and a communication server run on a VME Power PC, which is accessed using a graphical user interface. This paper describes the system as a whole and presents some recent uses and results from the SPS run in 2000.

1. INTRODUCTION

Since 1999 the PS pre-injector complex has been able to produce proton beams for LHC [1]. The LHC batch, consisting of 72 bunches spaced by 25ns is generated in the PS at 26 GeV/c and transferred to the SPS. Following three or four of such injections, the SPS is ramped in energy to 450 GeV/c, after which injection to the LHC will take place (see Fig. 1).

The Individual Bunch Measurement System (IBMS) was designed for a continuous monitoring of the intensity of each bunch of each LHC batch. The total range of intensities involved is summarised in Table 1.

Beam Type	Intensity per bunch ($\times10^{11}$ppb)	Max Nb of Bunches	Total Current (mA)
Pilot	0.03	1	0.05
Set-up	0.03	72	3.6
Commissioning	0.17	288	34
Nominal	1.05	288	209
Ultimate	1.7	288	340

Table 1: Bunch intensity for LHC type beams.

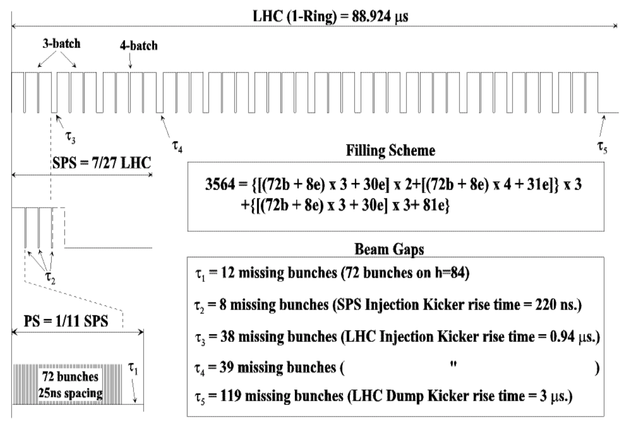

Figure 1: Bunch disposition in the LHC, SPS and PS.

The system is able to measure all bunches for all injected batches in the PS to SPS transfer lines, and a selected number of turns in the SPS ring, or up to 16 selected bunches for all turns in the SPS.

2. INSTALLATION

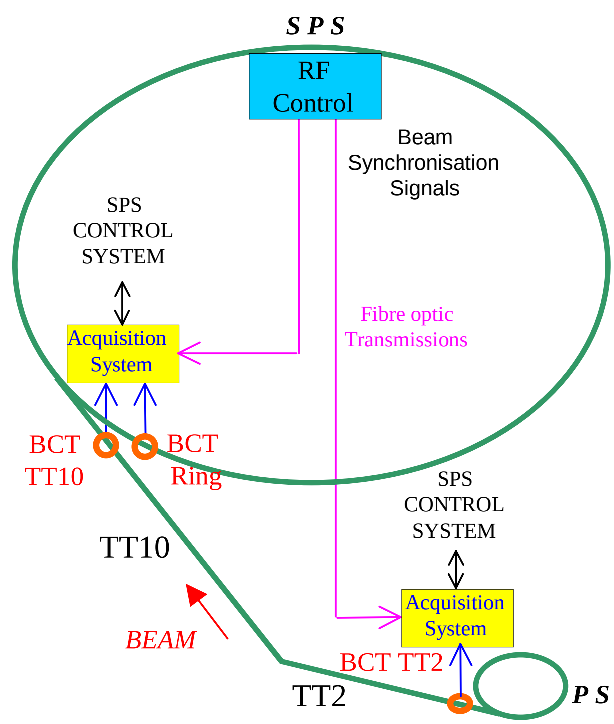

Figure 2: Layout of the installation.

The layout of the current installation is shown in Fig. 2. Three existing Fast Beam Current Transformers (FBCTs) were used: one at the beginning of the TT2 transfer line, one at the end of the TT10 transfer line, and one after a complete revolution in the SPS. The acquisition systems were installed in the nearest surface building to minimise the cable lengths required.

3. ANALOGUE FBCT SIGNALS

The first measurements for the IBMS project where performed on a prototype transformer integrated into an existing CERN-SPS DCCT housing. An LHC batch with 72 bunches spaced by 25ns shows an important droop of 5%/µs which needs to be much lower for precise measurements (Fig. 3(a)). The ringing between the bunches of the same batch is essentially due to the resonance of the big cavity formed by the wall-current bypass and the outer side of the vacuum chamber (Fig. 3(b)). The signal therefore needed to be filtered before sampling.

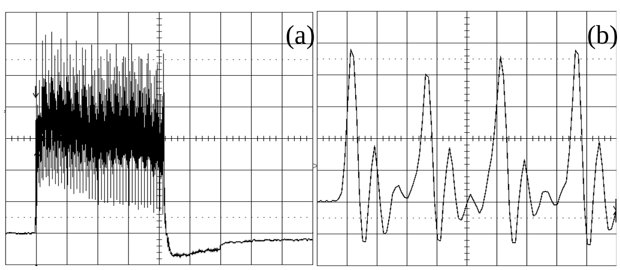

Figure 3: a) 72 bunches showing 5%/us droop.
b) zoom showing ringing between bunches.

A new housing, Fig. 4(a), has now been designed, with a much smaller cavity between the vacuum chamber and the wall-current bypass. By integrating a low droop transformer into such a housing, a good bunch to bunch signal can be obtained even without filtering (Fig. 4(b)). Such a system will be installed in the CERN-SPS for tests in 2001.

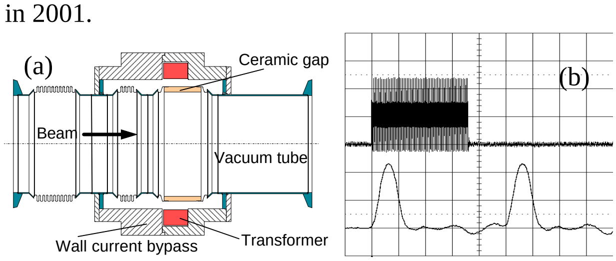

Figure 4: a) new FBCT housing.
b) resulting signals with new housing.

4. THE ACQUISITION SYSTEM

A 60 MHz low-pass filter is used treat the noisy signal (see Fig. 3(b)) coming from the FBCT to maintain the zero level between two consecutive bunches. A 50Ω splitter and a 12.5ns delay then provide the two phase shifted signals, for the synchronisation of the simultaneous sampling. Two 12-bit ADCs using an external 40MHz clock convert the data to digital format, and write into a 4096 location FIFO. A PowerPC running under Lynx/OS is then used to transfer the FIFO contents each time it is half-full. The read-out from the FIFO has to be faster than or equal to the rate of the incoming data. This limit is in fact reached when collecting 16 bunches on a turn-by-turn basis. If more bunches are to be collected, the time between acquisitions has to be increased. For example, in order to collect the data from all 72 bunches, the acquisition can only be performed every 7 turns. The exact delay between the revolution frequency and the sampling time is controlled via an adjustable phase shift of the 200MHz RF acceleration frequency providing the external clock.

5. GRAPHICAL USER INTERFACE

Two user applications (GUI's) have been built in order to visualise remotely acquired data in different fashions. A third GUI is necessary to set up the delays required for the synchronisation of the top and valley acquisitions (see Fig. 5).

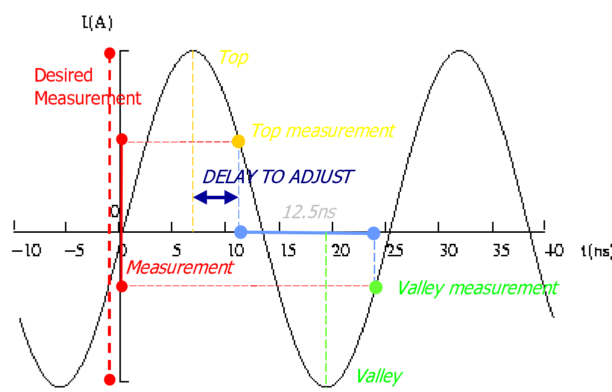

Figure 5: Delay adjustment requirements.

The first of the user applications, allows the visualisation of data from a single system for a configuration where bunches, number of turns and acquisition time can be selected. The same data can be viewed in different ways: measurement of all bunches and turns acquired as shown; measurement of up to eight selected bunches (out of the acquired bunches) for all turns; raw data (top, valley and measurement) for all bunches on a given turn (see Fig. 6).

The second application provides information from all three systems installed at the same time. Measurements are gathered for the same injection in the transfer lines and at any of the first four turns in the SPS ring. This user application therefore automatically configures the acquisition parameters to obtain a one batch measurement from all the systems. Cross-calibration of the systems has not yet been performed, hence only the shape of the acquisition curve could be used to find out if there were losses at injection.

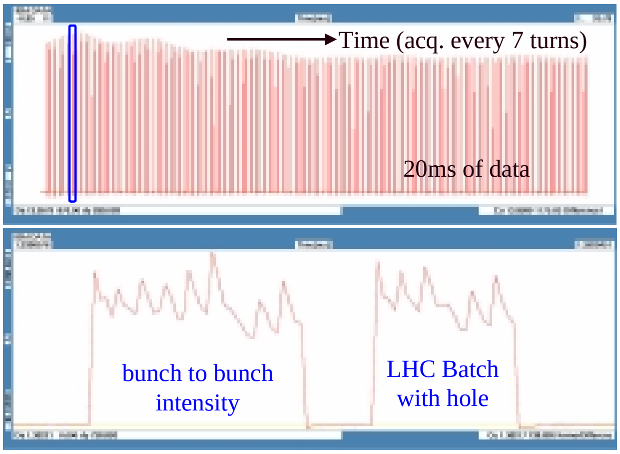

Figure 6: Example of a typical acquisition, in this case with a missing PS booster injection.

6. RESULTS

The capability of the system permits the measurement of single bunch intensities for a few thousand consecutive turns in the case where only a few bunches from the batch have been selected, or the whole cycle for the complete batch if the acquisition frequency remains low enough. This bunch-by-bunch capability has been extensively used during SPS operation in 2000, to study the injection of LHC type beams, and their stability while circulating. Fig. 7 shows an acquisition where the total batch intensity is seen to decrease during the cycle. Looking in more detail at specific bunches within the batch shows that the loss is concentrated at the tail of the batch. This type of instability was linked to the electron cloud effect [2], where secondary electrons are accelerated by successive bunches, hit the vacuum chamber and produce even more secondaries, leading to a cloud build-up along the batch.

There are, however, also some problems with the current system using the peak and valley approach. It is very sensitive to any bunch length variations, as can be seen at the start of the graphs in Figs. 6&7, where the intensity is seen to oscillate due to bunch length variations linked to longitudinal mismatch at injection. It is also sensitive to any phase differences between the beam and RF frequency. This arises during acceleration, where the time taken for the RF signals to reach the acquisition crate remains fixed, but the beam time-of-flight changes. Such errors can be corrected by modifying the delay parameter according to the momentum increase during the acquisition if the ramp function is known. Such a solution will be adopted for the IBMS system in 2001.

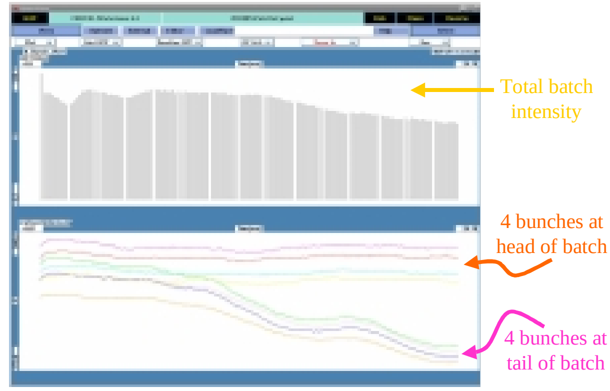

Figure 7: IBMS acquisition for a complete SPS cycle, showing beam loss at the tail of the batch.

7. CONCLUSIONS

The IBMS has proved very useful for a first evaluation of the LHC beam in the transfer lines and the SPS. However, the current system is not optimised, and several changes will be made during the coming years. Notably, the FBCTs currently used will be replace by three identical, low-droop FBCTs, all housed in a purpose built assembly. The top and valley acquisition system which is very sensitive to the timing adjustment and bunch length will be replace by a new system based on a fast integration and digitalisation of the signal from each bunch. In addition a Digital Acquisition Board (DAB), designed for the LHC beam position monitor system [3], will replace the current digital storage system based on a FIFO.

8. REFERENCES

[1] The Large Hadron Collider Project http://lhc.web.cern.ch/lhc/
[2] G. Arduini et al. “Electron Cloud : Observations with LHC-Type Beams in the SPS”, Pres. at: 7th European Particle Accelerator Conference, Vienna, Austria, CERN-LHC-Project-Report-434, 2000.
[3] D. Cocq et al., “First beam tests for the prototype LHC orbit and trajectory system in the CERN-SPS”, in these proceedings, DIPAC 2001, Grenoble, 2001.

CONTROL MODULES FOR SCINTILLATION COUNTERS IN THE SPS EXPERIMENTAL AREAS

G. Baribaud, C. Beugnet, A. Cojan, G.P. Ferri, J. Fullerton,
A. Manarin, J. Spanggaard
CERN Laboratory - CH - 1211 Geneva 23

Abstract

The hardware used in the SPS Experimental Areas to control the beam instrumentation electronics and mechanics of the particle detectors is based on CAMAC and NIM modules. The maintenance of this hardware now presents very serious problems. The modules used to operate the Experimental Areas are numerous and older than 20 years so many of them cannot be repaired any more and CAMAC is no longer well supported by industry. The fast evolution of technology and a better understanding of the detectors allow a new equipment-oriented approach, which is more favourable for maintenance purposes and presents fewer data handling problems. VME and IP Modules were selected as standard components to implement the new electronics to control and read out the particle detectors. The first application implemented in this way concerns the instrumentation for the Scintillation Counters (formerly referred to as triggers). The fundamental options and the design features will be presented.

1 MOTIVATION AND HISTORY

Most of the detectors in the Experimental Areas of the SPS were implemented more than twenty years ago. At that time many detectors were at an experimental stage and the implementation of their control electronics and data acquisition were not yet in a final state. It was therefore convenient to have building blocks that made it easy to add new features whenever needed. The electronics were therefore implemented in a function-oriented way (see chapter 2), where many different systems, often located in different racks, constituted the building blocks of the detector control.

Our detectors are now well known and implemented in a well-defined manner. The advantage of the function-oriented approach has now vanished and has turned into a time consuming problem when it comes to maintenance and troubleshooting. For some detectors more than hundred cables are needed to interconnect their functional building blocks making fault finding very difficult.

Scintillation Counters are rather simple devices used to count the number of particles in a beam. They are made up of a scintillator that can be moved in or out of the beam and a photomultiplier to pick-up the scintillation light produced by each charged particle. When put in coincidence two Scintillation Counters are often used to strobe a more complex detector (see Fig. 1). The old function-oriented approach presently implemented for the Scintillation Counters requires the interconnection of seventeen different electronic modules for their control and data acquisition (see chapter 2.1).

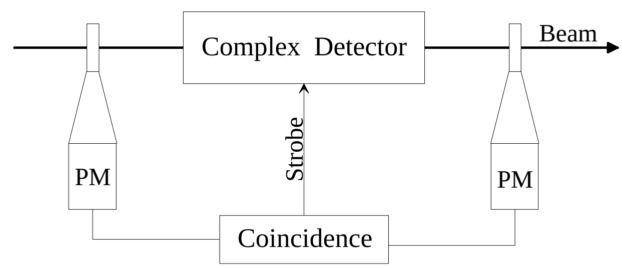

Figure 1: Scintillation Counters in coincidence.

2 FUNCTION ORIENTED APPROACH

2.1 Modules used for the old implementation

In the old function-oriented approach the different systems like Discriminators, Delays, DACs and ADCs have many channels connected to signals from many different types of equipment.

For the Scintillation Counter the electronic modules needed to implement the old function-oriented systems are listed below:

- Discriminator. 8 ch NIM module.
- Delay Driver. 64 ch CAMAC module.
- Quad Delay. 4 channel 19” chassis.
- Coincidence. 4 ch NIM module.
- Scaler. 6 ch CAMAC module.
- Programmable Fan Out. 16 ch Camac module.
- Led Driver. 16 ch NIM module.
- ADC. CAMAC module.
- Multiplexer Driver. 1024 ch CAMAC module.
- ADC multiplexer. 64 ch 19” chassis.
- Analogue MPX PP. 32 ch 19” chassis.
- DAC. 12 ch. CAMAC module.
- Output Register. 128 ch CAMAC module.
- Input Gate. 256 ch CAMAC module.
- Timing Repeater. 4 ch NIM module.
- Line Survey. 128 ch CAMAC module.
- I/O Motor Driver. Two ch NIM module.

2.2 Complex troubleshooting

These seventeen modules are located in different chassis and in different racks mixed with other types of equipment. In some cases the control electronics of a Scintillation Counter is located in one barrack whereas the data acquisition is located in another. This is what make troubleshooting extremely difficult and time consuming.

3 IP MODULES

3.1 Evolution of electronics

New electronic components now allow a designer to pack much more functionality in less space with increased reliability at reduced cost. This allows to move the function-oriented approach from the module level to the sub-module level.

3.2 From daughter boards to IP Modules

Many companies have developed electronic modules using daughter boards either to gain space for higher integration or in order to implement a standard functionality that can be re-used for another member of the same product family.

The trademark IndustryPacks, introduced as an open standard for daughter boards by GreenSpring Computers back in 1988, has now grown to a widely used industrial standard called IP Modules [1]. In the mid-nineties around 100 firms had adopted the standard and put IP Modules on their product program. Today you find a lot of standard functions implemented as general purpose IP Modules and some firms even offers custom design of daughter boards in this standard. In the case of a VME motherboard a maximum of four IP Modules can be added on (see Fig. 2).

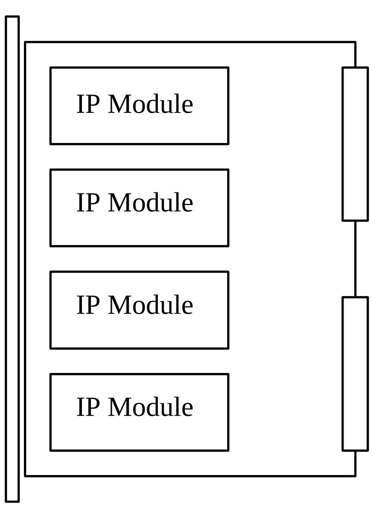

Figure 2: VME board with IP Modules.

4 EQUIPMENT ORIENTED APPROACH

4.1 Advantages

The aim of the new equipment-oriented approach is that one module only serves one equipment or at least one type of equipment. This approach has a number of advantages:

- Simplify the system structure.
- Decouple different types of equipment.
- Reduce the number of electronic modules.
- Suppress interconnecting cabling.
- Reduce the number of standards used.
- Regroup the electronics of equipment.
- Simplify the database and software.
- Increase reliability.

4.2 Module specifications

The main requirements for the new equipment-oriented module for the Scintillation Counters are:

- Dual equipment module to ease coincidence.
- High voltage control for the photomultipliers.
- Motor control of in/out movements.
- Signal discrimination and coincidence control.
- Count number of particles.
- Perform spill measurement (see chapter 5).

4.3 Collaboration with industry

As in most research laboratories the resources are getting rare so collaboration with industry is encouraged for new electronic developments. Standard industrial modules, modules designed from CERN specifications and a minimum of home design have therefore been key words for our new electronics.

For the update of the old function-oriented hardware of the Scintillation Counters the IP Modules represent an interesting choice. Other types of detectors based on photomultipliers will also be able to profit from these sub-modules to replace the functions originally implemented in NIM, CAMAC or 19 inch chassis. We have therefore tried to find partners in industry to produce IP Modules that fulfils most of the functionality needed for this family of detectors.

4.4 Implementation in VME

The new equipment-oriented module for the Scintillation Counters has been implemented as a VME board with three IP Modules:

- IP-A is a general-purpose input/output/counter module from Actis. This module features eight 12-bit DACs, eight 12-bit ADCs, three counters/timers and up to twenty digital inputs or outputs [2].

- IP-B is quad 100 MHz spill counter from Develco. It contains four individual counters plus a FIFO[3]. The contents of all four counters are transferred to the FIFO at the rate of the programmed sampling frequency from IP-A. The use of this new feature is described in chapter 5.
- IP-C is a dual discriminator and delay module developed at CERN. It features 100MHz signal processing of the photomultiplier signals and conditioning of the signals for the coincidence and the counters. The programmable delay and pulse width is implemented with an ASIC delay generator [4].

These three IP Modules fulfil most of the needs for the Scintillator control and data acquisition whereas the remaining equipment specific features are implemented on the motherboard. This is the case for the power stage for the motor control.

The interface from the VME-bus to the individual IP Modules is implemented in an Xilinx capable of controlling four IP Modules. In order to simplify the internal addressing, the functions implemented on the motherboard are controlled as a virtual IP-D module.

5 NEW FEATURES

The Scintillation Counters are used for the fixed target physics in the Experimental Areas of the SPS. Protons are extracted from the SPS accelerator towards a fixed target during a 2.4 seconds period referred to as the spill. From the Target Area the secondary beams are transported through long beam lines to the Experimental Areas. Each beam line is equipped with several Scintillation Counters in order to count the number of particles at different positions. As explained in chapter 1, they are also used to strobe more complex detectors.

As a new feature, it was requested that the Scintillation Counter Control Module could measure the stability of the beam extraction and the beam transport in order to know the intensity variation during the spill. This spill measurement has been implemented in the new module by storing away the counter content at regular intervals. By transferring the counter content to a FIFO every millisecond, useful information about the spill quality can be obtained. Fig.3 shows a spill measurement from a secondary beam line during the 2.4 second extraction from the SPS towards the West Experimental Area. The first half of the spill shows normal stable beam intensity whereas the second half indicates a magnet problem in the beam transport.

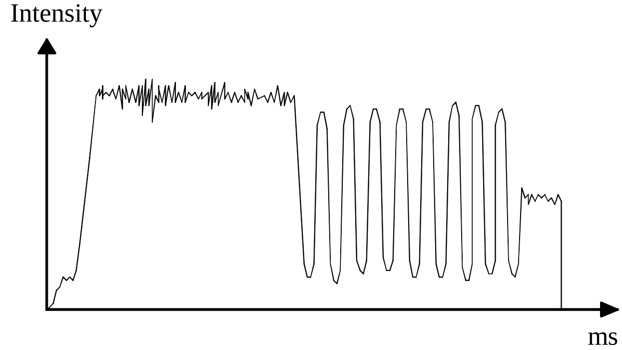

Figure 3: Spill measurement with a scintillation detector.

6 CONCLUSION

One single new control module for the Scintillation Counters replaces seventeen old CAMAC and NIM modules. The complex cabling between these old modules is suppressed and the new equipment-oriented design makes troubleshooting much easier and limits the number of industrial standards. Using the same standard IP Modules on other dedicated VME boards, several detectors will profit from the same upgrade in the future. The new equipment-oriented approach will increase the reliability of the electronics and make the overall maintenance load significantly smaller.

REFERENCES

[1] ANSI / VITA 4-1995: IP Modules.

[2] A. Manarin: Analog and digital I/O module, an IP Module. SL-spec 2000-02. CERN January 2000.

[3] A. Manarin: 32-bit counters with FIFO, an IP Module. SPS-spec 99-21. CERN November 1999.

[4] T. Toifl et al.: A 4-channel rad-hard delay generator ASIC with 1 ns minimum time step for LHC experiments. CERN 1998.

LHC BEAM LOSS MONITORS

A. Arauzo Garcia, B. Dehning, G. Ferioli, E. Gschwendtner, CERN, Geneva, Switzerland

Abstract

At the Large Hadron Collider (LHC) a beam loss system will be installed for a continuous surveillance of particle losses. These beam particles deposit their energy in the super-conducting coils leading to temperature increase, possible magnet quenches and damages. Detailed simulations have shown that a set of six detectors outside the cryostats of the quadrupole magnets in the regular arc cells are needed to completely diagnose the expected beam losses and hence protect the magnets.

To characterize the quench levels different loss rates are identified. In order to cover all possible quench scenarios the dynamic range of the beam loss monitors has to be matched to the simulated loss rates. For that purpose different detector systems (PIN-diodes and ionization chambers) are compared.

1 LHC PARAMETERS

1.1 Quench levels

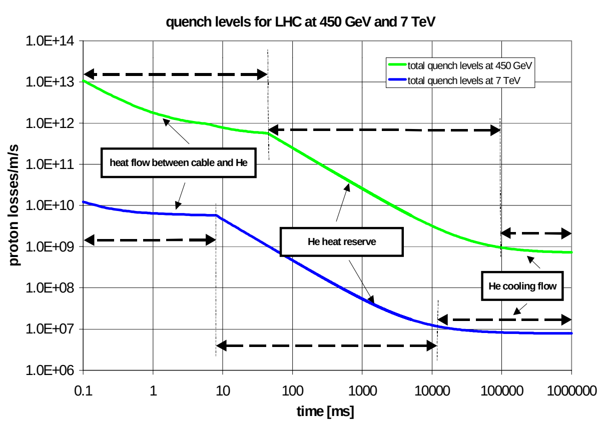

Figure 1: Different quench levels for 450GeV and 7TeV.

Super-conducting magnets can quench if a local deposition of energy due to beam particle losses increases the temperature to a critical value. Figure 1 shows the maximal allowed proton losses/m/s at 450GeV and 7TeV for quenches being reached after different time scales. These quench levels are determined by the coil materials and the coil cooling. The main effects are[1]:

1. At short time scales (τ<50ms at 450GeV, τ<8ms at 7TeV) the maximal allowed proton loss rate is limited by the heat reserve of the cables as well as by the heat flow between the super-conducting cables and the helium.
2. At intermediate time-scales (τ>50ms at 450GeV, τ>10ms at 7TeV) the limited heat reserve of the helium determines the quench levels.
3. The maximal helium flow to evacuate the heat across the insulation defines the allowed proton losses at times above seconds.

The proton loss rate extends over six orders of magnitude. An uncertainty of 50% is considered for the levels.

1.2 Operation conditions

The magnet protection must cover the different filling schemes for LHC shown in Table 1 at injection, ramping and top energy.

Table 1: Different filling schemes for the LHC.

filling scheme	Number of bunches	number of protons/bunch
pilot bunch	1	$5\cdot10^{9}$
TOTEM	36	$1\cdot10^{10}$
batch	243	$1\cdot10^{11}$
nominal	2835	$1.1\cdot10^{11}$

2 SIMULATION OF BEAM LOSSES AND DETECTOR LOCATIONS

With the Monte Carlo code GEANT 3.21 the impact of beam protons on the aperture of the super-conducting magnets has been simulated[2]. In order to detect the beam losses outside the cryostat the shower development in the magnets has been computed in consideration of the main different geometries and magnetic field configurations. These calculations allow determining the suitable positions of the beam loss detectors as well as the needed number of monitors. The results show that a set of six monitors outside the cryostat of the quadrupole magnets in the arc cells are needed to completely diagnose the expected beam loss.

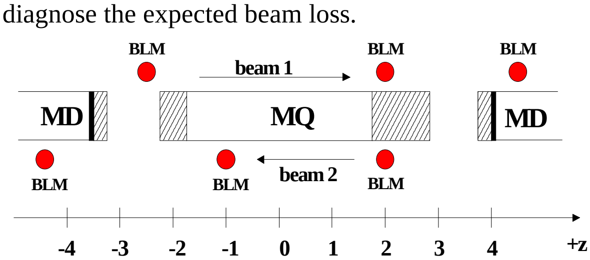

Figure 2: Proposed beam loss monitor locations around the quadrupoles.

The proposed beam loss detector locations in the arc shown in Figure 2 cover aperture limitations in the quadrupole magnets where the betatronic function has a maximum value and also misalignment errors between the bending and quadrupole magnets. The locations are also optimized to allow distinction between the counter-rotating beams.

The averaged expected shower particles (MIPs) per lost beam proton per cm^2 reaching the detectors are shown in Table 2. The number of protons depend on the magnet configuration and the different monitor locations. The statistical error on the simulation is between 5% and 10%.

Table 2: Simulated shower particles per lost beam proton per cm^2.

beam energy	$MIPs/p/cm^2$ min	$MIPs/p/cm^2$ max
450 GeV	$5\cdot10^{-4}$	$3\cdot10^{-3}$
7 TeV	$8\cdot10^{-3}$	$4\cdot10^{-2}$

3 BEAM LOSS DETECTORS

The dynamic range of the detection system must be 10^7; six orders are due to the quench levels and a factor 10 comes from the sensitivity for low level losses.

In the following sections the performance and the dynamic range of two different beam loss detector systems are investigated; PIN-diodes are compared with ionization chambers at different quench levels.

3.1 Charge threshold counters

PIN-diode beam loss monitors consist of two reverse-biased PIN-diodes mounted face-to-face[3]. Charged particles that cross the two detectors produce a coincidence signal. The dark counts from random coincidences are very low of the order of 10^{-3}/10ms. The efficiency of the PIN-diodes for minimum ionizing particles in coincidence is measured to be 35%[4].

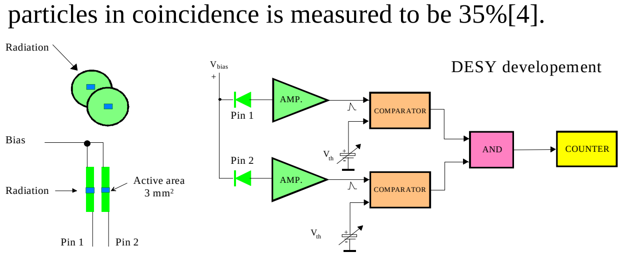

Figure 3: Read-out chain for the two PIN-diodes.

The time resolution of the PIN-diode detectors can be as high as 40MHz. However, since the diodes give per bunch crossing either no hit or only one hit (and not several hits that are proportional to the lost beam protons) the maximum count rate is limited to the bunch passage frequency. This is at nominal LHC conditions 2835×11235.5Hz=32MHz.

However, this threshold can be raised by almost one order of magnitude when applying Poisson statistics (see in details in [5]).

Table 3 shows the expected PIN-diode counts **R** induced by lost protons equivalent to the quench levels in 10ms. **R** is calculated according to

$$\mathbf{R = F\times P = F\,[1-e^{-np}]},$$

where **F** is the number of bunch passages in a certain time window and **P** is the probability for at least one hit in the diodes per bunch crossing. **P** depends on the number of lost protons **n** per bunch crossing and on the probability **p** for a hit in the diodes per one lost proton. We see that the exact knowledge of the number of bunch passages **F** is important.

The PIN read-out will saturate, if the counts **R** are equal to the number of bunch passages **F** (in Table 3 at the pilot filling scheme, at TOTEM for 450GeV and for a batch with 450GeV). In these cases **n** or **p** is very high and hence the probability **P** becomes unity. Applying Poisson statistics is then redundant and no predictions can be made about the number of lost protons and the quench levels.

Table 3: Expected PIN-diode counts in case of a quench caused in 10ms.

filling schemes	max. PIN counts F in 10ms	PIN counts R for a quench caused in 10ms: 450 GeV	PIN counts R for a quench caused in 10ms: 7 TeV
pilot	112	*112*	*112*
TOTEM	$4\cdot10^3$	$4\cdot10^3$	$3.9\cdot10^3$
batch	$2.7\cdot10^4$	$2.7\cdot10^4$	$1.1\cdot10^4$
nominal	$3.2\cdot10^5$	$1.7\cdot10^5$	$1.4\cdot10^5$

The saturation effects shown in Table 3 can be improved by taking advantage of the angular distribution of the MIPs that hit the detectors. Using two diodes with a distance of e.g. 2cm and with different sizes (e.g. $10mm^2$ and $3mm^2$) decreases the probability for hits in the diodes and hence the counting rate (up to a factor 10). Saturation happens then only at the pilot filling scheme.

At the smallest quench level read-out (quench level in 1s at 7TeV, pilot filling scheme) the signal to noise ratio is $S/N=3\cdot10^4$.

3.2 Charge integration counters

The proposed ionization chambers (SPS type) have a surface of $30cm^2$ and a length of 30cm. The air-filled detectors are polarized at V_{bias}=800V. One MIP produces ~2000 electron/ion-pairs. Tests[6] have shown that the response of the ionization chamber is linear up to 10^{12}–10^{13} $MIP/s/cm^2$. The maximal expected rate is at the order of 10^{11} $MIP/s/cm^2$.

The read-out chain is shown in Figure 4. An Integrator integrates the ionization chamber current during a gate length of 10ms. In case it saturates at 5V within this gate, the capacity of the integrator is discharged and a 12bit counter is incremented. At the end of the 10ms gate the counter is read out and a 12bit ADC samples the integrator output.

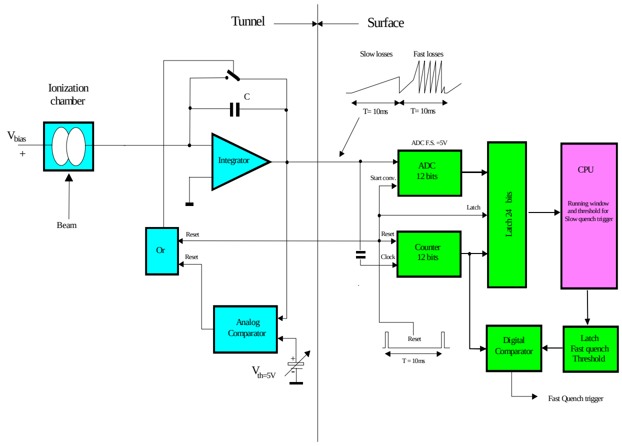

Figure 4: Read-out chain for the ionization chamber.

In case of very large signals the ADC value becomes irrelevant and the counter can be even read out in smaller time intervals (like every turn = 89µs). Figure 5 shows the output integrator results in bits depending on the input current relevant for LHC. We see that at very high currents dead-time corrections have to be applied due to the capacitor discharge duration. However, all quench levels are well in the linear range.

The counter together with the ADC allow a very large dynamic range of the order of 10^7. The time resolution ranges between 0.1ms and several seconds. The noise level is in the range of $\pm$ 2mV, hence the signal to noise ratio for the smallest quench level signal (ie. quench levels reached in 1s at 7 TeV) is $S/N=1.3\cdot10^3$.

Figure 5: Integrator output signal for the ionization chamber versus input current.

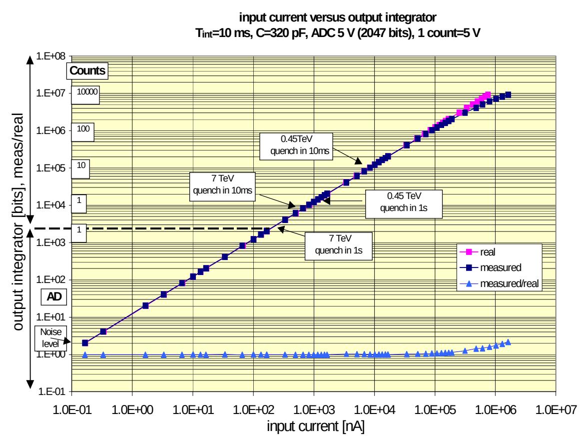

5 SUMMARY

Table 4 summarizes the characteristics of the PIN-diodes and the ionization chamber.

Since the diodes are 1-hit/no-hit devices they saturate at quenches reached in 10ms for the pilot filling scheme. Very fast loss detection (1 turn) is not possible due to these saturation effects. The ionization chambers cover all possible filling schemes. Although the diodes have a single bunch loss resolution, this is not of importance for the arc monitors at LHC. In addition the significance is little because of the saturation effects.

The electronics for both detector systems will be installed below the central quadrupole magnet where the radiation dose is expected to be only 5-10 Gy/year[7].

Both detector systems are very reliable. Practical experience from SPS shows that during 12 years of operation no ionization detector elements have been exchanged due to ageing effects. At DESY no PIN-diode detector failures were observed during 8 years of operation.

Comparing the performance of the two detector systems shows that the choice will be mainly driven by cost estimates.

Table 4: Comparison between PIN-diodes and ionization chamber.

PROPERTIES	PIN-diodes	ionization chamber
signal read-out	1-hit/no-hit mode	proportional mode
protection of quenches caused in 10ms	not for pilot	yes
Protection of quenches caused in 1s	yes	yes
read-out resolution	bunch	1 turn (89µs)
first turn detection	no	yes
additional needed information	nr. of bunches	-
signal/noise ratio S/N	$3\cdot10^4$	$1.3\cdot10^3$
cabling	fibre optics	twisted pair cables

ACKNOWLEDGMENTS

We acknowledge the many fruitful discussions about quench levels with Bernard Jeannert.

REFERENCES

[1] J. B. Jeanneret et al., LHC Project Report 44, CERN, (1996).
[2] A. Arauzo Garcia et al., LHC Project Note 213, CERN, (2000).
[3] K. Wittenburg, Nucl. Instr. and Meth. A 345 (1994) 226-229, (1994).
[4] F. Ridoutt, Int. Report, PKTR Note No. 91, (1993).
[5] H. Burkhardt, I. Reichel, SL Note 96-26 OP, (1996).
[6] V. Agoritsas, MPS-66-23, CERN, (1966).
[7] C. Fynbo, G. Stevenson, LHC Project Note 251 CERN, (2001).

SENSITIVITY STUDIES WITH THE SPS REST GAS PROFILE MONITOR

G. Ferioli, C. Fischer, J. Koopman, M. Sillanoli, CERN, Geneva, Switzerland

Abstract

During the SPS run in the year 2000 further test measurements were performed with the rest gas monitor.

First, profiles of single circulating proton bunches were measured and the bunch charge progressively reduced, in order to determine the smallest bunch intensity which can be scanned under the present operating conditions. The image detector in this case was a CMOS camera.

Using a multi-anode strip photo-multiplier with fast read-out electronics, the possibility to record profiles on a single beam passage and on consecutive turns was also investigated. This paper presents the results of these tests and discusses the expected improvements for the operation in 2001.

Moreover, the issue of micro channel plate ageing effects was tackled and a calibration system based on electron emission from a heating wire is proposed. The gained experience will be used for the specification of a new monitor with optimised design, to be operated both in the SPS and in the LHC.

1 INTRODUCTION

A residual gas ionisation beam profile monitor (IPM) is considered as one of the instruments for measuring the transverse beam size of the proton beams in the SPS and in the LHC. A monitor from DESY has been modified and is under test in the SPS [1][2]. Previous measurement campaigns have shown that adequate accuracy and resolution can be achieved. During 2000 the sensitivity limit of the monitor was probed. It was operated in both a high spatial resolution read-out mode, using a standard CMOS camera, and a high speed read-out mode, employing a miniature photo-multiplier tube with 16 anode strips.

In the LHC the instrument will have to deal with beam intensities varying from one pilot bunch, (5×10^{9} protons), up to 2808 bunches of 1.67×10^{11} protons each (ultimate current): a dynamic range in the order of 10^{5}.

The acquisition speed is another important issue, since the device may also be used to verify the quality of the betatron matching at injection into the SPS and the LHC [3]. For that purpose a single nominal bunch, (1.1×10^{11} protons), should be measured on a turn by turn basis (23.1 μs in the SPS and 88.9 μs in the LHC).

One of the problems encountered, when exploiting IPM monitors, is the ageing of the micro channel plate (MCP). This ageing affects the area of the MCP where the beam is imaged. To track this effect and correct for it, a remote controlled built-in calibration system would be very useful. A method is proposed using a heating wire acting as an electron source. The feasibility of such a correction system has been checked in a dedicated laboratory set-up.

2 SENSITIVITY LIMIT

2.1 High spatial resolution read-out set-up.

In the first half of the 2000 SPS run, a read-out system integrating a standard CMOS camera, with a 25 Hz frame rate associated to CERN designed acquisition electronics, was installed. Beam profiles, integrated over 866 SPS turns, were provided every 40 ms. Figure 1 shows 108 consecutive horizontal profiles acquired during the SPS acceleration cycle, starting at injection.

These measurements are performed on a single bunch

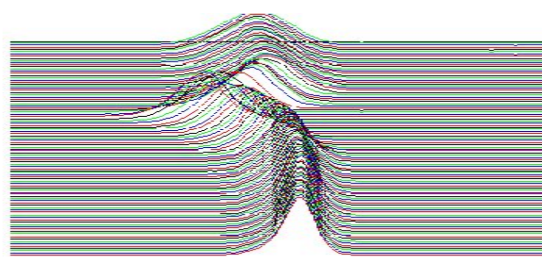

Figure 1: 108 consecutive horizontal profiles of a bunch of 6×10^{10} protons accelerated in the SPS.

of 6×10^{10} protons, (half the nominal LHC intensity). Profiles are very well defined, as can be seen in Figure 2, and the shrinking of the r.m.s. beam size (from 1.2 to 0.7 mm) during acceleration can be easily distinguished.

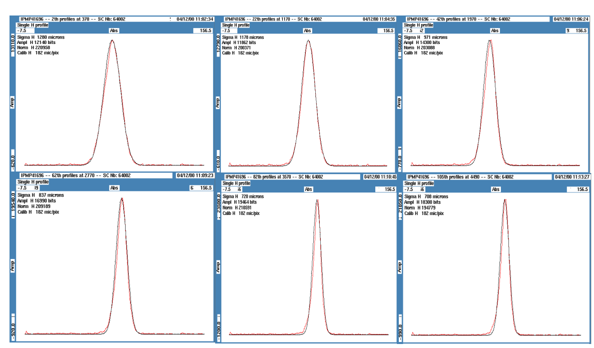

Figure 2: Six horizontal individual bunch profiles of a bunch of 6×10^{10} protons accelerated in the SPS.

The profile of a bunch of 6.10^{9} protons, nearly an LHC pilot bunch, is displayed in Figure 3. This measurement was performed with all gains set at maximum, while maintaining the nominal SPS rest gas pressure of 10^{-8} hPa. The signal, although rather noisy, is still exploitable. This confirms that this set-up is suitable for transverse profile measurements throughout the full intensity range of LHC beams. The large dynamic range can be handled with by acting on several parameters: the MCP gain, the phosphor screen gain, the camera lens diaphragm opening, and the video gain. A further possibility is to locally increase the residual gas pressure by injection of gas (N2). This will allow for precision measurements at low beam intensities, (pilot bunches), in the LHC where the residual pressure will be lower than in the SPS by at least one order of magnitude.

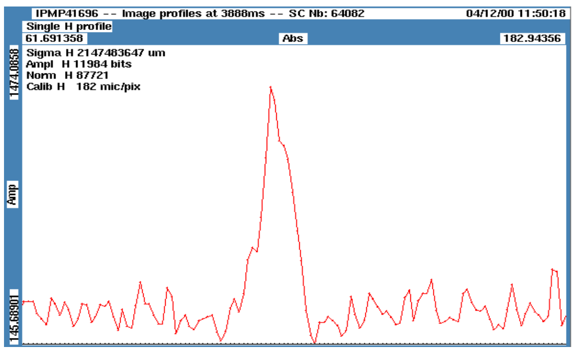

Figure 3: Horizontal profile of a bunch of 6×10^9 protons.

2.2 High speed read-out set-up.

In the second half of the SPS run a Photo Multiplier Tube (PMT) with 16 anode strips and dedicated, CERN designed, high speed acquisition electronics [4], were associated to the IPM. The phosphor used was of the P46 type, claimed to have a decay time of 0.3 µs down to 10% and 90 µs down to 1%. This set-up allowed for profile measurements at the SPS beam revolution frequency (43.3 kHz). Such profiles measured at injection on 6 consecutive SPS turns, with good definition, are represented in Figure 4.

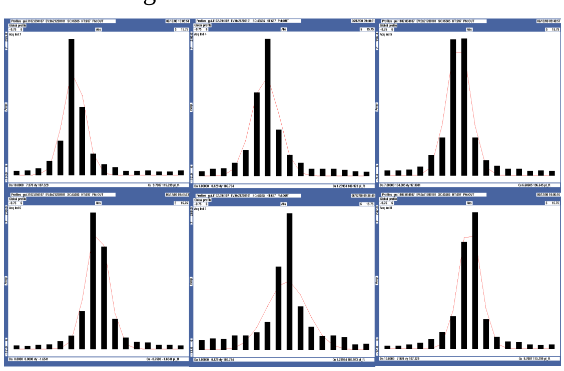

Figure 4: Horizontal profiles of a beam of 1.5×10^{12} protons (40 bunches), on six consecutive SPS turns.

Beam size and position oscillations following injection can be observed in Figure 5, (time axis from upper right to down left corner). Figure 6 represents the associated average position oscillation with a maximum excursion of ±3mm.

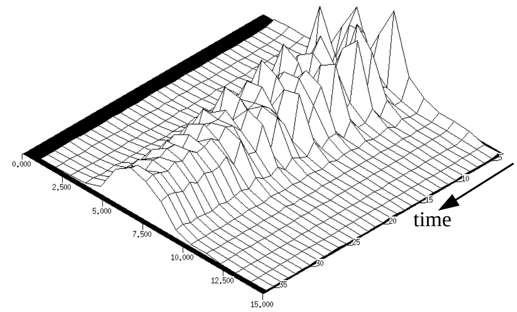

Figure 5: Profiles measured on 37 consecutive turns after injection of a beam of 1.5×10^{12} protons (40 bunches).

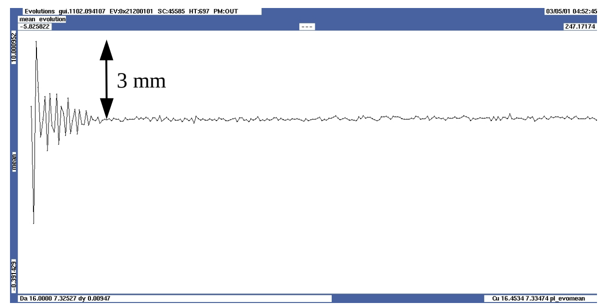

Figure 6: Corresponding oscillations in average position (±3mm maximum amplitude).

The previous measurements were carried out with a beam of 1.5×10^{12} protons consisting of 40 bunches. They were repeated with a single bunch of 3.5×10^{10} protons. Results are displayed in Figure 7. The signal is somewhat noisier, with a few random spikes, but it is still exploitable.

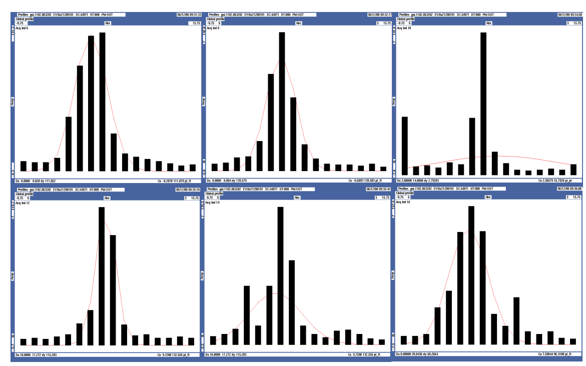

Figure 7: Horizontal profiles of a bunch of 3.5×10^{10} protons, on six consecutive SPS turns.

The evolution of the bunch size measured over 195 SPS turns just after injection is represented in Figure 8. A blow-up of about 5 mm, created deliberately, is clearly observed on the rms value.

One drawback of this high speed read-out system was its low spatial resolution. Both position oscillations and beam-size variations had to be coped with. A range of 50.5 mm at the beam level was covered with the 16 channels of the PMT, resulting in a resolution of 3.16 mm/strip. Reducing this range to 40 mm should be acceptable. Moreover, a new design is under way that uses

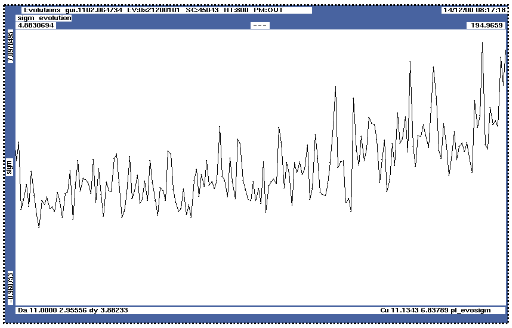

Figure 8: Evolution of the horizontal rms value of a bunch of 3.5×10^{10} protons over 195 turns.

a PMT with 32 channels. Hence, the optics of the system can be modified to reach a resolution of 1.25 mm/strip.

3 MCP CALIBRATION SYSTEM.

One recurrent problem with instruments employing micro channel plates is ageing. MCP's lose gain after having delivered a certain amount of charge, resulting in erroneous measurements. To correct for this phenomena a built-in remote controlled electron source could be employed. This source must deliver a uniform and, even more important, stable distribution of electrons onto the MCP input face. One of the most simple electron sources is a glowing wire. Applying an electrical extraction field with sufficient strength will induce enough energy to the liberated electrons to excite the MCP.

A laboratory set-up was built to test the principle. Inside a windowed vacuum tank, a wire made of an alloy of Tungsten (75%) and Rhenium (25%), with a diameter of 50 µm, was stretched in a 80 mm wide supporting fork. This fork was placed on a carriage allowing the distance between MCP-input and wire to be varied from 5 mm to 60 mm. A DC voltage was applied to the wire ends inducing a current of 0.5 A, causing the wire glow red. Behind the wire and around the input face of the MCP, two large parallel plates were mounted to ensure the uniformity of the extraction field. A voltage of a few tens of Volts was applied on the wire with respect to the plate behind it in order to reject the emitted electrons towards the MCP. An extraction field of several hundreds of Volts was applied between the wire and the MCP input, thus giving enough energy to the electrons to excite the MCP. The phosphor behind the MCP was of the P46 type and could be observed through the window.

The first results are encouraging. Figure 9(a) shows an image of the light density distribution from the phosphor obtained with the glowing wire at a distance of 60 mm from the MCP input face. The distribution looks fairly homogeneous. The exercise has been repeated a few weeks later under the same conditions. No alteration of the pattern was observed, indicating that the distribution may be reproducible with time. Ageing of the wire should not be an issue, since it is operated only for very short periods of time.

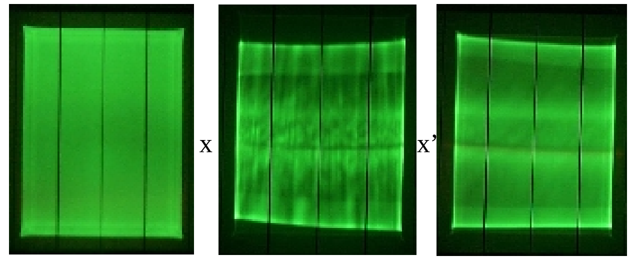

(a) (b) (c)

Figure 9: Light density distributions from the phosphor.

One of the problems encountered in this set-up was an erratic emission pattern along the wire in the xx' direction, Figure 9(b), clearly observable when it was placed at 5mm from the MCP input face. Neither polishing nor cleaning the wire in a solvent cleared the problem. Heating the wire for some minutes at a very high temperature, the wire was then lighting up white, did, however, improve the emission pattern: Figure 9(c).

The obtained light density distribution is not homogeneous enough yet to be used as an absolute calibration system. A peak to peak modulation of about 25% can be measured. It should be sufficient, however, to track the ageing of the MCP. Using two or more wires in parallel at some distance may improve the uniformity of the light distribution. The principle of this system will be integrated into a new IPM design, under preparation, to be installed next year in the SPS.

4 CONCLUSION.

The tests carried out in the SPS during the year 2000 with the rest gas monitor, show that it will probably be possible to acquire profiles down to the LHC pilot bunch level (5×10^{9} p). In the turn by turn mode, an improvement of the resolution by a factor of 2.5 is expected, in order to also use the device for injection matching studies.

A future rest gas monitor design will incorporate two parallel heating wires, emitting electrons, to track and correct for the ageing of the micro channel plate.

REFERENCES

[1] Fischer, C., Koopman, J., Measurements made in the SPS with a Rest Gas Profile Monitor by collecting Electrons, BIW 2000, Boston, USA, May 2000.

[2] K. Wittenburg, Emittance measurement in the Proton Accelerator in DESY, Emittance in Circ. Accel., KEK 95-7, Sept. 1995.

[3] Bovet, C., Jung, R., A new Diagnostic for Betatron Phase Space matching at Injection into a circular Accelerator, EPAC '96 Sitges, Spain, Jun 1996.

[4] Ferioli, G. et Al., Beam profile measurements at 40 MHz in the PS to SPS transfer channel, DIPAC'99. Chester, UK, May 1999.

THE MEASUREMENT AND OPTIMISATION OF LATTICE PARAMETERS ON THE ISIS SYNCHROTRON

D.J. Adams, K.Tilley, C.M.Warsop, Rutherford Appleton Laboratory, Oxfordshire, UK.

Abstract

The ISIS Synchrotron accelerates a high intensity proton beam from 70 to 800 MeV at 50 Hz. Recent hardware upgrades to the diagnostics, instrumentation and computing have allowed turn by turn transverse position measurements to be made. A special low intensity beam can also be injected for detailed diagnostic measurements. The analysis of such data at many points around the ring has allowed the extraction of lattice parameters. This information will have significant application for improved beam control. The methods of analysis as well as some applications for setting up and optimising the machine are described in this paper. Future plans and relevance for high intensity performance is also given.

1 INTRODUCTION

The ISIS Synchrotron [1] accelerates 2.5×10^{13} protons per pulse at 50 Hz, corresponding to a mean current of 200 µA. To establish high intensity beam, particles are accumulated via charge exchange injection over 120 turns. Beam is then bunched and accelerated from 70 to 800 MeV in 10 ms, extracted in a single turn and transported to the target.

In optimising the machine, extensive use is made of special low intensity 'diagnostic' beams [2]. These are provided by 'chopping' the normal 200 µs injection pulse to ~100 ns (less than one turn) with an electrostatic kicker. The injection painting provides the initial 'kick', and measurement of the turn by turn, transverse motion at a position monitor then allows extraction of numerous ring parameters. Allowance has to be made for the apparent damping caused by the finite Q-spread in the beam. Fitting a suitable function allows the centroid betatron amplitude, the closed orbit position, the betatron Q and phase to be extracted.

This paper describes new measurements and beam control applications, made possible with recent upgrades to the synchrotron diagnostics data acquisition system [3]. These use the low intensity beam at injection together with the new facility to take turn by turn measurements at many position monitors around the ring. The relevance of these measurements to high intensity operation is described in Section 5.

2 PHASE SPACE MEASUREMENTS

2.1 Basic Measurements

On the ISIS Synchrotron we have two sets of beam position monitors separated by drift spaces, one set per transverse plane. By using the signals from these monitors, it is possible to reconstruct (y_n, y_n') on each turn. The apparent Q-spread damping over many turns can be removed with appropriate use of fitted parameters. The 'corrected' (y_n, y_n') are then fitted with a suitable ellipse to extract alpha, beta and centroid emittance.

Measured phase space ellipses for the vertical plane are shown in Figure 1. In this case measurements were taken with the lattice in two distinct configurations. The first under normal configuration, and the second, with a low field tuning (trim) quadrupole switched off.

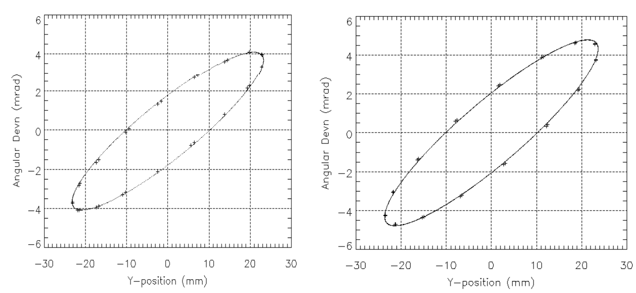

Figure 1. Measured Vertical Phase Space Ellipse. Left: Normal. Right: Trim Quad off.

To check the measurement, the extracted parameters were compared with the results of a MAD model [4]. The results are shown in Table 1.

Table 1: Fitted parameters and MAD predictions.

	Alpha		Beta (m)	
Optics	**MAD**	**Measured**	**MAD**	**Measured**
Normal	-2.09	-2.05+/-0.2	13.37	13+/-1.0
TQ Off	-1.92	-2.1+/-0.2	12.43	11.5+/-1.0

This shows the measurement gives good agreement with theory. Systematic differences are consistent with measured lattice errors, see Section 4.

2.2 Further Work

Work is now continuing to extend these measurements to the horizontal plane, and with analysis techniques to take full account of the beam damping.

3 BETA AND PHASE FUNCTION MEASUREMENTS

3.1 Basic Measurements

To demonstrate the basic measurement of beta and phase, a set of measurements were made with the synchrotron in a normal configuration and then with one trim quadrupole (tq) switched off. It can be shown that the change in the horizontal beta function is given by:

$$\frac{\Delta\beta(s)}{\beta(s)} = -\frac{\Delta k(s_{tq})\beta(s_{tq})l}{2\sin 2\pi Q}\cos 2(|\phi(s_{tq})-\phi(s)|-\pi Q) \qquad (1)$$

where the notation is standard [5]. The change in the phase follows a similar form, although 90 degrees ahead of (1). The results of the experiment are shown in Figure 2, together with the fitted functions. The measurements were taken at equivalent lattice positions in each superperiod.

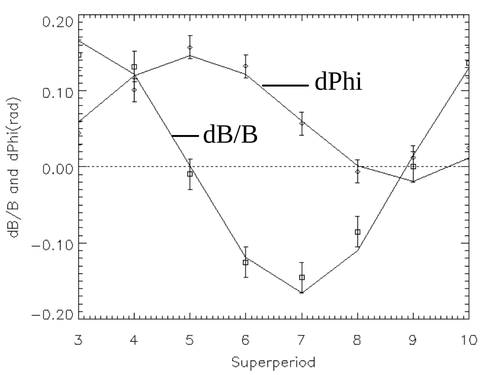

Figure 2: Δβ/β and change in phase (dPhi) around the ring with one trim quadrupole switched off.

The two measurements show the expected form and the extracted parameters agree well with expected values.

3.2 Future Plans

We plan to use these measurements to identify isolated lattice errors. Additionally, the measurement of lattice phase can also be used to calculate the transverse impedance around the ring [6].

4 BETA FUNCTION CORRECTION

4.1 Background

Perturbations in the beta function can be expressed in a harmonic formulation, which shows clearly the resonant nature of the system. From this, one sees the largest contributions to perturbations are given by lattice errors, $\Delta k_{Err}(s)$, distributed around the ring with spatial frequencies near 2Q. This is described by the following formulae [5]:

$$\frac{\Delta\beta(s)}{\beta(s)} = \frac{Q}{2}\sum_q \frac{F_q e^{iq\phi(s)}}{Q^2-(q/2)^2} \qquad (2)$$

where F_q is given by:

$$Q\beta^2(s)\Delta k_{Err}(s) = \sum_q F_q e^{iq\phi(s)} \qquad (3)$$

It follows therefore that we can make deliberate large changes to beta if the lattice is excited with an additional perturbation Δk(s) with the appropriate frequency q. This then forms the basis of a correction system, which cancels out the dominant harmonics of the lattice errors.

4.2 Application of Harmonic Perturbation

The ISIS synchrotron has 2 sets of 10 trim quadrupoles distributed at regularly spaced intervals around the lattice. These are connected to a system which can apply a modulation at a number of spatial harmonics (q), and thereby generate an additional harmonic focusing Δk(s) around the ring.

The modulation in the beta function due to the application of a single harmonic function of the form Δk_j= 0.0162 SIN (2π 0.8 j) m^{-2}, (where j is the j^{th} trim quadrupole) has been measured and is shown in Figure 3.

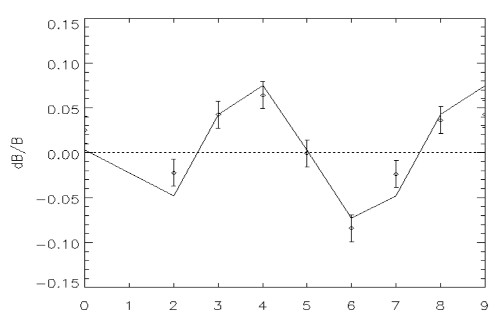

Figure 3: Application of a known perturbation with the predicted and measured changes in beta.

The result shows a strong induced oscillation at q=2, consistent with the expected undersampled or ‘aliased’ q=8. Thus the beta function resonates strongly as per equation (2) with Qh=4.31. Agreement between the predicted and measured data sets is good.

4.3 Normal Configuration

Using the above approach, we aim to develop a correction system to control the variation of the beta function in the ring. A typical measurement of beta perturbation during normal running is shown in Figure 4.

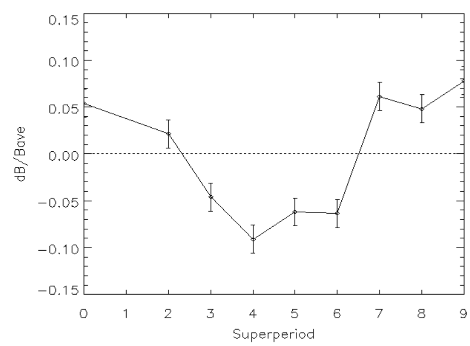

Figure 4: Variation of Horizontal beta function.

The data is from equivalent lattice positions in each superperiod, where values are expected to be the same. We can see that it varies by up to 10%, and shows a strong oscillation describing approximately one full cycle. The variation here is consistent with an aliased 9th harmonic, showing that under normal conditions the beta function is resonating strongly due to lattice errors near 2Q. The application of another 9th harmonic with the appropriate amplitude and phase could be used to cancel the driving errors.

4.4 Proposed Correction Method

A harmonic correction system for beta, based on the above ideas is presently being developed. The first step uses the low intensity beam to measure beta at equivalent points in each superperiod as in Figure 4. The aim is to minimise $\Delta\beta(s)/\beta(s)$. The required corrections $\Delta k(s)$ can then be estimated using the alternative formulation of equation.(2) [5]:

$$\frac{\Delta\beta(s_i)}{\beta(s_i)} = \mp\frac{1}{2\sin 2\pi Q}\oint \Delta k(\sigma)\beta(\sigma)\cos 2[|\phi(\sigma)-\phi(s_i)|-\pi Q]d\sigma \quad (4)$$

which can be expressed as a matrix equation:

$$\left(\frac{\Delta\beta}{\beta}\right)_i = M_{ij}\sum_j \Delta k_j \quad (5)$$

where *i* corresponds to the monitor, and *j* the trim quad. Parameters defining the correction coefficients M_{ij} are also measured.

The resulting Δk_j's are then fourier analysed to obtain the dominant harmonics of $\Delta k(s)$ required for correction. Once these values have been fed back into the system, the values of the beta function can then be re-measured, and thus form part of an iterative process.

4.5 Status and Future Plans

Preliminary attempts to control the beta function using this method have been promising. Once fully operational, the aim will turn to optimising the beta function to minimise beam loss. As part of a future upgrade, individually powered trim quadrupole units will allow alternative correction methods to be considered.

5 RELEVANCE TO HIGH INTENSITY OPTIMISATION

Low intensity diagnostic beam measurements provide much detailed information on the synchrotron set up, i.e. checks on the lattice and injection set up [2].

In principal many of the measurements described here are possible at high intensity, however high intensity effects modify beam motion and therefore measured parameters. It is therefore useful to have measurements at both low and high intensity: the former define machine set up, whilst the latter provide information related to minimising beam loss.

6 CONCLUSIONS

The use of low intensity beams, together with turn by turn position measurements at many points around the ring has enabled the determination of lattice parameters at injection. A system to correct the beta function using these measurements is in development. This work will improve the understanding and optimisation of the machine for high intensity operation.

REFERENCES

[1] Spallation Neutron Source, Description of Accelerator and Target, B Boardman, RAL Report RL-82-006
[2] Low Intensity and Injection Studies on the ISIS Synchrotron, C M Warsop, Proc ICANS XII, RAL Report RAL 94-025
[3] The ISIS Synchrotron Beam Control and Study Programme, D.J. Adams, K Tilley, C.M.Warsop, PAC'99, New York, March 1999.
[4] The MAD Program Version 8.23 User's Reference Manual, H. Grote, F.C.Iselin, CERN/SL/90-13(AP) Rev5. 125 (1996)
[5] Particle Accelerator Physics 1, Ch 7., H. Wiedermann
[6] Multiturn Measurements at the CERN SPS, J.Klem, G.Arduini, G. Morpurgo, EPAC2000

FIRST BEAM TESTS FOR THE PROTOTYPE LHC ORBIT AND TRAJECTORY SYSTEM IN THE CERN-SPS

D. Cocq, L. Jensen, R. Jones, J.J. Savioz, CERN, Geneva, Switzerland
D. Bishop, B. Roberts, G. Waters, TRIUMF, Vancouver, Canada

Abstract

The first beam tests for the prototype LHC orbit and trajectory system were performed during the year 2000 in the CERN-SPS. The system is composed of a wide-band time normaliser, which converts the analogue pick-up signals into a 10 bit position at 40MHz, and a digital acquisition board, which is used to process and store the relevant data. This paper describes the hardware involved and presents the results of the first tests with beam.

1 INTRODUCTION

The LHC Orbit and trajectory prototype system is divided into two parts; an analogue front-end module (WBTN) that processes the signal from the four-button pick-up to produce digitised position data at 40MHz and a Digital Acquisition Board (DAB) that selects, stores and pre-processes the position data. The DAB module is developed at TRIUMF (Vancouver, Canada) using CERN specifications as part of the Canadian contribution to the LHC whereas the WBTN is developed entirely at CERN. An overview of the whole system is shown in Fig. 1. The initial signal is provided by a button pick-up, which is then processed by a wide-band time normaliser, converting the beam position into a pulse modulation at 40MHz. A 10-bit ADC then digitises this signal before a digital acquisition board is used to sort and store the data in memory.

2 WIDE BAND TIME NORMALISER

The principle of the Wide-Band Time Normaliser (WBTN) is explained in [1]. The WBTN is used to convert the amplitude ratios of the two signals provided by a pair of electrodes, into a variation in time. In this application an excursion over the full aperture of the BPM corresponds to a pulse width modulation of ~3ns. This variation is measured with an integrator and digitised with a 10-bit ADC at 40MHz. Within a dynamic range in intensity of 40dB, the systematic error measured at the centre is less than 1% (see Fig. 2). This covers the foreseen operating bunch intensities of the LHC, from the pilot bunch at 5×10^{9} protons per bunch to the ultimate 1.7×10^{11} protons per bunch. As the system works at 40MHz, measuring each individual bunch, there is no need to take into account the filling pattern when considering the dynamic range. The RMS random error due to noise remains well below 1% for the nominal and ultimate bunch intensities, rising to 1.3% for the pilot bunch, as can be seen in Fig. 3. The measured position is corrected using a 3rd order polynomial following the theory outlined in [1]. The systematic error can thereby be reduced to around 1% (see Fig. 4).

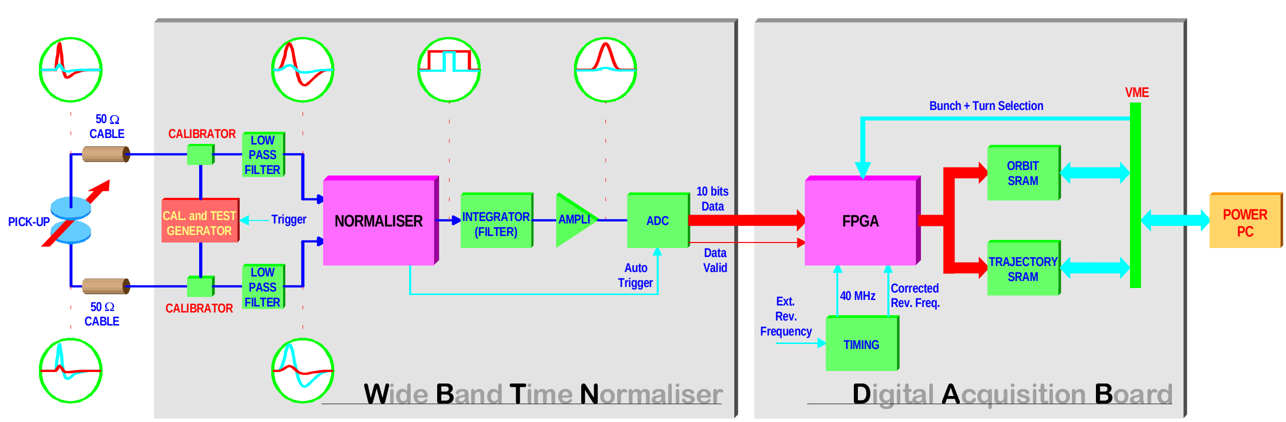

Figure 1: Schematic of the prototype LHC beam position system installed in the CERN-SPS

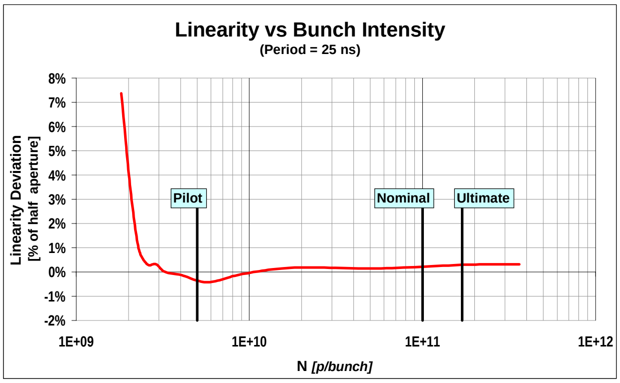

Figure 2: WBTN linearity as a function of intensity.

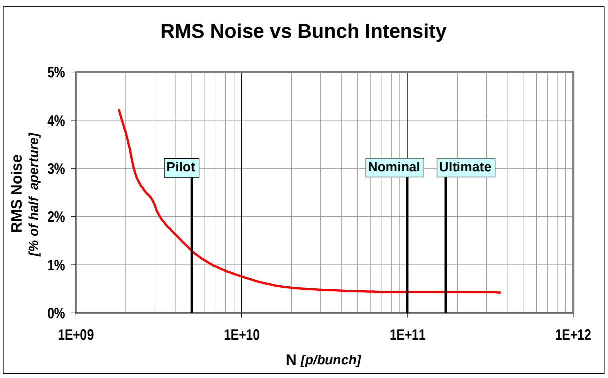

Figure 3: WBTN RMS noise as a function of intensity.

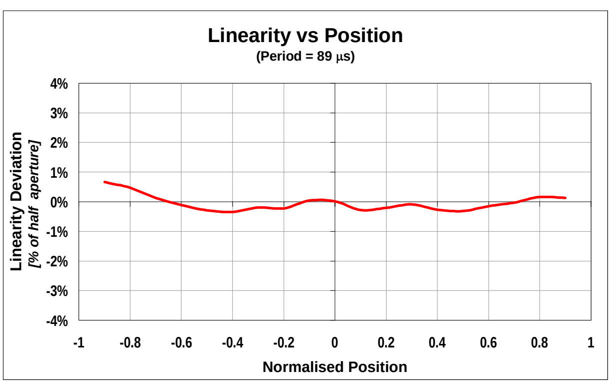

Figure 4: WBTN Linearity as a function of position.

3 DIGITAL ACQUISITION BOARD

The Digital Acquisition Board (DAB) is responsible for selecting, storing and pre-processing the position information that is provided by the WBTN. In the first generation of the DAB module, that became available during the summer of 2000, only the capture (random) acquisition mode was implemented. This allows N bunches to be acquired over T consecutive turns where $N \times T \leq 64000$. This number comes from the available memory on the DAB module. In future versions, an orbit acquisition mode will be added, which will be capable of providing real-time closed orbit measurements at 10Hz.

Two Altera FPGAs handle the intelligence on the DAB module: one for the bunch selection and storage, the other for the VME access to registers and memory. An on-board low-jitter PLL circuit creates the 40MHz bunch-clock from the 44kHz SPS revolution frequency, and is used to handle the synchronisation with the WBTN. A dedicated bus had been specified on the VME P2 bus to transfer the ADC values and status bits to from the WBTN to the DAB module.

4 INITIAL TESTS

The prototype WBTN module contains a generator that can be controlled from the DAB module. This generator will be used for calibrating the measurement chain by setting values on the WBTN output that correspond to the two extreme positions (left/right or up/down) and the centre of the BPM. With a 10-bit unipolar ADC the values we expect are between 0 and 1023. In Fig. 5 one can see the distribution of ADC values in calibration mode, before correction, for a centred beam with a signal strength equivalent to an intensity of 5×10^{10} protons per bunch. This was recorded by the DAB after the complete chain of acquisition electronics. The distribution sigma of 2 bins corresponds to an RMS noise of 40µm for the 83mm diameter BPM that was used for the measurements in the SPS.

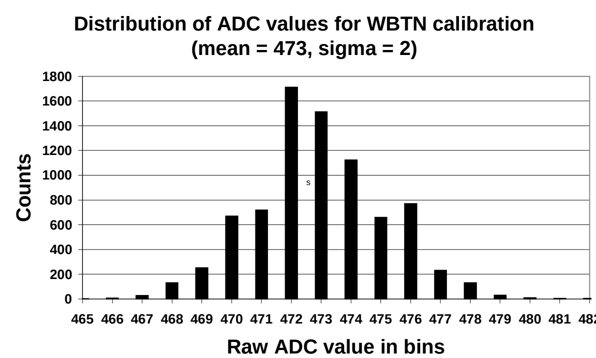

Figure 5: Distribution of ADC values after the complete acquisition chain.

5 MEASUREMENTS ON THE BEAM

The system linearity was measured using local orbit bumps and comparing the results obtained with calibrated readings from the existing CERN-SPS MOPOS orbit acquisition system. Good agreement, even without non-linear correction, can be seen in Fig. 6, for orbit deviations representing up to 15% of the BPM half-aperture.

The capabilities of the prototype system allowed several interesting machine development studies to be performed. A typical result from an LHC batch (72 bunches spaced by 25ns) affected by instabilities is shown in Fig. 7 for four selected bunches. The first bunch in the batch is seen to be stable, while later are affected by the electron cloud phenomenon [2], giving rise to transverse instabilities. The re-stabilisation of these bunches further along in the cycle can be explained by the decrease in their intensity due to beam loss.

Another experiment that profited from the capabilities of the prototype LHC beam position measurement system concerned so-called “AC-Dipole” excitation. This, in principle, allows the excitation of transverse oscillations to large (several σ) excursions without emittance blow-up. The idea was originally proposed and tested at BNL for resonance crossing with polarised beams, using an orbit corrector dipole with an excitation frequency close to the betatron tune, hence the term “AC-Dipole”. This technique was tested in the SPS using the transverse damper as an “AC-Dipole” providing the fixed frequency excitation [3]. Fig. 8 shows the beam response, measured with the prototype LHC beam position measurement system for a single bunch over 22000 turns. A single, one-turn, Q-kick excitation for measuring the tune is also visible at then end of the excitation.

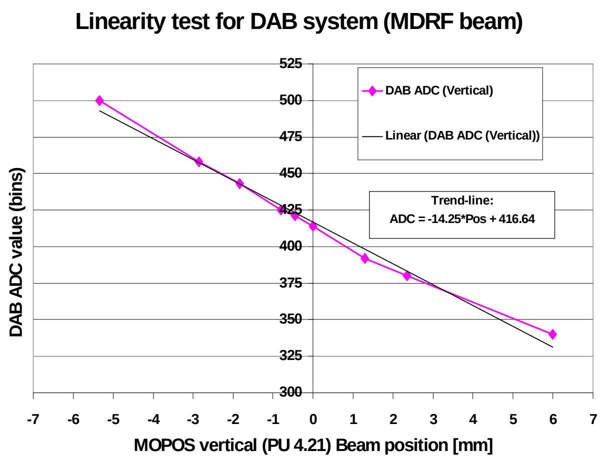

Figure 6: Linearity comparison with SPS closed orbit acquisition system (MOPOS).

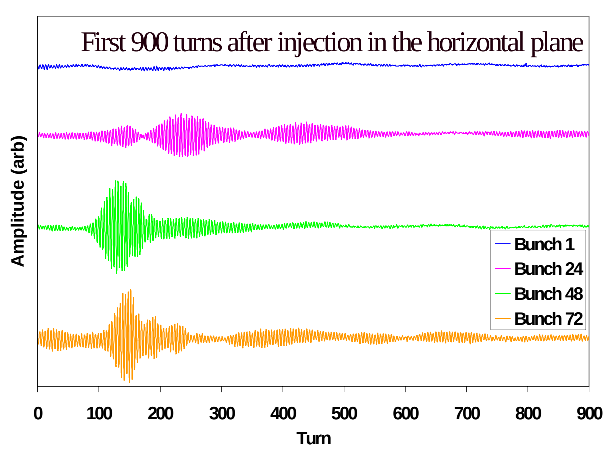

Figure 7: Observation of an instability caused by the electron cloud phenomenon using the prototype LHC beam position measurement system.

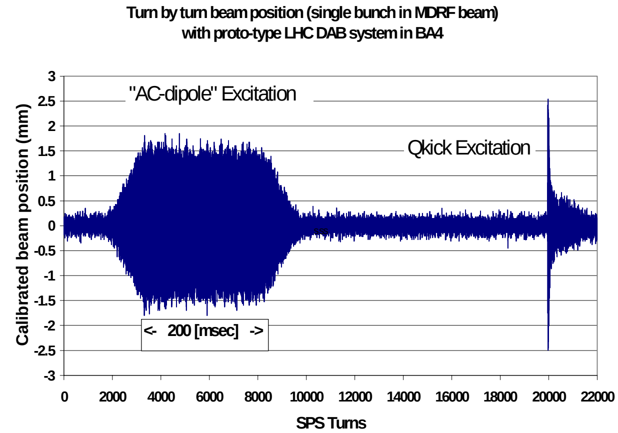

Figure 8: The investigation of “AC-Dipole” excitation.

6 CONCLUSIONS

Installing a prototype LHC beam position measurement system in the CERN-SPS has proved very useful for testing the two main components of the final LHC Orbit acquisition system, namely the wide band time normaliser and the digital acquisition board. The auto-trigger mechanism of the WBTN and the flexibility of the DAB module have also meant that this prototype became an important tool during machine studies. To this end a dedicated SPS system based on the same acquisition electronics will be installed in the CERN-SPS in the near future.

7 REFERENCES

[1] D. Cocq, “The Wide Band Normaliser : a New Circuit to Measure Transverse Bunch Position in Accelerators and Colliders”, Nucl. Instrum. Methods Phys. Res., A 416, 1998.

[2] G. Arduini, "Observations in the SPS: Beam Emittance, Instabilities", Proceedings of the Workshop on LEP-SPS Performance - Chamonix XI, Chamonix, January 2001, CERN-SL-2001-003 DI.

[3] O. Berrig, W. Hofle, R. Jones, J. Koopman, J-P Koutchouk, F. Schmidt, “Emittance-Conserving Transverse Excitation using the ‘AC-Dipole’ Principle”, SL-Note-2000-062 MD, 2000.

BEAM DIAGNOSTICS FOR LOW-INTENSITY RADIOACTIVE BEAMS

L.Cosentino, P.Finocchiaro, LNS - INFN, Catania, Italy

Abstract

In order to perform imaging, profiling and identification of low intensity ($I_{beam}<10^5$ pps) Radioactive Ion Beams (RIB), we have developed a series of diagnostics devices, operating in a range of beam energy from 50 keV up to 8 MeV/A. These characteristics do them especially suitable for ISOL RIB facilities.

1 INTRODUCTION

At INFN - LNS Catania the ISOL (Isotope Separator On-Line) EXCYT facility (EXotics with CYclotron and Tandem) is under development [1]. It allows the production of radioactive beams with energies from 0.2 up to 8 MeV/A, emittance less than 1π mm·mrad and energy spread below 10^{-4}.

The radioactive beam is produced by stopping a stable primary beam (A < 48, E $\leq$ 80 MeV/A) inside a thick target. The produced radioactive species are extracted and transported to a high resolution magnetic isobar separator ($\Delta M/M$ = 1/20000), which separates the ions of interest from the isobaric contaminants. The separator consists of two main stages composed of two magnetic dipoles each one, arranged so that the first stage is placed on a 250 kV platform, while the second is grounded. After it the radioactive beam has a kinetic energy of 300 keV and can be directly used for the experiments or accelerated by the 15 MV Tandem. Its intensity falls in a range from 10^3 pps up to 10^8 pps, depending on the intensity of the primary beam (< 1 pμA), on the production cross section in the target and on the overall extraction efficiency from the ion source.

In this paper we report on diagnostics devices developed for the beam pipe before the acceleration (kinetic energy from 50 keV to 300 keV), and for the accelerated beams (up to 8 MeV/A).

For the low energy regime, a device for imaging/identification of the beam has been developed. It is based on a CsI(Tl) scintillator plate and exploits the decay of radioactive ions of the beam, since the energy of the emitted radiation (β and γ) is typically above 1 MeV, enough to produce a detectable signal.

Regarding the high energy range, we make use of a couple of devices, capable of identifying and profiling the beam by directly detecting the accelerated ions. The background due to radioactive ions implanted inside the devices does not represent a problem, since its contribution to the overall signal is negligible.

2 PREACCELERATION BEAM IMAGING AND IDENTIFICATION

2.1 The LEBI device

The beam diagnostics in the preacceleration stage (low energy) is a crucial point, since a quick beam tuning needs an efficient real-time check of the beam properties. The devices should be able to locate the beam position, to measure its transversal size and to identify its nuclear composition. The device named LEBI (Low Energy Beam Imager / Identifier) permits to attain the beam imaging and identification by exploiting the radiation emitted by the radioactive ions, Fig. 1. The core of this system is a scintillator plate of CsI(Tl) and a thin mylar tape arranged in front of the plate. When the film and the scintillator are placed along the beam line in order to intercept the beam, the ions get implanted onto a small film area, which thus becomes a radioactive source. The emitted radiation (mainly β and γ rays) crosses the plate, so producing a light spot. A CCD camera watching the plate allows to determine the beam location and roughly measure its transversal size.

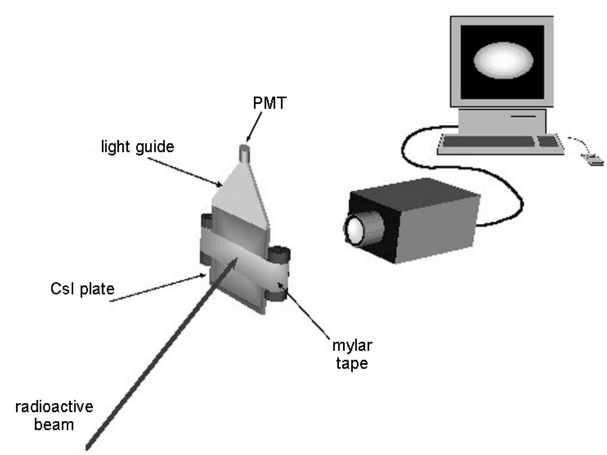

Figure 1: Sketch of the LEBI device for low energy beam imaging and identification.

In order to get as much information as possible to identify the beam, a small photomultiplier (Hamamatsu R7400) used in pulse counting mode is optically coupled to a side of the plate, by means of a light guide. Its main application concerns the identification of implanted nuclear species, by measuring the particle count rate at fixed time intervals, in order to estimate the decay constant λ.

For decays in which the daughter nuclei emit gamma ray, a couple of high purity germanium detectors installed close to the plate, allow a most suitable identification of the isotopes. Since the gamma ray spectrum is typical of each nucleus, the recognition of well defined peaks by means of gamma spectroscopy allows the identification of the different nuclear species present in the beam.

2.2 Off line testing and simulation

The spatial resolution of LEBI is rather modest, mainly because the radiation is emitted isotropically. So, if we use a hypothetical point like source placed in front of the plate, the radiation crosses the plate in all directions (the plate covers a solid angle of about 2π sr), thus producing a light spot with a halo around it. The FWHM of the spot is of the order of the plate thickness.

An experimental test has been performed by using a 1mm collimated ^{90}Sr, which emits a β particles micro beam with intensity below 10^3 pps. It was placed in front of a CsI plate of thickness 2 mm. The light spot was observed by a CCD camera and had a FWHM ≈ 1.8 mm. Using the rule of the sum of the squares, we calculated a spatial resolution of about 1.5 mm.

The germanium detectors for gamma identification are positioned very close to the mylar tape, at a relative angle of 90°. They should collect events with at least two gamma rays emitted in coincidence, so that the background can be strongly reduced, highlighting the gamma cascades bound to the selected gammas. In such a way it is possible to perform a strong selection of the nuclear species, provided that it has at least a couple of gamma rays in cascade. We have tested this technique with two germanium detectors and a ^{60}Co source, showing that it is reliable.

We have also developed a Monte Carlo simulation code, based on the energy loss of beta rays inside the crystal, which is capable of simulating the shape of the light spot produced when the plate is crossed by the radiation. As an example where a realistic beam is simulated, we assumed to produce a ^{18}F beam that contains ^{18}N as a contaminant, see Fig. 2. The predominance of the contribution due to ^{18}N ions depends on the value of its decay constant (λ_{18N} = 1.11 sec^{-1}), much larger than ^{18}F (λ_{18F} = 1.05 10^{-4} sec^{-1}).

2.3 The prototype

The LEBI prototype we have built is made of a spherical vacuum chamber containing the plate-tape set-up. The tape is rolled up in two spools and can be slid on by means of a DC motor (Minimotor 3557K012), whenever it becomes contaminated. An external high sensitivity CCD camera (Watec WAT – 902H, sensitivity of $3\cdot10^{-4}$ lux) watches the plate and is connected to a frame grabber for the acquisition by a pc. A pneumatic cylinder allows to insert and remove the plate-tape set-up from the beam line, via a remote control. The germanium detectors are arranged by using two cups assembled in the vacuum chamber.

When LEBI will be operative, a set of software tools will offer enough flexibility for managing the different peculiarities of each produced beam.

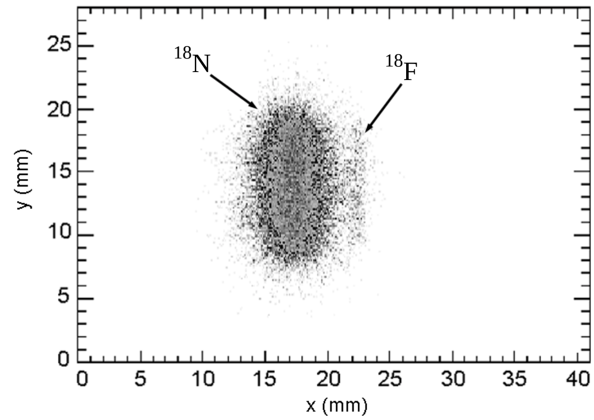

Figure 2: Simulated response of LEBI for a ^{18}F beam and its contaminant ^{18}N.

3 POST-ACCELERATION

3.1 Beam profiling

In order to develop new beam diagnostics tools, which should be able to cover the wide intensity range of the beams, different techniques have been considered based on gas detectors, secondary emission and scintillators.

In gas detectors the signal is produced by ionization due to the energy lost by the ions in a chamber, filled with a suitable gas, or by interaction with the residual gas present along the beam pipe. In the last case, the very few ionizing collision events need some sort of physical amplification; therefore a microchannel plate (MCP) is generally used, onto which the incoming electrons or ions produced by ionization are driven by a transverse electric field [2]. Another technique, that requires a MCP for low intensity beams, exploits the secondary emission of electrons from wires (tungsten) and/or thin foils (carbon or aluminium) when hit by energetic particles [3].

Thin scintillator plates and thicker Scintillating FiberOptic Plates (SFOP) that the beam directly impinges on, have been characterized and they showed to be useful for low intensity beam imaging with CCD cameras. The device named SBBS (Scintillator Based Beam Sensor) is a moving slit sensor, and consists of a CsI(Tl) plate placed behind a thick graphite screen with a 0.5 mm slit. The scintillator is optically coupled with a compact photomultiplier, and the whole structure can be moved to scan the beam. It allows the self-calibration (light versus counts) for very low beam intensity (<10^6 pps). We also proved that this device could operate at very low energy, by easily sensing a 1 pA beam of ^{12}C at 50 keV [4].

The Glass FIbre Based Beam Sensor (GFIBBS) [5] allows to reconstruct the X and Y beam profiles in a single scan with high sensitivity ($I_{beam} < 10^5$ pps). It is based on a pair of glass or plastic scintillating fibres scanning the beam. The two fibres are mutually perpendicular and are readout by means of a single compact PMT.

3.2 *Beam identification*

The beam identification after acceleration has to be performed from a device named HEBI (High Energy Beam Identifier), based on a high resolution silicon telescope, that can revolve around a target. The capability of this system to identify the nuclei with high efficiency, allows to determine the nuclear species present in the beam. It can be accurately positioned around a target (typically gold) placed along the beam line, so being able to intercept the scattered ions.

In order to study the discrimination efficiency, a test has been done performing elastic scattering from the reaction $^{16}O + ^{196}Au$, see Fig. 3. An alpha source placed close to the telescope has been used to perform the calibration procedure of the system. These data have allowed to measure the experimental error, useful for extrapolating the foreseen errors of other hypothetical elements hitting the telescope, since one wants to study the performance of HEBI for the nuclear species produced with EXCYT. We have taken into consideration the elements: ^{11}Be, ^{17}F and ^{18}F. For each of these and their isobaric contaminants, we calculated the energy loss in the ΔE detector, in order to build the relative ΔE-E plot with the error bands, as shown in Fig. 4. These plots have allowed to calculate the probability of misidentification, that between the contiguous elements is always below 10^{-10}.

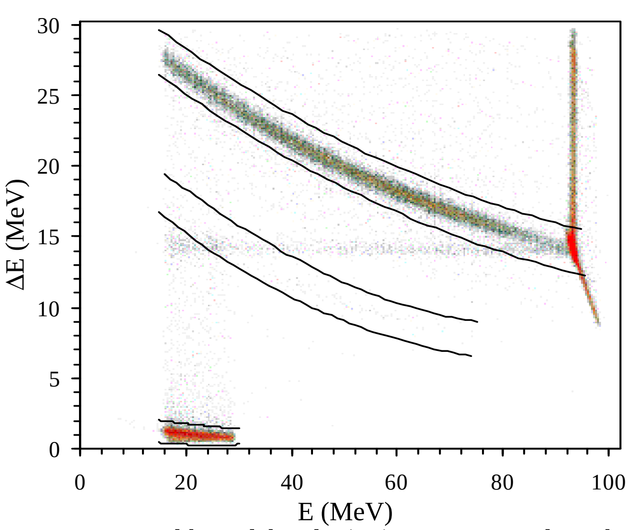

Figure 3: Calibrated bands ($\pm\sigma$) superimposed to the experimental data taken with HEBI. From the ^{16}O+^{196}Au reaction we get mainly elastic scattering, plus many alphas and some C product.

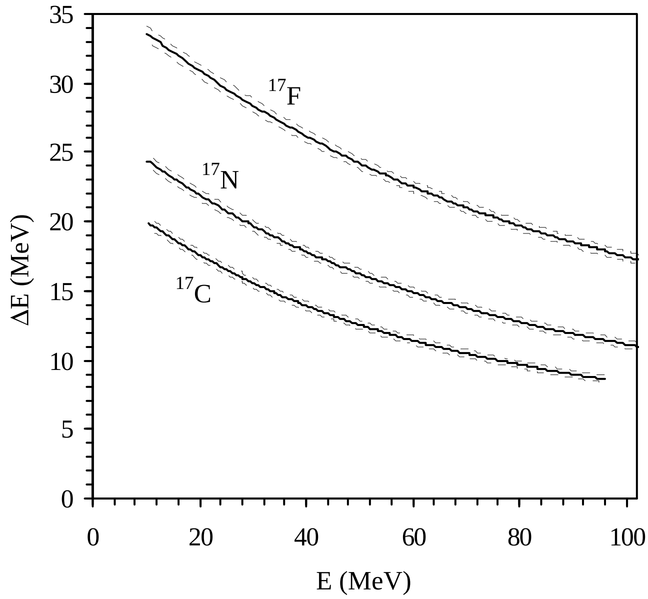

Figure 4: Discrimination plot ($\pm\sigma$) for ^{17}F. The two main contaminants are shown.

REFERENCES

[1] G. Ciavola et al., Nucl. Instr. and Meth. B126 (1997) 258-261;

[2] P. Finocchiaro, DIPAC 97, 3rd European Workshop on Beam Diagnostic and Instr. for Particle Accel., Lab. Naz: Frascati, October 14th, 1997;

[3] P. Finocchiaro, CAARI 98, 15th Internat. Conf. on the Appl. of Accel. In Research and Industry, Univ. of North Texas Denton, November 4-7, 1998;

[4] P. Finocchiaro et al., Nucl. Instr. and Meth. A437 (1999) 552-556.

[5] P. Finocchiaro et al., Nucl. Instr. and Meth. A419 (1998) 83-90.

THE DYNAMIC TRACKING ACQUISITION SYSTEM FOR DAΦNE E+ / E- COLLIDER

A. Drago, A. Stella, Istituto Nazionale di Fisica Nucleare, Laboratori Nazionali di Frascati, Italy

Abstract

The goal of this paper is to describe the dynamic tracking acquisition system implemented for the DaΦne e+/e- collider at LNF/INFN. We have been using the system since last year and it has been possible to collect useful information to tune-up the machine.

A four-button BPM is used to obtain the sum and difference signals in both the transverse planes. The signals are acquired and recorded by a LeCroy LC574A oscilloscope with the capability to sample the input waveforms using a beam synchronous external clock generated by the DaΦne Timing System. The start of acquisition is synchronised to a horizontal kick given by an injection kicker. After capturing up to 5000 consecutive turns, data are sent through a GPIB interface to a PC, for processing, presentation and storage. A calibration routine permits to convert voltage data to millimetres values. The acquisition and control program first shows the decay time in number of turns. Then it draws a trajectory in the phase space (position and speed) in both the transverse planes. To do this the software builds a data vector relative to a second "virtual" monitor advanced by 90 degrees. This is done by two alternative ways: applying the Hilbert transform or using the transport matrix method. Examples of data acquired during the collider tune-up are shown.

1 INTRODUCTION

DaΦne is a Φ factory presently in operation at the Laboratori Nazionali di Frascati of I.N.F.N. In the last two years it alternated machine development and data taking shifts: during these periods it produces e+/e- collisions to give luminosity to one of the two installed experiments, KLOE in the Interaction Point 1 and DEAR in the Interaction Point 2. Recently DaΦne has reached in the IP1 a peak luminosity of $2.1 \cdot 10^{31}$ cm^{-2} sec^{-1}, with an integrated luminosity up to 1.3 pbarn^{-1} per day. The maximum stored current is more than 1 A for electrons and for positrons.

For the non-linear optics studies, a transverse monitor has been installed to record and analyze the dynamic characteristics of the beam by varying the machine parameters.

In this paper we describe the dynamic tracking monitor and acquisition system implemented for DaΦne and show some example of taken data. The system has been used since last year allowing collecting useful information to tune-up the machine.

2 DYNAMIC TRACKING

A coherent signal proportional to the transverse displacement of the bunch can be obtained by processing the signal from the beam position monitor electrodes.

The method of dynamic tracking [1] consists in exciting a free transverse betatron oscillation by kicking the beam and recording the transverse displacements at two different azimuths in the storage ring. If the two monitors have π/2 betatron phase difference, then the transverse beam position at the second monitor is proportional to the angle of the beam at the first monitor. Plotting the first monitor data versus the second ones (on turn by turn basis) is equivalent to a phase space plot at the azimuth of the first monitor. A dynamic tracking system makes possible to perform studies on the non-linear beam dynamics [2]. In particular, the tune dependence on amplitude is found by fitting the decay of the coherent signal as a function of the number of turns (an example of a recorded data sequence is shown in Fig.1). The dynamic aperture is defined as the maximum displacement amplitude (the stable acceptance) without intensity loss.

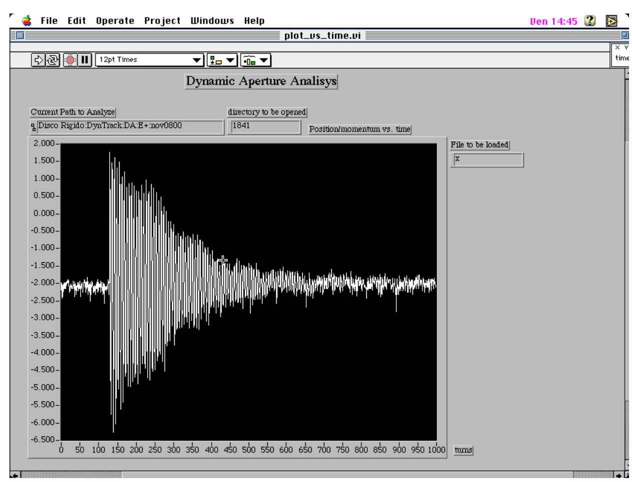

Figure 1: Horizontal displacement (in mm) after a kick versus number of turns.

3 SYSTEM DESCRIPTION

3.1 Signal acquisition

A four-button Beam Position Monitor is used to obtain transverse signals at the passage of a beam. Using hybrid junction components, it is possible to produce sum and difference signals in the two transverse planes at one azimuth of the storage ring. The signals are acquired and recorded by a four channels LeCroy LC574A oscilloscope with the capability to sample the input waveforms using a beam synchronous external clock generated by the DaΦne Timing System [3]. The digitizer accepts frequencies in the 50:500 MHz range, and the DaΦne RF is 368 MHz. The lowest frequency fitting as clock is RF/6 and the harmonic number is 120, hence 19 values over 20 have to be discarded because for now we limit the analysis to the single bunch case. However, multibunch analysis is also possible [4]. A phase shifter with a range of 20 nsec is used to time correctly the acquisition of the signals generated by the selected bunch.

The start of acquisition is synchronised to a horizontal kick given by one of the injection kickers. Usually the kick has a peak voltage in the range from 2 to 6 kV corresponding to an angle from ~1 to ~3 mrad.

After capturing up to 5000 consecutive turns, data are sent through a GPIB interface to a personal computer, for processing, presentation and storage. In Fig. 2 a simplified scheme of the acquisition system is shown.

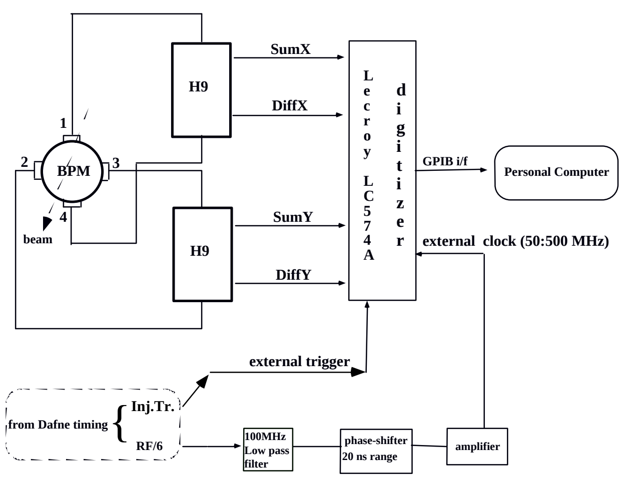

Figure 2: The acquisition system.

3.2 The virtual monitor

Two monitors at $\pi/2$ of betatron phase can be used to produce a plot in the phase space. Since our system acquires data from the only BPM, our second monitor is "virtual" and has to be calculated. To do this the software builds a data vector relative to a second monitor advanced by 90 degrees. This is done by two alternative ways: by applying the Hilbert transform or using the transport matrix method.

The Hilbert Transform [5] applied to a data sequence produces a second data sequence with a 90 degrees phase shift with the same frequency and amplitude content. This gives the interesting advantage to have phase space plots already normalized.

The transport matrix method uses the Twiss parameters α, β at the monitor position as computed with the machine model.

The transport matrix formula is

$$x'(i) = \frac{x(i+1) - (\cos(2\pi Q) + \alpha \sin(2\pi Q))\, x(i)}{\beta \sin(2\pi Q)}$$

where α, β are the horizontal or vertical Twiss parameters, and Q is the tune. A preliminary comparison has shown a good agreement between the results of the two methods.

2.3 Signal processing

After the oscilloscope has captured the transient, data are downloaded to a personal computer following an operator request. A calibration routine allows converting data from voltage to millimetres. The acquisition and control program first shows the decay time in number of turns. It is important to have this plot in real time to understand if the captured data are correct. Then the program draws a trajectory representation in the phase space (position and angle) in both the transverse planes. In the Fig. 3 it is shown a typical pattern with seven arms.

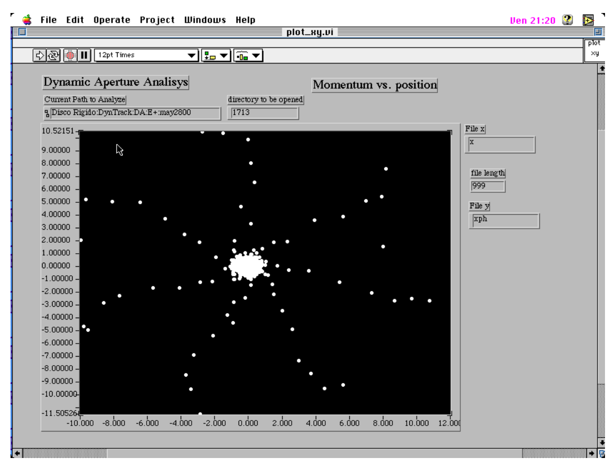

Figure 3: Horizontal phase space plot drawn using the Hilbert transform.

All the recorded data are stored in a database ordered according to the record time. It is possible, of course, to analyze the collected data with different machine parameters from the local workstation or from a remote computer.

4 RESULTS

The dynamic tracking system has made possible to perform studies on the non-linear beam dynamics in DaΦne.

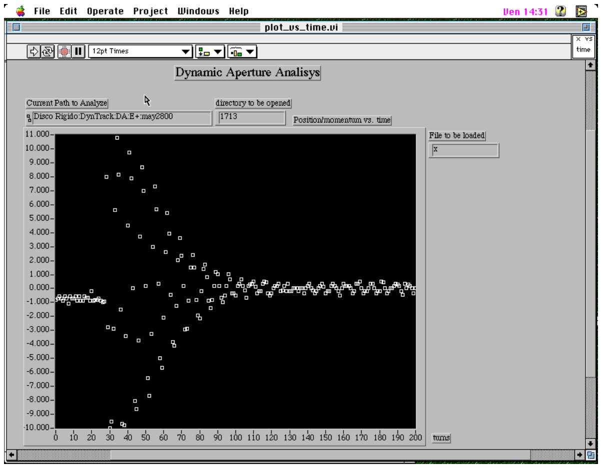

Figure 4: A coherent signal decay due to non-linear filamentation (displacements versus turns), data are from the same record of Fig. 3 .

Optics measurements on new configurations of the main rings are usually started with this tool [6], [7] to understand better the behaviour of the machine. The coherent oscillation amplitude decay through non-linear filamentation (see Fig. 4) helps to estimate directly nonlinearity strength and tune spread [8], and provides a quick tool to modify the dynamic aperture by varying sextupole settings.

The decoherence time is an indirect measurement of the tune on oscillation amplitude dependence, related to the nonlinearity of the ring. A study of the wiggler field nonlinearity and optimization of the sextupoles settings are among the most relevant results providing by the dynamic tracking system. Fig. 5 shows two distinct cases, corresponding to two different configurations of the rings.

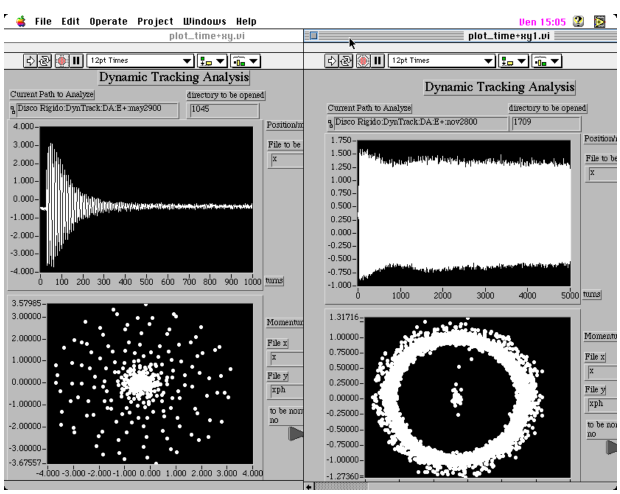

Figure 5: A comparison between optics with wigglers turned on and wigglers turned off.

5 CONCLUSIONS

The dynamic tracking acquisition system has shown to be a very useful tool to investigate the non-linear behaviour of the DaΦne rings and to improve their performances. Upgrade of the system will be provided in the next future. First of all, a more powerful workstation will be installed, to download data more quickly from the oscilloscope and to exchange data with the machine real time database in the control system. Then, a second oscilloscope will be used with the goal to have up to eight channels to acquire signals from two BPM's. We also plan to start multibunch software development to extend the use of the system to the transverse modal analysis.

5 ACKNOWLEDGEMENTS

The authors wish to thank Oscar Coiro and Donato Pellegrini for the realization of the set-up, very critical on the equalization of the cables. Thanks also to Mario Serio for many ideas and suggestions during the system implementation and to Mikhail Zobov for the interesting and useful discussions during the set-up of the system.

REFERENCES

[1] P.L.Morton, J.-L.Pellegrin, T.Raubenheimer, L.Rivkin, M.Ross, R.D.Ruth, W.L.Spence, "A Diagnostic for Dynamic Aperture", 1985 Particle Accelerator Conference, Vancouver, B.C., Canada, May 13-16, 1985.

[2] P.Tran, C.Pellegrini, M.Cornacchia, M.Lee, W.Corbett, "Nonlinear Beam Dynamics Experimental Program at SPEAR", SLAC-PUB-95-6720, 1994.

[3] G.Di Pirro, A.Drago, A.Gallo, A.Ghigo, F.Sannibale, M.Serio, "Implementation and Performance of the DaΦne Timing System", EPAC98, Stockholm, Sweden, 22-26 June 1998. LNF-98/023.

[4] S.Prabhakar, J.D. Fox, D.Teytelman, A.Young, "Phase Space Tracking of Coupled Bunch Instabilities", Phys.Rev.Spec.Top.-Acc. and Beam, Vol 2, 1999.

[5] R.T.Burgess, "The Hilbert Transform in Tracking, Mapping and Multiturn Beam Measurements", C.E.R.N., SL-Note-99-048 AP, Geneva, Switzerland, 22 October 1999.

[6] C.Milardi, G.Benedetti, C.Biscari, S.Di Mitri, M.Boscolo, A.Drago, S.Guiducci, F.Marcellini, G.Mazzitelli, M.Preger, C.Vaccarezza, G.Vignola, M.Zobov, "Optics Measurements in DaΦne", EPAC 2000, Vienna, Austria, 26-30 June 2000. LNF-00/021(P).

[7] S.Di Mitri, "Dinamica trasversa di singola particella in presenza di non linearita' sestupolari nell'acceleratore circolare DAΦNE", tesi di laurea, Univ. di Pisa, A.A. 1999-2000.

[8] A.-S. Muller, J.Wenninger, "Measurements of Tune Shifts with Amplitude at LEP", PAC'99. New York, 1999.

A HIGH DYNAMIC RANGE BUNCH PURITY TOOL

B.Joly, G.A.Naylor. ESRF, Grenoble, France.

Abstract

The European synchrotron radiation facility uses a stored electron beam in order to produce x-rays for the study of matter. Some experiments make use of the time structure of the x-ray beam which is a direct reflection of the time structure in the electron beam itself. Avalanche photo-diodes have been used in an x-ray beam in a photon counting arrangement to measure the purity of single or few bunch filling modes. Conventional techniques measuring the photon arrival times with a time to analogue converter (TAC) achieve dynamic ranges in the 10^{-6} range. We report here the use of a gated high count rate device achieving a measurement capability of 10^{-10}. Such high purity filling modes are required in synchrotron light sources producing x-ray pulses for experiments looking at very weak decay signals as seen in Mossbauer experiments..

1 INTRODUCTION

An avalanche photodiode, collects scattered x-ray photons from an x-ray absorber on an unused bending magnet beam-line (fig 1, 2) and is used to measure bunch purity in few bunch modes. The x-ray photons collected by the photodiode create a hundred to a thousand carriers which are then multiplied by avalanche in the junction. An avalanche photodiode is chosen with a thin (10µm) depletion layer to achieve a fast time response (HAMAMATSU model S5343SPL, ref 1). The subsequent electric pulse is amplified (fig 3) and sent to a photon arrival time electronic acquisition time (fig 4).

Such an acquisition system is frequently used in high dynamic range time resolved user experiments (ref 2) and can be used in two different operating regimes:

1) Low count rate mode where the probability of detecting a photon is much less than one per main pulse revolution. The arrival time of all photons is stored and a profile of the time dependent x-ray emission is determined and hence the electron bunch intensity profile as a function of time determined with a very high dynamic range (fig 4). Since photon pile up is rare the plot is fairly linear and accurate with moderate acquisition times (a few minutes) over around 6 orders of magnitude. This is an important diagnostic tool in determining the purity of the main bunch with respect to neighbouring bunches.

2) High count rate where the probability of detecting a photon from the main pulse is much more than one. In this case there is a great non-linearity between the measurement of the main pulse and subsequent pulses. By applying a gate to the discriminator the incoming photon counts can be accepted or de-validated. A gate can then be applied to only allow counts during a specified period after the main pulse. These validated counts are then at a rate much less than 1 per revolution and so the trace becomes linear again but with a much greater sensitivity (up to 10 orders of magnitude below the intensity of the main pulse. Since the main pulse now has an amplitude much higher than the subsequent pulses to be counted (due to the fact that it represents many photons) the gate can only be applied some 10-20ns after the main pulse due to the decay and possible oscillations following the main pulse. Such a diagnostic is then not useable for determining the population in neighbouring electron bunches but is very sensitive to occupancy in bunches more than 20ns following the main pulse up until the neighbouring pulse prior to the next main pulse.

2 DIAGNOSTIC CONFIGURATION

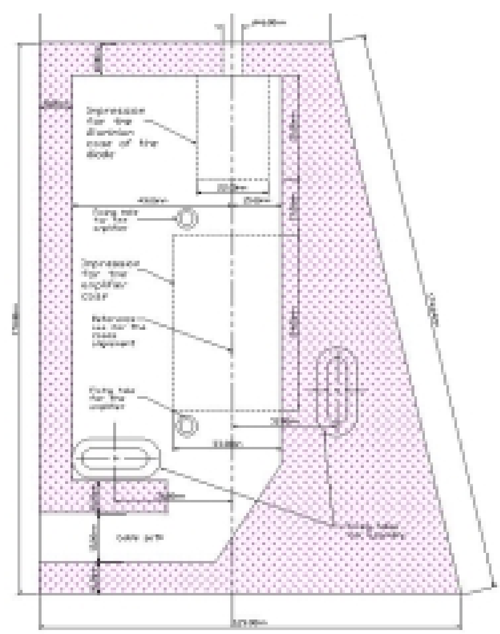

Figure 1: Avalanche photo-diode in lead shielding

A bunch purity diagnostic tool using the first mode of operation is installed on beam line D19. This paper concerns the performance of a bunch purity diagnostic used in the second counting mode. A high count rate is achieved on the D4 beam line (fig 1) using a beryllium window to allow the high flux of Cu K alpha fluorescence photons to be detected. As seen in figure 5, an aluminium window will effectively transmit a moderate flux of Compton scattered photons from the Cu absorber surface.

The cross section for x-ray interaction with the copper surface is however much higher via the photo-electric emission than for Compton scattering. The remaining excited Cu+ ion (electron removed from an inner shell) can decay by auger emission or by the re-emission of an x-ray fluorescence photon. Assuming there to be not to much delay in the fluorescence emission (due to the very short excited state lifetime of the Cu+) this fluorescence is still characteristic of the temporal profile of the electron bunch (though in practice may lead in part to the tail of the main pulse detected by the avalanche photodiode.

Figure 2: Avalanche Photodiode

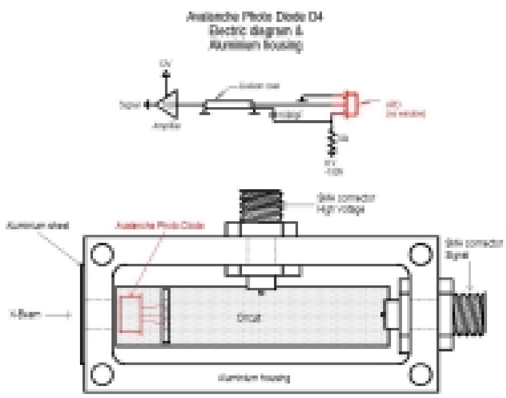

Figure 3 Time to analogue converter

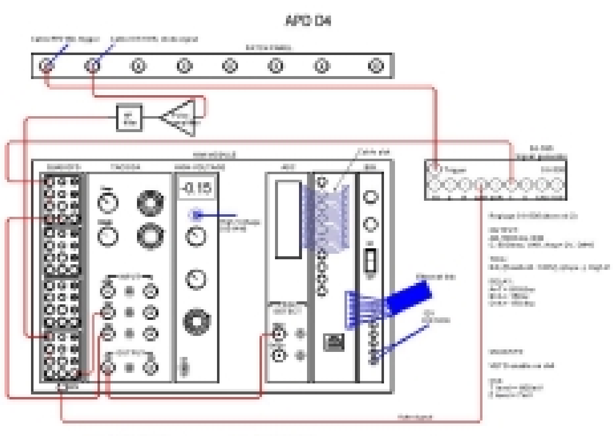

A significant fraction of the incident scattered x-rays is then scattered in-elastically into Cu K alpha x-rays at an energy below the peak of the bending magnet emission. These photons will be heavily attenuated by the aluminium window yet strongly transmitted by a beryllium window. The avalanche photodiode must be protected within a thick lead housing to prevent erroneous counting from x-rays scattered from other sources than the Cu absorber surface (that would not have the correct timing) as well as Bremstrahlung gamma rays coming directly from the electron beam impacting residual gas atoms in the storage ring.

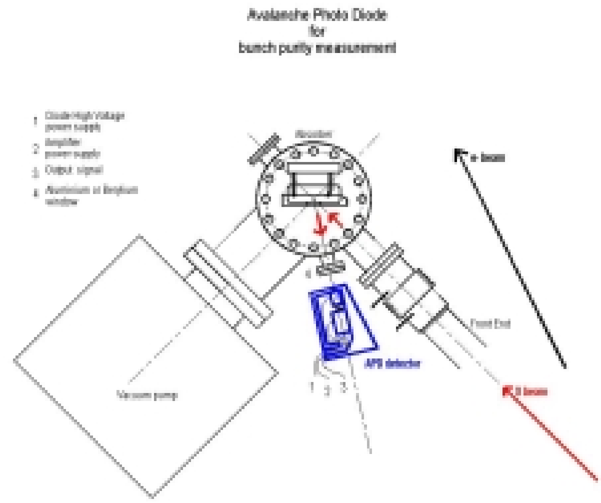

Figure 4 Collection of scattered x-rays on beam port

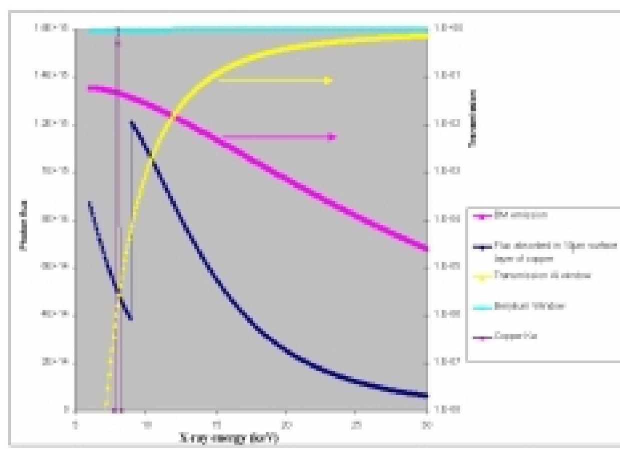

Figure 5 Cu Ka line transmitted by Be window.

3 MEASUREMENTS

The received count rates as a function of time must be calibrated at low current so as to avoid non-linearity effects due to photon pile up. This is done by injecting a low current in a multibunch mode (one third filling) and looking at the trail off in intensity of the bunches at the end of the pulse train. The count rate was calibrated by injecting 20mA of 2/3rd fill and scraping down to 0.4mA. The count rate in the 150ns window was 1600per sec equivalent to 50Hz/µA or 16Hz/pC. This corresponds to a count rate of 50 times that on D19.

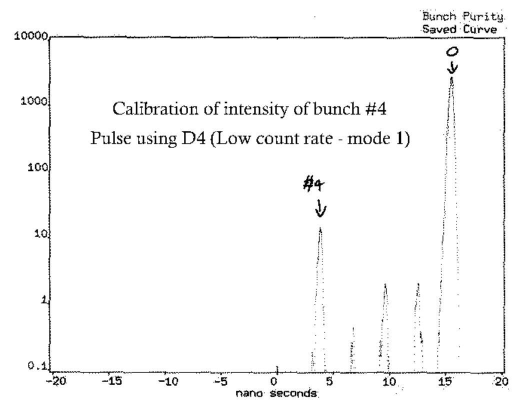

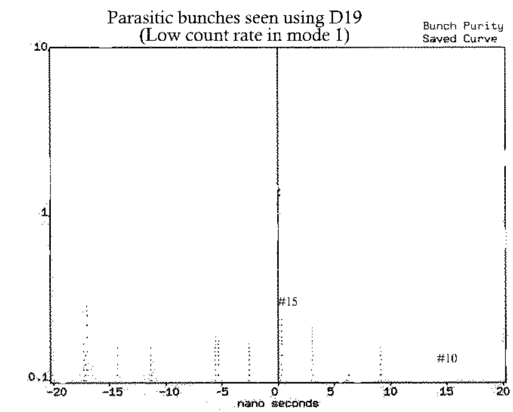

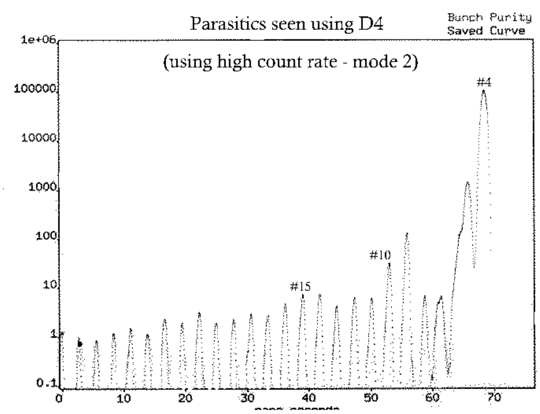

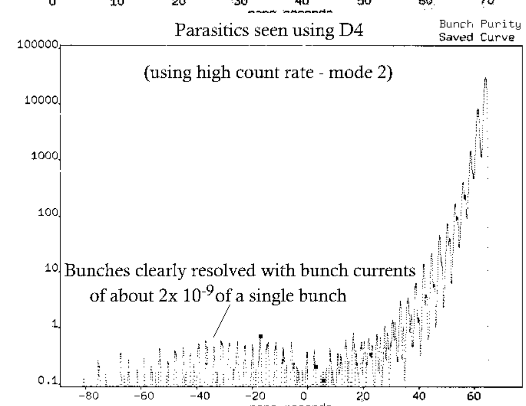

Figure 7 Resolution of 10^{-9} in high counting mode

The beam was further scraped down to 3Hz within the 150ns period. This corresponds to a remaining current of 1nA per bunch. A single bunch was injected as a reference pulse (#0). With a fill of 10mA this would correspond to parasitic bunches each at 10^{-7} of the main pulse. Figure 2 and 3 show the visualization of these parasitic bunches using D4 and D19. While barely detectable on D19 using the counting mode i) these pulses are easily visible with the high count rate device D4 using mode ii) described above. The detector D4 can usefully determine the purity ratio of bunch #4 to bunch #0 by lowering the count rate using an attenuator to be in the linear counting regime with no pile up. The purity detector D4 is then able to detect the ratio of the parasitic bunches #10 and #15 to the weak pulse #4 in the high count rate regime. Pulses with an intensity of 10^{-9} of the intensity of a single bunch can be detected in this way.

4 CONCLUSIONS

The Avalanche photodiode on D19 gives a good linear detection of the bunch purity and is sensitive to parasitic bunches immediately following the main pulse with a detection limit of about 10^{-7} or 1nA per bunch in absolute terms (3pC). The D4 avalanche photodiode is heavily saturated by the main pulse and successive ripples on the signal prevent correct counting during the 20ns period immediately following the main pulse. The D4 APD does have greater sensitivity allowing parasitic bunches at the 10^{-9} level to be easily measured in a 200s-integration period. Further tests measuring the total count rate within the 150ns gate window and using a high count rate gives a resolution in the 10^{-9} range in single bunch and the 10^{-10} range in 16 bunch. The mode of operation i) is therefore able to detect impurities down to 10^{-6} while mode ii) allow the impurity detection limit to be extended from 10^{-6} to 10^{-}

5 ACKNOWLEDGEMENTS

Discussions with R.Rueffer and J.L. Revol have been essential in the development of this diagnostic tool.

6 REFERENCES

[1] 'Bunch Purity measurements of Synchrotron X-ray beams with an avalanche photodiode detector'
S. Kishimoto, NIM PR A351 pp 554-558
[2] 'An avalanche Photodiode detector for x-ray timing measurements' S.Kishimoto, NIM PR A 309 pp603-605
[3] 'Report on the X-ray efficiency and time response of a 1cm2 reach through avalanche diode' A.Q.R. Baron, NIM PR A352 pp665-667
[4] 'Photon counting detectors for fill structure measurements at visible wavelengths' H.L.Owen, conf proc. DIPAC99 Chester pp137-139

DSP AND FPGA BASED BUNCH CURRENT SIGNAL PROCESSING

G.A.Naylor ESRF, Grenoble, FRANCE

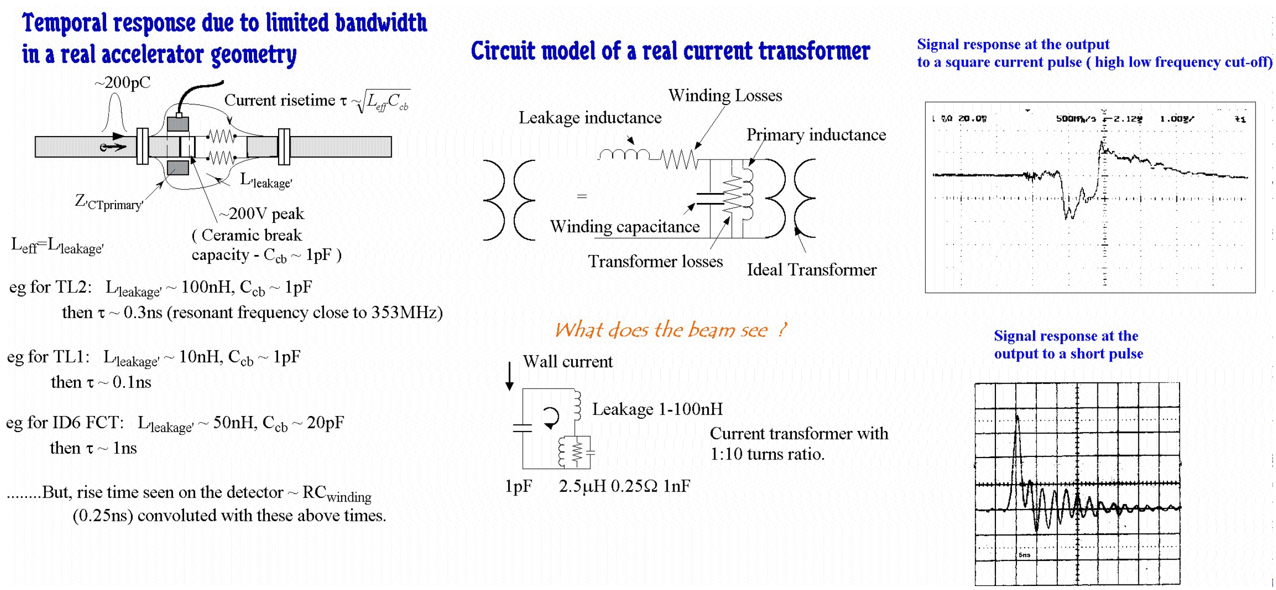

Figure 1 Principles of a fast current transformer to resolve a complex filling pattern

Abstract

The current in electron storage rings used as synchrotron light sources must be measured to a very high precision in order to determine the stored beam lifetime. This is especially so in high-energy machines in which the lifetime may be very high. Parametric current transformers (PCT) have traditionally been used to measure the DC or average current in the machine, which offer a very high resolution. Unfortunately these do not allow the different components of a complex filling pattern to be measured separately. A hybrid filling mode delivered at the ESRF consists of one third of the ring filled with bunches with a single highly populated bunch in the middle of the two-thirds gap. The lifetime of these two components may be very different. Similarly the two components are injected separately and can be monitored separately using a fast current transformer (FCT) or an integrating current transformer (ICT). The signals from these devices can be analysed using high speed analogue to digital converters operating at up to 100MHz and digital signal processing (DSP) techniques involving the use of field programmable gate arrays (FPGAs) in order to process the continuous data stream from the converters.

1 A NEW CURRENT TRANSFORMER ACQUISITION SYSTEM

There is a need at the ESRF to improve the data acquisition system measuring the current in the various elements of the injection system as well as the storage ring. The requirement is to measure the injection efficiency with a greater precision and reliability in order to provide an interlock against too low an injection efficiency.

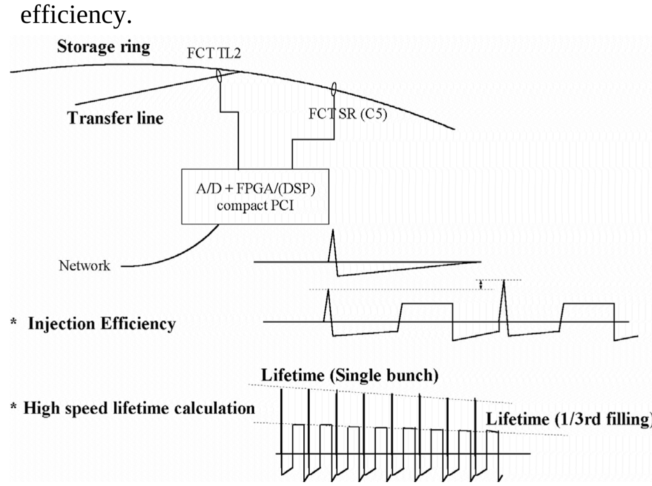

Figure 2 Fast current transformers to compare beam in the transfer line and storage ring

The machine division is examining the feasibility of operating the machine in a ‘topping up’ mode, for which a reliable and accurate measure of the injection efficiency is required. The existing diagnostic acquisition chain based on analogue gating techniques does not provide a sufficiently reliable measurement when different filling patterns may be injected giving different pulse shape responses due to the limited band-pass of the current transformers (fig 1). Recent advances in high-speed digital acquisition and processing techniques allow the measurement to be performed digitally and with a much greater precision. The limited frequency response of the current transformers can be compensated in the time domain using correlation (fig 2,3). The measured pulse is numerically cross-correlated with a waveform of the anticipated pulse shape. The cross-correlation gives then a measure of the total injected charge and is fairly immune to noise that may be present on the signal. The measurement is immune both to high frequency noise and low frequency noise (the latter which gives rise to uncertainty in the base-line offset. The much greater precision afforded by such techniques will also allow the lifetime to be determined more quickly. This is important in the optimisation of machine parameters.

2 CALCULATION OF THE CROSS-CORRELATION

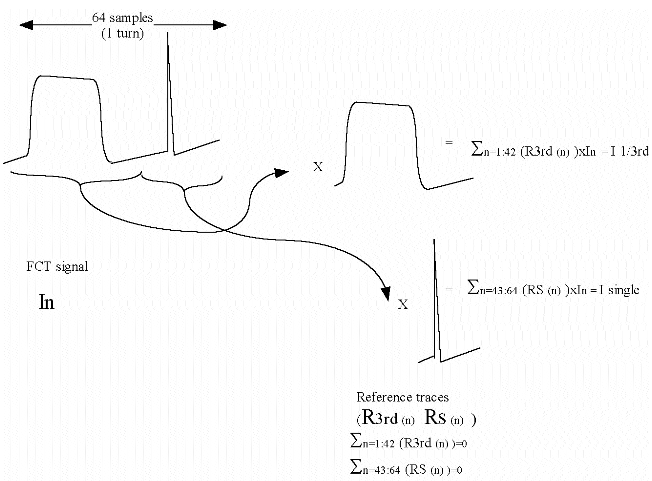

Figure 3 The cross correlation measures a part of the beam structure

In order to take the cross-correlation of the current waveform in the storage ring as measured by the current transformer, its signal is acquired using an analogue to digital (A/D) converter. In order to resolve the shape in all filling modes (including 16-bunch mode) 64 acquisitions will be taken per revolution period. In the case of the ESRF, this corresponds to an acquisition frequency of 22.7MHz. This is well within the capabilities of modern A/D chips. The data rate that this represents would however be difficult to treat on a continuous basis with Digital Signal Processing boards that are currently available. It is possible to perform the high data rate multiply and accumulate computations (that form the correlation) using a field programmable gate array (FPGA). The compressed data output (representing the charge bunch structure) may either then be processed using a conventional DSP or Pentium processor on a cPCI system. A server program running on the cPCI will make bunch current, injection efficiency and lifetime available to applications running in the control room. Programming of the FPGA is a task for specialists using hardware description languages such as VHDL, though the use of "System Generator" (a product of XILINX), it should be possible to define the model using Simulink (a product of Mathworks) in order to define a model at a high level (see fig 4).

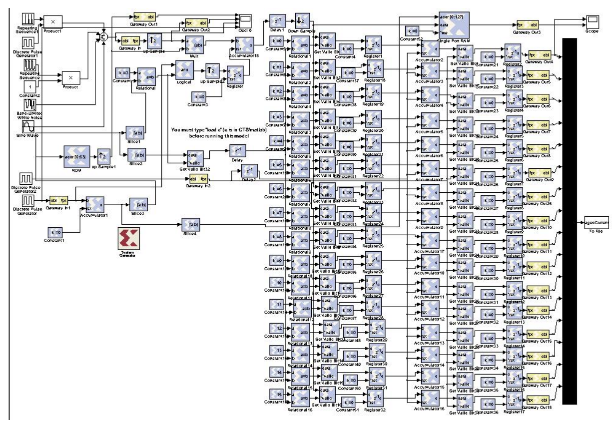

Figure 4: Use of Simulink to define the model

3 RESULTS FROM SIMULATION

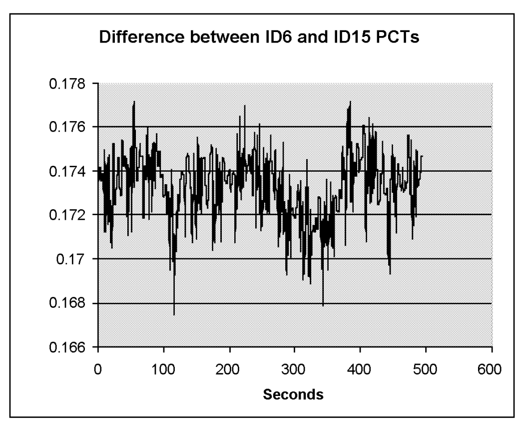

Figure 5: Noise using a conventional Bergoz Parametric current transformer

Real data was recorded using a digital oscilloscope and the correlation calculated off-line using Matlab. The rms noise on the current reading determined from a 64 point cross-correlation calculation was 1.3 x 10-3.

A total of 57 data points were taken over a 50 minute period. The current was about 70mA so that the rms current noise per turn measurement was 90µA. This gives an equivalent noise if each reading was taken over one second of 0.15 µA. This corresponds favourably to what can be achieved using very-high resolution Parametric current transformers (1.1µA rms measured over a 10 minute period, each reading being averaged over 1s see fig 5). An improvement in the noise figure by a factor 2 will allow the lifetime to be determined 4 times quicker and with a 3 times reduction in noise allows the lifetime to be determined practically an order of magnitude times faster.

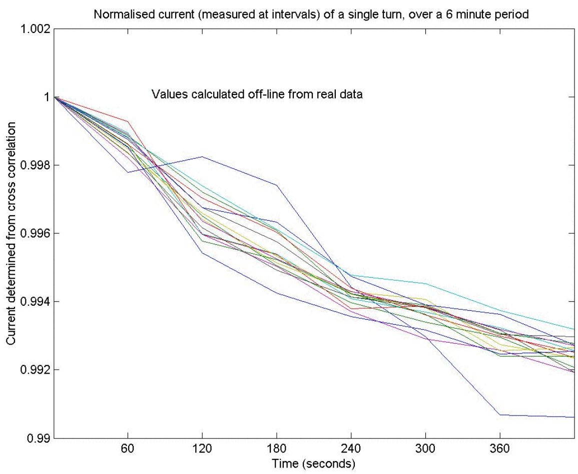

4 ACKNOWLEDGEMENTS

This project is inspired by many discussions with J.M.Koch and C.Herve

DISCUSSION 1 : MONDAY AFTERNOON (16.30HRS - 18.00HRS)

Orbit Feedbacks for Synchrotron Light Sources

Discussion animators: Micha Dehler, Daniele Bulfone

The session is meant to serve as a survey giving an overview on the current status of closed orbit stabilisation and on future needs. Therefore we would be interested to have from each laboratory/project, where appropriate, transparencies on the following discussion topics.

The first general part are noise sources for the beam and requirements with the following items

?? Ground spectra at the different labs, e.g. function of ground humidity, natural seismic noise, man made noise by e.g. external traffic.
?? Transfer function between ground noise and resulting beam movement influenced by the girder design and magnet movement.
?? Beam coupling values, theoretical and real.
?? Thermal drifts due to cooling and variations in the air temperature.
?? Noise from the mains via e.g. the corrector power supplies requiring feedback at 50 Hz and upper harmonics.
?? Other sources of high frequency noise.
?? Resulting bandwidth requirements for feedbacks
?? Feedback compensating for loose and cheap design?

The second part concentrates on closed orbit feedbacks including components and is meant to cover:
?? Requirements for the BPM system: Sampling rates, fast interfacing, self calibration and compensation of e.g. current dependencies.
?? Use of photon BPMs
?? Power supplies: Mains rejection, bandwidth, resolution.
?? Performance of current systems as well features of planned systems.
?? Strategies: Local vs. global feedback systems
?? Feed forward techniques
?? Interference between orbit feedbacks and other feedbacks, e.g. local ones for the stabilisation of optical beam lines or experiments.

DISCUSSION 2 : MONDAY AFTERNOON (16.30HRS - 18.00HRS)

Emittance Measurement Techniques

I. Physical questions.

Short review of the existing techniques, methods and approaches (imaging, interference, projection, betatron coupling) with their advantages and limitations.

New promising methods of emittance diagnostics (short contributions / messages from participants are expected).

How to go from beam profile (size, divergence, etc.) measurements to emittance ? Problems of indirect measurements.

II. Practical questions.

Emittance, brightness (brilliance), luminosity are very important "passport" characteristics of an accelerator.
In practice, however, lack of time, man-power, sometimes low priority, make it not so easy to construct and maintain a good, reliable emittance diagnostic system.
How this situation can be improved ?

What can be shared (ideas, software, hardware, personnel) ?

How to shorten a long way from a bright idea to a reliable system ?

Can final beam users (e.g. SR users) contribute / share their diagnostics systems or data ?

DISCUSSION 3 : MONDAY AFTERNOON (16.30HRS - 18.00HRS)

Industrial Products for Beam Instrumentation

In various branches of high technology industry there has been considerable progress in the past years which could be used for beam instrumentation.

The subject will be introduced by two short demonstrations:

1) a demonstration of modern audio electronics

with 24bit-96kHz ADC, digital signal electronics and application programs under windows on a PC, which allow to change the parameters of the signal treatment.

Potential applications are data monitoring at constant sampling frequency, orbit feedbacks (including high power audio amplifiers), noise reduction on beam current transformers....

2) digital treatment of video signals

webcams, frame grabbers, CCD-data via USB, all one needs for image acquisitions, in particular interesting for profile measurements.

These introductory demonstrations will not last longer than 30 minutes.

The remaining time will be used to pass through the audience collecting information into a two dimensional table, which shall contain as row index the accelerator and as column index the type of measurement.

The contents of the table will be the "of the shelf" industrial product, that has been used/will be used to perform the task.

This table with some explanation will be put into the conference proceedings, such that the interested parties can take the necessary contacts.

DISCUSSION 4 : TUESDAY MORNING (11.30HRS - 13.00HRS)

Calibration and Stability of Diagnostics Equipment

Topics are divided in 3 categories: *BPMs*, *Current Monitors* and *Optical Monitors*. The animators, Volker Schlott (volker.schlott@psi.ch) and Laurent Farvacque (laurent@esrf.fr) have here below listed issues as a basis for discussion.
Further suggestions and/or contributions are welcome and can be communicated to the animators (preferably before DIPAC in order to adapt the schedule and to allow a proper planning of the discussion session).

Beam Position Monitors (BPMs):

- Is there a need for calibration of BPM chambers on a test bench?
- Are mechanical resp. machining tolerances (< 0.05 mm) good enough to simply apply theoretical calibration factors, which are derived from EM-simulation codes like MAFIA, POISSON etc…?
- Is the initial error on the complete BPM system, including mechanics and electronics, low enough to store beam (in case of a storage ring) and simply apply the method of *beam based alignment* (BBA) to solve all further calibration issues of the system?
- To what accuracy leads BBA? How often should it be repeated in order to guarantee always a well "calibrated" system?
- How is BBA actually implemented in the different labs?
- Is online calibration of BPM electronics necessary (e.g.: new calibration for each change in gain settings)?
- How often should this procedure be repeated and to what level of accuracy? Is a (short) "time-out" in the position measurement tolerable?
- Are BPM electronics in general stable enough to be only calibrated once (before installation)?
- How important are *absolute* position measurements (with respect to the magnetic center of an accelerator)?
- How important is the reproducibility of a (absolute) "golden orbit"? How close is such a "golden orbit" to a calibrated "BBA" orbit?
- How are drifts resp. movements of the vacuum system (BPM block) considered in determination of beam positions (golden orbits)?
- Usually drifts occur in case of temperature gradients in the vacuum chamber (heat load from the beam) and/or changes in the ambient (tunnel) temperature - locally and globally after a shut-down.
Should these mechanical drift be monitored and corrected?

Current Monitors

- How are calibrations of current monitors (DC to wide BW monitors) usually done?

- A short description of successful techniques and implementations in the labs or on the machines would be appreciated !!!

- How precise and how reproducible are calibration procedures of current monitors?
- In case of lab calibrations: How close are the calibrations to the measurements on the machine?
- In case of online calibration: How much do calibration features influence the actual measurement on the beam?
- How often do the calibrations need to be repeated?
- Is cross calibration desirable or even necessary?

- What influences most the stability and reproducibility of current measurements (temperature, bunch pattern etc…)?
- What are the (easiest) cures to these problems?

Are there universal monitor design criteria for current monitors of different kinds (DC to wide BW) to obtain optimum results?

Optical Monitors

- What is the best way of calibrating an optical monitor (screen moniotr or synchrotron radiation monitor)?
- In case of a fixed optical set-up (magnification) : in the lab…?
- In case of a flexible optical set-up (telescope optics…) : online with the use of calibration grids etc…?

- What are the stability requirements for optical set-ups in terms of mechanical and timing stability?
- Stability considerations for different optical set-ups and different machine environments would be appreciated!!!

- How well do we have to know about timing electronics in case of “fast optical measurements”?
- Is there a well tested timing unit with lowest jitter (?? ps)?

- How much should we and can we learn from our experimentalists (especially in case of storage rings)?

- Should we resign on doing optical monitoring for cases like beam size, emmittance, stability and let the experimentalists take over?

DISCUSSION 5 : TUESDAY MORNING (11:30HRS – 13:00HRS)

Digital Signal Treatment in Beam Instrumentation

Digital Signal Processing has grown dramatically over the last five years. The evolution of digital logic and processors has opened up the use of digital signal processing in domains, which were reserved to analog signal processing.

In this discussion session we would like to review digital signal treatment for beam diagnostics application.
Participants are encouraged to present their different approaches and their motivation to do it in one or the other way.

Emphasis shall be put on the following subjects:

?? **Digital Signal Processing for :**

- image processing	**- BPMs**	**- current monitors**
- beam loss monitors	**- feedback systems**	**- others**

What are the advantages/disadvantages with respect to their analog counterpart?

?? Digital Signal Processing – Overkill versus more flexibility?
?? Can digital signal processing provide better calibration methods?
?? Do commercial products suit the beam diagnostic needs or are in-house developments inevitable?
?? The fields of digital systems are manifold, different expertise on different levels is needed. Does a digital system need more manpower than a conventional analog system?
?? Trend in digital signal processing:
DSP / General Purpose Processor (PowerPC, Pentium MMX, etc.) / Field Programmable Gate Arrays (FPGA)?
?? Coding dilemma in DSP based systems:
- benefits and drawbacks of low- and high-level programming?
- benefits and drawbacks of using an operating system?
?? How risky is the use of newest commercial products or should one better rely on established hardware/tools with better software environment?
?? Integration into control systems:
What are the possibilities today for the communication with the 'control room'?
How easy is remote debugging?
?? Next generation of diagnostic devices: Could a modular design of a digital signal processing device (general processing unit + customizable signal conditioning hardware) be used as a general purpose diagnostic device?

DISCUSSION 6 : TUESDAY MORNING (11.30HRS - 13.00HRS)

Beam Loss Monitors

1) A very brief review of different beam loss monitors.

Which, how fast, sensitivity, experiences, reliability, ...

2) Where can beam loss monitors help us?

Beside of the information about the intensity and the position of beam losses, what else can beam loss monitors tell us?
BLMs are used for very different kinds of measurements: Tail scans, beam orbit oscillations, ground spectra, tune scans, protection of superconducting magnets, beam lifetime, beam steering, 'dust' detection, dosimetry, beam energy, transversal and longitudinal beam dynamics...

Typically, BLMs are required in case of unwanted beam conditions. However, BLM systems might give a lot of more information.

This discussion session should give a forum for ideas to use the special information from BLM systems to improve and/or understand the behavior of accelerators/storage rings/extraction lines.

Therefore we would be interested to have from different laboratories and projects a short presentation of their use of BLMs and what kind of (beam related) information is extracted.

Further suggestions and/or contributions are welcome and can be communicated to the animators. (Kay.Wittenburg@desy.de)

List of Authors

Bold papercodes indicate primary authors

Institutes List

ANL
Argonne National Laboratory, Argonne, Illinois, USA

- Decker, G.
- Lill, R.
- Singh, O.

BESSY
Berlin, Germany

- Feikes, J.
- Holldack, K.
- Kuske, P.
- Peatman, W.B.

BNL
Brookhaven National Laboratory, Upton, NY, USA

- Cameron, P.
- Cerniglia, P.
- Connolly, R.
- Cupolo, J.
- Degen, C.
- Drees, K.A.
- Gassner, D.
- Grau, M.
- Kesselmann, M.
- Lee, R.
- Liaw, C-J.
- Satogata, T.
- Sikora, R.

Bergoz
Bergoz Instrumentation, St. Genis Pouilly, France

- Bergoz, J.
- Unser, K.

CERN
Geneva, Switzerland

- Angoletta, M.E.
- Barbero, E.
- Baribaud, G.
- Benedikt, M.
- Berrig, O.
- Beugnet, C.
- Carli, Ch.
- Cocq, D.
- Cojan, A.
- Dehning, B.
- Dutriat, Ch.
- Ferioli, G.
- Ferri, G.P.
- Fischer, C.
- Fullerton, J.
- Garcia, A.A.
- Giovannozzi, M.
- Gschwendtner, E.
- Guerrero, A.
- Höfle, W.
- Jakob, H.
- Jansson, A.
- Jensen, L.
- Jones, R.
- Koopman, J.
- Koutchouk, J.-P.
- Ludwig, M.
- Madsen, N.
- Manarin, A.
- Marqversen, O.
- Martini, M.
- Pedersen, F.
- Prochnow, J.
- Raich, U.
- Rossa, E.
- Savioz, J.J.
- Schmickler, H.
- Schmidt, F.
- Sillanoli, M.
- Spanggaard, J.
- Søby, L.
- Vismara, G.
- Williams, D.J.

DELTA
Institute for Accelerator Physics and Synchrotron Radiation, University of Dortmund, Dortmund, Germany

- Berges, U.
- Wille, K.
- Kasel, E.
- Schirmer, D.
- Schmidt, G.
- Wille, K.

DESY
Deutsches Elektronen-Synchrotron, Hamburg, Germany

- Flöttmann, K.
- Werner, M.
- Wittenburg, K.
- Körfer, M.
- Wendt, M.
- Wittenburg, K.

DESY-Zeuthen
Deutsches Elektronen-Synchrotron, Zeuthen, Germany

- Bohnet, I.
- Bähr, J.
- Lipka, D.
- Lüdecke, H.
- Stephan, F.
- Zhao, Q.

ELETTRA
Sincrotrone Trieste, Trieste, Italy

- Bocchetta, C.J.
- Bressanutti, R.

- Bulfone, D.
- Carniel, A.
- Cautero, G.
- D'Auria, G.
- De Monte, R.
- DeMonte, R.
- Fabris, A.
- Ferianis, M.
- Gambitta, A.
- Giuressi, D.
- Loda, G.
- Lonza, M.
- Mazzolini, F.
- Mian, G.
- Pangos, N.
- Rossi, C.
- Sergo, R.
- Smaluk, V.
- Tommasini, R.
- Tosi, L.
- Zambon, L.

ESRF
European Synchrotron Radiation Facility, Grenoble, France

- Chubar, O.
- Drakopoulos, M.
- Plouviez, E.
- Snigirev, A.
- Weitkamp, T.
- Chubar, O.
- Farvacque, L.
- Joly, B.
- Kuznetsov, S.
- Nagaoka, R.
- Naylor, G.A.
- Scheidt, K.
- Snigirev, A.
- Weitkamp, T.

FZR
Forschungszentrum Rossendorf, Dresden, Germany

- Büchner, A.
- Büttig, H.
- Evtushenko, P.
- Michel, P.
- Schurig, R.
- Wustmann, B.

Fraunhofer-INT
Euskirchen, Germany

- Henschel, H.

GAC
General Atomics Corporation, San Diego, CA, USA

- Kamperschroer, J.
- Senior, R.

GSI
Gesellschaft für Schwerionenforschung, Darmstadt, Germany

- Bank, A.
- Forck, P.
- Hoffmann, T.
- Nolden, F.
- Peters, A.
- Reeg, H.
- Schneider, N.
- Weiss, A.

HC
Honeywell Corporation, USA

- Gruchalla, M.
- O'Hara, J.

HMI
Hahn-Meitner Institut, Berlin, Germany

- Wulf, F.

I-Tech
Instrumentation Technologies, Solkan, Slovenia

- Košiček, A.
- Uršič, R.

IKP
Forschungszentrum Jülich GmbH, Jülich, Germany

- Bojowald, J.
- Dietrich, J.
- Klehr, F.
- Mohos, I.

INFN-LNF
Laboratori Nazionali di Frascati, Frascati, Italy

- Castellano, M.
- Drago, A.
- Serio, M.
- Stella, A.
- Verzilov, V.

INFN-LNS
Laboratori Nazionali del Sud, Catania, Italy

- Cosentino, L.
- Finocchiaro, P.

INFN-Roma2
Roma, Italy

- Catani, L.
- Cianchi, A.

ITEP
Institute for Theoretical and Experimental Physics, Moscow, Russia

- Liakin, D.A.

JLAB
Jefferson Lab., Virginia, USA
- Cuevas, C.
- Denard, J.-C.
- Freyberger, A.P.
- Sharabian, Y.
- Jordan, K.

KEK
High Energy Accelerator Research Organization, Ibaraki, Japan
- Kasuga, T.
- Mochihashi, M.
- Obina, T.
- Tanimoto, Y.
- Mitsuhashi, T.

LANL
Los Alamos National Laboratory, Los Alamos, NM, USA
- Barr, D.
- Day, L.
- Gilpatrick, J.D.
- Kerstiens, D.
- Sellyey, W.C.
- Stettler, M.
- Valdiviez, R.

LETI
Grenoble, France
- Brambilla, A.
- Mongellaz, F.
- Verger, L.

LURE
Service de Photons, Atomes et Molécules, Saclay Lab. d'Utilisation du Rayonnement Électromagnétique, Orsay, France
- Couprie, M.E.

NRNE
Institute for Nuclear Reseach and Nuclear Energy of the Bulgarian Academy of Science, Sofia, Bulgaria
- Tsakov, I.

PSI
Paul Scherrer Institut, Villigen, Switzerland
- Dach, M.
- Dehler, M.
- Dölling, R.
- Kramert, R.
- Pollet, P.
- Schilcher, T.
- Schlott, V.
- Uršič, R.

PSI-LMN
Laboratory for Micro- and Nanotechnology, Paul Scherrer Institute, Villigen, Switzerland
- David, C.

PSI-SLS
Swiss Light Source, Paul Scherrer Institute, Villigen, Switzerland
- Jaggi, A.
- Schlott, V.

RAL
Rutherford Appleton Lab., Oxfordshire, UK
- Adams, D.J.
- Tilley, K.
- Warsop, C.M.
- Matheson, J.

RRC
Russian Research Center 'Kurchatov Institute', Moscow
- Kohn, V.

RWTH-Aachen
III. Physik Institut, Aachen, Germany
- Hüning, M.

SLAC
Stanford Linear Accelerator, Stanford, CA, USA
- Anderson, D.
- Anderson, S.D.
- Anderson, S.R.
- Araki, S.
- Naito, H.T.
- Nelson, J.
- Ross, M.
- Smith, S.R.
- Smith, T.J.
- Terunuma, N.
- Young, A.

SPring
Japan Synchrotron Radiation Research Institute SPring-8, Japan
- Masaki, M.
- Takano, S.
- Masaki, M.
- Ohkuma, H.
- Sasaki, S.
- Shoji, M.
- Takano, S.
- Tamura, K.

SRRC
Synchrotron Radiation Research Center, Hsinchu, Taiwan, ROC
- Chen, C.S.

- Chen, J.
- Hsu, K.T.
- Hu, K.H.
- Kuo, C.H.
- Lee, D.
- Lin, K.K.

SRRI
Japan Synchrotron Radiation Research Institute, Mikazuki, Hyogo, Japan

- Asak, T.
- Dewa, H.
- Hanaki, H.
- Hori, T.
- Kobayashi, T.
- Mizuno, A.
- Sasaki, S.
- Suzuki, S.
- Takashima, T.
- Taniushi, T.
- Tomizawa, H.
- Yanagida, K.

TRIUMF
Vancouver, Canada

- Bishop, D.
- Roberts, B.
- Waters, G.

UChicago
University of Chicago, IL, USA

- Torrence, E.